

# Abstract

---

Pagosa Springs, Colorado is famous for the hydrothermal activity in its groundwater system, though the system is poorly understood. At present, the hot water flow is used for both tourism and the heating of some buildings, but further expansion of the springs' usage could reduce the effective energy produced in both cases. To better understand the nature and extent of the hydrothermal flow, several geophysical methods were designed and implemented, including: Gravity, magnetics, electromagnetics, seismic, Direct Current (DC) resistivity, and ground penetrating radar (GPR), all of which were tied in with global positioning system (GPS) data. The surveys were designed to determine the structural geology, the locations of water sources, and the direction and magnitude of that flow. These geophysical surveys were employed to give students a better understanding of geophysical methods as well as assisting Pagosa Springs in learning more about the complexion of the springs so as to better utilize the hydrothermal energy without damaging, and hopefully improving, the existing infrastructures.

The data of the geophysical methods was processed, interpreted and integrated by students to attain a plausible explanation of the results and the geothermal system the results describe. At the Stevens Airport and the Barn 3, a survey site far to the south of town, it was shown that the Eightmile Mesa Fault, as well as nearby faults, likely penetrate into the basement geology which could provide a conduit for deep hot water transport. At another site three kilometers south of Pagosa where there were geothermal springs cooler than the Pagosa springs, the data entertains the possibility that there is water flowing from the ridge to the east toward the river to the west. The data also shows that there is likely a fault to the east of the Pagosa Mother Spring. The Pagosa Mother Spring is the main spring in the town that was measured to be at least 1,000 feet deep. Closer to the Mother Spring, on the field southwest and east of the river, the flow of water in the subsurface near the spring was surveyed. Two conduits were expressed in the data: one running east-west and the other going north-south. Finally, one line indicated the possibility of two additional faults north of Pagosa, though further investigation is necessary to better define these results. These integrations can be used to sum up a plausible explanation of the hydrothermal system, however, there are several studies that could still be done in this area to better understand the hydrothermal system as well as hopefully improve the current geothermal usage in Pagosa.

# Acknowledgements

---

The Students of the geophysics field camp, 2012 would like to thank the organizations and individuals who contributed to the success of this field camp.

We are grateful for the primary support provided by:

Archuleta County: Mike Whiting and Greg Schulte

Archuleta County Airport at Stevens Field: Mark Lavato and Chris Torres

Archuleta School District 50 Joint: Linda Reed

Pagosa Springs Geothermal District: Phil Starks

We greatly appreciate the financial support provided by:

Colorado School of Mines

Colorado School of Mines, Department of Geophysics

Imperial College London

SEG Foundation

US Department of Energy

We are grateful for the equipment and services that the different intuitions and companies provided. We are also grateful for the knowledge and time they provided to help make this field camp run smoothly and efficiently, this includes:

CGGVeritas

Ion Geophysical / Hans Ecke

Sercel

Zonge

We are grateful for the help and support from:

Coach America

Century Link

CSU Archuleta Extension: Terry Schaaf

First Inn: Lou Woodard

Pagosa Baking Company: Kathy Keyes, Kirsten Skeeahan

Pagosa High School: Laura Rand and kitchen staff

San Juan Motel: Kiel Steck

We are grateful for the support of the Pagosa Springs community who provided access to roads and their private properties. Special thanks go to:

Aspen Cascade Ranch: J.R. Ford

Chimney Rock Archaeological Area: Wendy Smith, US Forest Service

Chimney Rock Interpretive Volunteers – Tannis and Allan

Davis Ranch

Geothermal Greenhouse Partnership

Goodman Ranch

Gerry Hutterer

Ken Levine

Kevin Khung, US Forest Service

KWUF

Pam Leschak, BLM Durango

Matt Mees

Overlook Hot Springs Pagosa Springs Chamber of Commerce: Mary Jo Coulehan

Pagosa Springs Community Development Corp: Rich Lindblad

Pagosa Springs Golf Club

Pagosa Sun: Jim McQuiggin

Reservoir River Ranch: Levine Family

Jerry Smith & Sally

Southern Ute Indian Nation: Nathan Strong Elk

Spring Creek Ranch: Donald Shahan

The Springs Resort: Carla Shaw

Kristen Swaim Pierce, BLM

Town of Pagosa Springs US Geological Survey: Warren Agena, Seth Haines, Norm Vance,  
pagosa.com

We would like to express our appreciation to the staff and faculty from Colorado School of Mines and Imperial College London who helped greatly, by providing their valuable time, knowledge and assistance, to make this project a success.

Professor Michael Batzle

Professor Terence Young

Professor Andre Revil

Professor Richard Krahenbuhl,

Professor Bob Raynolds

Professor Dave Hale

Professor Paul Sava  
Professor Jeff Andrews-Hanna  
Professor John Stockwell  
University Emeritus Professor Ken Lerner,  
Professor Charles Oden  
Dawn Umpleby  
Brian Passerella

Professor Helmut Jakubowicz  
Dr. Jonathan Carter  
Professor Adam Booth

The assistance of the following graduate students and teaching assistants has been greatly appreciated:

Cerica Martinez  
Joyce Hoopes  
Ashley Fish  
Matthew Wisniewski  
Joseph Capriotti  
Gordon Osterman  
Marios Karaoulis  
Brent Putman  
Dionisio Carlos



Finally, all the students who participated in the field camp:

**CSM students (last name, first name):**

Abdulla, Mohamed  
Aldossary, Norah  
Almumtin, Hamid  
Alqatari, Hala  
Arias, Elias  
Atshan, Ihmad  
Cuttler, Stephen  
Douma, Johannes  
Doyle, Matt  
Emmett, Matt  
Fleury, Clement  
Gallastegui, Arantxa  
Gayer, James  
Graziano, Chris  
Grazulis, Allie  
Ittharat, Dettchai  
Johnson, Heather  
Knaak, Alison  
Lambert, Jasmine  
Maag, Liz  
Mah, Russell  
Martinez, Gabe  
Meier, Paul  
Moll, Karen  
Patterson, Lindsay  
Pengfei, Cai  
Perrone, Francesco  
Rapstine, Thomas  
Shannon, Dan  
Wheeler, Lorealee  
Zelenak, Georgie  
Zhou, Jieyi

**Imperial students (last name, first name):**

Al Hooti, Khalil  
Caratge, Astrid  
Ceyhan, Uygur  
Eres Guardia, Karin Maria  
Franca, Camila  
Kaewprain, Phansakorn  
Kanafina, Saniya  
Karalis, Petros  
Kim, Junghee  
Kokoshina, Elena  
Li, Nanxin  
Loh, Jia Long  
Masri, Iskandar  
Ngeri, Aminayanasa  
Northall, John  
Oakley, Eleanor  
Omofoma, Veronica  
Phillips, Jack  
Polisano, Gustav  
Prise, Siobhan  
Rajesh Kumar, Litty  
Rasheed, Haroon  
Studer, Florian  
Tamunobereton-ari, Noble  
Watson, Angus  
Zhang, Liang

**RMIT University (Melbourne) student:**

Kratzer, Terence

# Disclaimer

---

The content of this report is derived from a summer field camp for undergraduate and graduate students in Geophysics at the Colorado School of Mines and Imperial College London. The main objective of this field camp was to introduce the students to many different geophysical methods that are used in exploration. All the data has been acquired, processed and interpreted mainly by the students from the Colorado School of Mines and Imperial College London. Therefore the content of this report should be regarded appropriately. The aforementioned schools do not guarantee the accuracy or validity of the data obtained or the interpretations and conclusions subsequently presented in this document.

# 1 Table of Contents

<b>1. Introduction .....</b>	<b>1</b>
1.1 Background Information .....	1
1.2 Objectives .....	2
1.3 Survey Locations .....	3
<b>2. Geology .....</b>	<b>6</b>
2.1 Geologic History and Overview .....	6
2.2 Hydrology .....	12
2.3 Geothermal Analysis.....	13
2.4 Field Observations .....	15
2.5 Hand Specimen Analysis .....	22
2.6 Petrophysics and Well Log Analysis .....	32
2.7 Geochemistry .....	36
<b>3. Surveying.....</b>	<b>38</b>
3.1 Introduction.....	38
3.2 Differential GPS (dGPS).....	38
3.3 Total Distance Measure (TDM).....	40
3.4 Surfer and Google Earth .....	41
3.5 Conclusions.....	42
<b>4. Deep Seismic.....</b>	<b>43</b>
4.1 Introduction.....	43
4.1.1 Wave Theory.....	43
4.1.2 Deep Seismic .....	44
4.1.3 2D Seismic Method.....	45
4.2 Survey Design.....	45
4.2.1 Stevens Airport: 2D Seismic Line .....	46
4.2.2 Barn 3: 2D Seismic Line.....	49
4.3 Processing .....	51
4.4 Uncertainties/Errors .....	54
4.5 Near surface model .....	55
4.6 Interpretations .....	56
4.6.1 Interpretation: Stevens Airport Seismic Line.....	57
4.6.2 Interpretation: Barn 3 Seismic Line .....	60

4.7	Conclusions and discussions .....	62
<b>5.</b>	<b>Shallow Seismic.....</b>	<b>64</b>
5.1	Introduction.....	64
5.2	Refraction survey sites .....	65
5.3	Survey Design.....	66
5.4	Processing .....	67
5.5	Uncertainties/Errors .....	70
5.6	Interpretation.....	70
5.7	Conclusions and Discussions .....	75
<b>6.</b>	<b>Gravity.....</b>	<b>77</b>
6.1	Introduction.....	77
6.2	Survey design.....	79
6.3	Processing/Data Reduction .....	82
6.3.1	Drift Correction.....	82
6.3.2	Latitude Correction .....	83
6.3.3	Free-Air Correction.....	83
6.3.4	Bouguer Correction.....	83
6.3.5	Terrain corrections .....	84
6.4	Uncertainties/Errors .....	84
6.4.1	Errors.....	84
6.4.2	Uncertainties .....	85
6.5	Data and Interpretation.....	86
6.5.1.	Stevens Airport .....	86
6.5.2.	Barn 3.....	87
6.5.3	PAGO01.....	88
6.5.4	PAGO02.....	89
6.5.5	PAGO05.....	90
6.5.6	Warm Springs .....	91
6.5.7	Zen Garden.....	92
6.6	Conclusion .....	99
<b>7.</b>	<b>Magnetics.....</b>	<b>101</b>
7.1	Introduction.....	101
7.2	Survey Sites .....	102
7.3	Survey Design.....	103
7.4	Processing .....	107
7.5	Uncertainties/Errors .....	110

7.6	Interpretations .....	112
7.6.1	Zen Garden.....	112
7.6.2	PAGO01, PAGO02, Barn 3 Deep Seismic, and Warm Springs .....	115
7.6.3	Steven’s Airport Deep Seismic .....	116
7.7	Conclusions and Discussions .....	117
7.7.1	Zen Garden.....	117
7.7.2	Steven’s Airport Deep Seismic .....	118
7.7.3	PAGO01, PAGO02, Barn 3 Deep Seismic, and Warm Springs .....	118
<b>8.</b>	<b>Electromagnetics.....</b>	<b>119</b>
8.1	Introduction.....	119
8.2	Instrumentation .....	121
8.2.1	EM31.....	121
8.2.2	EM34.....	122
8.2.3	EM47.....	123
8.3	Survey design.....	124
8.3.1	FEM methods.....	125
8.3.2	TEM methods.....	126
8.4	Processing .....	127
8.4.1	FEM processing .....	127
8.4.2	TEM processing .....	127
8.5	Uncertainties/Errors .....	128
8.5.1	EM31 & EM34 .....	128
8.5.2	EM47.....	128
8.6	Interpretations .....	128
8.6.1	Zen Garden.....	128
8.6.2	PAGO01.....	131
8.6.3	PAGO02.....	132
8.6.4	Stevens Airport .....	134
8.6.5	Barn 3 .....	135
8.6.6	Warm Springs .....	136
8.7	Conclusions and discussions.....	137
<b>9</b>	<b>DC Resistivity.....</b>	<b>139</b>
9.1	Introduction.....	139
9.2	Sites method was completed at.....	140
9.3	Survey design.....	141
9.3.1	Hot Springs .....	141

9.3.2	Warm Springs .....	143
9.3.3	Zen Garden.....	145
9.4	Processing .....	147
9.4.1	Downloading Data and Data Formatting .....	147
9.4.2	Data Reduction.....	148
9.4.3	2D Inversion.....	150
9.4.4	Kriging .....	151
9.4.5	3D Inversion.....	151
9.5	Uncertainties/Errors .....	152
9.6	Interpretations .....	152
9.6.1	Hot Springs .....	152
9.6.2	Warm Springs .....	163
9.6.3	Stevens Airport .....	168
9.6.4	Zen Garden.....	168
9.7	Conclusions and discussions.....	178
9.7.1	Hot Springs, Warm Springs, and Stevens Airport .....	178
9.7.2	Zen Garden.....	180
<b>10</b>	<b>Self-Potential.....</b>	<b>182</b>
10.1	Introduction.....	182
10.2	Survey Design .....	183
10.3	Processing .....	185
10.4	Uncertainties/Errors .....	188
10.5	Interpretations .....	188
10.6	Conclusions and discussions.....	194
<b>11</b>	<b>Ground Penetrating Radar.....</b>	<b>196</b>
11.1	Introduction.....	196
11.2	Survey design.....	197
11.3	Processing .....	201
11.4	Uncertainties/Errors .....	206
11.5	Interpretations .....	206
11.5.1	Airport Line and Barn 3 Line.....	206
11.5.2	Zen Garden.....	208
11.6	Conclusions and discussions.....	211
<b>12</b>	<b>Integrated Site Conclusions .....</b>	<b>212</b>
12.1	Stevens Airport .....	212
12.2	Hot Springs .....	218

12.3	Warm Springs .....	223
12.3.1	Introduction.....	223
12.3.2	Shallow Seismic.....	224
12.3.3	Gravity .....	224
12.3.4	Resistivity profiles .....	225
12.3.5	SP profile .....	226
12.3.6	Conclusion .....	227
12.4	Zen Garden.....	228
12.5	Barn 3.....	237
12.5.1	Data acquired .....	237
12.5.2	Interpretation.....	237
12.5.3	Conclusions.....	241
12.6	North Line Hot Springs.....	242
<b>13.</b>	<b>Conclusions.....</b>	<b>244</b>
<b>14.</b>	<b>Recommendations.....</b>	<b>250</b>
<b>Appendix A</b> .....	<b>252</b>	
<b>Appendix B</b> .....	<b>265</b>	
<b>Appendix C</b> .....	<b>270</b>	
<b>Appendix D</b> .....	<b>274</b>	
<b>Appendix E</b> .....	<b>277</b>	
<b>Appendix F</b> .....	<b>285</b>	
<b>Appendix G</b> .....	<b>294</b>	
<b>References</b> .....	<b>300</b>	

# Table of Figures

---

Figure 1. 1 Google Earth image of Pagosa Springs location in relation to Denver and Golden, where the Colorado School of Mines is located. ....	2
Figure 1. 2 Google map image of the Pagosa Springs area of investigation with the location of all the survey sites.....	3
Figure 2. 1 Regional map of the structures within the San Juan Basin with the area of interest outlined in red. ....	7
Figure 2. 2 Regional map showing the Archuleta anticlinorium in relation to the San Juan Basin and other basin with the area of interested outlined in red. ....	8
Figure 2. 3 Stratigraphic column of the geology discovered in well P-1 drilled within Pagosa Springs city limits. ....	10
Figure 2. 4 Hydrologic map of Pagosa Springs, which includes much of the area of interest. [6].....	13
Figure 2. 5 Geothermal map of Pagosa Springs, which includes much of the area of interest. [6].....	15
Figure 2. 6 Left: Steven’s Airfield cross-section line. Right: General Pagosa Springs cross-section line. ....	17
Figure 2. 7 General cross-section of Pagosa Springs. Vertical scale has been exaggerated to show features in larger detail. ....	18
Figure 2. 8 Cross-section of Steven’s Airfield. Vertical scale has been exaggerated to show features in larger detail.....	19
Figure 2. 9 Locations of wells used to create cross-sections and elsewhere in the study: P-1 Well [6] and the Mizar-Schick (provided by Dr. Batzle). ....	21
Figure 2. 10 General overview of sample locations collected during investigation. ....	24
Figure 2. 11 Samples #1 and #2. Samples of Dakota Sandstone collected by Thomas Rapstine north of the Barn 3 Line. ....	25
Figure 2. 12 Locations of Samples #1 and #2.....	25
Figure 2. 13 Samples #3, #4, and #9. Samples of the Mancos shale and Limestone units collected by Thomas Raptine (#3 and #9) and Matt Emmett (#4).....	26
Figure 2. 14 Samples #5, #6, and #7. Sample #5: intermediate igneous rock collected by Elias Arias on Pago 1. Sample #6: pyroclastic tuff collected by Stephen Cuttler near Wolf Creek Pass. Sample #7: intermediate altered igneous rock collected by Stephen Cuttler south of Wolf Creek Pass. ....	27
Figure 2. 15 Left: Locations of samples #3 and 4#. Right: Locations of samples #5, #6, and #7.....	28
Figure 2. 16 Samples #8, #10a-b, and #11. Samples #8 and #11 are examples of crystalline calcite collected by Matt Emmett on the Pago8 line. Samples #10a-b are further examples of crystalline calcite collected by Joyce Hoopes on the Pago8 line. ....	29
Figure 2. 17 Samples #12, #13, and #14. All samples collected by Matt Emmett on the Pago8 line and demonstrate examples of crystalline calcite within the Mancos Shale. ....	30
Figure 2. 18 Locations of Samples #8, #10a-b, #11, #12, #13, and #14.....	31
Figure 2. 19 Sample #15: Mancos Shale with gypsum filling in preserved mudcracks or joints. Collected by Elias Arias on the Pago7 line.....	31
Figure 2. 20 Locations of Sample #15. ....	31



Figure 2. 21 Samples used in petrophysical analysis. M= Mancos, D= Dakota, V= Igneous (Sample 5), B= Igneous (Sample 7).....	33
Figure 2. 22 Left: Sample on scale balance. Right: Vacuum used to remove air. ....	33
Figure 3. 1 Left- Group of students setting up a dGPS base station at the Hot Springs location. Right – Student using the rover to measure a survey point at the Hot Springs location.....	39
Figure 3. 2 Students surveying a location on the Northern HS hammer seismic line using the TDM.....	40
Figure 3. 3 Google Earth example map of Zen Garden survey location, a map used as a reference in processing and analysing the student site. ....	42
Figure 4. 1 : Land Seismic Acquisition Set Up .....	45
Figure 4. 2: Satellite view of Pagosa Springs Region. Red lines indicated location of seismic survey lines. ....	46
Figure 4. 3: Satellite view of Steven Airport Seismic Line. The red line indicates the extend of the survey line.....	47
Figure 4. 4 : Elevation profile for Stevens Airport survey line .....	48
Figure 4. 5 : Satellite view of Barn 3 Seismic Line. The red line indicates the extend of the survey line.....	50
Figure 4. 6: Elevation Profile of the Barn 3 survey line .....	50
Figure 4. 7: Seismic processing sequence for Stevens Airport line and Barn 3 line .....	53
Figure 4. 8: Final Stevens Airport Seismic Line migrated image without AGC .....	53
Figure 4. 9: Final Barn 3 Seismic Line migrated image without AGC .....	54
Figure 4. 10: Stevens Airport Seismic Line migrated image.....	57
Figure 4. 11: Stevens Airport migrated image after depth conversion .....	57
Figure 4. 12: Interpretation of Stevens Airport Seismic Line.....	58
Figure 4. 13: Barn 3 seismic line migrated image .....	60
Figure 4. 14: Barn 3 seismic line migrated image after depth conversion .....	60
Figure 4. 15: Rough Geologic Cross Section of Barn 3 line .....	61
Figure 4. 16: Interpretation of migrated image with time converted to Depth. ....	61
Figure 5. 1 Difference between refracted and reflected raypaths when they encounter a higher velocity layer in the subsurface. [14] .....	64
Figure 5. 2: Regional map of the Pagosa Springs area, displaying the relative positions of each hammer seismic survey site. ....	66
Figure 5. 3: Vertical hammer strike on a metal plate, generating primary seismic waves. ....	66
Figure 5. 4: Raw S-Wave shot record from the Zen Garden Line 1 dataset. The hammer strike occurred in the center of the line.....	68
Figure 5. 5: Zen Garden Line 2 shot record 1. Trace numbers 13, 27 and 28 were faulty and contained high frequency noise in each shot record in this dataset. These traces were muted; their amplitude was given a zero value over the entire record length. ....	69
Figure 5. 6: Zen Garden Line 2 Shot 1 before (left figure) and after the application of a bandpass filter (right figure). Some of the high and low frequency noise that were previously dominating the shot record have been removed. ....	69
Figure 5. 7: Zen Garden Line 2 Shot 1 p-wave record after processing, with velocity trends interpreted across the first breaks. In this shot record two layers have been identified; a shallow layer with a velocity of 421 m/s, and a deeper layer with a velocity of 29 .....	71

Figure 5. 8: Subsurface model derived from the interpretation of the Zen Garden Line 1 dataset .....	72
Figure 5. 9: Subsurface model derived from the interpretation of the Zen Garden Line 2 dataset .....	73
Figure 5. 10: Subsurface model derived from the interpretation of the Barn 3 Anisotropy North-South dataset .....	74
Figure 5. 11: Subsurface model derived from the interpretation of the Barn 3 Anisotropy East-West dataset .....	74
Figure 5. 12: Subsurface model derived from the interpretation of the Warm Springs dataset .....	75
Figure 6.1 Simple Astatic Gravity Meter .....	78
Figure 6.2 LaCoste-Romberg gravimeter [20] .....	78
Figure 6.3 CG-5 gravimeter [21] .....	79
Figure 6.4 GPS map of sites the gravity method was completed .....	80
Figure 6.5 Zen Garden grid: red dots show gravity data collection points .....	81
Figure 6.6 Students working with the CG-5 gravimeter .....	82
Figure 6. 7 Gravity data from Stevens airport (black points) superimposed with the synthetic gravity anomaly (black continuous line) calculated from the geological model (bottom portion) .....	87
Figure 6. 8 Gravity data from Barn 3 (black points) superimposed with the synthetic gravity anomaly (black continuous line) calculated from the geological model (bottom portion) .....	88
Figure 6. 9 Gravity data from PAGO01 (black points) superimposed with the synthetic gravity anomaly (black continuous line) calculated from the geological model (bottom portion) .....	89
Figure 6. 10 Gravity data from PAGO02 (black points) superimposed with the synthetic gravity anomaly (black continuous line) calculated from the geological model (bottom portion) .....	90
Figure 6. 11 Gravity data from PAGO05 (black points) superimposed with the synthetic gravity anomaly (black continuous line) calculated from the geological model (bottom portion) .....	91
Figure 6. 12 Gravity data from Warm Springs (black points) superimposed with the synthetic gravity anomaly (black continuous line) calculated from the geological model (bottom portion) .....	91
Figure 6. 13 Entire gravity measurements conducted over Zen Garden site. ....	92
Figure 6. 14 Mesh used for Zen Garden 3D inversion process. ....	93
Figure 6. 15 3D Entire Zen Garden site inversion process. ....	94
Figure 6. 16 Inverted gravity data with interpretation over the Zen Garden site .....	95
Figure 6. 17 Correlated gravity and EM data over the Zen Garden site. ....	96
Figure 6. 18 Location of travertine on the Zen Garden site in relation to the San Juan River. ....	97
Figure 6. 19 Fracture location in reference to inverted gravity data at the Zen Garden site. ....	97
Figure 6. 20 5x5 Subsection of finely sampled gravity data with known locations of landmarks in the Zen Garden site. ....	98
Figure 6. 21 5x5 Subsection of the finely sampled gravity data with known locations and close up of crack in the Zen Garden site. ....	99
Figure 7. 1 The set-up of the roving cesium magnetometer. ....	102
Figure 7. 2 Map of the Pagosa Springs area showing locations where magnetics surveys were performed. ....	102

Figure 7. 3 Map of the Zen Garden survey site (black diamonds indicate flag locations). ...	103
Figure 7.4 Map of the location of the Steven's Airport magnetic survey.....	104
Figure 7. 5 Map that shows the locations of Pago01 and Pago02. ....	105
Figure 7. 6 Map of the location of the Barn 3 deep seismic line located south of Pagosa Springs. ....	106
Figure 7. 7 Map of the warm springs site. The line used in the forward modelling of the gravity and magnetics data is the fourth one from the left. ....	107
Figure 7.8 The Top DNL data for the Barn 3 deep seismic line.....	109
Figure 7.9 Plot that shows the Top DNL data for the PAGO01 line. ....	110
Figure 7.10 Plot that shows the Top DNL data for the PAGO02 line. ....	110
Figure 7. 11 Magnetic data after the GPS offset correction. The black circles indicate locations of noisy data most likely due to surface rock piles. ....	112
Figure 7.12 Image showing the inverted magnetic data at the surface of the Zen Garden site. ....	113
Figure 7.13 6 m depth slice. Image that shows the inverted magnetic data at the Zen Garden site at 6 m depth. ....	114
Figure 7.14 15 m depth slice. Image that shows the inverted magnetic data at the Zen Garden site at a depth of 15 m. ....	115
Figure 7. 15 Model created using GM-SYS modelling software. The top tile of the image shows the magnetic data and response, the middle tile shows the gravity data and response, and the bottom tile shows the geologic model.....	117
Figure 8. 1 Example of TEM acquisition, showing path of decaying current [33]. ....	119
Figure 8. 2 An example of FEM acquisition scenario in Horizontal Coplanar using EM 34. ....	120
Figure 8. 3 Students using the EM31 in the field. ....	121
Figure 8. 4 Students walking the EM34 transmitter and receiver coils to a new station.....	122
Figure 8. 5 EM47 instrument setup.....	123
Figure 8. 6 A map view of the survey site locations where EM methods were performed. PAGO01 and PAGO02 are shown as white and purple lines repectively. ....	125
Figure 8. 7 Students setting up the 3-component receiver used in the TEM surveys.....	126
Figure 8. 8 EM31 apparent conductivity over the Zen Garden area near the hot springs. EM31 data is approximately the first 6 m from surface. The red to yellow (20 to 70 mS/m) is characteristic of the Mancos Shale that is in this area, and therefore the highly conductive blue area indicates an anomaly. The black outline represents the area over which the EM34 survey was undertaken (see Figure 8. 9), and the star represents the location for the TEM EM47 inversion of Figure 8. 11. ....	129
Figure 8. 9 EM34 vertical dipole survey for Zen Garden area. Depth of investigation is 15m. ....	129
Figure 8. 10 In-phase component of the EM31 data. Strong negative data indicates subsurface metallic objects, and strong positive data indicates near-surface metallics. ....	130
Figure 8. 11 EM47 inversion for south-east corner of the Zen Garden. This shows a resistive layer beginning at about 75m depth. ....	131
Figure 8. 12 EM31 conductivity for Hot Springs PAGO01. ....	132
Figure 8. 13 EM34 apparent conductivity pseudosection for Hot Springs PAGO01. ....	132
Figure 8. 14 A comparison of EM31 and EM34 apparent conductivities on the PAGO02 line. ....	133
Figure 8. 15 The inverted EM47 data along the PAGO02 line. This profile matches the geology known in the area. The resistive area directly in the middle of the profile is probably the sandstone in the region.....	133

Figure 8. 16 EM31 in-phase data indicating locations of magnetic pipes and Stevens Airport boundary. ....	135
Figure 8. 17 EM34 apparent conductivity for the Barn 3 site. Conductivity does not correlate with expected geology. The resistive body may indicate a sand/gravel deposit. ....	135
Figure 8. 18 Time series plot for the Warm Springs site. ....	136
Figure 9. 1 Resistivity survey map .....	140
Figure 9. 2 Map of the resistivity surveys in the Hot Springs area.....	142
Figure 9. 3 Map of the resistivity surveys in the Warm Springs area.....	144
Figure 9. 4 Map of Zen Garden Site .....	146
Figure 9. 5 Exterminate bad data points feature for RES2DINV .....	148
Figure 9. 6 Inverted resistivity profile of PAGO04 .....	153
Figure 9. 7 SP and inverted resistivity profiles of PAGO01.....	154
Figure 9. 8 SP and inverted resistivity profiles of PAGO02.....	155
Figure 9. 9 Inverted resistivity profile of PAGO05 .....	156
Figure 9. 10 Inverted resistivity profile of PAGO06 .....	157
Figure 9. 11 Inverted IP resistivity profile of PAGO06.....	157
Figure 9. 12 Normalized chargeability profile for PAGO06 .....	158
Figure 9. 13 Inverted resistivity profile of PAGO07 .....	159
Figure 9. 14 Inverted resistivity profile of PAGO08 .....	159
Figure 9. 15: Interpolated resistivity slice at elevation 2100m for the Hot Springs site.....	161
Figure 9. 16: Interpreted resistivity slice at elevation 2125m for the Hot Springs site .....	162
Figure 9. 17: Interpreted resistivity slice at elevation 2050m for the Hot Springs site .....	163
Figure 9. 18 Warm Springs 2D profiles.....	165
Figure 9. 19 PONC 03 annotated resistivity section.....	166
Figure 9. 20 PONC 07 annotated resistivity section.....	166
Figure 9. 21 Warm Springs 3D profile .....	167
Figure 9. 22 PAGO03 (Stevens Airport) 2D profile.....	168
Figure 9. 23 Near surface geology of the Zen Garden depicted by a dipole-dipole DC Resistivity survey. Warm colours indicate resistive materials and cool colours indicate conductive materials. Conductivity units are S/m. ....	170
Figure 9. 24 Conductivity at ten meters depth. Notice how the cooler colors are beginning to dominate the scene. Units are S/m. ....	171
Figure 9. 25 Conductivity at 20 meters depth for the Zen Garden. Apart from some slightly resistive areas, the conductive materials almost completely dominate the scene. Units are S/m. ....	172
Figure 9. 26 Conductivity at 30 meters depth. The resistive bodies are nearly non existent besides a small region in the north east corner of the scene. Units are S/m. ....	173
Figure 9. 27 3D resistivity model of the Zen Garden where the middle-range values have been left out. Notice the ring of resistive material that caps the conductive regions beneath. Units are S/m.....	174
Figure 9. 28 Cross section along the surface fracture at the Zen Garden. Notice the conductive body that rises to the surface along the cross section near the western end of the fracture: this is near the location of the pipe mentioned earlier.....	175
Figure 9. 29 3D conductivity model displaying the top ten meters of the Zen Garden site. Notice the dominance of resistive material. Units are S/m.....	176
Figure 9. 30 3D conductivity model displaying all depths except the top ten meters of the Zen Garden site. Notice the increase in conductivity with depth. Units are S/m. ....	177
Figure 9. 31 Fault map of Pagosa Springs .....	179
Figure 9. 32 Scheme of the probable geothermal system taking place at Pagosa Springs ....	180

Figure 10. 1: This figure shows the types of anomalies seen with Self-potential data in areas with geothermal activity. [39]	183
Figure 10. 2: Google Earth image showing the locations where the SP data was completed.	184
Figure 10. 3 This figure shows the need of the reference correction within SP data. The orange arrows are showing the shift of the data. [5]	186
Figure 10. 4 This figure is showing the need for the closure correction within SP data with a closed profile composed of 10 data points. Point 0 and point 10 are geographically in the same place. [40].	187
Figure 10. 5: SP plot and DC Resistivity inversion along the profile PAGO 01	188
Figure 10. 6: SP plot and DC Resistivity inversion along the profile PAGO 02	189
Figure 10. 7: SP plot and DC Resistivity inversion for the profile along the Stevens Airport line	190
Figure 10. 8: 2D Kriging Map of the SP data at the Warm Springs Site	191
Figure 10. 9: Variogram for the 2D Kriging Map of the SP data at the Warm Springs Site	192
Figure 10. 10: 3D representation of SP data at the Warm Springs Site made in MatLab. ....	192
Figure 10. 11: SP plots and DC Resistivity inversions of profiles 1-4 at the Warm Springs Site.	193
Figure 10. 12: SP plots and DC Resistivity inversions of profiles 5-7 at the Warm Springs Site.	194
Figure 10. 13: Fault map for the Pagosa Springs area.	195
Figure 11. 1 A schematic diagram of a radar acquisition comprising of the radar components and the analogue interpretation of a radar time section.	196
Figure 11. 2 Sites at which GPR was completed	197
Figure 11. 3 Stevens Airport survey line	198
Figure 11. 4 Barn 3 survey line	198
Figure 11. 5 GPR subsection of Zen Garden survey grid	199
Figure 11. 6 Central rectangle outlines the GPR grid in reference to the entire Zen Garden.	201
Figure 11. 7	202
Figure 11. 8	204
Figure 11. 9	204
Figure 11. 10 (a) A radar section obtained from Barn 3 line (a) with its interpreted section (b).	207
Figure 11.11 A migrated radar cross section with topographical correction obtained from the Zen Garden (a) with its interpreted section (b).	209
Figure 11. 12 Depth slices of the Travertine deposit (a) with its interpreted section (b). The black lines in section (b) highlight beneath the fracture. The change between depth of 1 m and 2 m shows that the fracture boundary spreads apart, and suggests it has a dome-shaped structure.	210
Figure 12.1 Shows the seismic section with depth on the y-axis	213
Figure 12.2 EM31 data for Stevens Airport line	214
Figure 12.3 EM34 data for Stevens Airport line	214
Figure 12.4 SP and resistivity data on the Stevens Airport line.	215
Figure 12.5 Forward model for the gravity and magnetic data	216
Figure 12.6 GPR image of Stevens Airport	216
Figure 12.7 Updated cross section based on results	217
Figure 12.8 SP and Inverted Resistivity Profiles of PAGO01	219

Figure 12. 9 SP and Inverted Resistivity Profiles of PAGO02 .....	219
Figure 12.10 Inverted resistivity profile of PAGO06 .....	220
Figure 12. 11 PAGO01, 02, and 06 Lines in Relation to the Fault.....	220
Figure 12.12 Normalized Chargeability Profile for PAGO06 .....	221
Figure 12.13 Kriging of PAGO 01, 02, 04, 05, 06, and 07.....	222
Figure 12.14 Hot Springs Site Overview .....	222
Figure 12. 15 Map of the Warm Springs site, showing the Grid and Hammer Seismic profile .....	223
Figure 12. 16 Subsurface model along the Warm Springs shallow seismic profile, showing the loose sediments and the underlying Dakota Sandstone .....	224
Figure 12. 17 Interpreted gravity data, with the Mancos Shale (Green), Dakota Sandstone (Yellow) and Morrison Formation (Red), with the gravity anomaly plotted above the figure. ....	225
Figure 12. 18 PONC 03 2D resistivity slice .....	226
Figure 12.19 Warm Spring 3D resistivity profile .....	226
Figure 12.20 Warm Spring 3D SP profile .....	227
Figure 12.21 Conductivity maps from quadrature EM31 (top) and EM34 (bottom) data display similar trends that diminish with depth. EM31 has an approximate depth of investigation of six meters and the EM34 has a depth of investigation close to fifteen meters. ....	229
Figure 12.22 EM47 data displaying the change in conductivity with depth at one point in the Zen Garden site. The Mancos Shale ranges from 15 meters to 60 meters in depth.....	230
Figure 12.23 GPR layer images of the fracture in the travertine. Results show the travertine extends approximately five and a half meters into the subsurface. ....	230
Figure 12. 24 Surface conductivity of the DC resistivity model. Notice the conductive trend running from the southwest to the northeast.....	231
Figure 12.25 20 meters depth of the DC resistivity model. Notice the conductive trend running from the southwest to the northeast.....	232
Figure 12.26 Line E of the DC resistivity survey. Notice the low conductivity on the edges, with a higher value in the middle.....	232
Figure 12. 27 Gravity model cross section (top) and top view at twenty meters depth (bottom) of the Zen Garden. Notice the high to low density trend from east to west. The low density anomaly could be due to the low porosity of the alluvial deposit that has the north/south conduit running through it. ....	233
Figure 12. 28 Surface magnetic susceptibility map (top) and in-phase EM31 map (bottom) of the Zen Garden. Notice the low susceptibility trend that runs from southeast to northwest. ....	234
Figure 12. 29 SP data (top) and DC resistivity (bottom) for PAGO 02. The Zen Garden is located within the red box. Notice the high SP anomaly, which is commonly associated with moving fluids. The DC model also indicates a conductive body moving into the page.....	235
Figure 12. 30 Geologic cross section (top) and map (bottom) based on the integration of the geophysical surveys preformed at the Zen Garden.....	236
Figure 12. 31 Seismic Section at Barn 3 and its interpretation in relation to the Dakota Sandstone.....	238
Figure 12. 32 Electrical conductivity measurements of the EM34 at Barn 3 and the interpretation of the geology.....	239
Figure 12.33 Interpreted Gravity data at Barn 3 .....	240
Figure 12. 34 Final depth converted migrated section of Barn 3 with interpretation.....	241
Figure 12. 35 (a) Location of Northline – PAGO 08 (blue line) on a Google earth image. (b) Northline with fault plane locations (red lines) superimposed on top.....	243

Figure 12.36 (a) 2D deep resistivity data collected at line PAGO 08, Northline site location. (b) Calciferous crystals samples found near both fault zones suggesting past hydrothermal system along fault planes .....	243
Figure 13. 1: Subset of geologic map showing locations of interpreted faults (in black). ....	246
Figure 13. 2 Interpretation of the location of the Victoire fault with the Hot Spring lines. ...	247
Figure 13. 3 Interpretation of the location of the Northline faults with the Northline survey. .....	248
Figure 13. 4 Geothermal system of the Pagosa Hot Springs with associated cross-section..	249

# List of Tables

---

Table 1. 1 Geophysical methods acquired at each survey site with the name of each line collected at each specific site.....	4
Table 2. 1 Table of values obtained from the petrophysical analysis. M= Mancos, D= Dakota, V= Igneous (Sample 5), B= Igneous (Sample 7). .....	35
Table 2. 2 Table of values obtained from the analysis of the Mizar Schick Well Log #1.....	35
Table 2. 3 Table of values obtained from several geochemical analysis of the thermal waters from the Mother Spring in Pagosa Springs Colorado at four different dates (provided by Paul Morgan of the Colorado Geological Survey) [11]......	37
Table 3. 1 Surveying locations and how they were surveyed.....	38
Table 3. 2 Sources of error and the uncertainty they cause. ....	39
Table 4. 1 : Seismic Line's Parameters.....	46
Table 4. 2: Acquisition parameters for Stevens Airport line .....	48
Table 4. 3:Acquisition parameters for Barn 3 seismic line.....	51
Table 6. 1 Density and thickness used on the forward modelling of the gravity data. ....	86
Table 8. 1 Spacing, depth of investigation, and frequencies used for the FEM instruments [36]......	122
Table 8. 2 All locations where EM methods were used specifying which instrument. ....	124
Table 9. 1 Resistivity survey map.....	141
Table 9. 2 Survey design parameters in the Hot Springs area. ....	142
Table 9. 3 Survey design parameters in the Warm Springs area .....	145
Table 9. 4 Survey design parameters for the Zen Garden site .....	147
Table 9. 5 Filtering parameters in the Warm Springs area .....	164



# 1. Introduction

---

## 1.1 Background Information

In May 2012, the Colorado School of Mines hosted a Geophysical field session comprised of both graduate and undergraduate students in association with the Colorado School of Mines and Imperial College London in the Pagosa Springs area, Archuleta County, Colorado, USA, Figure 1. 1

The group visited Pagosa Springs, Archuleta County, Colorado from May 13<sup>th</sup> to May 24<sup>th</sup>. The goal was to investigate the geological structure of the Upper San Juan Basin and the geothermal fluid movement in the Pagosa Springs area in order to better characterize the geothermal resources and provide the Pagosa Springs community with a better understanding of the potential geothermal reserves. The field camp is an invaluable experience for students, which allows knowledge and theory gained through lessons and lectures to be put into practice in the field and hence refining and reinforcing the geophysical skills and techniques of each student.

The United States gets only 4% of its electricity from wind, solar and biomass; however the state of Colorado has a target of achieving 30% renewable energy by 2020 [1]. Exploiting geothermal energy is one way to help reach this target. Geothermal power is a clean, cost effective, reliable and sustainable energy source. With recent technological advances the range and size of viable resources has dramatically expanded especially for applications such as home heating [2].

Pagosa Springs, Archuleta County, is of great interest to the state of Colorado because of its geothermal potential. Pagosa Springs is a town visited by thousands of people every year for recreational purposes, utilizing the geothermal resources for bathing and it has the largest and deepest hot springs in the world. Since December of 1982, the city of Pagosa Springs has maintained and operated a geothermal system to provide heating to the community. This system was funded primarily by the Department of Energy (DOE) and also by Archuleta County and the Town [3]. For decades this town has worked to utilize its resources, but is now turning to Colorado School of Mines and Imperial College for ways to expand its geothermal energy industry.

The 2012 Geophysical field session was split into two sections. Approximately two weeks were spent in the field at six primary survey sites in the Pagosa Springs area, shown in Figure 1. 2. Table 1. 1 shows the thirteen different geophysical techniques conducted at each site location within these two weeks. Data reduction, processing and interpretation were performed over an additional two weeks at

the Colorado School of Mines. The students' research in the Pagosa Springs area was presented on June 8<sup>th</sup> at the Colorado School of Mines campus.

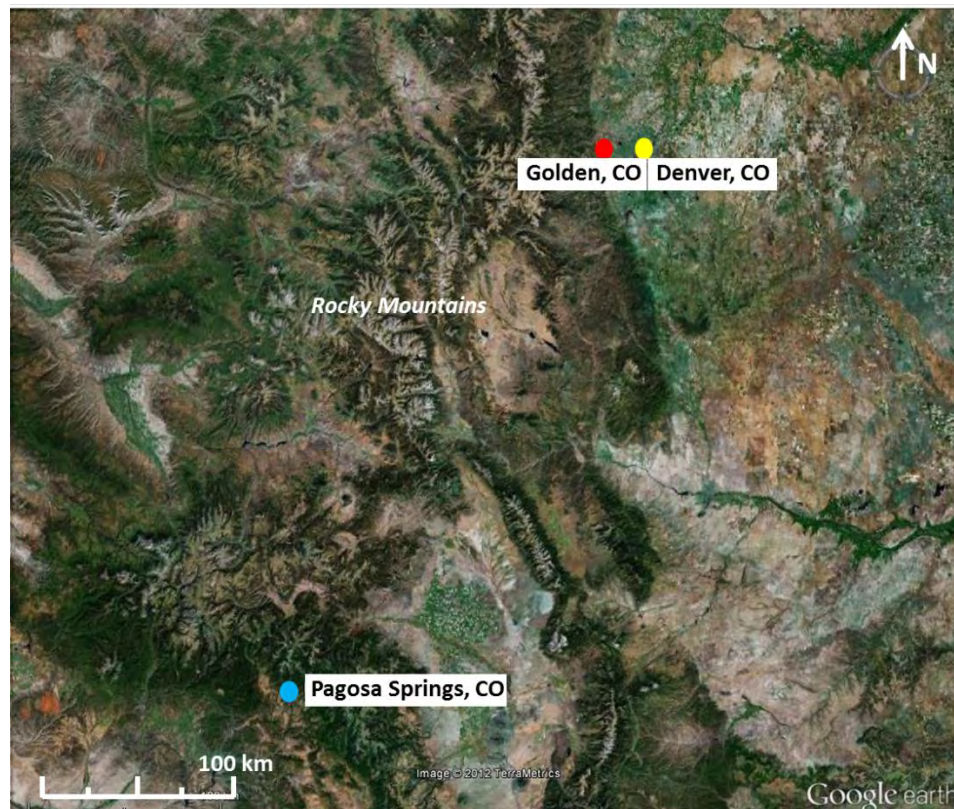


Figure 1. 1 Google Earth image of Pagosa Springs location in relation to Denver and Golden, where the Colorado School of Mines is located.

## 1.2 Objectives

There are two main objectives of the 2012 Colorado School of Mines and Imperial College London field camp. The principal purpose of this field camp enables the participating students to put knowledge and theory gained through lectures into practice in the field, hence refining and reinforcing the geophysical skills and techniques of each student. The field work completed in the first two weeks provided hands on experience of different acquisition techniques of a variety of different geophysical methods while learning the importance of field safety and management strategies. The final two weeks completed at the Colorado School of Mines provided experience in data processing, interpretation, integration and management of multiple data types.

The geophysical objective of this field camp was to characterize the geological structure of the Upper San Juan Basin in the Pagosa Springs area, specifically focusing on obtaining a better understanding of the geothermal fluid movement within the basin structure. Geophysical investigations were completed with the primary objective of better characterizing the main fault system in the Pagosa Springs area. A comprehensive understanding of the fault structure and system in this area allows an

accurate interpretation of the fluid movement within the subsurface and hence better characterization of the geothermal resources. This will provide the Pagosa Springs community with a better understanding of their potential geothermal reserves.

### 1.3 Survey Locations

Geophysical data was collected in the Pagosa Springs area from six main site locations, shown in Figure 1. 2. Thirteen different geophysical techniques were used in order to collect a wide variety of geophysical data about the subsurface in this area. Table 1. 1 shows each different geophysical method acquired at each different site location.

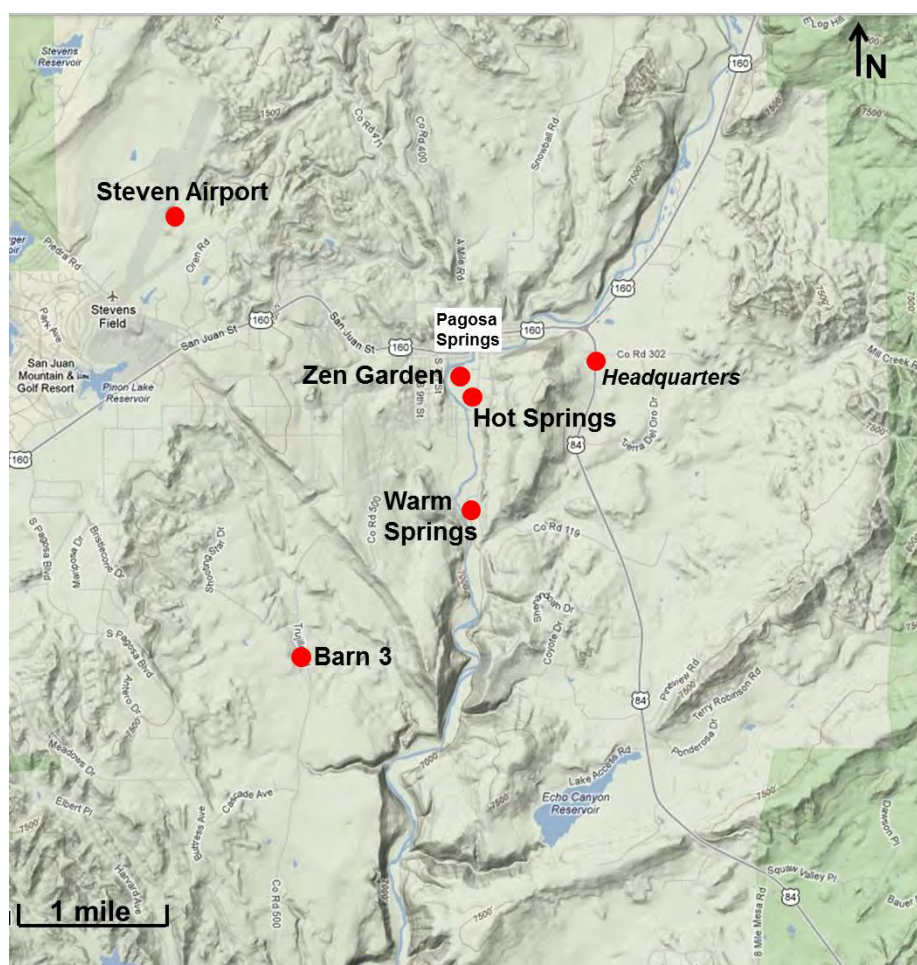


Figure 1. 2 Google map image of the Pagosa Springs area of investigation with the location of all the survey sites.

**Table 1. 1 Geophysical methods acquired at each survey site with the name of each line collected at each specific site.**

<b>Geophysical methods acquired at each site location</b>						
<b>Geophysical Method</b>	<b>Stevens Airport</b>	<b>Hot Springs</b>	<b>Warm Springs</b>	<b>Barn 3</b>	<b>Zen Garden</b>	<b>North Line</b>
<b>Gravity</b>	Airport	PAGO01 PAGO02 PAGO05	Line 4	Barn 3	Lines 1-10, A-M	
<b>Magnetics</b>	Airport	Data collected	Data collected	Barn 3	Data collected	
<b>EM31</b>	Airport	PAGO01 PAGO02		Barn 3	Data collected	
<b>EM34</b>	Airport	PAGO01 PAGO02		Barn 3	Lines 1-10, A-R	
<b>EM47</b>		PAGO02 PAGO03	Line 1			
<b>Deep Seismic</b>	Airport			Barn 3		
<b>Hammer Seismic</b>		Data collected		Barn 3	Data collected	
<b>Resistivity</b>	PAGO03 Airport Deep Seismic Line	PAGO01 PAGO02 PAGO04 PAGO05 PAGO06 PAGO07	Lines (Profiles) 1-7			PAGO08
<b>IP</b>		PAGO06				
<b>SP</b>	PAGO03 Airport Deep Seismic Line	PAGO01 PAGO02	Lines (Profiles) 1-7			
<b>SuperSting</b>					Lines A-L	
<b>GPR</b>	Airport	Data collected		Barn 3	Data collected	
<b>GPS</b>	Airport	Data collected	Data collected	Barn 3	Data collected	Data collected

The main objectives of this study were achieved by using all the different geophysical techniques shown in Table 1. 1 along with accurate survey design at each site location.

The Steven Airport site is located next to the Steven Airport main runway; Figure 1. 2. The survey design of this site was directed towards deep seismic acquisition, with other geophysical techniques acquired along the line. This site was chosen due to its flat surface where a long distance, obstacle free deep seismic line can be acquired. The south and north ends of the line extends into the Pagosa Springs golf course and forested area. The objective of this site was to image the main fault in this area, called the 8 Mile Mesa Fault. This lies south of the Steven airport runway and is thought to have an important influence on the geothermal fluid movement i.e. provide a migration path for the fluid in the Pagosa Springs area.

The Barn 3 site is located by the Alpine ranch, shown in Figure 1. 2. This site was chosen during the field camp by the survey design team. The objective of this site was to better image the 8 Mile Mesa Fault and structural geology in the Pagosa Springs area. The survey design of this site was mainly directed towards deep seismic acquisition, with other geophysical techniques acquired along the line. The 8 Mile Mesa Fault is found within the north east of the ranch suggesting that it can be imaged by



2D deep seismic acquisition running perpendicular to the fault plane. The survey line runs south west to north east and is bisected by the Colorado County Road 500.

The Hot Springs site is located in the large field to the south of the Mother spring and The Springs hotel, Figure 1. 2. This area was selected as one of the main geophysical acquisition sites where all the different geophysical methods in this field camp were used, except for deep seismic. The objective of this site was to characterize and understand the subsurface geothermal fluid movement around the Mother spring and other hot springs in this area. Throughout the two weeks spent on field acquisition new surveys were designed at this site in order to get a better idea of the direction of the subsurface fluid flow and determine if there is any connectivity between the Mother spring and other hot springs around it.

The Warm Springs site is located roughly 2 km south of the Hot Springs site, Figure 1. 2. In this area there is a small warm spring that breaks out next to the river. The objective of this site was to achieve a preliminary study of the fluid movement around the small warm spring in order to try and characterize the fluid flow and to see if it is connected to the Mother Spring at the Hot Springs site. The main geophysical techniques used at this site were DC resistivity, SP, Gravity, Magnetics and EM 47.

The North Line site is located by the Goodman property, shown in Figure 1. 2. This site was chosen by the DC resistivity team in order to better characterize the subsurface north of the Pagosa Springs area. Specifically there was thought to be another fault yet to be imaged at this site which could have an effect on the geothermal fluid migration paths in the Pagosa Springs area. Due to time limitations DC resistivity was the only method completed at this site.

The Zen Gardens site is located in the large field to the south of the mother spring and The Springs hotel. This area was selected for the student site after the property owner pointed out a surface crack in the travertine leading away from the mother spring. In addition there was a large PVC pipe angled into the ground through which water could be heard flowing and sulfur could be smelled. It was determined that these two features would make excellent targets for near-surface investigation using multiple geophysical methods. Magnetics, gravity, DC-resistivity, electromagnetics, GPR, and hammer seismic were all used at this site in order to better characterize the fracture in the travertine and the suspected near-surface movement of water at the pipe.

## 2. Geology

---

### 2.1 Geologic History and Overview

The area of study around the city of Pagosa Springs lies on the northeast edge of the San Juan Basin, a large depositional basin concentrated in western New Mexico and the Four Corners region of the western United States. This basin is bordered to the north by the San Juan Mountains of southern Colorado, to the northeast by the Chama Basin, to the east by the Nacimiento and San Pedro Uplifts, to the south by the Zuni Uplift and the Zuni Mountains of New Mexico, and to the west by the Defiance Uplift of eastern Arizona and western New Mexico (Figure 2-1) [4]. Although a variety of uplifts, anticlines, and other structural features form the border of this basin, the central basin with the deepest sedimentary units lies primarily in north western New Mexico and a small part of southern Colorado. This basin formed as the result of uplift of mountain ranges nearby prior to the Cambrian age and the transgression of multiple seaways beginning in the late Cambrian age, both of which provided the sediment that composes the basin [5]. Because of this, the basin includes a nearly continuous column of sedimentary units beginning in the late Cambrian and continuing until the orogenies and glaciations of the late Cenezoic.

Pagosa Springs lies on the northeast edge of this basin on the Archuleta anticlinorium. The Archuleta anticlinorium hugs the edge of the San Juan Basin beginning in southern Colorado with a north-northwest trend, continuing into north central Arizona (Figure 2-2). This structure serves as the division between the San Juan Basin to the southwest and the San Juan Sag to the northeast, the Brazos Uplift to the east, and the Chama Basin to the southwest [5]. The region lies 15 miles west of the Continental Divide with the San Juan River serving as the primary stream system as it flows from the Divide to the Pacific Ocean to the Southwest. The most significant characteristic of this structure is its allochthonous folding over the underlying basement [4]. This produces a shallow north-north western trending anticline through Pagosa Springs, giving the 12000ft of sedimentary units in the area a dip of approximately 5-10° towards the San Juan Mountains in the north eastern half of the anticlinorium and a similar dip towards the basin on the south western half. To the north the units thin and merge with the surrounding basins beneath the San Juan Mountains while to the south the units increase in dip as they move towards the main basin.

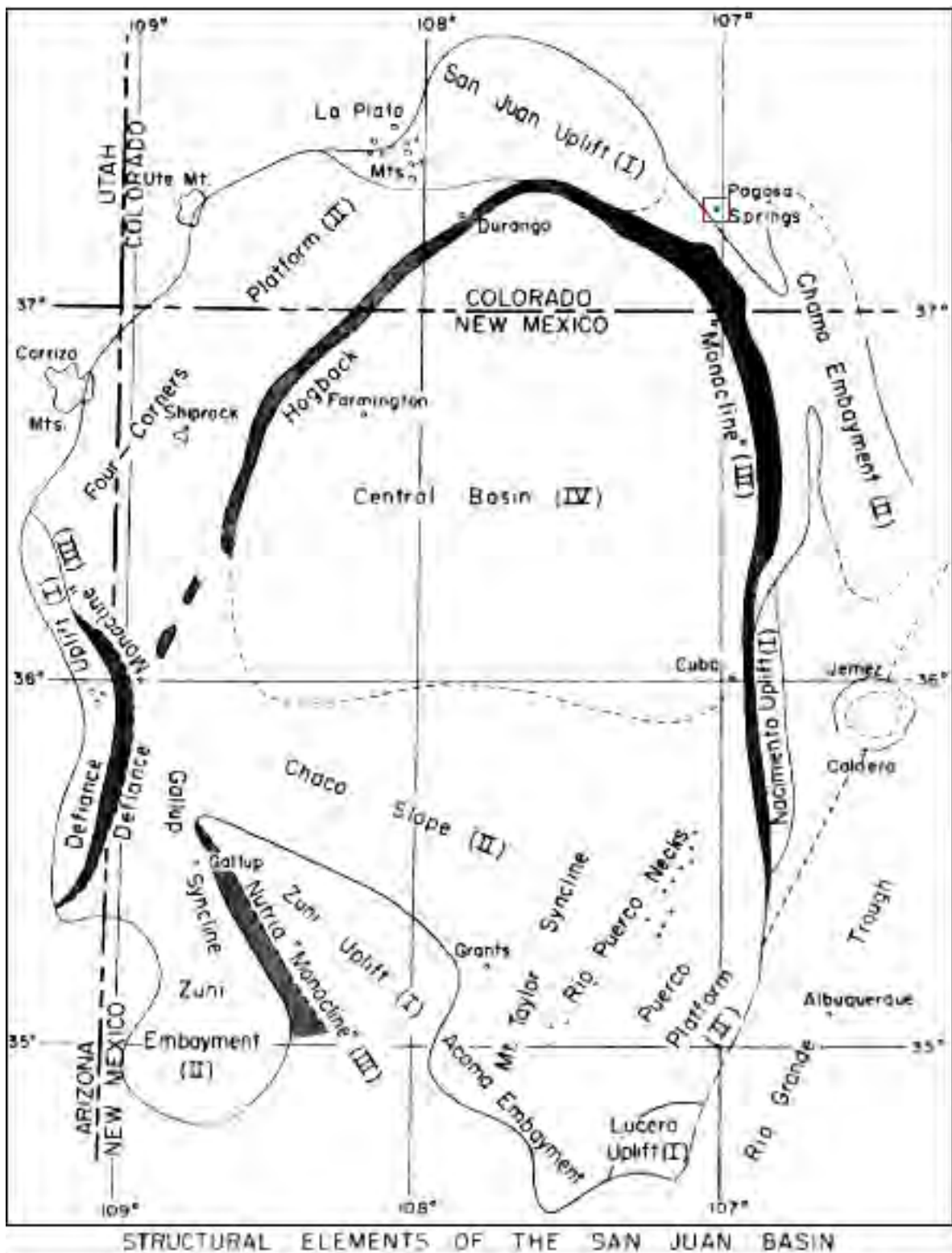


Figure 2. 1 Regional map of the structures within the San Juan Basin with the area of interest outlined in red.

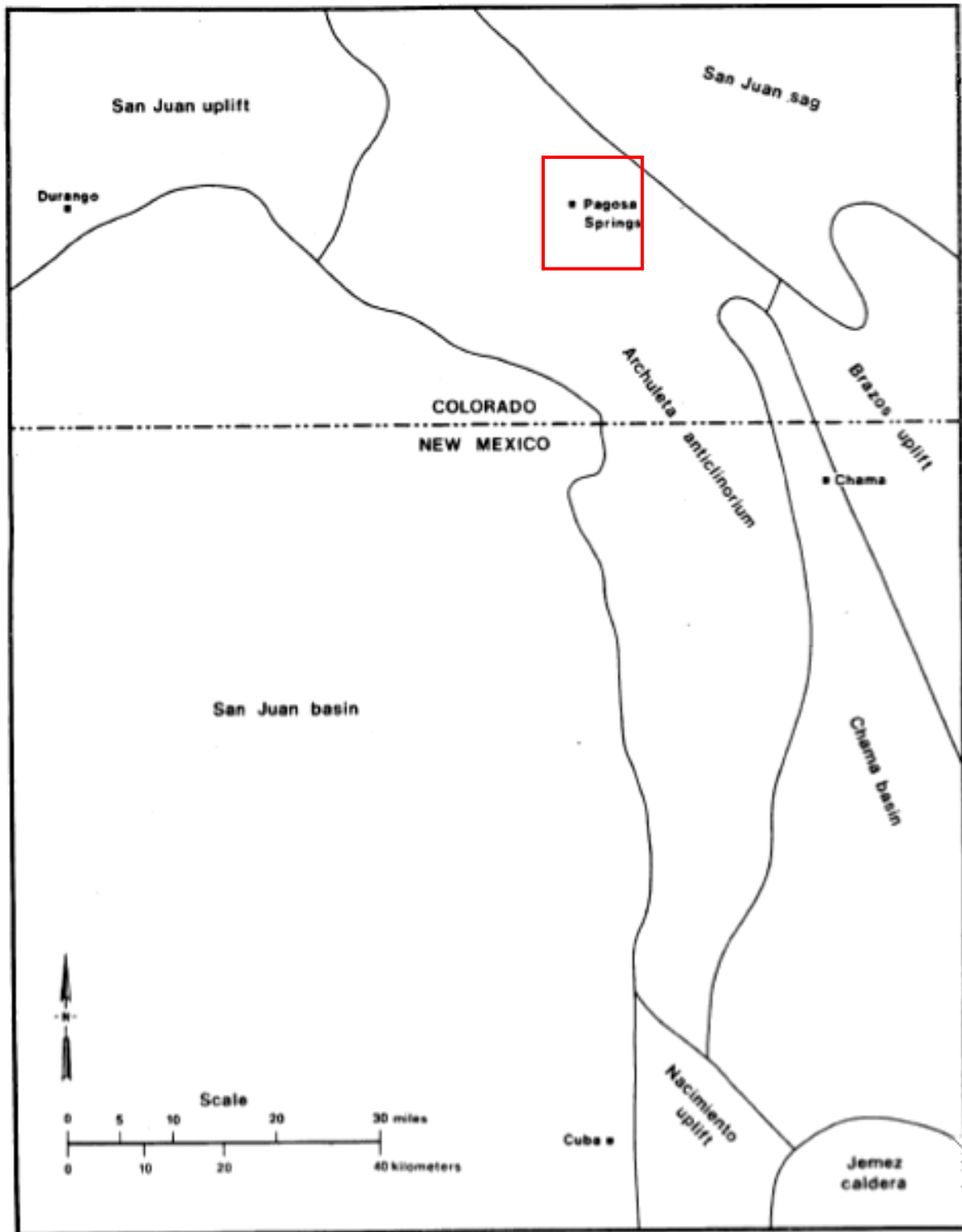


Figure 2. 2 Regional map showing the Archuleta anticlinorium in relation to the San Juan Basin and other basin with the area of interested outlined in red.

The primary sedimentary units of Pagosa Springs are underlain disconformably by a crystalline Pre-Cambrian basement. In Pagosa Springs this basement occurs at relatively shallower depths compared to other areas of the basins, with exploratory wells encountering the basement at depths as shallow as 1300ft [6]. The majority of this basement is igneous and metamorphic crystalline rock, which Kelly



estimates to be 45% granite and granitic rocks, 30% schist and gneiss, 15% quartzite and phyllite, and 10% greenstone. Particularly in the San Juan mountain region, this pre-Cambrian material can be separated into three primary divisions: Archean schists and gneiss, Irving Greenstone, and the Needle Mountains group. The Archean schists and gneiss is the oldest and deepest of these divisions, and is composed of a complex mixture of highly metamorphosed schist, gneiss, and some sedimentary units from very different ages. The Irving Greenstone dates to the Proterozoic Algonkian age and is primarily composed of highly metamorphosed volcanic material of andesitic composition. The Needle Mountain group, also of Proterozoic Algonkian age, can be divided into the Vallecito Conglomerate and the Uncompahgre Formation. The Vallecito contains large pebbles of greenstone and schist, while the Uncompahgre is heavy in quartzite, jasper, hematite, and magnetite [7]. According to Galloway, the Needle Mountain Group is rare to non-existent below Pagosa Springs but is prominent elsewhere in the San Juan Mountains, particularly to the west where the San Juan Mountains are composed of this material [6].

Throughout much of the San Juan Basin the sedimentary units begin with the late Cambrian formations. However, in Pagosa Springs and the surrounding area all units prior to the Entrada Formation of the late Jurassic are absent. This is likely due to a series of uplifts culminating in the Uncompahgre Uplift of the Triassic period that raised the area and caused it to become a place of erosion instead of deposition. It was during this time that the region became a source of sediments for many of the units found deeper in the basin, and therefore many of the pre-Jurassic units eroded away until the Pre-Cambrian material was exposed. The nearest rocks of older ages can be found to the south in surface exposures of the Triassic Dolores Formation in Piedra Canyon [8].

The first sedimentary formations present in the area of investigation are the Entrada and Wanakah formations, both of Jurassic age. The Entrada formation disconformably overlays the Pre-Cambrian formation and is underlain by the Wanakah formation. Both units are part of the San Rafael group, though the oldest and youngest units of this group—the Carmel Formation and the Summerville Equivalent respectively—are absent in this area [9]. The Entrada formation is a buff, grey, or white mottled sandstone with massive crossbedding which has a reported thickness of approximately 150ft in wells drilled under Pagosa Springs. The overlaying Wanakah formation is composed of a light red sandstone and shale member with reported limestone and gypsum layers in other areas, and occurs in a layer approximately 100ft thick below the area of investigation (Figure 2-3). Neither formation has surface exposures in the study area, with the nearest exposures south of Pagosa Springs in the Piedra Canyon [6].

AGE	FORMATION	THICKNESS ft	LITHOLOGY	DESCRIPTION
QUATERNARY	ALLUVIUM	10		Soil, sand, gravel, rounded boulders.
UPPER CRETACEOUS	MANCOS SHALE	227		Shale, soft, very dark brownish gray, fissile. Locally contains some detrital sand, flakes of biotite. Pyrite in tiny (0.2 mm or less) clusters of cubes at 105 to 120 ft. Shale calcareous at 120 ft, and white calcite veinlets 120 to 150 ft.
	DAKOTA SANDSTONE	198		237 Fine- to medium-grained, well-sorted arkosic sandstone with clots and streaks of carbonaceous matter. Some shales show slickensides, hydrothermal euhedral quartz and pyrite crusts up to 1 mm thick on fragments of sandstone and shale. Barite clots occur with Pyrite and euhedral quartz, up to 1mm long.  Sandstone, quartzite, light gray, medium- to coarse-grained, slightly arkosic. Sparse carbonaceous and shaly laminations. Pyrite on fractures at 399-402 ft. Shale, black, with abundant quartz, silt and sand. 435
JURASSIC	MORRISON	681		Sandstone, light greenish gray, very poorly sorted, poorly rounded, frosted grains. Some white and light greenish clays. Sparse disseminated pyrite cubes.  Shale, medium gray and medium greenish gray, soapy, swells and disintegrates in water. Sandstone, white, well rounded, frosted grains, medium- to coarse-grained, cemented by soft white clay, 20% chert pebbles. Pyrite in clots and single euhedral crystals on fragments.  30% sandstone, medium-grained, well sorted, calcareous cement, 20% sandstone, white, hard, chalcedonic(?) cement and altered white chalky lithic grains. 50% siltstone, medium dark brownish red.  Lithic arenaceous sandstone, fine- to medium-grained, light to medium bluish grayish green, some gray and reddish brown. Well sorted, slightly to very calcareous.  Sandstone, arkosic, light gray, medium-grained, well sorted. Sericitized feldspar and lithic fragments. Euhedral pyrite on fractured surfaces. Siltstone, dark purplish gray with pale green streaks, poorly sorted. Abundant fine-grained mica in some fragments.  Alternating shales, sandstones and siltstones as above.  Shale, medium to reddish brown, slightly to very calcareous. 1116
	WANAKAH	96		1212 Limestones-anhydrite. White crystalline anhydrite in nodules 2-5 mm with fetid medium to dark gray finely crystalline limestone. Ave. 40% anhydrite. 1128-1138 ft, 60-70% anhydrite.
	ENTRADA	159		1371 Sandstone, light gray, fine- to coarse-grained, very poorly sorted, well rounded, high sphericity, frosted grains, calcareous. At 1288 ft. rock is pale pink, arkosic, very hard, non-calcareous. Rock is carbonaceous at 1218 ft. Pyrite is found as tiny disseminated crystals, interstitial grains and 1-2 mm thick pyrite veinlets from 1228 to 1258 ft. 1258-1358 ft. rare disseminated crystals.
PRE-CAMBRIAN				1483-TD Gneiss. 40% fine-grained foliated biotite, 40% feldspar porphyroblasts. 0.5-1 mm, including 10% pink to orange to red microcline and 30% plagioclase, locally sericitized. 20% clear, glassy quartz in small grains in biotite. Red apite at 1390 ft. Granite, fine-grained, weak foliation. Migmatite lenses of pegmatitic orange microcline and quartz in biotite schist and gray granite schist. Biotite gneiss.

Figure 2. 3 Stratigraphic column of the geology discovered in well P-1 drilled within Pagosa Springs city limits.

During the Jurassic period, the Ancestral Rocky Mountains locally rejuvenated, causing the seaway at the time to regress [5]. The combination formed the Morrison Formation, a Jurassic unit that conformably overlies the Wananka Formation. This unit is primarily composed of white sandstone in the lower member and a variegated sandstone and shale member in the upper portion of the unit. In Pagosa Springs the Morrison Formation is approximately 700ft thick, and has few surface expressions in the area [6].

After the deposition of the Morrison Formation, some uplift and arching during the early Cretaceous removed some of the deposited material, resulting in a disconformity above the Morrison Formation. The transgression of the Cretaceous seaway in the early Cretaceous then deposited the Dakota Formation: a 200ft thick layer of sandstone that can be divided into three members. The lower member is a layer of cross-bedded, medium to coarse-grained conglomerates, the middle member is a layer of dark grey carbonaceous silty shale, and the top member is a cross-bedded massive, medium to fine grained sandstone [6]. Though the unit primarily lies approximately 200-300ft below the surface, the upper member of the Dakota Sandstone has numerous exposures throughout the area of study, particularly along known fault planes.

As the seaway continued to advance towards the east and southeast, the beach environment shifted and the marine calcareous muds and silts deposited the Mancos Shale [5], a unit of dark grey to black, carbonaceous, massive to fissile shale that conformably overlays the Dakota formation. In areas north of Pagosa Springs the unit can reach thicknesses in excess of 2000ft, but in Pagosa Springs erosion has whittled the unit down to a thickness of 400ft or less. The Mancos Shale makes up the majority of surface exposures throughout the area of investigation [6].

Mountains rising to the south and west of the San Juan Basin provided the material for the Mesa Verde Group, a buff to grey sandstone of varying thicknesses that interbeds with the Mancos and Lewis Shale. Generally it is approximately 300-400ft thick, but this is difficult to verify due to its interbedded nature at Pagosa. The Mesa Verde Formation only produces a few surface exposures in the study area, mostly to the far north of the area. The Lewis Shale, which generally overlays the Mesa Verde Group, is similar in composition to the Mancos Shale and in locations farther north and west of the study area merges with the Mancos to produce one cohesive unit. This unit represents the final marine transgression in the area, occurring in the late Cretaceous [4].

No younger sedimentary units occur in the study area. To the north, units from the late Cretaceous such as the Picture Cliffs, Kirtland, and Picture Cliffs Formations have surface exposures, but due to erosion these units have neither surface exposures nor do they occur in the subsurface [6]. As the Cretaceous came to an end, the Laramide Orogeny that produced the current Rocky Mountains began

to occur. This initiated the Archuleta Anticlinorium and likely caused the majority of faulting and structural deformations present in the area, though some sources claim that this faulting occurred later during the Eocene as brittle stratigraphic beds flexed over the Archuleta Anticlinorium [6]. At the same time, the area began to increase in elevation, and much of the deposition of previous ages ceased. It was during this time that the San Juan Mountains formed [4]. These mountains are composed of andesitic to mafic volcanic rocks, primarily volcanic tuffs formed from pyroclastic flows produced by Mt. Princeton during the early Cenozoic. Numerous dikes occurred in the area during this time, mostly to the north near Wolf Creek Pass in the San Juan Mountains. These formations were later carved by the glaciations that covered most of the Rocky Mountains during the Pleistocene and later by the San River that flows through the resulting glacial valley. Fluvial and glacial deposits of the above units are present throughout the area of investigation as Quaternary exposures.

Today the area is an area of erosion, carved by the San Juan River that flows through the center of Pagosa Springs (Figure 2-4). The primary structural features include the Eight Mile Mesa Fault that trends north to northwest through the center of our area of investigation and several small folds including the Sunetha anticline and the Stinking Springs anticline in the south portion of the study area (3).

## 2.2 Hydrology

The surface groundwater in Pagosa Springs is dominated by the San Juan River, its tributaries, and by local structures. The main aquifers are the Mancos Shale and the Dakota Sandstone.

The Mancos Shale is exposed over much of the mapped area, particularly around Pagosa Springs. On this layer groundwater flow is the result of both fracture and inter-granular porosity. The fractures may interconnect isolated porous units sufficiently to “smooth out” water pressures within the numerous Mancos aquifers, allowing the formation to become nearly homogeneous [6].

The water surface map suggests areas of local recharge to the west, north, and east of Pagosa Springs (Figure 2.4). This could include the areas of Mancos exposure adjacent to the Eight Mile Fault southwest of Pagosa Springs. A local discharge occurs about 2km south of Pagosa Springs’ San Juan River, while recharge may occur along most of its course through Mancos Shale.

Water quality is generally poor. Total dissolved solids range from 1000 to 2500 mg/l, with particular high concentrations of sodium, calcium, iron, and sulphate. Dissolved hydrogen sulphide is also common [5].



The Dakota Sandstone is exposed along the Sunetha and Stinking Springs anticlines, and on the northeast side of the Eight Mile Mesa Fault. Groundwater flow in the Dakota Sandstone is the result of fracture porosity and is confined. Individual aquifers cannot be identified, but it is probable that at least two semi-independent aquifer (fracture) systems exist, separated by black shale sequences. Areas of recharge, as defined by piezometric surface map correspond extremely well with exposures of Dakota Sandstone. Pagosa Springs may be an area of regional discharge from the Dakota Sandstone. The Dakota is not exposed in this area suggesting discharge occurs through fractures and/or faults in Mancos Shale and possibly the surface. Water quality is highly variable. It appears to be similar to Mancos' but with some water with much lower dissolved solids and similar to drinking water standards.

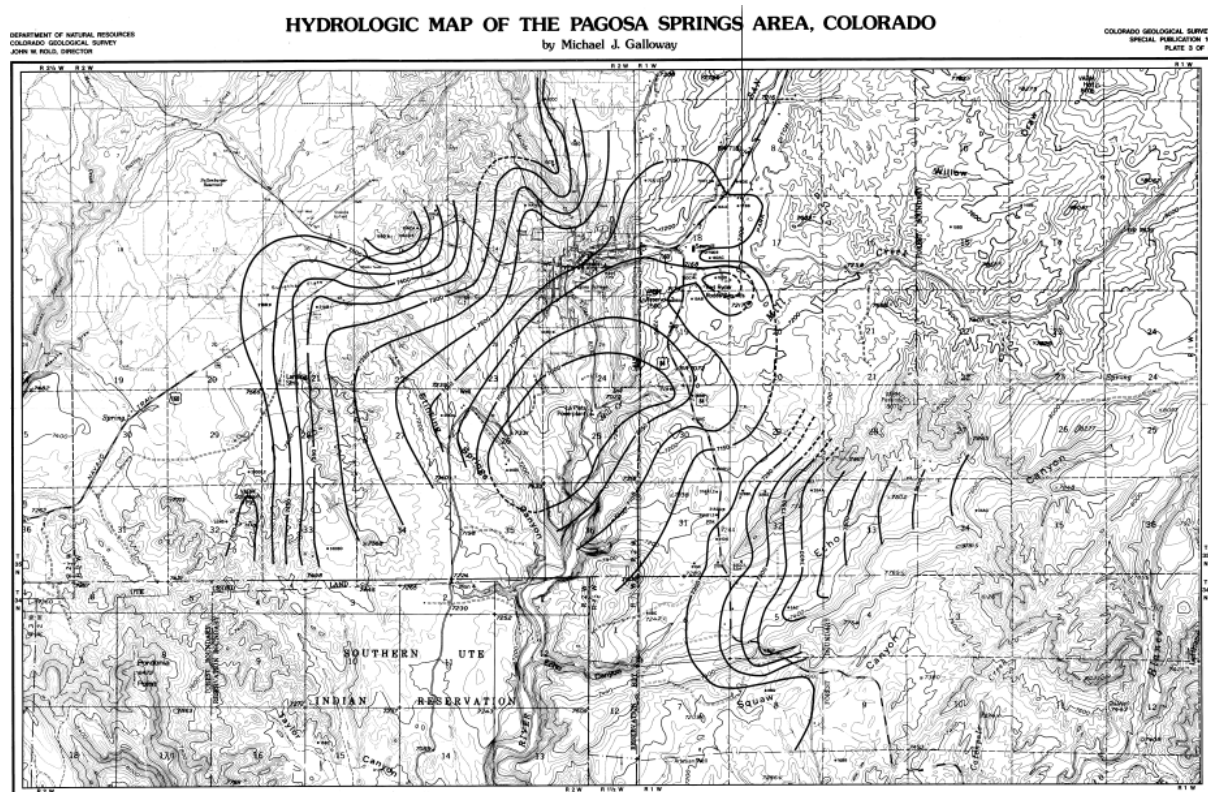


Figure 2. 4 Hydrologic map of Pagosa Springs, which includes much of the area of interest. [6]

## 2.3 Geothermal Analysis

Geothermal energy has been used on Pagosa Springs since the 1800's. Main thermal spring is located on the east side of the San Juan River. The area contains hot springs and hot wells (Figure 2.5).

The mound of the hot springs covers 0.03 mi<sup>2</sup> (0.07 km<sup>2</sup>) mostly on the south side of the river. Other travertine mounds can be seen on the other side of the river but it is unknown if they are in situ. The elevation of the mounds is 7055 ft (2153 m) to 7077 ft (2158 m). The diameter of the main spring

ranges from 25-35 ft (8-10 m) and the depth is unknown but estimates are 100 ft (38 m) and 850 ft (260 m) [6]. The spring discharges from fractures and caverns below the surface, and likely feeds springs located at the periphery of the mound.

The temperatures of the springs range throughout the year from 54° C to 58° C (129.2° F to 136.4° F). Various geo-thermometer analyses (chalcedonia-silica, Na-K and Na-K-Ca) give high estimates that suggest a temperature at depth between 80° C (176 F) and 150° C (302 F). The discharged waters contain between 3,040 to 3,310 mg/l of dissolved mineral matter and are a sodium-sulphate type. The mineral matter in the water appears to be derived from the Mancos Shale. According to various well owners and the interpretation of the geologic conditions of the area, it appears that the thermal waters are coming from the Dakota Formation [10].

The area of the hot wells is approximately 0.04 mi<sup>2</sup> (0.1 km<sup>2</sup>). On the fringes of this area, warm water was found in wells 13 DBAC (18), 13 CBDC (17), and 13 DCCC (25). Outside of this area only cold water was found. The chemical analysis of 2 wells (13 CADC1 and 13 DBCD1) indicates that composition is not different from the spring water.

In 1978 the Colorado Geological Survey drilled two wells (one at 780 ft and another at 1,483 ft) behind the courthouse across the San Juan River from the spring. The longest well bottomed in Precambrian granite and metamorphic rocks. The wells encountered hot water (56° C, 133.8 F) at the Mancos Shale and the Dakota Formation. The temperature dropped to 45° C (113 F) below the Dakota Sandstone. Although all the layers carried some water, only the Mancos and Dakota Formations contained the hottest water. Pearl believes that the Mancos is a secondary aquifer and that the primary shallow aquifer in the area is the Dakota Formation. The layers were also highly fractured, but did not appear to be faulted, thus it could be possible that the waters move up from the depths along fractures zones and into the Dakota Formation.

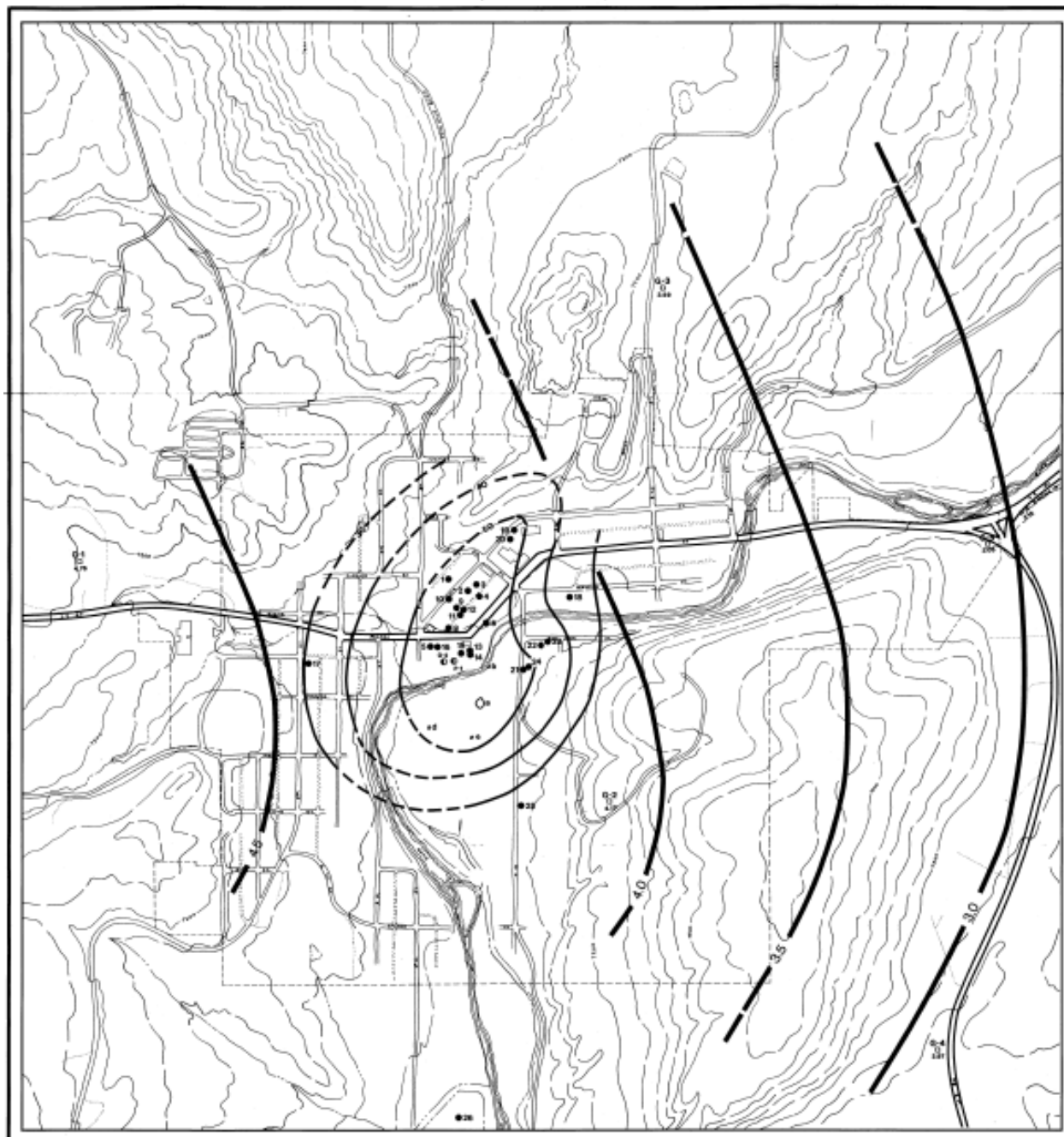


Figure 2. 5 Geothermal map of Pagosa Springs, which includes much of the area of interest. [6]

## 2.4 Field Observations

Prior to performing any geophysical surveys in the Pagosa Springs area, we needed to examine the local geology and confirm the placement of stratigraphic units and structural features within the area of interest. In particular, we focused on two lines: line paralleling Steven's airfield northwest of Pagosa Springs beginning southwest of the golf course and ending northeast of the north end of the

airfield (Figure 2.6), and a general line beginning at Burns Canyon in the San Juan National Forest southwest of Pagosa Springs and ending in Wolf Creek Pass northwest of Pagosa Springs (Figure 2.6). We chose the general section because it provided a general overview of the stratigraphy of the Pagosa Springs area over which many of our survey lines would later cross. We chose the section paralleling the airfield because we planned to perform our first deep seismic survey along this line, and having a good understanding of the structures and stratigraphy of the area would be necessary to correctly interpret the resulting seismic data.

In general the stratigraphy and structural geology of the Pagosa Springs area is somewhat simple. The main folding features in the area include the Stinking Springs Anticline, which is present just south of Pagosa Springs on the general cross-section and on the extreme south end of the airport cross section (Figure 2.7) (Figure 2.8). This again represents the border that separates the features of the San Juan Basin to the southwest from the features of the San Juan Sag to the northeast as the stratigraphic units approach the San Juan Mountains. This is a gentle fold trending north to northwest that formed during the late Cretaceous at the same time as the Laramide Orogeny, and caused the sedimentary units in the area to dip at approximately 5-10° on either side of the fold axis.

Structurally, the area is dominated by a series of small normal faults, the largest of which is the Eight Mile Mesa Fault that trends north to northwest and passes south of the city of Pagosa Springs. This is the largest and longest trending fault in Pagosa Springs, beginning west to northwest of Pagosa Springs and continues directly south of Pagosa Springs until it bisects Eightmile Mesa, for which it gives its name. Based on surface examinations, the fault is largely independent of surface topography, indicating that it dips nearly vertical and has nearly 300ft of vertical displacement [6]. However, the depth that this fault penetrates is yet unknown, though it is suspected that it penetrates through the stratigraphic layers into the Pre-Cambrian basement. Most of the other known faults in the area occur south of the Eight Mile Mesa Fault and are significantly smaller in length, throw, and likely depth of penetration. These faults also trend north to northwest and are primarily normal faults.





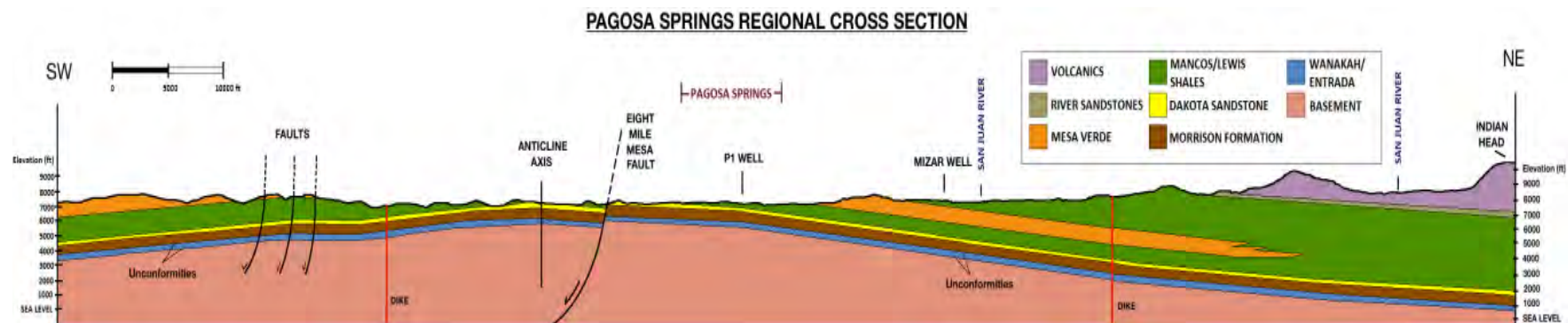


Figure 2. 7 General cross-section of Pagosa Springs. Vertical scale has been exaggerated to show features in larger detail.

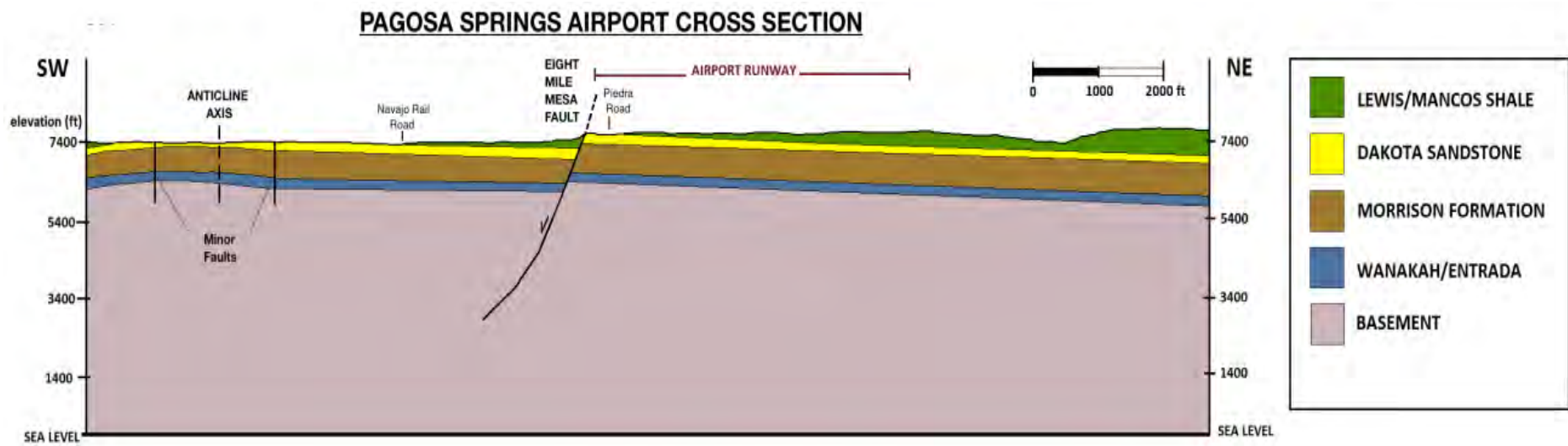


Figure 2. 8 Cross-section of Steven's Airfield. Vertical scale has been exaggerated to show features in larger detail.

To aid our investigations, we used the well log results of two wells drilled near the city of Pagosa Springs: Well P-1 and the Schick-Mizar Well #1. Schick-Mizar Well #1, with a total depth of approximately 2300ft, was drilled northeast of Pagosa Springs (Figure 2.9) in 1981 and encountered primarily Mancos Shale and the underlying Dakota formation in addition to a thin layer of Quaternary sediments. The P-1 well, with a total depth of approximately 1480ft, was drilled within Pagosa Springs between the San Juan River and the county courthouse in 1978 [6]. This well encountered very little of the Mancos Shale and penetrated through the Dakota, Morrison, Wananka, and Entrada Formations to encounter the Pre-Cambrian Basement shortly before reaching total depth. This confirms the slight folding structure in the region, as the Schick-Mizar Well #1 penetrated deeper than the P-1 well yet did not intersect the Morrison Formation, let alone the underlying formations and the Pre-Cambrian Basement.



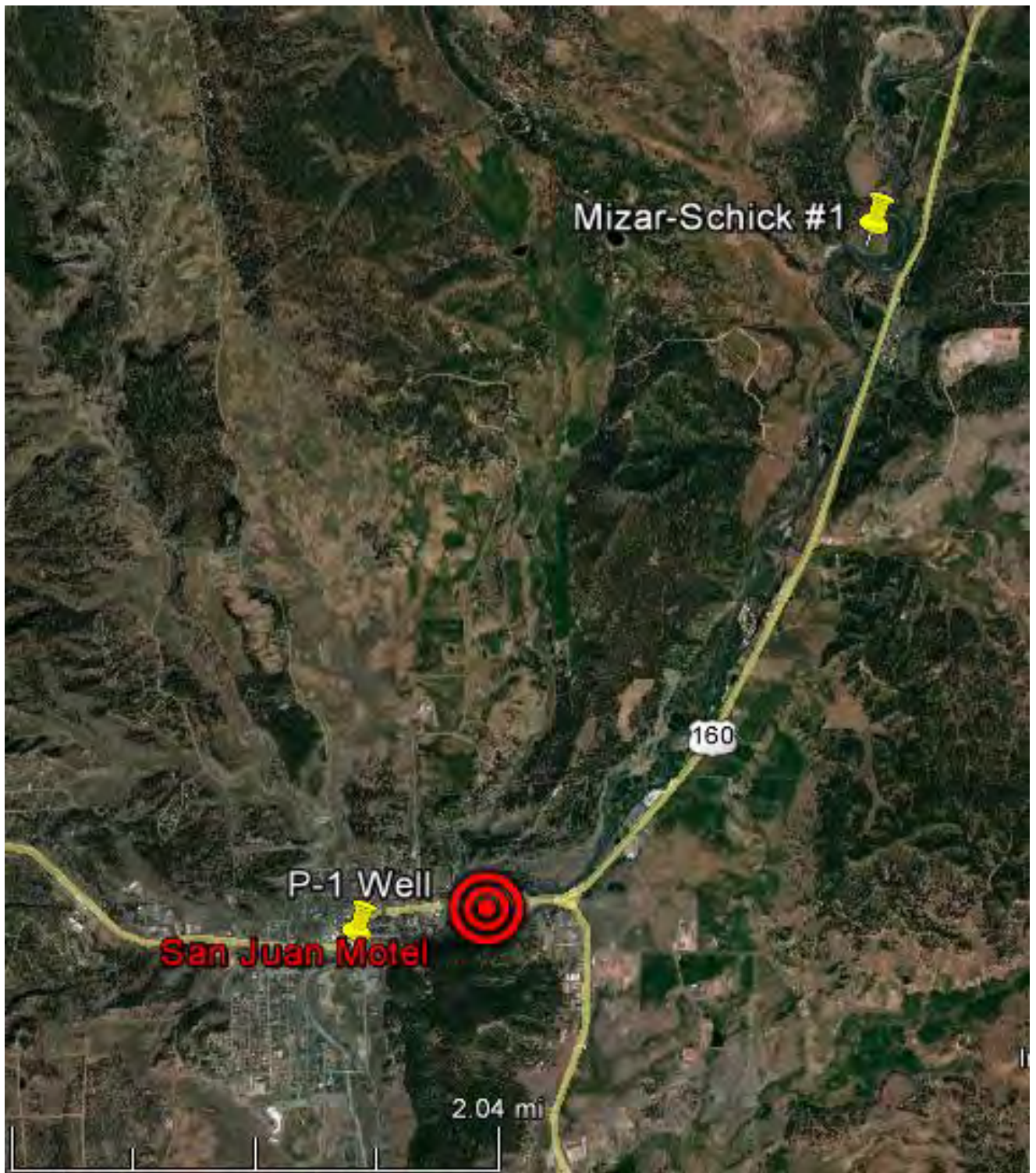


Figure 2. 9 Locations of wells used to create cross-sections and elsewhere in the study: P-1 Well [6] and the Mizar-Schick (provided by Dr. Batzle).

## 2.5 Hand Specimen Analysis

During investigation, a variety of hand specimens were collected around the area of investigation and from surrounding areas (Figure 2.10). Each hand specimen was collected either to clarify better the properties and characteristics of the known rock units or to provide evidence for anomalous formations in the study area. Each sample was collected by students participating in the investigation during the investigation and was analysed by Stephen Cuttler, Dr. Andre Revil, and Dr. Bruce Geller of the Colorado School of Mines Geology Museum.

Samples 1 and 2 (Figure 2.11) are hand samples of the Dakota Sandstone collected on exposures north of the Barn 3 line by Thomas Rapstine, where a prominent exposure of the Dakota Sandstone is present (Figure 2.12). These samples appear to part of the Dakota Sandstone's upper member, and are red to tan coloured, fine to medium grained sandstones rich in quartz and potassium feldspars. Along several of the faces of the samples the sandstone shows evidence of recrystallization, primarily through the large quartz crystals that give the Dakota Sandstone its characteristic "sparkle." This alteration is likely due to water, and because the Dakota Sandstone is highly jointed, it is likely that this occurred as water flowed through these joints as part of the aquifer. However, it is unclear without further samples and research whether this alteration occurred early or late in the history of these samples, or if the alteration is due to meteoric or geothermal waters.

Samples 3, 4, and 9 (Figure 2.13) are hand samples of the Mancos shale collected by Thomas Rapstine near the mother spring site and Matt Emmett on the Pagosa Springs 8 line north of Pagosa Springs (Figure 2.15), and appear to be black to dark grey carbonaceous, fissile shale samples. When the Mancos weathers, it gains a light brown to tan "skin" which chips easily to reveal the still dark unweathered material underneath. Larger exposures show that the unit shows a strong trend towards thin, horizontal layering. Sample 4 in particular appears to be from a small limestone unit within the Mancos shale, as indicated by Galloway. It contains numerous clam and mollusk fossils and reacts with hydrochloric acid (HCl) indicating carbonaceous material, both of which are prominent characteristics of common limestones.

Samples 5, 6, and 7 are samples of igneous rocks collected in the area (Figure 2.14). Sample 5 was collected by Elias Arias on Pago 1 (Figure 2.15), and appears to be an extrusive, aphanitic to porphyritic intermediate andesite with alterations due to water. The majority of the sample appears to be black hornblendes and amphiboles (85%), with some white plagioclase feldspar (10%) and some green chlorite (10%). The presence of chlorite indicates that this unit has been exposed to and altered by water over a prolonged period of time, and the uniform composition indicates that this is not due to water flowing over surface exposures. This sample is also highly magnetic—it visibly attracts even a low strength magnet—indicating the presence of magnetite within the sample. This is supported by

the exposed surface, which is a slight shade of red. Because magnetite is not the final oxidation stage of iron bearing minerals, the magnetite will continue to oxidize into hematite and goethite when exposed to water and air. A volcanic bomb was also found near Sample 5, but because it was not found in situ, it is unlikely to be related and only indicates that volcanic activity occurred in the region, which is confirmed by the eruption of Mount Princeton during the Cenezoic era. Sample 7 is a similar sample collected by Stephen Cuttler from an igneous dike just south of Wolf Creek Pass. Though this was not within the area of investigation, this sample has a very similar composition to Sample 5. Sample 7 is a porphyritic, extrusive, intermediate andesite with visible glassy porphyries of plagioclase feldspar. It has a higher magnetism than Sample 5. However, the chlorite is absent, indicating that no water flows through this structure. If these two samples are from the same or similar volcanic period, then the presence of chlorite in Sample 5 indicates that the dike it came from was likely a conduit for water. Sample 7 is a sample of the pyroclastic andesitic volcanic tuff that composes much of the San Juan Mountains collected at Wolf Creek Pass by Stephen Cuttler. Angular to sub-rounded clasts are visible throughout the fine grained matrix, and it bears little resemblance to Samples 5 and 7.

Samples 8, 10a-b, 11, 12, 13, and 14 (Figure 2.16 and 2.17) are samples of calcite collected by Matt Emmett and Joyce Hoopes along the Pago8 line north of Pagosa Springs (Figure 2.18). All of the above samples were collected within the Mancos shale. Samples 11 and 12 clearly show the tetrahedral crystal form characteristic of transparent to semi-transparent calcite. The presence of calcite within the Mancos shale indicates the presence of fluid flow within the system. Because the Mancos shale is largely impermeable, this indicates the flow of fluid via fractures, the necessary conduits for a geothermal system. Samples 10a-b and particularly Sample 8 show this well, as both samples show massive crystals of transparent to semi-transparent calcite sandwiched between layers of Mancos shale, indicating that the crystals filled a small fracture as water flowed through the fracture. Samples 10a-b and Sample 14 show a different crystal form for the calcite, indicating that the area where that crystal formed did not fill the entire void space. The green in Sample 14 is thought not to be a coloring of the mineral but rather the presence of algae which absorb the abundant nutrients within calcite. All samples react with hydrochloric acid (HCl), confirming the presence of calcium carbonate ( $\text{CaCO}_3$ ), the primary chemical unit of calcite.

Sample 15 (Figure 2-19) was collected by Elias Arias on the Pago7 line (Figure 2-20). It appears to be a unit of the Mancos shale with either joints or mud cracks preserved by cementation and filled in with a duo layer of gypsum after cementation. Gypsum can easily form from meteoric water, and therefore this sample only indicates that meteoric water flowed through these faults. Therefore, this sample is of little use to our investigation.



Samples of the Morrison, Wanakah, Entrada, or Pre-Cambrian formations were not collected due to a lack of surface exposures in the survey area, nor were they encountered in recognizable outcrops during several exploratory investigations outside of our area of investigation. The same is true for younger formations, such as the Mesa Verde, Kirtland, and Picture Cliffs Formations. No other anomalous mineral specimens besides the calcite specimens collected by Matt Emmett and Joyce.



Figure 2. 10 General overview of sample locations collected during investigation.





Figure 2. 11 Samples #1 and #2. Samples of Dakota Sandstone collected by Thomas Rapstine north of the Barn 3 Line.

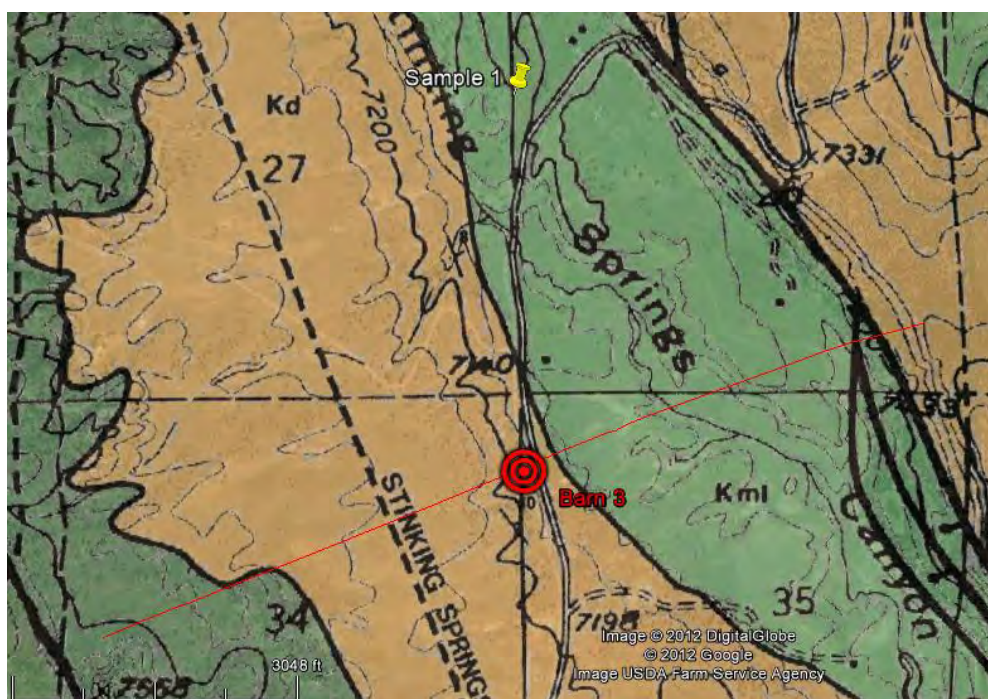


Figure 2. 12 Locations of Samples #1 and #2.





Figure 2. 13 Samples #3, #4, and #9. Samples of the Mancos shale and Limestone units collected by Thomas Raptine (#3 and #9) and Matt Emmett (#4).



**Figure 2. 14 Samples #5, #6, and #7. Sample #5: intermediate igneous rock collected by Elias Arias on Pago 1. Sample #6: pyroclastic tuff collected by Stephen Cuttler near Wolf Creek Pass. Sample #7: intermediate altered igneous rock collected by Stephen Cuttler south of Wolf Creek Pass.**





Figure 2. 15 Left: Locations of samples #3 and 4#. Right: Locations of samples #5, #6, and #7.



Figure 2. 16 Samples #8, #10a-b, and #11. Samples #8 and #11 are examples of crystalline calcite collected by Matt Emmett on the Pago8 line. Samples #10a-b are further examples of crystalline calcite collected by Joyce Hoopes on the Pago8 line.





**Figure 2. 17 Samples #12, #13, and #14. All samples collected by Matt Emmett on the Pago8 line and demonstrate examples of crystalline calcite within the Mancos Shale.**



Figure 2. 18 Locations of Samples #8, #10a-b, #11, #12, #13, and #14.



Figure 2. 19 Sample #15: Mancos Shale with gypsum filling in preserved mudcracks or joints. Collected by Elias Arias on the Pago7 line.

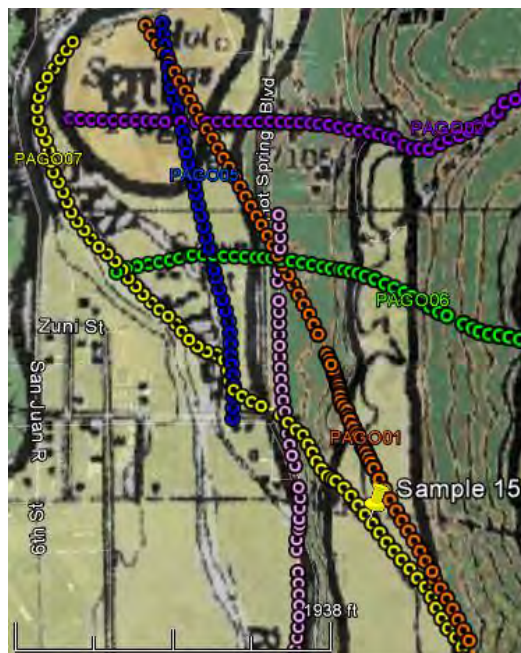


Figure 2. 20 Locations of Sample #15.



## 2.6 Petrophysics and Well Log Analysis

To further examine the physical characteristics of the rock units in the area, a preliminary petrophysical examination was performed by Stephen Cuttler and Arantxa Gallastegui with the help and equipment of Dr. Mike Batzle. To do this, we selected four samples for testing. The first sample was a sample of the Dakota Sandstone collected by Stephen Cuttler near the Barn 3 Deep Seismic line. Sample 2 was a sample of the Mancos Shale collected by Thomas Rapstine. Sample 3 was a sample of a volcanic dike south of Wolf Creek Pass collected by Stephen Cuttler similar to Sample 7 in Section 2.5. Sample 4 was an igneous sample collected by Elias Arias along one of the DC/SP lines similar in composition to Sample 5 Section: Hand Specimens. These four samples were selected because they represented several of the primary exposures present within the area of investigation and their properties were likely the properties to be measured by the shallow geophysical surveys.

To test these samples, each sample was broken into several pieces (Figure 2.21). From each, we selected three miniature samples each approximately the size of a grape to walnut. Each sample was immediately weighed on a mass scale for their dry mass (Figure 2.22). Each sample was then placed into a sealed container, which was then connected to a vacuum (Figure 2.22). The samples remained under the vacuum for 24 minutes to remove as much air as possible from the pore spaces of the samples. We then switched the vacuum off and added water to the container until the pressure within the container was approximately 1000psi. The samples were left in this container for 1 hour 44 minutes to allow the water to force itself into the pore spaces of the samples and completely saturate them. The samples were then removed from the container and placed on the mass balance within a beaker of water (zeroed to remove the mass of the beaker and water) to gain a second mass reading with the saturated samples. The samples were then measured as suspended weights within water to get their volume. Finally, the samples were allowed to dry overnight and were re-measured again the following day. The results of this experiment are shown in Table 2.1.

Several errors could have occurred during this experiment. First of all, the scale required zeroing between each measurement particularly because it was easy to add or remove water from the system between measurements, and if this was forgotten or performed prematurely, the measurement of the mass of the sample would be incorrect. Second, all external water needed to be removed from the saturated sample before measuring. If this was not performed, then the sample will appear to be more massive than it actually was. Third, if small parts of the rock were broken off the main sample at any point between the measurement of the dry mass and the final measurements, any following measurements will be less than the actual measure.





Figure 2. 21 Samples used in petrophysical analysis. M= Mancos, D= Dakota, V= Igneous (Sample 5), B= Igneous (Sample 7).



Figure 2. 22 Left: Sample on scale balance. Right: Vacuum used to remove air.

This is only a preliminary petrophysical investigation intended to examine the density and pore space of the given samples. For a proper investigation, the samples should be heated up and vacuumed for a longer period of time before any measurements and left under pressure for a longer period of time. However, due to time constraints, we were unable to perform this properly, and would recommend future investigations of the petrophysical properties of the gathered samples.

To compare and verify the properties gathered during the petrophysical investigation, we also gathered data concerning the petrophysical characteristics of the rocks from well logs gathered within the area of investigation from previous investigations. In particular, we focused on the Schick Mizar Well #1, which had borehole geophysical tests performed on it between August and November of 1981. These well logs were provided to us by Dr. Mike Baztle both in electronic form and via a paper copy. To examine these, we made generalizations about the values of the well logs by averaging general trends throughout the data. By combining these series of average values and once again averaging them, we could get values of the porosity, conductivity, gamma ray, and wave velocity. The results of this examination are shown in Table 2.2.

When comparing the two, the only property that overlaps is the value for the porosity derived from density. For the Mancos shale, this is stark, differing by approximately 123%. The Dakota Sandstone differs by only 16%. These differences may be largely due to the procedure used to test these properties in the petrophysical investigation: as stated above, more thorough testing will be necessary for accurate results. The other samples do not overlap because neither volcanic sample was encountered during the drilling of this well. Also, no other properties were tested during the petrophysical investigation due to the lack of time and equipment. Therefore, we recommend that the results gained from the well-log analysis are more accurate and should be used in further investigations and testing.

**Table 2. 1** Table of values obtained from the petrophysical analysis. M= Mancos, D= Dakota, V= Igneous (Sample 5), B= Igneous (Sample 7).

Sample	Volume (cm3)	Pore Space Volume (cm3)	Porosity	Grain Density (g/cm3)
M1	2.49	0.17	0.068273092	2.642241379
M2	7.82	0.68	0.086956522	2.708683473
M3	7.39	0.68	0.092016238	2.715350224
<b>M Average</b>	---	<b>0.51</b>	<b>0.082415284</b>	<b>2.688758359</b>
D1	10.95	0.87	0.079452055	2.642857143
D2	8.31	0.65	0.078219013	2.647519582
D3	11.4	0.83	0.072807018	2.640491958
<b>D Average</b>	---	<b>0.783333333</b>	<b>0.076826029</b>	<b>2.643622894</b>
V1	4.42	0.25	0.056561086	2.618705036
V2	8.54	0.16	0.018735363	2.633651551
V3	20.08	0.76	0.037848606	2.627846791
<b>V Average</b>	---	<b>0.39</b>	<b>0.037715018</b>	<b>2.626734459</b>
B1	15.57	0.99	0.063583815	2.705075446
B2	4.19	0.3	0.071599045	2.686375321
<b>B Average</b>	---	<b>0.645</b>	<b>0.06759143</b>	<b>2.695725384</b>

**Table 2. 2** Table of values obtained from the analysis of the Mizar Schick Well Log #1.

Rock Unit	Gamma Ray	Porosity	Conductivity (S/m)	Velocity (km/sec)
<b>Mancos Shale</b>	126.3636364	0.036923077	0.083181818	3.735006284
<b>Dakota Sandstone</b>	40	0.092	0.044666667	3.529779642

## 2.7 Geochemistry

Very little was performed with the geochemistry of water found in the naturally occurring hot springs, and nothing was done with geochemistry applied to the rock and mineral units. However, Paul Morgan of the Colorado Geologic survey provided us with geochemical data collected in the region in 1975, which we can then correlate with Galloway's predictions of the geochemical signature of meteoric water. According to Galloway, the water at the hot springs needs to have the chemical signatures of both the near surface and deep material in order to indicate that the water circulates from the surface, deep into the basement material, and then back to the surface. To indicate near-surface circulation, the water needs high amounts of sulfates, as well as elements such as Ca, Fe, K, and Mg (Geller). The data provided shows that the concentrations of Ca are approximately 230 mg/L, Fe approximately 20-80 µg/L, K approximately 87 mg/L, and Mg approximately 24 mg/L. The only one of these that occurs at significantly higher concentrations than other elements is Ca at 230 mg/L. This concentration explains the occurrence of crystalline calcite discussed in previous sections. However, sulfates are extremely high, occurring at approximately 1500 mg/L, correlating with the predictions. However, Galloway also mentions that high concentrations of elements such as Li, B, and F indicate circulation deep in the basement material (Galloway). The data provided shows that the concentration of Li to be approximately 2900 µg/L, B approximately 2000 µg/L, and F approximately 4.8 mg/L. Without reference to other water samples, it is impossible to determine whether these are abnormally high concentrations, and further geochemical testing and examination is needed to obtain any conclusive results. For a full description of the geochemical characteristics of the Pagosa Springs waters, please see Table 2.3.

Table 2. 3 Table of values obtained from several geochemical analysis of the thermal waters from the Mother Spring in Pagosa Springs Colorado at four different dates (provided by Paul Morgan of the Colorado Geological Survey) [11].

Table 1. Physical Properties and Chemical Analysis of Thermal Waters in Colorado.

Pagosa Springs: Big Spring

Location: 37°15'52"N. Latitude; 107°00'37"W. Longitude; T. 35 N., R. 2 W., Sec. 13cd, N.M.P.M., Archuleta County

	Date Sampled			
	8/75	10/75	1/76	4/76
Arsenic (As), (UG/L):	120	130	-	-
Boron (B), (UG/L):	1,800	1,700	2,000	2,300
Cadium (Cd), (UG/L):	0	0	-	-
Calcium (Ca), (MG/L):	230	210	240	230
Chloride (Cl), (MG/L):	180	180	190	180
Fluoride (F), (MG/L):	4.3		5	4.8
Iron (Fe), (UG/L):	80	20	20	20
Lithium (Li), (UG/L):	2,900	3,200	-	-
Magnesium (Mg), (MG/L):	25	23	2.6	24
Manganese (Mn), (UG/L):	230	220	220	200
Mercury (Hg), (UG/L):	0.1	0	-	-
Nitrogen (N), (MG/L):	0.02	-	0.01	0.01
Phosphate (PO <sub>4</sub> )				
Ortho diss. as P, (MG/L):	0.07	-	0.03	0.07
Ortho, (MG/L):	0.21	-	0.09	0.21
Potassium (K), (MG/L):	90	87	87	85
Selenium (Se), (UG/L):	0	-	-	-
Silica (SiO <sub>2</sub> ), (MG/L):	54	-	58	59
Sodium (Na), (MG/L):	790	780	800	730
Sulfate (SO <sub>4</sub> ), (MG/L):	1,400	1,500	1,500	1,300
Zinc (Zn), (UG/L):	10	20	-	-
Alkalinity				
As Calcium Carbonate, (MG/L):	701	705	707	702
As Bicarbonate, (MG/L):	855	859	862	856
Hardness				
Noncarbonate, (MG/L):	0	0	0	0
Total, (MG/L):	680	620	610	670
Specific conductance (Micromohs):	5,810	4,000	4,200	4,340
Total dissolved solids (TDS), (MG/L):	3,200		3,310	3,040
pH, Field	6.5	6.9	6.6	6.5
Discharge (gpm):	265	226	241	260
Temperature (°C):	58	57	55	54

Remarks:

## 3. Surveying

---

### 3.1 Introduction

When it comes to trying to find something, it helps to know where you are. Surveying is vital to the accuracy of all of our geophysical techniques and their interpretation. Surveying is used to obtain accurate locations, elevations, and total distances for all the points used in the surveys. A variety of techniques and technologies allow accurate locations to be obtained with precisions of up to centimeters. Global Positioning System (GPS), Differential GPS (dGPS), Total Distance Measure (TDM), and Geographic Information System (GIS) software; allow the user to define points to a high but necessary degree of accuracy. Table 3. 1 shows which surveying techniques were applied where.

**Table 3. 1 Surveying locations and how they were surveyed.**

Survey Location	Techniques
Airport	dGPS
Barn 3	dGPS
PAGO01	dGPS
PAGO02	dGPS and TDM
PAGO04	dGPS
PAGO05	dGPS
PAGO06	dGPS and TDM
PAGO07	dGPS
PAGO08	GPS
Zen Garden	dGPS and GIS
Warm Springs	dGPS and GIS
Hammer Seismic Lines	dGPS

The surveying techniques used at each location depended on the accuracy and survey detail needed for each of the geophysical methods.

### 3.2 Differential GPS (dGPS)

Basic GPS is useful in obtaining a basic location; the accuracy is low but is useful as a first step in surveying a predefined line. It allows the user to generally follow a predetermined path. GPS employs a constellation of mid-ranged satellites sending out a microwave signal in order to determine a location on the surface of the earth. This constellation of satellites comes from the Global Navigation Satellite System (GNSS). The GPS must make contact with at least four satellites to obtain XYZ coordinates. The more satellites used the greater the locational accuracy. These communications give a distance by calculating the time it takes the microwaves to travel the distance from the satellite and GPS receiver. It corrects for time differences by sending out a pattern and analysing the phasing of the signal when it returns. Using these distances and the satellite locations the GPS is able to triangulate the position of the user or station.



GPS has an accuracy of about ten meters [12]. Table 3.2 shows sources of error that decrease the accuracy of the GPS:

**Table 3. 2 Sources of error and the uncertainty they cause.**

Source	Uncertainty
Ionospheric Effects	$\pm 5$ Meters
Ephemeris Errors	$\pm 2.5$ Meters
Satellite Clock Errors	$\pm 2$ Meters
Multi-Path Distortion	$\pm 1$ Meter
Numerical Errors	$\pm 1.5$ Meter

- Ionospheric/Tropospheric Effects- Signal slowing due to passing through the different layers of the atmosphere.
- Ephemeris Errors – Inaccuracies in satellite position
- Satellite Clock errors – Differences in the GPS clock and satellite clock
- Multi-Path Distortion – Error due to receiving signal from reflections of the satellite signal rather than a direct signal.
- Numerical errors – Normally caused by having fewer satellites or signals being blocked by trees or buildings.

The ten meter error caused by these errors is not accurate enough for most of the geophysical methods. As a result of this, Differential Global Positioning System, dGPS, was utilized, this technique increases the accuracy of GPS by an order of magnitude. The dGPS uses a base station in order to reduce the error at the mobile receiver (rover), as seen in Figure 3.1. Using the difference in measurements of the base station and rover the dGPS is able to correct for many of the errors that the standard GPS suffers from.



**Figure 3. 1 Left- Group of students setting up a dGPS base station at the Hot Springs location. Right – Student using the rover to measure a survey point at the Hot Springs location.**

This system allows for corrections of the ionospheric, ephemeris, satellite clock, multi-path, and some numerical errors, because the base station is able to provide additional signals and the differences in signal can be used to remove many of the effects that cause error in the dGPS measurements of  $\pm 2\text{m}$  [13]. This is allowable error for all geophysical methods except gravity and GPR, however if we are in an open field and near the base station the errors are often even smaller and usually allowable for the methods that require the greatest accuracy.

### 3.3 Total Distance Measure (TDM)

Though many of the survey locations in Pagosa Springs were open fields that only required dGPS data to have a high enough degree of accuracy for the methods being performed, there were a few lines that required a higher degree of accuracy. The Total Distance Measure, TDM, was used to enhance and correct the GPS data further. The TDM is a device that measures the total distance between two points to  $\pm 0.001\text{m}$ . It also measures the angle between the line of the two points and the azimuthal angle, as well as, the angle from vertical in order to calculate the elevation change. Figure 3. 2 shows two students using the TDM to measure a point. One person operates the TDM and fires the laser while the other holds a special prism to reflect the laser back to take a measurement. This information can be applied to points that have a high standard deviation in the GPS data in order to correct for the dGPS errors. This tool was not utilized at every site, because it requires a lot time to collect and process and is sometimes hard to interpret.

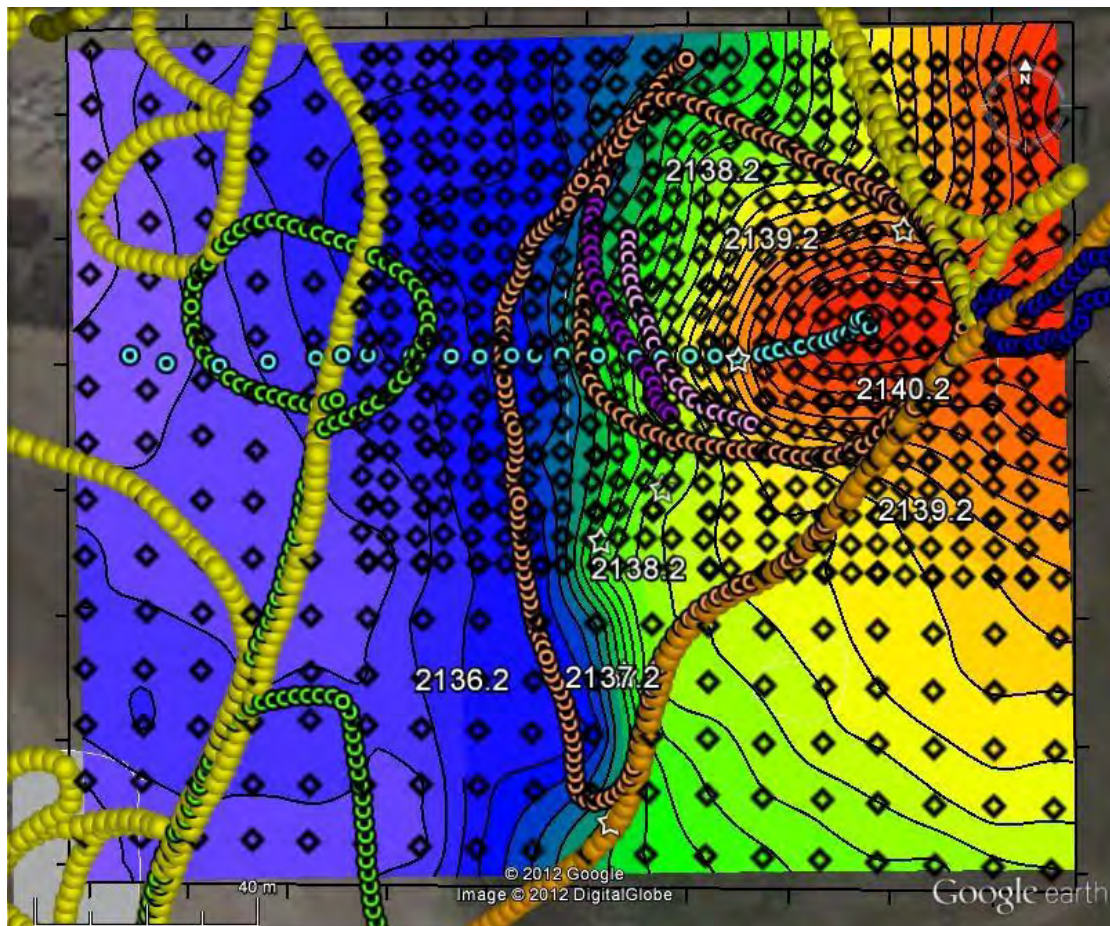


Figure 3. 2 Students surveying a location on the Northern HS hammer seismic line using the TDM.



### 3.4 Surfer and Google Earth

The GIS software used to enhance and plot the survey locations was Surfer and Google Earth. Surfer was used for its coordinate transform capabilities and to make digital depth models (DDMs). Google Earth was used to plot GPS data, the satellite images were also used to make maps to assist in interpretation, and make the maps for this report. Surfer was able to convert from one coordinate system to another just by loading a spread sheet or comma separated variables (csv) file and denoting the coordinates it was in and what coordinates to convert to. In this case the coordinates were mostly surveyed in WGS84UTM N13, so anything that was not surveyed using this coordinate system needed to be converted. Latitude and longitude were also converted to allow the data to be plotted in Google Earth. Surfer also has software preprogramed to create an interpolated DDMs model. Surfer performs a kriging interpolation of the elevation in the data. This process interpolates a grid from data values using their standard deviation to fill in the gaps. This was required for the Zen Garden to get a finely spaced grid that GPR and gravity used. Google Earth was used to plot the data on the satellite images to make our maps. Google Earth is free software that allows individuals to interactively navigate the maps, while being an easy medium to create the maps. It was used to plot the GPS data, to point out important points during interpretation, and to generate maps for this report. Below is an example map used for the interpretation of the Zen Garden.



**Figure 3. 3 Google Earth example map of Zen Garden survey location, a map used as a reference in processing and analysing the student site.**

In Figure 3. 3, each colour and symbol is used to denote a different feature noted at the surface of the Zen Garden. The black diamonds show the station locations, and the color gradient map in the background is the contour map of the area with higher elevations appearing as red and lower elevations appearing as blue. This allows an individual analysing the data to see where in the survey line major surficial features or other obstacles were crossed. This lets the interpretations ignore the clutter of the image above and only look at features that appear to be subsurface and therefore far more intriguing in a subsurface survey.

### 3.5 Conclusions

Surveying serves as a vital tool in the processing and interpretation of all the geophysics methods. Errors that occur in the GPS data continue through all of the other geophysical methods that used the GPS data in their data processing, making its accuracy essential. With the tools used to survey, the accuracy of surveying is above the minimum standards of the geophysical methods used allowing for more accurate geophysical results.

# 4. Deep Seismic

---

## 4.1 Introduction

The seismic method uses vibrational energy propagating through the Earth to create an image of the subsurface. The source of this energy can be either artificially generated or come from natural events such as earthquakes. The nature of the energy source provides a control on the depth of investigation of a seismic survey; shallow seismic sources like weight drops or hammer strikes allow imaging on the order of tens of meters, deep seismic sources like Vibroseis, marine airguns or dynamite allow us to image on the scale of tens of kilometers, whilst earthquakes permit the imaging of Earth's core.

Vibrational energy propagates through the Earth as various wave types, momentarily displacing particles from their resting position and transferring energy to immediate neighbors. Whilst more exotic types are possible, the waves are mainly compressional (longitudinal “p-waves”), shear (transverse “s-waves”) or Rayleigh (surface). Critically, all modes of propagation obey fundamental principles of wave theory and, therefore, undergo phenomena such as reflection, refraction and diffraction. These events occur where there are changes in rock properties known as acoustic impedance. A change in rock type, i.e. density, leads to a change in acoustic impedance and results in some of the incident energy being reflected back towards the surface. Thus, by measuring how long it takes for a wave to leave a source, travel into the subsurface and be reflected back to a receiver, we can begin to learn about the positions of geological boundaries beneath the surface.

### 4.1.1 Wave Theory

As discussed, energy travels through the subsurface as a wave and must obey well understood physical laws. The two wave effects of most use are reflection and refraction, each giving a different piece of information about the rocks below.

When a wave is incident on an interface between two different media, for example two rock types, some energy is reflected and what remains travels into the second medium, perhaps to be reflected at a deeper interface. The property which governs the occurrence of a reflection

is known as the acoustic impedance of a rock and is the product of its density and p-wave velocity. The travel time and amplitude of the reflected waves may then be recorded at the surface by receivers known as geophones on land and hydrophones in marine surveys. The travel time provides information about the position of a change in rock type, whilst the amplitude of the reflection can give us information about the rock types involved as higher amplitudes indicate larger contrasts in acoustic impedance.

During a reflection, the angle of incidence of an incoming wave on the interface equals the angle of reflection. However, if the angle of incidence equals a critical angle, the wave is instead refracted and travels along the interface before being diverted towards the surface as a head wave. The refracted wave travels along the interface at the velocity of a wave travelling purely in the second medium and this may be calculated as the inverse of the slope of the first breaks of a shot record. Thus, refractions are a useful tool to create a velocity model of the near subsurface and to calculate time shifts for static corrections due to surface topography.

Not only is the type of wave important, but also the frequency. Subsurface resolution is approximately equal to one quarter of the wavelength; hence higher frequencies allow imaging of smaller structures. However, high frequencies are attenuated faster than low frequencies and thereby, reducing the depth of investigation. Therefore, the depth and size of any subsurface target are important considerations when selecting which type of seismic survey to conduct.

#### **4.1.2 Deep Seismic**

A 2D deep seismic survey is a single line of acquisition that creates a two dimensional image of the subsurface. It is considered a deep survey because the depth of investigation of a 2D seismic line is approximately equal to the maximum source receiver offset, which commonly spans for several kilometers. Deep seismic data is acquired to help determine subsurface stratigraphy and identify structures such as faults. Over the course of this field camp, two 2D seismic lines were acquired with the aim of imaging the 8 mile Mesa Fault, smaller faults, stratigraphy and better assessing any impact these structures may have on the occurrence of the local geothermal system.

### 4.1.3 2D Seismic Method

Two dimensional land seismic surveys are acquired by laying many geophones in a single straight line. Travel times from source to receiver are then recorded and later processed to create a full image of the subsurface beneath the acquisition line. The final image is then interpreted to understand the geology below.

## 4.2 Survey Design

Guiding the practice of designing a seismic survey is the objective of imaging the selected subsurface target in the most economic and time efficient way. The type of acquisition designed and carried out in Pagosa was 2D land seismic. In land seismic acquisition a shot is fired from a seismic source as a p-wave and the down going energy is reflected on boundaries between lithological layers and recorded at receiver stations on the surface by geophones. The geophone stations are positioned along a line. This set up is illustrated in Figure 4. 1 : Land Seismic Acquisition Set Up. When the source is in line with a receiver, a 2D profile through the earth is generated.

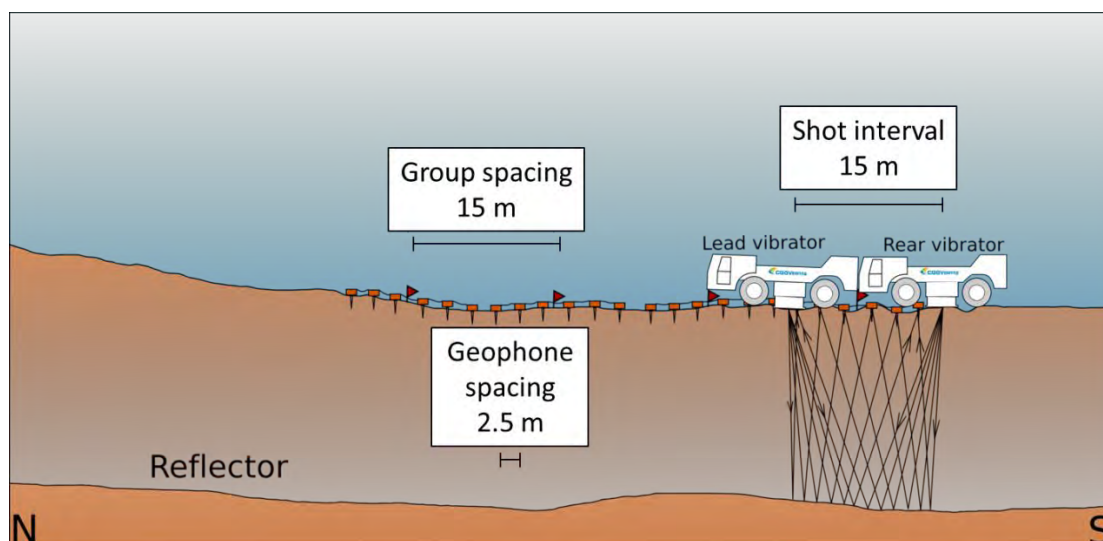


Figure 4. 1 : Land Seismic Acquisition Set Up

The overall aim of both deep seismic survey sites was to create high fold interpreted depth sections to image the structural geology of the Pagosa area. We designed and acquired 2D seismic data at two separate seismic lines; Stevens Airport and at the Barn 3 location south of Pagosa as shown in Figure 4. 2. Both land surveys were acquired in fields, close to populated communities and through private property hence operations were only conducted in daylight. The parameters of these lines are shown in Table 4. 1.



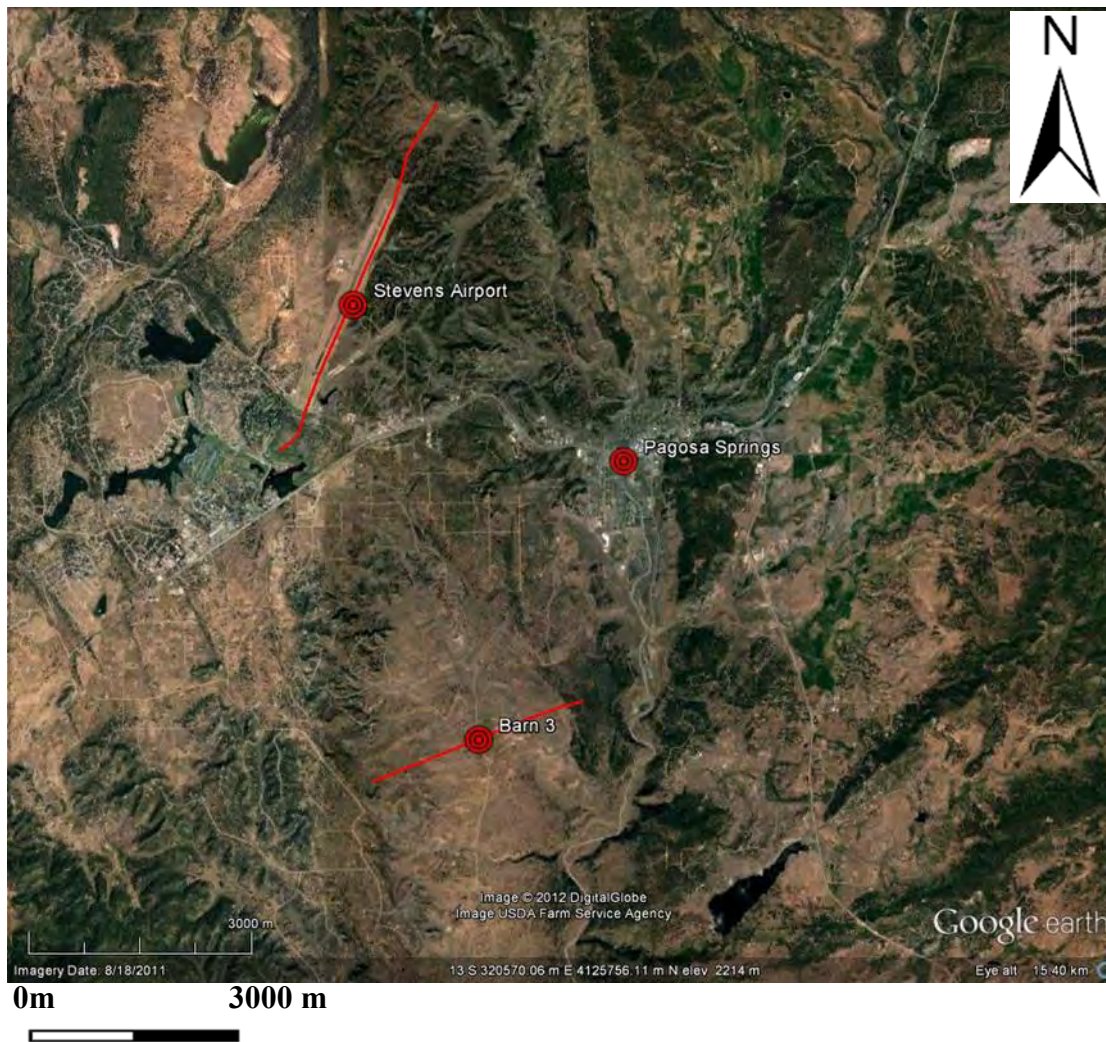


Figure 4. 2: Satellite view of Pagosa Springs Region. Red lines indicated location of seismic survey lines.

Table 4. 1 : Seismic Line's Parameters

Line name	Shooting direction	Total receiver stations	Total shot stations	Receiver station numbers	Shot station numbers	Line length
Stevens Airport	23° North East	342	213	954:1295	1003:1217	5.1 km
Barn 3	68° North East	223	173	1:223	3:144 147:163 168:190	3.3 km

#### 4.2.1 Stevens Airport: 2D Seismic Line

This section will describe the location and survey design for the airport line. The airport seismic line ran parallel to the runway as shown in Figure 4. 3: Satellite view of Steven

Airport Seismic Line. The red line indicates the extend of the survey line.. The line was a distance of 235 ft away from the centre of the runway. This distance was decided upon because the airport regulations required a region of safety that was prohibited to access. This region extended 200 ft from the centre of the runway. Additionally, approximately 260 ft from the centre of the runway there is a sewage line and steep banks. The Vibroseis trucks preferably acquire over a horizontal surface, avoiding crossing and damaging buried pipelines as well as steep gradients. The airport line was picked because we were given permits to run Vibroseis trucks on the land and place geophones. However, we primarily picked the line based on geological features in the regions. We knew where the 8 mile Mesa Fault was located and we made sure our line ran approximately perpendicular to the strike of the fault to enable the imaging of the fault correctly. Additionally, the layers in the subsurface around that region were dipping northeast. Thus, our line ran perpendicular to the strike of the layers.



Figure 4. 3: Satellite view of Steven Airport Seismic Line. The red line indicates the extend of the survey line.



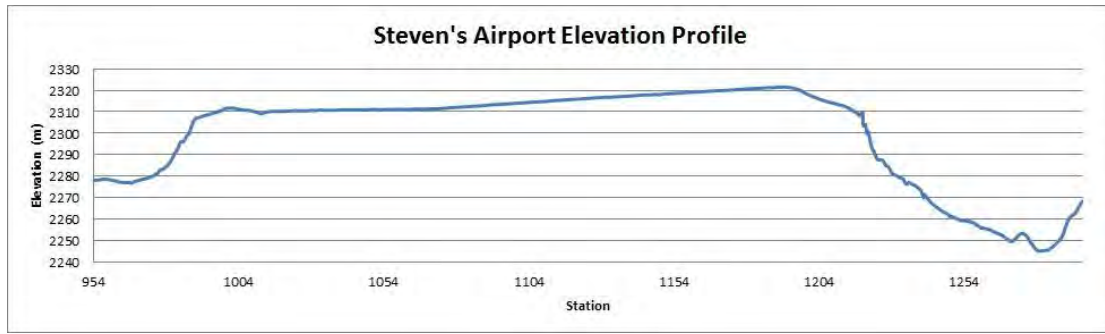


Figure 4. 4 : Elevation profile for Stevens Airport survey line

The line was 5.1 km long and ran southwest to north east. It began at flag 954 and ended at flag 1295 as seen in Figure 4. 4 : Elevation profile for Stevens Airport survey line. These flags were spaced 15 m apart and represented the stations. The line extends both north and south of the airport boundary. The southern section of the line runs through a golf course and a residential estate. The north end of the line runs through privately owned ranches. For both ends, we obtained permits to place geophones but not to run vibroseis trucks. The line consists of 342 group stations separated by 15 m each containing 6 geophones 2.5 m apart recording for all shots acquired. The 6 geophones act as an array cancelling horizontal energy (noise) and reinforcing vertical energy (signal). Each geophone has a natural recording frequency of 10 Hz. The Vibroseis trucks ran only within the boundaries of the airport which was ideal because the surface was flat. The part of the line that the Vibroseis trucks shot from was 3.2 km long and ran from station 1003 to station 1217 (station 1000 being the first station within the airport boundary). The two Vibroseis trucks were utilized as one source by having them drive behind one another. Both trucks swept from low to high frequencies (8 to 80 Hz) for 10 s. The geophones listened for 8s. GPS coordinates and elevation were recorded at each station for geometry during processing. As the maximum offset of the line is 5 km, a rough estimate of depth of recoverable energy is 5 km. Details of the acquisition parameters are presented in Table 4. 2: Acquisition parameters for Stevens Airport line

Table 4. 2: Acquisition parameters for Stevens Airport line

<b>Line length</b>	5.1 km
<b>Orientation</b>	23° north east
<b>Angle to fault plane</b>	~ 90°
<b>Group spacing</b>	15 m
<b>Station numbers</b>	954 - 1295 south west to north east



<b>Source</b>	vibroiseis
<b>Sweep type</b>	10 up sweeps of 8 - 80 Hz
<b>Sweep length</b>	10 s
<b>Record length</b>	8 s
<b>Shot spacing</b>	15 m
<b>Spread</b>	Asymmetric split spread
<b>Max offset</b>	4.4km
<b>Fold</b>	213

#### 4.2.2 Barn 3: 2D Seismic Line

During the field camp a number of locations were considered for the acquisition of a second 2D seismic line. Permits for access to the xx ranch south of Pagosa were obtained and several lines were considered within the ranch boundaries. The objective of this second line was to better image the 8 mile Mesa Fault in the Pagosa area as it may be poorly imaged on the airport line. The fault is found within the north east of the ranch suggesting that it can be imaged by 2D acquisition. Figure 4. 6 illustrates the topography and landmarks associated with this survey. The line runs from station 1 to 223 south west to north east and is bisected by the Colorado County Road 500.

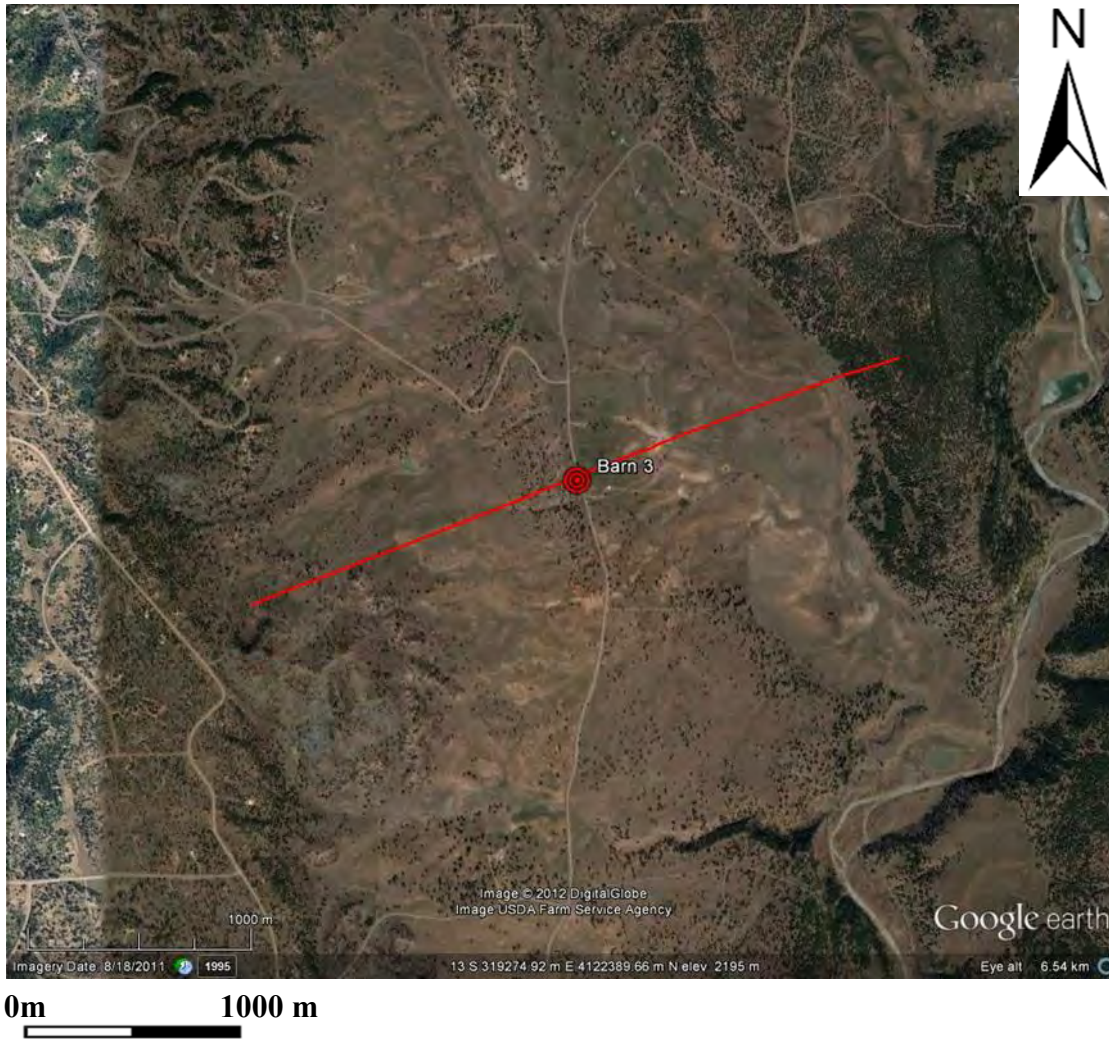


Figure 4. 5 : Satellite view of Barn 3 Seismic Line. The red line indicates the extend of the survey line.

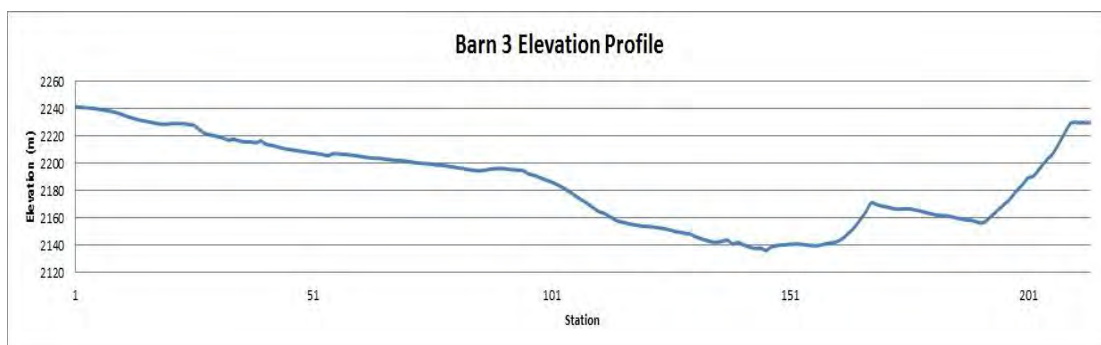


Figure 4. 6: Elevation Profile of the Barn 3 survey line

The geology associated with the line is consistent with the region as described in Section 2. The line itself runs close to perpendicular to the fault,  $80^{\circ}$ , which is required to retrieve a well-defined fault in the processed line. From the geological map the seismic line lies over

and perpendicular to the Stinking Springs Anticline (Dakota Sandstone) and the Mancos shale to the north east and south west.

There were few obstacles and environmental issues to consider when designing the survey. However, as the ranch was home to cattle, they were arranged to be away from the survey area at the times of acquisition. Two significant obstacles on the path of the line were a small lake and high ridge as shown in Figure 4. 5 : Satellite view of Barn 3 Seismic Line. The red line indicates the extend of the survey line..

The line was acquired using the same acquisition parameters as the airport line. These parameters are shown in Figure 4.3. The line consists of 223 group stations separated by 15 m each containing 6 geophones 2.5 m apart recording for all shots acquired. Where the fault and tree line begins at the north east end of the line the trucks were not able to shoot. GPS coordinates and elevation were recorded at each station for geometry during processing. As the maximum offset of the line is 3.3 km, a rough estimate of depth of recoverable energy is approximately 3.3 km.

**Table 4. 3:Acquisition parameters for Barn 3 seismic line**

<b>Line length</b>	3.3 km
<b>Orientation</b>	69° north east
<b>Angle to fault plane</b>	80°
<b>Group spacing</b>	15 m
<b>Station numbers</b>	1 - 223 south west to north east
<b>Source</b>	vibroseis
<b>Sweep type</b>	10 up sweeps of 8 - 80 Hz
<b>Sweep length</b>	10 s
<b>Record length</b>	8 s
<b>Shot spacing</b>	15 m
<b>Spread</b>	Asymmetric split spread
<b>Min/max offset</b>	3.3km
<b>Fold</b>	173

### 4.3 Processing

Seismic data processing was carried out on the ProMAX package, both at the Colorado School of Mines and at the Denver offices of ION GX Technologies. Processing involves a

wide range of techniques to correct for several physical effects and create an image which is faithful to the subsurface.

The processing sequence which was carried out for both the Stevens Field Airport line and the Barn 3 line are shown in

Figure 4. 7: Seismic processing sequence for Stevens Airport line and Barn 3 line. A more detailed description of the seismic data processing can be found in the seismic Appendix.

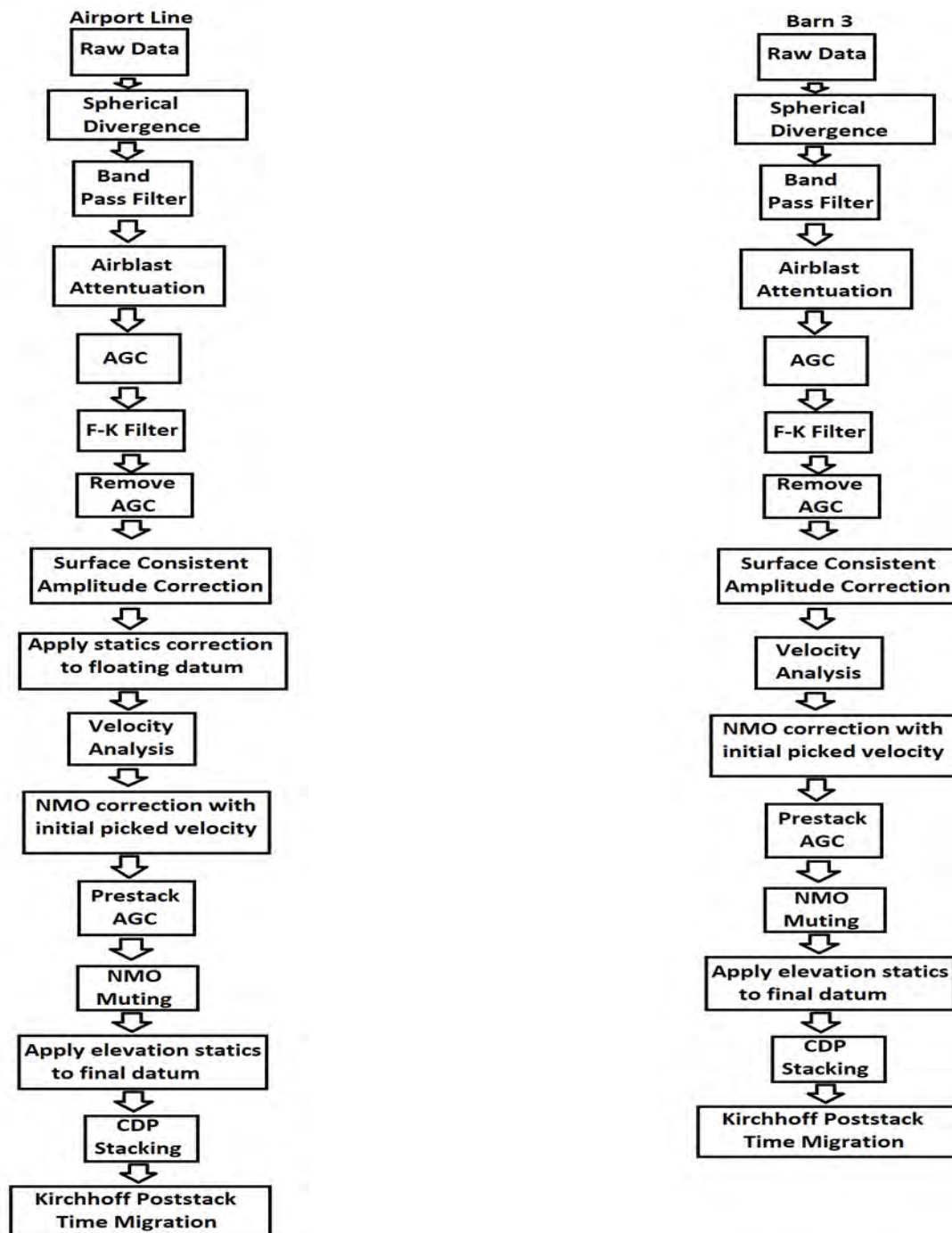


Figure 4. 7: Seismic processing sequence for Stevens Airport line and Barn 3 line

The final processed images are shown below as Figure 4. 8: Final Stevens Aiport Seismic Line migrated image without AGC and Figure 4. 9: Final Barn 3 Seismic Line migrated image without AGC Their interpretation is discussed in Section 4.6.

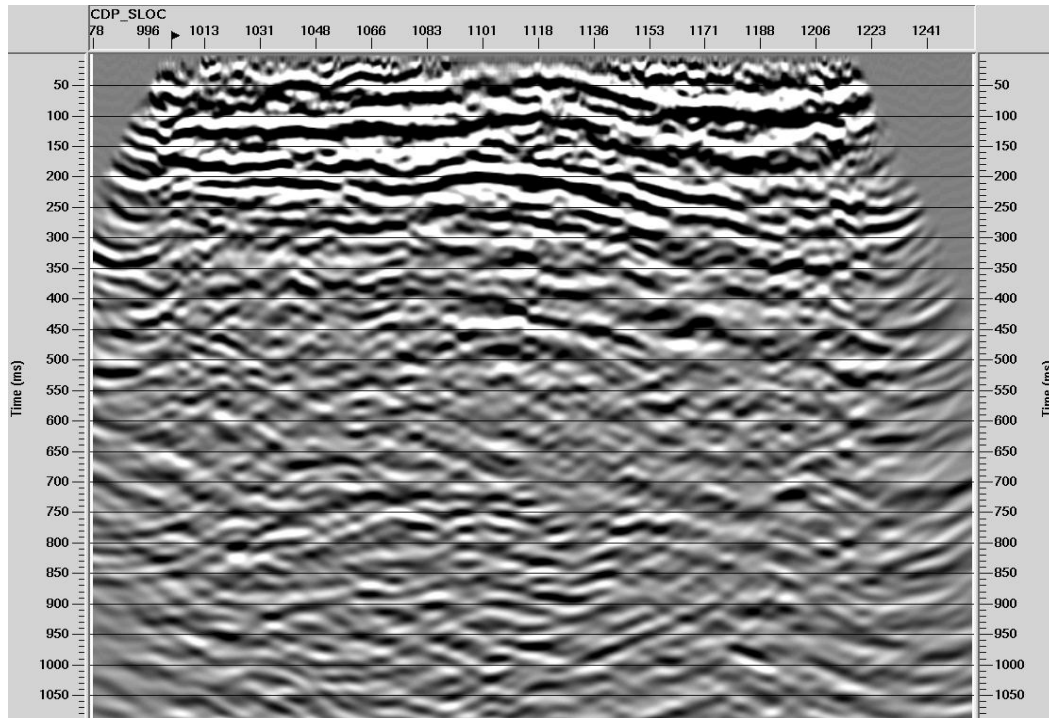


Figure 4. 8: Final Stevens Aiport Seismic Line migrated image without AGC



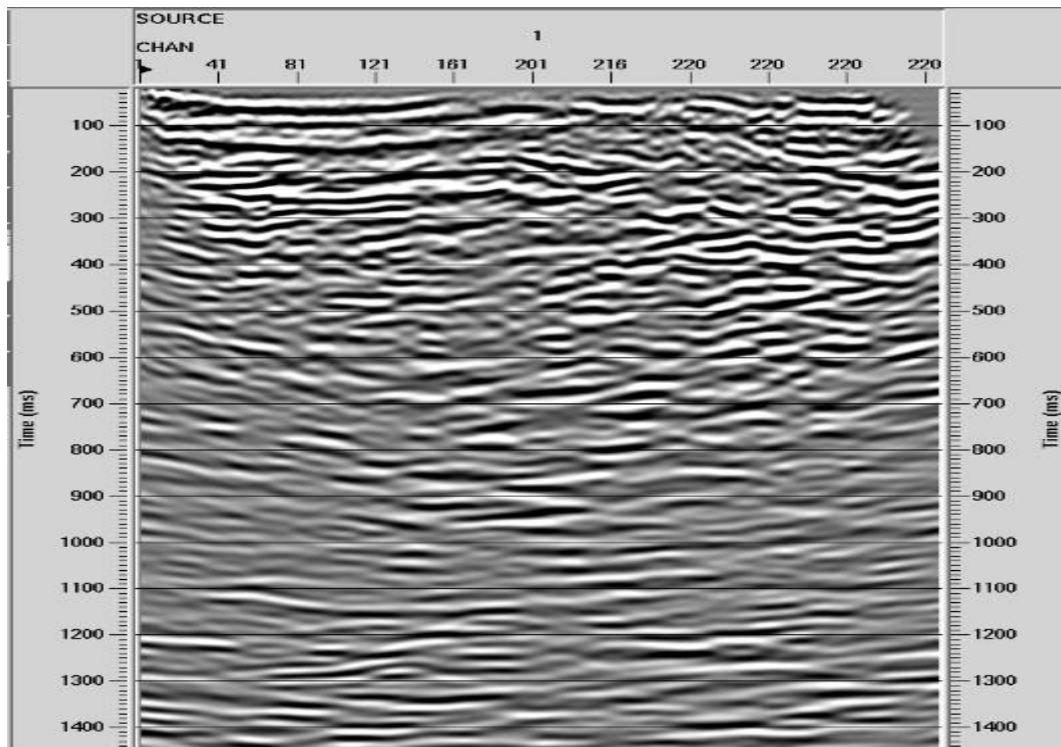


Figure 4. 9: Final Barn 3 Seismic Line migrated image without AGC

#### 4.4 Uncertainties/Errors

There is no definitive answer when it comes to seismic interpretation. Multiple geophysicists can look at the exact same seismic line and come up with different conclusions. Thus, there are always uncertainties in interpreting seismic data.

Seismic processing does produce one unique seismic line. The final image depends on the parameters chosen during processing and the accuracy of velocity and first time arrival picking.

The problems that were encountered during processing of the seismic data included reducing the noise, dealing with statics and velocity picking.

Noise is always an issue that is present in seismic processing. One tries to handle the noise as best as they can. However, even in the final processed image, there is still noise present that could not be filtered out without losing data.

Statics is another source of possible error in land seismic. One first has to interactively pick first arrivals times which can lead to human errors. If the noise is really bad for a survey or shot, or there are large elevation changes, the first arrival time picking can become a challenging task to complete. We had this problem with Barn 3 line. Thus, there is quite a high level of uncertainty/error in our final image for the Barn 3 line.

Another source of possible error is velocity picking. One has to interactively pick velocities as well. Thus, this can be a cause of human error. The change in final images can be quite dramatic depending on the velocities one picked. This was clearly visible during our processing stages where people processing the data with very similar or even identical parameters were getting different images because they picked slightly different velocities.

Finally, other sources of error that could impact our final results include slight geometry errors which were mostly corrected for during processing. However, slight offsets most likely still remain. Long period multiples are be attenuated during CDP stacking and short period multiples or reverberations are targeted by gapped deconvolution. However, they may still appear and thus one should be careful interpreting a section. One does not want to interpret a multiple as a reflection for they do not represent a physical surface.

In conclusion, there are a number of sources of uncertainty and error in our data. One cannot quantify the amount of error present in the data. However, due to the amount of interactive steps required during seismic processing, one knows there will be human error present in the data. Thus, one just has to accept that there will be errors present in the data.

## 4.5 Near surface model

Hammer, GPR, first break picks.

The velocity of the near surface layer is very important during seismic processing, particularly when computing offsets or dealing with ground roll. Above the rock layers of the subsurface sits the “weathered layer”; it is usually poorly consolidated and of a very low velocity due to erosion. Information about the weathered layer including velocity, depth and structure was obtained during this field camp from both hammer seismic and GPR techniques.



## 4.6 Interpretations

We know from our geologic cross-section and well log data the approximate depth and velocity of the geological layers in the subsurface of the Stevens airport. At Stevens Airport, the Mancos shale ranges from a thickness of 0m up to 170 m thick and has a velocity of approximately 3.74 km/s. After the Mancos shale comes the Dakota sandstone formation, the Dakota is approximately 70 m thick throughout the Stevens airport line and has a velocity of approximately 3.53 km/s. We however do not have well log data in Pagosa Springs of the Morrison and Entrada/Wananka formation. Thus, we do not have the velocity information for these layers. We do know the thicknesses of these formations. The Morrison formation is approximately 230 m thick and the Entrada/Wananka is approximately 50m thick. After these formations, one would hit the basement. Using this information, we can calculate when we would approximately expect to see the reflections of these layers. We predict to see a reflection representing the Mancos-Dakota boundary at a time of 0s up to 0.09s. We then would predict to see the Dakota-Morrison reflection at a time of approximately 0.04s up to 0.13s. We cannot make a prediction for the Morrison-Entrada/Wananka reflection because we do not know the velocity of the Morrison formation.

We also have information about the depths of the layers for the Barn 3 line. We assume the velocities are the same for the layers of Barn 3 as for the Stevens Airport line. On the barn 3 geologic cross-section, there is an anticline present named the Stinking Springs anticline. This anticline makes the depths of the layers vary throughout the region. Thus, we will make an approximation of the depths to get a rough idea at what time to expect the reflections to occur. The bottom of the Mancos shale layer is at a depth of approximately 0-20 m. The Dakota sandstone layer is approximately 70 m thick thus located at a depth of 70 m - 90 m. The Morrison formation is approximately 230 m thick and we would expect the bottom of this layer to be at approximately a depth of 300 m - 320 m. We then have the Entrada/Wananka layer that is approximately 50 m thick thus putting it at a depth of approximately 350 m-370 m. Using the same velocities as for the Stevens Airport line, we predict to see a reflection representing the Mancos-Dakota boundary at a time of 0 s up to .01 s. We then would predict to see the Dakota-Morrison reflection at a time of approximately .04 s up to .05 s. Again, we cannot make a prediction for the Morrison-Entrada/Wananka reflection because we do not know the velocity of the Morrison formation. We also do not

have the velocity for the Entrada/Wananka formation so we cannot make a prediction as to what time we would expect to see the basement reflection.

#### 4.6.1 Interpretation: Stevens Airport Seismic Line

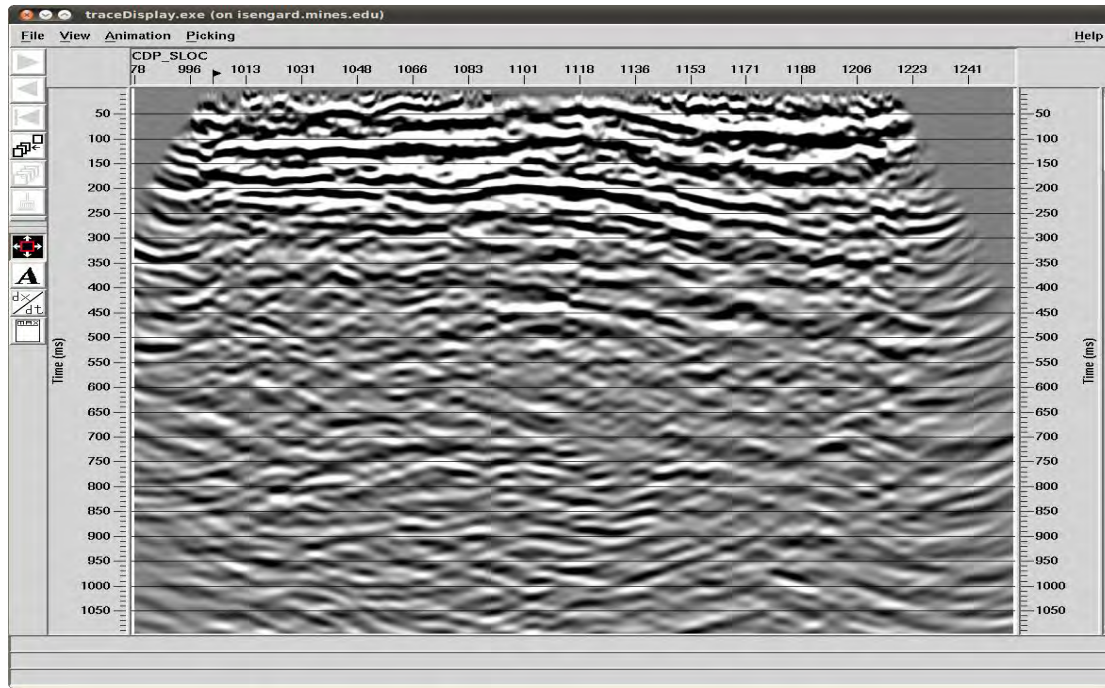


Figure 4.10: Stevens Airport Seismic Line migrated image

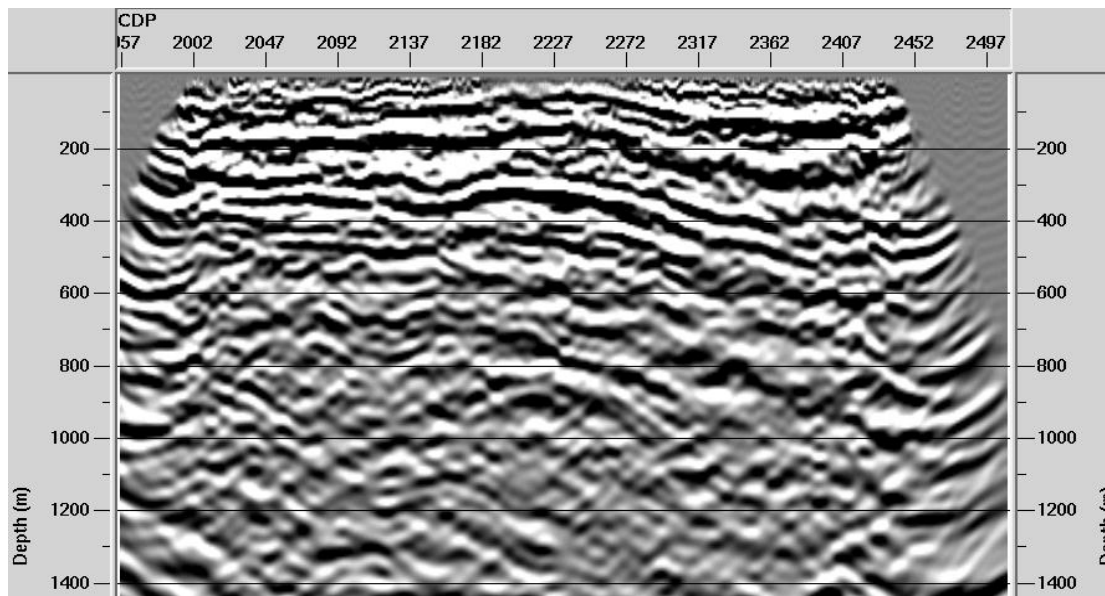


Figure 4.11: Stevens Airport migrated image after depth conversion

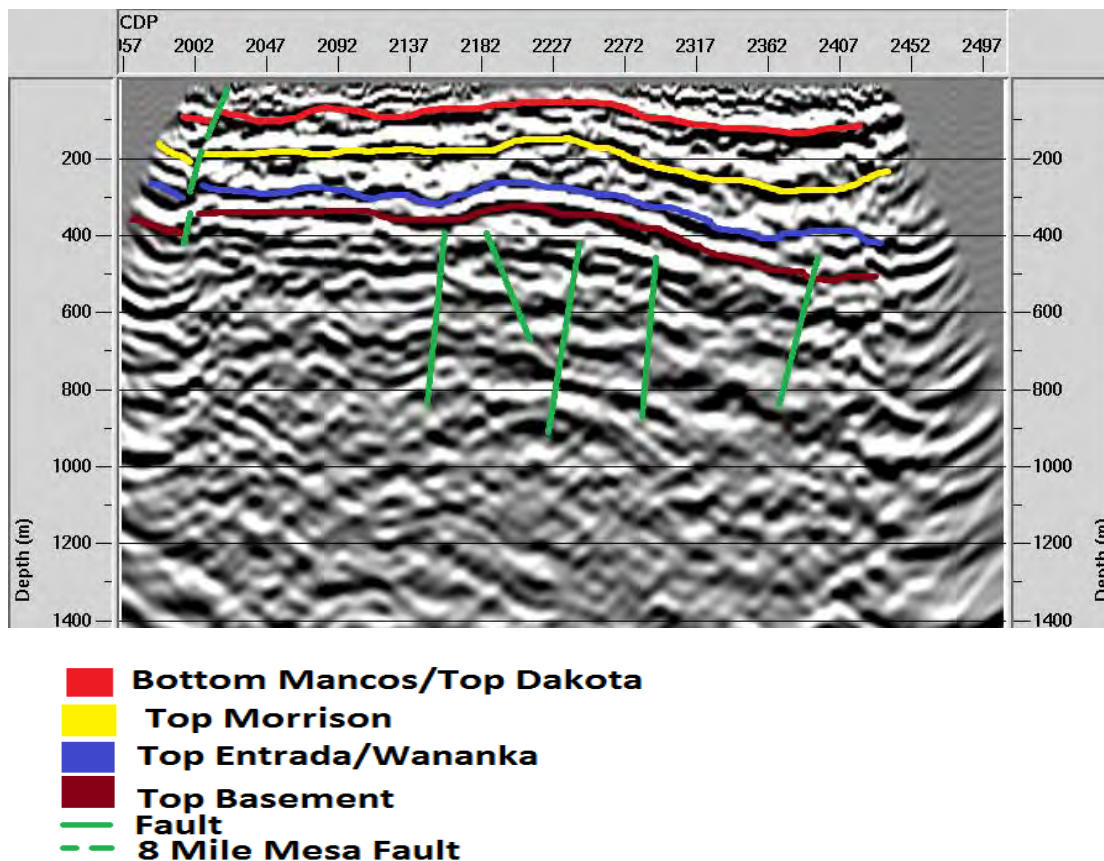


Figure 4. 12: Interpretation of Stevens Airport Seismic Line

The geological information available to us prior to the survey indicated a normal fault at the south end of the line. It was also indicated that the crystalline basement could be highly fractured. Whilst the fault would be detectable in another survey, the design of this particular survey was not optimal for this purpose. This is because the fault sat south of the first source position and very close to the end of the geophone line. Consequently, there is a very low fold recovery where we expect to see the fault and thus this area of the section is not reliable for structural interpretation. This fact is highlighted by the presence of migration smiles at both extremes of the image, indicating that an interpretation here would not be entirely reliable. We would also expect the layers in the subsurface to be gently dipping towards the north east with an angle of approximately 8 degrees.

Figure 4. 10 shows the time migrated image for the Stevens Airport Seismic line. We then did a time to depth conversion explained in the seismic Appendix to get Figure 4. 11. We interpreted this figure. One can see our interpretation for the Stevens airport line in Figure 4. 12.

Our interpretation correlates to our geologic cross section for the airport and our prediction for the depth of the layers. The Mancos, Dakota, Morrison, Entrada/Wananka and the basement layers are approximately at the depth that we predicted in the previous section. One can also see that the layers are gently dipping. They are not consistently dipping 8 degrees but this is caused by not being able to do refraction statics correction. This correction would probably remove this inconsistency. The basement is highly fractured with faults which is what we would have expected to see.

As discussed, the survey is not designed optimally for imaging the 8 Mile Mesa Fault to the south of the line. However, as we know a fault to be present there from our study of the local geology and we see some circumstantial evidence on the seismic section, we have decided to include it on the interpreted section as a dashed line.

In conclusion, the migrated image of the Stevens Airport Seismic line correlates to our geologic interpretation of the region and the reflections correspond to our predictions of the depth we would expect to see them occur. Even though there are still errors present in the data, overall a good job was done processing the data with the allowed time.



#### 4.6.2 Interpretation: Barn 3 Seismic Line

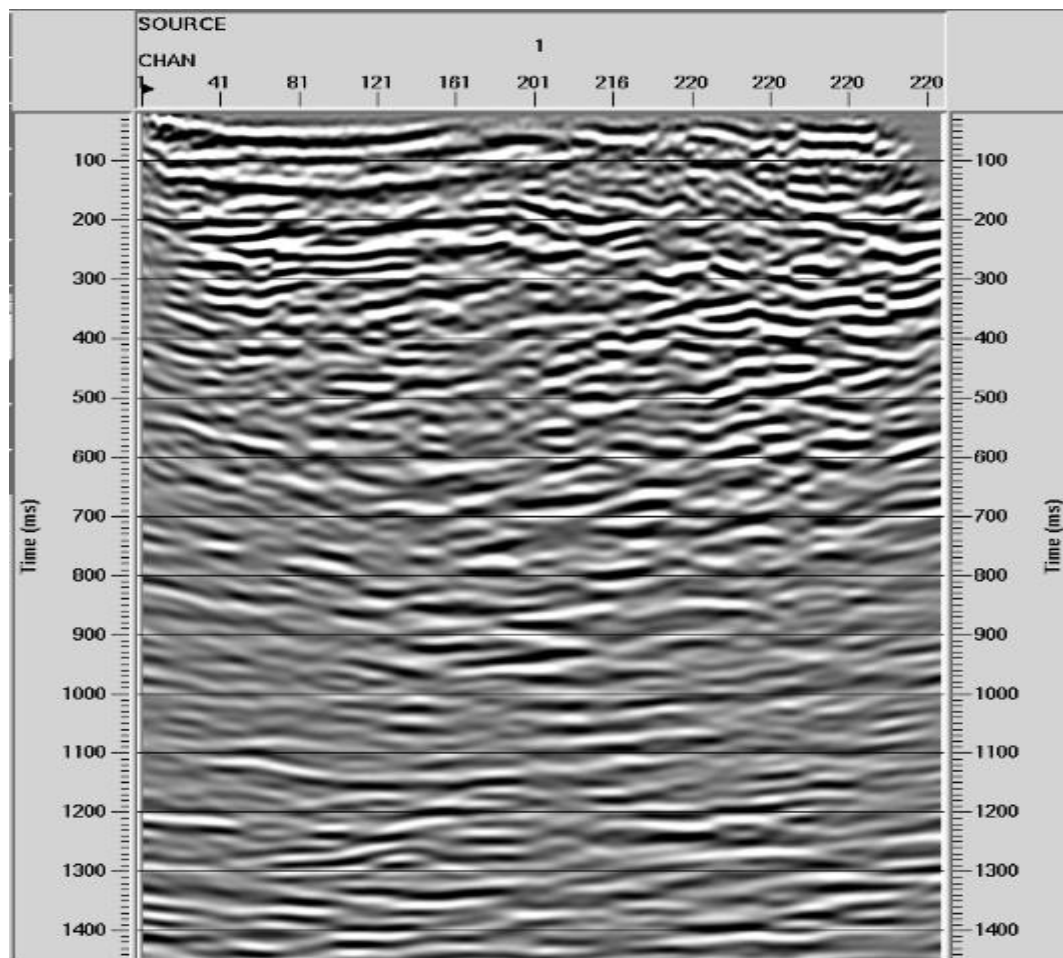


Figure 4. 13: Barn 3 seismic line migrated image

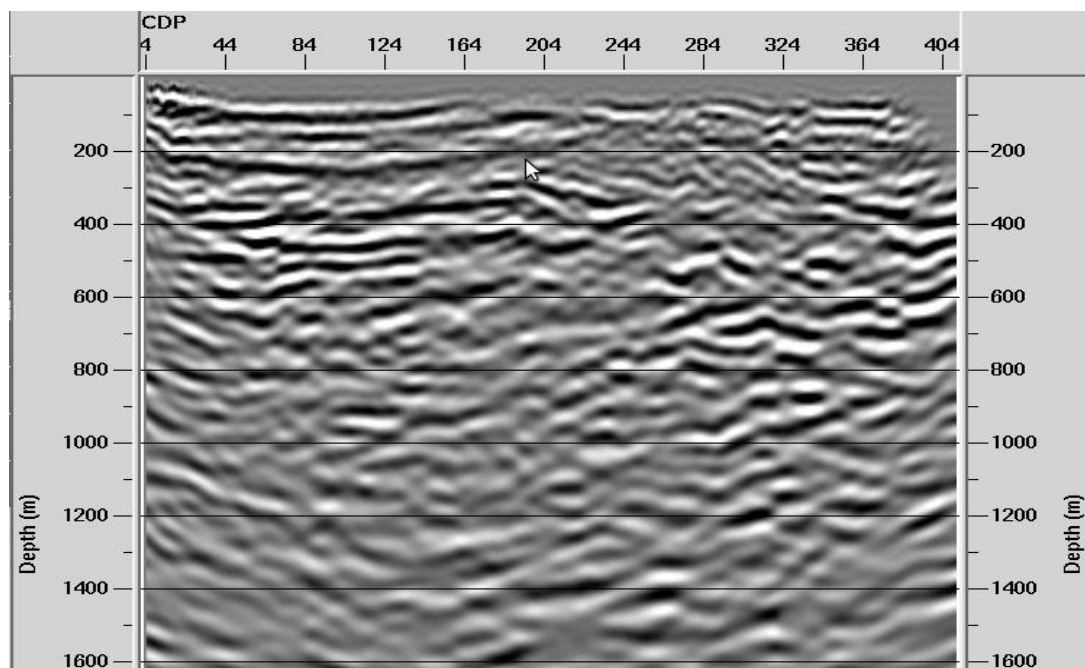


Figure 4. 14: Barn 3 seismic line migrated image after depth conversion

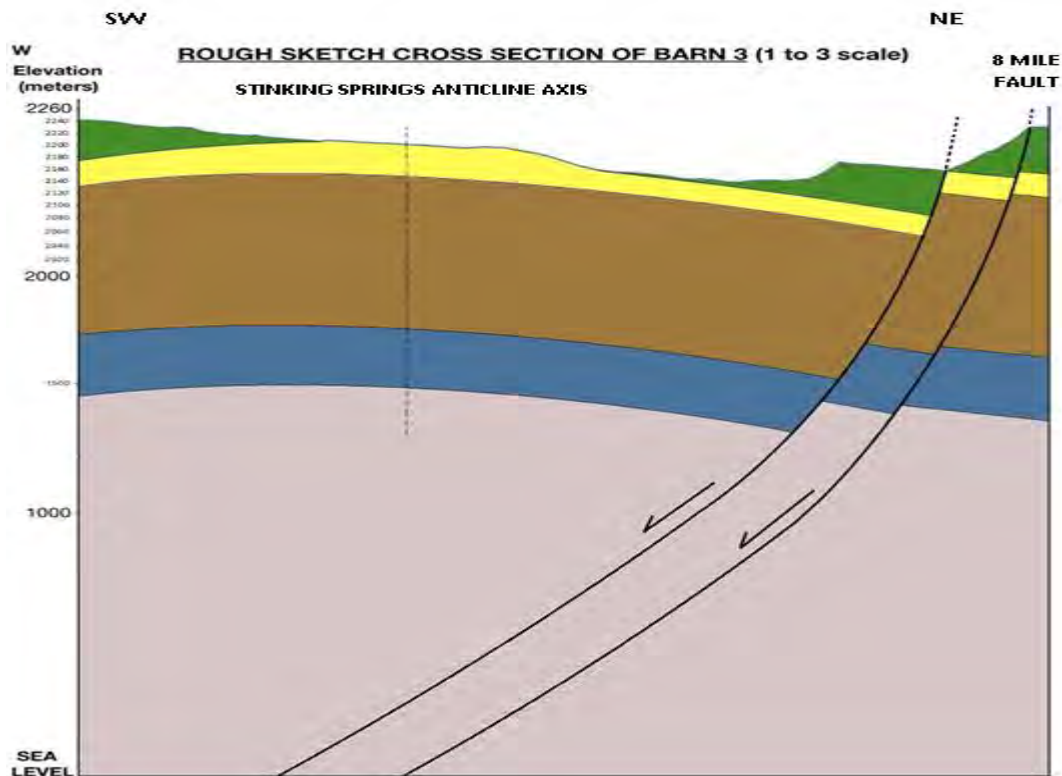


Figure 4. 15: Rough Geologic Cross Section of Barn 3 line

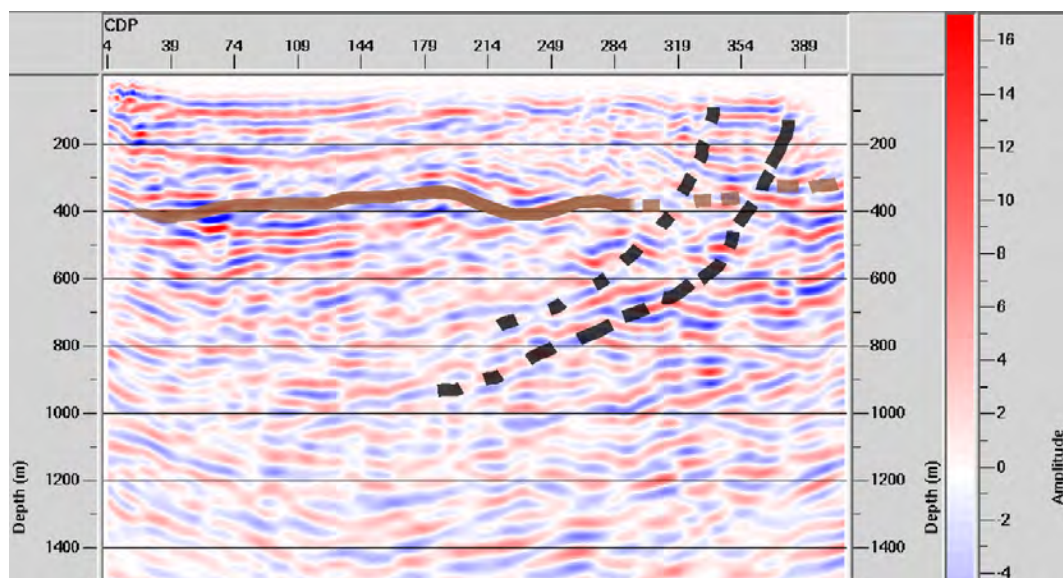


Figure 4. 16: Interpretation of migrated image with time converted to Depth.

Barn 3 seismic line has significant elevation changes. Having a steep hill on the East side of the line, which is the right side of the figures shown above, where the fault is located and a gently dipping hill on the West side which is the left side of the figures shown above. This elevation profile can be seen in Figure 4. 6: Elevation Profile of the Barn 3 survey line.



Although we were not able to do an accurate interpretation of the data due to issues with the geometric information provided by ION GX Technologies, we made a rough interpretation which is shown in Figure 4. 16 which is based on the geologic cross section of the region shown in Figure 4. 15. In our interpreted image we have indicated with a brown line where we believe to see the basement. On the right of the figure, we have drawn where we expect the faults to be based on our geologic cross section. It is important to reiterate that this is a rough interpretation. This interpretation is based on the geologic cross section but is much harder to actually see in the migrated image itself. The reason this isn't an accurate interpretation is because of issues such as elevation statics, refraction statics and residual statics.

Elevation statics correction updates the apparent arrival times. It does so by applying the major elevation change of survey topography. Due to the rough elevation profile from the Barn 3 survey, elevation statics correction is an important and necessary process to correct for the general topography of the survey and the arrival times of the seismic events.

Refraction statics correction is the method to control the refraction of a heterogeneous layer and arrival time errors from the subsurface. In general, sediment layers deposited on the top of target area will deviate the correct arrival times of the survey. Therefore, if we ignore the effect of the sediment refraction, we will acquire the wrong data for further seismic processing such as normal move out correction, CDP stacking, and migration. This can lead to possible errors in interpreting the geological structures in the subsurface. Finally, residual statics correction time shifts the traces to correlate with each other as a final statics correction.

In conclusion, we cannot accurately interpret the migrated section from Barn 3 survey, shown in Figure 4. 14, because we have not included the statics corrections which are very important due to the rough topography of the survey line. However, we did a rough interpretation which is shown in Figure 4. 16.

## **4.7 Conclusions and discussions**

The deep seismic method allowed us to image very deep into the Earth's subsurface, more so than any other geophysical method employed during our field camp. Even though there were

a large variety of errors possible, the processed deep seismic data was accurate enough to correlate to our prediction. Our interpretation of the Stevens Airport seismic line ties in very well with the existing geologic model. The reflection boundaries occurred at the times we predicted using the geological cross section and well log data. However, the Barn 3 processed data could not be interpreted accurately because we were not able to apply statics to correct for the rough topography of the region.

# 5. Shallow Seismic

## 5.1 Introduction

The “layer cake” geological model involves an increase in compaction with greater depth, as older strata are squashed by overlying layers. This should give an increase in the velocity of acoustic waves for deeper layers, as seismic velocity increases with density. For shallow layers, the layer cake model regularly holds true, with hard rock overlain by weathered rock and unconsolidated sediments, enabling imaging of the underlying strata through seismic refraction surveys.

Refraction surveys start with a seismic source, such as a hammer strike or a weight drop, which generate acoustic waves in the subsurface. When the incident wave hits a deeper layer with a higher seismic velocity, they are usually reflected. When the incident wave hits the boundary at a critical angle, it is refracted along the top of the layer.

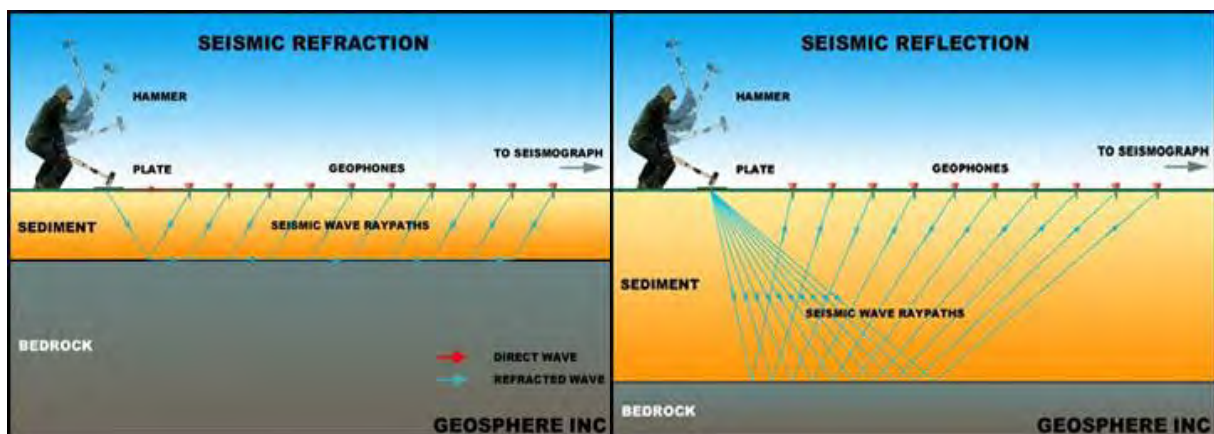


Figure 5. 1 Difference between refracted and reflected raypaths when they encounter a higher velocity layer in the subsurface. [14]

The refracted wave continually transmits energy to the surface; the velocity of the layer in which the refracted wave travels can be measured by placing receivers (geophones) at the surface, which detect acoustic waves transmitted from layers in the subsurface. By correlating the measured velocity of subsurface strata with geological information and knowledge of the typical velocities of rocks, it is possible to construct a model of the subsurface beneath a refraction survey.

## 5.2 Refraction survey sites

The choice of field sites to conduct the hammer seismic geophysical survey was dependent on the anomalous features thought to be present in the area. The survey locations were as follows:

- (1) Zen Garden: The Zen Garden location included two survey lines.

Line 1 was chosen with an N-S orientation with the first geophone placed on the south end of the line. It was 72 meters long. This line was a pilot study to check the data quality and acquisition system on the field. The main goal of this survey line was to help understand the background characteristics of the subsurface away from known fracture locations on the site.

Line 2 on the Zen Garden site was 96 meters long and was placed in an N-S orientation crossing the travertine fissure feature.

For both lines, the objectives were to characterize the primary wave-shear wave velocity ratio of the site including the fissure and travertine area which could indicate some velocity dependence on fractures in the subsurface.

- (2) A survey was conducted near the Barn 3 Deep Seismic line in two orientations; 48 meter lines running North-South and East-West. There were fractures present in this site, trending North-South. The aim of this survey was to identify any anisotropy in the velocity of the Dakota Sandstone at this location, as the N-S trending line ran in line with the fractures, and the E-W line ran perpendicular to them. The site was chosen for its flat surface topography and its proximity to an outcrop of the Dakota Sandstone, indicating that the sandstone was near the surface and therefore more easily imaged.

- (3) Warm Springs: A 48 meter North-South line was chosen at the warm springs site, the purpose of which was to further characterize the Dakota Sandstone horizon, and to image any potential anomalies that may have been associated with the warm springs.

Maps of the site areas are given in Appendix B.1.



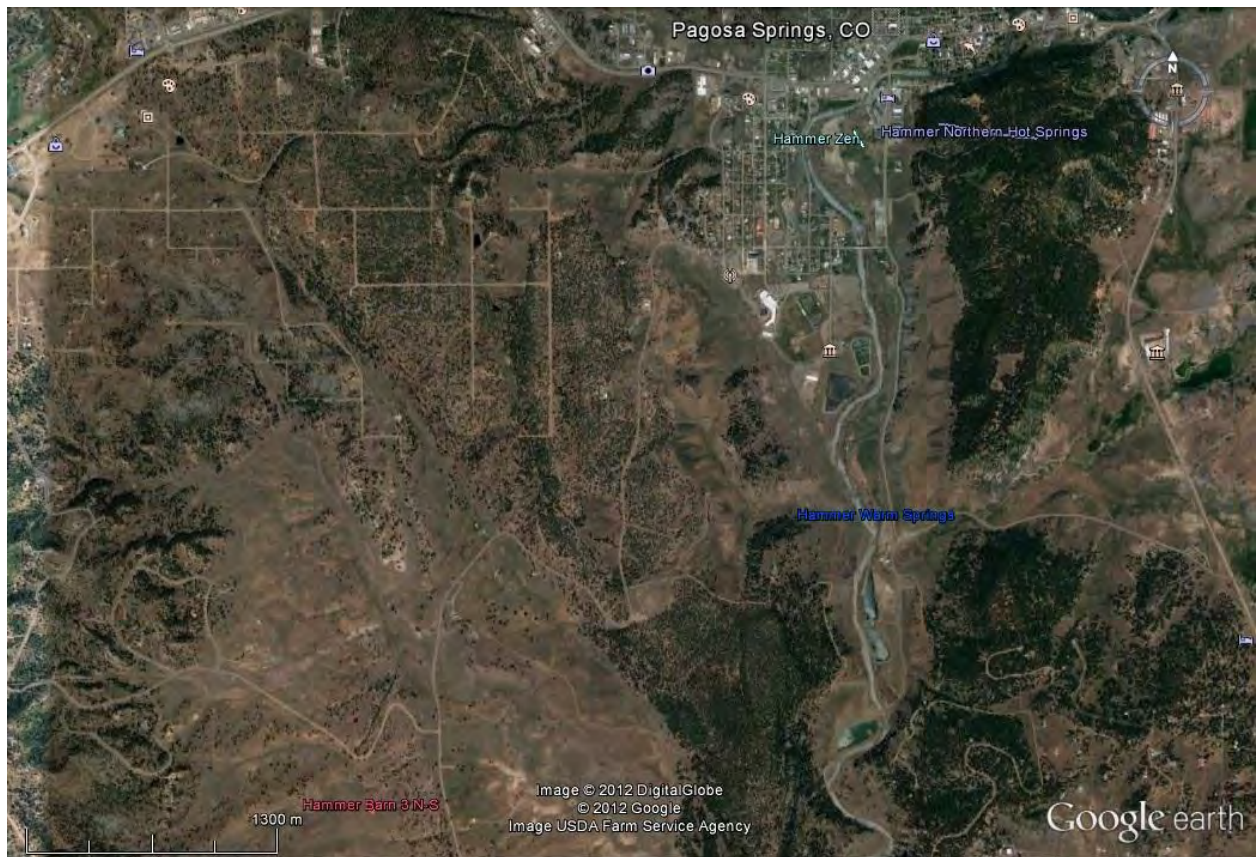


Figure 5. 2: Regional map of the Pagosa Springs area, displaying the relative positions of each hammer seismic survey site.

### 5.3 Survey Design

Survey lines were flagged out at a chosen spacing between flags. Geophones were deployed in an end on geometry (in line) at each flag, with the shot point, the point of the hammer strike, being placed between the geophones.

A Geometrics geode system was used to record the data, with 24 channels per geode. Therefore in the longer surveys that contained more geophones multiple geodes were used.



Figure 5. 3: Vertical hammer strike on a metal plate, generating primary seismic waves.

Vertical geophones were used for the primary (P-wave) surveys, with a combination of 10Hz and 40Hz geophones used. The seismic source was vertical impacts of a sledgehammer on a metal plate. Two hammers were used, the larger weighing 16lbs, the smaller weighing 4lbs. 3 hammer strikes were carried out at each shot point; the 3 records were stacked in the lab after an initial QC.

For shear wave (S-wave) data, the seismic source was a series of semi-horizontal impacts on a metal plate as described by Haines [15]. The receivers were horizontal geophones with a natural frequency of 10Hz, sensitive to horizontal ground motion. Sources and phones were deployed perpendicular to the seismic line, so as to target the horizontally-polarized shear waves propagating along the line after a hammer strike. 3 strikes were carried out on each side of the source, stacking the data for each side and then differencing the two results to enhance the shear waves and reduce the primary waves. The acquisition parameters specific to each survey are listed in Appendix B.2.

## 5.4 Processing

The raw data generated by the geophones after each seismic shot were assigned a geometry consistent with the acquisition parameters of that survey, to create shot records of P and S wave data.



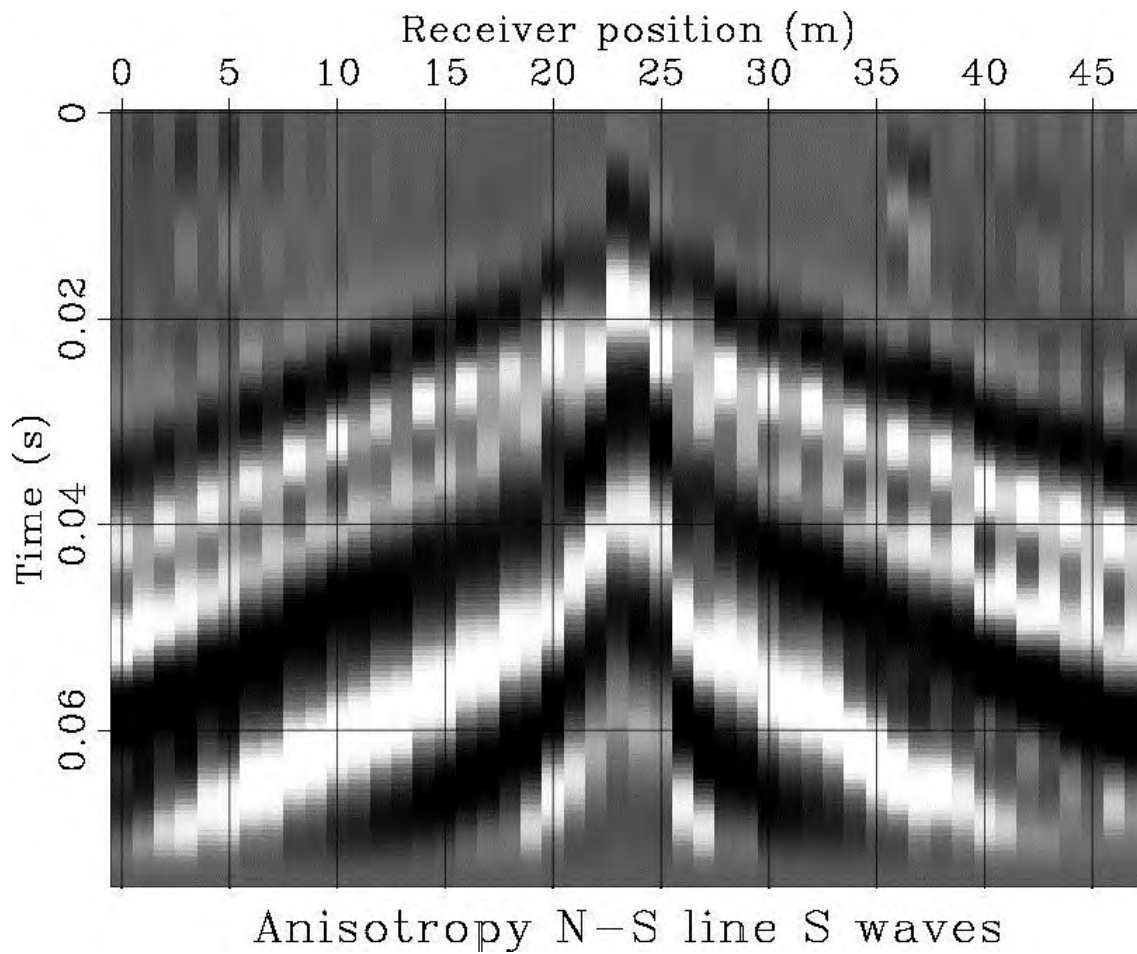


Figure 5. 4: Raw S-Wave shot record from the Zen Garden Line 1 dataset. The hammer strike occurred in the center of the line.

The shot records gathered from each survey were analyzed to identify the necessary processing steps that would enable an accurate interpretation of the data. In most cases a bandpass filter to attenuate low and high frequency noise, and balancing of the amplitudes of the traces, were sufficient.

Some datasets had traces that contained excessive noise in each shot record. These traces were determined to be faulty and had to be muted out to enable confidence in the interpretation of the data.

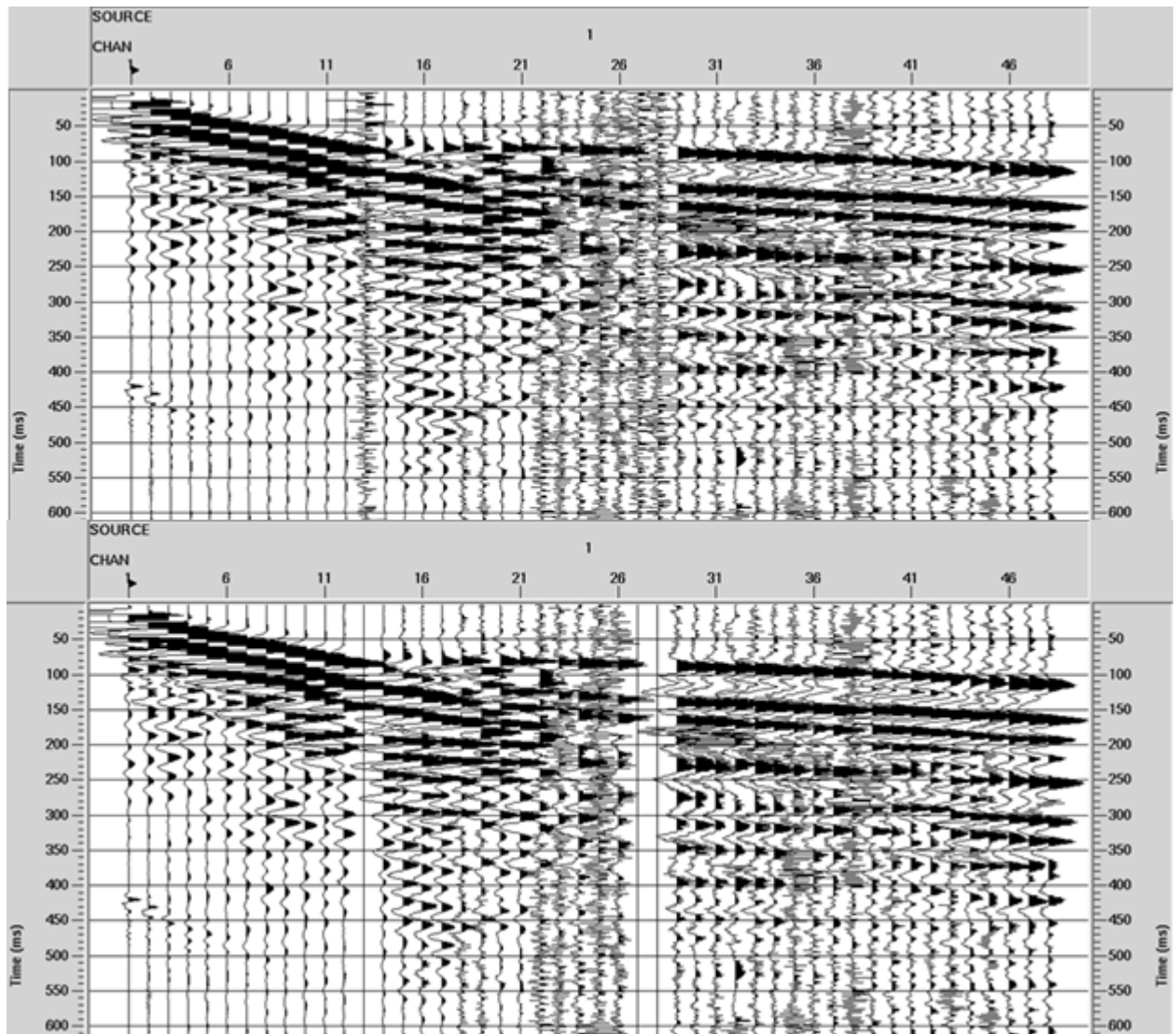


Figure 5. 5: Zen Garden Line 2 shot record 1. Trace numbers 13, 27 and 28 were faulty and contained high frequency noise in each shot record in this dataset. These traces were muted; their amplitude was given a zero value over the entire record length.

A bandpass filter was applied to each shot record to remove low and high frequency noise. Low frequency noise can arise from people walking along the line whilst recording is taking place. Excessive wind during the survey can result in high frequency noise.

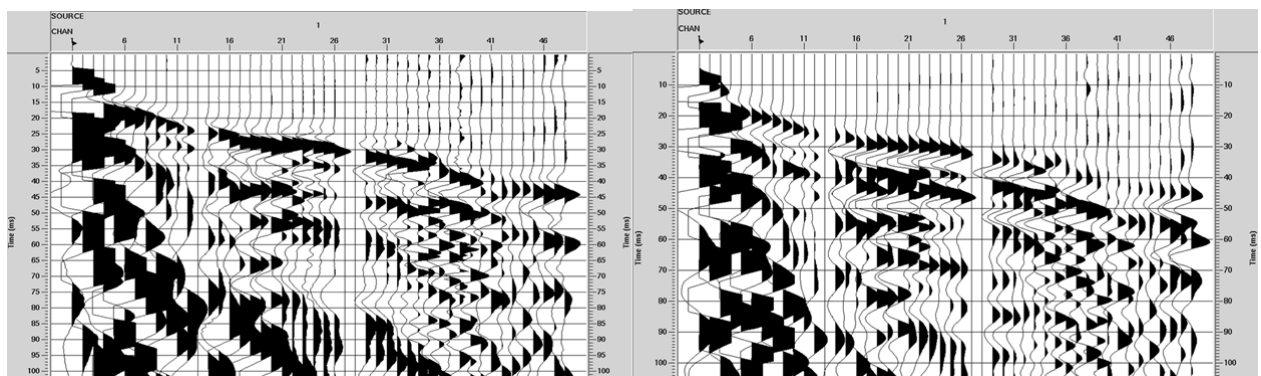


Figure 5. 6: Zen Garden Line 2 Shot 1 before (left figure) and after the application of a bandpass filter (right figure). Some of the high and low frequency noise that were previously dominating the shot record have been removed.

For a list of the processing steps applied to each shot record refer to Appendix B.3.

## 5.5 Uncertainties/Errors

Errors in the results arose from the ambiguity in the velocity trend picked from the shot record, and in the intercept time where the velocity crossed zero offset on the shot record.

This gave an uncertainty in the depths calculated in the subsurface models. If two variables  $x$  and  $y$  combine to give  $z$ , the uncertainty in  $z$  is given by the formula:

$$\frac{\sigma x^2}{x^2} + \frac{\sigma y^2}{y^2} = \frac{\sigma z^2}{z^2}$$

Where  $\sigma x$ =uncertainty in  $x$ ,  $\sigma y$ =uncertainty in  $y$  and  $\sigma z$ =uncertainty in  $z$ .

Inserting an error of  $\pm 50$  m/s into the velocity value, and an error of  $\pm 0.001$  ms into the intercept time, the above formula shows the depths in the models to be correct to within 0.507 meters.

## 5.6 Interpretation

Energy refracted from subsurface layers was identified by the first break from zero on each processed shot record, and a line was assigned to each layer to give a velocity.

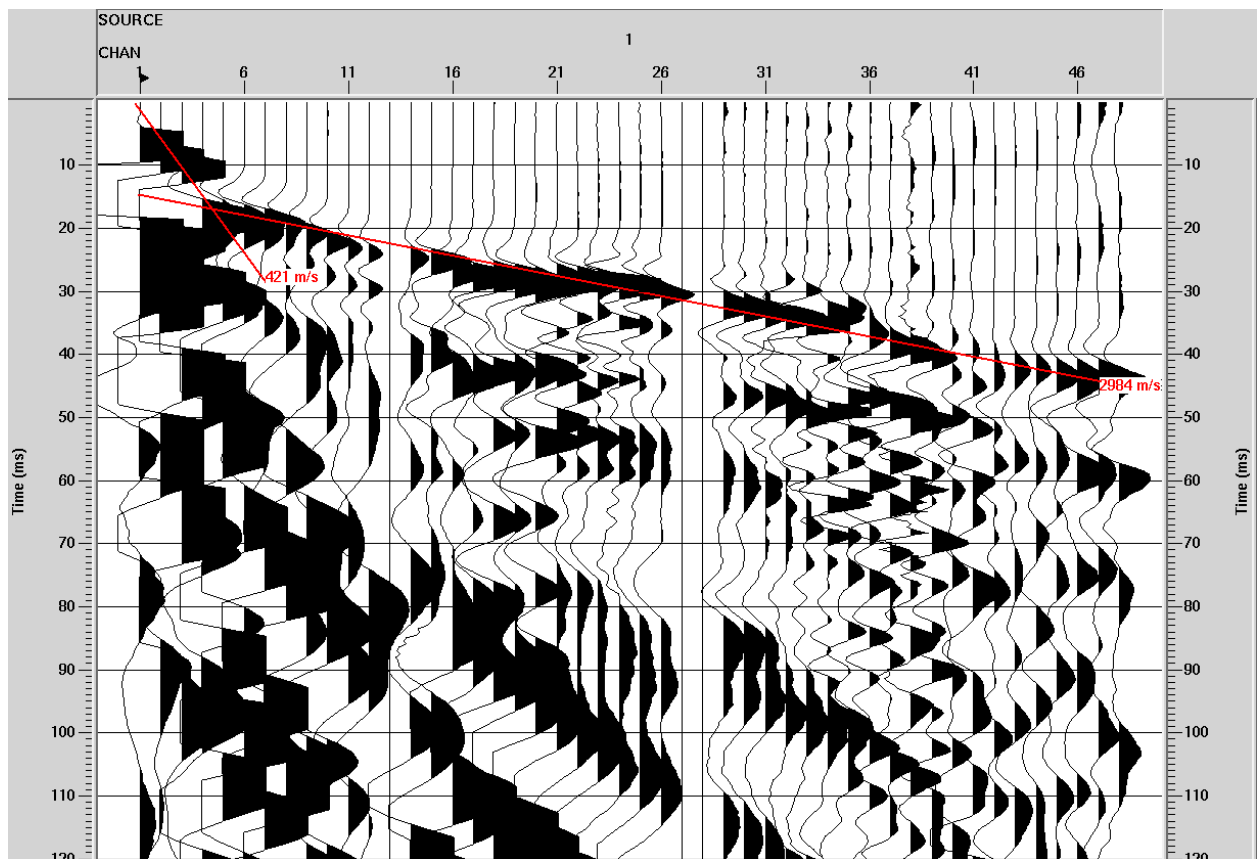


Figure 5. 7: Zen Garden Line 2 Shot 1 p-wave record after processing, with velocity trends interpreted across the first breaks. In this shot record two layers have been identified; a shallow layer with a velocity of 421 m/s, and a deeper layer with a velocity of 29

Once velocity lines had been picked the point where the lines intersected zero offset where noted. Using the velocity values and the intersect times, the velocity and thickness of each layer in the survey could be calculated to generate subsurface models using the equations given by Burger 2007 [16]. For a list of the equations used in the calculation of layer thickness refer to Appendix B.4.

### Zen Garden 1 Subsurface Model

Three layers were identified in the Zen Garden site, the first being a veneer of unconsolidated sediments extending to 1.4 meters depth. Below this there is an increase in velocity, interpreted as being due to greater compaction of the sediments and the presence of water in the pore spaces between grains. It should be noted that the increase in s-wave velocity across the water table cannot be attributed to the presence of water, as water has no shear modulus. The increase in s-wave velocity is purely due to greater compaction in the sediment. At approximately 10 meters depth there is a sharp increase in velocity as the Dakota Sandstone horizon is reached. The Dakota horizon is interpreted as having a slight dip to the South.

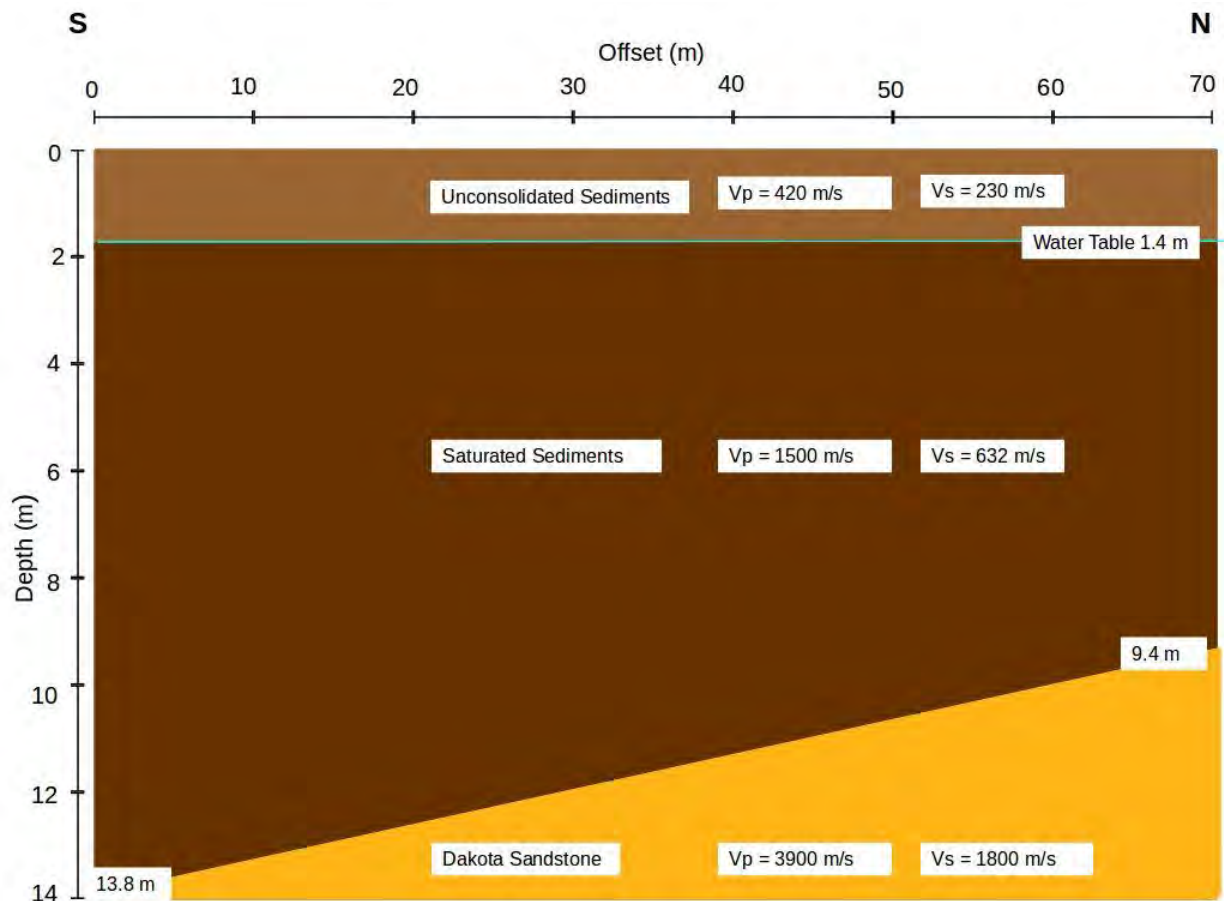


Figure 5. 8: Subsurface model derived from the interpretation of the Zen Garden Line 1 dataset

### Zen Garden 2 Subsurface Model

The second survey at Zen Garden shows a similar geology, the main difference being a shallower Dakota horizon. There is probably a component of dip in the East direction that could explain this, but a small fault is also possible. The lower velocity values in the Dakota Sandstone given by this line could be explained by the fact that it crosses the travertine fissure area, which will reduce the velocity. Primary wave velocities will be particularly affected by fractures.



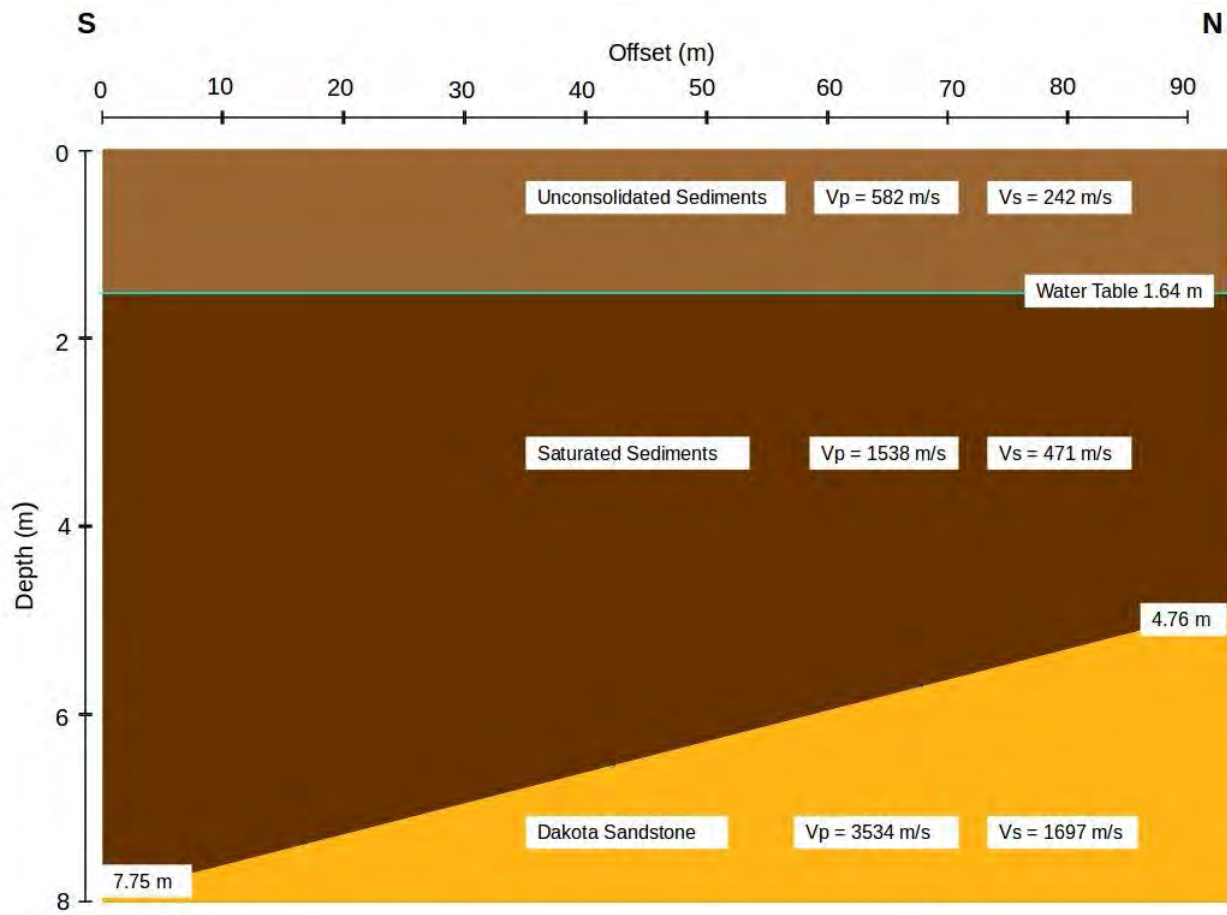


Figure 5. 9: Subsurface model derived from the interpretation of the Zen Garden Line 2 dataset

### Barn 3 Anisotropy N-S

The survey conducted parallel to the fractures near the Barn 3 deep seismic line displayed a two layer model with a shallow Dakota Sandstone overlain by unconsolidated sediments. The Dakota Sandstone had a much lower p-wave velocity than the same horizon in the Zen Garden.

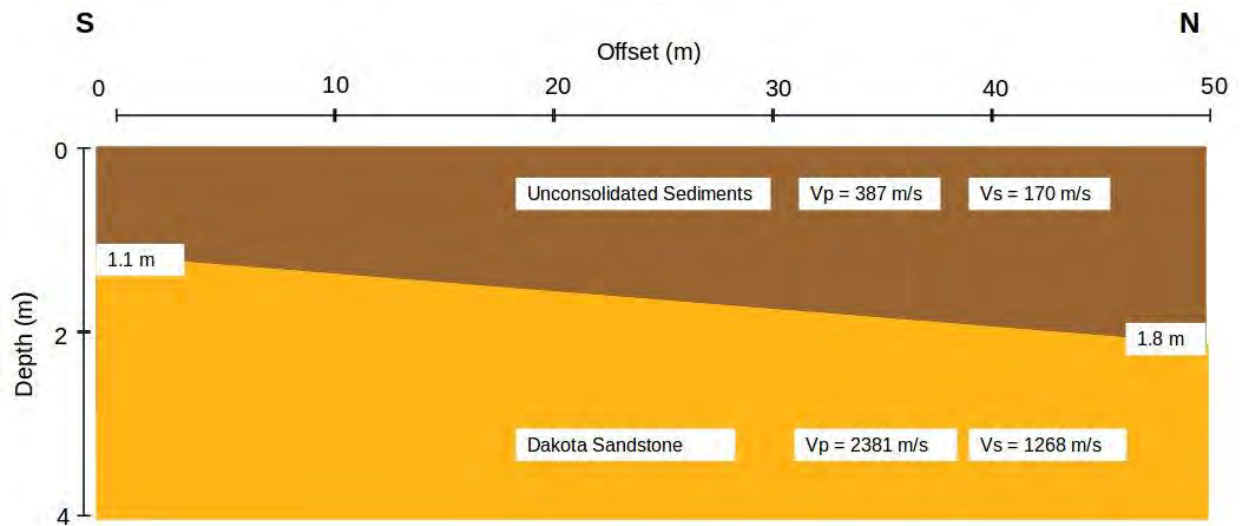


Figure 5. 10: Subsurface model derived from the interpretation of the Barn 3 Anisotropy North-South dataset

### Barn 3 Anisotropy W-E

The survey conducted perpendicular to the fractures gave a lower p-wave velocity for the Dakota Sandstone. This is due to the reduced compaction of the rock in the area near the fractures, slowing the compressional p-waves down. The shear waves were relatively unaffected by the orientation of the survey, as they depend on side to side motion, not compression.

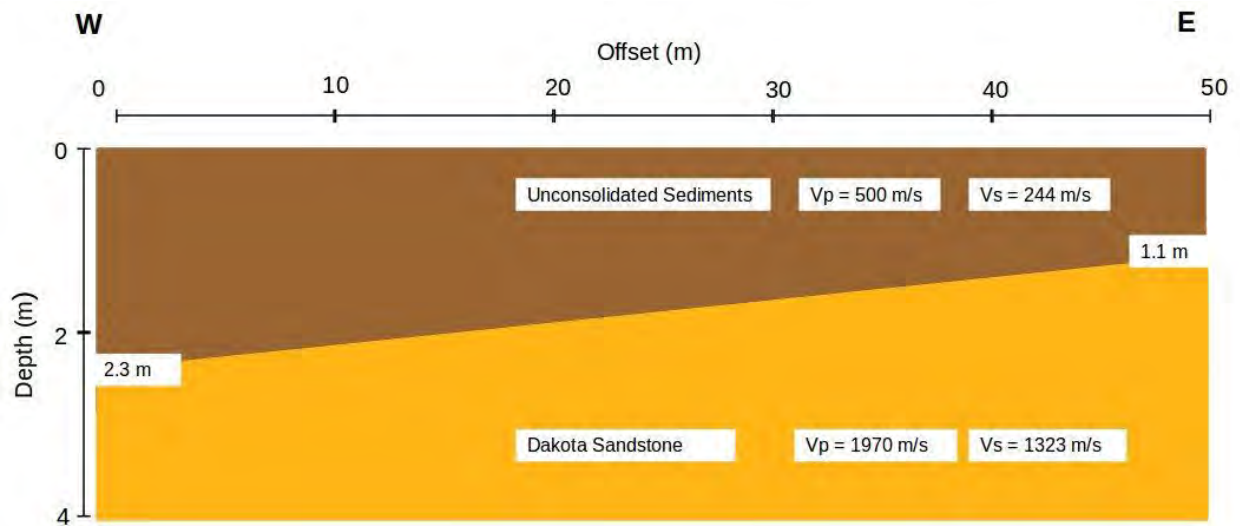


Figure 5. 11: Subsurface model derived from the interpretation of the Barn 3 Anisotropy East-West dataset

## Warm Springs

The warm springs site gave a two layer model, with a shallow Dakota Sandstone. The velocity of the sandstone is between the values given from the surveys at Zen Garden and Barn 3.

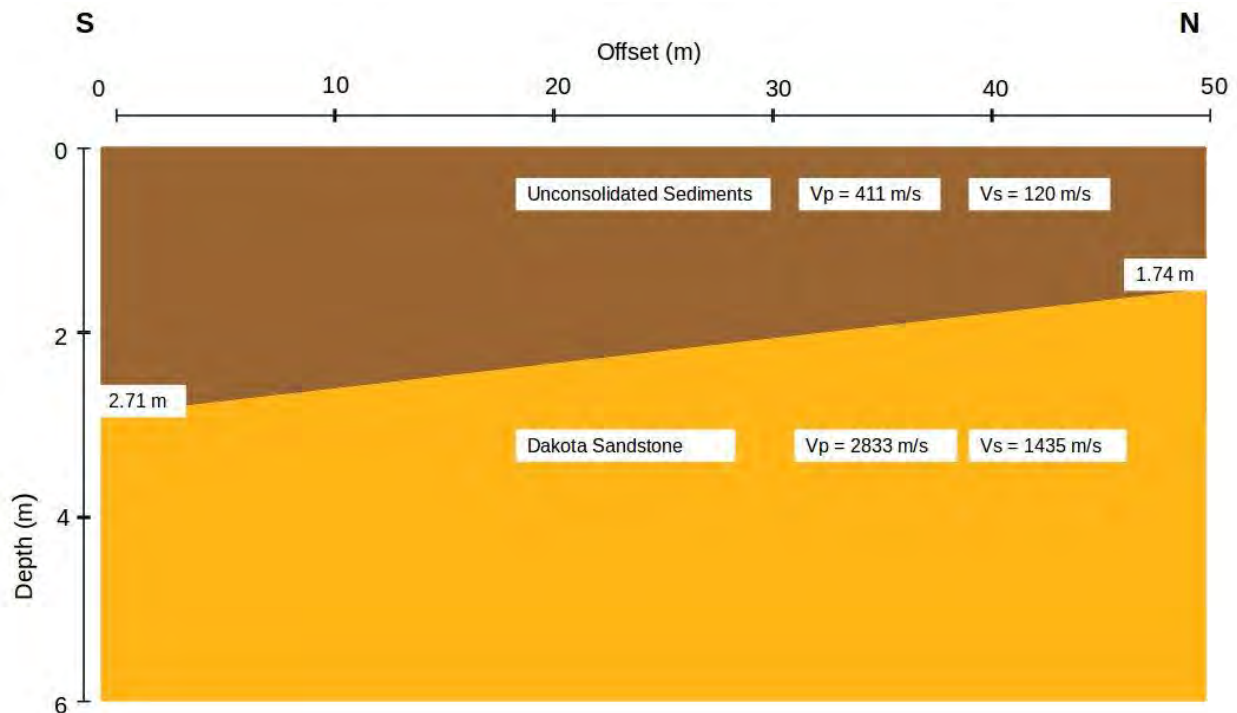


Figure 5. 12: Subsurface model derived from the interpretation of the Warm Springs dataset

## 5.7 Conclusions and Discussions

### Zen Garden

The two seismic lines show the Dakota Sandstone to be deeper at this location than at any of the other refraction survey sites, with a Depth ranging from 4.71 meters at the North end and 13.8 meters to the South. This suggests a southerly dip to the Dakota at this region, but this difference at each end could also be attributed to topography in the Dakota horizon or some small scale faulting.

The velocity values in the range of 3500-4000m/s show the Dakota to be a well compacted sandstone. Some lateral velocity changes were also observed, a possible result of variations in the dip along the line or some weathering.

### **Barn 3 Anisotropy Survey**

The two lines at this location show a thin veneer of unconsolidated sediment lying on top of the Dakota Sandstone, which ranges from 1.1 meters to 2.3 meters in depth. There is some dip displayed by both the N-S and E-W trending cross sections, however a change of approximately 1 meter in depth at either end of a 48 meter profile leads to the conclusion that any apparent dip is more likely due to topography on the top of the Dakota Sandstone.

The velocity of the sandstone was much lower, ranging from 1970-2381 m/s, which can be explained by the shallow level of the Dakota. It is probable that being closer to the surface has resulted in greater weathering of the rock, reducing its seismic velocity.

### **Warm Springs**

The Dakota Sandstone is also shallow at the Warm Springs site, with a depth range of 1.74-2.71 meters. Here the sandstone also displays some dip to the south. The velocity of 2833 m/s indicated that the Dakota in this location had undergone some weathering, consistent with its position, but had not been weathered to the same extent it had at the Barn 3 site.

### **Overall Conclusions**

The fact that an element of dip was observed at both the Zen Garden and Warm Springs sites leads to the conclusion that it cannot be completely explained by topography in the sandstone, therefore a dip to the south of less than  $10^\circ$  is a reasonable assumption.

The velocity of the Dakota Sandstone varied greatly between hammer seismic surveys conducted at different sites. This is most likely attributable to the variation in the depth and the extent of weathering that the sandstone had been exposed to.

The p-wave velocity of the Dakota Sandstone is lower in the presence of fractures when the waves run perpendicular to the fractures.

This spread of velocities is worth bearing in mind for the processing of the deep seismic line, especially around any known faults or fracture zones.

# 6. Gravity

---

## 6.1 Introduction

Gravity is an attractive force between masses which creates a gravitational field [17]. The equation for the gravitational force follows:

$$F = \frac{G \times M \times m}{R^2}$$

Equation 6.1 Equation of Gravitational force

$G$  is a gravitational constant equal to  $6.67384 \times 10^{-11} \text{ m}^3 \text{ kg}^{-1} \text{ s}^{-2}$

$M$  and  $m$  are two point masses

$R$  is the distance between the two masses

The gravity method is used to measure the small changes in the Earth's gravitational field that are produced by differences in rock densities. These values can be measured by instruments called gravimeters, and these gravity variations are used to identify anomalies. The anomalies highlight variations in the strength of the gravitational force over the surface of the Earth. These occur in areas where there are great concentrations of mass that cause a change in density [18]. Different types of rocks have different densities. For example, basalt has a higher density than sand or shale. With this knowledge we look at our anomalous data and determine the basic structure of the sub-surface. Gravity methods are often used in mineral, oil and gas exploration, as well as in archaeology and other geological surveys. Gravity was chosen as a method for this field camp because of the geothermal resources in Pagosa Springs. The density contrast data helped us to interpret the geology of the area and to better understand the hot springs resources and water location.

There were two different instruments used for data collection with the gravity method; the LaCoste-Romberg gravimeter (L&R) and the Scintrex CG-5 gravimeter (CG-5). L&R gravimeters are the only manually operated gravimeters still in use today. It has a steel astatic spring system which means it uses zero-length main springs. The tension in the zero-length spring is proportional to its length (see figure 6.1). The measurements are made by rotating the dial. This will create a force as the measuring spring is raised or lowered [19].



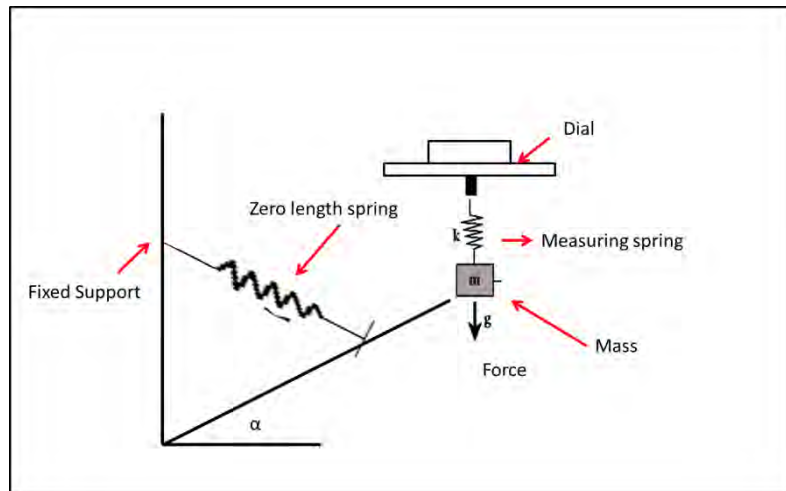


Figure 6.1 Simple Astatic Gravity Meter

To use the L&R you must first level the instrument by using the three levelling screws. Next, look through the eye piece and adjust the dial until you see the cross hair at 2.4. The components of the L&R are shown below in Figure 6.2.

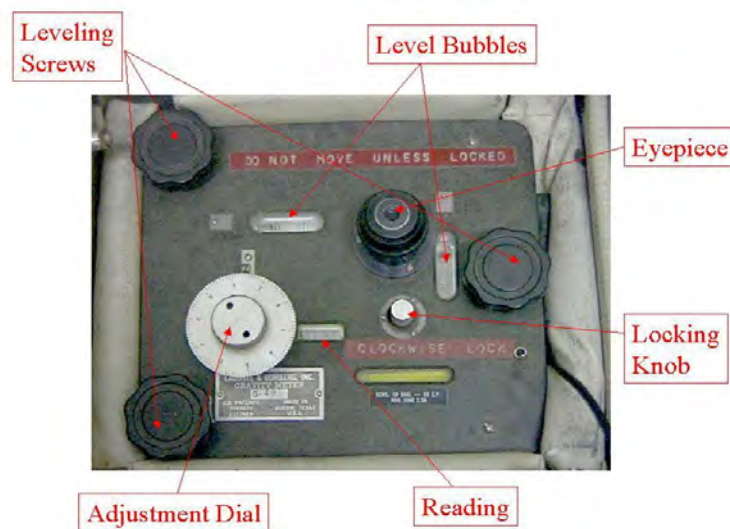


Figure 6.2 LaCoste-Romberg gravimeter [20]

The other gravimeter used in the field was the CG-5. This is an automatic meter, which means everything is stored in one carrying case and the readings are stored instantly in the meter's memory system. Levelling and taking a reading with the CG-5 is considerably easier than with the L&R. A detailed description of collecting data with both meters will be discussed in Appendix C.



Figure 6.3 CG-5 gravimeter [21]

Another important piece of the gravity method is the base station. To have an accurate gravity survey you must return to your base station approximately every three hours. The Earth's gravitational field is constantly changing and in order to complete the appropriate data corrections you must have multiple base station readings where you can see how these values have changed. It is also imperative that, each day a new survey begins, one of the first readings taken is at one of the same locations where data was previously collected. This allows your data to be connected and when it comes to inversion your data set can be one complete survey. Base station values are used specifically in the drift correction. The drift correction accounts for instrument drift which is mainly due to temperature changes. This correction is subtracted from the anomaly value and helps to eliminate errors in the measurement. Drift correction as well as the other corrections used in processing are discussed in section 6.4.

## 6.2 Survey design

Gravity data was collected at many different sites in Pagosa Springs. CG-5 data was collected at the airport, PAGO01, PAGO02, warm springs and the Zen Garden. L&R data was collected at the airport, PAGO01, PAGO02, and Barn3. One of the main sites was the Zen Garden. This was the site where the students planned and developed their own survey. It was near the hot springs and the river and was laid out over a large fracture. The survey sites were chosen based on known hot spring locations, expected geologic features and accessible land. Below is a GPS map showing the exact locations of the survey lines.



Figure 6.4 GPS map of sites the gravity method was completed

The Zen Garden was a grid 170 m x 140 m. The Zen Garden started out having 15 stations per line with 10 m station spacing and 10 m line spacing; 18 lines total. This survey grid was then altered to allow for more data collection. The new grid had 5 m station spacing and 5 m line spacing for lines A-E. Because of time restrictions the gravity measurements were only collected up to flag 10 of each line over lines A-M. Since the Zen Garden site was a grid, a 3D inversion was performed on this data. This was very useful for geologic interpretation because we were able to look at much more of the sub-surface. Below is a figure showing the entire Zen Garden grid marked with red dots where gravity measurements were taken. The mother spring is just off the NE corner of the grid and the river is just to the west of the grid.

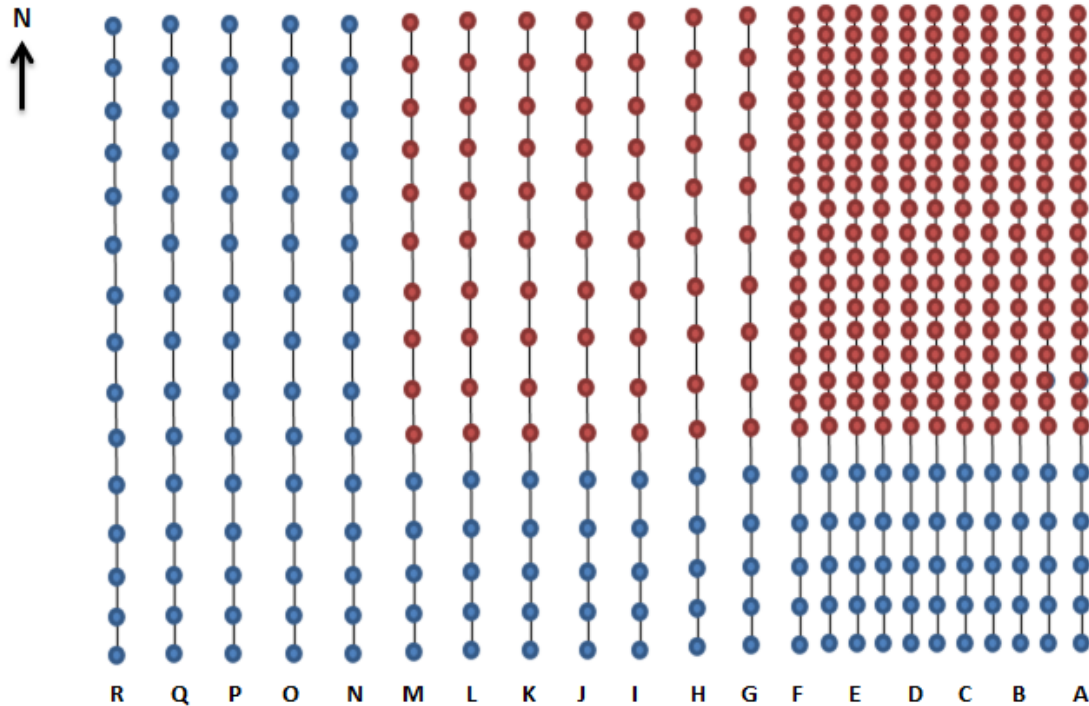


Figure 6.5 Zen Garden grid: red dots show gravity data collection points

The other survey designs were 2D lines. This included the lines at the hot springs, airport, Barn3 and warm springs. There were three different lines at the hot springs site: PAGO01, PAGO02, and PAGO05. PAGO01 and PAGO02 ran from the river, across the road and up reservoir hill. PAGO01 ran north-south and PAGO02 ran roughly east-west. PAGO05 ran along a flat surface next to the river. All three of these lines had 20 m spacing. The hot springs site was chosen because of its proximity to the river and mother spring. Also, there was a possible fault in the area. Data was collected at the airport line at every other pink flag, which was 60 m spacing. Barn3 was the second deep seismic line where again we took gravity measurements every 60 m. The seismic lines were too long to have any smaller spacing than that due to time constraints. The last site was the warm springs, where not much data was collected. Gravity measurements were taken at the warm springs every 10 m for half of line 4; this was approximately in the middle of the field.





Figure 6.6 Students working with the CG-5 gravimeter

## 6.3 Processing/Data Reduction

Before the results of gravity survey can be interpreted it is necessary to correct for all variations in the Earth's gravitational field which do not result from the differences of density in the underlying rocks [26]. This process is known as data reduction.

### 6.3.1 Drift Correction

The first correction applied to the raw data set was the drift correction/tide correction. Observed gravity changes as a function of time at a given location, these changes are due to tidal effects, instrument drift, and in some cases real changes (e.g. motions on faults, swelling magma chambers) [30]. Corrections for instrumental drift is based on repeated readings at a base station at recorded times throughout the day. The meter reading is plotted against time and drift is assumed to be linear between consecutive base readings [26]. The Drift correction is subtracted from the observed value. The Equation 6.26.2 presents the drift correction subtracted from the gravity observations.

$$\Delta gD = g_b = (t - t_b) \frac{g_e - g_b}{t_e - t_b} - g_1$$

Equation 6.2 Drift correction [29].



Where  $t$  is the time of the measurement (min),  $gb$  and  $ge$  are the gravity reading (mGal) at the beginning and end of the survey loop, at times  $tb$  and  $te$  respectively,  $g_1$  is the reading in (mGal) at the first recorded instance of the base station.

### 6.3.2 Latitude Correction

Gravity varies with latitude because of the non-spherical shape of the Earth. The angular velocity of the point on the earth's surface decreases from a maximum at the equator to zero at the poles. The centripetal acceleration generated by Earth's rotation has a negative radial component that causes gravity to decrease from pole to equator [26]. Equation 6.36.3 presents the approximate gravity correction for latitude.

$$\Delta gl = 0.001626 \sin \theta \cos \theta \Delta y$$

Equation 6.3 Latitude Correction [29].

Where  $\Delta gl$  is the latitude correction to be applied to the data,  $\theta$  is the latitude of the station in degrees and  $\Delta y$  is the local, or relative, northing in reference to one station.

### 6.3.3 Free-Air Correction

The free air correction (FAC) corrects for the decrease in gravity resulting from increased distance from the centre of the earth, according to Newton's Law[26].The correction for a point with elevation  $h$  is given by Equation 6.4.

$$\Delta g_{FA} = -0.3086h$$

Equation 6.4 Free Air Correction[29].

Where  $h$  is the station elevation above the sea level (m). The constant 0.3086 takes into account the radius of the Earth and the average acceleration of the gravity.  $\Delta g_{FA}$  is the Free-air correction to be subtracted to the data in mGal.

### 6.3.4 Bouguer Correction

The Bouguer correction (BC) together with the terrain correction (TC) removes the gravitational effect of the background density below the topographic surface down to sea level [29]. The BC takes into account the gravity of materials between gravity stations and the datum plane that was established in the Free Air Correction. This is done by assuming there is a continuous slab of material with constant density in the space. The density was

assumed to be the average density of continental crust ( $2.67\text{g/cm}^3$ ). The gravitational effect of a slab with thickness  $h$  and infinite horizontal extent is given by Equation 6.5.

$$\Delta g_s = 2\pi\gamma\rho_b h$$

$$\text{Assuming } \rho = \frac{2.67\text{g}}{\text{cm}^3}$$

$$\Delta g_s = 0.1119h$$

#### Equation 6.5 Bouger Correction

In Equation 6.5  $h$  is the station elevation above the sea level (m) and  $\Delta g_B$  is in mGal.

### 6.3.5 Terrain corrections

The Terrain Correction accounts for the effect of excess and deficient mass introduced by the terrain relative to the infinite slab used in the Bouguer correction. The precise elevations of the line were provided by a digital elevation map from the USGS seamless server with a spatial resolution of 10m. Oasis Montaj software from Geosoft was used to correct the data by utilizing local and regional grids. The algorithm calculated the effects of the terrain by breaking into sloping triangular sections and calculating the gravity for square prisms comprising the terrain under the stations [27].

## 6.4 Uncertainties/Errors

### 6.4.1 Errors

The main errors observed in exploration gravity data are:

- Instrument Errors:

#### **LaCoste & Romberg Graviton- EG**

- Precision of  $0.1\ \mu\text{Gal}$
- Resolution of  $1.0\ \mu\text{Gal}$
- Present minimum error budget  $<+- 1.0\ \mu\text{Gal}$
- Random errors  $= +1\ \mu\text{Gal}$
- Systematic errors  $<+-0.1\ \mu\text{Gal}$

#### **SCINTREX CG-5**

- Resolution  $1\ \mu\text{Gal}$

- Human Sources of Errors:
  - Survey design errors
  - Sampling errors
  - Processing algorithm errors
  - Levelling error
  - Manual recording errors
  
- Positioning errors include inaccuracies in the operation of the TDM and GPS collecting the coordinates of the station locations.
  
- Temporal Mass Changes:
  - Global (spatial extension  $\geq 10^3$  Km)
  - Regional and local
  - Typically product of hydrologic changes, effects of atmospheric pressure.
  
- Noise: acquisition of other surveys such as magnetics and hammer seismic in the Student Site area during the acquisition of the gravity data could produce errors in the gravity observation points.
  
- Weather: factors such as the presence of wind and drastic changes in temperature during the day can also be causing errors in the gravity data.

#### **6.4.2 Uncertainties**

For most inversion problems the Earth is digitized with more cells than data values. Therefore, it will be impossible to find a unique value for each cell without additional information [28]. This issue is referred to non-uniqueness. Problems with more unknowns than data are called "under-determined," and will have an infinite number of possible solutions. Furthermore, there will be errors associated with every data point.

The forward modelling of gravity data also can generate several non-unique geologic models. To minimize uncertainty, the model must be constrained by suspected values of the density of the rock and geologic observations. Restricting the boundaries of possible density values decrease the variability in the geologic models produced. Forward modelling can also be

conducted by taking into consideration magnetics data. Conducting a forward model fitting both of these datasets reduces the uncertainty and increases the confidence in the model produced.

## 6.5 Data and Interpretation

As mentioned in section 6.2, gravity data was collected on seven different sites (**Error! Reference source not found.**). In Zen Garden a 3D profile was created and inverted over its 3 dimensional distribution of density contrast; making use of the suite of algorithms GRAV3D developed at the UBC Geophysical Investigation Facility. The other six 2D profiles were modelled in the program GM-SYS developed by Geosoft, together with the magnetic data. The forward modelling started by first testing the response of the gravity to a geological model designed based on field observations, dip measurements and the USGS geological map of the area in the scale 1:24.000 [6], the thickness of each sedimentary unit was based on the P1 and Mizar wells, Figure 2.9. Density values for each different unit were derived by laboratory measurements of hand samples; the values used for the forward modelling can be seen in Table 6. 1.

**Table 6. 1 Density and thickness used on the forward modelling of the gravity data.**

<b>Geological Unit</b>	<b>Density</b>	<b>Thickness</b>
<b>Mancos Shale</b>	2.68	0-3000
<b>Dakota Sandstone</b>	2.64	~ 200
<b>Morison Formation</b>	2.68	~ 700
<b>Wanakah/Entrada</b>	2.62	~ 250
<b>Volcanics (intrusions and alluvial deposits)</b>	2.63- 2.8	-
<b>Metamorphic basement</b>	2.7 - 3	-

By adjusting density parameters, inside a reasonable range, and slightly modifying the primary geological model to best fit the data while keeping a realistic geological model, the final 2D models were created. The low density of the gravity measurements are one of the largest uncertainties in the data, given that gravity values outside of the main trend can be considered noisy data. These were not taken into consideration for the final modelling.

### 6.5.1. Stevens Airport

According to the geological map of the area, Stevens Airport area crosses, at its southern portion, the Eight Mile Mesa Fault. This can be seen by the delineation of the topography in

the area since the hanging wall of this fault generates a positive relief by the near outcropping of the Dakota Sandstone. The layers at the north end of the fault are dipping at about eight degrees to the north, and outcrops of Mancos shale are observed along the airport section.

A slight difference in the gravity anomaly can be observed at the suggested location of the Eight Mile Mesa Fault, confirming the primary position of this fault. This difference is due to the relatively lighter Dakota Sandstone being closer to the surface at the hanging wall and the existence of a larger section of heavier Mancos shale in the foot wall area (Table 6. 1). Additionally, a decrease on the magnetic anomaly is observed on the foot wall zone, related with the deeper basement on this region (Figure 6. 7).

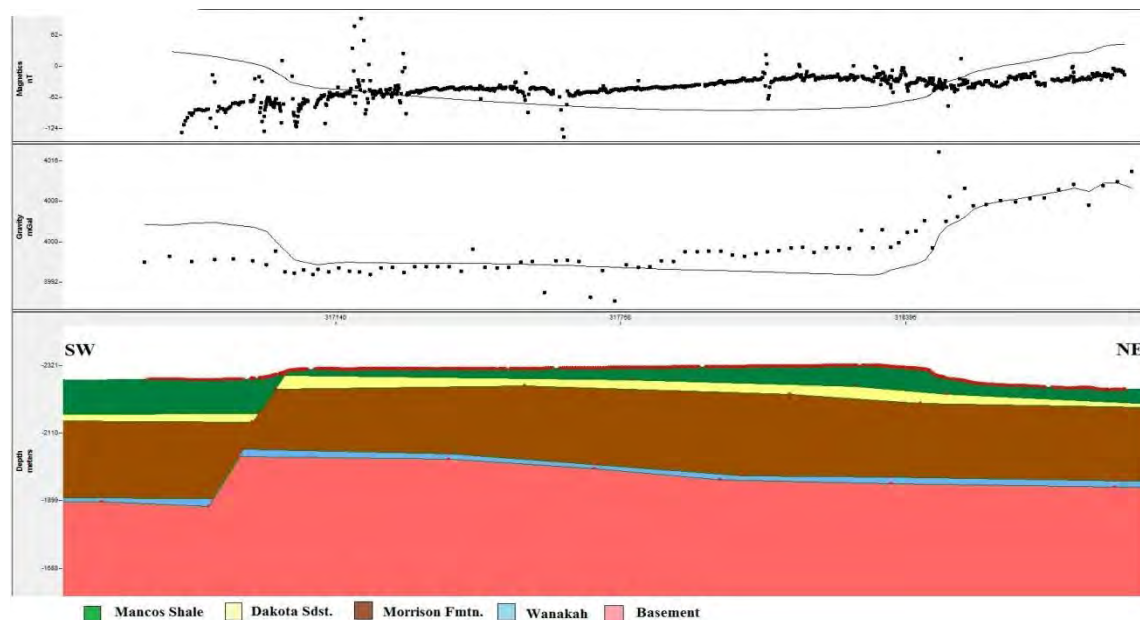


Figure 6. 7 Gravity data from Stevens airport (black points) superimposed with the synthetic gravity anomaly (black continuous line) calculated from the geological model (bottom portion).

### 6.5.2. Barn 3

The Eight Mile Mesa Fault crosses the Eastern portion of the Barn 3 line, and the surface geology of the area shows that a low angle anticline structure occurs on this region. This model predicted the high gravity anomalies observed east of the fault, probably generated by a basement uplift of this area.

The western portion of the profile shows a decreasing trend of the gravity values that suggests a deepening of the basement to west of the area, and towards the centre of the San



Juan Basin. Given the existence of a large negative gravity anomaly on the central portion of the line and an anomaly in the magnetic data, a sudden increase of the basin thickness is proposed in the area. This could be generated by a small fault in the basement (Figure 6. 8).

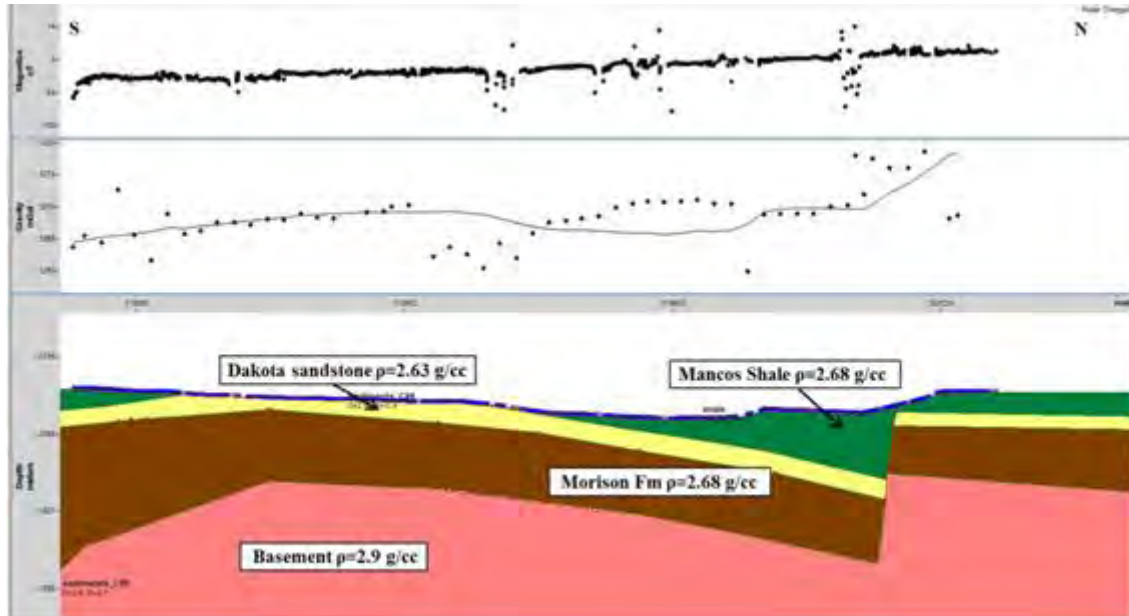


Figure 6. 8 Gravity data from Barn 3 (black points) superimposed with the synthetic gravity anomaly (black continuous line) calculated from the geological model (bottom portion).

### 6.5.3 PAGO01

The gravity data acquired on the PAGO01 line only had coherent values on the southern portion of the line; therefore the data acquired on the North part of the line was not used on this interpretation. As observed in **Error! Reference source not found.**, the PAGO01 line follows the regional strike of the dipping formations; hence the apparent dip of this section is sub-horizontal. The southern portion of this section shows a very flat gravity anomaly, confirming the hypothesis that the line is crossing a very laterally homogeneous area.

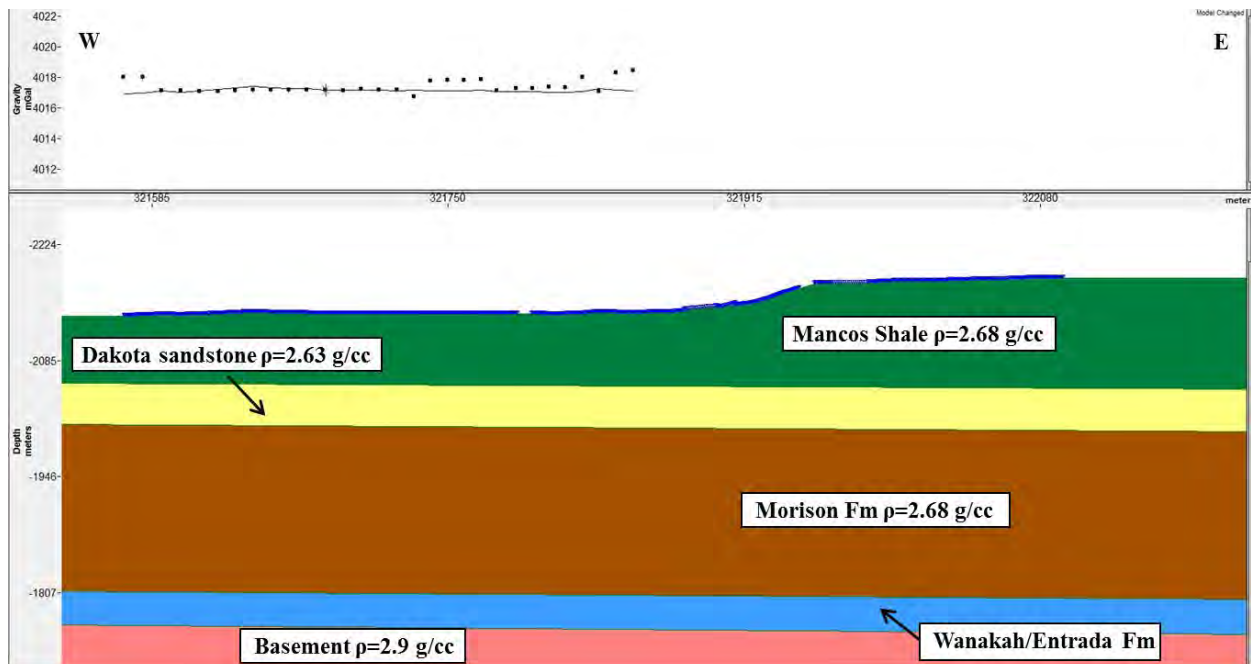


Figure 6. 9 Gravity data from PAGO01 (black points) superimposed with the synthetic gravity anomaly (black continuous line) calculated from the geological model (bottom portion).

#### 6.5.4 PAGO02

The PAGO02 line starts close to the San Juan River in the west and runs to the east side of a hill. The crest of the hill is formed by alluvial deposits of rounded boulders, rich in volcanic material, suggesting that those hills are the leftovers of a former location of the San Juan River. On both sides of the hill outcrops of Mancos shale can be observed. Resistivity measurements on this line showed a large resistivity contrast between the conductive Mancos Shale and the resistive alluvial deposits. This is evidence for the presence of a fault on the western portion of the hill.

The gravity data on the area decreases slightly in the presence of low density, unconsolidated deposits. However, the low density contrast of the region does not allow the gravity data to be used as a key survey to detect such fault, as can be observed in Figure 6. 10.

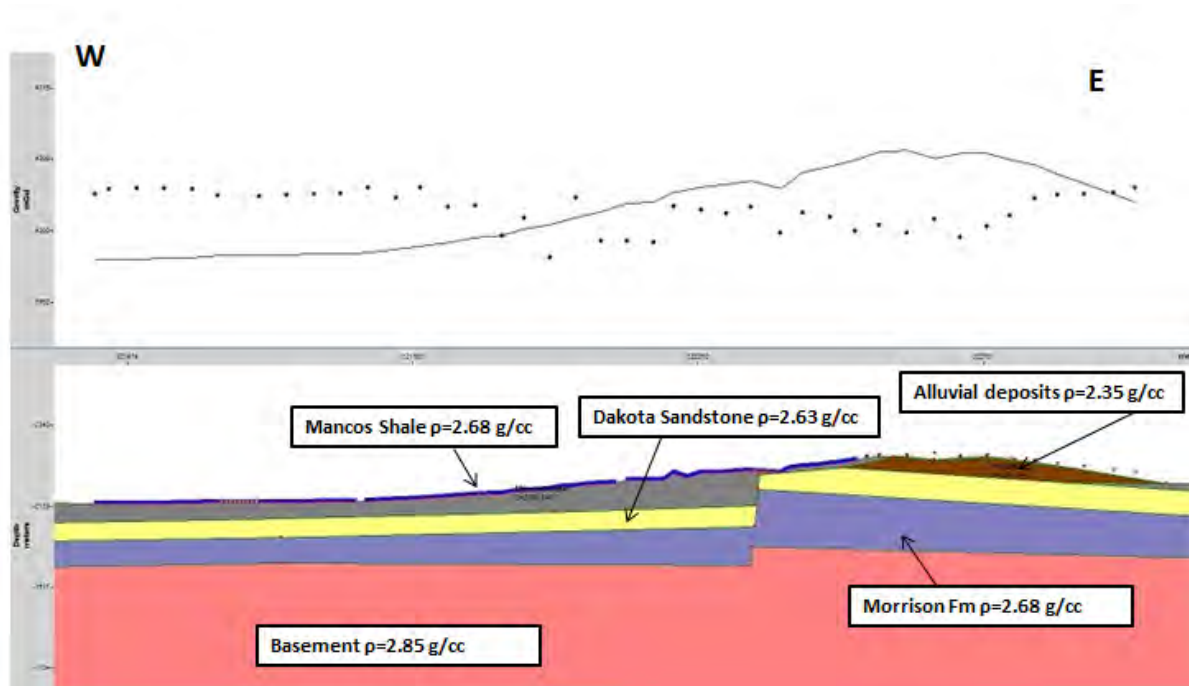


Figure 6. 10 Gravity data from PAGO02 (black points) superimposed with the synthetic gravity anomaly (black continuous line) calculated from the geological model (bottom portion).

### 6.5.5 PAGO05

Similar to the PAGO01 section, PAGO05 is located perpendicular to the dip direction, therefore the apparent dip of the geological layers are flat. On the west side, this simple model can predict the flat subsurface, and a low gravity anomaly given by the presence of a highly porous travertine. However, from the middle of the survey line on the data starts to increase away from the models predicted readings. This trend could be due to compacted soil next to the buildings on the east side of the survey line.

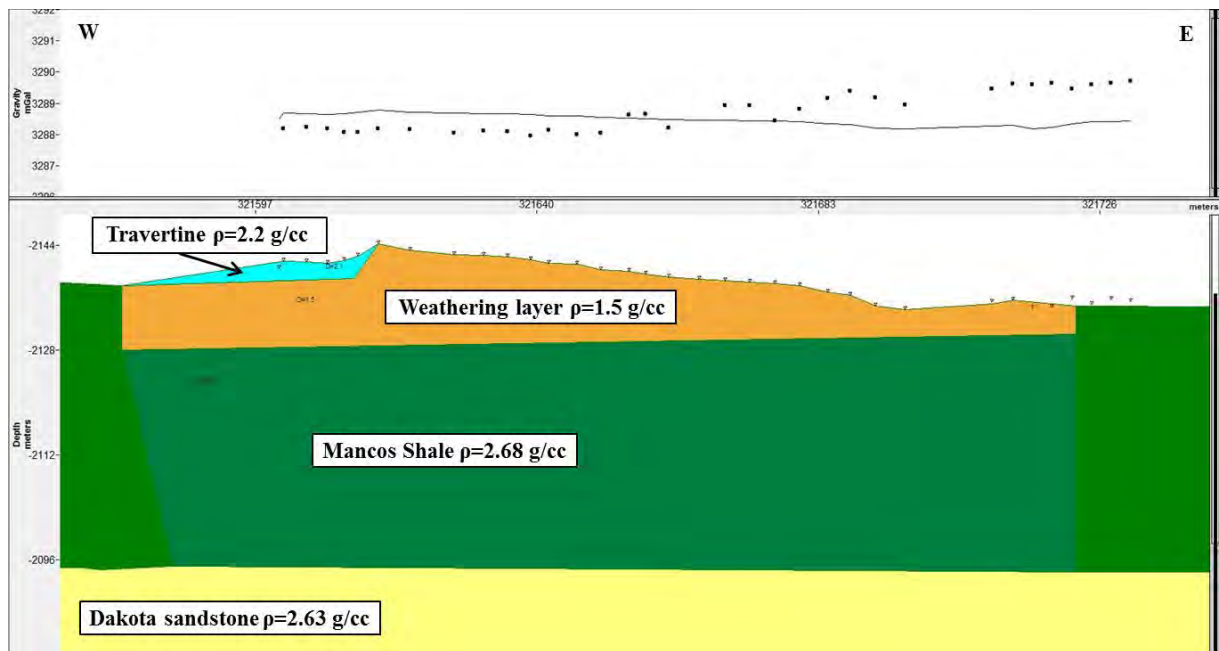


Figure 6. 11 Gravity data from PAGO05 (black points) superimposed with the synthetic gravity anomaly (black continuous line) calculated from the geological model (bottom portion).

### 6.5.6 Warm Springs

The gravity survey on the Warm Springs site was taken on line 4 of the Warm Springs Grid, until station 30, both the geological model and the shallow hammer seismic suggested that the dipping of the area is sub-horizontal up to 8 degrees NEE. There does not seem to be a large gravity anomaly in the area, but there are slightly higher gravity values to the north that could be due to the increase in thickness of the relatively denser Mancos shale in this area (Figure 6. 12). It is important to understand that since this line was not very extensive, the measured gravity anomalies are related only with shallow features.

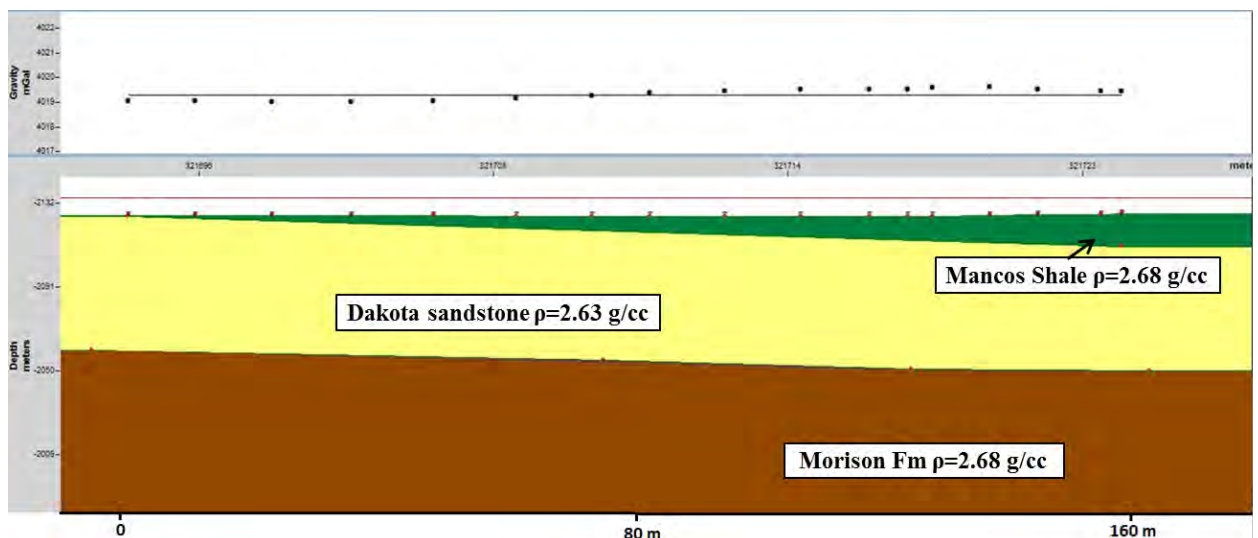


Figure 6. 12 Gravity data from Warm Springs (black points) superimposed with the synthetic gravity anomaly (black continuous line) calculated from the geological model (bottom portion).

### 6.5.7 Zen Garden

The gravity data from the Zen Garden location was acquired on a 3D grid. This grid has 10 m spacing on the central and west portions, and 5 m spacing on the eastern portion. Figure 6.13 shows the gravity data acquired from the Zen Garden area. The data points correspond to the locations where the observations were taken. The highlighted areas correspond to the location of rock piles that produced very high anomalies, which are outliers. These points were deleted for the inversion modelling. In addition to the general inversion, the finely sampled section, known as the 5x5 meter grid, was sectioned off and run in a separate inversion to be discussed.

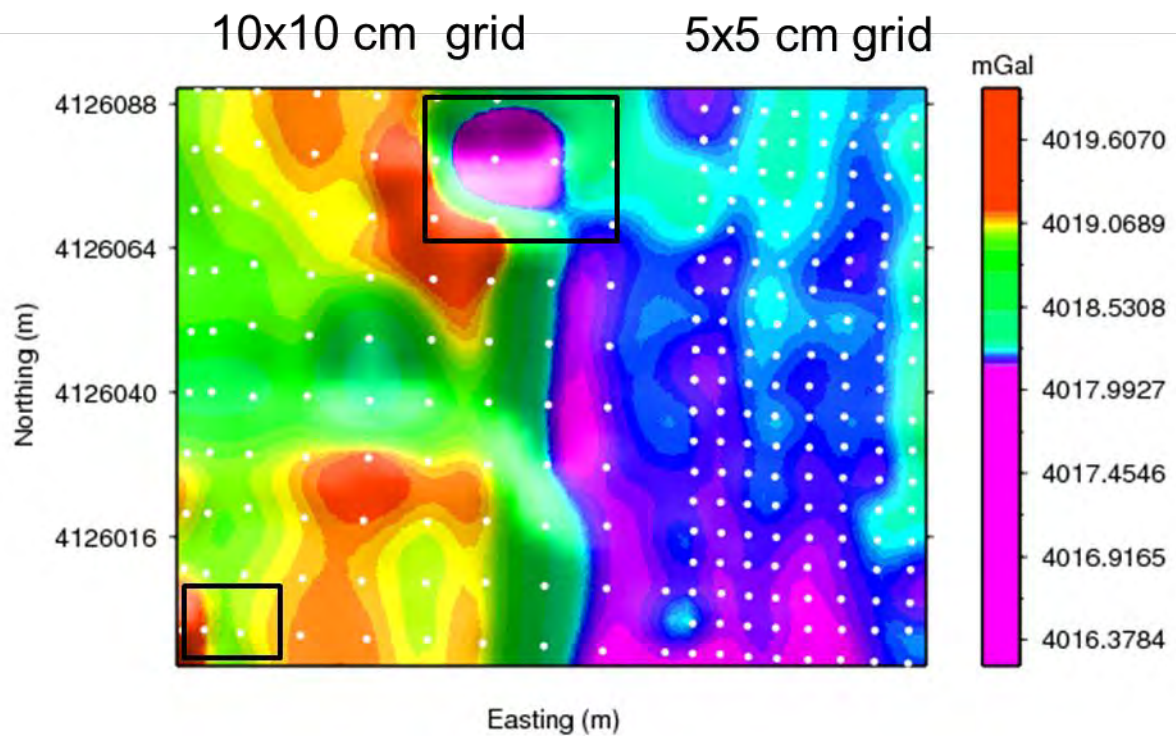


Figure 6.13 Entire gravity measurements conducted over Zen Garden site.

### Gravity inversion

The goal of the gravity inversion was to obtain, from the extracted anomaly data, quantitative information about the distribution of the anomalous density in the ground.

Two specific programs in the algorithm suite were used. GZSEN3D calculated the sensitivity matrix for use of the inversion and GZINV3D inverted the anomalous gravity field to generate a density model.



In order to construct the sensitivity matrix it was necessary to construct a mesh file. The mesh used had 83 cells in the easting direction, 54 cells in northing direction and 39 cells in the vertical direction. The mesh selected can be observed in Figure 6.14.

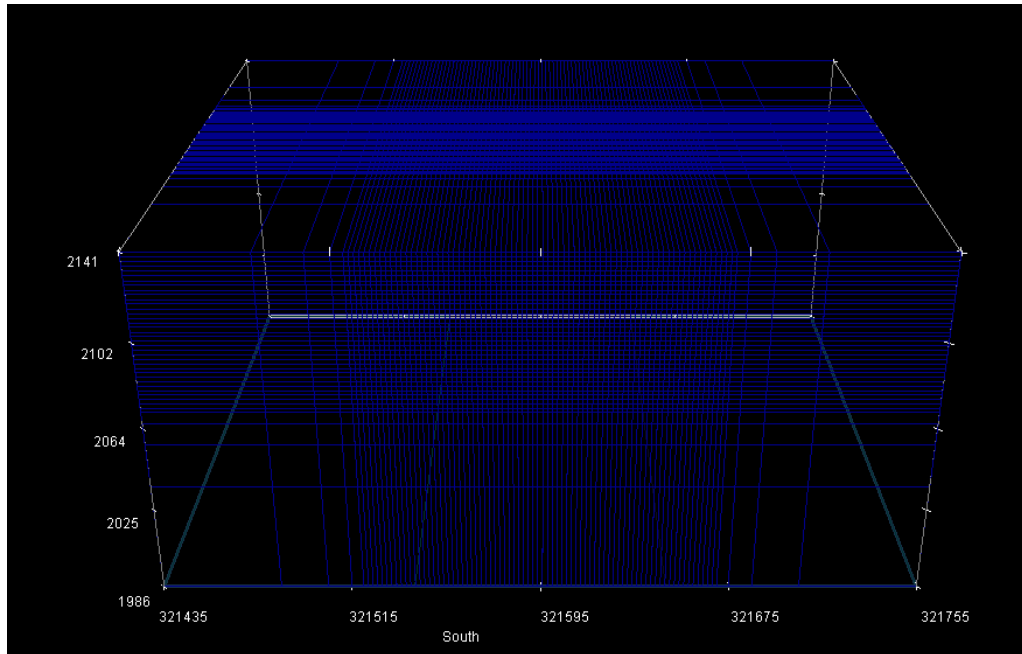


**Figure 6. 14 Mesh used for Zen Garden 3D inversion process.**

In order to perform the inversion of the gravity data it was necessary to include a regularization that imposes stability to yield accurate approximate solutions. The regularization used was the Tikhonov's Regularization. The choice of the regularization parameter  $\beta$  ultimately depends upon the magnitude of the error associated with the data. The inversion of noisier data requires heavier regularization, thus a greater value of  $\beta$  is required. Different inversions were performed using different regularization parameters ranging from 0.000001 to 1000000. The data misfit vs. model norm was plotted on a log-log scale with the function in order to find the optimal regularization parameter at the maximum curvature. The  $\beta$  selected was 100 for the Tikhonov's curve because it preserved the overall geological structure of the model, as well as ignored features in the surface that may not be real and are products of noise and errors in the data. Figure 6.15 presents the gravity observations, model, and the difference between the two. It is possible to observe that the model fits the data and just ignores possible artifacts or erroneous observations.

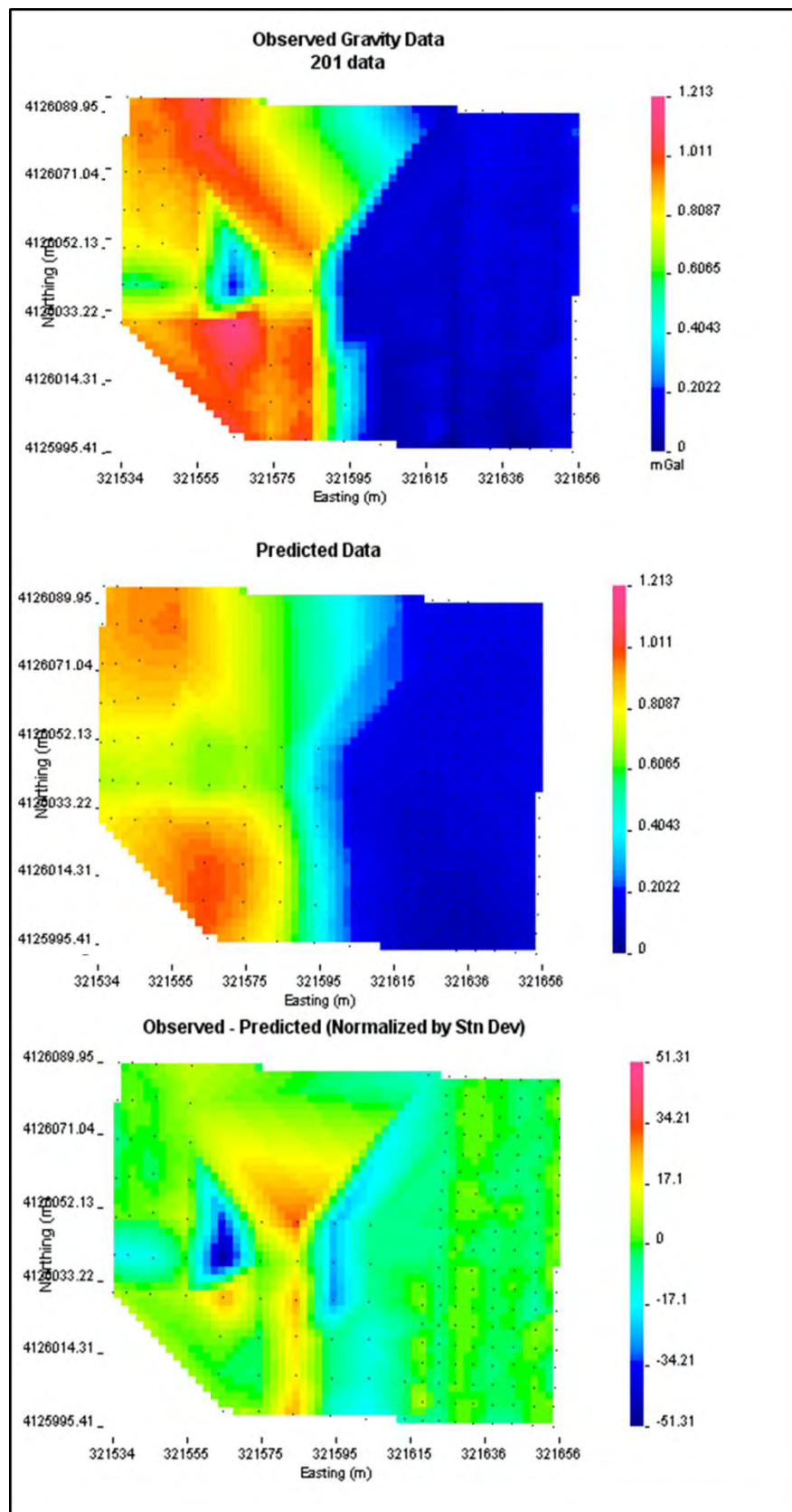


Figure 6. 15 3D Entire Zen Garden site inversion process.

## Results and interpretation

The eastern part of the density model showed a low density contrast that corresponded with the high resistivity area in EM-31 data. This part of the model was interpreted to have a large volume of travertine that could possibly have great pore volume around 30% that produced low density values between 1.8 to 2.1 g/cc. Hot springs at the surface possibly formed the great scattered volume of travertine at the east side. The water level dropped due to production of hot water in surrounding wells. Therefore, it is not possible to observe hot springs at the surface in the eastern part of the survey. However, it is possible to interpret that the hot water is circulating through the travertine in horizontal fractures toward the west side where the hot water pipe was found (Figure 6.16). Also, it is interpreted from the DC resistivity inverted data that there is a possible conduit of water running north-south (Figure 6.19). In the west side of the model it is possible to observe a great contrast between low density and high density rocks or layers. This could be interpreted as the contact between a region with a large amount of travertine and the Mancos shale, or a shale-prominent region with higher values of density between 2.68 and 2.72 g/cc. (Values known from well log interpretation). Also, it is possible to observe these changes in resistivity in the EM31 data.

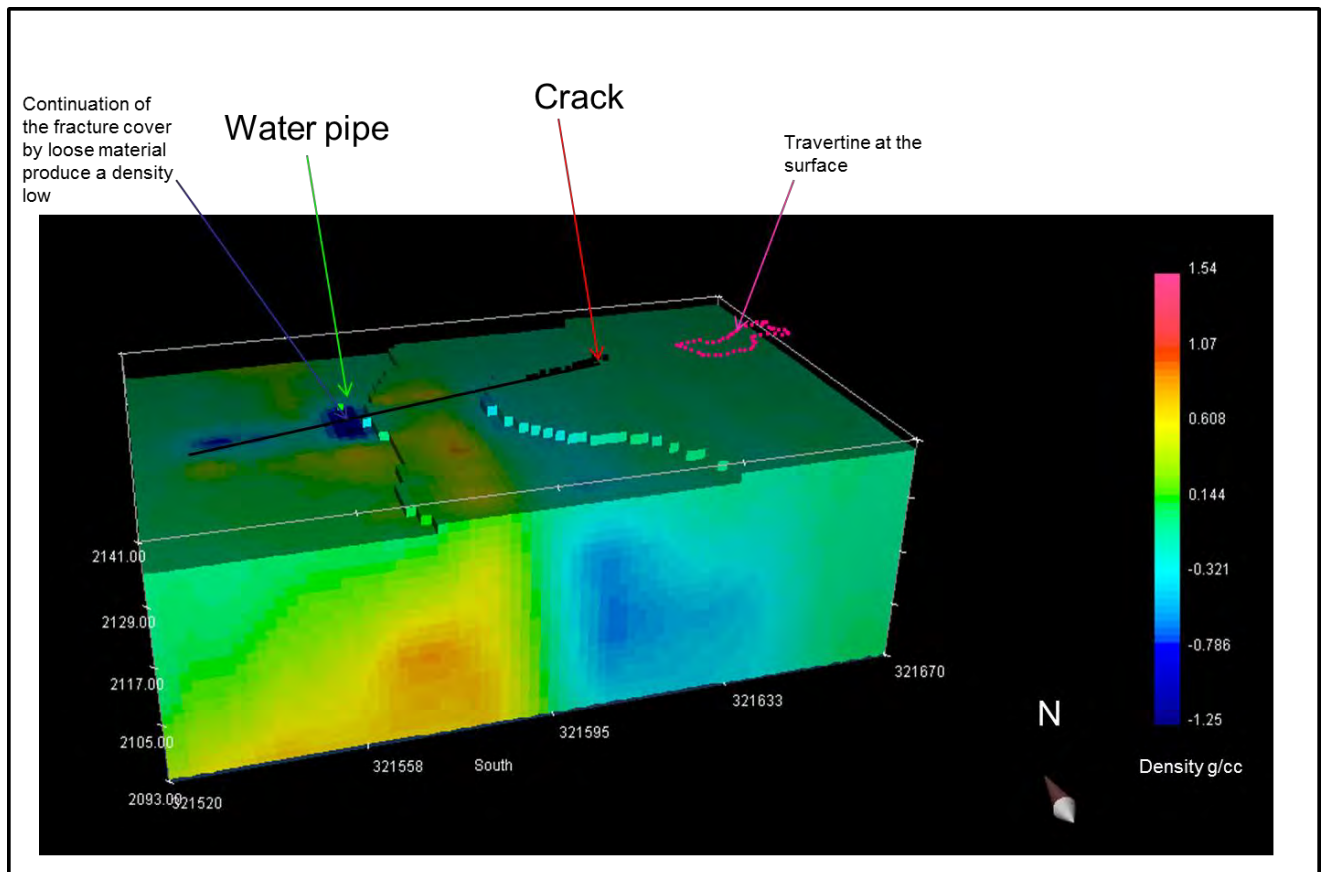


Figure 6. 16 Inverted gravity data with interpretation over the Zen Garden site.

The EM-31 data shows a transition between a resistive material to the east to less resistive material to the west. This could be interpreted to be the transition between an area with high volumes of travertine (resistive) to a shale-prominent formation. This could be covered by river sediments or deposits. Human activity in the area may affect the gravity data, like materials brought in from external locations, for example to fill voids. Also, construction materials on the site probably affected the gravity observations. A schematic interpretation is presented in Figure 6.17 and Figure 6.18.

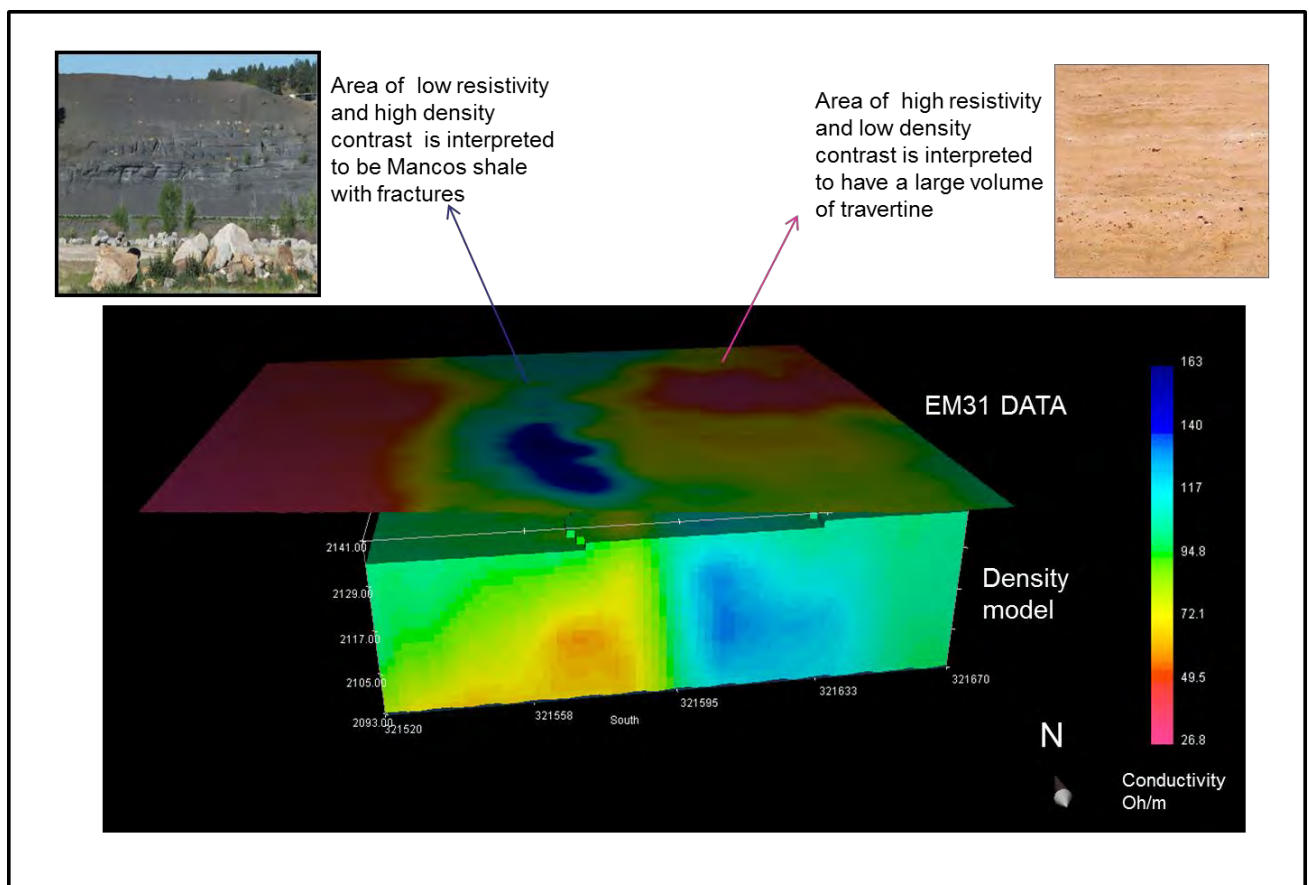


Figure 6. 17 Correlated gravity and EM data over the Zen Garden site.

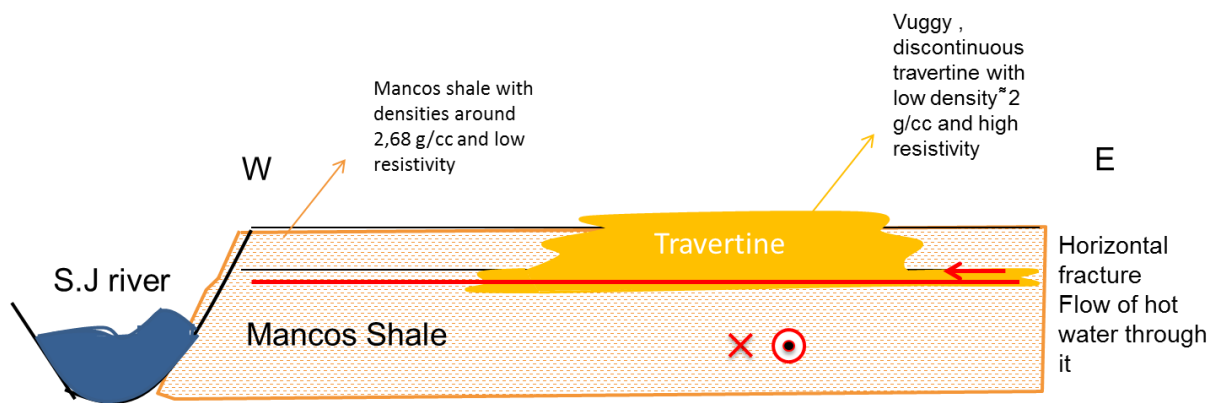


Figure 6.18 Location of travertine on the Zen Garden site in relation to the San Juan River.

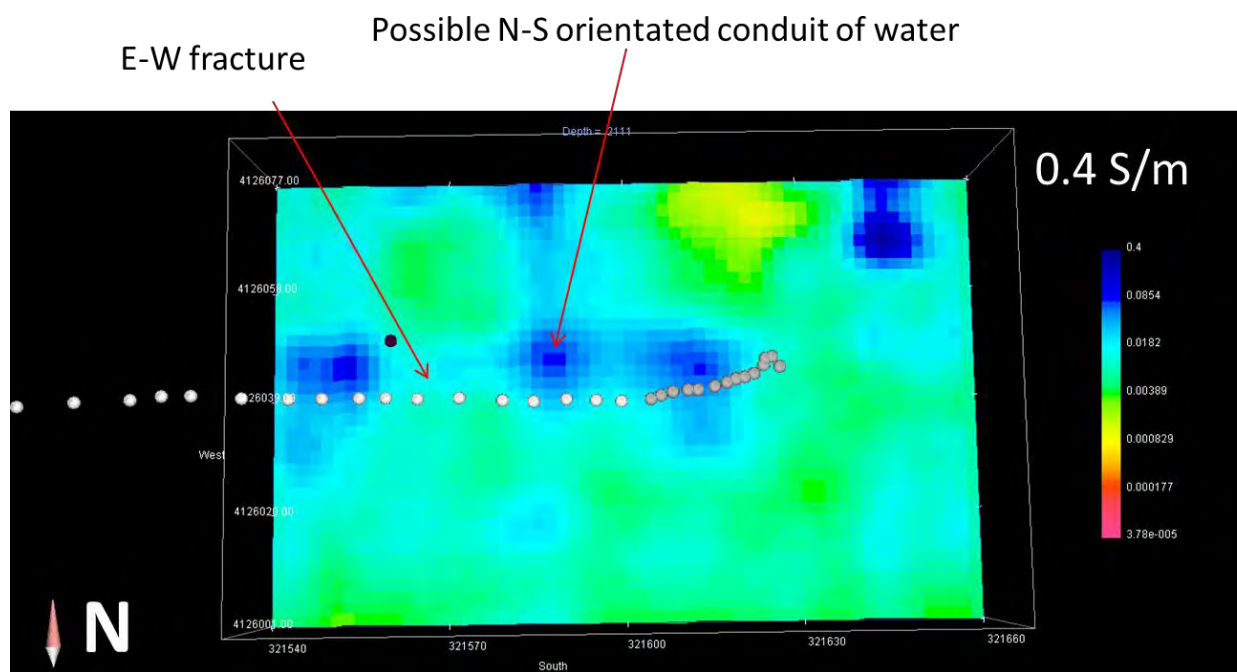


Figure 6.19 Fracture location in reference to inverted gravity data at the Zen Garden site.

In addition to the general interpretation of the entire Zen Garden region where gravity data was collected, the finely sampled 5x5 m subsection that was sectioned off and inverted, gives a few additional insights into the area. The inversion process used a similar style mesh used in the full site inversion and ran the same programs to retrieve the gravity density model, but in this case a regularization parameter of 10 was used. Within the subsection it can be seen that there is a similar pattern of density contrasts in the area. The higher density portions are seen in yellow and the lower density portions are contrasted in a blue green shade as seen in Figure 6.20. It can be concluded that the higher density sections are likely to be the locations of the travertine but there are still questions concerning sources of error. These sources still



include possible fill in sites of the past hot springs and filled roads in the area. The most important conclusion that can come from this section is that it can be seen that the location of the crack, seen in Figure 6.21, crosses an area that decreases in density and widens to the south, which was the conclusion also reached by GPR data in the area. Overall this is a variable region but a few simple conclusions can be made in the area.

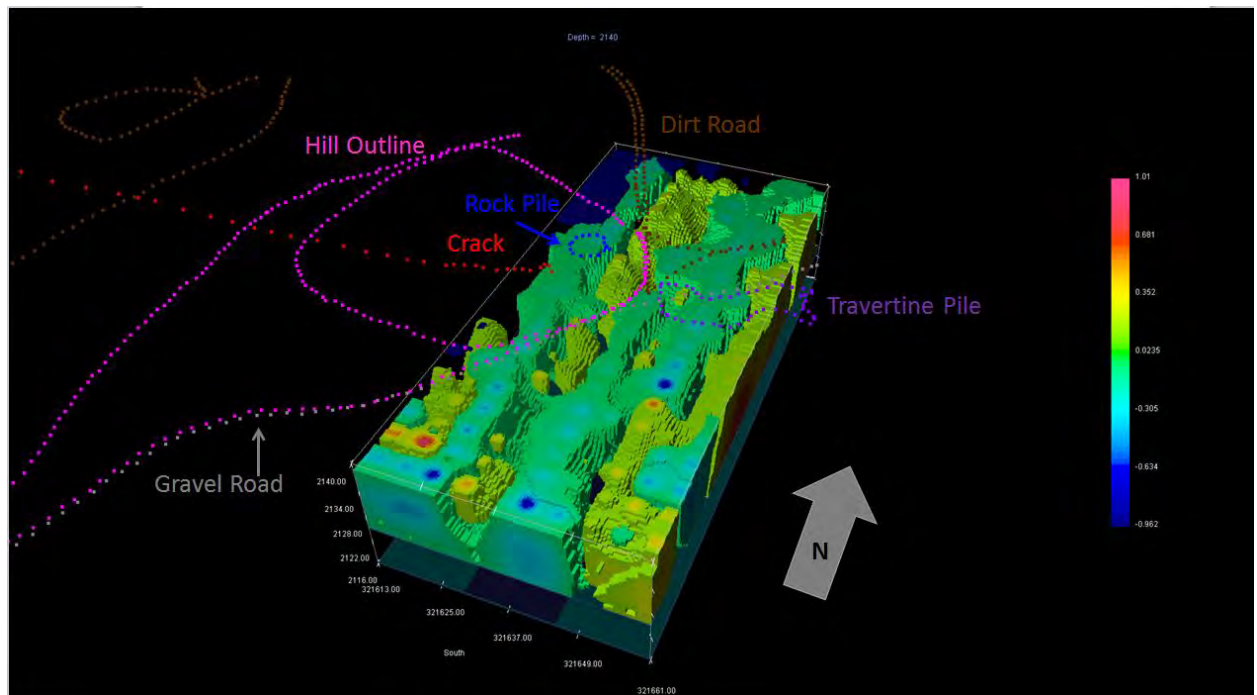


Figure 6. 20 5x5 Subsection of finely sampled gravity data with known locations of landmarks in the Zen Garden site.

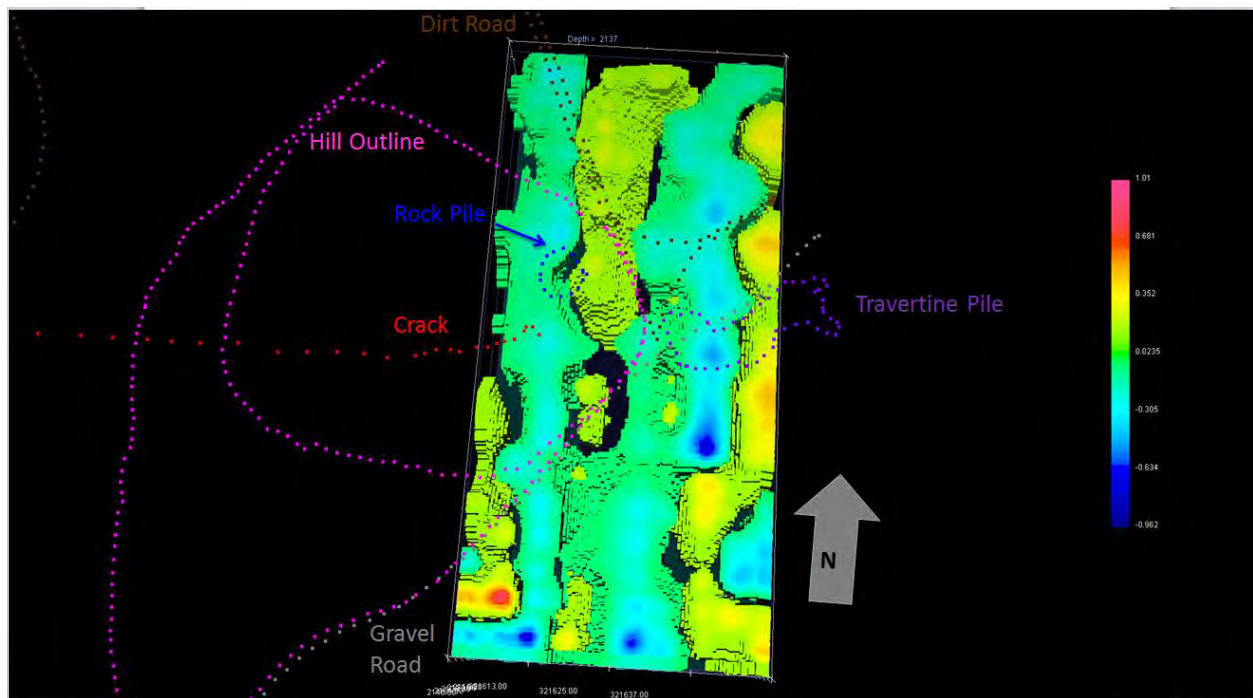


Figure 6. 21 5x5 Subsection of the finely sampled gravity data with known locations and close up of crack in the Zen Garden site.

## 6.6 Conclusion

The gravity data collected throughout this camp helped form a better understanding of the sub-surface geology of the Pagosa Springs area. The inversion and forward modelling that was conducted were able to confirm some of our original geologic interpretations of the area.

**Airport:** The southern portion of the airport crossed the Eight Mile Mesa Fault, which can be confirmed by the slight difference in the gravity anomaly. This is caused by the lighter Dakota Sandstone being close to the surface and the heavier Mancos shale existing at the footwall.

**Barn3:** This line crossed the Eight Mile Mesa Fault as well. There were high gravity anomalies observed to the east of the fault which indicate basement uplift. Toward the west section of the line the gravity values began to decrease, suggesting a deepening of the basement. A large negative anomaly showed a sudden increase in the basin thickness over this area, possibly generated by a small graben structure.

**Hot Springs:** There were three lines of gravity data obtained at the hot springs site: PAGO01, PAGO02 and PAGO03. The PAGO01 and PAGO05 lines had relatively simple

and flat layering geology. PAGO02 data showed a decrease in gravity data over the potential fault. This data had such a low density contrast that it could not really be used to detect the fault. On this line magnetics data was very useful to help with the fault interpretation.

**Warm Springs:** The gravity survey on this site was very short, so not much data was collected. The gravity anomaly for this area was very small. There were slightly higher values to the north where the heavier Mancos shale was found. The measured gravity anomalies at this site were only related with shallow features.

**Zen Garden:** There was a visible density anomaly from east to west. This was a transition from a less dense material to a denser material that is interpreted to be a contact between an area with large volumes of travertine and Mancos shale. It is also possible to observe a contrast of low density around where the water pipe was found.

A recommendation for surveys in the future would be to have a consistent base station. Also, sites on flat, open areas would be ideal so that there could be accurate GPS readings for each station. It is also recommended to apply a regional residual separation to the data as an additional correction to the gravity observations. For the gravity inversion at the Zen Garden it is recommended to extend the grid to the west side in order to obtain more density contrast information. Overall, the gravity method proved useful and was a valuable learning opportunity for all students. The gravity data and interpretations will help in the characterization of the geothermal energy system in the Pagosa Springs area.

# 7. Magnetism

---

## 7.1 Introduction

The primary goals of the magnetism investigation in the area surrounding Pagosa Springs were to confirm the location of suspected faults, identify areas of previous or current water flow, and to determine the depth and shape of the pre-Cambrian crystalline basement. Magnetic surveys usually cannot identify areas of water flow, but because the water at Pagosa Springs came from a great depth it likely had magnetic minerals dissolved in it. These waters that solidified into travertine should still contain a magnetic signature. The presence of magnetic minerals in the pre-Cambrian basement is one of the main reasons that magnetism can be used to determine the basement structure. Magnetic surveys can also see the sharp contrasts between different types of sedimentary rocks that accompany faults.

Magnetic surveys measure a physical property known as magnetic susceptibility. Magnetic susceptibility is defined as the scaling factor between the magnetization of a material and the magnetic field it is placed in. All rocks are initially created or deposited with magnetic information specific to that time. The orientation of the magnetic dipoles within the rock indicates the direction of the ambient magnetic field. These directions can be changed if significant heat and pressure are applied to the rock. The magnetic susceptibilities of rocks depend highly on the amount of magnetic minerals present. The most common of these is magnetite. More information on the science behind the magnetic method can be found in Appendix D [19].

There were two different types of magnetometers used in the surveys at Pagosa Springs. The first, a cesium magnetometer, was a G-858 MagMapper. This magnetometer is ideal for continuous collection because of its high sampling rate. The second, a proton precession magnetometer, was a G-856 AX. This magnetometer has difficulty collecting higher frequency magnetic data making it ideal for base station corrections [31]. The proton magnetometer was used as a base station at each site in order to monitor the changes in the earth's magnetic field. The cesium magnetometer was used as the rover in all of the surveys and put on continuous collection mode in order to collect a constant stream of data. More information on the magnetometers used can be found in Appendix D. The cesium magnetometer was placed in vertical gradient mode so that it collected data from a top sensor and a bottom sensor. These data points were then used to calculate the vertical gradient between the two sensors. A picture of the set-up is shown in **Error! Reference source not found.**



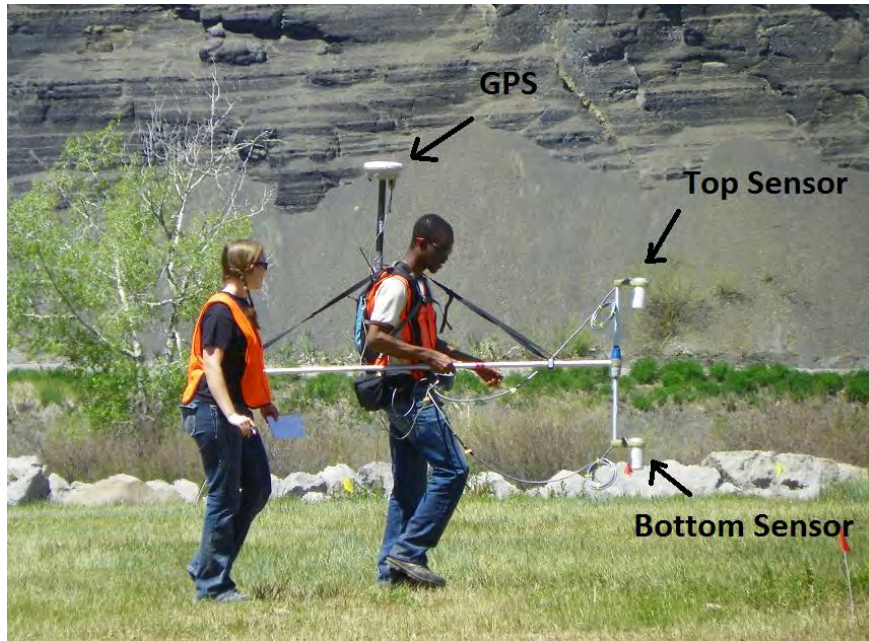


Figure 7. 1 The set-up of the roving cesium magnetometer.

## 7.2 Survey Sites

Magnetic surveys were performed at the following locations: Zen Garden, warm springs, PAGO01, PAGO02, Steven's Airport Seismic, and Barn3 Deep Seismic. The picture in **Error! Reference source not found.** shows the locations of all of these sites.

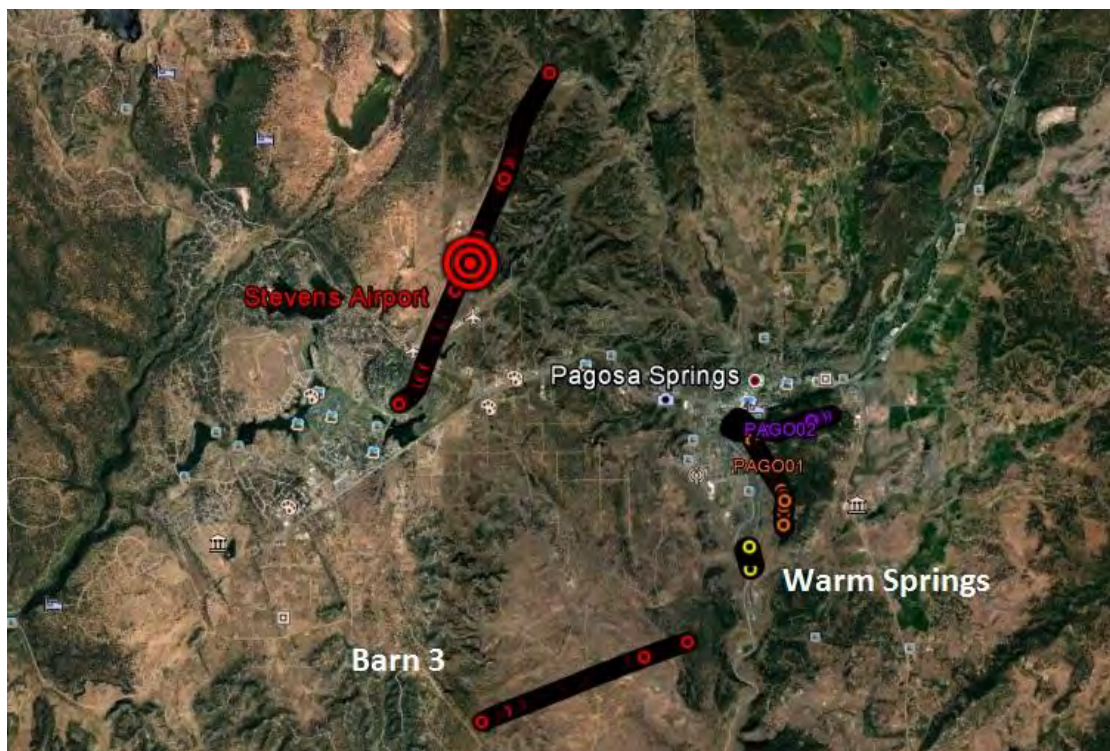


Figure 7. 2 Map of the Pagosa Springs area showing locations where magnetics surveys were performed.



### 7.3 Survey Design

The survey at the Zen Garden was designed to give a better understanding of the extent of the travertine in the field and the behaviour of the fracture within the travertine. **Error! Reference source not found.** shows a map of the location and survey points of this grid. The two primary targets were believed to be relatively shallow and the fracture had a small surface expression. This indicated that a tightly-spaced survey should be used to increase resolution across the area. Because the cesium magnetometer can be operated quickly it was determined that the entire Zen Garden grid could be surveyed at 5m spacing in a relatively short period of time. The complete 140m x170m grid was therefore studied. It was determined that the best data would be collected if the instrument were run in continuous mode. To account for the uncertainty in location one would expect with this collection method it was determined that a GPS rover would be carried with the instrument so that each measurement in the field could be correctly correlated to an accurate position.

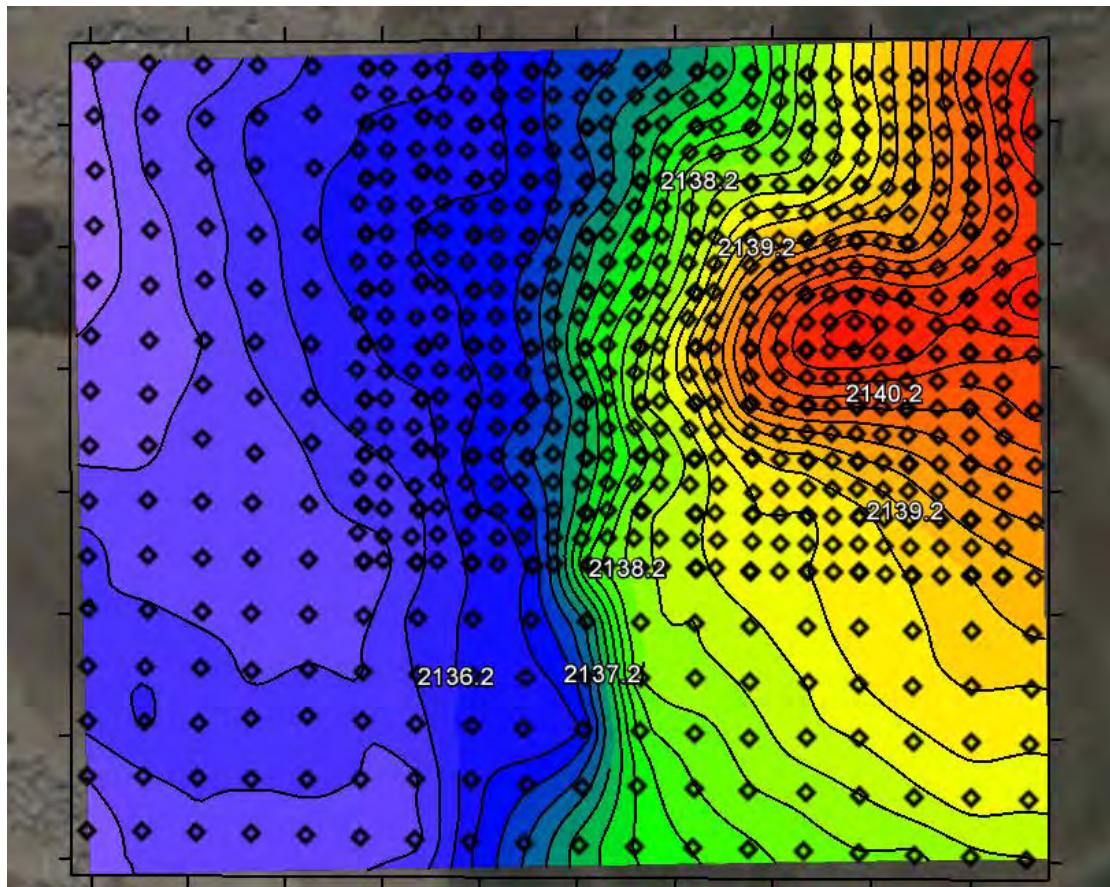


Figure 7. 3 Map of the Zen Garden survey site (black diamonds indicate flag locations).

At the Stevens Airport site the magnetics design was set up to correlate well with the seismic line that had already been established. This correlation would include the identification of the known fault and the characterization of the depth of the basement. **Error! Reference source not found.** shows a map of the location of this survey line. The line had takeouts every 15m with flags alternating between blue

and pink. It was determined that for this survey line it would be appropriate for the magnetometer to mark every 30m, meaning every other flag. It was decided that pink flags would be used as they would be more visible from a distance in areas with higher grass or brush.



Figure 7.4 Map of the location of the Steven's Airport magnetic survey.

The hot springs sites have magnetic survey lines that ran along the DC resistivity survey lines. These surveys were carried out at PAGO01 and PAGO02. Figure 7.5 shows a map of both of these lines, with the yellow and blue colors along their respective lines showing where magnetics was collected. The purpose of these two lines is to see if the magnetics can help identify the location of faults in the area and then to see if these locations match the locations that the DC resistivity surveys indicated. The markers on these lines were taken at every other flag. These flags were the locations of the electrodes for the DC lines and were spaced 20 meters apart. This gave the magnetic surveys a separation of 40 meters between markers. PAGO01 started near the river on the west side then ran through the student site, across the road and then encountered some terrain. It was run over a steep



hill and stopped about halfway across the plateau. PAGO02 also started at the student site, but was bearing nearly due east. After crossing the road, it ran to the south of the entrance road to the Frisbee park, up the gulch, and then continued winding its way to the top of the hill and partway down the other side.

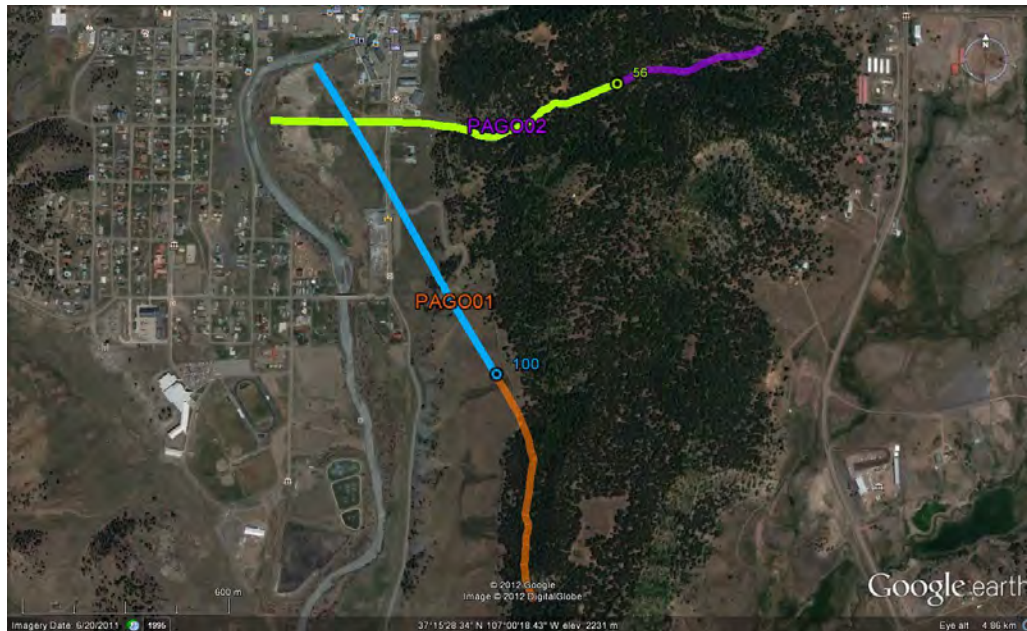


Figure 7. 5 Map that shows the locations of Pago01 and Pago02.

The survey at the Barn 3 deep seismic site was designed similarly to the Steven's Airport line in that it would help to determine the location of the fault and what layers existed in the subsurface. The original seismic line stopped on the east side slightly before the forest begins, but the seismic line was later extended to the location it is now. This change in the length of the line caused the data here to be collected in two different segments several hours apart.



Figure 7. 6 Map of the location of the Barn 3 deep seismic line located south of Pagosa Springs.

The survey at the warm springs site contained seven survey lines that had markers on each line spaced 20 meters apart. The flags at this site were space five meters apart so markers were taken at every fourth flag. The purpose of this survey was to characterize why there was a localized area of warm water at the surface and entering the river at this site. Because of time constraints only one of the lines of magnetics data was used in the modelling/inversion. The map of entire warm springs site is shown below in **Error! Reference source not found.** The fourth line from the left is that one that was intended to be used in the forward modelling of the gravity and magnetics.

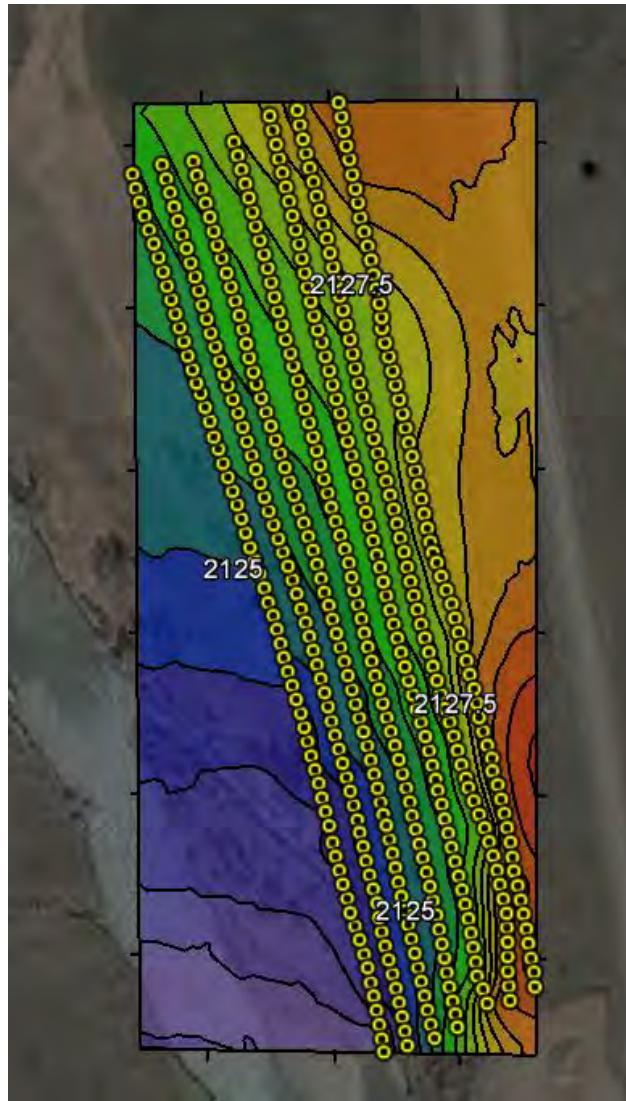


Figure 7. 7 Map of the warm springs site. The line used in the forward modelling of the gravity and magnetics data is the fourth one from the left.

## 7.4 Processing

All of the data that was collected was first uploaded from the magnetometer into MagMap2000. MagMap2000 offers a default program that automatically takes into account how the data was collected and assigns relative positions to these values. This program was ignored for all of the sites. The individual points were assigned UTM coordinates later. At each of the survey sites there was a base station set up that monitored the change in the ambient magnetic field. The base station data was used to correct the recorded magnetic data for each site. MagMap takes each data point recorded by the rover and searches for a base station reading with the same, or very close, time stamp. It then subtracts the base station reading from the rover data point which creates a diurnal reading. If no exact reading for a given time stamp is available, MagMap will linearly interpolate what the base station reading should be.



For all of the sites except for Zen Garden a program was written in Matlab that reads in the magnetic data file and a GPS file of all of the marker locations. It then calculates the distance between each marker and the time it took to get from one marker to the next. The program then determines the amount of time that passed since the previous marker and the data point that was collected during continuous collection using the time stamp associated with that point. This time is multiplied by the velocity of the magnetometer in order to come up with the exact position of the data point in Northing, Easting, and elevation. This Matlab program was used for the following locations: Warm Springs, PAGO01, PAGO02, Airport Deep Seismic, and Barn 3 Deep Seismic.

After a GPS location was associated with each data point, the data was opened in Microsoft Excel and the top sensor, bottom sensor, and gradient data were plotted in order to identify dropouts i.e. locations where there is a zero reading or a very low reading. If multiple dropouts occurred in succession these points were deleted from the data file, but if there was only one dropout bordered by usable data the values for this data point were linearly interpolated. If a line of data was collected in parts, the multiple lines were sewn together into one continuous line of data.

The Zen Garden magnetic data was collected with a continuous GPS device on the surveyors back. This simplified the processing for this site. Once the base station corrections had been made in MagMap the file was plotted using CGEMaestro software. In all plots the grid increment was set to 1.25, as the grid spacing during the survey was 5m. When the plot had been made it was determined that the heading errors were minimal, which removed the need for a levelling correction. It was noticed in the plot that GPS offset may have been occurring. The fracture in the travertine should have appeared as a continuous line in the data, but instead it was seen as a series of dots about 4m apart along the north/south lines. During the magnetics survey at the Zen Garden, the GPS device was carried in a strap bag hanging 1.6 m above the bottom sensor. It is also located about 0.25 m to the East when walking towards North and 0.25 m to the West of the sensors when walking southwards. Along the direction of acquisition (Northing) the GPS was 1.4 m behind the sensors. Hence the GPS offset of about 4 m observed in the data can be explained by the horizontal difference in distance between the GPS and the sensors as we move towards North and South.

To correct for these offsets, the corresponding differences in the GPS location and the sensors were systematically added or subtracted to the data location. The same corrections were made in the Easting direction which has a difference of 0.25 m and the height with difference of 1.6 m. Displaying our observed data after these corrections shows the observed anomalies to be relatively linear as opposed to the offsets observed before the corrections were made.

Inversions for the Zen Garden site were completed using software from the University of British Columbia and Geophysical Inversion Facility. Within the Geophysical Inversion Facility the Mag3D

software was used. After inversion the results were plotted using the Generic Mapping Tool within the CGEMaestro software. The data errors for all measurements were set to 7.5nT. The mesh and topography used were coordinated with the SuperSting DC-Resistivity and CG-5 gravity groups working on the student site to allow for easy integration of the three methods.

The data from the Steven's Airport, Barn 3 deep seismic, PAGO01, and PAGO02 were all uploaded into the Oasis Montaj software, GM-SYS. This is a forward modelling software that utilizes a user inputted geological model and determines what the gravity and magnetic response should be from this model. The user draws the model in the program and chooses density and magnetic susceptibility values that are associated with specific rock types. The predicted magnetic data from the model is plotted on the same graph as the observed magnetic data and similarly with the gravity data. The user then changes the model until the predicted and observed data match up best for gravity and magnetics. This model can then be used as a geologic cross section for interpretation. Because of a malfunction with the forward modelling program, the PAGO01, PAGO02, and Barn 3 lines were unable to be modelled. The plots of these lines are shown in Figure 7.8, Figure 7.9, and Figure 7.10. These plots show the general trends in the data as well as locations where there were large, localized anomalies.

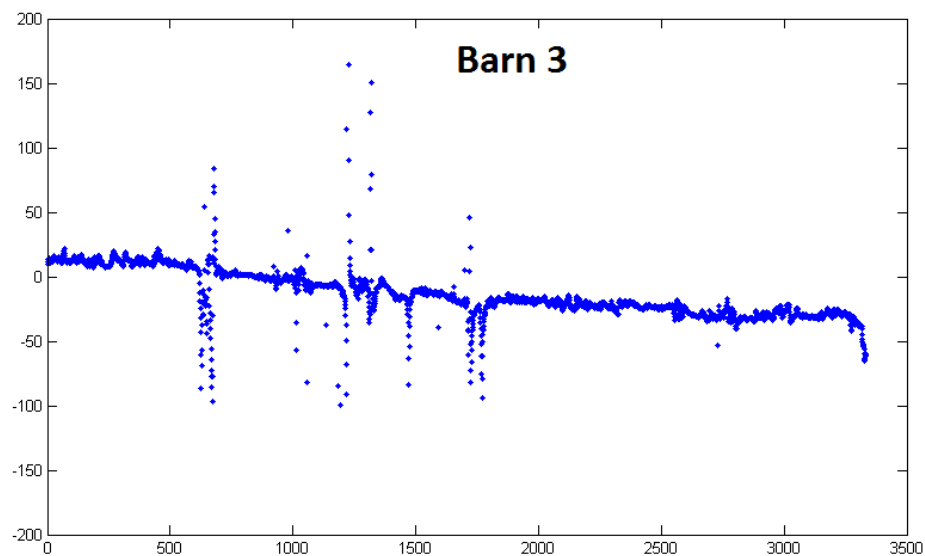


Figure 7.8 The Top DNL data for the Barn 3 deep seismic line.

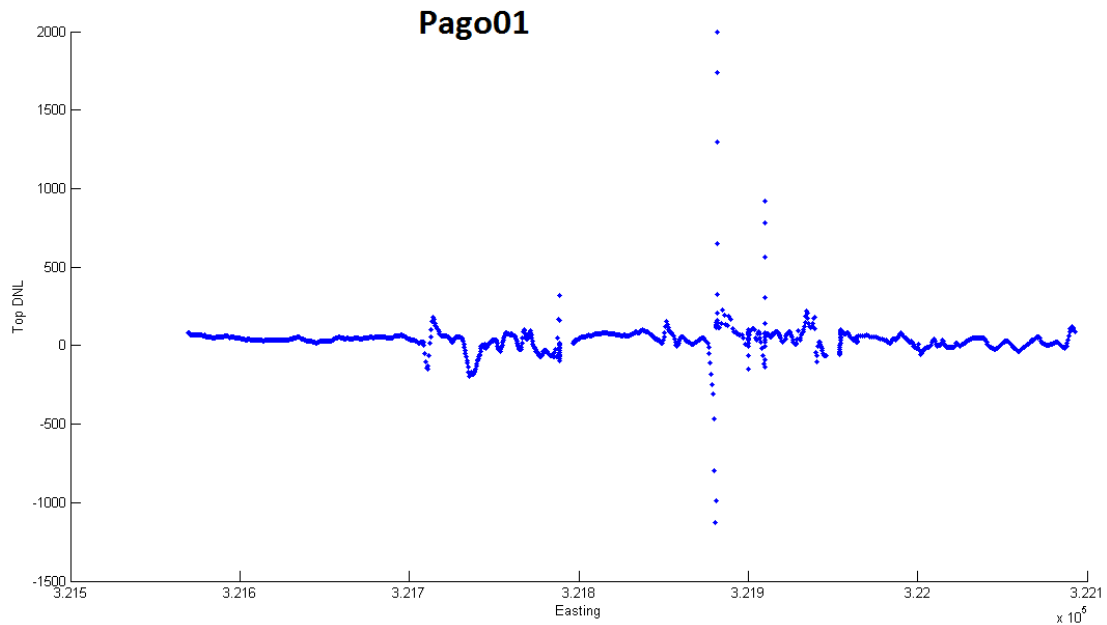


Figure 7.9 Plot that shows the Top DNL data for the PAGO01 line.

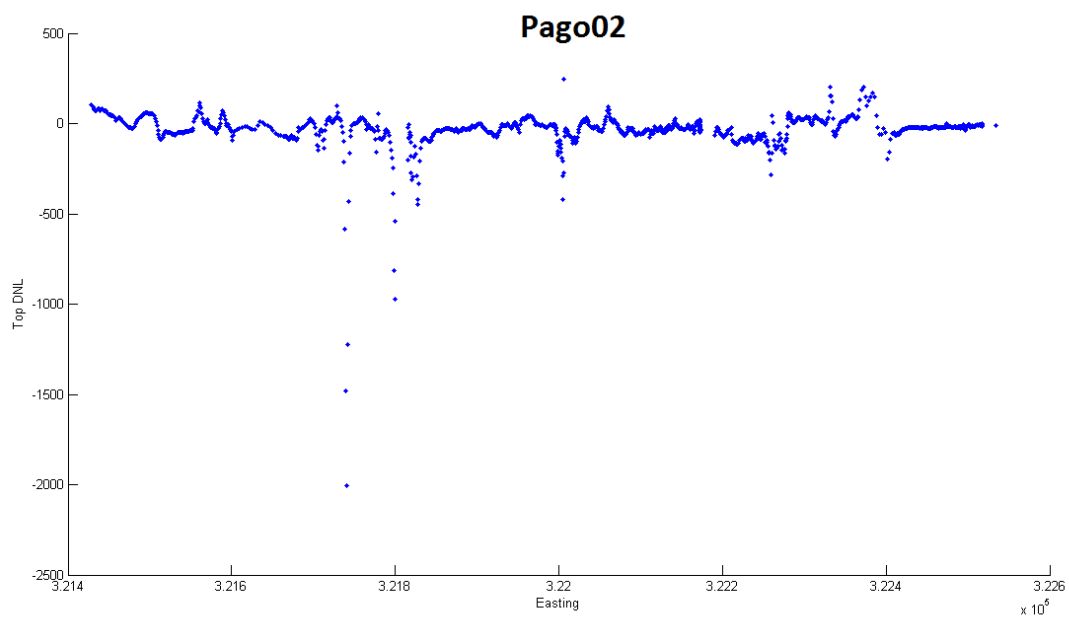


Figure 7.10 Plot that shows the Top DNL data for the PAGO02 line.

## 7.5 Uncertainties/Errors

The magnetometer that was used to collect data along all of the surveys uses continuous collection. The user of the roving magnetometer maintained an average walking speed of approximately 2 m/s. At this speed and with a collection frequency of every second it would be difficult for the magnetometer to observe any anomalies that are smaller than 1 m. Absolute location such as flags, are noted with a marker on the machine. A roving GPS collects data at each of these flag locations

and then later the GPS locations for each of the magnetic data values is interpolated by assuming a constant walking speed and the amount of time between the previous marker and the current time stamp. Because of elevation and other hazards, the person collecting data is not always walking at a constant speed. This can cause data points to be pushed together or spread out too far between marker points.

Another large uncertainty was where exactly each marker was measuring. Due to a lack of knowledge of what marker the surveyor was on, the notes for these surveys are often very confusing. At the airport site, what the notes say and what the magnetic data says about what marker they are on is already off by the time that the survey reaches the 40<sup>th</sup> flag. On the PAGO02 line and warm springs site there was a large problem of identifying which flags the markers were taken. The original collector and note-taker did not completely agree with which where these markers were taken. At the Barn 3 deep seismic site there were a lot of pauses due to fences and abrupt changes in topography or obstacles. These pauses made it very difficult to determine which markers were created because the users actually arrived at the correct location, or if they were just pausing and hit the incorrect button. The time stamps of each data value were used in order to answer this question best. Because the Barn 3 was created and then later extended, the magnetic data on this line was collected in two sections.

After all of the lines of data were initially processed they were forward modelled along with the gravity data. In the forward modelling of the Stevens Airport deep seismic line there was an over trend in the gravity data from an unknown source that caused the observed data to be shifted from the predicted model by a significant amount. This shift appeared to be a rotation that may have been caused by the surrounding topography and/or large scale geologic features like the mountains located to the northeast.

The student site, Zen Gardens, used the magnetometer with a roving GPS on the back of the person collecting the data. This GPS did not collect elevations along with the northings and eastings. This made it necessary to use a topographic model of the area and not actual data collected at the same time.

There were several locations of noisy data at the Zen Garden site due to surface rock piles. These locations are circled in the magnetic data in Figure 7. 1111

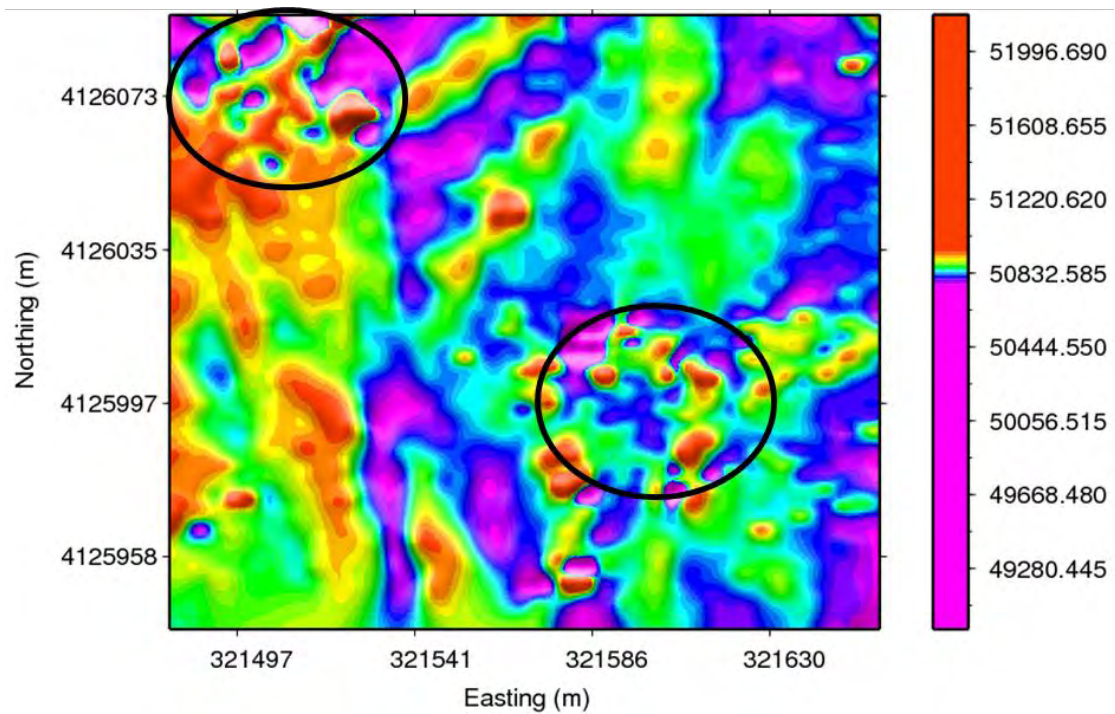


Figure 7.11 Magnetic data after the GPS offset correction. The black circles indicate locations of noisy data most likely due to surface rock piles.

The heading errors were not corrected in the Zen Garden data. These errors did not affect the data greatly and would not have changed much if removed, but it could have removed some of the uncertainty of the inversion.

## 7.6 Interpretations

### 7.6.1 Zen Garden

The large rock piles and multiple roads at the Zen Garden site created very noisy data that is difficult to interpret reliably. The most accurate inversion found several rings of higher susceptibility in the south east quadrant of the grid. An image of these rings and obstacles is shown in Figure 7.12. The image shows the locations of the surface rock piles using red circles. It is believed that the rings of higher susceptibility are not true geologic features, but are instead caused by the instrument varying slightly from the grid in order to move around the rock piles. This would lead to the computer program interpolating a few points in order to fill in the area that had not been directly surveyed. It is possible that a few slightly higher or slightly lower susceptibility data points near these voids in the data collection led to these anomalies in the inversion. The northern rock pile has a high magnetic susceptibility associated with it while the southern rock pile has a low. The reason for the low susceptibility of the southern rock pile is unknown. The solid red line indicates the gravel road that runs through the southeast corner of the site. The dotted red line northeast of the north rock pile is the surface crack. This feature does not show up in the data before or after inversion. This could be because it is below the resolution of the equipment. The inclined surface pipe is labelled in the image



and the anomaly associated with it is most likely due to the flowing water that was discovered at the bottom of it.

Immediately to the west of this surface pipe there is linear feature of low magnetic susceptibility. This feature also shows up in the EM31 data. It cannot be said that this area of low susceptibility is water itself, as it is possible that during the long cycle of being heated and traveling to the surface magnetic minerals dissolved in the water. There is the possibility; however, that this area of lower susceptibility is showing a change in the surrounding rock due to the presence of water.

The dotted red line in the northwest corner of Figure 7.1212 is a dirt road that winds around/through rock piles. The red circles are locations of surface rock piles. The broken lines in the top left corner are part of a dirt road path. The solid lines running from the top right of the image down and to the left are the gravel road. These piles are likely the cause of the chaotic data observed. The presence of such large features on the surface meant that the survey could not directly follow the grid, again possibly leading to the problem of the software interpolating a few data points. This portion of the inversion should therefore also be viewed cautiously.

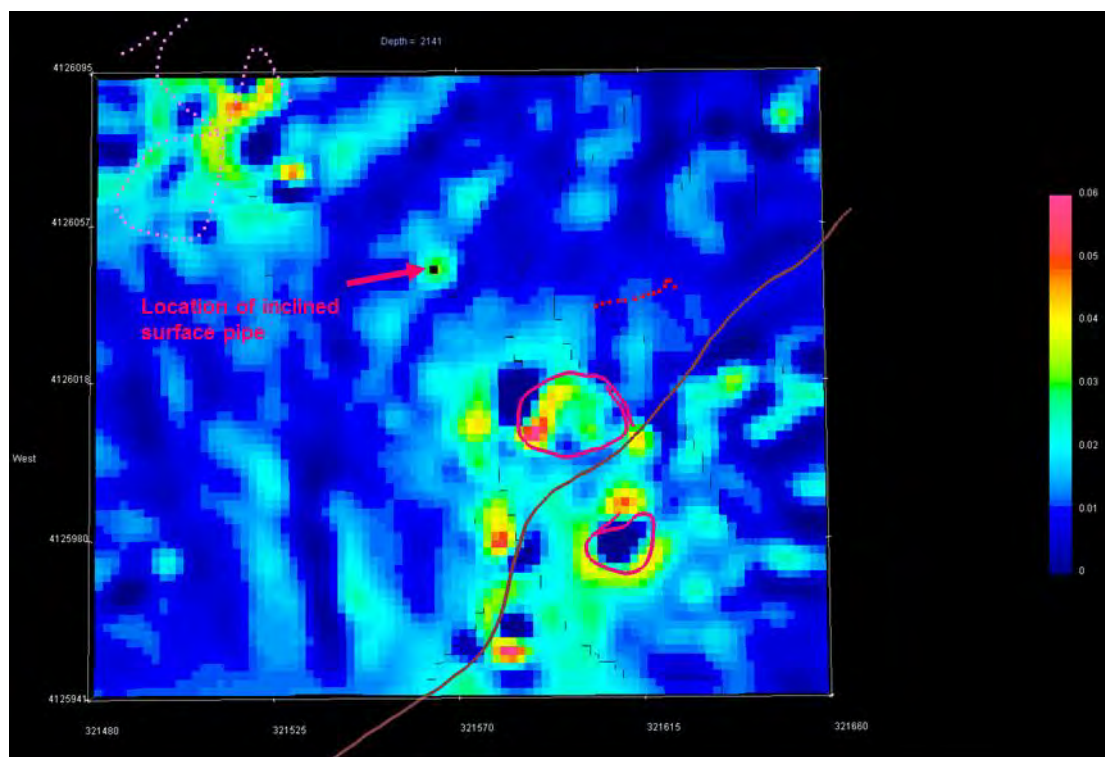


Figure 7.12 Image showing the inverted magnetic data at the surface of the Zen Garden site.

Figure 7.133 shows a 6 m depth slice of the same inverted magnetic data. The middle susceptibility values were removed in this image in order to highlight the highs and the lows. The same high and low features can still be seen at this depth. The anomalies in the EM31 data at 6 m are also in the

same location. After observing the same anomalies as the EM31 at 6 m depth we looked at a depth slice of 15 m and observed consistent anomalies with the EM34 data. The 15 m depth slice of the inverted magnetic data is shown in Figure 7.144. The low susceptibility anomalies (circular rings) get wider in diameter as you look deeper in the subsurface. A possible interpretation to this phenomenon could be the presence of geothermal vents. Similar structures are observed in the GPR data, but the locations of these structures on both data are inconsistent.

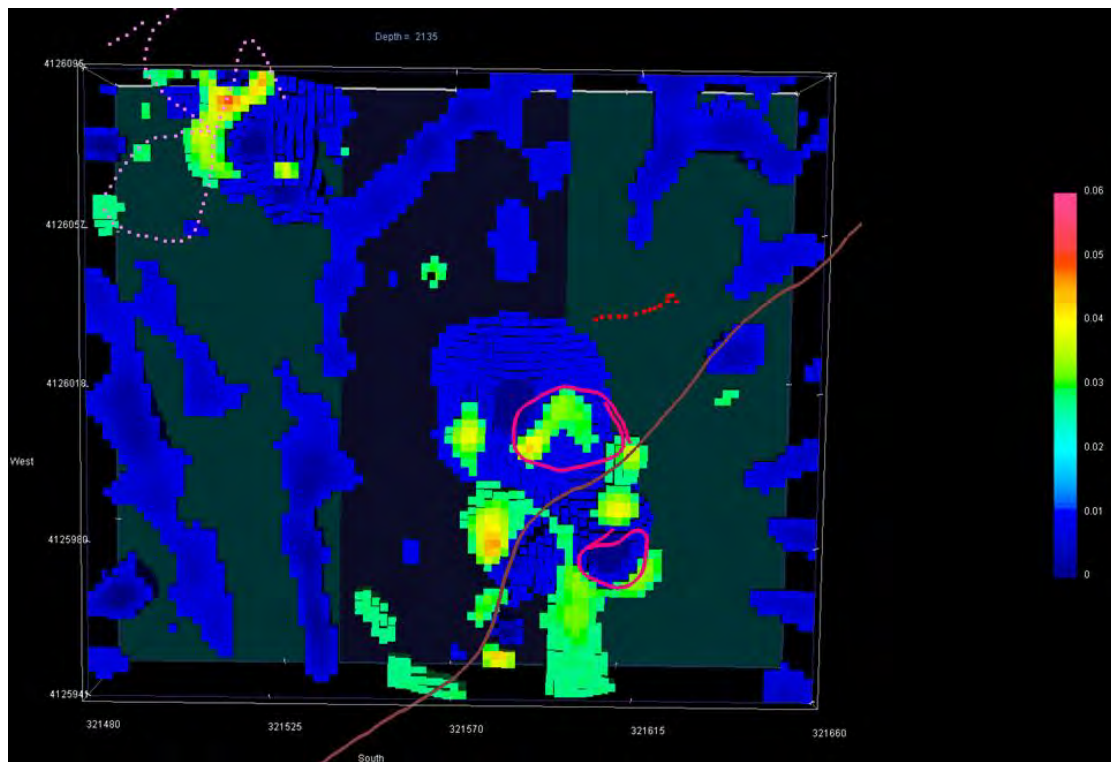


Figure 7.13 6 m depth slice. Image that shows the inverted magnetic data at the Zen Garden site at 6 m depth.

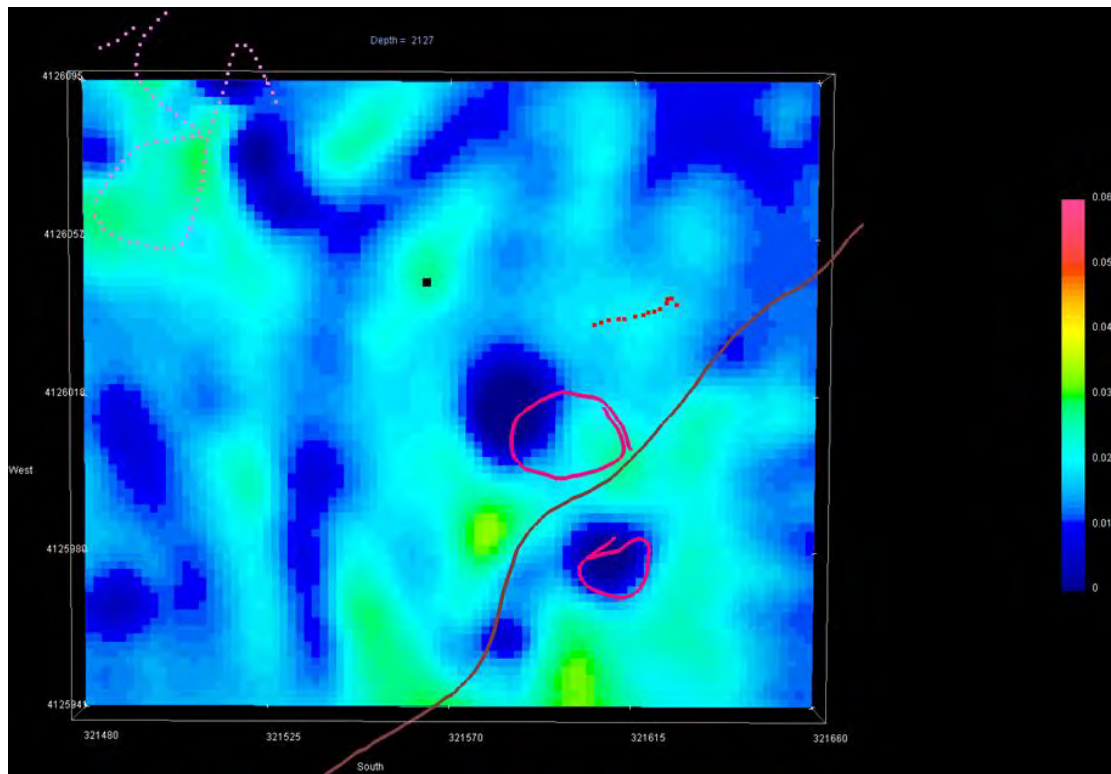


Figure 7.14 15 m depth slice. Image that shows the inverted magnetic data at the Zen Garden site at a depth of 15 m.

## 7.6.2 PAG001, PAG002, Barn 3 Deep Seismic, and Warm Springs

At this point in the forward modelling something went wrong with the program and did not allow us to properly model the magnetic response to our model. The incorrect model is shown in **Error! Reference source not found.15**. The program also incorrectly modelled the magnetic data from the Barn 3 site.

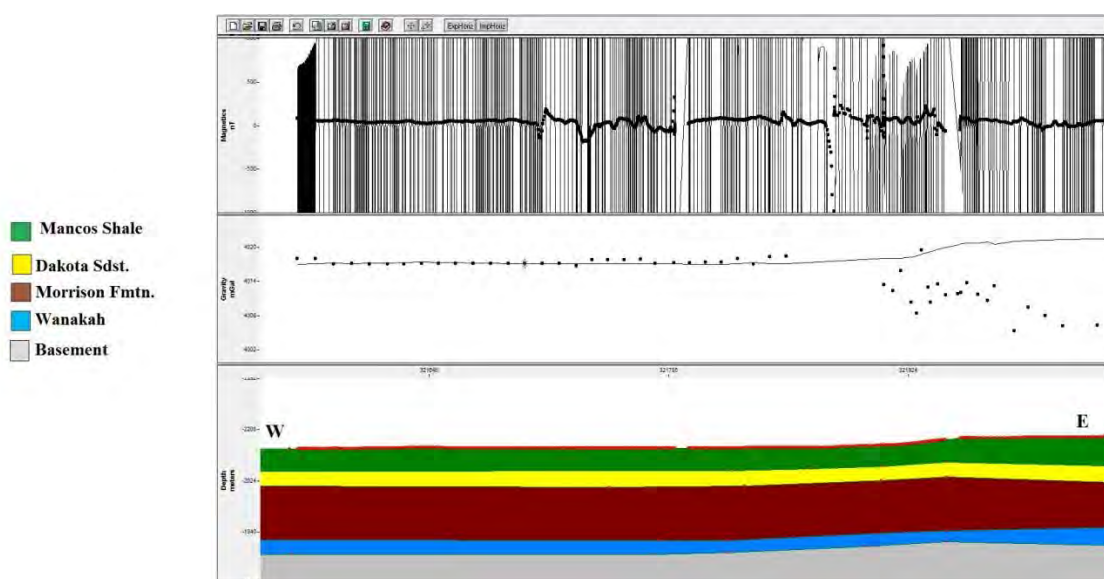


Figure 7.15 The magnetic data is shown in the top tile with the gravity data below that and the model below that.

Because of this error in the GM-SYS program, the magnetics data was not used to create the model that is shown in **Error! Reference source not found.16**. In this top tile of this image, the gravity data that was collected is indicated by black dots and the calculated gravity from the model is shown by the black line. The right half of the black dots drop off significantly and are very erratic. This is because of the second half of the data being collected on a different day and because the terrain it was collected on was very uneven and difficult to keep the machine steady.

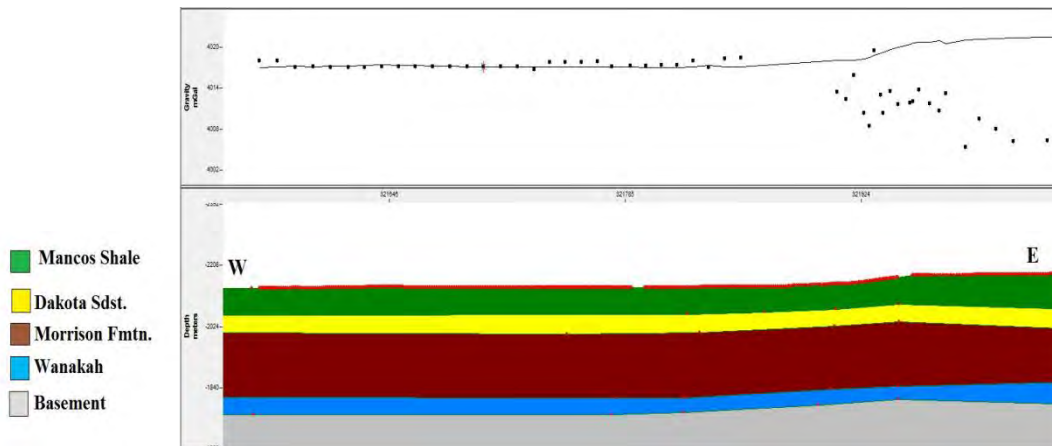


Figure 7.16 Model that was created at the Pago01 site using only gravity data.

### 7.6.3 Steven's Airport Deep Seismic

The modelling of the gravity and magnetic data at Steven's Airport was quite successful. The full image of the model and data is shown below in Figure 7.15. The top tile of the image shows the collected magnetic data as dots and the magnetic response to the model as a black line. The middle tile shows the collected gravity data as dots and the gravity response to the geologic model as a black line. The bottom tile shows the created geologic model. This model shows the fault that is known on the left southwest side of the line and a slight depression in the basement northeast of there. In the magnetics data there are many small anomalies that were not taken out of the data, but left in so that they might later be associated with similar anomalies in other methods. The airport line was one of the locations that a cross section was originally constructed so there were some parameters that were known before the model was created. One of these parameters is the presence of all of the layers shown in the model. All of these layers must be there, but the thicknesses and locations were able to be changed. It was also known that the Dakota sandstone was just below the surface of the runway. The left and right sides of the magnetic model are higher than they should be in order to fit the data, but a model could not be found that lowered one without raising the other.

The gravity model on this line fits the data very well except for a general overall trend of the model being rotated a few degrees clockwise from the data. The trend could not be corrected by inserting

the terrain to the northeast and southwest into the model. It is suspected that the trend occurs from the topography that is located off of the line.

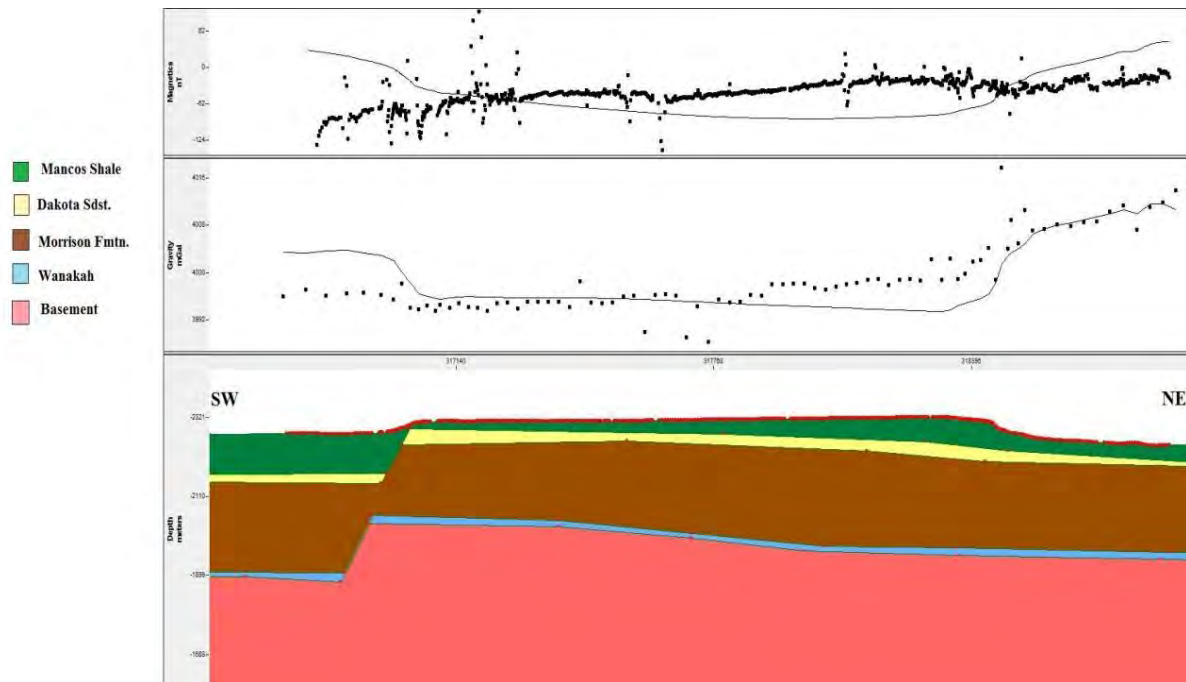


Figure 7. 15 Model created using GM-SYS modelling software. The top tile of the image shows the magnetic data and response, the middle tile shows the gravity data and response, and the bottom tile shows the geologic model

The magnetic and susceptibility values that were used for each of the rock formations in this model are shown in Table 7. 1

Table 7. 1 Magnetic susceptibility and density values for rock formations used during forward modelling.

Formation	Magnetic Susceptibility	Density ( $g/cm^3$ )
Mancos Shale	0.7 cgs	2.68
Dakota Sandstone	0.36 cgs	2.64
Morrison Formation	0.7 cgs	2.66
Wanakah and Entrada	0.14 cgs	2.62
Precambrian Basement	0.54 cgs	2.85

## 7.7 Conclusions and Discussions

### 7.7.1 Zen Garden

Using 3D inversion of the magnetic data we were able to come up with a usable model that gave us insight in to the structure of the area under the Zen Garden. The inversion did not image the crack that was on the surface most likely because the resolution of the instrument was not good enough. The inverted model did image a linear feature that ran the extent of the survey area roughly north to south. This linear feature has a low magnetic susceptibility and



shows up at the surface and at depths of 6 m and 15 m. This feature is also present in the corresponding electromagnetic data. A point of interest in these images is the PVC pipe that breaches the surface and extends down to running water. This pipe is in the middle of a localized high magnetic susceptibility and bordered by the low linear feature to the west.

### **7.7.2 Steven's Airport Deep Seismic**

The magnetic survey and subsequent forward modelling of the data successfully identified the location of the fault that exists on the southeast end of the Steven's Airport deep seismic line. The fault reaches the surface at an easting of about 3170303. The dip was harder to classify in the forward modelling, but is approximately 60 degrees.

### **7.7.3 PAGO01, PAGO02, Barn 3 Deep Seismic, and Warm Springs**

During the forward modelling of the magnetics and gravity data the GM-SYS software began malfunctioning and there was no way to correctly model the magnetics data. Because of this there are no conclusions about the magnetic susceptibility that can be drawn from the surveys completed at PAGO01, PAGO02, Barn 3 deep seismic, or Warm Springs.

# 8. Electromagnetics

---

## 8.1 Introduction

Electromagnetic (EM) methods exploit the properties of magnetic fields associated with alternating currents to determine the contrasts in conductivity in either geologic layers or in anomalous bodies. EM methods use the properties of electromagnetic waves which are composed of an electric and magnetic field. By measuring the changes in the magnetic fields created by an electrical source the apparent conductivity of the earth can be calculated. There are two ways in which data can be collected in electromagnetics: time-domain EM (TDEM), also called transient EM (TEM) and frequency-domain EM (FEM).

In TEM, a constant current is initially maintained, and then rapidly shut off. Generally it is acceptable to assume that the current is instantaneously shut-off. The primary current then decays down in a 'smoke ring' fashion, as shown in **Error! Reference source not found.** This primary current decay results in a time varying magnetic field in the subsurface, which subsequently induces eddy currents, resulting in a secondary current that sits on the skin of the surface [32]. This then produces a secondary decaying magnetic field, which can be measured at the receiver loop in the center of a larger transmitter loop

as shown in **Figure 8. 1**. When looking at anomalous bodies in TEM, the strength of the initial current only depends on the size of the object, but the decay of the current is dependent upon both the size and conductivity of the object. In more resistive bodies, the current disperses out faster, while in more conductive bodies, the current will decay at a slower rate. This phenomenon is explained by the diffuse vs. wave components detailed in the appendix

---

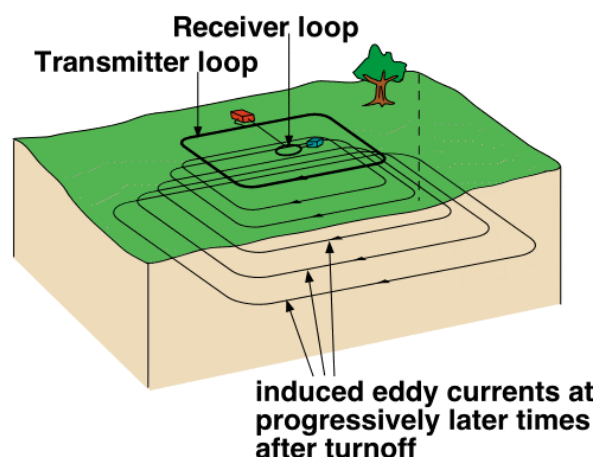


Figure 8. 1 Example of TEM acquisition, showing path of decaying current [33].

FEM involves having an alternating current pass through a coil of wire, which produces a time varying primary magnetic field that passes through objects of interest in the subsurface. This primary magnetic field then induces a secondary alternating current (eddy current) in the object, resulting in a secondary magnetic field [32]. Both the change of the primary and secondary magnetic fields over time is measured at the receiver. A diagram of a frequency-domain acquisition can be seen in **Error! Reference source not found.** Note how the receiver coil (Rx) picks up both the primary magnetic field (blue) and the secondary magnetic field (red).

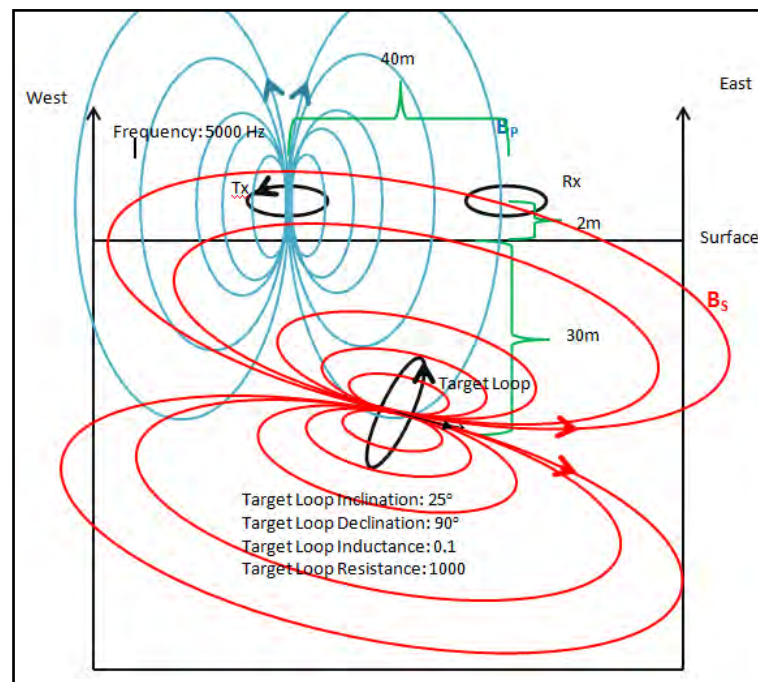


Figure 8. 2 An example of FEM acquisition scenario in Horizontal Coplanar using EM 34.

The apparent conductivity can be assessed by looking at the ratio of the primary and secondary magnetic fields ( $H_p$  and  $H_s$ , respectively). Note that  $H$  represents the magnetic field, while  $B$  represents the magnetic flux density.  $H$  is equivalent to  $B$  scaled by  $1/\mu$ , or  $1/\text{magnetic susceptibility}$ . The apparent conductivity is also known as the quadrature component of the ratio, (assuming no magnetic susceptibility), which is explained in further detail in appendix

.

EM methods were useful in analysing both faults and hydrothermal flow patterns in the subsurface of Pagosa Springs, CO. Three different electromagnetic instruments were used at this site: EM31, EM34, and EM47. The EM31 and EM34 were used to acquire FEM data, while the EM47 was used to collect TEM data.

## 8.2 Instrumentation

### 8.2.1 EM31

The EM31-MK2, manufactured by Geonics Ltd, is an inductive FEM instrument that operates at 9.8 kHz, with a fixed coil spacing of 3.7 m, giving it an effective depth of investigation down to approximately 6 m and a radius of investigation of approximately 3 m. It is operated by one person, and can be walked at normal speed through a survey area. The data is obtained instantly, and no processing is required. This means that it is ideal for near-surface surveys, quick reconnaissance surveys, and in areas where vegetation and terrain limit other methods.

The limitations of the EM31 system are similar to those for FEM induction systems generally: limited dynamic range and an inability to conduct an accurate zero setting. In addition to this, the EM31 has fixed coil spacing, limiting the vertical sounding capability to a fixed depth of investigation.

Both in-phase and quadrature data are recorded by the EM31 on-board datalogger. Accuracy is quoted by the manufacturer as  $\pm 5\%$  at 20 mS/m [34]. The instrument can be set up to stack an operator-determined number of readings, thus increasing the signal-to-noise ratio. The instrument can also be set up to take continuous measurements, allowing a very high along-line spatial data density.

Although it is important to note that the EM31 measures *apparent* conductivity, actual conductivity varies very little from apparent conductivity for this particular instrument.



Figure 8. 3 Students using the EM31 in the field.

### 8.2.2 EM34

In addition to the use of EM31, EM34 data was also collected at several survey sites in Pagosa Springs. The instrument used was the Geonics Limited EM34-3 which implements the same induction method as the EM31-MKS. The EM34 instrument consists of two coils, transmitter and receiver and instrument boxes as shown in Figure 8. 4.

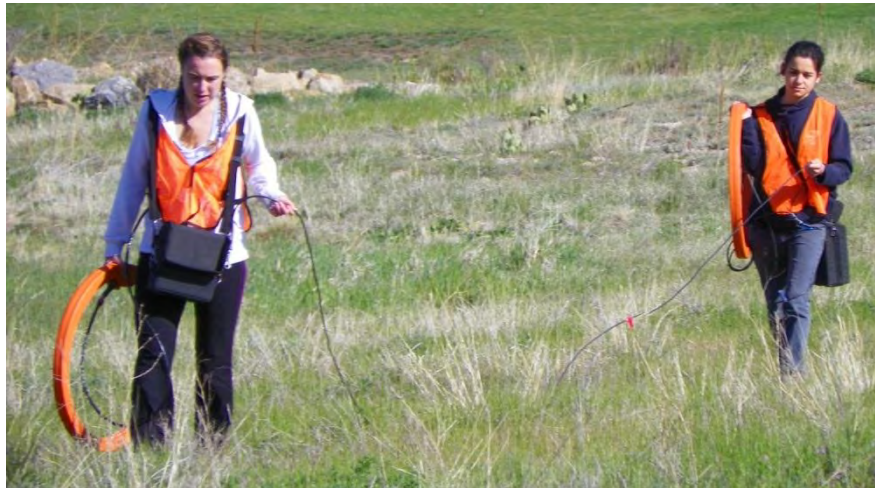


Figure 8. 4 Students walking the EM34 transmitter and receiver coils to a new station.

The EM34 can be operated in either Horizontal Coplanar mode or Vertical Coplanar mode. The Horizontal Coplanar mode creates a vertical dipole in the earth which is sensitive to vertical geologic anomalies [35]. The vertical dipole is used when trying to locate groundwater in fractured bedrock [35]. This is the mode used for all survey sites in Pagosa Springs because the goal of all the surveys completed with EM34 is to characterize the geothermal potential of the hot springs. The advantage of the EM34 over EM31 is the ability to varying the coil spacing which allows for different depths of investigation listed in Table 8. 1.

Table 8. 1 Spacing, depth of investigation, and frequencies used for the FEM instruments [36].

Instrument	Spacing	Depth of Investigation	Frequency
EM31	3.7m	6m	9.8kHz
EM34	10m	15m	6.4kHz
EM34	20m	30m	1.6kHz
EM34	40m	60m	0.4kHz

Different receiver and transmitter coil spacing can be used to create a pseudo-section of the apparent conductivity at depth. This was completed at the survey line called PAGO01 nearby to the Mother Springs. The instrument has several steps that must be completed before use on



the survey line. The EM34 must be calibrated before use. To do this it was taken to a location with minimal potential for interference, and calibrated to vertical dipole (VD), Horizontal Coplanar mode. Once the instrument is calibrated then measurements can be taken along the survey line or grid. The measurements are taken by placing the coils horizontally on the ground at the specified spacing. The apparent conductivity is then recorded manually in a field notebook.

### 8.2.3 EM47

The time-domain surveys used the Geonics Protem EM-47 instrument. Time-domain electromagnetics varies from frequency domain method by an instantaneous shut off of current rather than a sinusoidal change in current. This instrument uses a square transmitter loop and a three-component receiver coil. A 12-volt battery is connected to the transmitter box, which controls the transmitter loop. The transmitter loop is a conductive wire which current is injected into and then cut-off instantaneously. Once the current is shut off, there is an induced current which flows down into the Earth and creates a secondary magnetic field. The receiver coil measures the decay of the secondary field induced, by taking readings at closely spaced intervals called time gates [37]. The primary current is turned on and off at a certain frequency (repetition rate). Once the readings from each of the frequencies have been recorded, the EM47 is moved to a different station, and the process of injecting current at certain repetition rates is repeated. The sounding is all of the data from each station, which is used to make interpretations. The protem transmitter box is kept as far away as the connector cable allows from the 3 component receiver coil to prevent interference [37].

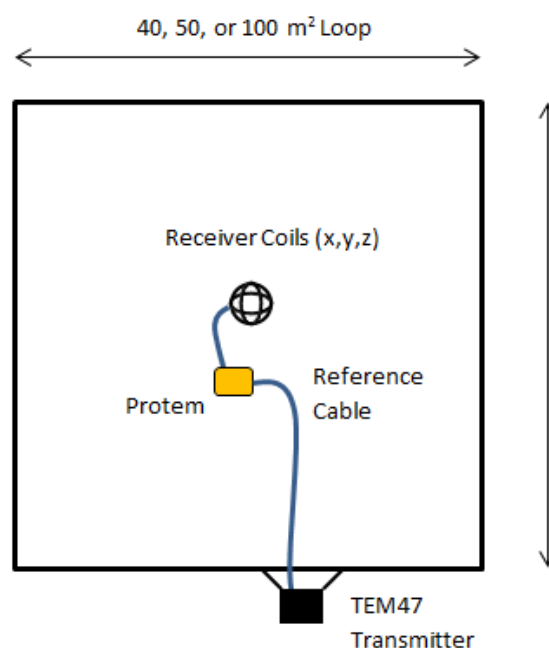


Figure 8. 5 EM47 instrument setup.

### 8.3 Survey design

All electromagnetic methods were carried out at each site, except the North Line near the Hot Springs site. The frequency domain instruments (EM31 and EM34) acquired data at Stevens Airport, the Hot Springs (PAGO01 and PAGO02), Barn 3, and the Zen Garden. The time domain method (EM47) also acquired data at the Hot Springs (PAGO01 AND PAGO02) and at the Warm Springs (Line 1). This is summarized in Table 8. 2.

**Table 8. 2 All locations where EM methods were used specifying which instrument.**

Survey Site	EM31	EM34	EM47
Stevens Airport	X	X	
Barn 3		X	
Zen Garden	X	X	
PAGO01	X	X	X
PAGO02	X	X	X
Warm Springs			X



**Figure 8. 6 A map view of the survey site locations where EM methods were performed. PAGO01 and PAGO02 are shown as white and purple lines respectively.**

The sites used were chosen based on both need and viability. The EM instruments were used at these sites to characterize the conductivity of the survey sites which gives important information about geology and groundwater helping to gain an overall picture of the subsurface structure at Pagosa Springs. The EM data can be correlated with the results found by resistivity surveys as well as magnetic and gravity surveys. A few sites were not chosen to perform EM acquisition because it was either impractical to set up the large loops required for TEM data, or there was too much interference from sources on the surface such as power lines, vehicles, other surveys, etc.

The survey design for electromagnetic methods is dependent on what instrument is being used (EM31, EM34, or EM47) and the location of the survey. Most of the surveys were completed on the same line or grid as other methods to make joint interpretation easier.

### **8.3.1 FEM methods**

The EM34 and EM31 instruments can be used for a line or grid of points. For EM34 the data is recorded manually at each point. The operators must place the two coils on the ground at the specified transmitter-receiver spacing and take a reading. This will create a profile of the line or grid at a depth of investigation which depends on the spacing of the coils. For EM31 the data is recorded automatically so the operator is only concerned with walking in a straight line with the transmitter-receiver pole level.

EM31 can be operated in continuous or manual mode. In continuous mode, the instrument takes readings at a specified time interval while the operator walks the line or grid. In manual mode, data is only recorded when the operator presses a button. The different modes were used at the operator discretion at the survey sites [34].

At each site the appropriate transmitter-receiver spacing for EM34 was determined by the assumed depth to important features. For the Zen Garden site, 10m spacing was chosen because the important features we wanted to characterize are in the shallow subsurface. At Stephens Airport, Barn 3, and PAGO02 sites the spacing was 40m so that we could see the geology deeper down. All three transmitter-receiver spacing were used at PAGO01 line because a possible fault was found by a resistivity survey and with multiple transmitter-receiver spacing a pseudo-section could be made that could delineate the extent of the fault.

### 8.3.2 TEM methods

The survey implementation of EM47 is more complicated than the frequency-domain methods. Either the X or Y components of the receiver loop need to be perpendicular to either one of the sides of the transmitter loop. At each station, all three components of the induced field are measured. At the Warm Springs site (referred to as Warm Springs Line1), the transmitter loop was 50m by 50m. PAGO01 used a 100m by 100m loop, while PAGO02 used a 40m by 40m loop. The size of the transmitter loop was restricted by the site location. PAGO02 used a smaller loop because of site size limitations, which was acceptable at this site because the valuable information was in the semi-shallow subsurface.

Each station (or sounding) uses three frequencies, and for each frequency used, the receiver measured 20 time gates. While Warm Springs had three soundings, PAGO01 had only one sounding, and PAGO02 had five soundings. The measurements started at 285Hz, decreased to 75Hz, and end with 30Hz. At the Warm Springs site the loop was oriented at 61°E. To find the ramp off time, the graph from the Geonics Protem47 manual was consulted. For example at the Warm Springs location, the current was shut off at 6μsec, and at 9μsec the flux was recorded. This slight time gap avoided measuring the primary current. The ramp off times for the other locations are dependent on the side lengths of the transmitter loop.



Figure 8. 7 Students setting up the 3-component receiver used in the TEM surveys.

## 8.4 Processing

### 8.4.1 FEM processing

The EM31 data collected from the Zen Garden near the Hot Springs was collected in continuous mode, over north-south lines. Very little processing is required for EM31 data, as conductivity calculations are performed in real-time by the instrument. Generally all that is required is matching the collected data to geological locations for easy comparison with other datasets. Normally this is achieved by using a ‘mark’ button when near a known location, which places a note in the data. In this case, problems with the operation of that particular feature meant that the notes were not properly stored. As a result, we had to locate data by assuming a constant walking speed throughout each line, interpolating between the ends of the lines, and placing each line of data across this interpolated line. The interpolated geographical data does not seem to have affected the data quality significantly (see Figure 8.8), as spatial coherence is very good and no north-south linear features are apparent.

The EM34 data is similarly simply processed as the EM31 data. The data points are matched to GPS and bad points are removed. For Pagosa Springs, most of the unuseable points were the results of interference from power lines or fences. The road between the river and ridge for PAGO01 and PAGO02 also caused poor data. These points were found by referring to the operator’s notes about the fluctuation of the readings. Some large negative conductivity values were also removed because it is theoretically impossible to have negative conductivity values.

### 8.4.2 TEM processing

All of the data from each of the three sites was first organized in a reasonable manner, by lines, soundings, and frequencies. At the Warm Springs location and PAGO01, the current in the transmitter loop did not get all the way up to 2A. This was accounted for in the processing of the data. For the first two lines, Warm Springs Line1 and PAGO01, the data was scaled by a factor of two divided by whatever the recorded current was. For example, at Line 2, at a repetition rate of 75Hz, the reading taken was multiplied by (2/1.65). The current varied with frequency. The standard deviations of each of the stations were calculated. Then, all of the data needed to be converted from readings of  $dB/dt$  to proper units of flux,  $nV/m^2$ . This was done using **Error! Reference source not found.**



$$\frac{dB}{dt} = \frac{19.2 * V_0}{E * 2^N}$$

Equation 8. 1

where  $V_0$  is the instrument reading (mV),  $E$  is the effective area of the receiver coil ( $31.4\text{m}^2$  in this case), and  $N$  is the gain selected (1 in this case). Once all of the data had been converted in this way, this formula was also applied to the standard deviations.

Before any inversions were done, the decay curves were plotted for each station. This was done to confirm that the current did have an exponential decay. The time gate values were also plotted for each line.

## 8.5 Uncertainties/Errors

### 8.5.1 EM31 & EM34

Errors in the EM31 and EM34 surveys came mostly from objects at the survey site. Power lines, fences, roads, and transformer boxes were all present in the survey sites. These could affect how the signal propagates in the ground and thus affecting the data recorded. Also vehicles, phones, and radios were kept away during EM31 and EM34 surveys but vehicles on the roads might have had an effect.

### 8.5.2 EM47

Errors in the EM47 surveys include the current amount, which was accounted for by scaling the data. The only other notable issue would be that the data collected for Warm Springs Line1 was interrupted by a thunderstorm. The data collection was paused for about an hour.

## 8.6 Interpretations

### 8.6.1 Zen Garden

The apparent conductivity data from the EM31, shows a region approximately 30-50 m wide of high apparent conductivity, set in a background of the conductivity expected in this geological setting – Mancos Shale in this region has a conductivity of approximate 50 - 80 mS/m.

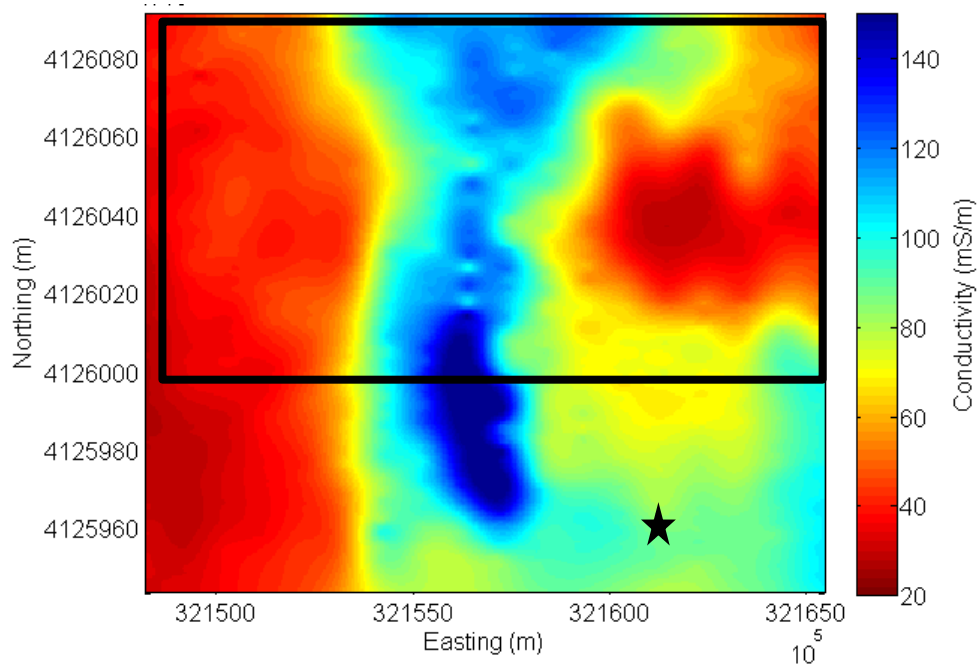


Figure 8. 8 EM31 apparent conductivity over the Zen Garden area near the hot springs. EM31 data is approximately the first 6 m from surface. The red to yellow (20 to 70 mS/m) is characteristic of the Mancos Shale that is in this area, and therefore the highly conductive blue area indicates an anomaly. The black outline represents the area over which the EM34 survey was undertaken (see Figure 8. 9), and the star represents the location for the TEM EM47 inversion of Figure 8. 11.

Further below the surface, the EM34 data at 15m depth(Figure 8. 9) shows that the large conductive anomaly is no longer present, and apparent conductivities revert to the expected range for Mancos Shale in the area, although there are areas of slightly higher conductivity that correlate well spatially with the conductive body closer to the surface. It should also be noted that EM34 vertical dipole configuration at the indicated apparent conductivities has significant departure from the true conductivities.

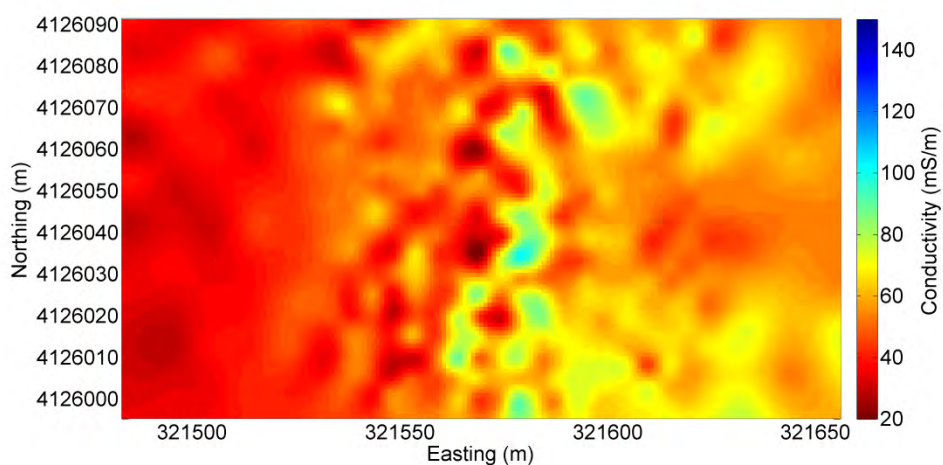


Figure 8. 9 EM34 vertical dipole survey for Zen Garden area. Depth of investigation is 15m.

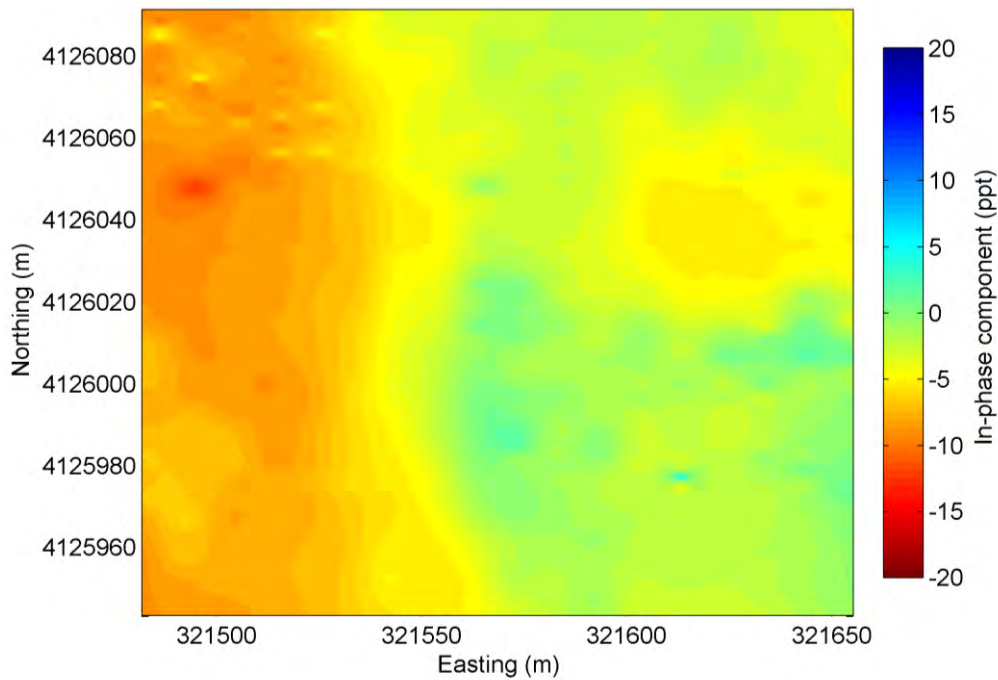


Figure 8. 10 In-phase component of the EM31 data. Strong negative data indicates subsurface metallic objects, and strong positive data indicates near-surface metallics.

The in-phase data is generally used in metal or waste detection. The EM31 has a range of -20 to 20 ppt for the in-phase data. A strong positive in-phase response indicates metallic objects very close to the surface, and a strong negative in-phase response indicates metallic objects beneath the surface. Figure 8. 10 shows the in-phase data for the Zen Garden. Most of the data is very close to zero, with the exception of a small strong (~15 ppt) negative anomaly in the north-west sector, which may indicate a sub-surface metallic object. There is also a moderate positive anomaly in the southeast sector possibly indicating a metal object near the surface.

An EM47 (Time-domain EM) reading was taken at a point near within the Zen Garden area (shown as a star in **Error! Reference source not found.**). The inverted results are shown in **Error! Reference source not found.**. The surface conductivity correlates well with the inverted EM47 data. Additionally, the inversion shows the conductivity decreasing rapidly from the surface until 25 m depth, before again decreasing until 150 m depth, and finally increasing up to high conductivities. This correlates with the expected geology at the Zen Garden site. The Mancos shale causes the higher conductivity near the surface. The conductivity then decreases as it approaches the Dakota sandstone after which the

conductivity decreases yet again as it finds the Morrison formation. The conductivity finally increases again when it reaches the basement.

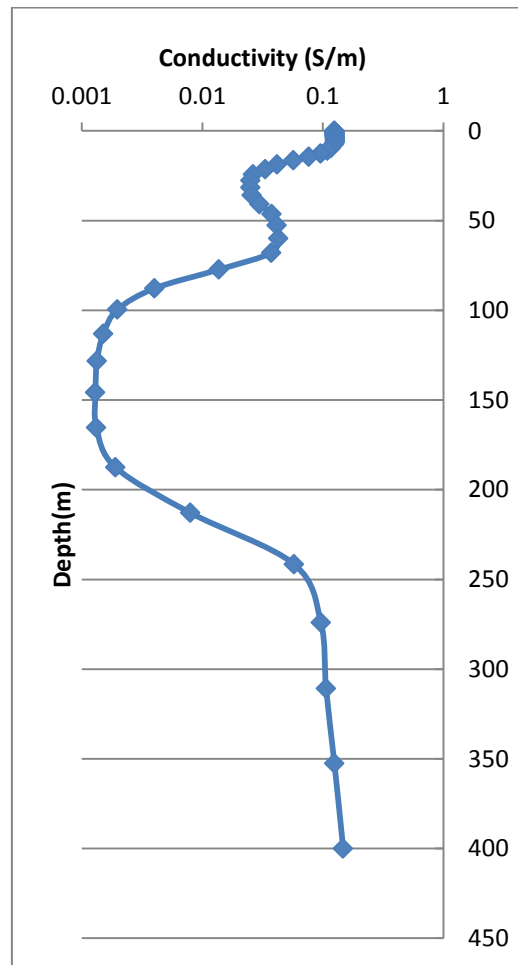


Figure 8. 11 EM47 inversion for south-east corner of the Zen Garden. This shows a resistive layer beginning at about 75m depth.

### 8.6.2 PAGO01

EM data for PAGO01 shows conductivity slightly below, but in the same order of magnitude, as expected for Mancos Shale in the area, for the southerly part of the line. As the line progresses north towards the hot springs and the river, conductivity increases likely due to moisture from the river. The bright red anomaly visible in Figure 8. 13 is caused by a paved asphalt road and should not be read as a geologic formation.

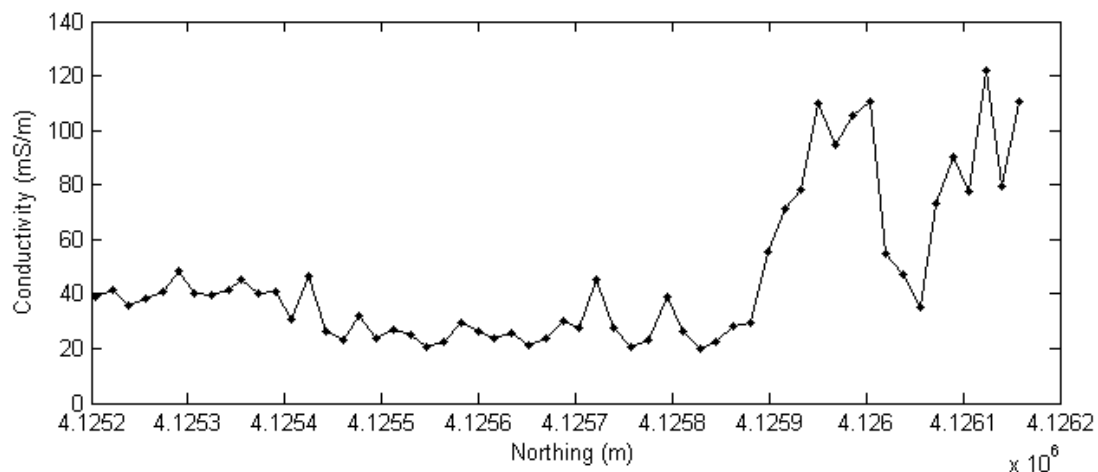


Figure 8.12 EM31 conductivity for Hot Springs PAGO01.

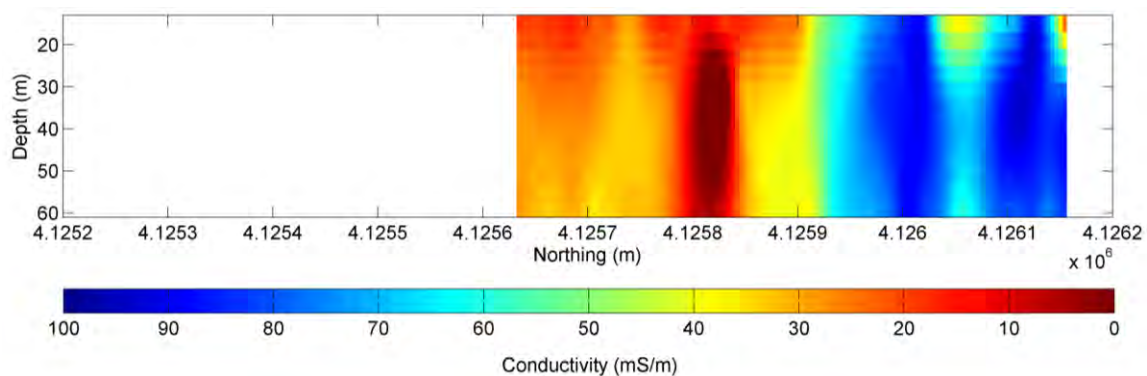


Figure 8.13 EM34 apparent conductivity pseudosection for Hot Springs PAGO01.

### 8.6.3 PAGO02

EM data for PAGO02 shows consistency with the geology of the area. Conductivity is high to the west near the river, and is lower to the east. The apparent conductivity is lower than that of the Mancos Shale, however this may be biased by alluvial deposits, particular in the 0 to 6 m depth range.

EM34 data (~10 m to 60 m depth) over PAGO02 has some significant outlying points, however the largest outliers appear to be due to power lines (~32180 m E) and a passing vehicle (~32200 m E), rather than geological features. Apart from these large outliers, conductivity at this depth appears consistent to the east with the shallow conductivities. Conductivities to the west do not seem to be as affected by the river as the shallow conductivities.



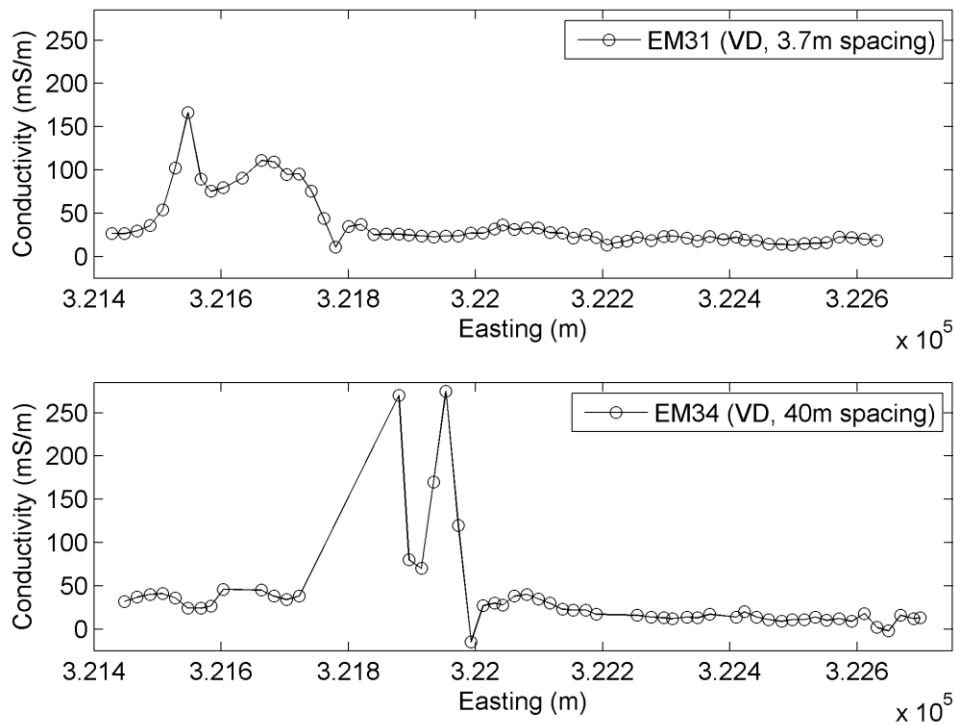


Figure 8. 14 A comparison of EM31 and EM34 apparent conductivities on the PAGO02 line.

The inverted EM47 data for the PAGO02 line has a resistive body located roughly in the middle of the line as shown in Figure 8. 15. It is supposed that it is the Dakota sandstone. This correlates with the lower conductivities found in the EM31 and EM34 results. The sandstone is most likely a continuous dipping layer in this area.

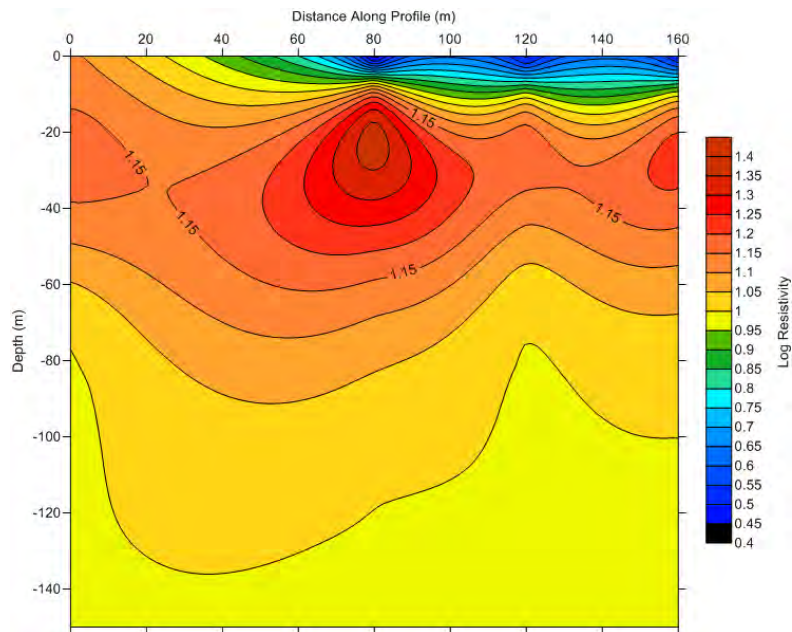
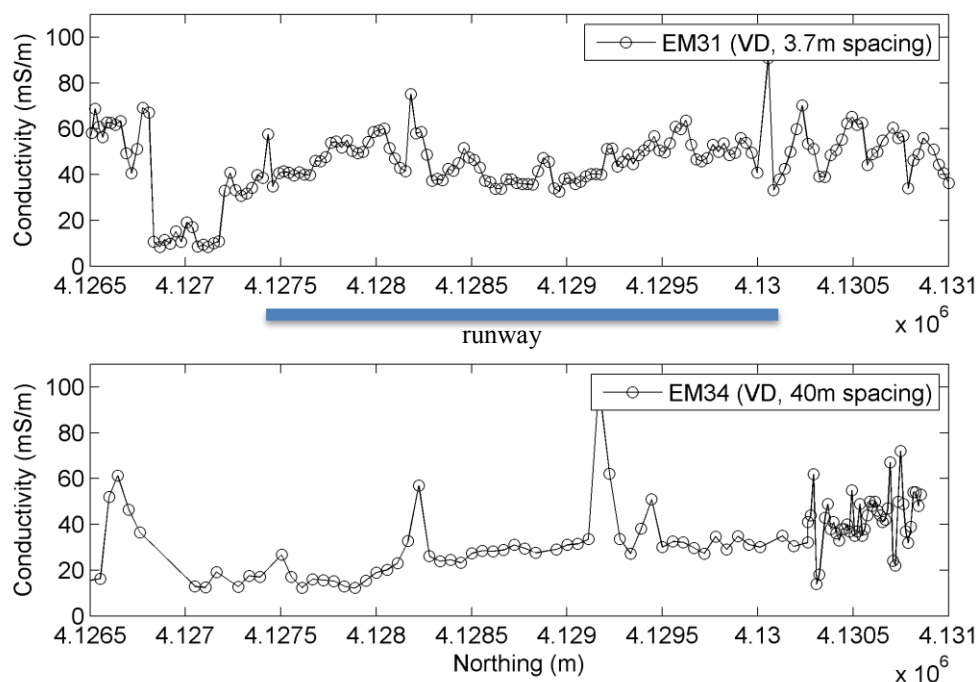


Figure 8. 15 The inverted EM47 data along the PAGO02 line. This profile matches the geology known in the area. The resistive area directly in the middle of the profile is probably the sandstone in the region.

#### 8.6.4 Stevens Airport

Apparent conductivities close to surface (0 to 6 m) show a fairly consistent range of 40 to 60 mS/m, with the exception of the 450 m to the south, where conductivity is significantly lower at approximately 10 mS/m for 450 m. This area is from the fairway to the south of the airport, to the southern taxiway feeding the runway. This data is probably due to the Eight Mile Mesa fault that runs south of the airport.



The in-phase data for the EM31, normally used to find metallic objects and anomalies, appears to qualitatively track the Mancos Shale as it thickens towards the north. It also appears to locate the Eight Mile Mesa fault, with a large discontinuity.

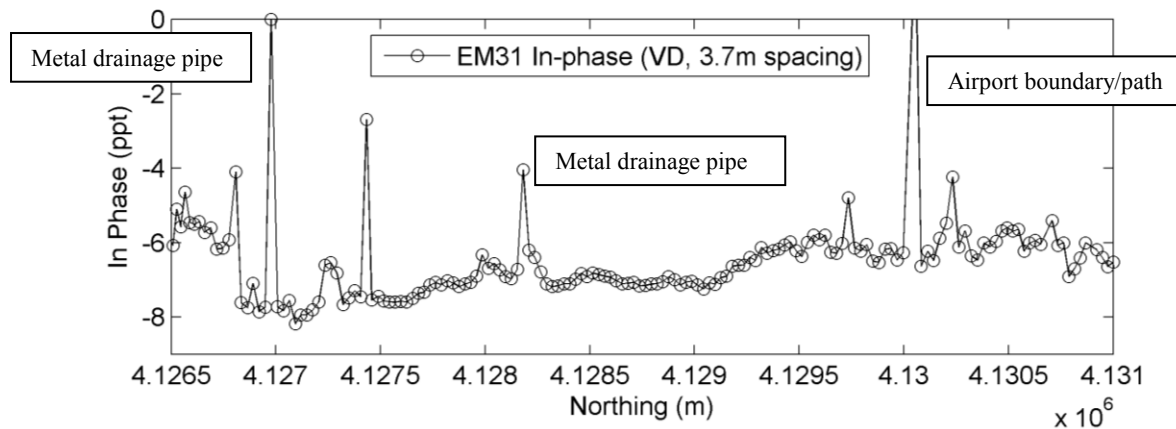


Figure 8. 16 EM31 in-phase data indicating locations of magnetic pipes and Stevens Airport boundary.

Further down, the EM34 data (40 m spacing vertical dipole) shows the obvious trend due to thickening Mancos Shale, as well as the Mesa fault. Several data points were unavailable to the south of this dataset, causing a gap where the edge of the fault is located.

### 8.6.5 Barn 3

The purpose of the survey site called Barn 3 is to more clearly define the Eight Mile Mesa Fault. The survey line heads in a northeastern direction crossing the fault near the end. EM34 is used to define the apparent conductivity of the area. A vertical dipole was used with 40m spacing. The result of the EM34 survey is shown in Figure 8. 17.

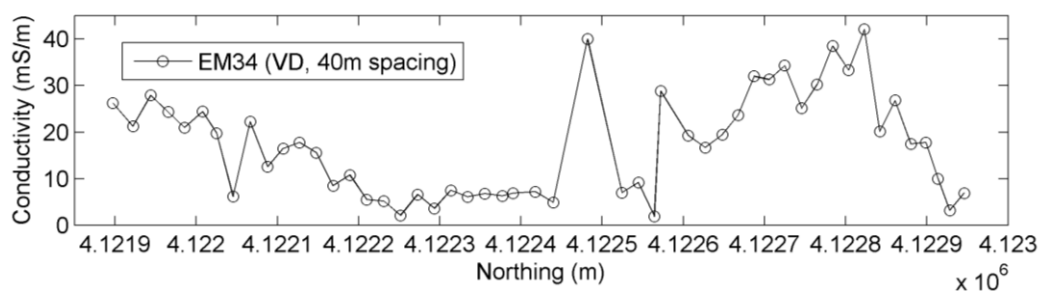


Figure 8. 17 EM34 apparent conductivity for the Barn 3 site. Conductivity does not correlate with expected geology. The resistive body may indicate a sand/gravel deposit.

The conductivity decreases levels out then increases again. This does not follow the prediction from geology. The edges of the line intersect Dakota sandstone which is less conductive than the Mancos/Lewis shale is in the middle. The EM34 data shows very low conductivity where the Mancos/Lewis shale is expected to be located. Such low readings would result from a large resistive body. One hypothesis is that the ground where the low

readings are located was extremely dry and may be resistive enough to effect the apparent conductivity. Another, maybe more plausible hypothesis is that there is a terrace deposit where the data is showing a resistive body. Terrace deposits are sand and gravel deposits from the Pleistocene era. Sand has low conductivity and could cause the conductivity low shown in Figure 8. 17. There are other sand deposits near to the survey site but this result must be correlated with other data before any conclusions can be drawn for the Barn 3 line.

### 8.6.6 Warm Springs

The only EM method used at the Warm Springs site was EM47. The purpose of using TEM at the site was to characterize the groundwater and geology near a hot spring that had gone cold. The inversion of the EM47 data was not successful because of poor data quality. However, a time/depth slice was able to be created which is shown in Figure 8. 18. There is a clear trend in the data of conductivity decreasing as distance increases. Remembering that the Warm Springs Line1 runs North-South, the best explanation to fit this trend is that there is a resistive layer dipping slightly to the North. This formation is fitting with the geology as most likely the Dakota Sandstone.

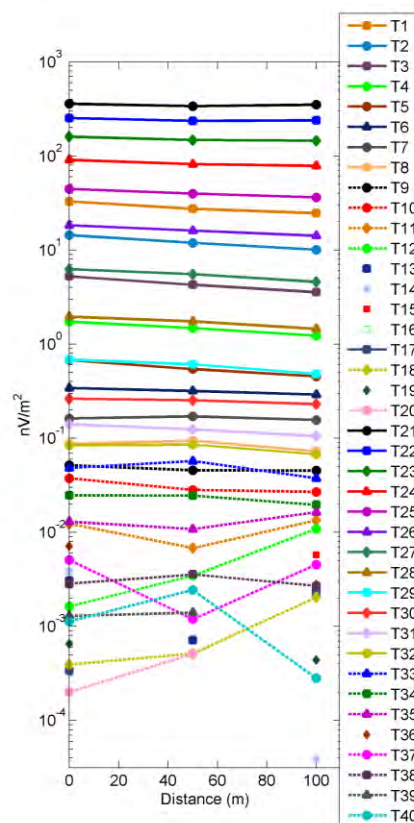


Figure 8. 18 Time series plot for the Warm Springs site.

## 8.7 Conclusions and discussions

The electromagnetic methods applied in Pagosa Springs, CO were able to identify what we think are geologic features and areas of ground water.

Zen Garden site shows a significant conductive feature running north-south. This is possibly associated with fluid flow. There are resistive feature to the northeast that is possibly associated with the know travertine formation in the area. The resistive section to the west may also be correlated with travertine although this is yet to be confirmed.

The EM34 data for the Stevens Airport site shows increasing conductivity towards the north which is consistent with the increasing thickness of the Mancos shale in that location. The EM31 data shows a significant drop in conductivity, as well as an anomaly in in-phase data, in the suspected location of the Eight Mile Mesa Fault.

The EM34 data from the Barn 3 site shows lower conductivities than was expected from geology. This might be because the Mancos and Dakota are dipping in the area or it could be from sand deposits. The data must be correlated with other geophysical techniques to be certain.

The EM31 and EM34 data from PAGO01 show resistive areas possibly associated with travertine formation near the San Juan river. There is a very obvious change conductivity from low to high that may be indicating the location of the water table. This conclusion is supported by the elevation profile of PAGO01 which flattens out around where the change in conductivity occurs.

The EM31 data from the PAGO02 line is consistent with expected geology and correlates with the EM31 data obtained from the Zen Garden site (the two overlap). The high conductive body seen at the Zen Garden site is also apparent in the data from PAGO02. The deeper EM34 data has some large data points that we attribute to noise or interference. It also correlates with the EM34 data collected at the Zen Garden site. The EM47 data identifies a resistive body at 40m depth. This may be the Dakota sandstone which is known to be around that deep in the area.



The EM47 data collected at the Warm Springs site can only give qualitative information but it does show conductivity generally decreases as distance increases. This indicates that there is a resistive body dipping opposite to the slope of the conductivities.

All of the EM information collected will aid in the characterization of the geothermal system in Pagosa Springs, CO.

# 9 DC Resistivity

---

## 9.1 Introduction

Materials in the subsurface can be characterized by their corresponding internal physical rock properties. The differences in the properties between materials can be used in order to image their distribution in the subsurface. Resistivity is one such property which describes a material's resistance to the flow of electricity. The DC Resistivity method exploits this property by injecting current into the ground along a specified array, while performing electrical potential measurements along the array in order to characterize how the resistivity of the subsurface changes laterally and with depth. This method was especially important for the investigation at Pagosa Springs, as the hot mineral rich geothermal water should register a very low resistivity compared to the surrounding geology.

Many DC Resistivity lines were completed in and around the Pagosa Springs area in order to characterize the distribution of the known geothermal system, as well as to image structures important to geothermal processes. Unlike with other methods, this process was very dynamic for the survey line locations and acquisition parameters. This is due to the easy set up and take down of the survey line, as well as, a quick acquisition time. Initially, survey lines were placed around the known hot springs area in order to characterize and get a better image of the area. From the basis of the preliminary results from the initial survey, further lines were placed to better image and get a larger local coverage of the area.

As with any geothermal system, faults and fractures are important structural components to harbour the storage and movements of hot water through the subsurface. With this in mind, initial surveys were placed to better image the geothermal distributions surrounding a large published normal fault which runs through town. As more information was gained as to the location of other possible faults, new survey lines were placed to better image these and explore for more structural features important to the geothermal system. Using measured resistivity values obtained from the geology of this area combined with the structural geologic information, the data was inverted into a resistivity model. This model allows mapping potential structures and fluid distribution related to geothermal effect throughout the area.

## 9.2 Sites method was completed at

The resistivity surveys can be divided into three main sites. The main site is located near the Mother Spring and contains the Hot Springs lines, the North line, and the Zen Garden lines. The other two sites are the Stevens Airport line and the Warm Springs area. Figure 9. 1 shows a map with the locations of the resistivity surveys, while Table 9. 1 summarizes the locations and names of all of the survey lines.

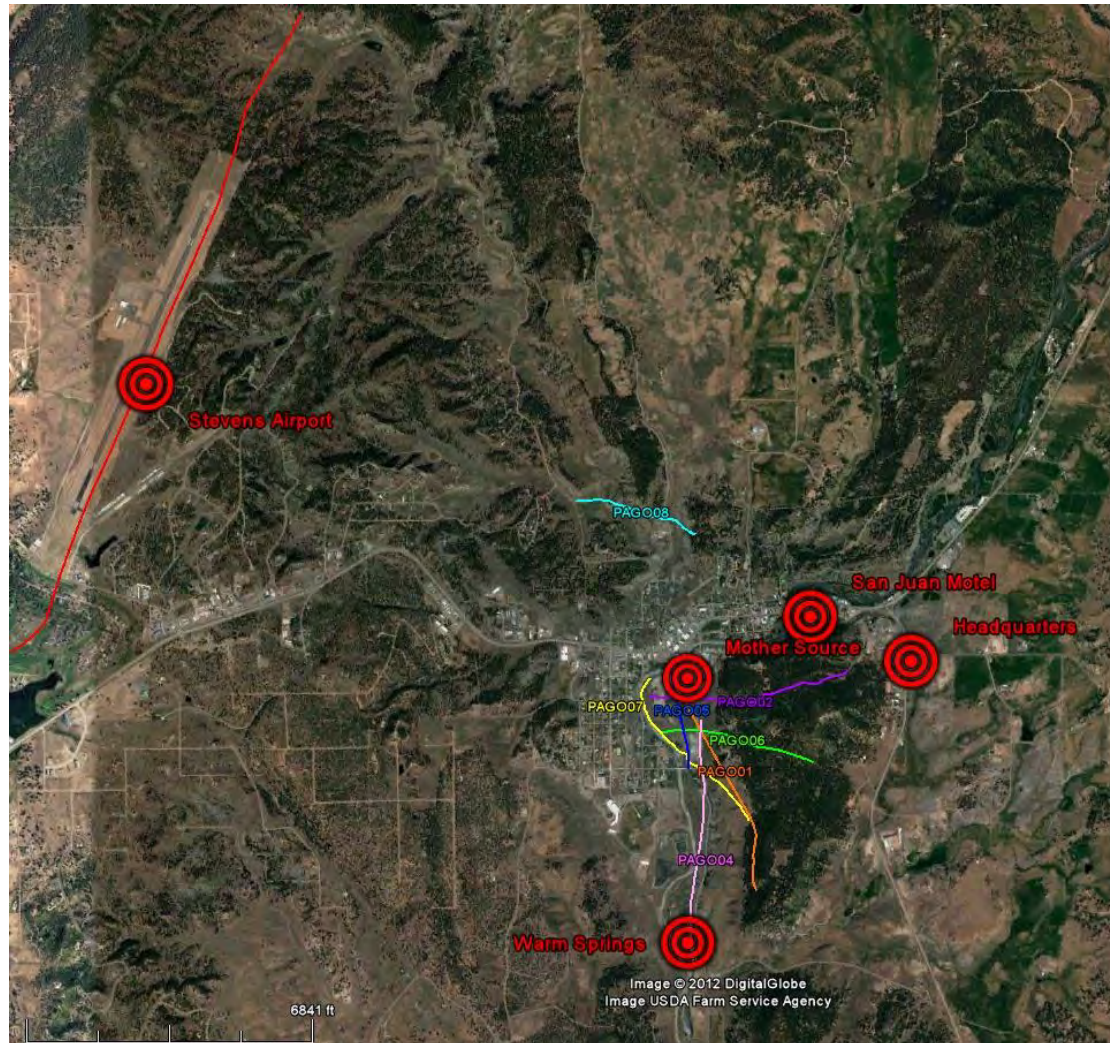


Figure 9. 1 Resistivity survey map

**Table 9.1 Resistivity survey map**

Area	Number of lines	Names of lines	Line length
Stevens Airport	1	PAGO03	3770m
Hot Springs	6	PAGO01, PAGO02, PAGO04, PAGO05, PAGO06, PAGO07	From 450m to 1440m
North Line	1	PAGO08	765m
Zen Garden	12	Line A, Line B, Line C, Line D, Line E, Line F, Line G, Line H, Line I, Line J, Line K, Line L	135m
Warm Springs	7	PONC01, PONC02, PONC03, PONC04, PONC05, PONC06, PONC07	315m

## **9.3 Survey design**

### **9.3.1 Hot Springs**

Water is a highly conductive medium. In order to locate the water around the Mother Spring, many different resistivity lines were ran in different directions and varying lengths to image it (Figure 9. 2, Table 9. 2).





Figure 9. 2 Map of the resistivity surveys in the Hot Springs area.

Table 9. 2 Survey design parameters in the Hot Springs area.

Line	Number of electrodes	Electrode spacing (m)	Topographic data	System	Acquisition type
PAGO 01	96	20	Altimeter	ABEM	Wenner
PAGO 02	80	20	Altimeter	ABEM	Wenner
PAGO 04	96	20	Altimeter	ABEM	Wenner
PAGO 05	30	20	Altimeter	ABEM	Wenner
PAGO 06	64	20	Altimeter	ABEM	Wenner
					Dipole-Dipole
					IP
PAGO 07	80	20	Altimeter	ABEM	Wenner



### 9.3.2 Warm Springs

It is known from a historical report of the region that a former hot water source is located on the southern side of Pagosa Springs. Assuming this geothermal system is related to the geothermal system supplying water to the Mother Spring, additional resistivity surveys were placed around the Warm Springs (Figure 9. 3, Table 9. 3). The results of these surveys are expected to help estimate the range of resistivity values within the shale and the sandstone located in the area. The layout of the lines as illustrated in Figure 9. 3, is an advantage and allows for a 3D inversion of the area to be performed.

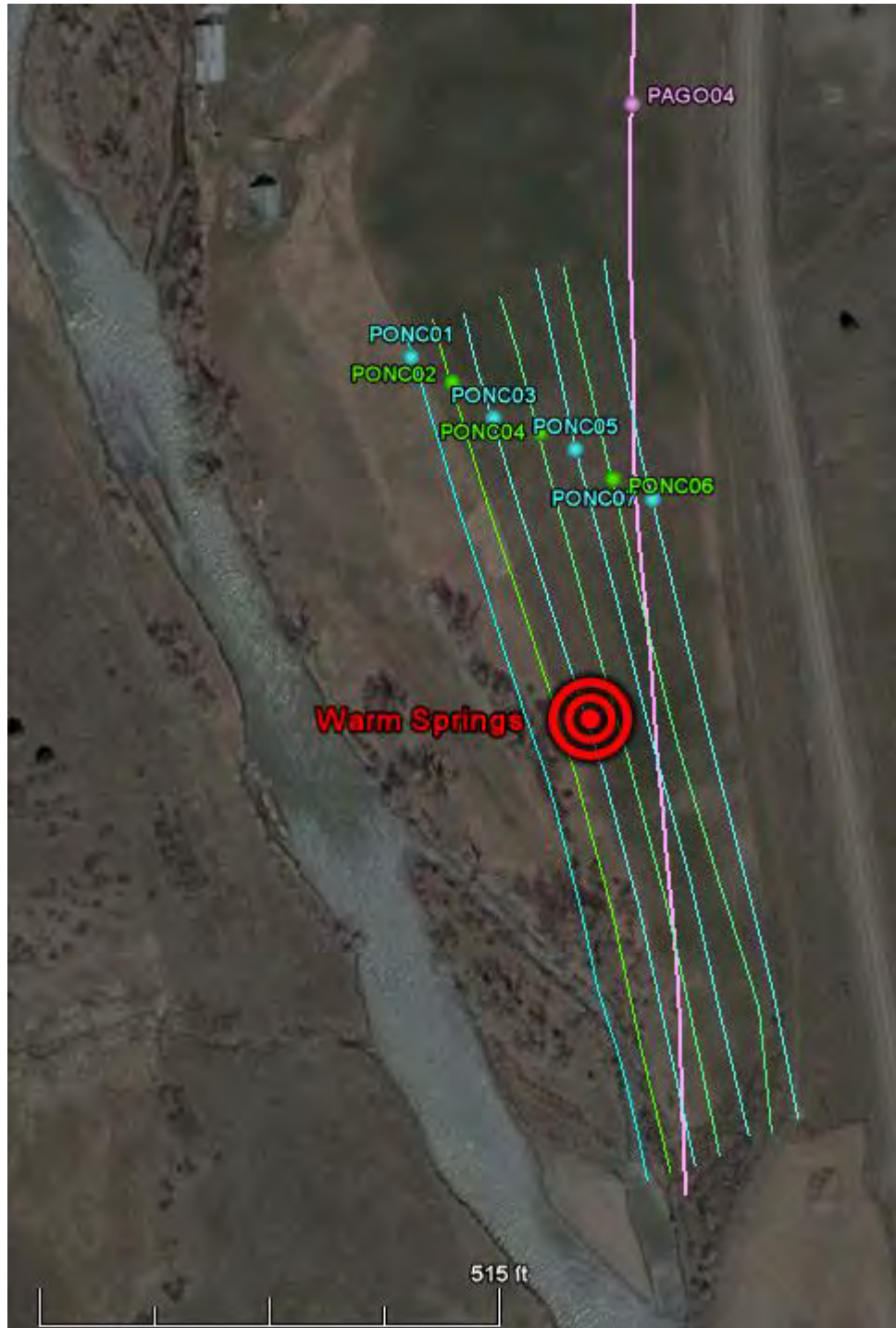


Figure 9. 3 Map of the resistivity surveys in the Warm Springs area

**Table 9.3 Survey design parameters in the Warm Springs area**

Line	Number of electrodes	Electrode spacing (m)	Topographic data	System	Acquisition type
PONC 01	64	5	Differential GPS	ABEM	Wenner
PONC 02	64	5	Differential GPS	ABEM	Wenner
PONC 03	64	5	Differential GPS	ABEM	Wenner
PONC 04	64	5	Differential GPS	ABEM	Wenner
PONC 05	64	5	Differential GPS	ABEM	Wenner
PONC 06	64	5	Differential GPS	ABEM	Wenner
PONC 07	64	5	Differential GPS	ABEM	Wenner

### **9.3.3 Zen Garden**

AGI's SuperSting 3D Resistivity Imaging System was used to gather DC resistivity data at the Zen Garden site, see Figure 9. 4. Data was collected for twelve lines, which were one hundred thirty-five meters in length. The eastern most line was called line A and the western most line was called line L. Ten meter spacing was used between each line. Twenty-eight electrodes, which were spaced five meters apart was used for each line. The northern most electrode was called electrode one. Acquisition started at line A and moved west towards line L. Both a Wenner and a Dipole-Dipole array acquisition was used for each line. Table 9. 4 shows the parameters for the DC survey performed at the Zen Garden site.

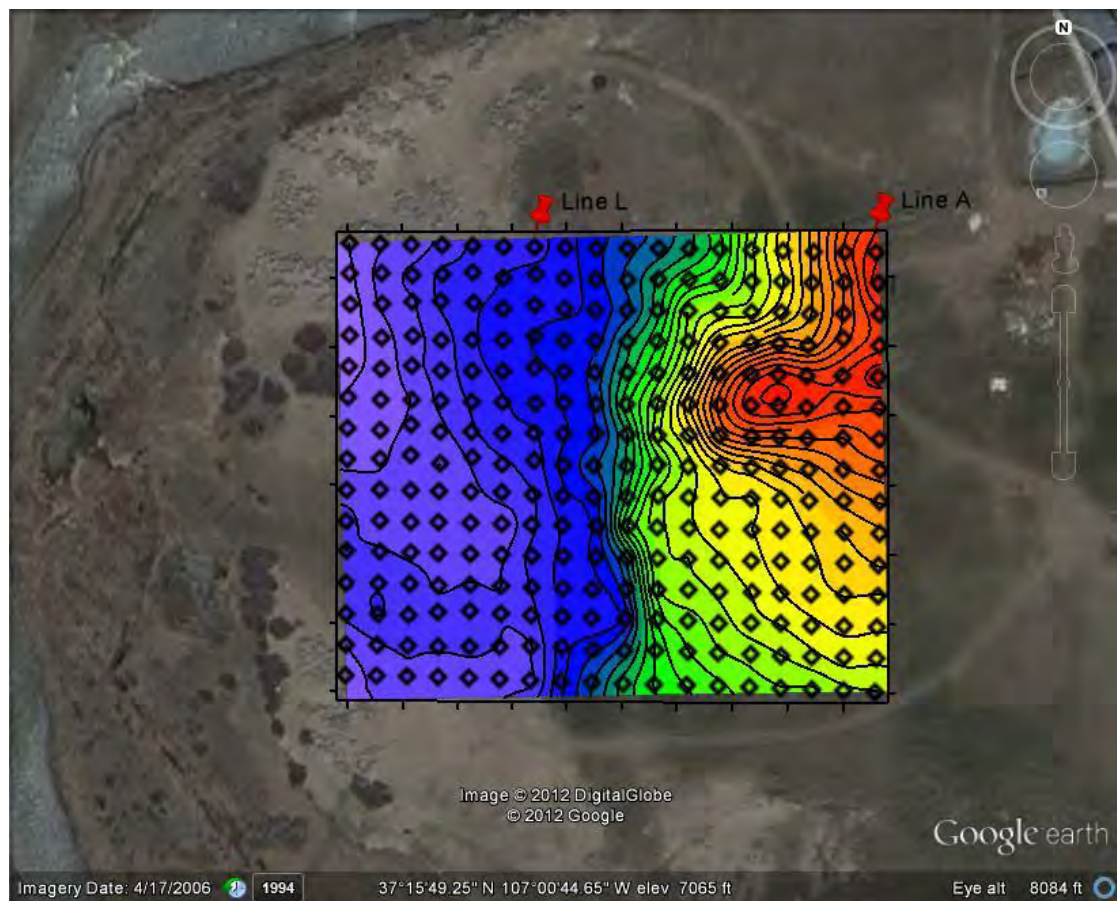


Figure 9. 4 Map of Zen Garden Site

**Table 9. 4 Survey design parameters for the Zen Garden site**

Line	Number of electrodes	Electrode spacing (m)	Topographic data	System	Acquisition type
Line A	28	5	Differential GPS	SuperSting	Wenner Dipole-Dipole
Line B	28	5	Differential GPS	SuperSting	Wenner Dipole-Dipole
Line C	28	5	Differential GPS	SuperSting	Wenner Dipole-Dipole
Line D	28	5	Differential GPS	SuperSting	Wenner Dipole-Dipole
Line E	28	5	Differential GPS	SuperSting	Wenner Dipole-Dipole
Line F	28	5	Differential GPS	SuperSting	Wenner Dipole-Dipole
Line G	28	5	Differential GPS	SuperSting	Wenner Dipole-Dipole
Line H	28	5	Differential GPS	SuperSting	Wenner Dipole-Dipole
Line I	28	5	Differential GPS	SuperSting	Wenner Dipole-Dipole
Line J	28	5	Differential GPS	SuperSting	Wenner Dipole-Dipole
Line K	28	5	Differential GPS	SuperSting	Wenner Dipole-Dipole
Line L	28	5	Differential GPS	SuperSting	Wenner Dipole-Dipole

The lines for the survey run North to South in order to be perpendicular to the crack in the travertine, which we are interested in imaging. The crack running through the travertine is relatively thin (~0.5m) and can be seen at the surface. This led to a five meter spacing between electrodes to be used. This spacing will give us good resolution at shallow depths. The length of the line was limited by the number of electrodes used in the line. This produced a line one hundred thirty-five meters long. Data was only acquired along twelve lines due to time constraints. A Wenner array was chosen to image the horizontal features of the area, while a Dipole-Dipole array was chosen to image the vertical features of the area. It is important to note that the Dipole-Dipole array has a poor signal to noise ratio. This survey was completed from May 21, 2012 to May 23, 2012.

## 9.4 Processing

### 9.4.1 Downloading Data and Data Formatting

#### ABEM

When a survey is completed using the ABEM Terrameter 4000 System, the data is extracted using the ABEM specific software SAS4000. SAS4000 simply converts the data format stored on the ABEM from .S4K to either .AMP or .DAT format. The data from all DC Resistivity profiles has been saved in all three formats in the [MASTER DATABASE NAME] for completeness and future use. The file



format .DAT was used in the inversions and quality checking of the data. Details on the SAS4000 software can be found in Appendix F.

## SuperSting

Data from the SuperSting is downloaded from the equipment formatted as .STG and is eventually converted to .DAT for the 3D resistivity inversion software. Each 3D inversion requires an input file .INP that contains the mesh .MSH and the .DAT data files. The input file may also contain a topography file .DAT, but for unknown reasons, our topography file is not compatible with the 3D inversion software. Two file types are required for the AGI Earth Imager 2D software - the original .STG files that contain the resistivity data and an accompanying topography file .TRN for each line of data.

### 9.4.2 Data Reduction

#### ABEM

Following the data downloading and format conversion, the data was reduced using Geotomo's inversion software RES2DINV. Within RES2DINV, the .DAT files were imported and examined for reliability. Once the data is imported, the quality of the data was checked using a quality checking feature in RES2DINV. This feature serves to remove erroneous data points. Figure 9. 5 show the “Exterminate bad data points” feature in RES2DINV.

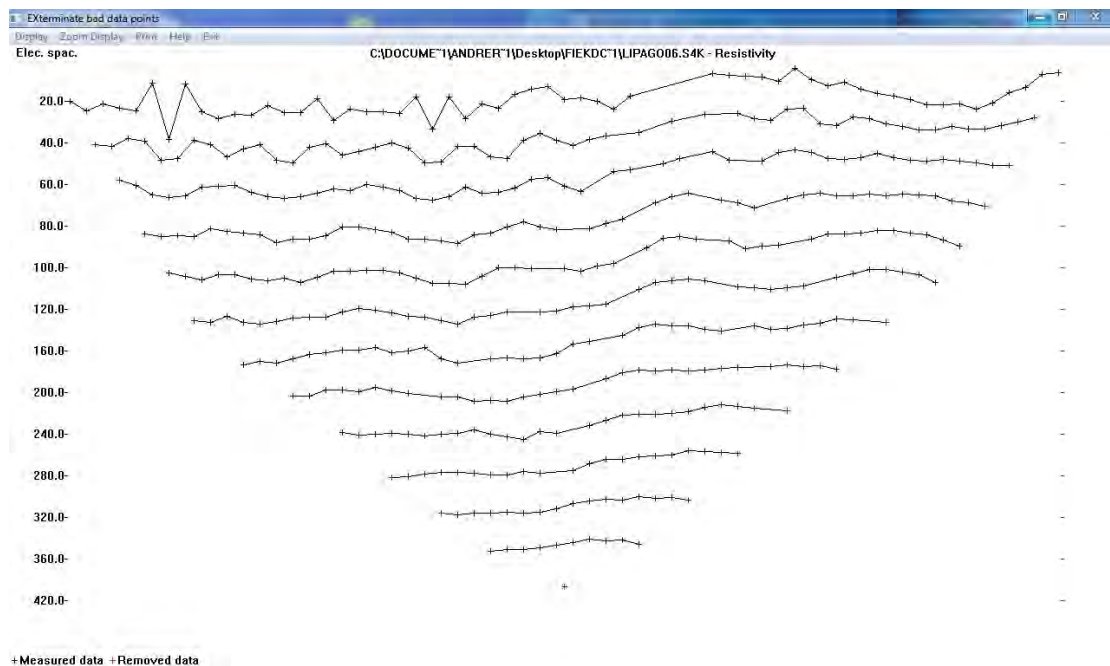


Figure 9. 5 Exterminate bad data points feature for RES2DINV

It is desirable to filter out data points that appear as large spikes on the pseudo-section. This data reduction was performed prior to any preliminary inversion. If the data set was reduced, a new .DAT data file was created with the newly reduced data while a raw copy of the data was retained to reprocess the data if needed.

After the initial data reduction, DGPS information was manually incorporated into the .DAT files via a text editor. The location data was necessary in order to take into account topography in the inversion process. The location information was added into the .DAT files in a format specified in the RES2DINV software manual.

Following the addition of location information, a preliminary inversion was conducted on the data sets. Multiple inversions were conducted on each data set in order to familiarize ourselves with the impact of different inversion parameters, and also allowed us to reduce the data to filter out noise. The inversion process is discussed in detail in the following section titled “2D Inversion”. Following the preliminary inversion, the resulting model was examined for sources of noise and uncertainty via the RMS percent error tool within RES2DINV. This tool allowed us to filter out the resulting data points that resulted in a large apparent resistivity RMS percent error for a given inversion model. Once the points were filtered out below a given percentage cut-off, a new data set was created, reimported, and re-inverted. It is desirable to eliminate data points that result in a high RMS percentage value because they increase the uncertainty in a given model and are likely a result of noise.

For IP data, an additional step of data reduction was required. Using the calculated normalized chargeability values, noise was eliminated by a manual filter of data in excel removing extreme values above a chosen arbitrary point. This allowed us to get a better idea of the chargeability over the section in finer detail. After filtering the data it was then presented in log scale and plotted into the section.

## **SuperSting**

In order to apply the inversion software to the data, it is necessary to replace the arbitrary X,Y,Z coordinates of the SuperSting electrode locations with the DGPS UTM coordinates. Most of the electrodes have DGPS coordinate locations, but a number of electrodes have UTM coordinates that have been interpolated based on two surrounding known electrode coordinates. Lines A-F maintains accurate five meter spacing based on differential GPS readings through electrode 19. The positions of electrodes 20, 22, 24, 26, and 28 of lines A-F have interpolated UTM coordinates. For lines G-L, every even numbered electrode has interpolated UTM coordinates. The coordinate replacements and interpolations were executed in Microsoft Excel. During the topography and UTM coordinate translations, a small number of the UTM values were doubled and this was fixed by dividing the

unreasonable values by two. Also, the DCIP3D inversion software indicated that a few source/receiver electrode pairs held the same location, so we deleted these data points.

To complete a 3D inversion with DCIP3D, we must create a mesh that covers the volume of the subsurface we are inverting over. The mesh defines the spatial resolution of the model we are generating from the data. The middle surface of the mesh has cells that are 2m x 2m x 1m and directly below that at the bottom of the mesh, the cells are 2m x 2m x 10m.

The 2D inversion topography files contain the elevation in meters, but the easting/northing UTM coordinates of the electrodes are considered tape measure positions based on five meter increments. This assumes that the lines are straight, but also takes into account the deviation from the true length that occurs when using a tape measure on a non-flat surface.

### 9.4.3 2D Inversion

#### **ABEM**

The Geotomo software RES2DINV was used to invert all of the 2D profiles. The specifics of the RES2DINV software are outlined in Appendix F.

A combined Marquardt and Occam inversion was performed on the data sets. The specifics of this inversion method are outlined in the Appendix F. This inversion took into account least-squares fitting and smoothness constraints. It is desirable to take into account smoothness in our inversions, since the majority of the geological features we are examining with resistivity are smooth in nature (with the exception of faults). Conveniently, this inversion option is built into the RES2DINV inversion software.

As noted in the “Data Reduction” section, if there was a significant amount of data points that resulted in a high apparent resistivity RMS percentage error, the data was modified and re-inverted. It is important to note that for IP the inversion process is exactly the same as listed here with only the added step of calculation of the normalized chargeability model.

For the purposes of processing and inversion, we assume that the geology outside the survey area is relatively constant (seen in the padding parameters of the inversion). Also concerning inversion, we assume that we can produce an accurate three dimensional model by connecting many individual two dimensional surveys.

#### **SuperSting**

2D inversions were completed for lines A-L of the Zen Garden for both the Dipole-Dipole array and the Wenner array using AGI Earth Imager 2D software. The specifics of AGI Earth Imager 2D are outlined in Appendix F.

The 2D inversions of Zen Garden are preliminary in nature and are primarily used to quickly check the progress and repeatability of the 3D inversions. Each inversion iterates until the error is below a specified value.

As with the ABEM 2D inversion, we assume that the geology outside the survey area is constant and linear, this can be seen in the padding cells.

#### 9.4.4 Kriging

##### **ABEM**

In addition to the 2D inversions of the data sets, Kriging was performed at both the Warm Springs site, and the Hot Springs profiles. The Kriging was performed using Microsoft Excel, MATLAB, Surfer, and Voxler. The Kriging data was obtained via the RES2DINV software used for inversion. After an inversion was performed and the results were satisfying, a .XYZ file was saved which simply gave the location of a data point along with its calculated resistivity value. Since our profiles were in 2D, we had to manually modify the .XYZ files in Microsoft Excel to include a y-coordinate along with the depth and line position of a given point. Following the modification of the .XYZ files, the Kriging of the data sets could be performed in MATLAB and Voxler. The Kriging gave us 3D models of the subsurface resistivities, which was useful when interpreting the data.

#### 9.4.5 3D Inversion

##### **SuperSting**

3D inversions of the Zen Garden data were performed using DCIP3D v2.5 software. The specifics of DCIP3D are outlined in Appendix F.

Three initial 3D inversions were performed on the dipole-dipole array SuperSting set with each inversion maintaining a constant percent error in the data (5, 10, and 20 percent). The inversion that allowed for 20% error in the data produce the most promising results - more than likely this is due to poor coupling between the electrodes and the highly resistive travertine that the electrodes were pounded into. From here we were able to develop a range of reasonable orders of magnitude for the generated model weighting factor  $\beta$ . If  $\beta$  is too small, then the model will be dominated by noise and if  $\beta$  is too large, then the model will be overly smooth. Four inversions were performed with  $\beta$  set to  $10^{-3}$ ,  $10^{-2}$ ,  $10^0$ , and  $10^1$ . For the 3D inversions, we did not use any data collected through the Wenner array system because the software did not accept the input files.

In order to accurately process and invert DC resistivity data, it is necessary to make several assumptions regarding the conditions of the survey design and parameters. One important assumption is that the survey areas cover subsurface features of interest that electrical methods can successfully capture. During acquisition, we assume that there are no major electrical disturbances in the area that

would skew the data, such as CSAMT and other electrical methods within the area. For the purposes of inversion, we assume that the geology outside the survey area is relatively constant (seen in the padding parameters of the inversion). Also concerning inversion, we assume that we can produce an accurate three dimensional model by connecting many individual two dimensional surveys.

## 9.5 Uncertainties/Errors

The greatest source of uncertainty in DC electrical methods is accuracy of station locations and elevations. Readings for this were taken on as many lines and grids as possible in Pagosa Springs using both a DGPS and a TDM system. In most cases the DGPS is accurate to a few centimeters in both the horizontal and vertical directions, however near buildings and in trees, the accuracy greatly decreases as it loses connection with GPS satellites. To remedy this, TDM data were taken along as many lines as possible. Though this process is time and labour intensive, there are frequent data gaps found throughout the area. To supplement, the DC group used a handheld GPS system combined with a barometric altimeter to get readings where other methods could not. The GPS group combined all these data sets to create the most accurate model they could. Using this, it is estimated that the error of station locations is well within error for subsurface measurements and should not be a problem for interpretation.

Another source which contributed to uncertainty in measurements is that of problems in the assumption of current line depth. This is affected by several influences such as electrode contact coupling, near surface conductivity, and subsurface anisotropy. In all cases it is true that resistivity and other electrical methods do not penetrate to exact depths of assumption. That being said, it is reasonable to conclude that with qualitative analysis and large enough survey layouts, this error of assumption can be negated to a certain degree for reasonable interpretation.

Other sources of error include bad electrode contact resistance, as well as, outlier measurements. These bad data are taken care of by both a hands on approach of qualitative analysis of manually removing visibly bad points from data, as well as with automated RMS error analysis identifying points which lie outside of a specified reasonable error range. From this, in inversion, smoothing functions and Kriging interpolations methods were applied in order to make a reasonable estimate of truth within error.

## 9.6 Interpretations

### 9.6.1 Hot Springs

The two main lithology present in this surveyed area are the Mancos Shale and the Dakota Sandstone. As the Mancos Shale has higher clay content than the Dakota Sandstone, we expect a lower resistivity



for the Mancos Shale. The Dakota Sandstone is fractured and therefore his conductivity is due to fluids occupying the pores. To be able to interpret properly the inverted sections, we need typical values for these two lithology.

According to our observations of the outcrops in this area, we know that the Dakota Sandstone is close to the surface near the Warm Springs and the Mancos Shale is at the surface near the Hot Spring. The line PAGO 04 is the only line with these two areas surveyed. Therefore, we use this line to estimate typical resistivity values for the Dakota Sandstone and the Mancos Shale.

### Results of line PAGO04

According to our geological observations in situ, we believe that the shallow resistive bodies present at the beginning of the profile correspond to the Dakota Sandstone and the less resistive area after 1200 m correspond to the Mancos Shale. The relatively deep resistive body shown between 1000 m and 1200 m cannot be correlated with other features observed within the other profile. Therefore, with the data we currently have, we are not able to interpret what could be this feature. The typical values we have from this interpretation are:

- Mancos Shale: log(resistivity) from 1.45 to 1.75 i.e. resistivity from 28 to 56  $\Omega \cdot m$
- Dakota Sandstone: log(resistivity) from 2.2 to 2.4 i.e. Resistivity from 160 to 250  $\Omega \cdot m$

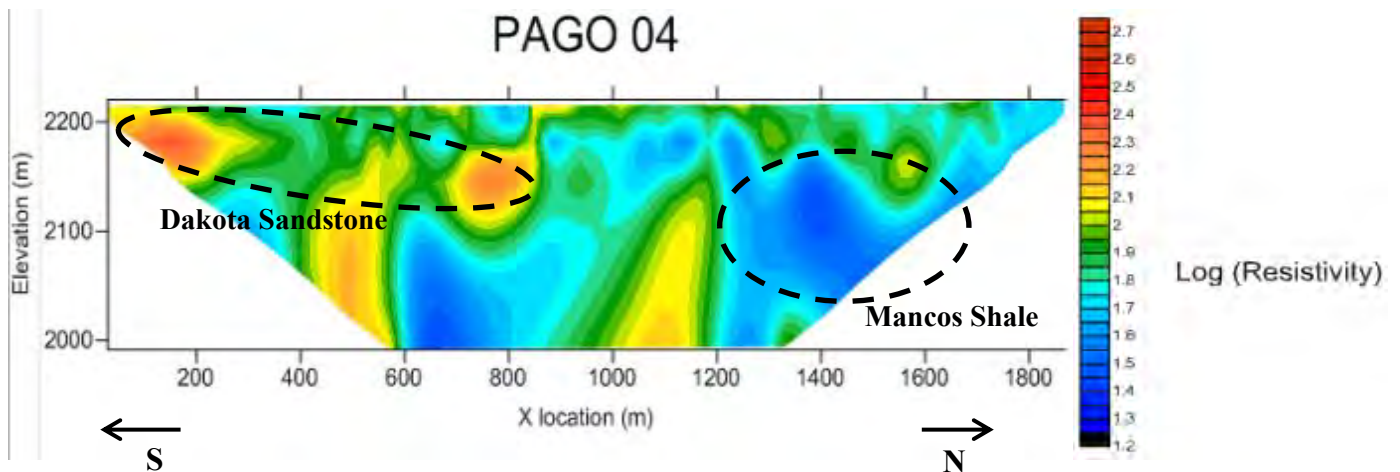


Figure 9. 6 Inverted resistivity profile of PAGO04

## Results of PAGO01

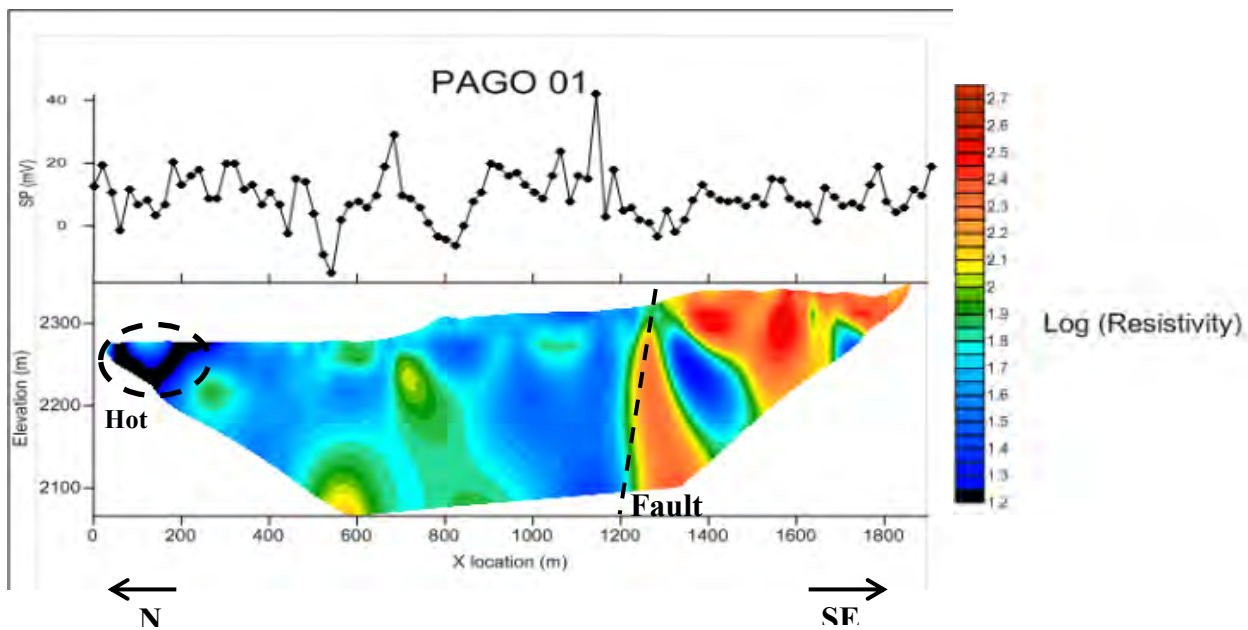


Figure 9. 7 SP and inverted resistivity profiles of PAGO01

Line is nearly 2km in length and runs approximately North-South from the Hot Springs site down to the South. The section is shows very low resistivity values, around 10  $\Omega.m$  at the beginning of the profile, likely due to the presence of hot water. From 200 m to 1200m, resistivity values are typical of expected values for the Mancos Shale. High resistivity values at the end of the profile and sharp vertical boundary between low and high values. It is likely to correspond to a normal fault bringing the Dakota sandstone closer to the surface. The SP data for this line indicates a lateral flow of water from 0 to 800 meters due to the horizontal trend in the data. The small positive anomaly from 800 to 1300 meters indicates water flow up along the fault seen in the figure above and also due to the fact that this area could be highly fractured. After this point the data shows another horizontal trend which would indicate no flow of water due to the high resistivity values of the Dakota Sandstone on this side of the profile. These high values show a non-saturated layer of Dakota with no fractures.

## Results of PAGO02

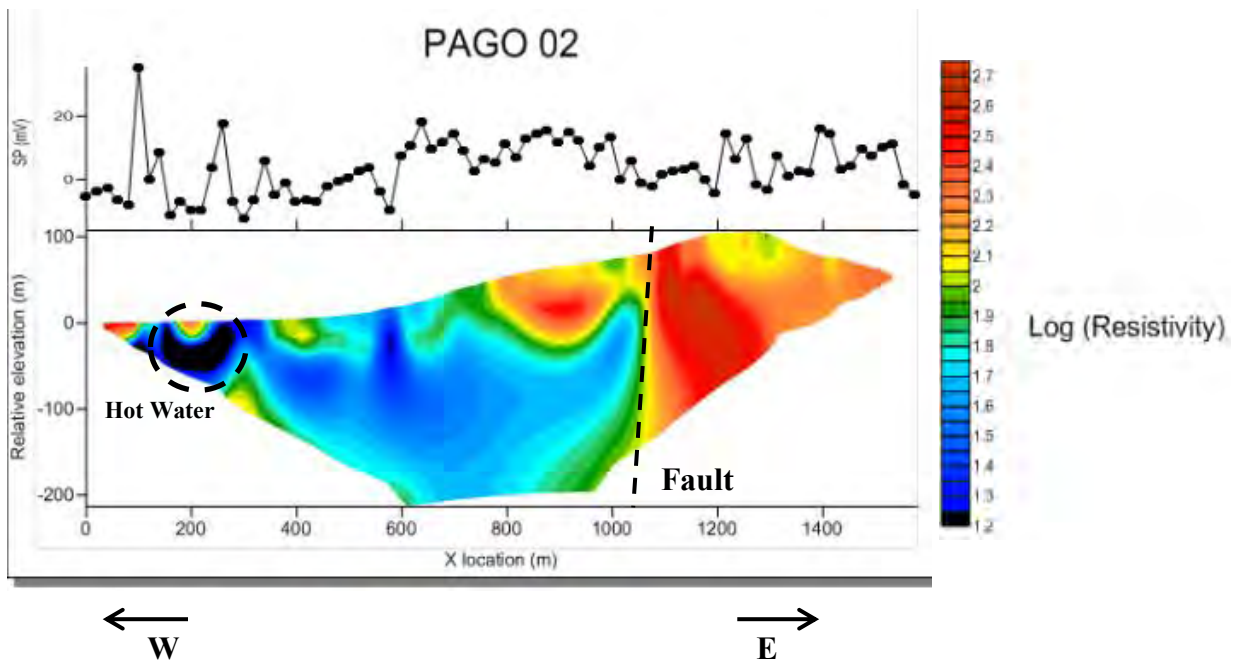


Figure 9. 8 SP and inverted resistivity profiles of PAGO02

Line is around 1500m long running East-West from the Hot Springs site up the hill to the East. This line is characterized by very low resistivity values, around 10  $\Omega\cdot\text{m}$  at the beginning of the profile, likely due to the presence of hot water. Small high resistive areas at the beginning of the profile are visible due to the presence of travertine mineralization and concretions. A sharp vertical conductivity contrast is seen at 1050m on the profile. This confirms the interpretation of a normal fault made for the line PAGO 01. The SP data in this profile shows an increasing trend in the data from 0 to 600 meters which indicates a flow of water from the fault location towards the West. From about 600 meters to about 900 meters there is a small positive anomaly that would indicate a localized vent of upwelling water just to the West of the fault location. Then the horizontal trend in the data after that indicates no flow of water after the fault location. This is due to the high values of resistivity in the Dakota Sandstone which means it is neither saturated nor fractured.

## Results of PAGO05

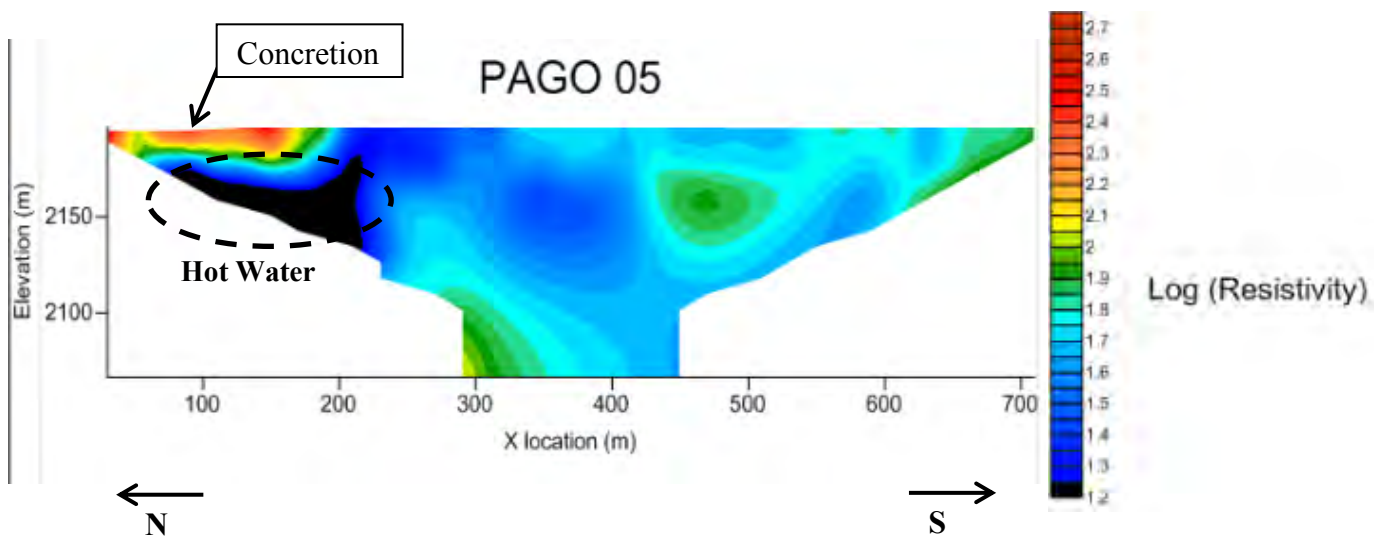


Figure 9. 9 Inverted resistivity profile of PAGO05

PAGO05 ran approximately north-south along the river from near the river at the mother spring site south towards the bridge. This line was approximately 700m long. Looking at the pseudo-section, we can see from north to south a layer of very resistive material on the north end of the line up to around 150 m down the line to the south about 20 m deep. This is interpreted to be from both resistive and physical observations layers interbedded with impermeable resistive concretions composed of travertine resulting from mineralization of the springs. Below this we can see a highly conductive layer which we interpret to represent the water from the hydrothermal system being both hot and minerally charged. As the line continues to the south away from the springs we can see the resistivity increases. The values of the rest of the profile correspond to the typical values for the Mancos Shale, which is the lithology we expect to find in the shallow subsurface along this profile. As the south end of the line approaches the river we can see the resistivity increase drastically representing the cold fresh water in the river.

## Results of PAGO06

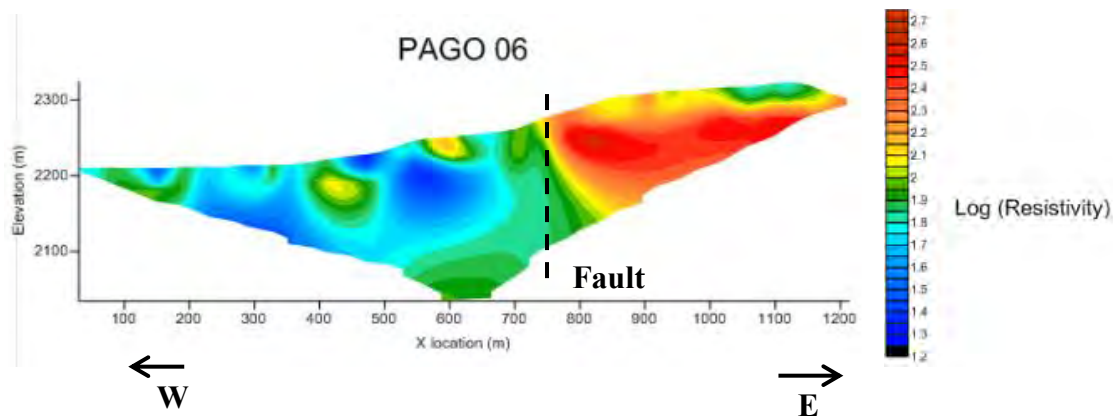


Figure 9. 10 Inverted resistivity profile of PAGO06

PAGO06 ran approximately East-West from the main hot springs area up the hill towards the East the line was around 1200m long. In this Wenner resistivity profile, we can see from west to east, a resistive layer of concretions and travertine around 20-30m deep for about 100m. Beyond this we see a conductive zone of Mancos shale with some spots of possible resistive concretions or calcifications throughout. East of this we can see a sharp boundary of a fault at about 800m down the line running the depth of our section. This shows a huge contrast in conductivity to the east of the fault. On top of this highly resistive material to the east of the fault we can see a thin layer of slightly more conductive Quaternary deposits as seen on the geologic map.

Figure 9-12 shows the resistivity model generated from the IP survey. This shows similar features to the previous Wenner model. All major features from both can be seen including Travertine deposits which can be seen on the western side of the plot as resistive anomalies. Also, the highly resistive layer to the east of the fault is a lot more apparent and is interpreted to coincide with the Dakota sandstone layer close to the surface.

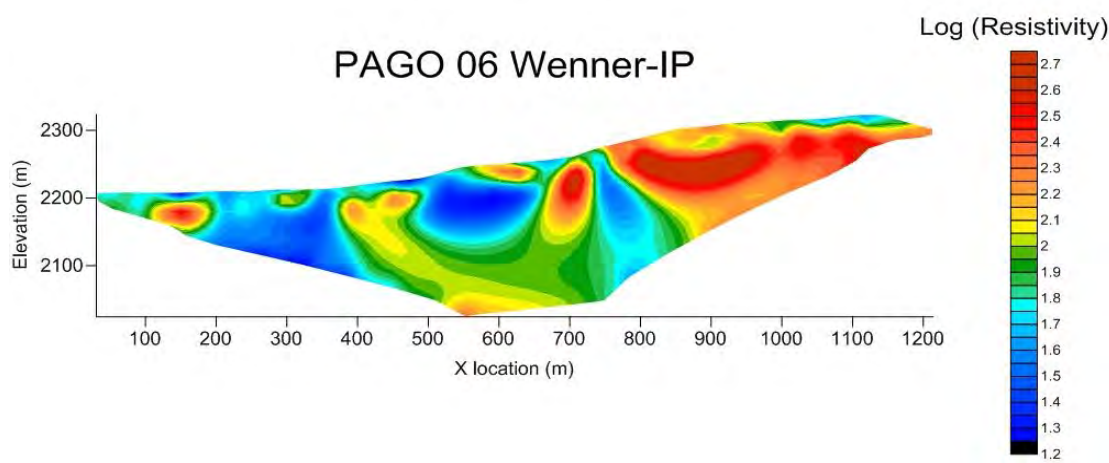


Figure 9. 11 Inverted IP resistivity profile of PAGO06



This shows the normalized chargeability generated from the IP survey inversion model. Chargeability should correlate directly with higher clay content and in this case, agrees with the expected Mancos geology. We can see the contribution of high chargeability in the clays in the Mancos on both sides of the fault. We can also see the slightly lower chargeability from the travertine deposits on the west side of the line, and the low chargeability of Dakota and Quaternary units on the east end of the fault. Another interesting feature we can see here is the fault fracture zone correlating with a low chargeability trend. We interpret this to be the contribution of the infilling of calciferous minerals from hydrothermal precipitation along the fracture zone.

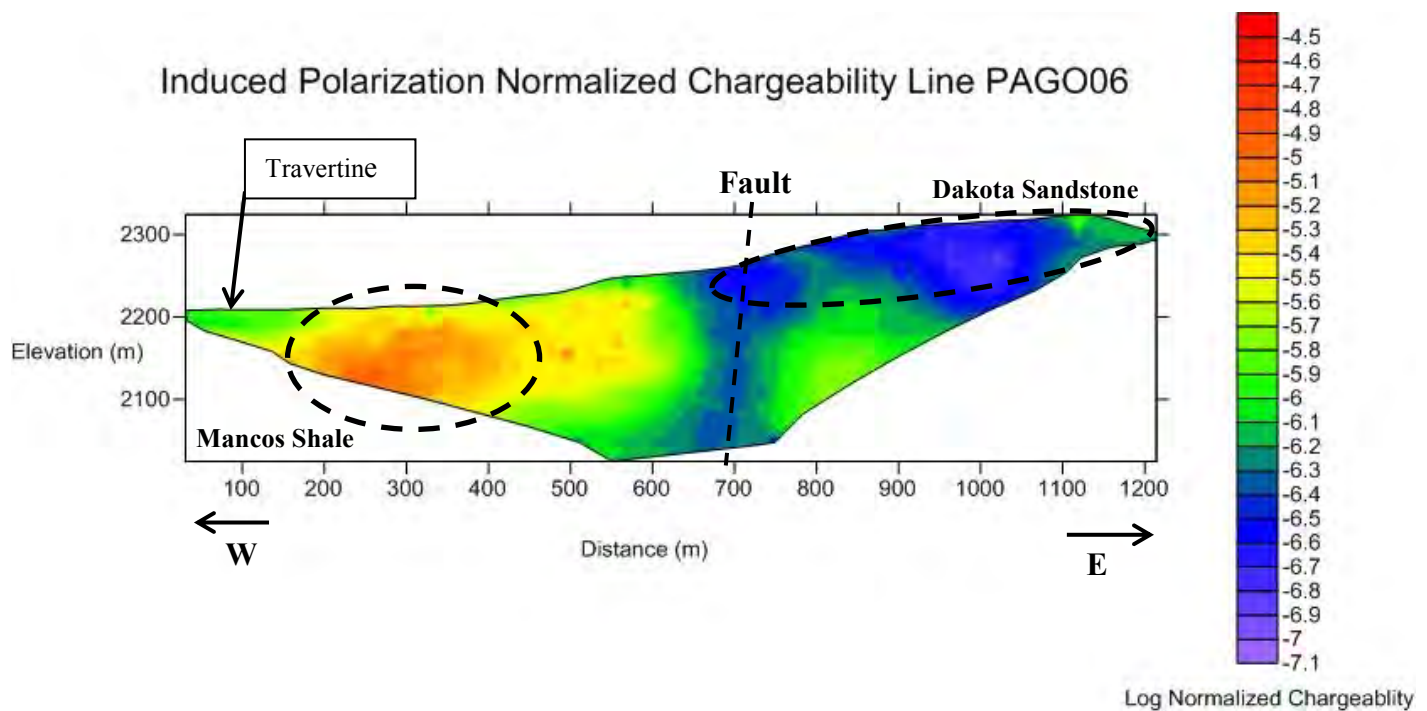


Figure 9. 12 Normalized chargeability profile for PAGO06

### Results of PAGO07

This line is 1500m long and runs approximately North-South along the river until it bends and then continues up the hill towards the Southeast towards the end of PAGO line 1. It is important to note that the profile does not reach the fault observed in the profiles 1, 2 and 6. Nevertheless, interpolating the data we have for the line PAGO 01, the fault might just after the end of this profile. The relatively high resistive body at 900m appears only on this profile. It is hard to tell what to interpret from this, however with known geology in the area; this shows similar resistivity to the travertine. Also, we can see this ends abruptly at a sharp conductivity contrast and therefore could suggest a fault system related to the one known past the edge of this profile.

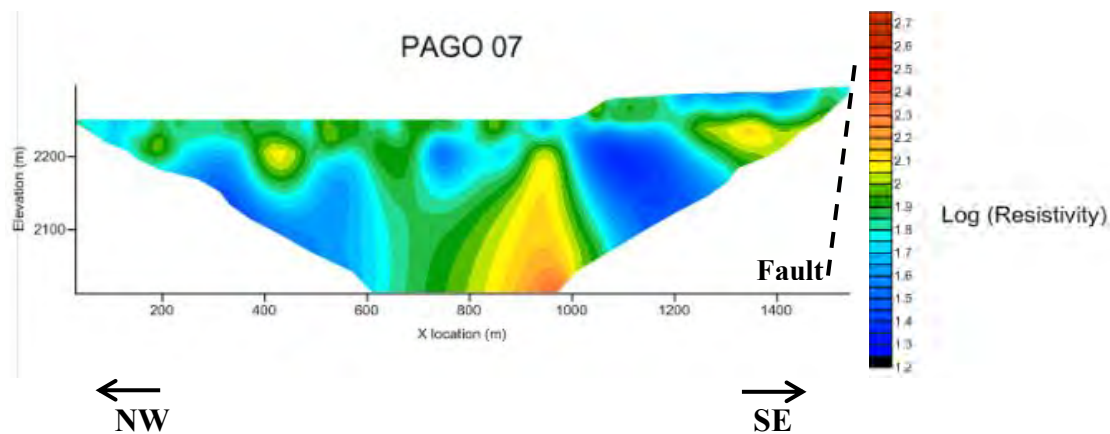


Figure 9. 13 Inverted resistivity profile of PAGO07

### Results of PAGO08

Line was around 1km long running approximately East-West just north of the Goodman property. The line was chosen to better characterizing the fault systems North of town. From this we can conclude interesting results as to previously uncharacterized faults and their orientations. From this section we found two faults located around 250m and 650m down the line respectively. The faults are characterized by sharp changes in conductivity similar to the results from fault found in the East-West PAGO lines located at the warm springs site. Also, sample of calciferous crystals were collected near each of these fault zone which suggest past and/or present hydrothermal water moving along the fracture zones. The most important result however is that we can assume due to local topography that these faults are oriented along the West edge of each ridge and move South towards Pagosa Springs where they likely meet and eventually converge with the large fault found in the other East-West PAGO hot spring lines. This could explain how the current hydrothermal system developed in Pagosa Springs characterized by splaying fracture zones which show evidence of past hydrothermal waters.

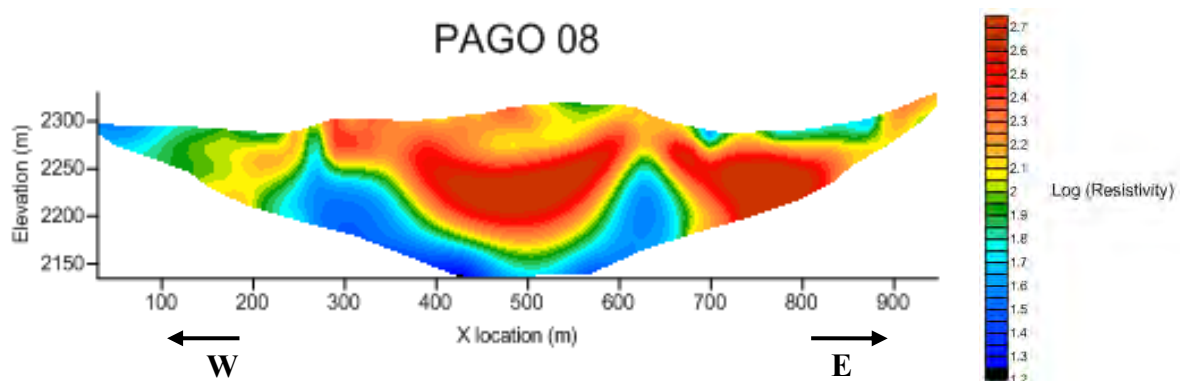
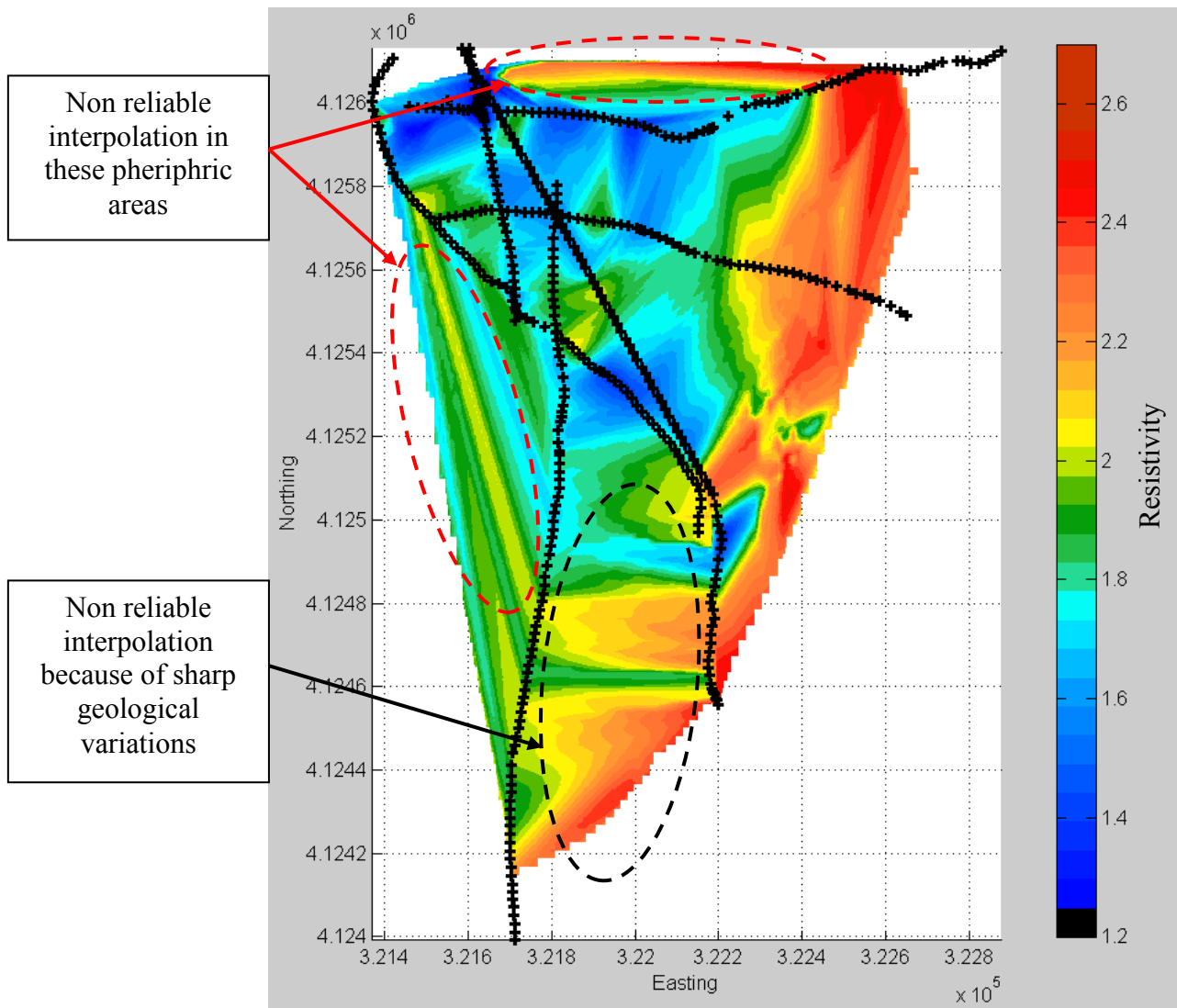


Figure 9. 14 Inverted resistivity profile of PAGO08

### **3D Model**

We then need to build a 3D resistivity model which integrates the results of all the 2D resistivity profiles. As the lines don't form a grid, we cannot perform a proper 3D inversion. Nevertheless, we have 6 lines which cover the Hot Springs site along various directions and create a rough grid over this site. Consequently, we can perform a 3D interpolation. To perform this interpolation, we use the grid of resistivity values provided for each profile by the 2D inversion with their respective depth and location in the UTM system. Different methods of interpolation were available with the software we used: linear, natural neighbor and nearest neighbor. We performed a linear interpolation because it gave relatively good results without having too long time of calculation. Indeed, due to the large distance in between each profile the other methods take a very longer time of calculation and the change in quality didn't justify this longer time.

As shown in Figure 9.16 the first thing to notice is that some interpolated areas are not reliable due to a too sparse grid. The interpolated data are not reliable especially within the periphery because it is an interpolation between two lines distant of a few kilometers. In between lines 1 and 4, the interpolation is not reliable neither because of sharp geological variations, e.g. the presence of what we interpret as a fault.



**Figure 9. 15: Interpolated resistivity slice at elevation 2100m for the Hot Springs site**

Looking at different slide at different elevations, we can correlate the features we observed within all the six 2D profiles, e.g. correlate the fault found in profiles 1, 2 and 6.

As shown in Figure 9.17, the slice at elevation 2125 m (for reference the surface elevation is around 2160m along the river) shows clearly the presence of hot water near the mother Hot Springs. But, in this slice, it is harder to interpret exactly where is the fault in between the lines, especially in the south of the site around line PAGO 01.

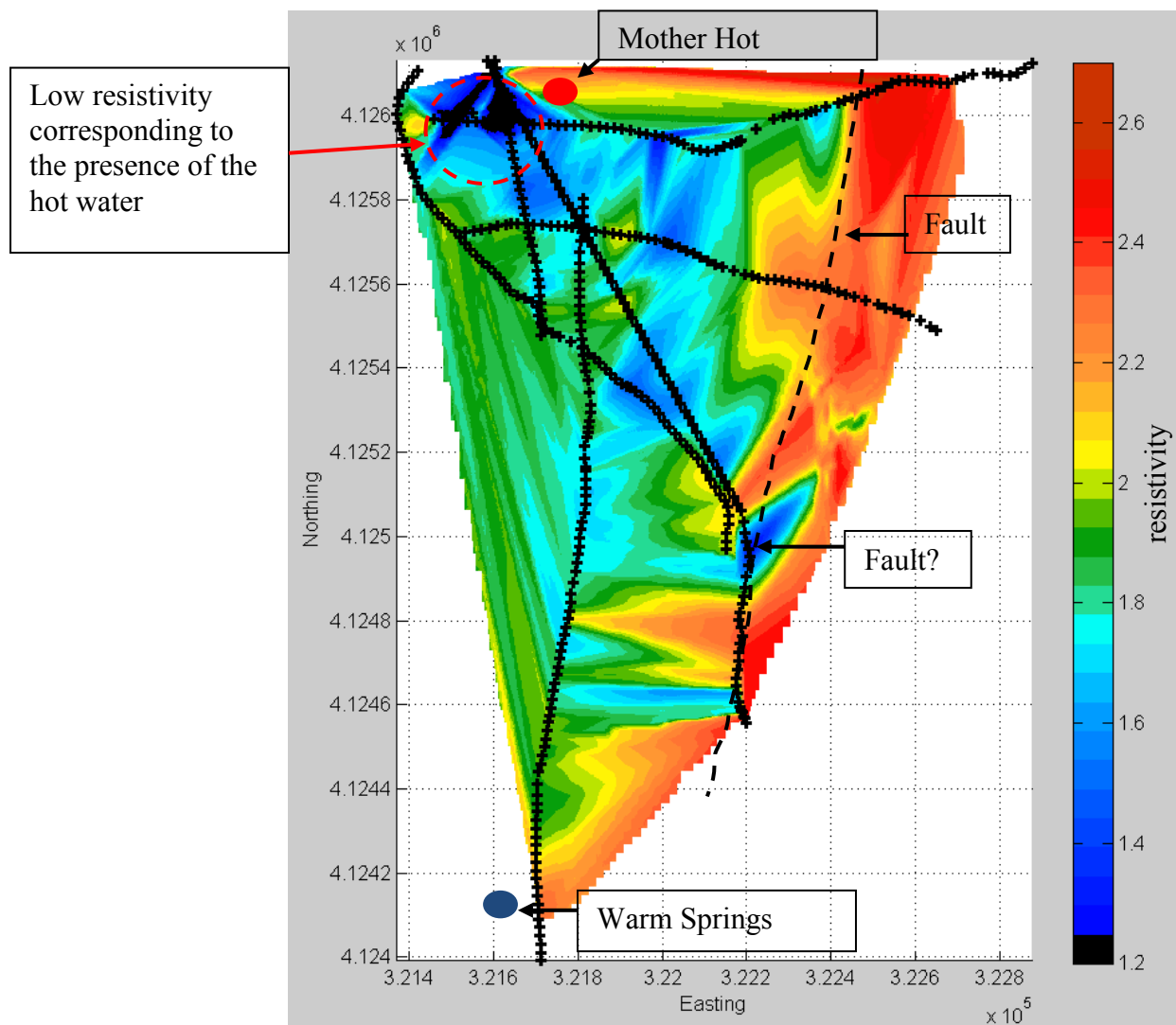


Figure 9. 16: Interpreted resistivity slice at elevation 2125m for the Hot Springs site

Looking at another slice, at elevation 2050m, the fault appears more clearly as shown in Figure 9.18. We can notice that line PAGO 01 seems to be roughly parallel to the fault which explains why the fault is not clearly identifiable for some slices, especially those closer to the surface.



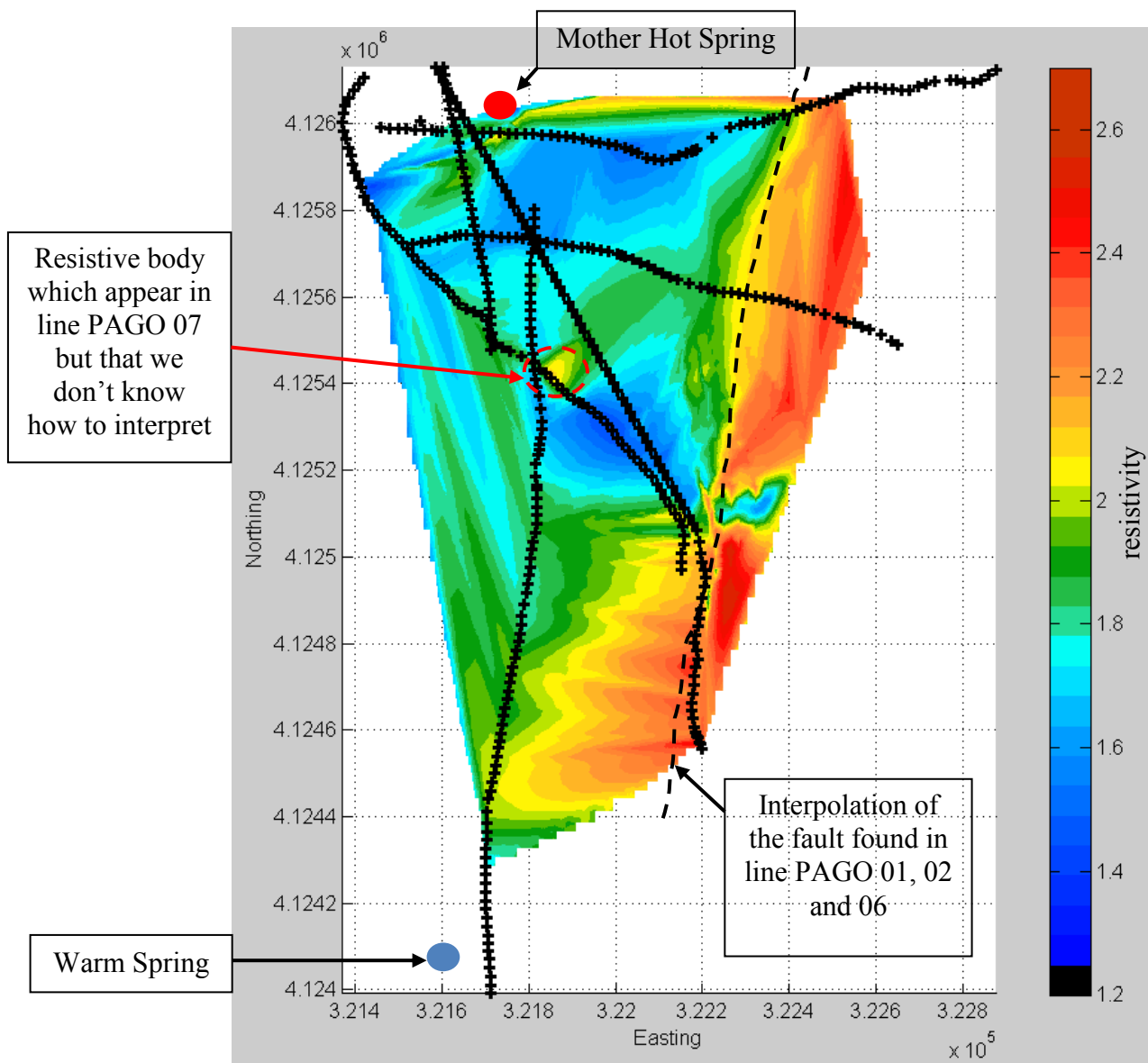


Figure 9. 17: Interpreted resistivity slice at elevation 2050m for the Hot Springs site

### 9.6.2 Warm Springs

Res2DInv software has been used to invert the data collected in the Warm Springs area. As described in the Appendix F, few parameters have to be chosen to perform the inversion. The best matches were found using a Smoothing function with a Combined Inversion method and a Least Squares Fitting. If necessary, the inversion results have then been filtered thanks to a RMS filtering

**Table 9. 5 Filtering parameters in the Warm Springs area**

Line	Filtering process
PONC 01	None
PONC 02	None
PONC 03	RMS cutoff at 35%
PONC 04	RMS cutoff at 16%
PONC 05	RMS cutoff at 20%
PONC 06	RMS cutoff at 14%
PONC 07	None

### **2D inversion results**

According to Figure 9. 18 , the four first profiles look relatively similar with a low resistivity thin layer (3-4m thickness, resistivity between 30 and 50 ohm-m), followed by a highly resistive body (20m thickness, resistivity between 300 and 500 ohm-m) while the lower layer is characterized by a medium resistivity (resistivity between 50 and 100 ohm-m) (Figure 9. 19). On the other hand, profiles 5, 6 and 7 are relatively different with a thicker shallow conductive layer (10m thickness) below which several bodies of relative average resistivity can be identified. There is no more a clear contrast between a high conductive layer and a high resistive one (Figure 9. 20).

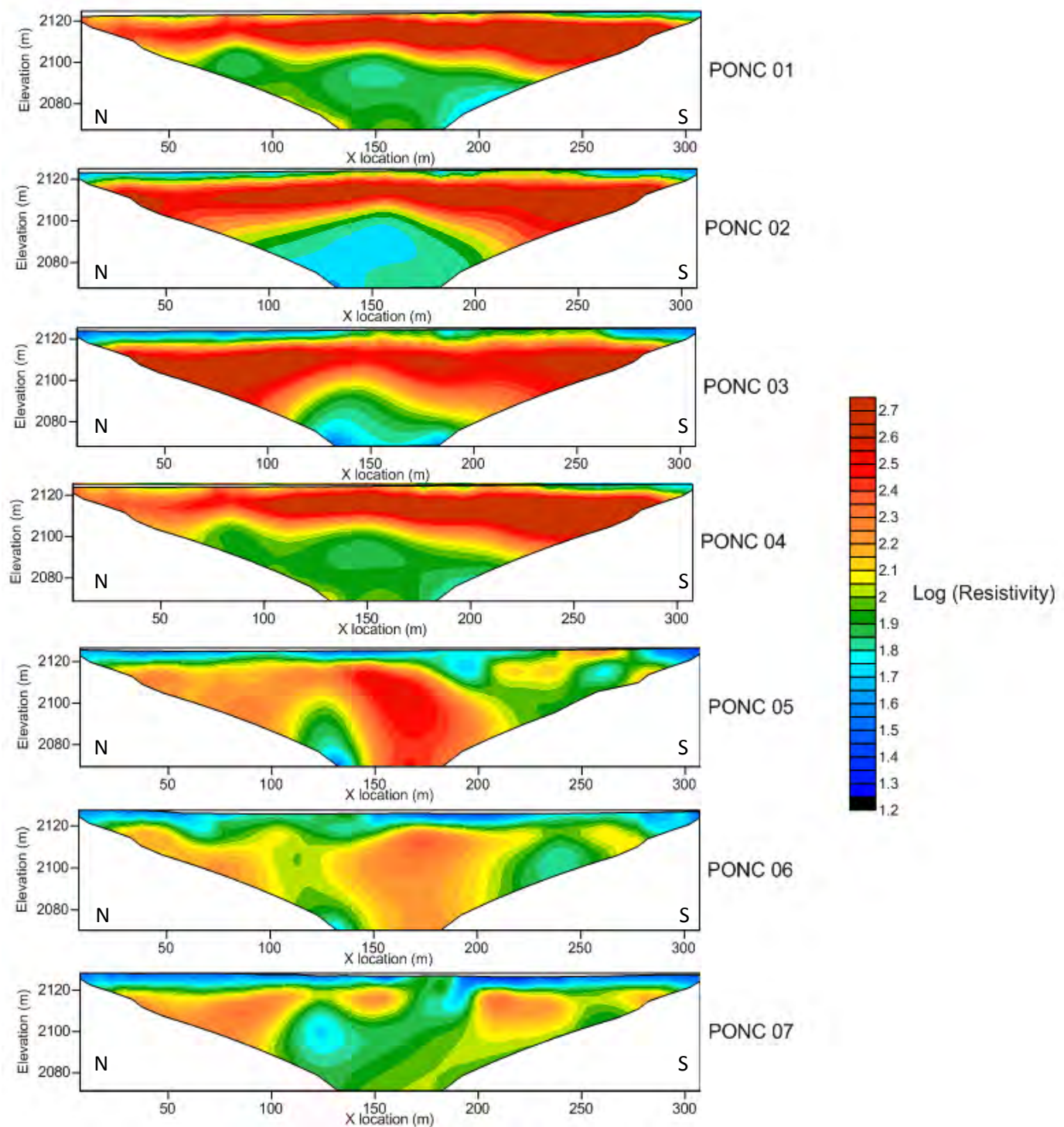


Figure 9. 18 Warm Springs 2D profiles

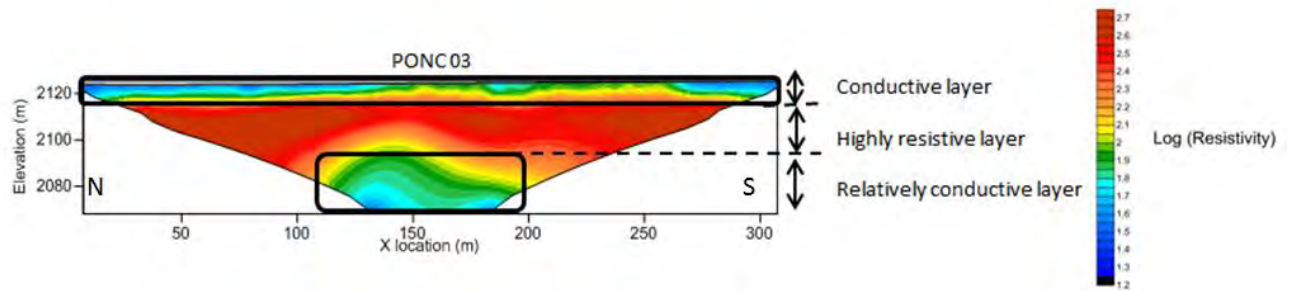


Figure 9. 19 PONC 03 annotated resistivity section

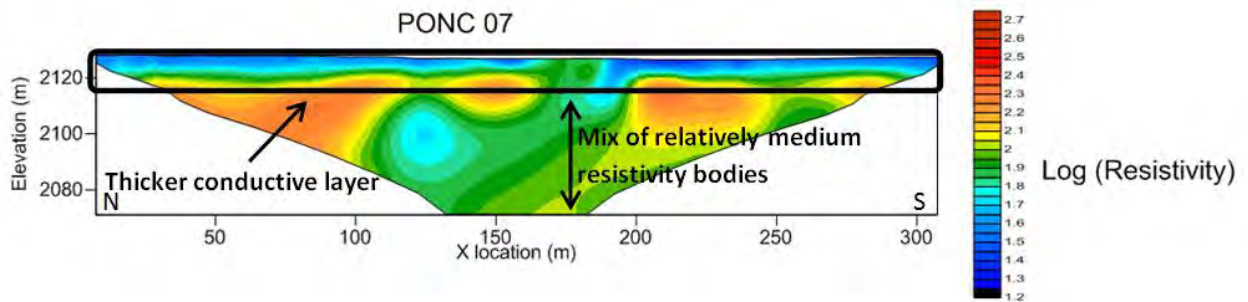


Figure 9. 20 PONC 07 annotated resistivity section

### 3D interpolation slices

The survey design of the Warm Spring area should theoretically allow us to perform a proper 3D inversion using software like RES3DINV. Nevertheless, RES3DINV did not manage to perform the 3D inversion with the data we have. Therefore, we did a 3D interpolation to correlate in 3D all the data acquired at the Warm Spring site and so build a 3D resistivity model of this area.

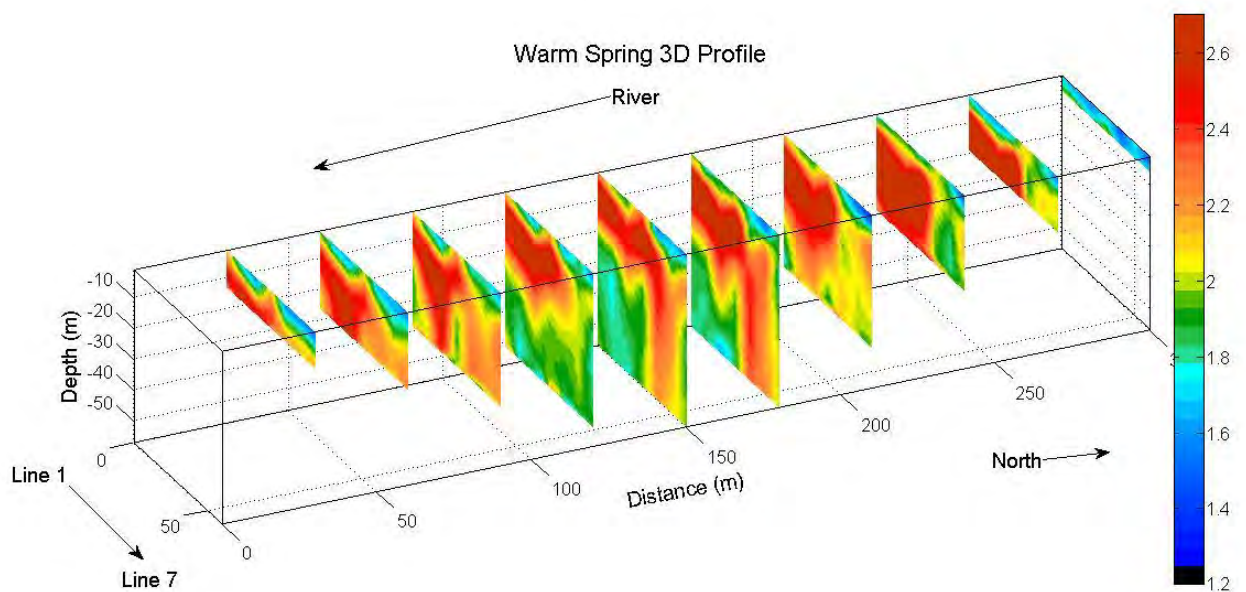


Figure 9. 21 Warm Springs 3D profile

The 2D inversion provides us a grid of resistivity values for each profile with their respective depth and location in the UTM system. We need then to interpolate in order to get resistivity values in between each profile. Different methods of interpolation were available with the software we used: linear, natural neighbour and nearest neighbour. We performed a linear interpolation because it gave good result without having too long time of calculation. The 3D interpolation allows us then to have a global model of this site.

From the P-I well data and the outcrop that can be seen on the other side of the river, only Mancos Shale and Dakota Sandstone are present in this area. Alluvial sediments can be observed in the slices but if so, only few meters can be expected (1-2 m). Thanks to this, we strongly believe that the thin blue conductive layer (resistivity below 60 ohm) can be identified as the shale and the 3D interpolation mixing the Hot Springs and the Warm Springs area confirms that. Moreover the increasing thickness of the layer towards the East (cf. 2D slices observation) is consistent with the dip given by the geological map (8 degrees towards NE)

Everything below is the Dakota sandstone formation. The resistivity contrast that can be observed between the red resistive area (resistivity above 251 ohm); the deeper green area (resistivity between 75 and 125 ohm) might then be explained by saturation changes. As the 3D model tends to show, the saturation contrast is really clear closed to the river (first lines) and becomes lighter when going East. In this case, we have then water circulation within the Dakota Sandstone closed to the river at around 30m deep.



This interpretation correlates the SP results in this area: water is flowing laterally (likely from the just discovered fault) through the Dakota Sandstone. As the layer is dipping towards NE, the water goes naturally up towards the river side. During its travel, the hot water might be mixed with cold ground water and get his pressure decreased; this can be an explanation of the relatively cold temperature and low flow observed around the geothermal sources of the Warm Spring area.

### 9.6.3 Stevens Airport

The PAGO03 line at the Stevens airport is about 3800m long, starting from the northeast end of the runway and ending southwest at the golf course at the same point where the seismic survey line begins, but it has about eight meters lateral offset from the seismic line. In the north part, low resistivity values from 0 to 2000 m are typical of expected values for the Mancos Shale. The underlying high resistivity layer is likely Dakota Sandstones. Subsurface layers are slightly dipping northeast, consistent with our geological observation. At the southwest side, the vertical boundary between high and low resistivity materials is quite clear, from this sharp change the normal fault between the airport and the golf course can be seen to some extent. Since there is only one 2D line at this area, even with information from other methods like gravity, magnetics or EM along the same 2D line, we still cannot draw many conclusions. Nevertheless, the SP data may tell us something about the hydrothermal flow and will be discussed in Section 10.

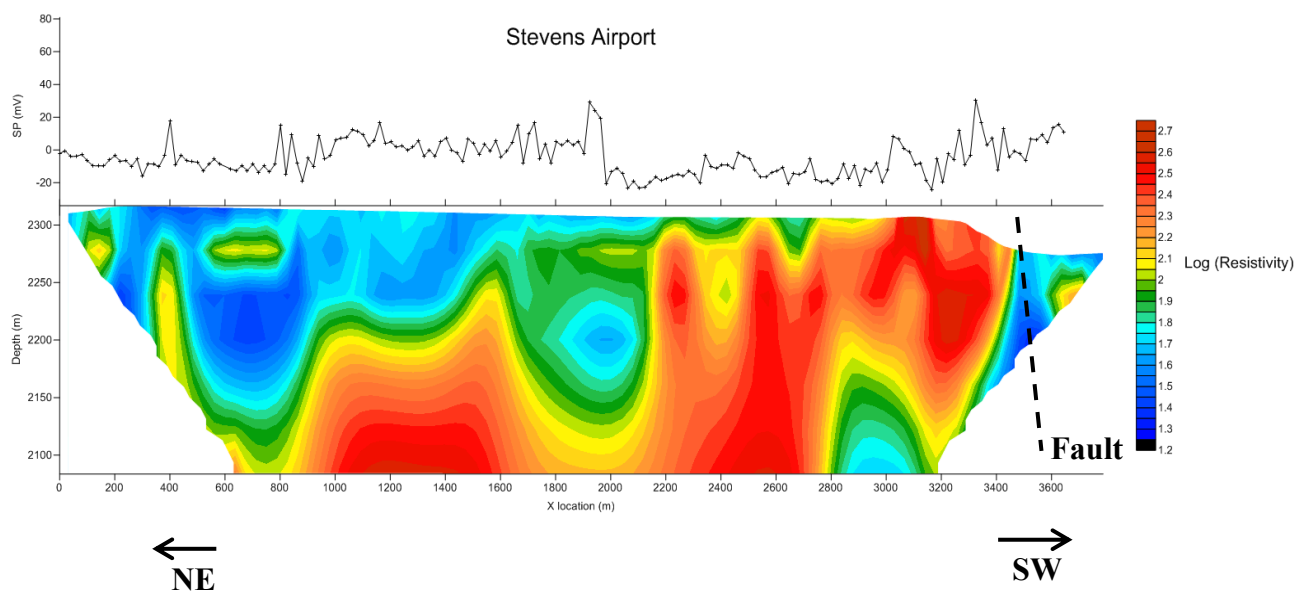


Figure 9.22 PAGO03 (Stevens Airport) 2D profile

### 9.6.4 Zen Garden

The interpretation we have derived is based upon a 3D inversion of twelve 2D dipole-dipole array surveys. The dipole-dipole array tends to emphasize vertical features more than lateral features. Our

depth of investigation for the Zen Garden is approximately thirty meters. No conclusive information came from the Wenner data.

The near surface geology of the Zen Garden shows a layer of highly resistive rock with a few small factions of conductive bodies that become more prevalent in the westward direction (Figure 9. 23). It is not surprising that the survey indicates that the surface geology is resistive because there are many outcrops of travertine (a resistive rock) within the survey area. Notice the two conductive bodies that lie on the north and south side of the extended fracture (indicated by the small blue dots). The eastern end of the fracture has known water running through it and a pipe extends into the ground at the western end where it is possible to hear running water. Water will appear as a highly conductive material because of the dissolved minerals that are good for conducting electricity.

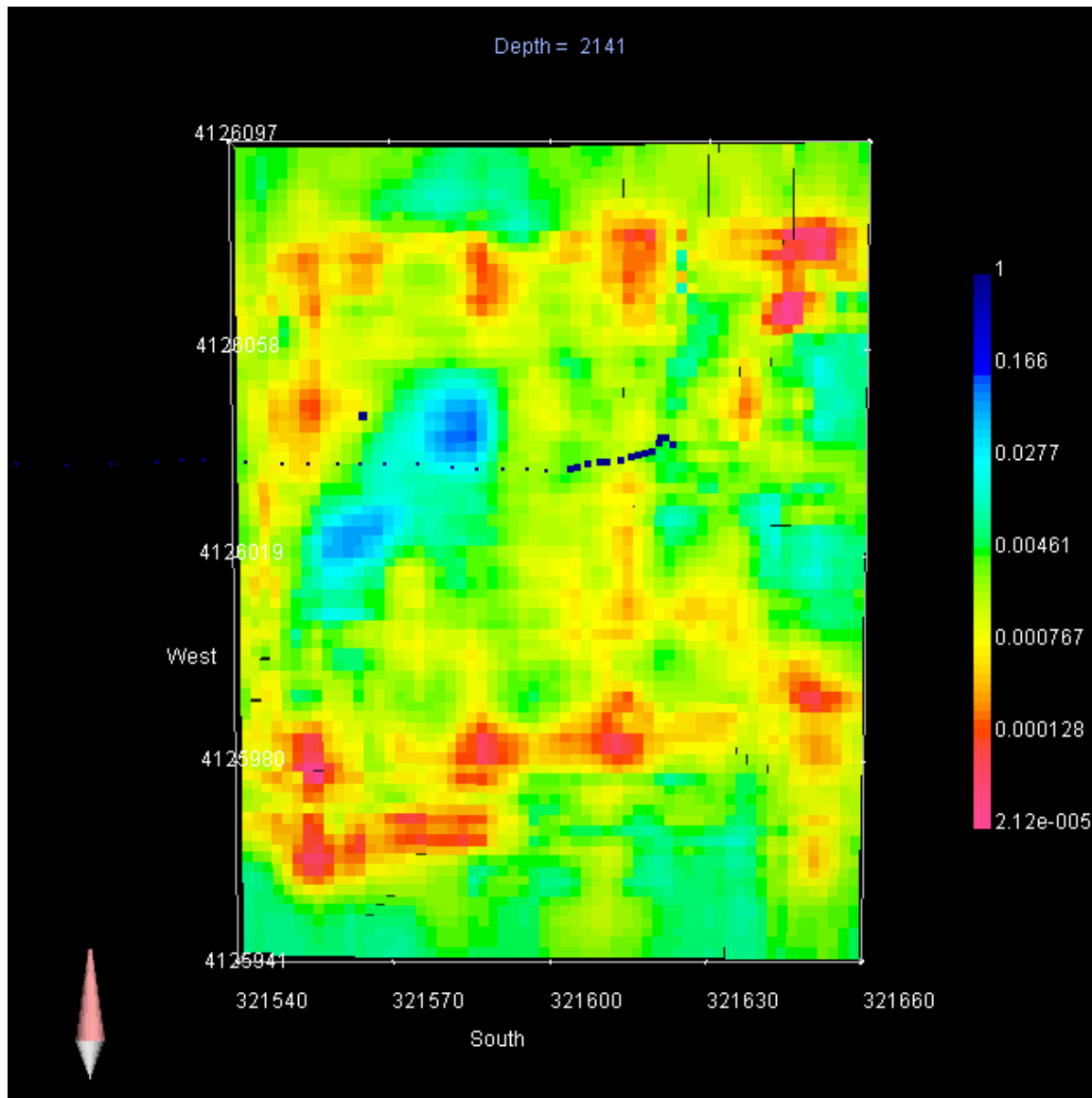


Figure 9. 23 Near surface geology of the Zen Garden depicted by a dipole-dipole DC Resistivity survey. Warm colours indicate resistive materials and cool colours indicate conductive materials. Conductivity units are S/m.

As we look further into the ground, the conductive materials begin to dominate the geology. The conductive saturation is promising for the truth of this survey since other surveys, such as EM31 and EM34, show similar patterns in the subsurface. Close to ten meters in depth there are still some resistive bodies, but the expanse of the conductive materials has grown substantially (Figure 9. 24). As we look deeper into the earth, it becomes apparent that the surfaces overall conductivity increases with depth (Figure 9. 25, Figure 9. 26).

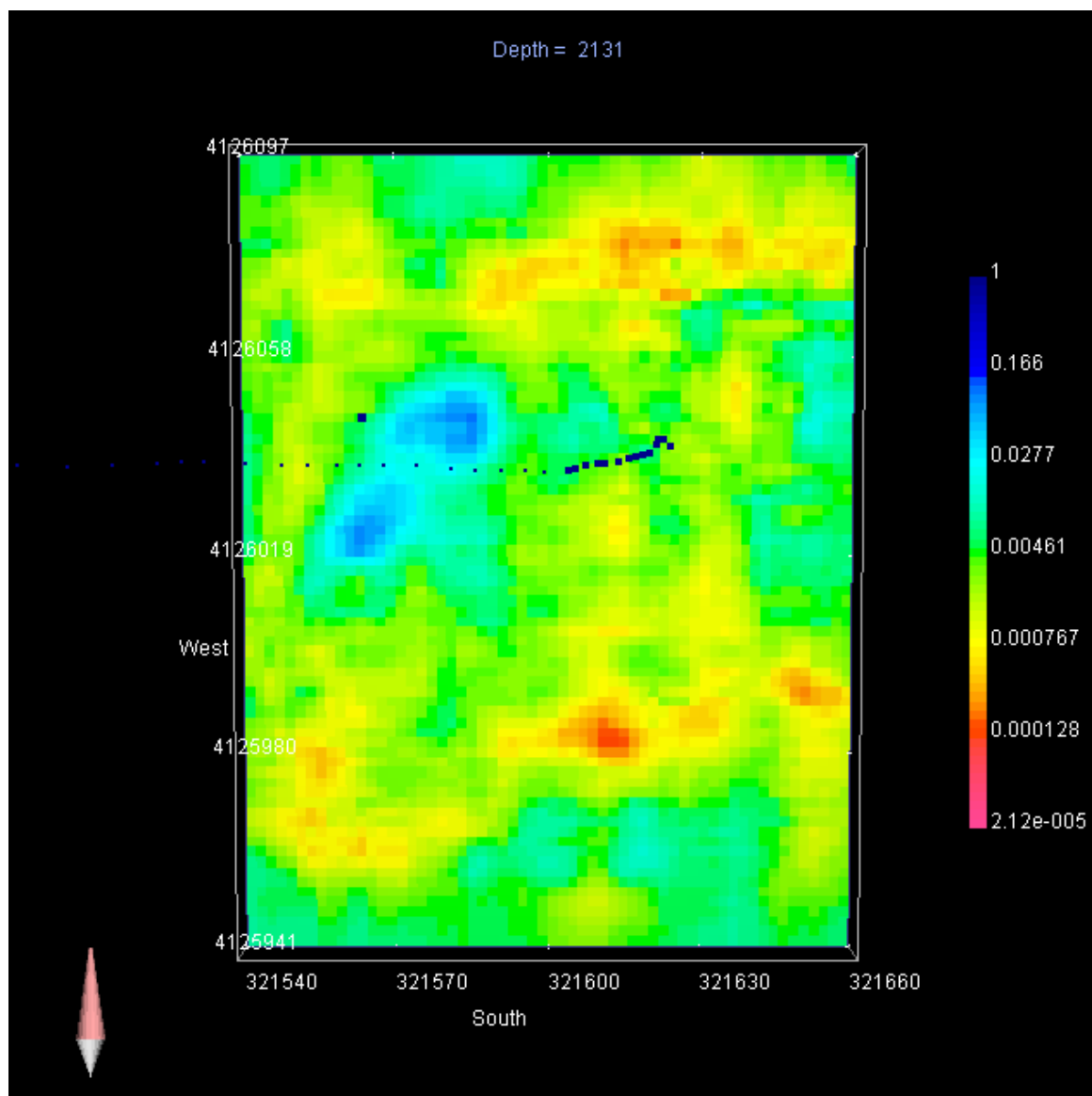


Figure 9. 24 Conductivity at ten meters depth. Notice how the cooler colors are beginning to dominate the scene. Units are S/m.

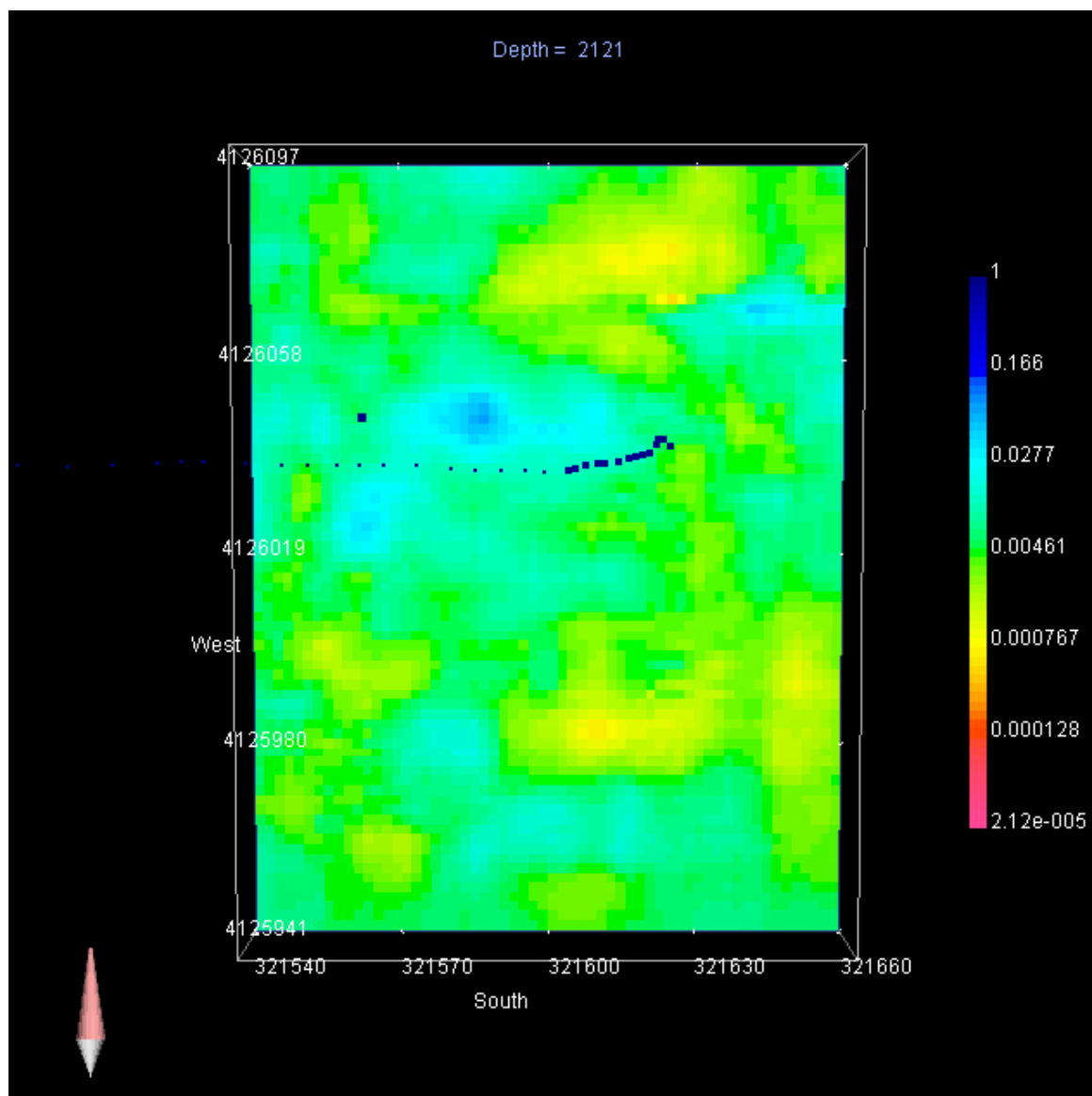


Figure 9. 25 Conductivity at 20 meters depth for the Zen Garden. Apart from some slightly resistive areas, the conductive materials almost completely dominate the scene. Units are S/m.



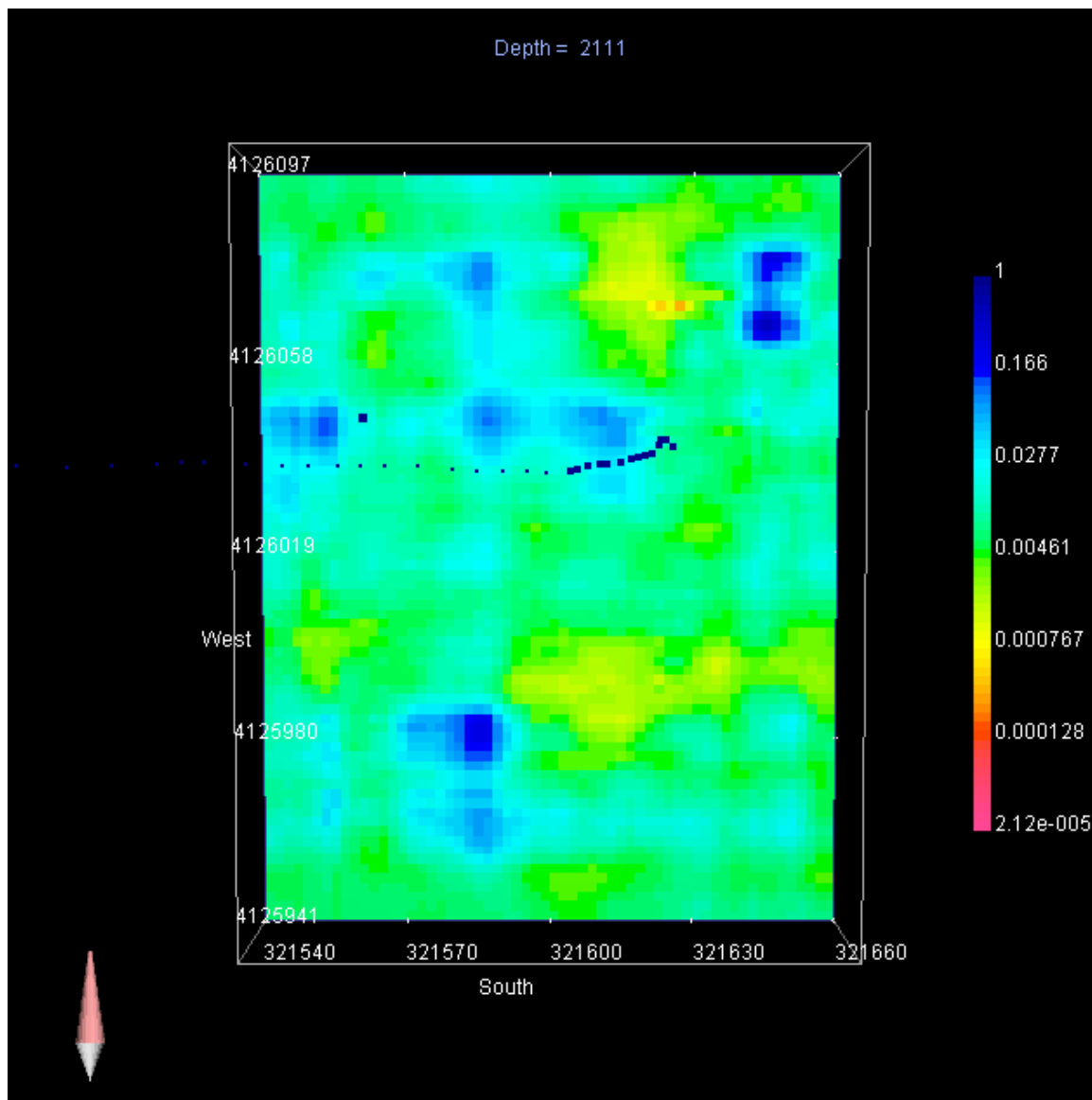


Figure 9. 26 Conductivity at 30 meters depth. The resistive bodies are nearly non existent besides a small region in the north east corner of the scene. Units are S/m.

When we examine a cut-off view of the 3D model, we can easily distinguish between regions of high and low conductivity (Figure 9. 27). Notice ring like structure of the resistive material that lies on top of the more conductive material. Along the known fracture path we expect to see a highly resistive body close to the surface because we know it is a void. Figure 9. 28 displays the same model as Figure 9. 27, but with the volume north of the fracture excluded from the image and allows us to see the conductivity cross section along the fracture. Almost directly above 321630 easting, there is a pocket of resistive material that dips into the surrounding material - this closely follows what we would expect to see for the fracture. Because we can see one fracture, it is possible that there are more fractures in the subsurface that would allow for water to travel through and thus appear as conductive material. GPR models produce results by showing a few more fractures that project south of the

surface fracture, but GPR shows the base of the resistive travertine at only three meters deep. It is possible that there is an internal layering system within the travertine. When we keep only the materials that have very high resistivity ( $\sim 10^{-4}$  S/m), we see that the possible travertine is 7 or 8 meters thick near the surface.

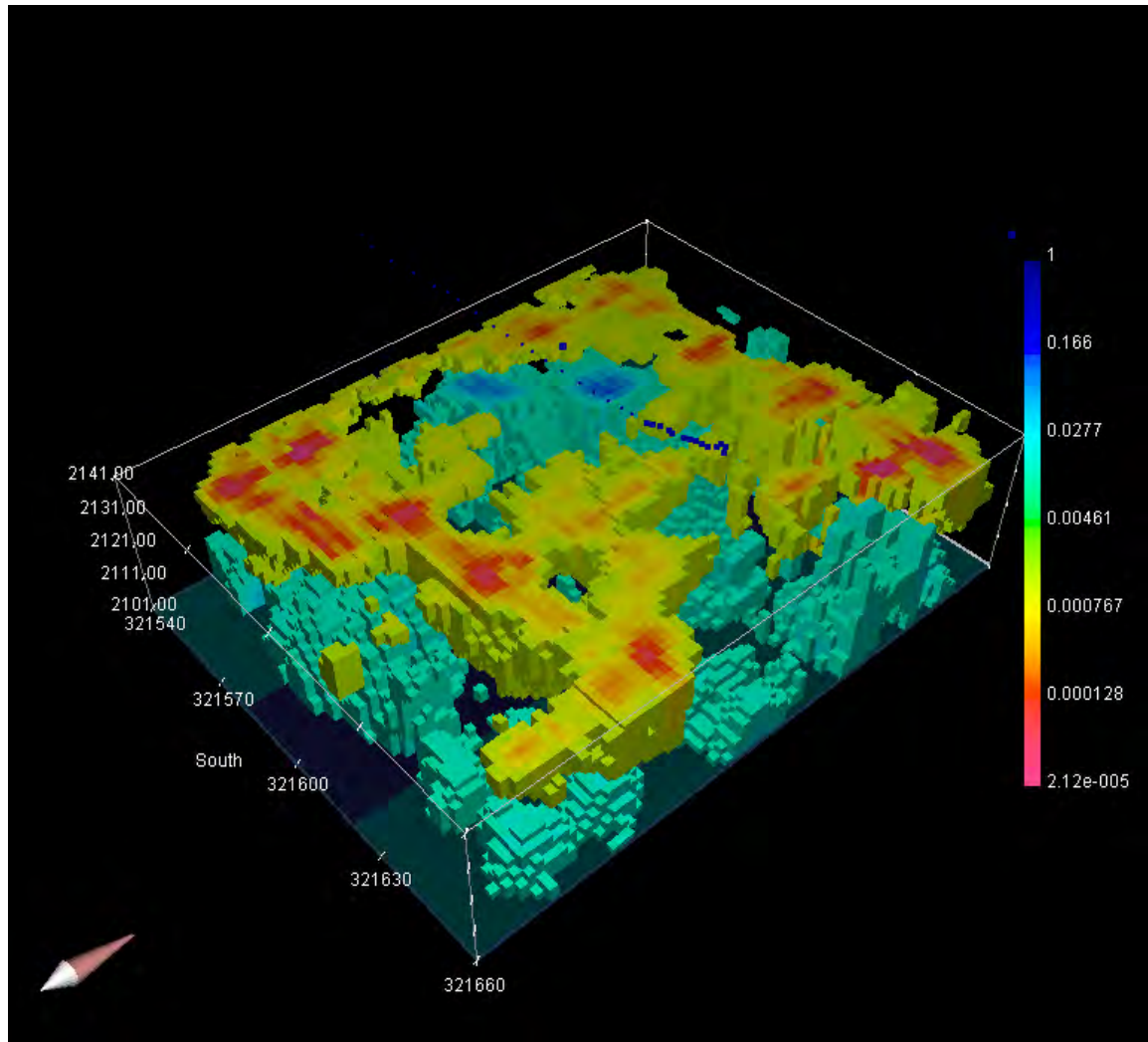
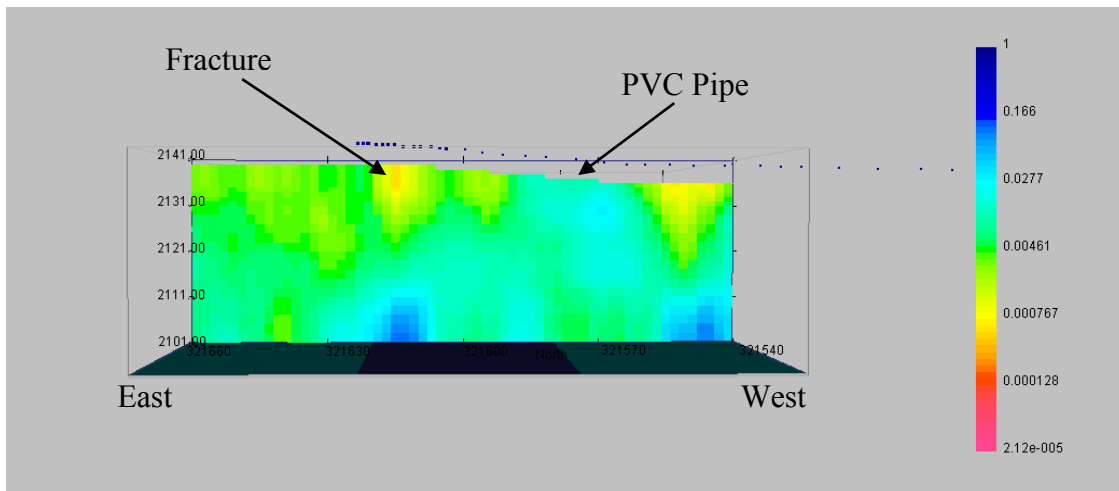


Figure 9. 27 3D resistivity model of the Zen Garden where the middle-range values have been left out. Notice the ring of resistive material that caps the conductive regions beneath. Units are S/m.



**Figure 9. 28** Cross section along the surface fracture at the Zen Garden. Notice the conductive body that rises to the surface along the cross section near the western end of the fracture: this is near the location of the pipe mentioned earlier.

Figure 9. 29 and Figure 9. 30 display the dichotomy that exists between the top ten resistive meters and the conductive layers at depth. In examining Figure 9. 29 and Figure 9. 30 together, we can see that there is a conductive body that follows the general east/west path of the surface fracture and diverges to the north. At the point of divergence a conductive body reaches towards the surface and is close to the location of the pipe. The resistive materials in Figure 9. 30 that continue deeper into the ground could possibly be a series of fractures that do not hold water, or they solid, impermeable rocks that act as guides for any sort of fluid flow.

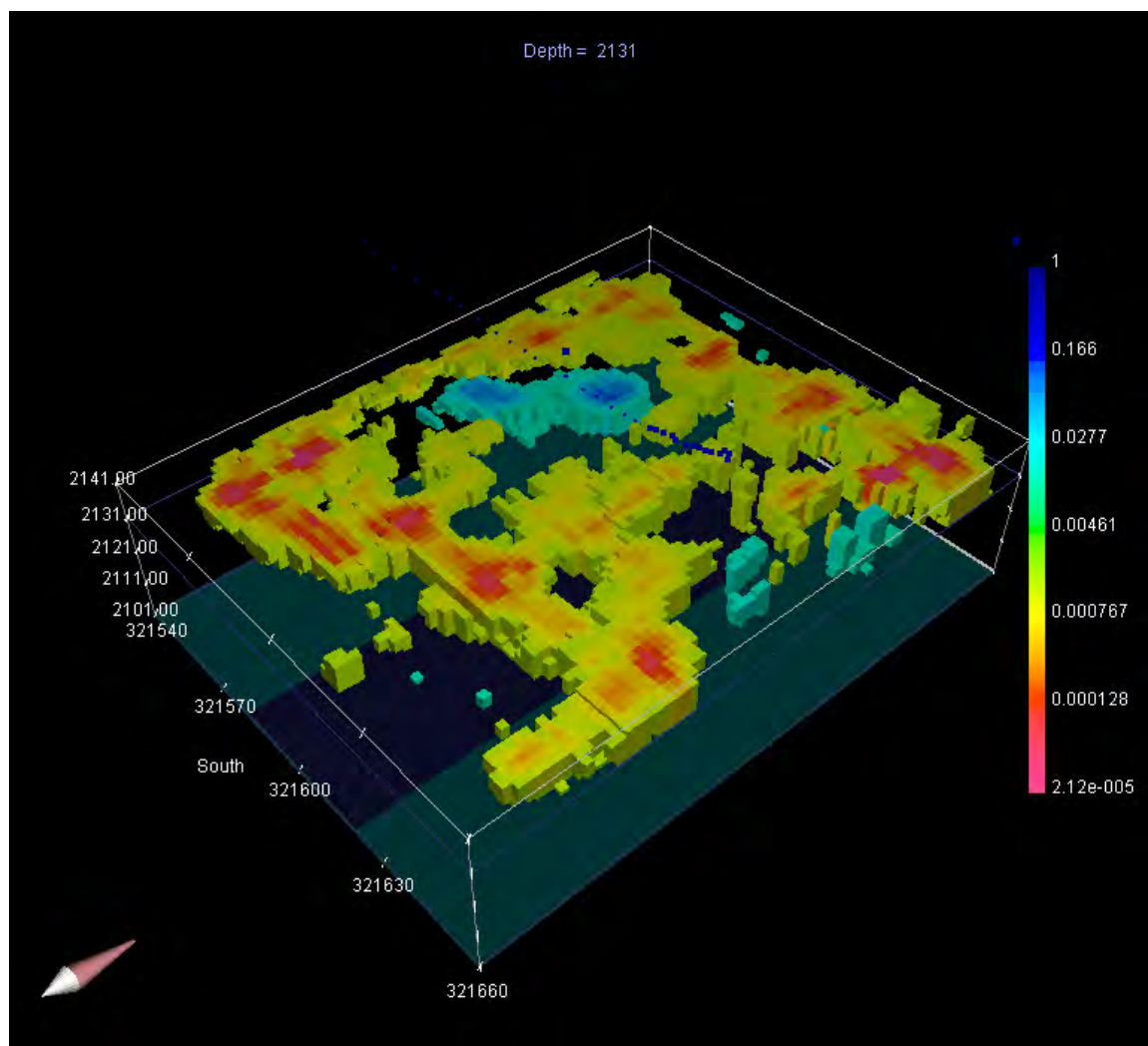
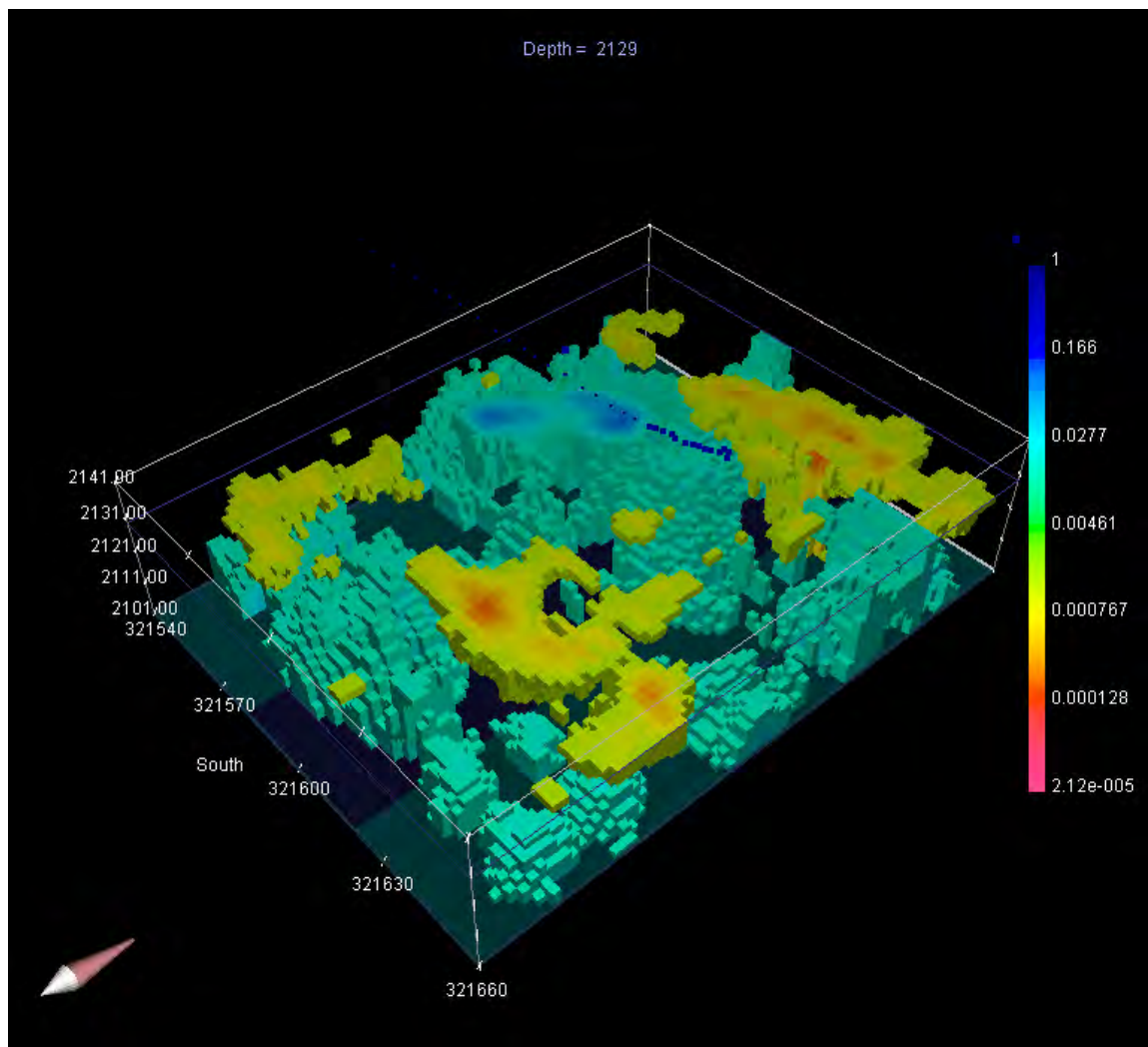


Figure 9. 29 3D conductivity model displaying the top ten meters of the Zen Garden site. Notice the dominance of resistive material. Units are S/m.



**Figure 9. 3D conductivity model displaying all depths except the top ten meters of the Zen Garden site. Notice the increase in conductivity with depth. Units are S/m.**

According to our geologists, the Zen Garden has a top layer of travertine that overlays a conductive alluvial deposit. The absolute thickness of the travertine and the alluvial deposit is unknown, but we can infer from the conductivity model that the travertine is approximately three to seven meters thick and that the alluvial deposit is at least twenty meters thick. Underlying the alluvial deposit is the Mancos shale. If the Mancos shale is more conductive than the alluvial deposit, then we may be seeing the top of the shale at depths of approximately 35 meters. This is assuming that the Mancos shale is more conductive than the alluvial deposit. Also, we must remember that our depth of investigation is approximately 30 meters, so any information gathered from deeper than 30 meters is not to be wholly trusted.

Much of the ground truth information we have coincides with the produced conductivity model, which allows us to trust the model at depths that we cannot physically touch.



According to our geologists, the Zen Garden has a top layer of travertine that overlays a conductive alluvial deposit. The absolute thickness of the travertine and the alluvial deposit is unknown, but we can infer from the conductivity model that the travertine is approximately three to seven meters thick and that the alluvial deposit is at least twenty meters thick. Underlying the alluvial deposit is the Mancos shale. If the Mancos shale is more conductive than the alluvial deposit, then we may be seeing the top of the shale at depths of approximately 30 meters (see Figure 4). This is assuming that the Mancos shale is more conductive than the alluvial deposit. Also, we must remember that our depth of investigation is approximately 30 meters, so any information gathered from deeper than 30 meters is not to be wholly trusted.

Much of the ground truth information we have coincides with the produced conductivity model, which allows us to trust the model at depths that we cannot physically touch. The PVC pipe is located near a rising conductive body and the area near the fracture appears as a highly resistive body, as voids should. Through geologic investigations and other methods, we know that there is a body of resistive travertine overlying a more conductive alluvial deposit and our conductivity model clearly displays the separation between the two layers.

## **9.7 Conclusions and discussions**

### **9.7.1 Hot Springs, Warm Springs, and Stevens Airport**

The DC Resistivity results in the Pagosa Springs area successfully confirmed the Eight Mile Mesa Fault, while also finding additional faults near the Mother Spring (Figure 9. 31). At the Stevens Airport area, the resistivity line supports the seismic results by confirming their fault description.

On the other hand, the various resistivity surveys around the mother source (which is our target) enabled us to locate an additional normal fault and to confirm its play in the geothermal system of the area. Indeed, this fault is likely to be deep enough to make the hot water flowing from the Precambrian basement to the base of a hole in the Mother Spring case or to the permeable Dakota Sandstone in the Warm Spring case (Figure 9. 32).

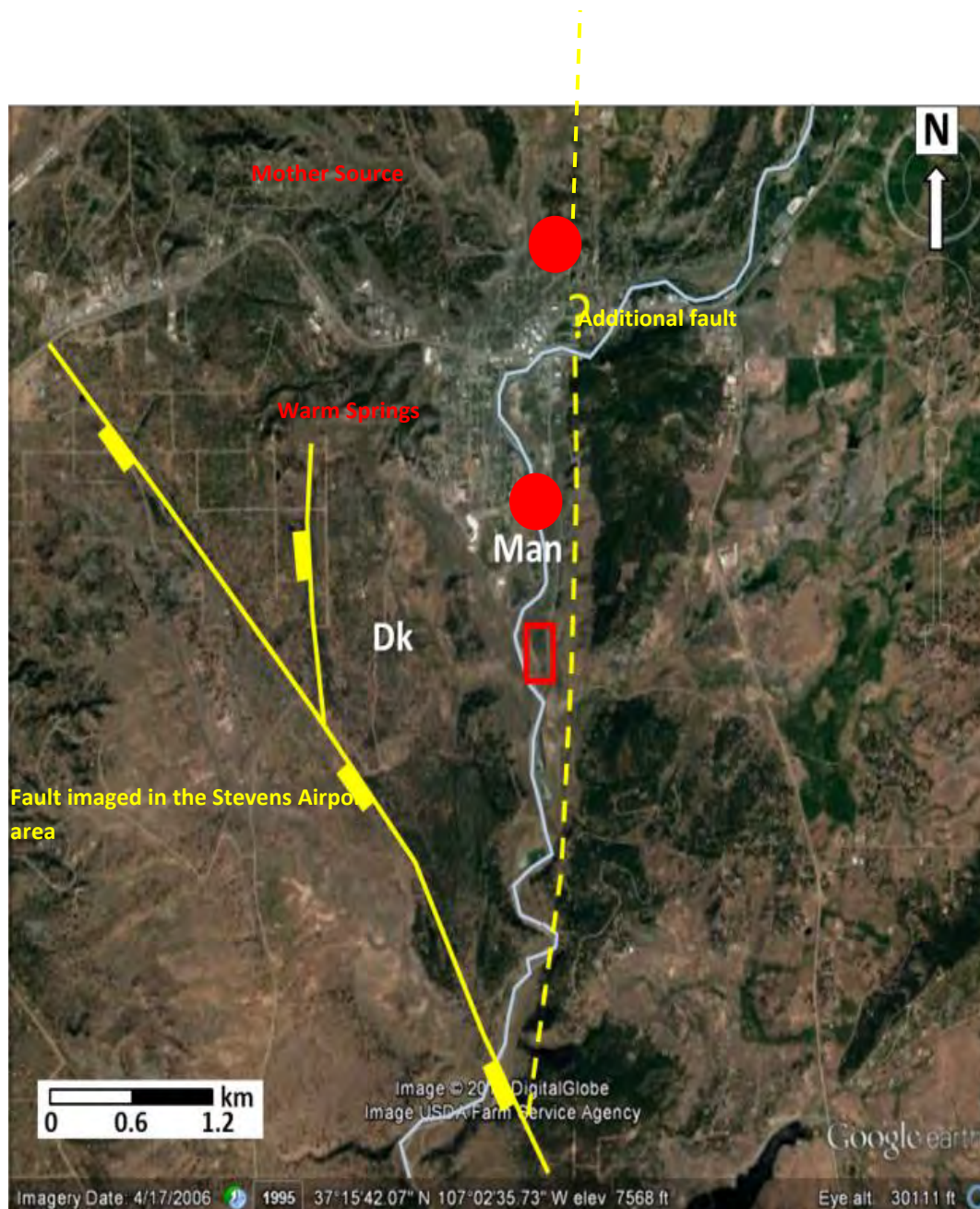


Figure 9. 31 Fault map of Pagosa Springs

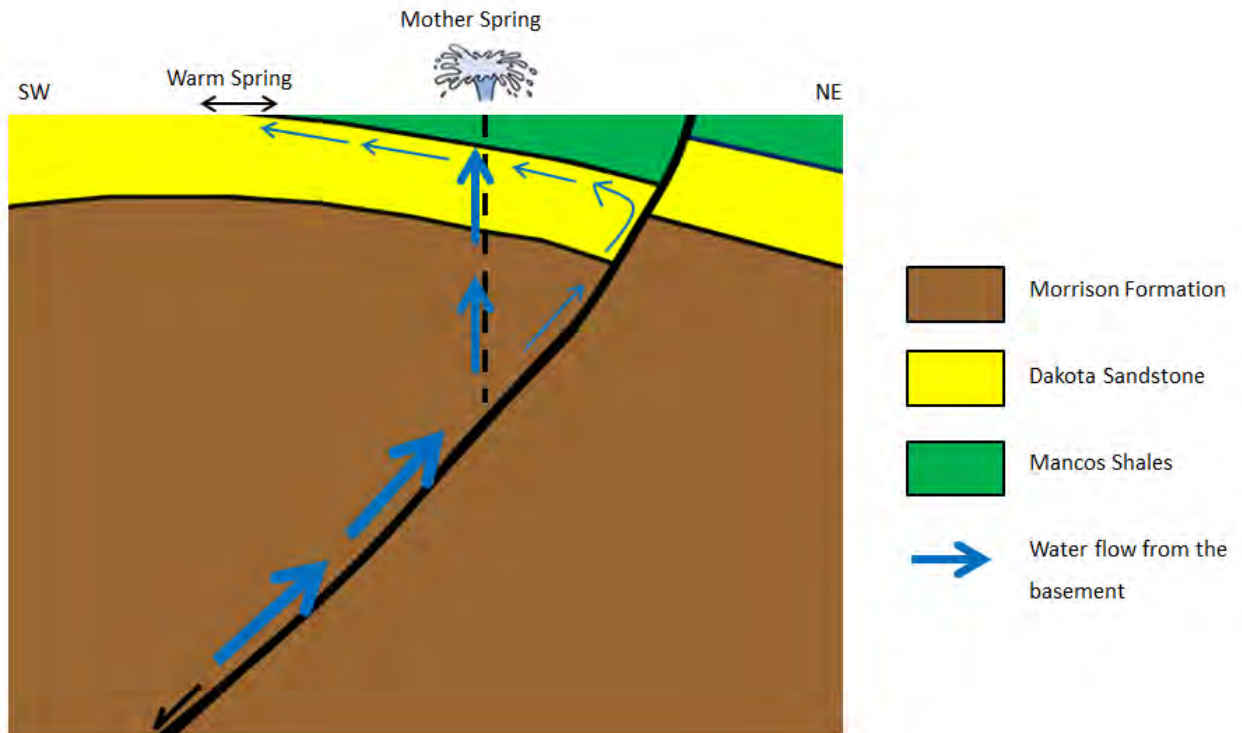


Figure 9.32 Scheme of the probable geothermal system taking place at Pagosa Springs

In order to confirm this preliminary interpretation, additional resistivity lines should be done on the northern side and eastern side. This would enable us to draw a precise description of the fault and how it can be linked to the other ones in the area. Other types of surveys such as gravity or electromagnetic would also bring further details concerning the play of the fault in the geothermal system.

### 9.7.2 Zen Garden

A 3D inversion of the twelve dipole-dipole DC resistivity surveys performed at the Zen Garden produces a model that displays many features that correlate well with the geology and the results of other geophysical methods that surveyed the area. The primary feature is the distinction between a top resistive layer that overlies a thicker conductive body. This contrast in conductivity coincides with the suspected geology of the site in that there is a layer of travertine (resistive) at the surface that caps an alluvial deposit (conductive). Because the Zen Garden is next to a river and is near the Mother Spring, it is not surprising that there is an alluvial deposit that is fairly conductive. Due to the complexity of the DC resistivity method, it is challenging to determine the thickness of the layers, but the model indicates that the travertine is seven to eight meters thick. The alluvial deposit is at least twenty meters thick, but our depth of investigation is approximately only thirty meters, so it would be

challenging to any make reliable conclusions concerning the conductivity of the subsurface at depths greater than thirty meters.

There is a surface fracture in the travertine that runs east/west and appears in the model as a resistive feature. The top of the fracture appears as a resistive feature because void spaces do not conduct current, but increases in conductivity with depth because of the change in layering and the possible presence of water. GPR results indicate that there are secondary fractures south of the surface fracture and our conductivity model shows similar results. More than likely, the subsequent fractures are void space and appear as resistive features. A PVC pipe near the north-eastern corner of the DC resistivity survey area allows us to hear running water in the ground, which reinforces the model of a conductive second layer. Another reinforcing factor as to the accuracy of our model is that it displays a conductive body that rises to the surface near the PVC pipe.

Although our survey design and model produced good results, there is always room for improvement. To increase the reliability of our model, it would be beneficial to run survey lines with an east/west orientation rather than north/south. Many features appear in the model that appear to be oriented in the north/south direction, so an east/west orientation would allow us to capture these features better. Also, coupling the electrodes was a major issue and resulted in bodies that appear as unreasonable highly resistive features. The poor coupling was due to a combination of the surface geology and the fact that the survey area was extremely dry at the surface. In the future it would be a good idea to complete the survey during a wetter season in order to achieve better coupling. Finally, a wider range of inversion parameters should be examined in the future, as well as generating models based on a Wenner array survey. This last point is purely a time and computing power constraint.

# 10 Self-Potential

---

## 10.1 Introduction

The Self-potential (SP) method, also called spontaneous polarization method, is widely used in groundwater and geothermal investigations [23]. It passively measures the electrical potential field in the ground created by the current that is associated with the groundwater flow [38]. Non-polarized electrodes are used in the survey, so that there is no voltage difference between the ground and the electrode. Voltmeters with millivolt sensitivity and high impedance are needed because the anomalies are usually less than 100 mV [19]. Voltage is measured between one fixed electrode as the reference and another electrode moving away from it with a regular interval. Reference corrections are required if more than one reference point is used in a survey line. Regional corrections are also needed to subtract the drift, or say the regional trend due to the telluric current [23]. Additionally, the non-zero voltage measured between two directly connected electrodes needs to be subtracted from all the data points. Nevertheless, the latter two corrections are usually numerically too small to have much influence in the results, so that can be neglected. Generally, in the corrected data, negative anomalies indicate water flowing down, away from the surface, while positive anomalies indicate upflows.



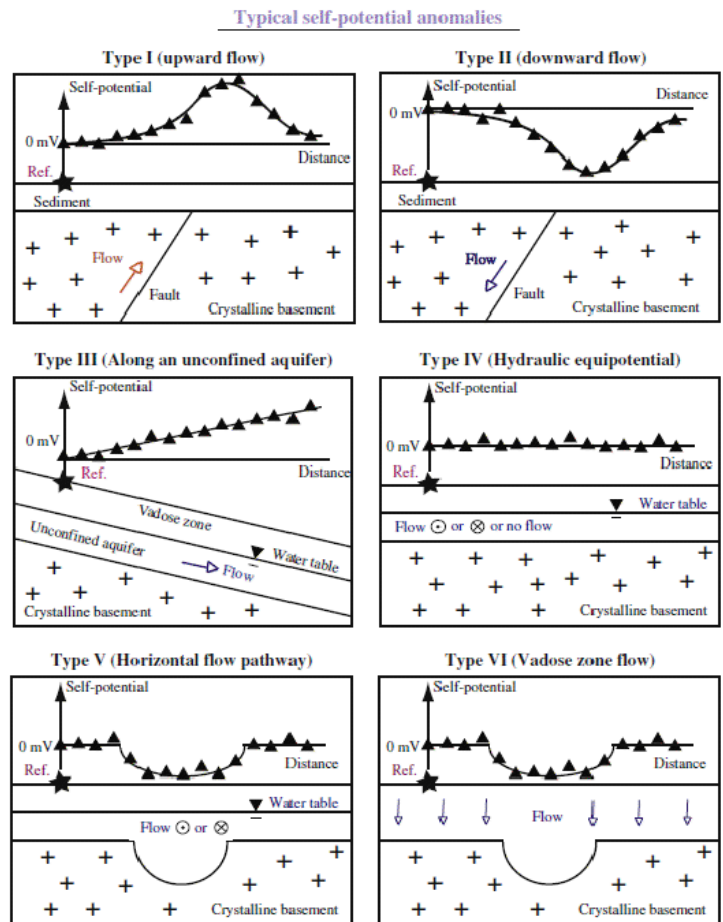


Figure 10. 1: This figure shows the types of anomalies seen with Self-potential data in areas with geothermal activity. [39]

## 10.2 Survey Design

In Pagosa Springs, three longer profiles and a grid of seven shorter profiles, where DC Resistivity surveys were done, were completed using the self-potential method. These profiles include PAGO 01, PAGO 02, Stevens Airport, and the Warm Springs Grid. Both PAGO 01 and PAGO 02 were chosen to help correlate with the DC Resistivity surveys but due to the time constraint out in the field, SP was not completed on the profiles PAGO 04 – 08. All of which did have DC Resistivity surveys completed on. This SP data will also help to correlate with any other methods that were completed on these lines to help with the interpretation of the subsurface in these areas. The line at Stevens Airport was also done to help correlate with the DC Resistivity survey but it was also done in this area to help with the interpretation of the first deep seismic line. However, this line was 1475 meters shorter than the deep seismic line; measurements were not done on the Davis Ranch to the North, and this line was 10 meters to the West of the seismic line. The Warm Springs grid was completed, again to correlate with the DC Resistivity surveys done on all seven profile and to help interpret the movement of water near the small warm spring found on the bank of the river to the West of the grid.



**Figure 10. 2: Google Earth image showing the locations where the SP data was completed.**

All of the SP profiles were completed using a pair of non-polarizing electrodes that do not generate self-potential effects and they are of a lead/lead chloride composition with a porous wood material at the base of the electrode. Along with these electrodes, a high impedance multimeter was used to connect the electrodes together using a long spool of orange cable. This was needed because one electrode is the reference electrode and is buried near the beginning of the survey line and the other electrode is the roaming electrode that you carry along the profile and connect it to the multimeter and the spool of cable.

For the profile PAGO 01 they used 96 electrodes at a spacing of 20 meters which made the profile a length of 1900 meters. This profile started on the bank of the river, near the bend close to the Hot Springs Hotel and ended just after the open field on Ken Levine's property. It also crossed the main

road named Hot Springs Blvd. The second line completed, PAGO 02, used 80 electrodes at a spacing of 20 meters, making it 1580 meters long. PAGO 02 started on the bank of the river (after the bend), crossed Hot Springs Blvd, followed Spring St up the hill, and then followed the small gulley until it ended in the forest at the top of the hill. The profile at Stevens Airport used 183 electrodes with a spacing of 20 meters for a length of 3640 meters. This profile was approximately 10-20 meters to the West of the deep seismic line and went from flag 954 to around flag 1197. At the Warm Springs site we had a grid of seven profiles going from West (next to the river) to East (next to the road, CO 119), orientated relatively North South. Each of the profiles had 64 electrodes at a spacing of 5 meters making the profiles have a length of 315 meters each. There was a spacing of 10 meters between each of the seven profiles within the grid.

### 10.3 Processing

During the processing of the self-potential data, Microsoft Excel 2010 and Surfer 10 (64 – bit) were used to process, correct, and plot the data. For all profiles including PAGO 01, PAGO 02, Stevens Airport, and the seven profiles at the Warm Springs Site the data from these profiles were put into Excel with the format of station number, distance from the first station, and the SP values in millivolts (mV). The corrections used to process this data include a reference correction, a closure correction (or drift), and a correction for the wet versus dry soils at the Warm Springs Site. A reference correction is needed with SP data whenever the reference electrode is moved to a new location when the survey is taking place or when the survey is completed over multiple days. Also to correct for the difference between the reference electrode and the roaming electrode, taken before the survey began. This value is subtracted from all values before a change in the reference electrode location takes place. After this point in the data, three values should be re-measured every time that reference electrode is relocated. The differences at these three locations are calculated and then the average is taken of these differences. Sometimes up to five locations are repeated in the field, but at least three should be repeated for this correction. Afterwards you take this average and subtract it from the values within the section that contained this specific reference location [40].

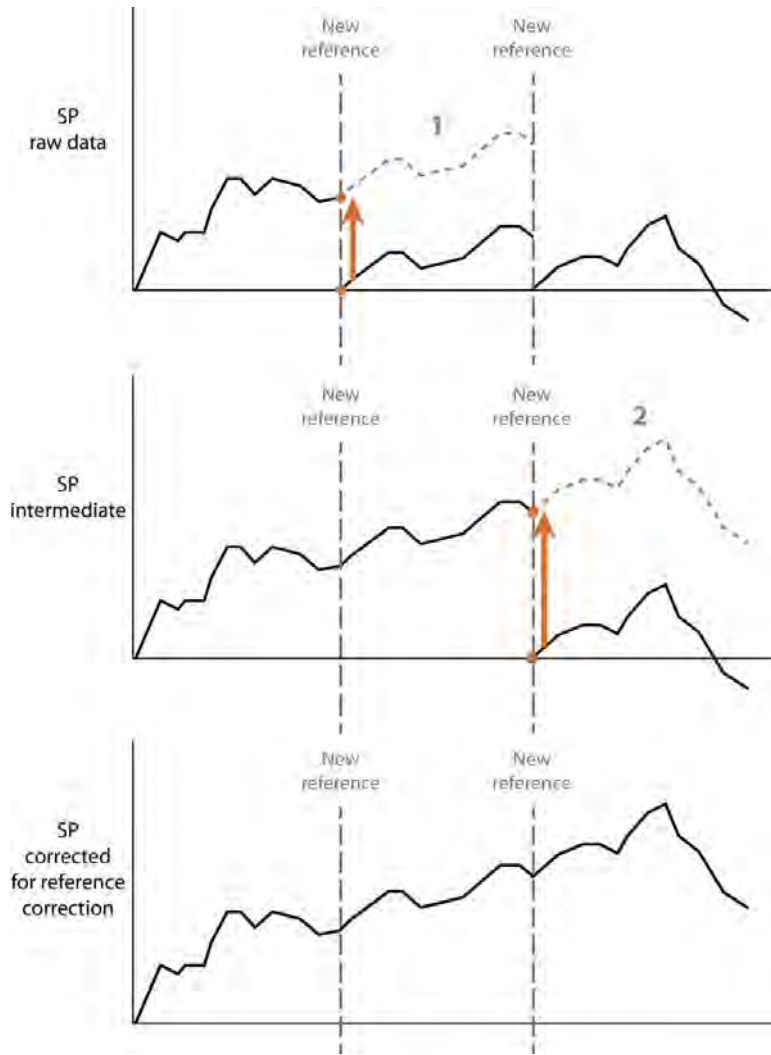


Figure 10. 3 This figure shows the need of the reference correction within SP data. The orange arrows are showing the shift of the data. [5]

The closure or drift correction was applied to the data. It is used to correct for the effect of drifting in the SP values between electrodes. The equation below was used for this correction.

$$SPc = SP_r - \frac{D}{N} * n$$

Equation 10. 1

Where SPc is the corrected SP value after the closure correction is applied, the SP<sub>r</sub> is the corrected SP value after the reference correction is applied, D is the drift of the difference in electrodes, N is the total number of SP values in the profile, and n is the location of the SP value in the profile. The drift is the total amount between the starting and ending differences between the electrodes. Then you just plot the distance in meters along the x-axis and the SPc values in mV along the y-axis [5]. One other correction that we had to apply specifically to the seven profiles at the Warm Springs Site was a



correction for the difference between the wet and dry soil. This was needed because the owner of the farm at this location used this field as a location for drainage of water and the North end of this grid was soaked with water during both the DC Resistivity surveys and the SP surveys. For each of the seven profiles, we labelled which areas were wet and which were dry based on the notes taken by the students during the surveys, these notes correlated well with the high values being the soaked parts and the low values with the dry parts. Where the change from dry to wet or vice versa happened we took the difference in the values and recorded it. Then we calculated the average of those differences for each profile and subtracted that average from every wet value on that particular profile. Afterwards it was plotted in the same way as before, with the distance in meters on the x-axis versus the SPc values in mV on the y-axis.

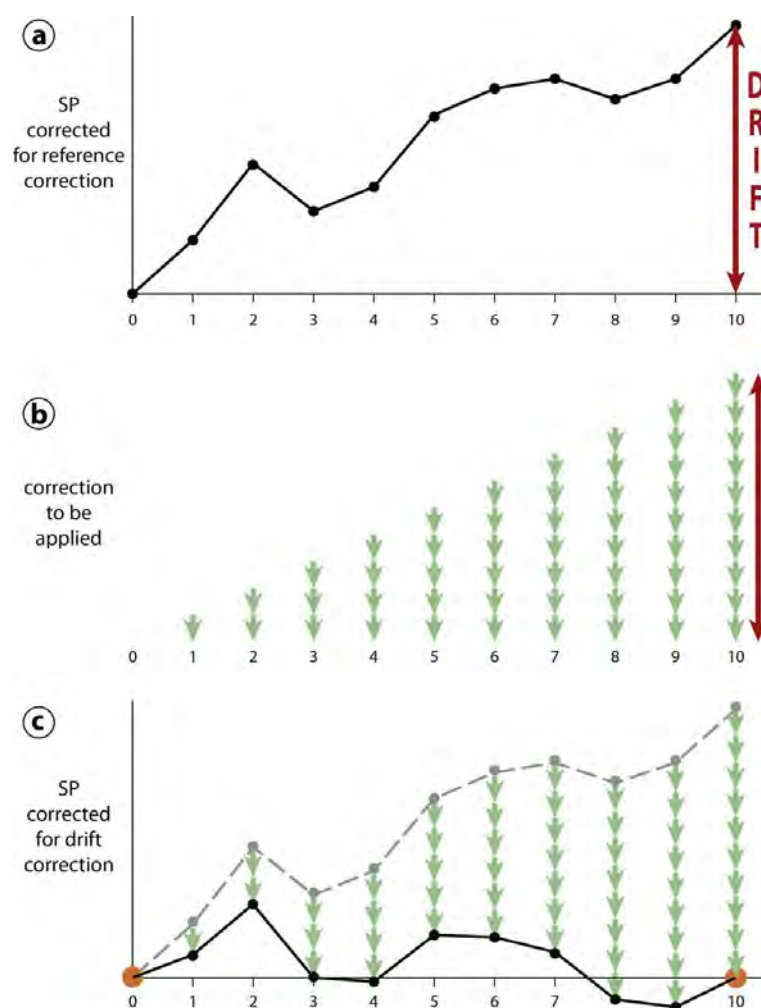


Figure 10. 4 This figure is showing the need for the closure correction within SP data with a closed profile composed of 10 data points. Point 0 and point 10 are geographically in the same place. [40].



## 10.4 Uncertainties/Errors

In self-potential surveys there are certain errors that you could see. These errors include cultural noise or contaminated soil (buried power lines or other cables carrying current), bad coupling or electrode resistance (between the lead/lead chloride electrodes and the ground surface), a large value for the difference in electrodes, a change in reference electrode location, or drift that might not be completely linear (which is our assumption). Site specific errors for this field camp include the DC Resistivity surveys could have been running at the same time due to poor communication between those members and the SP crew. This error could have occurred at all sites during field camp. Another error could have been the large difference in values between the SP values for the wet and dry soil at the Warm Springs Site due to the drainage of water.

## 10.5 Interpretations

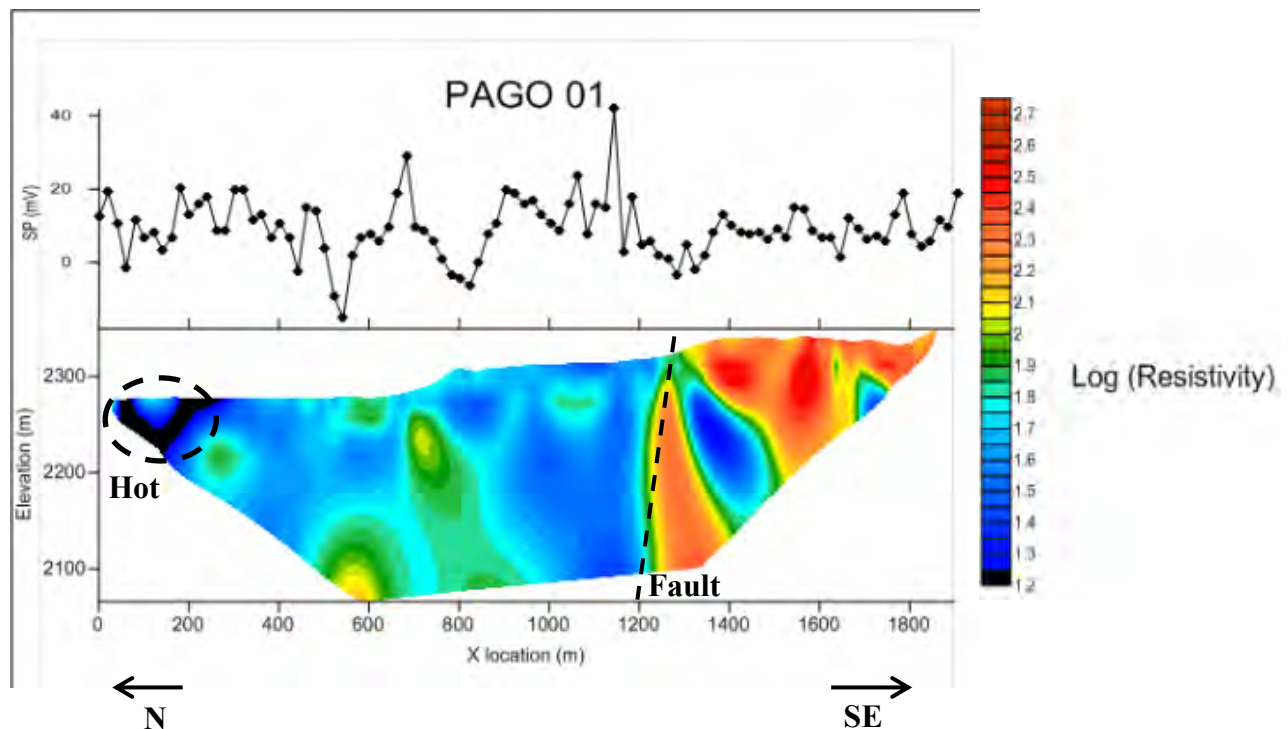


Figure 10. 5: SP plot and DC Resistivity inversion along the profile PAGO 01.

This profile line is nearly 2km in length and runs approximately North-South from the Hot Springs site down to the South. The section is showing very low resistivity values, around  $10 \Omega\text{m}$  at the beginning of the profile, likely due to the presence of hot water. From 200 m to 1200m, resistivity values are typical of expected values for the Mancos Shale. The high resistivity values at the end of the profile and the sharp vertical boundary between low and high values, most likely corresponds to a normal fault bringing the Dakota sandstone closer to the surface. The SP data for this line indicates a lateral flow of water from 0 to 800 meters due to the relatively horizontal trend in the data. The small

positive anomaly from 800 to 1300 meters indicates water flow up along the fault seen in the figure above and also due to the fact that this area could be highly fractured from being near the fault. After this point the data shows another horizontal trend which would indicate no flow of water in this region due solely to the fact that the resistivity values are much higher than on the left and do not indicate saturated Dakota Sandstone.

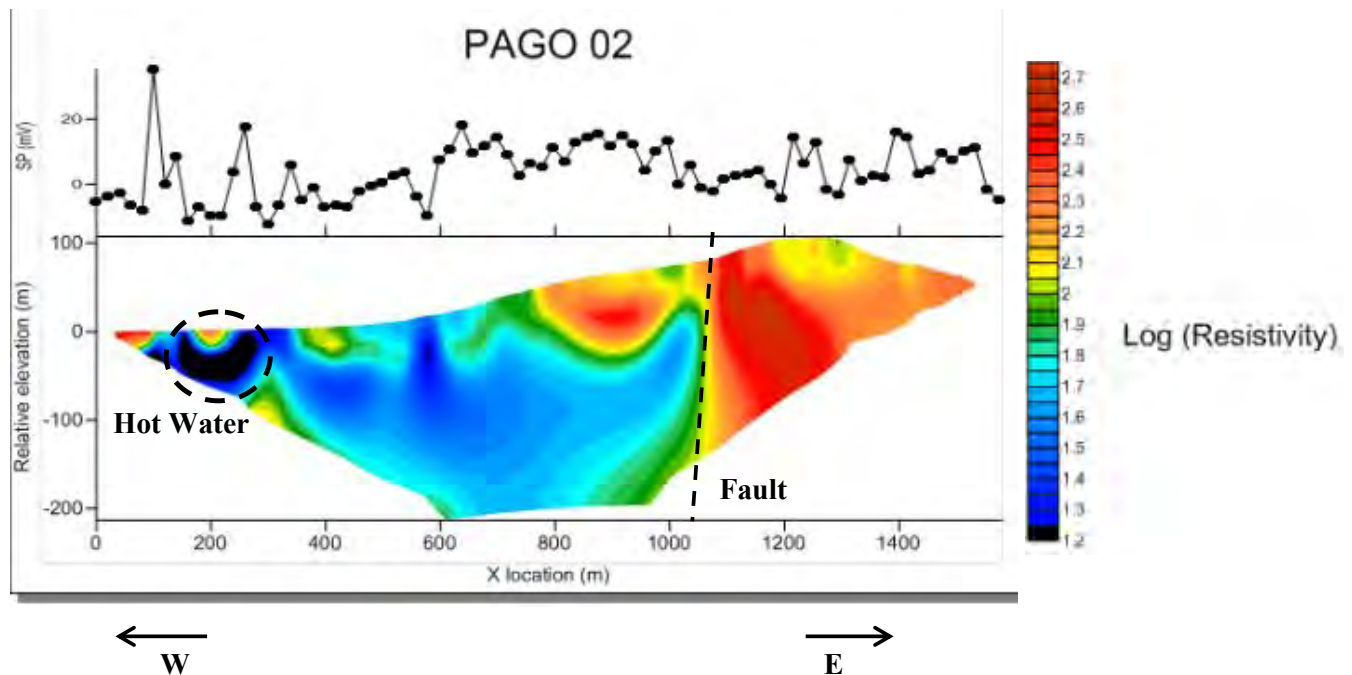


Figure 10. 6: SP plot and DC Resistivity inversion along the profile PAGO 02.

This line is around 1500m long running East-West from the Hot Springs site up the hill to the East. This line is characterized by very low resistivity values, around 10  $\Omega\text{m}$  at the beginning of the profile, most likely due to the presence of hot water again. The small areas of high resistivity values at the beginning of the profile are visible due to the presence of travertine mineralization and concretions. A sharp vertical conductivity contrast is seen at 1050m on the profile. This confirms the interpretation of a normal fault made from the line PAGO 01. The SP data in this profile shows an increasing trend in the data from 0 to 600 meters which indicates a flow of water from the fault location towards the West or the Hot Springs area. From about 600 meters to about 900 meters the small positive anomaly indicates a localized vent of upwelling water just west of the fault location. Later in the profile, the horizontal trend in the data indicates an area where there is no flow because the resistivity values indicate a non-saturated Dakota Sandstone.

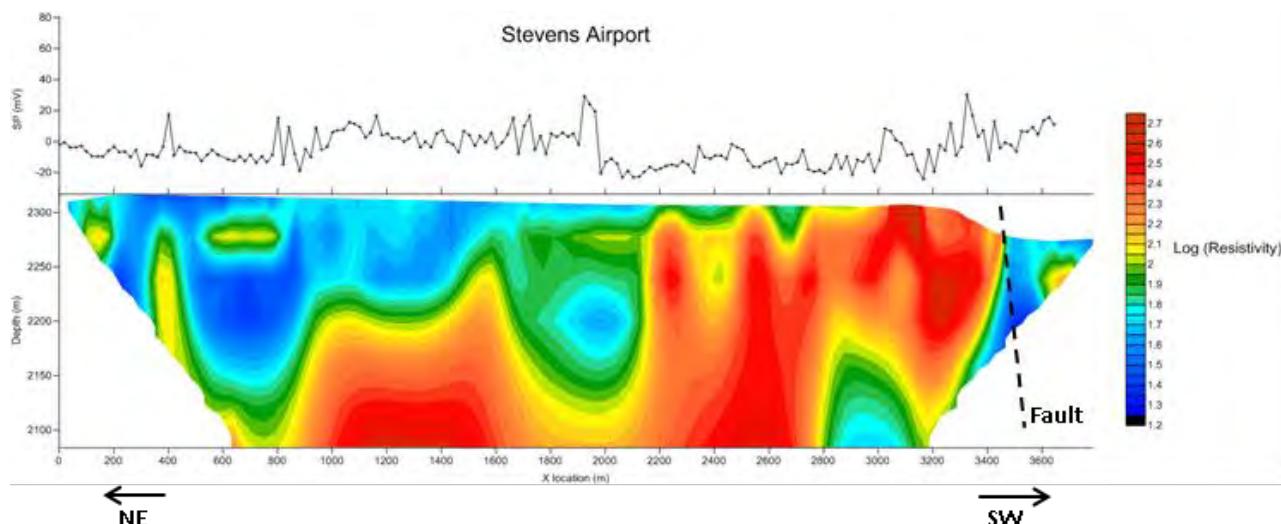
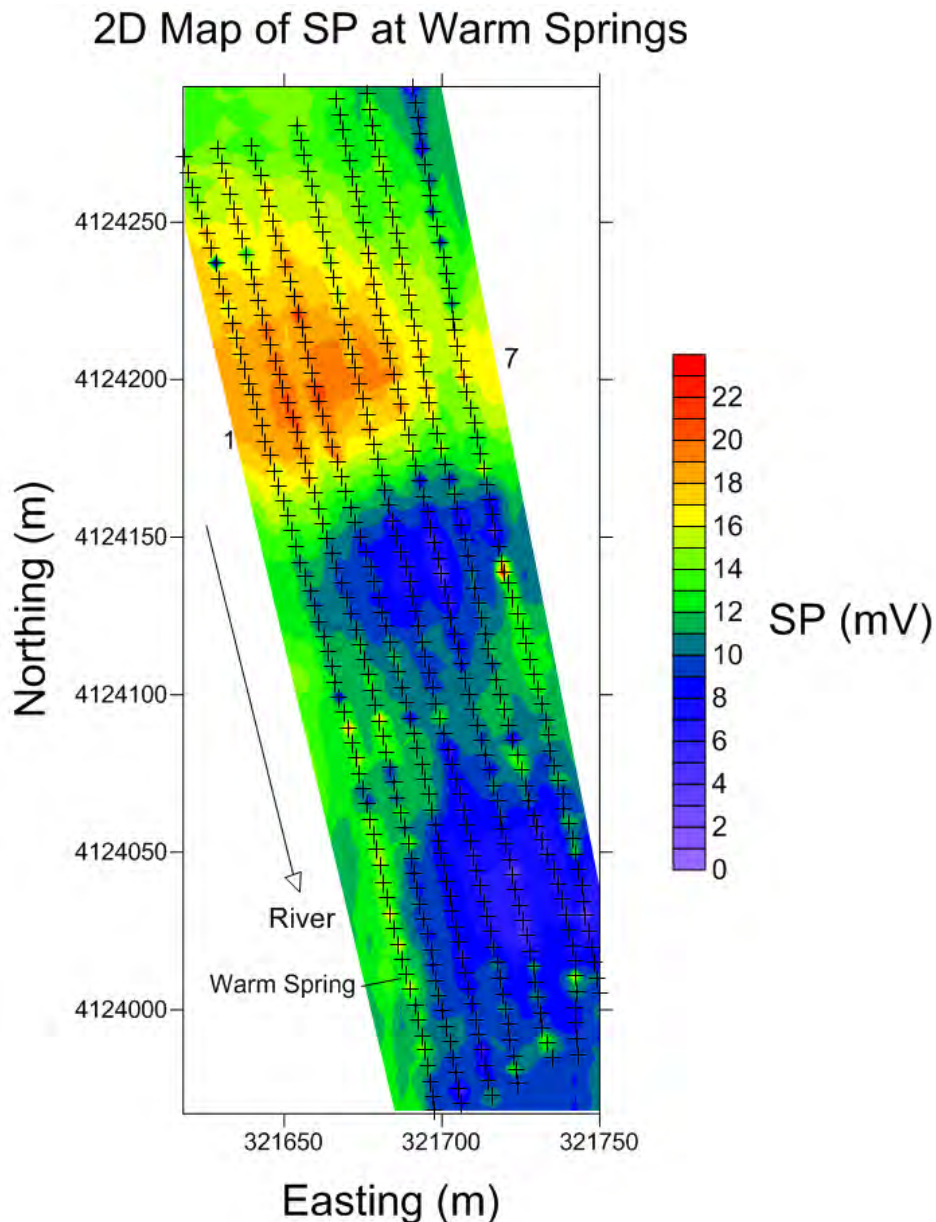


Figure 10. 7: SP plot and DC Resistivity inversion for the profile along the Stevens Airport line.

As you can see in the Stevens Airport line above, the low resistivity values from 0 to 2000 meters are typical of the expected values for the Mancos Shale. The underlying high resistivity layers are most likely Dakota Sandstone. The layers in the subsurface are dipping eight degrees to the Northeast, which is consistent with geological observation and cross-section. At the Southwest end of the profile, you can see a vertical boundary between the high and low resistivity materials which is quite clear. From this sharp change, the normal fault between the airport and the golf course can be seen to some extent with this inversion. The SP data shows certain trends for the water flow in the subsurface at this location. On the left of the profile the SP data has a slight dip down and to the right which indicates a water flow with a slight dip up and to the right in the subsurface. This occurs from approximately 0 meters to about 900 meters within the profile. Afterwards you see broad, low amplitude, positive anomaly from about 900 meters to 2100 meters that might be caused from the Dakota Sandstone being fractured at this location and these fractures allow water to flow through. Then from about 2100 meters on the SP data begins to increase and this might be the start of another larger positive anomaly due to water flowing up the large fault seen on the golf course. More data would have been useful after the fault to see the full wavelength of this feature.



**Figure 10. 8: 2D Kriging Map of the SP data at the Warm Springs Site.**

From this 2D kriging map of the SP data at the Warm Springs site we can see how the water is flowing in this area. The blue areas indicate a low SP value, which is measured in millivolts (mV) and the orange/red areas indicate high SP values. A warm spring is located at station ten along the first line (seen in the figure above), and it is coming out on the bank of the river and then flowing into the river which is just to the left of line one. The lower blue area on this map is showing the flow of the water which is coming from the right of the figure or Northeast and is moving left or Southwest towards the warm spring. There are higher values shown in green over the area where the warm spring is located which may indicate that this water within the layer of Dakota Sandstone is upwelling and therefore creating this spring.



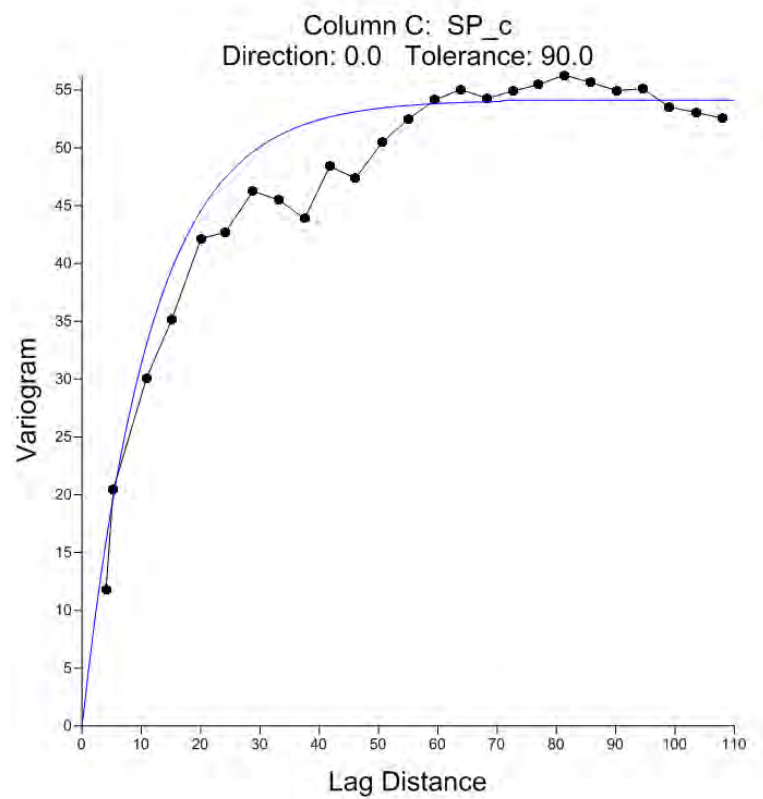


Figure 10. 9: Variogram for the 2D Kriging Map of the SP data at the Warm Springs Site.

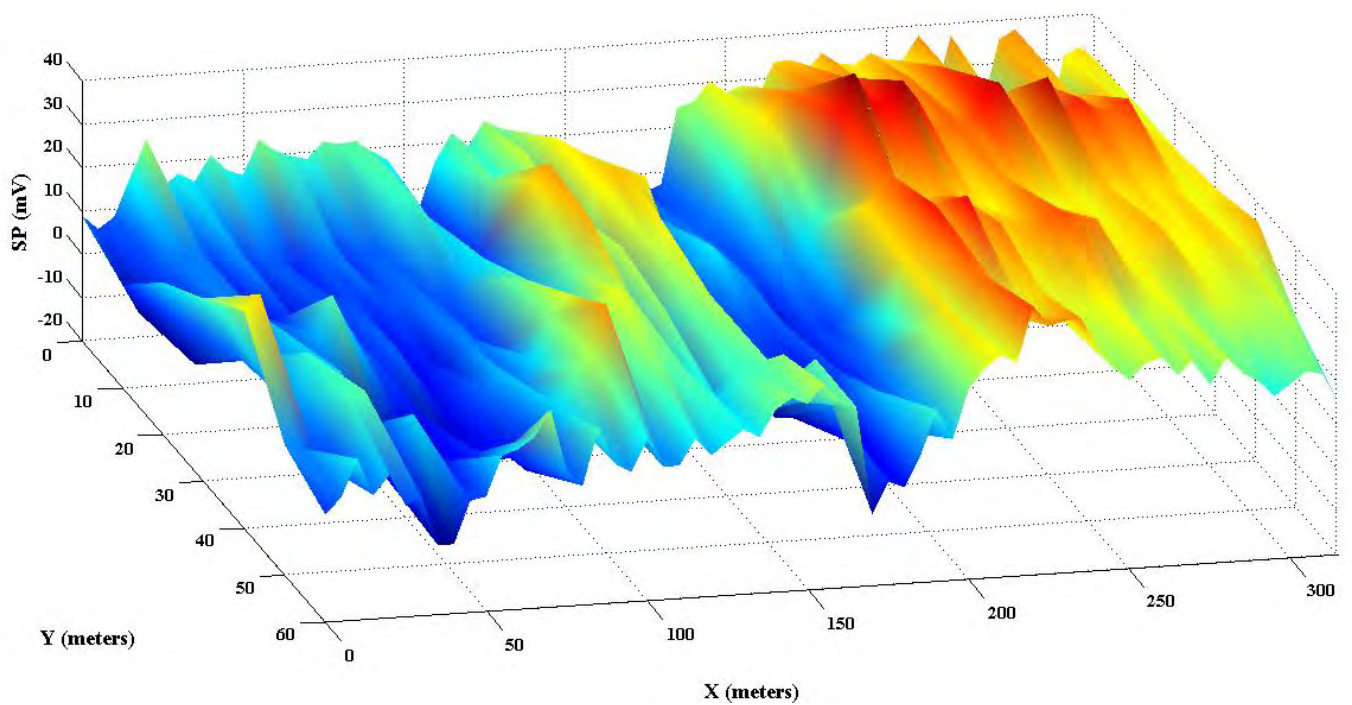


Figure 10. 10: 3D representation of SP data at the Warm Springs Site made in MatLab.



This is a model made in MatLab, which is also showing the SP data but now in 3D, with the location of all the measurements within the grid and the SP values in millivolts (mV). With this figure the blue areas still show lower or negative values and the red areas show the higher values of SP. In this figure, you can also see the flow the water is following in the subsurface. It travels laterally, into the page between the 50 meter mark and the 100 meter mark on the x-axis, and then upwells to the surface near the zero meter mark on the y-axis, which is where the warm spring is located. Therefore it follows the blue area from line seven to line one or the 60 meter mark to the zero meter mark on the y-axis.

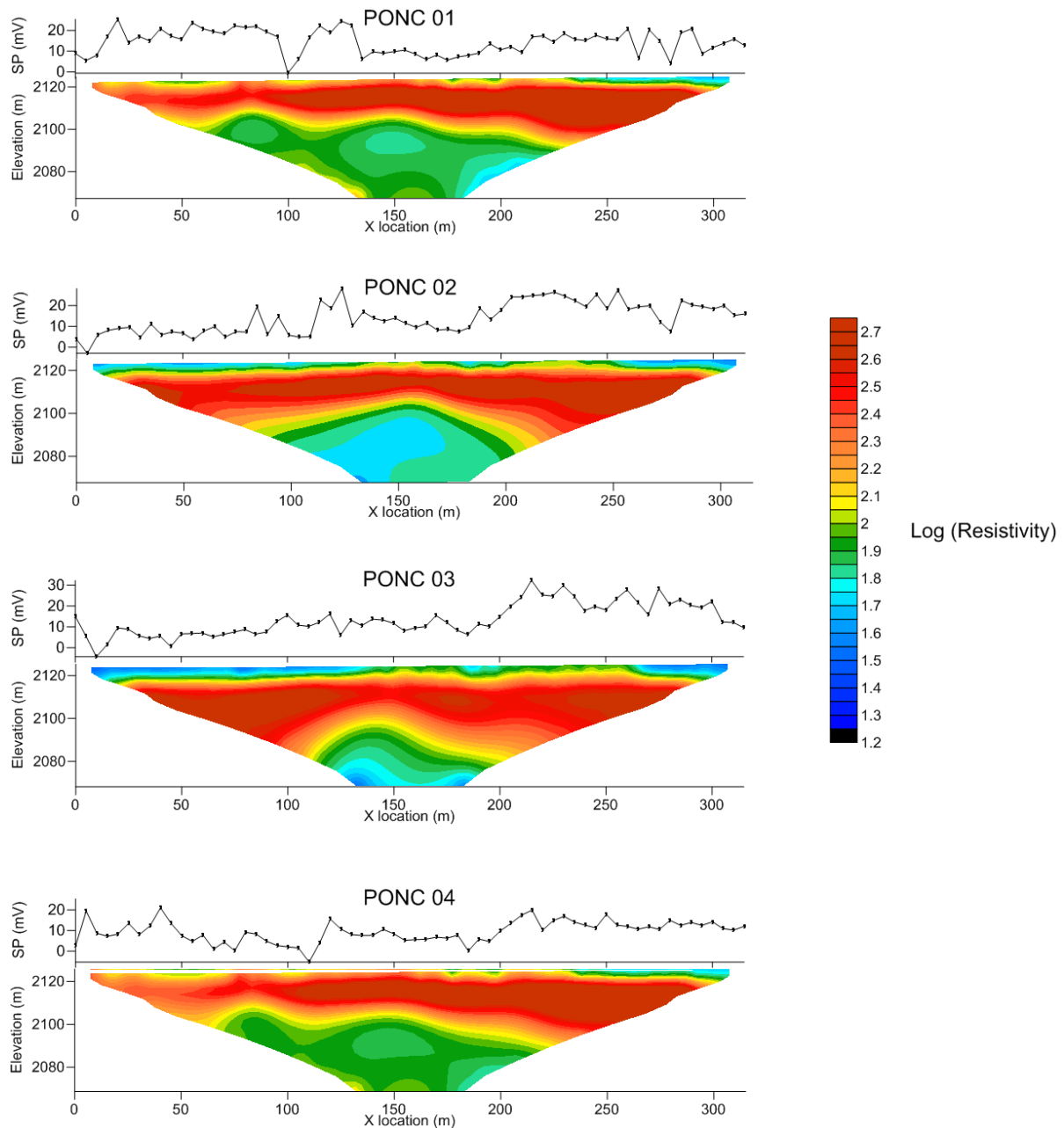
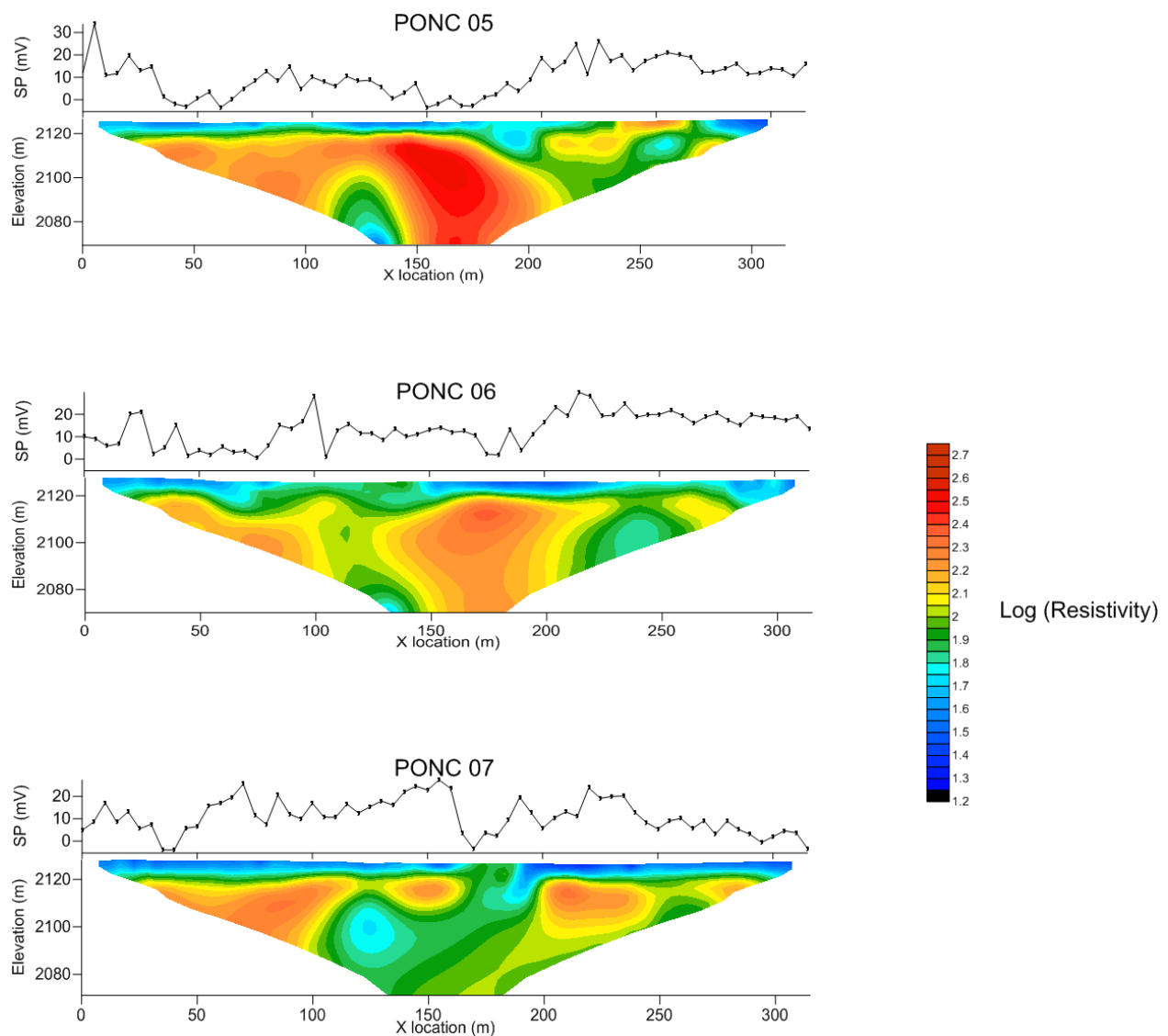


Figure 10. 11: SP plots and DC Resistivity inversions of profiles 1-4 at the Warm Springs Site.



**Figure 10. 12: SP plots and DC Resistivity inversions of profiles 5-7 at the Warm Springs Site.**

For the two figures seen above, the SP data just shows partially from this side view of these seven profiles how the water is moving from profile seven to profile one at approximately 40 to 75 meters along the x-axis.

## 10.6 Conclusions and discussions

The DC Resistivity along with the SP surveys and the results from these surveys in the Pagosa Springs area successfully confirm the Eight Mile Mesa Fault while also finding additional faults near the Mother Hot Springs. On one hand, in the Stevens Airport area, the line where both DC Resistivity and SP were completed is supporting the seismic results by confirming their fault description.

On the other hand, the various resistivity surveys around the mother source (which is our target) enable us to locate an additional normal fault and to confirm its play in the geothermal system of the

area. Indeed, this fault is likely to be deep enough to make the hot water flowing from the Precambrian basement to the base of a hole in the Mother Spring case or to the permeable Dakota Sandstone in the Warm Spring case, shown in Figure 9.33.

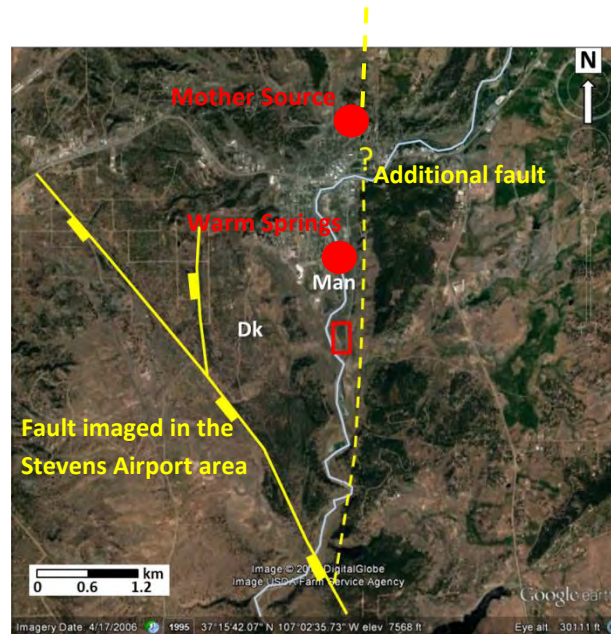


**Figure 10. 13: Fault map for the Pagosa Springs area.**

In order to confirm this preliminary interpretation, additional resistivity lines should be considered on the Northern side and the Eastern side of the main Hot Springs area. Also more Self-Potential surveys should be considered on all of the lines that the DC Resistivity surveys were completed at to get a better idea of the regional water flow especially in the main Hot Springs area and then completed at the surveys that are proposed above for more DC Resistivity surveys. This would enable us to draw a more precise description of the fault found here and how it can be linked to the other ones in the area. Some other types of surveys such as gravity, magnetics, or electromagnetics would also bring further details concerning how this fault plays in the geothermal system in Pagosa Springs.

# 11. Ground Penetrating Radar

## 11.1 Introduction

Ground penetrating radar (GPR) is a non-invasive geophysical method that uses the propagation of electromagnetic (EM) waves to image the subsurface. [GPR surveys can be executed by aircraft or satellite, within a borehole, or with vehicle or by hand on land.] In this report, the GPR was pulled along the ground, with a transmitting antenna emitting a short, high frequency EM pulse into the ground every 0.05 m. The EM wave is reflected, diffracted, and refracted when there is a contrast in the dielectric permittivity within the subsurface. The receiver continuously records the reflected waves at the ground surface. Preliminary data is shown on the display as a wiggle plot. This process is modelled in Figure 11.1. Images created from GPR data resemble those created from seismic data. All seismic processing techniques can be applied directly, or with relatively little modification, to GPR data. The major differences between seismic imaging and GPR imaging are the depth of investigation and resolution.

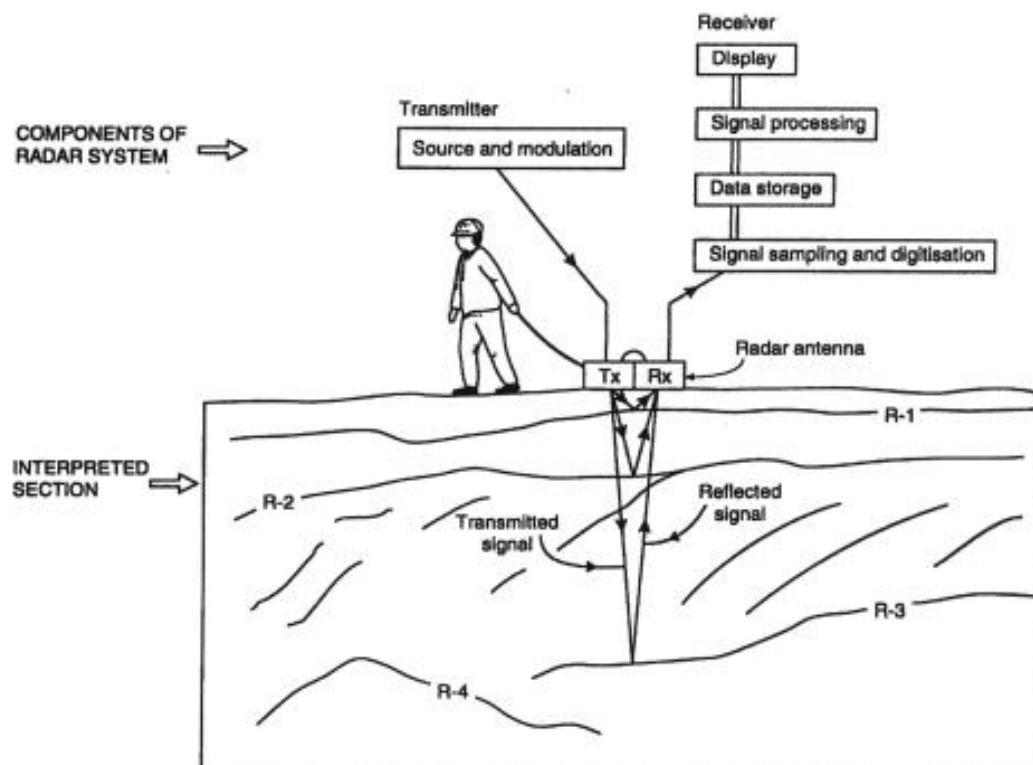


Figure 11. 1 A schematic diagram of a radar acquisition comprising of the radar components and the analogue interpretation of a radar time section.

GPR is mostly used to analyse the shallow subsurface. The depth of investigation (DOI) varies from less than a meter to 5400 m depending on the electrical properties of the targeted medium and the equipment parameters. DOI is largely dependent on subsurface electrical conductivity. In conductive mediums, electromagnetic energy dissipates into heat, causing a loss of signal and therefore a shallower DOI. EM wave frequency has a significant effect on DOI as well. High frequency EM waves attenuate faster than low frequency EM waves, again decreasing DOI. Although DOI is reduced, the resolution of the data is increased due to a smaller wavelength. GPR has the highest resolution of all geophysical methods, generally on the order of centimeters. After migration of the data has been completed applied, the resolution is about one fourth of the wavelength.

## 11.2 Survey design

GPR surveys were completed along the Stevens Airport line, Barn 3 line, and a subsection of the Zen Garden grid. All areas at which GPR was completed can be seen in Figure 11.2. Individual sites can be seen in better detail in Figures 11.3 – 11.5.



Figure 11.2 Sites at which GPR was completed



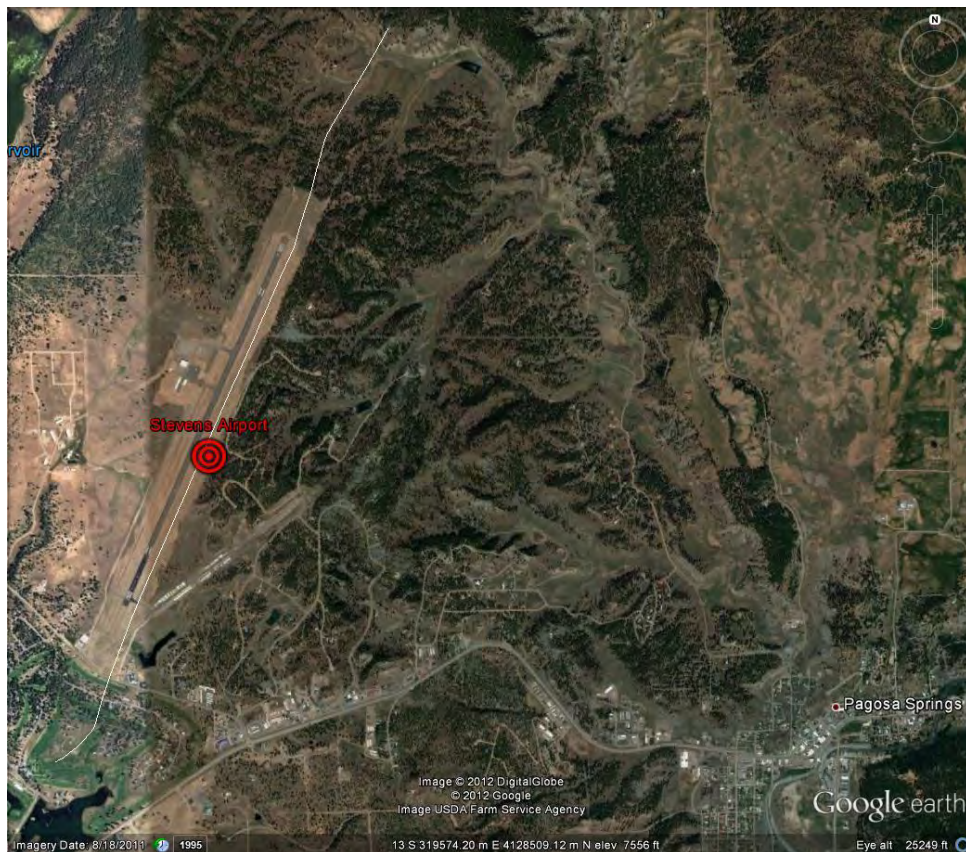


Figure 11. 3 Stevens Airport survey line

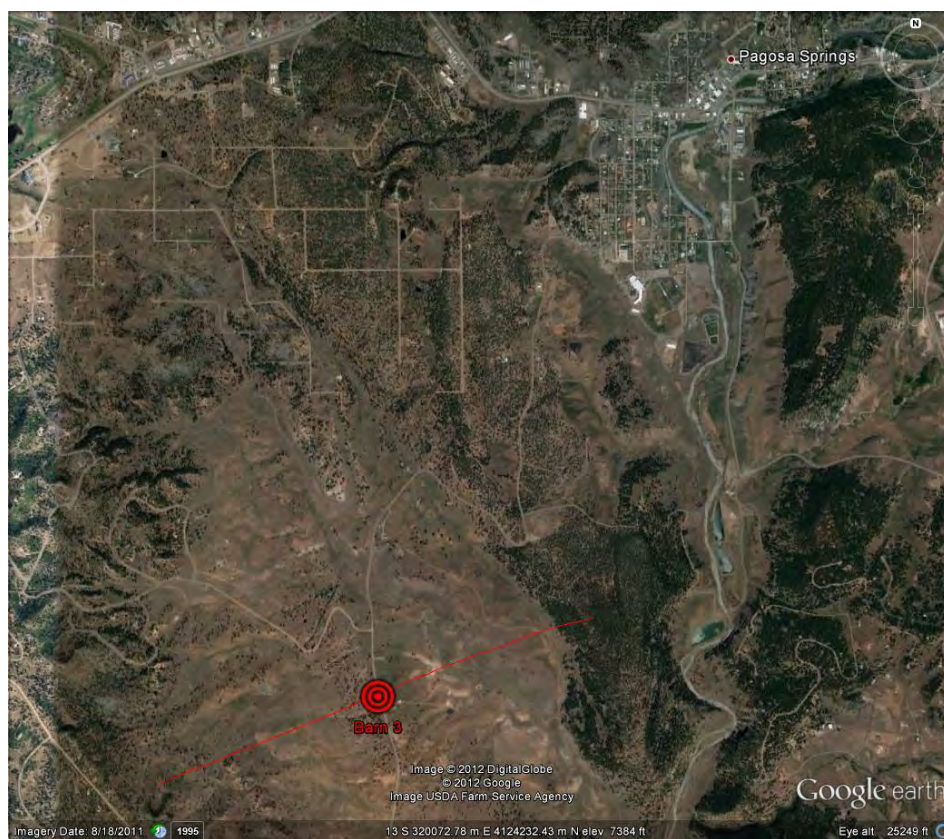


Figure 11. 4 Barn 3 survey line





**Figure 11. 5 GPR subsection of Zen Garden survey grid**

GPR surveys were primarily conducted in three locations: The Zen Garden, Barn 3, and Stevens Airport. In some locations multiple GPR surveys were conducted. The two survey types that were implemented were the common offset survey (the standard method of acquiring GPR profiles), and the common midpoint (CMP) survey (to measure GPR propagation velocity). In all common offset surveys, the GPR was mounted in a sled that fixed the transmitter-receiver offset at 23 cm. Along-line distances were monitored using the built-in odometer wheel. Acquisition speed is a slow walking pace, and raw data is shown on a console that allows the survey team to monitor data recording.

At Stevens Airport and Barn 3 sites, the GPR was used as a reconnaissance tool in support of the deep seismic acquisitions to identify hazards. One of such hazards would be buried gas lines along the seismic line which may rupture due to the weight and vibration of the vibroseis trucks. GPR may also be used to examine consistency in the seismic shots, given shallow variations in subsurface structure. At Stevens Airport (Figure 11.3), GPR was acquired along most of the deep seismic line (except where access was restricted), providing a profile 3275 m in length, sampled every 5 cm. The equivalent survey was performed at Barn 3 (Figure 11.4), and the total profile length at this site was 3300 m.

The common offset surveys conducted in the Zen Garden (Figure 11.5) were conducted in a grid of dimension 86.5 by 30 m. The grid comprised 173 lines, separated by half of a meter, and each 30 m long. Each line was sampled every 5 cm, providing roughly 600 traces per line (there is some variation due to changing topography),

The common midpoint surveys were different with respect to the scale in which they were used, and their purpose. In the case of the Pagosa Springs surveys, the CMP survey was used in order to determine the velocity of the different subsurface units. The determination of velocity from CMP will further be discussed in section 11.4. Rather than using a traditional common midpoint survey, the team incorporated a common-source gather survey. For this, the transmitter unit and the receiver unit were removed from their constant separation sled so that they may be able to move independently. The transmitter was then placed at a fixed location along a measuring tape. The receiver was then placed 7cm away from the transmitter. This equates to a 30cm initial offset as the centers of the transmitters and receivers are separated by 23 cm when their housings are touching. The receiver was then slowly, and at a constant pace, offset from the transmitter with distances monitored by the odometer wheel. These common-source gathers were conducted on different materials in order to find their GPR velocity; specifically, for Dakota Sandstone, the Travertine unit, and the Mancos Shale. The Dakota Sandstone common-source gather survey was conducted on an outcrop of the unit near the Barn 3 line. The CMP section of the Dakota Sandstone is illustrated in figures 11.4.2 and 11.4.3. The Travertine common-source gather survey was conducted on top of the travertine deposit in the Zen Garden location. The Mancos Shale survey was also conducted at the Zen Garden site, but on top of a portion of the Mancos Shale unit. See Figure 11.6 for location of travertine and Mancos Shale CMP gathers.



Figure 11. 6 Central rectangle outlines the GPR grid in reference to the entire Zen Garden.

### 11.3 Processing

The processing of the GPR data was done using the Sandmeier Software Reflexw processing program. Initially all of the data was subject to the same pre-processing routine regardless of its survey type. This routine consisted of: 1. Dewow, 2. Band Pass Frequency Filtering, and 3. Move Start time.

A dewow filter is applied to remove the low-frequency ( $< 5$  MHz) cross-talk between closely-spaced transmitter and receiver antennas: this cross-talk is termed 'wow'. Without applying the dewow filter the data would appear to be shifted from their zero-axis and bowed. The dewow filter is a form of a high-pass filter, which allows for high frequencies to pass and attenuates low frequency signals. The cut-off for the filter is dependent on the frequency of the antennas. When providing a value for the dewow filter it was given in terms of time corresponding to a period. The antennas were of 500 MHz, which corresponds to a period of 2 nanoseconds. This can be shown through:  $T = \frac{1}{f}$ . Knowing that a greater period corresponds to a lower frequency, the processing team decided that a period of 5 nanoseconds or greater would correspond to the low-frequency noise associated with the cross-talk between the transmitter and receiver. After applying the dewow filter, it then gave the processing

team the ability to do further corrections in the frequency domain and for those corrections to have the desired effect.

The band-pass filter operates on the frequencies determined to be outside of the useful signal bandwidth. The purpose of the band-pass filter is to reduce low and high frequency noise. In order for the filter to be applied, it must first define a range of frequencies which are allowed. This range of frequencies is referred to as the passband. The passband is defined as the region between the lower plateau and upper plateau. Within this region the frequency has zero attenuation and is allowed to be fully expressed in the data. The rest of the filter is defined by the lower cut-off and the upper cut-off. The lower cut-off is a frequency that is below the lower plateau and the upper cut-off is a frequency which is above the upper plateau. Frequencies outside of the range of the lower and upper cut-off are completely attenuated and not expressed. Frequencies that fall within the area between the lower cut-off and the lower plateau are partially attenuated. The amount at which the frequencies are attenuated depends upon where the frequency falls on the ramp. This is dependent on the slope of the ramp which is the produced from the linear line connecting the lower cut-off and the lower plateau points. The same can be said for the area between the upper plateau and the upper cut-off. As a general rule of thumb the upper cut-off should be twice the value of the upper plateau, which should be twice the value of the lower plateau, which should be twice the value of the lower cut-off. Frequencies may exceed the doubling pattern but should not be less than. See Figure 11.7 for diagrammatic explanation of band-pass filter.

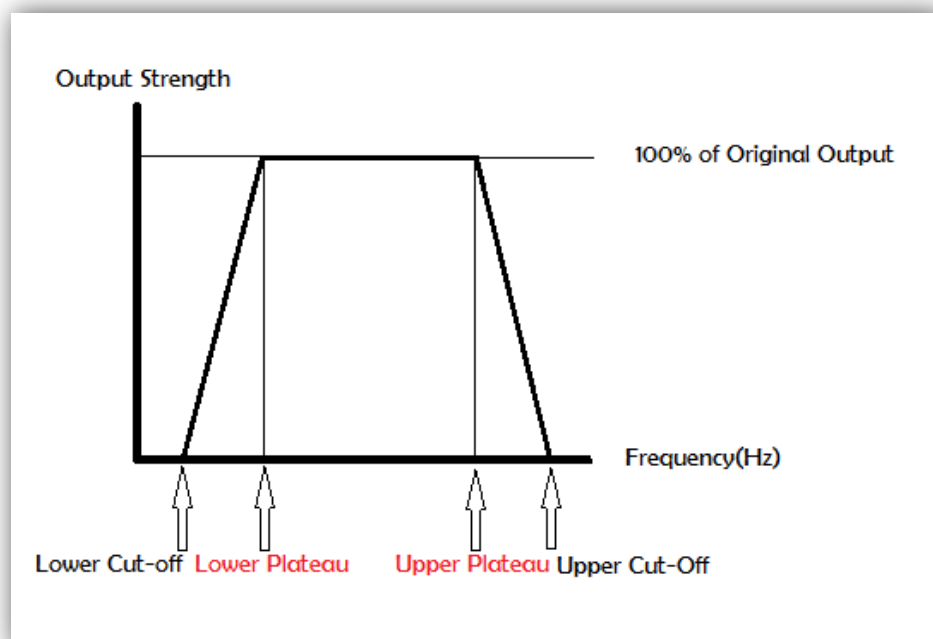


Figure 11. 7



The Start time has to be shifted to remove excess time at the start of each trace. Initially in the data acquisition the start time of the transmitted wavelet was delayed for each trace to be after the data began recording. The transmitted wavelet was delayed so that the entire waveform was able to be seen. This helps so that the entirety of the subsurface is able to be imaged. However once the processing begins it is not necessary to have extra time before the trace was transmitted. In order to get the correct time sequence the section had to be viewed in its wavelet form. From this wavelet it was then possible to identify a time for which the first break occurred. With the time known of the first break, the time the wave is in air going from transmitter to receiver must then be subtracted. Since GPR waves are actually electromagnetic waves moving at the speed of light, their velocity in air is known to be 0.3 m/ns. As was discussed in section 11.3, the separation of the antennas at a constant offset is 0.23 m. converting that separation distance to time, it is known that it takes roughly .767 ns for the wave to travel from transmitter to receiver in air. The whole set is then statically corrected in time by the value of the equation: *Static Time = First Break – Traveltime in Air*. The static time value is subtracted from the sections to remove the excess time at the start.

In order for the sections to be migrated a velocity for each rock unit must be obtained. For this reason, all of the CMP's were conducted on outcrops of the different rock units so that the processing group may perform a velocity analysis. Prior to any velocity analysis, the sections must have undergone the pre-processing routine described above. The velocity analysis performed on the sections is based on semblance. Semblance aims to pick out coherent signal amongst the noise. The semblance velocity analysis allowed for the processing team to pick out an interval velocity. The CMP gather from the Dakota Sandstone had the most coherent signal and it was easy to determine an interval velocity from it. An image of the raw CMP gather may be seen in Figure 11.9 for the Dakota Sandstone. Figure 11.8 displays the same section after it has undergone the pre-processing. The semblance velocity analysis was completed for the travertine deposit and the shale at the Zen Garden site as well. From the CMP the processing team was able to determine an interval velocity. In the shale unit an interval velocity was not able to be determined. A coherent signal was not able to be identified in the shale due to its composition. The shale is composed of a significant amount of clay. Clay is highly conductive and quickly attenuates the radar signal penetrating it. In data acquisition this equated to a significantly shallower depth of investigation than the travertine layer. In figure 2 of Appendix H this difference in depth of investigation can clearly be seen. At roughly meter 22 the section transitions from the travertine on the east to the shale layer on the west.

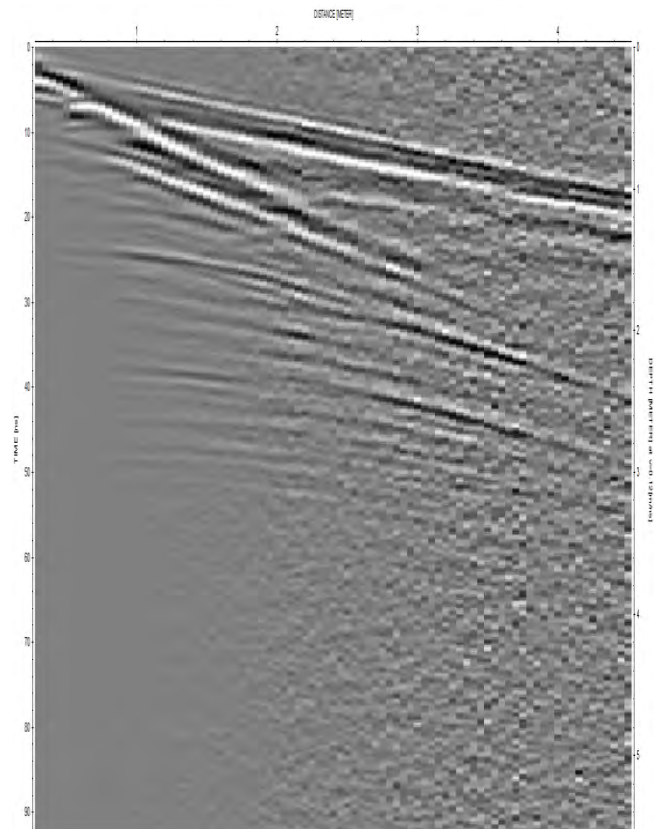


Figure 11. 8

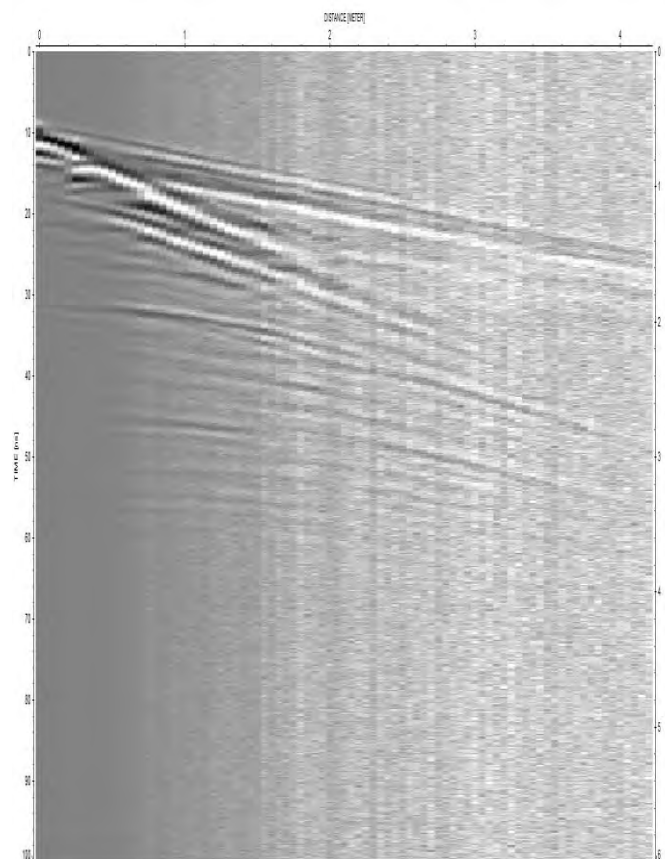


Figure 11. 9

Once the pre-processing was completed and the interval velocity was known, the processing team began processing the common offset survey data. In order to properly view the section gain must typically be added. In this instance, after multiple trials, the processing team determined that an energy decay gain correction was the best type of gain correction to use. The amplitude of the wavelet is greatest at the shallowest depths. As time progresses, and accordingly as depth increases, the amplitude of the wavelet will decrease. The purpose of applying gain is to try and balance the amplitude of the wavelets. This is done to amplify reflections deeper in the subsurface and tone down reflections from the shallow subsurface.

After the energy decay gain correction has been applied to the pre-processed data, the section is then able to be migrated using the interval velocities that were found. The purpose of migration is to shift reflection events to their correct location and dimensions. For this migration, the Kirchhoff migration algorithm was incorporated. The Kirchhoff algorithm states that the data can be produced from point reflections. The final reflected image is the sum of all of the points. Before the migration may begin, the processing team must examine the diffraction hyperbolas. From the diffraction, the widths of the hyperbolas must be found in order to perform the migration. With the widths of the diffraction hyperbolas and an interval velocity, the migration may then be performed. In the case of the Zen Garden the velocity of the travertine was used for the migration, because the travertine structure would be the structure which would feel the effects of the migration. The shale zone, since it quickly attenuated the signal. In the Airport line and the Barn 3 line the velocity of the Dakota Sandstone was used, because once again, the Dakota unit is where the migration would have its effect.

Once all of the processing and migration has occurred the processing group proceeded to apply static corrections to all of the lines and grid areas. Up until the static correction is applied, the sections have been viewed as if they were along a flat surface. Realistically the sections were far from flat and a bit of topographic variation. With the help of a young woman with a GPS unit strapped to her back, the GPS team was able to produce elevations for each GPR survey site. With the elevations of the survey sites known, each site had its elevations made relative to its respective highest point. The highest point was designated an elevation of 0.0 m and the rest of the points were given elevations corresponding to their difference from the elevation of the site maximum. In order for the static correction to be applied the elevations must be converted into traveltimes of the wavelets. When converting to traveltimes the processing team had to take into account the two way traveltimes. With this in mind, the traveltimes were calculated incorporating the equation,  $t = \frac{-2d}{v}$ . Where  $d$  is the elevation relative to the maximum point at the site and  $v$  is the velocity of the rock unit that the correction is being applied to. In this case, the correction was being applied using the same velocity as was in the migration. Figure 2 of appendix H displays a section in the Zen Garden which has been

migrated, completely processed, and has had static corrections applied to it. This figure also corresponds to a complete and final line in the survey grid.

## **11.4 Uncertainties/Errors**

During acquisition, if the transmitter or receiver units are not directly touching the ground surface, a large amount of the EM energy will be transmitted into the air instead of the ground. There is always a small amount of energy transmitted into the air, even if the transmitter and receiver remain on the ground surface. This energy appears in the raw data as airwaves and tends to cloud the subsurface information. Along the Barn 3 survey line, there were several obstacles such as piles of timber that blocked access to the ground. These areas were omitted from the GPR survey line.

Parameters for initial processing are chosen visually by estimating the areas of most importance in the data. Useful sections of data have the possibility to be muted if these parameters are chosen incorrectly. Velocity picking on the common shot gathers (CMPs) is one of the largest sources of error in GPR subsurface images. Since multiples appear as clearly in the semblance plot as reflections, it becomes increasingly difficult to pick the correct peaks on the semblance plot. Also, the last layer of the velocity model will always be the least accurate since there is no layer beyond that one for the program to compare velocities to. Picking velocities by matching widths of hyperbolas in the raw data is also a potential source of error. It is extremely difficult to get a perfect representation of the velocity with this technique therefore it is used as a preliminary value to complete initial processing.

## **11.5 Interpretations**

### **11.5.1 Airport Line and Barn 3 Line**

The main purpose of the GPR acquisition in these lines was to identify hazards as these lines corresponds to the seismic acquisition site. Vibroseis or Thump trucks transmit powerful signals into the ground. This may mean that any near surface objects lying beneath the vibroseis could be damaged. For safety reasons, GPR surveys were conducted.

Identification of hazards such as gas pipe, sewage pipes, drainage lines and power line using GPR method are therefore useful. However, based on the results, it failed to identify these features and thus did not produce any risk hazards for the seismic acquisition. This may mean that the features are deep beneath the ground such that the structures are beyond the depth of GPR penetration.

On the other hand, the transition between geological features such as between the Dakota Sandstone and Mancos shale can be seen clearly. This is primarily because of the contrast in electrical

conductivity between the Dakota sandstone and the Mancos shale; Mancos shale being more conductive than the Dakota sandstone.

As an example, Figure 11.10a illustrates a radar section that was obtained from the Barn 3 line. It shows the varying contrasts between the recorded radar signals. Three main reflectors were identified and interpreted as shown in Figure 11.10b. The coherent reflectors with irregular surface as seen in figure 1a are interpreted as the fractured Dakota sandstone. The reason for the irregularity in the reflectors is due to the presence of void spaces that allows radar waves to pass through. From the radar section, the thickness of the fractured Dakota sandstone was found to be in the magnitude of ca. 1m.

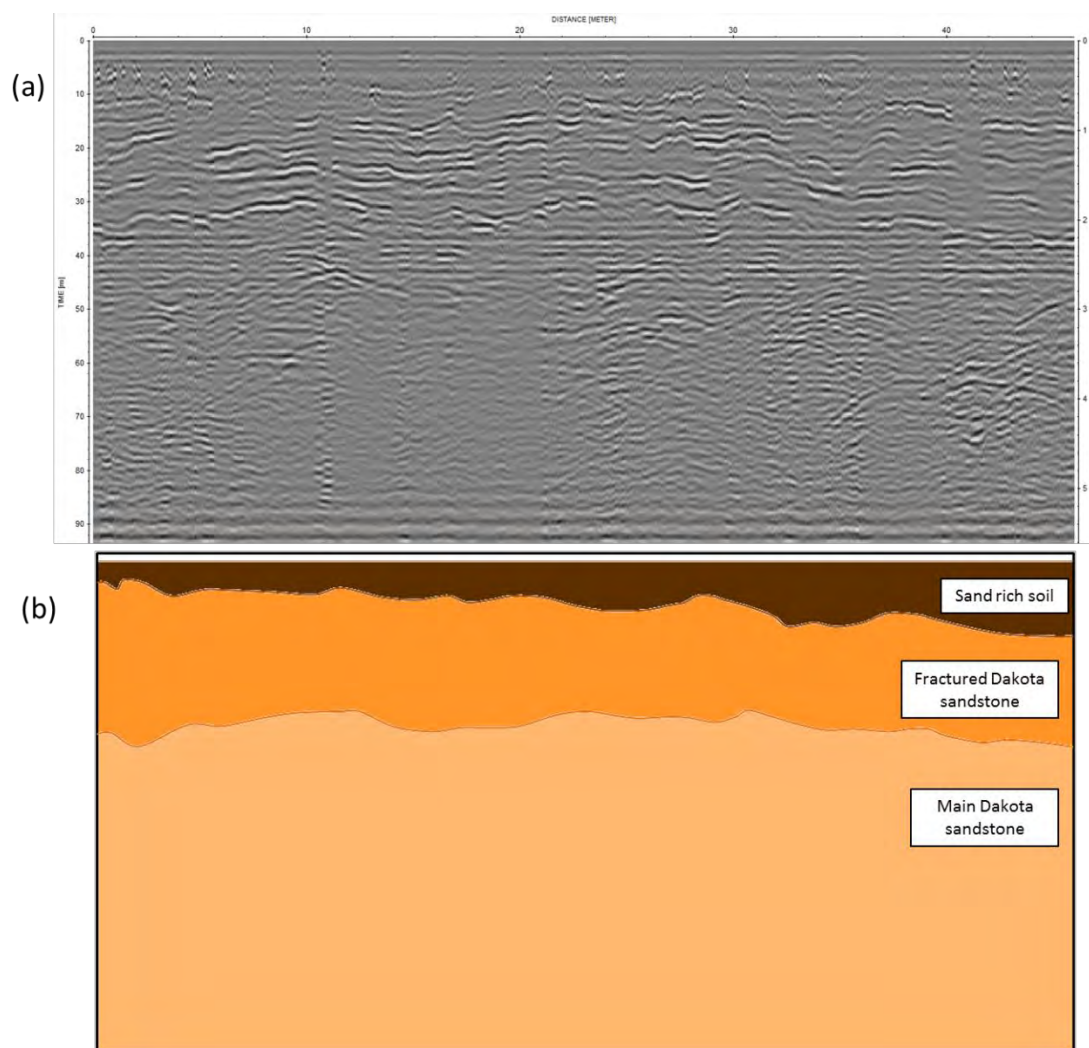


Figure 11. 10 (a) A radar section obtained from Barn 3 line (a) with its interpreted section (b).



### 11.5.2 Zen Garden

This site is located near to the pagosa springs. Its main objective is to map the travertine deposit as it has a direct relationship to the geothermally active aquifer. It serves to pin point the distribution of this deposit. Figure 11.11 illustrates the radar section that was obtained from this site. In Figure 11.11a, it was found that the low, attenuated signal corresponds to the Mancos shale as interpreted in the Figure 11.11b. The Mancos shale has a high electrical conductivity which effectively attenuates the radar signal. With the Travertine deposit, its electrical conductivity is lower than that of the Mancos shale making it to produce prominent coherent signals that can be picked easily. Within the Travertine deposit, minor structures are present. This is marked by relative pinch outs and high reflective surface within the radar section. This is interpreted as its episodic behaviour during its formation.

Figure 11.12 illustrates the depth slices across the travertine deposit. The extent of the travertine deposit is marked by the region of strong GPR reflectivity. The amplitude of the travertine layer diminishes at depth greater than 3m. At 500 MHz of transmission frequency, the effective depth of penetration is 2m-3m. At this depth is where the majority of the energy comes from. This is the effect of the radar wave getting attenuated at deeper depth. Large travertine structures were also found with thicknesses of more than 5m. Fracture features observed in the field was also found in the radar section. It progresses deep beneath the ground as illustrated in figure 11.11b.

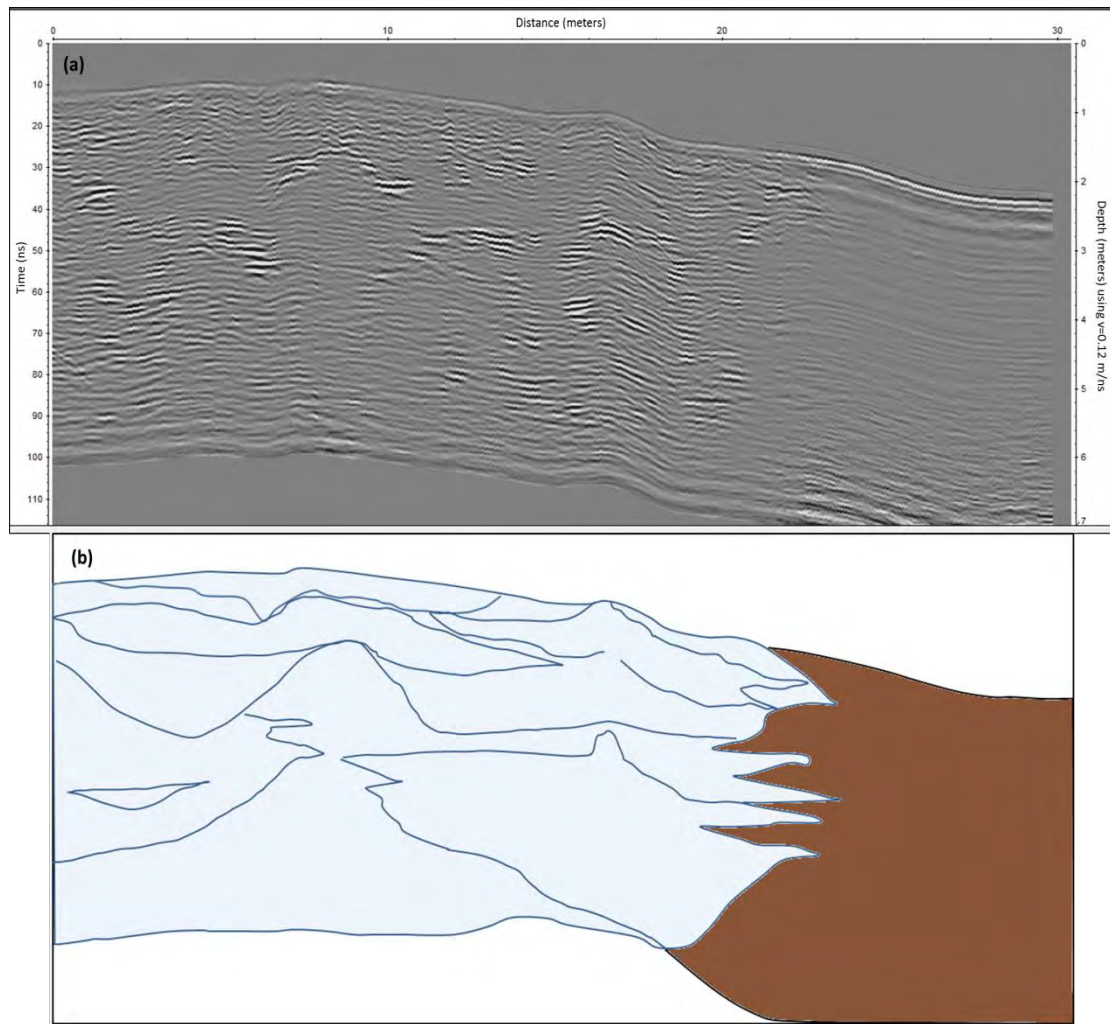


Figure 11.11 A migrated radar cross section with topographical correction obtained from the Zen Garden (a) with its interpreted section (b).

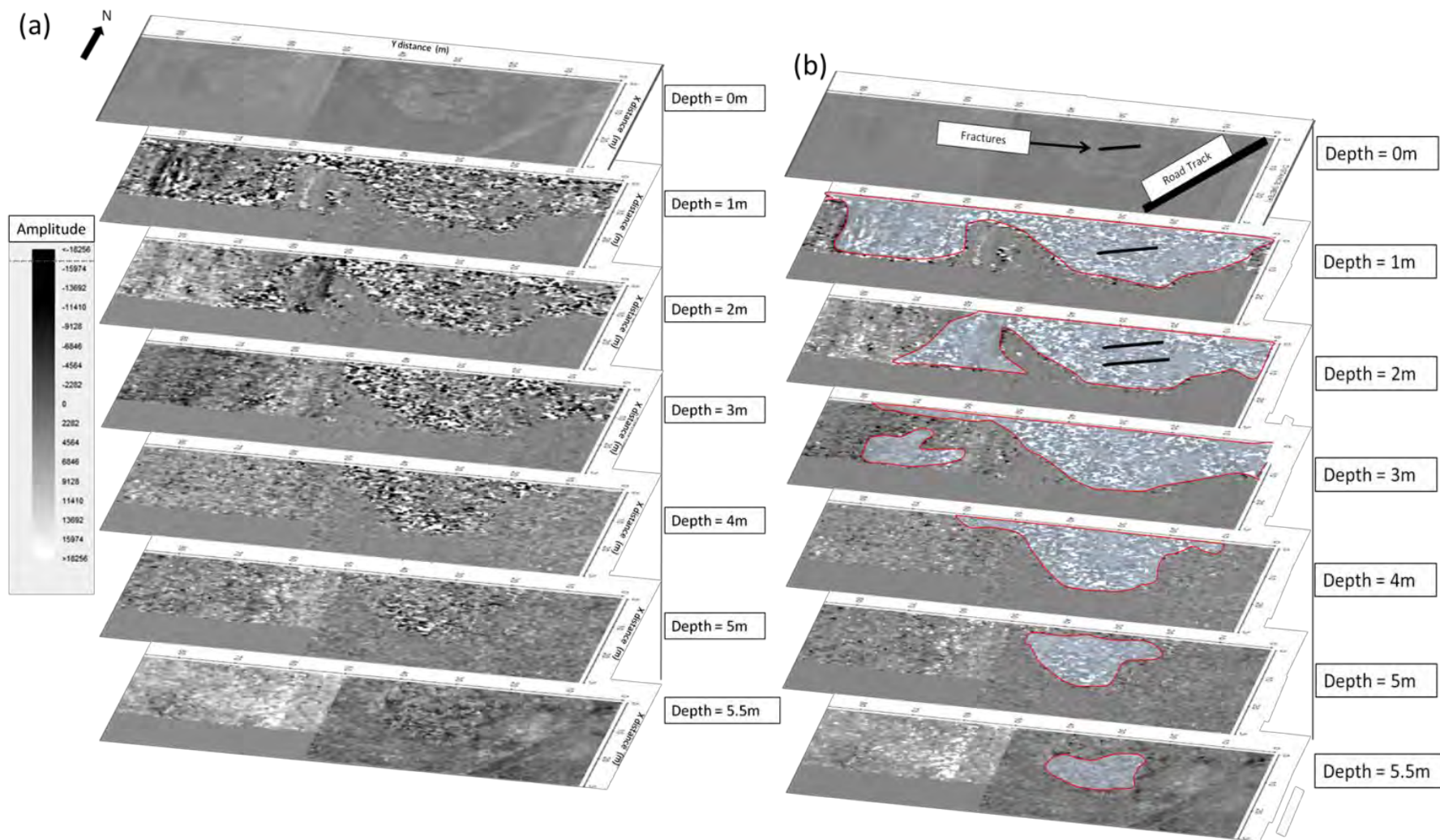


Figure 11. 12 Depth slices of the Travertine deposit (a) with its interpreted section (b). The black lines in section (b) highlight beneath the fracture. The change between depth of 1 m and 2 m shows that the fracture boundary spreads apart, and suggests it has a dome-shaped structure.

## 11.6 Conclusions and discussions

At the Stevens Airport and Barn 3 sites, the main objective of the GPR survey was to identify potential hazards ahead of the seismic survey. No such hazards were identified along either line, although such an assessment could only be made within the upper 1 m of the subsurface given the limited penetration depth of GPR through the clay-rich shale soil.

At Barn 3 specifically, deeper penetration was observed over outcrops of Dakota sandstone. Together with GPR velocities, derived from a CMP analysis, internal layers were observed within the Dakota sandstone unit and interpreted as being transitions between weathered and unweathered rock. The thickness of weathered material is  $\sim 1$  m, and it is itself overlain by a sandy soil layer. These observations may prove highly useful for determining static corrections for the processing the co-located deep seismic line.

At the Zen Garden site, the primary objective of the GPR survey was to image a travertine deposit and investigate the continuity of a fracture through it. Numerous internal reflective horizons were identified within the travertine deposit which suggests the episodic behaviour of the travertine during deposition. This trend is parallel with the surface fracture. The travertine deposit is expected to be at least 5 m thick, and other geophysical surveys at the site are in accordance with this assertion.

# 12. Integrated Site Conclusions

---

## 12.1 Stevens Airport

The goal of the Stevens Airport survey site was to identify the location and trend of the Eightmile Mesa fault, map the shape and depth of the basement and other layers, and to determine if there were any other faults present that could be geothermal flow path.

By analyzing the seismic depth section in Figure 12.1 we have interpreted a normal fault starting at the surface at about the start of the runway that dips to the southwest. According to the time to depth migrated section we see the top of the Dakota and bottom of the Mancos Shale at approximately 80-90 m. The top of the Morrison and bottom of the Dakota is at approximately 200 m in the southwest and increasing in depth to the northeast to about 300 m. The basement is at an approximate depth of 350 meters to the southwest and then moves down to about 500 meters to the northeast. The geologic cross section that was created shows the basement at 400-500 meters depth along the airport line. The calculated seismic depths fall within the expected range of the cross section. The depth values calculated from the seismic section are approximate because a refraction statics correction was not applied and the velocity model was manually picked. The Wanakah and Entrada Formations are located immediately above the basement. We have identified multiple faults that are within the basement. These faults could extend deep enough in the subsurface to be a source of geothermal water.



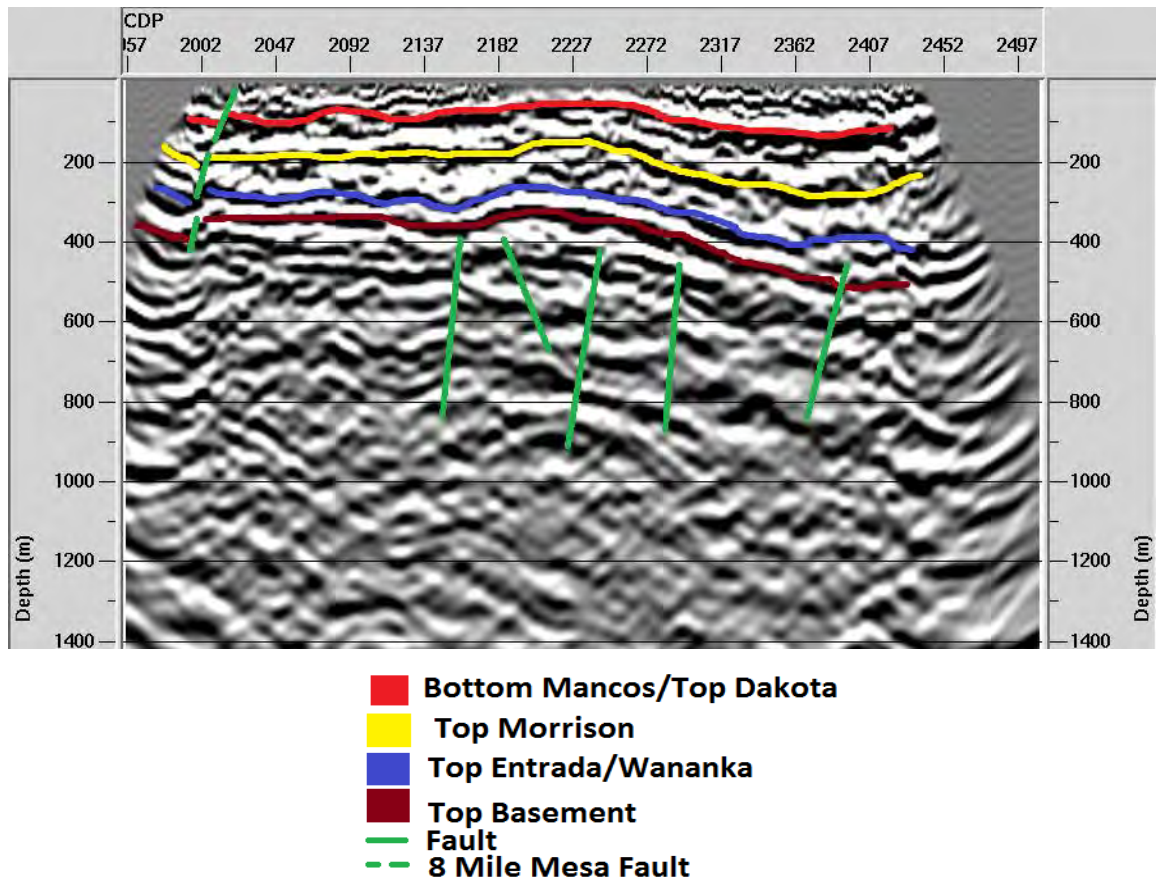


Figure 12.1 Shows the seismic section with depth on the y-axis.

The EM31 data in Figure 12.2 shows a relatively constant conductivity moving from northeast to southwest until you reach a sharp drop which could indicate the change from Mancos Shale to Dakota Sandstone. This sharp drop is better interpreted as a general trend of decreasing conductivity towards the southwest. Southwest of this low there is an abrupt change to a region of high conductivity. We believe this to be the change back to the Mancos Shale and the location of the normal fault. This trend of decreasing conductivity moving southwest and then an abrupt change to high conductivity is present in the EM34 data as well, as seen in Figure 3. This supports the idea of a slight dip of the beds to the northeast.

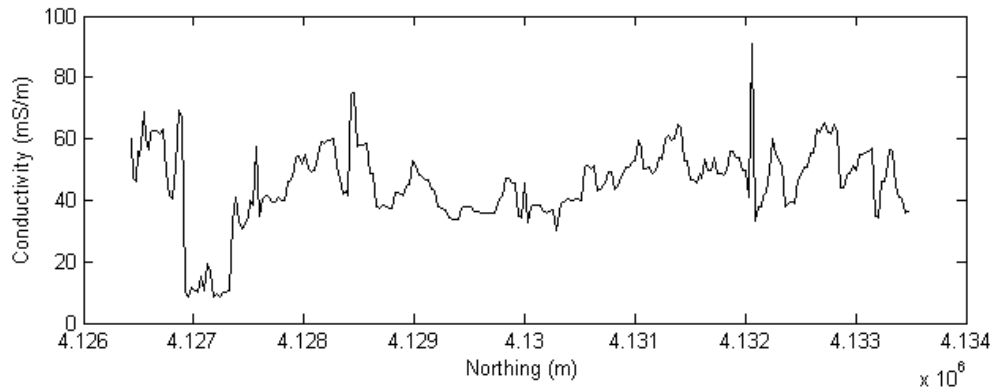


Figure 12.2 EM31 data for Stevens Airport line.

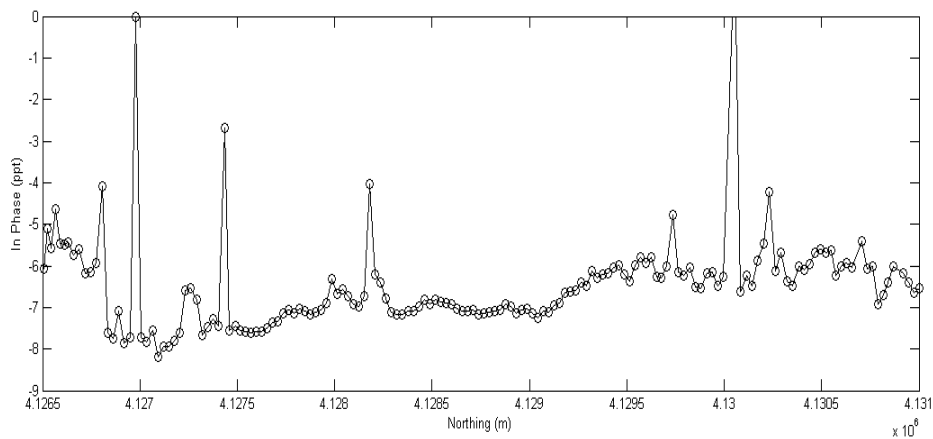


Figure 12.3 EM34 data for Stevens Airport line.

The DC resistivity and SP data in Figure 12.4 shows the location of the fault in between the golf course and the run way from the Stevens Airport. We can see the contact of the Dakota Sandstone and the Mancos Shale toward northeast. The Dakota Sandstone has a higher resistivity than the Mancos Shale, which leads us to conclude that the horizontal features of higher resistivity are the Dakota. Spontaneous potential surveys are designed to detect the movement of water. There is a lower trend of SP toward the northeast region. The SP data decreases for 900 m as you move along the seismic line to the southwest. This indicates that water has risen from a lower depth and begins to upwell in the fractured Dakota. We expect this water to be moving through the Dakota Sandstone because the highly resistive layer in the DC data turns into a low resistivity layer in this area. This general high trend stops at the location where the region of high resistivity starts. We can assume that after this point there is no water in the Dakota. From this point there is a broad increase in the SP data moving towards the fault. This might indicate water moving up the fault.

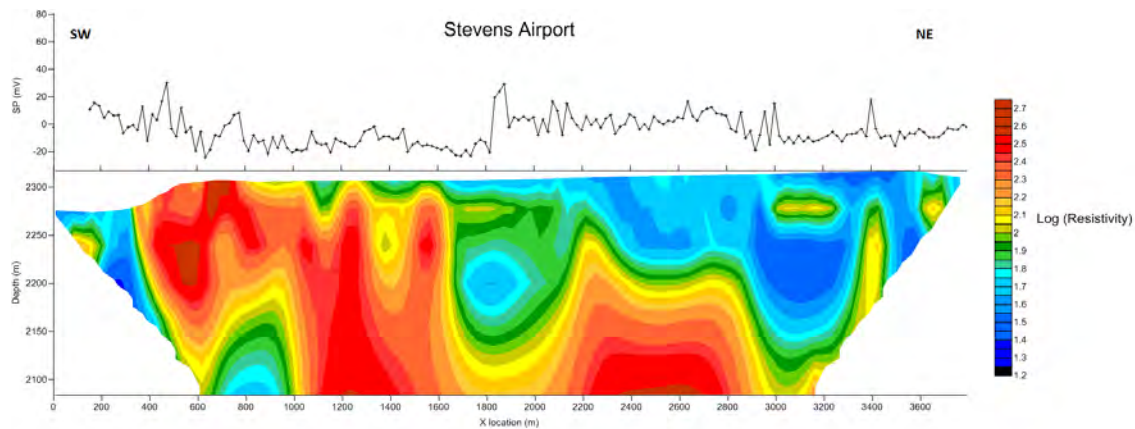


Figure 12.4 SP and resistivity data on the Stevens Airport line.

The forward model for the gravity and magnetic data (Figure 12.5) indicates a normal fault dipping to the southwest at approximately 60 degrees in the same location as the fault found with DC resistivity. The gravity model that was created is slightly rotated clockwise from the processed gravity data. This is most likely due to a 2D solution being applied to a 3D problem. It should be noted that there were mountains in the surrounding area that may have had an effect on the gravity measurements. The initial model for the gravity and magnetic data was created using information about the Precambrian basement from the seismic section. This model was then altered in order to better fit the gravity and magnetic data. Because gravity and magnetics are nonlinear and are affected by things off of the survey line there is no 2D solution that perfectly fits both sets of data.

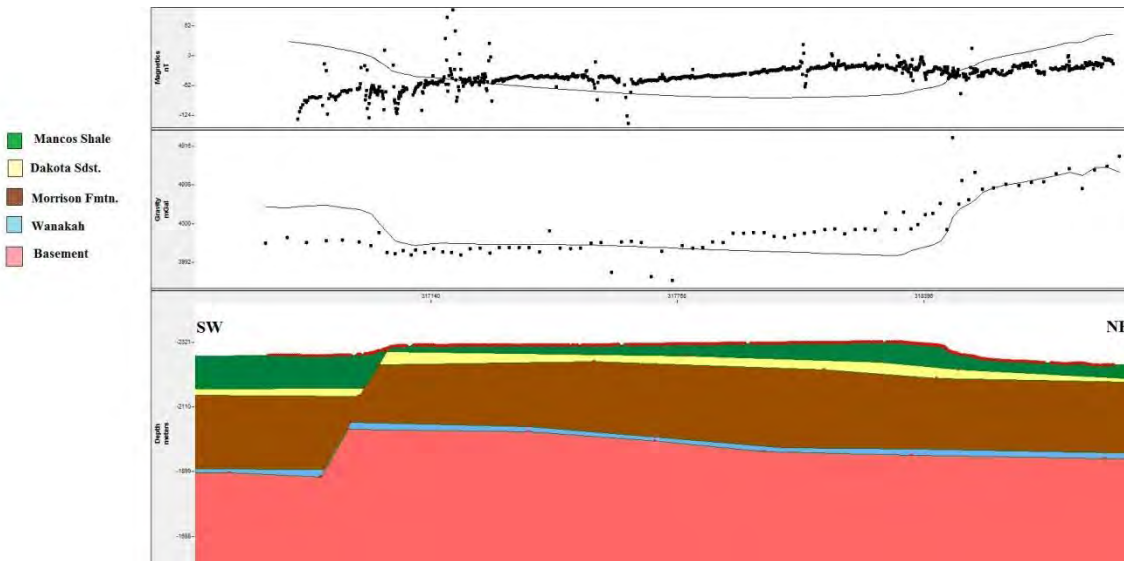


Figure 12.5 Forward model for the gravity and magnetic data.

The GPR survey was performed prior to the Vibroseis trucks acquiring data in order to determine whether there were buried pipes or obstacles underneath the survey line. Nothing was found at the site.

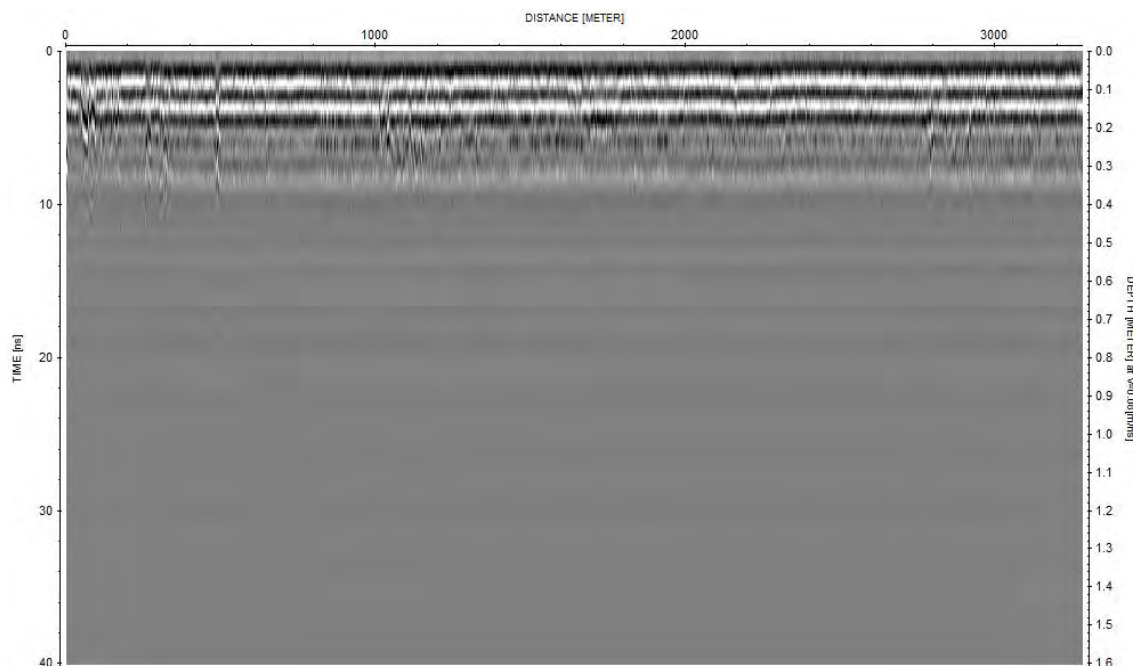


Figure 12.6 GPR image of Stevens Airport

After the analysis of the data from the different methods performed at the site there are several conclusions that can be drawn. The updated cross section based on our interpretations is shown in Figure 12.7. There is a normal fault at the south western end of the survey line that dips

approximately 60 degrees to the southwest. Evidence of this fault (the 8 Mile Mesa Fault) is present in the EM, gravity, magnetics, and DC resistivity data. The dip of the fault was found from the forward modelling of the gravity and magnetic data and a broad positive section in the SP data may indicate water travelling up the fault. The seismic section also identified several normal faults within the basement. The extent of these faults is unknown, but they may be the source of the geothermal water in this area. In Figure 12.7 the relative thickness of the Mancos Shale was determined from the EM and DC resistivity data. It has also been determined that there is water rising from depth along the north eastern 900 m of the seismic line. At this point the water has entered the Dakota Sandstone and there is upwelling in the fractures. The upwelling of the water stops 2100 m from the north eastern end and the Dakota becomes resistive. Future collaboration with property owners and businesses to the south of the airport could allow for additional sources on the hanging wall of the fault. This could provide better imaging of the Eightmile Mesa Fault, perhaps confirming these conclusions.

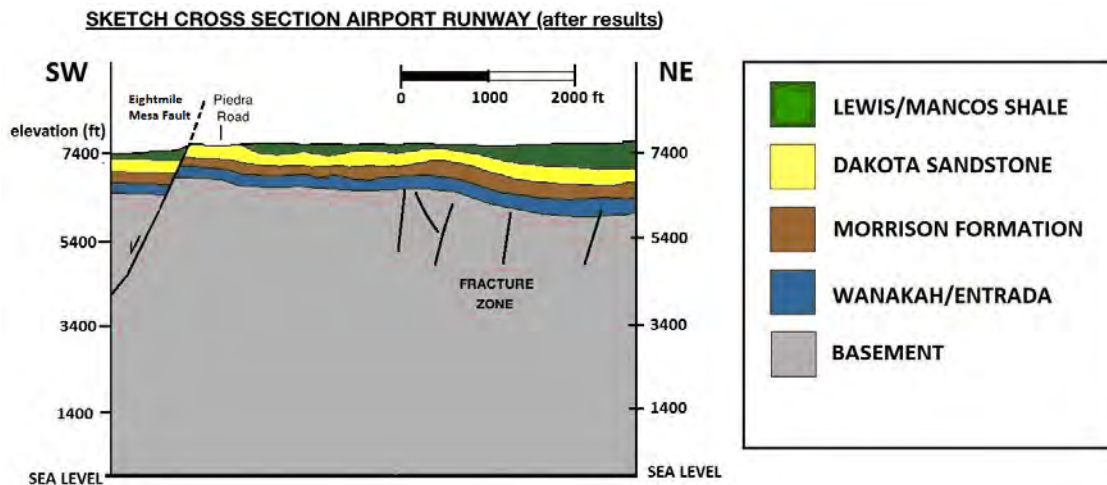


Figure 12.7 Updated cross section based on results



## 12.2 Hot Springs

The Hot Springs area consisted of survey lines PAGO 01, 02, 04, 05, 06, and 07, as seen in Figure 12.14 Hot Springs Site Overview and had a wide range of survey instruments including DC Resistivity, Self Potential (SP), Induced Polarization (IP), Electromagnetism (EM), Gravity, and Magnetics. Although the Gravity and Magnetics methods were not able to detect the location of any hot water features or faults, the DC Resistivity, Self Potential, and Induced Polarization methods were extremely useful in locating these features of interest.

On survey lines PAGO 01, 02, and 06, the hot water and fault were able to be detected with multiple methods. The fault can be seen in Figure 12.8, Figure 12.9, and Figure 12.10 where there is a large contrast in resistivity on either side of the fault, the conductive side on the footwall block and the resistive side on the hanging wall block. This fault is the same fault in each of these survey lines that is running North South, East of the Mother Springs, as seen in Figure 12.11, where the fault is the white line. The fault presence can also be seen in the Kriging of PAGO lines 01, 02, 04, 05, 06, and 07 at an elevation of 2125 meters, which is 30 meters below the surface, as seen in Figure 12.12 Kriging of PAGO 01, 02, 04, 05, 06, and 07, but it is unknown as to whether this fault will continue on its known projection. Another feature that is associated with the fault is the possible presence of hot water flowing through the fault. This image can be seen in Figure 12.12, where the blue feature, running along the fault, could be due to the calciferous minerals that precipitate from hydrothermal flow. This image also shows a clear image of the Dakota Sandstone, which is a possible formation for the water to flow through and the Mancos Shale. On the North side of the PAGO01 line and on the West side of the PAGO02 line, a highly conductive material was detected in the resistivity profiles as seen in Figure 12.8 and Figure 12.9. This hot water anomaly could be from the hot spring and would be consistent with what was observed in the Zen Garden. There is also indication of up welling of hot water in the SP portion of Figure 12.9. From 600 meters to 1000 meters a positive anomaly occurs, which could be a fracture system of hot water flowing upwards towards the surface.

This data is able to suggest that there is definitely up welling in the Hot Springs area and water flowing through the fault. The direction of this flow is thought to go up dip, through the Dakota Sandstone as cold water until it hits the fault and flows down to the basement, where it gets heated up and flows back up through the fault as warm water. This warm water will hit the Dakota Sandstone and get pushed through it until it hits the fracture system in the Mancos Shale, where it will get pushed up to the surface to create

the Mother Spring, the upwelling feature in PAGO02, and the hot spring that is thought to be in the Zen Garden.

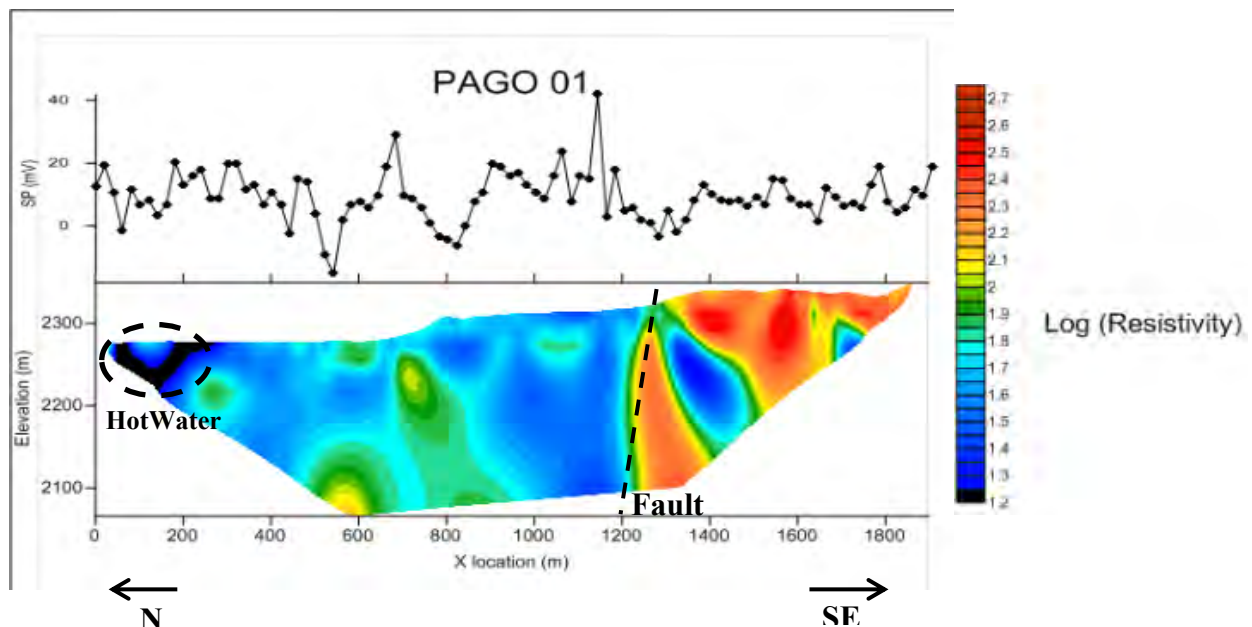


Figure 12.8 SP and Inverted Resistivity Profiles of PAGO01

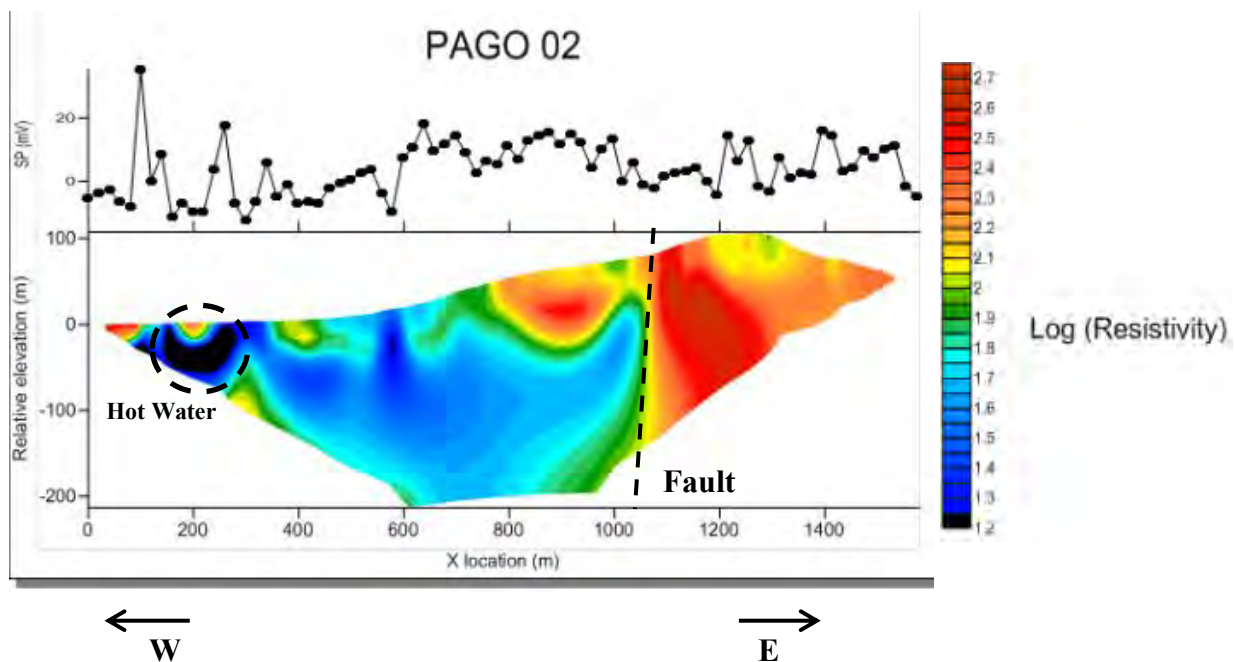


Figure 12.9 SP and Inverted Resistivity Profiles of PAGO02

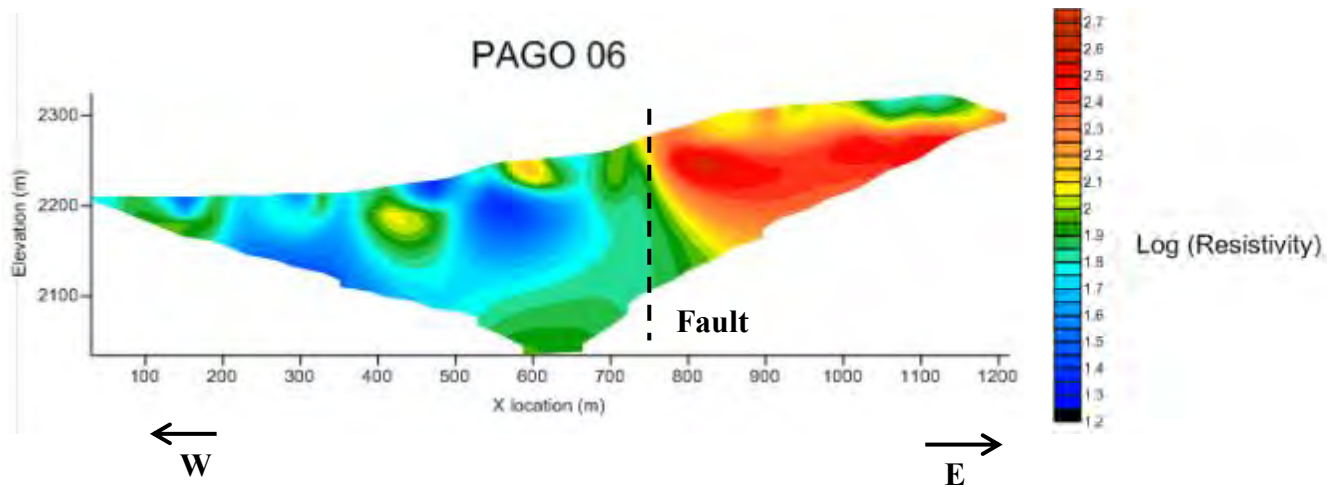


Figure 12.10 Inverted resistivity profile of PAGO06

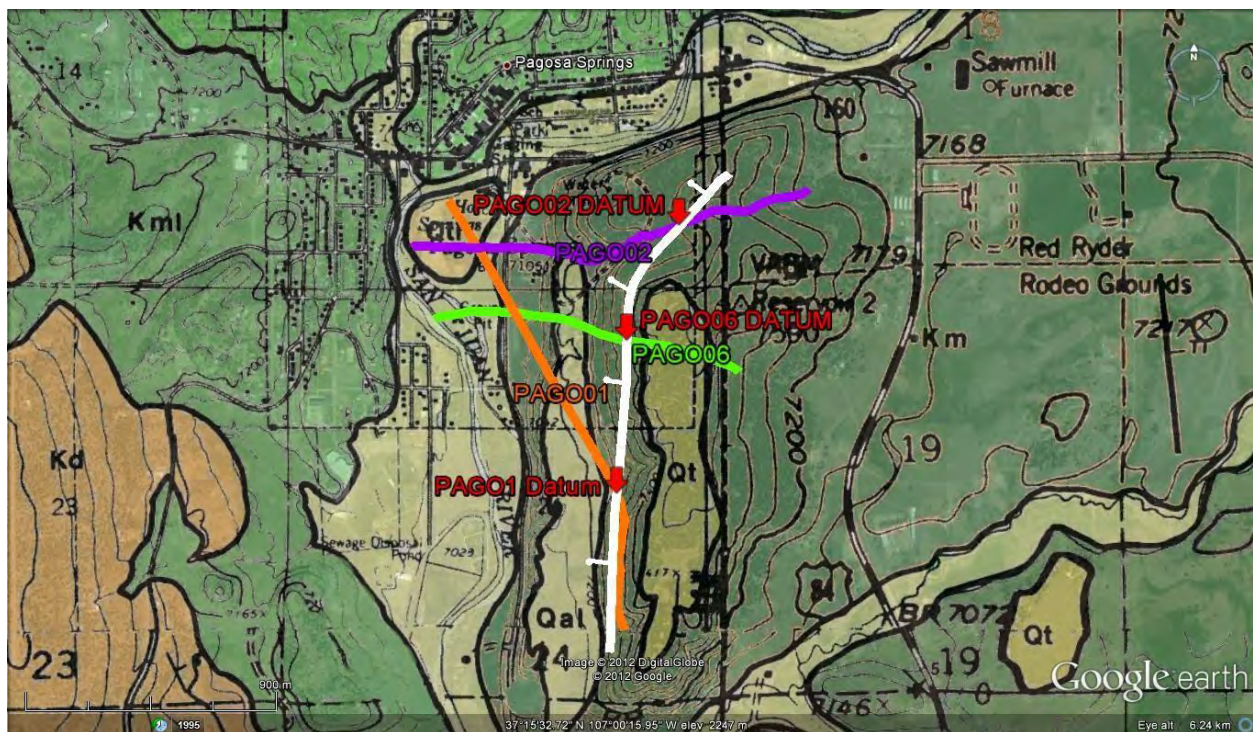


Figure 12. 11 PAGO01, 02, and 06 Lines in Relation to the Fault

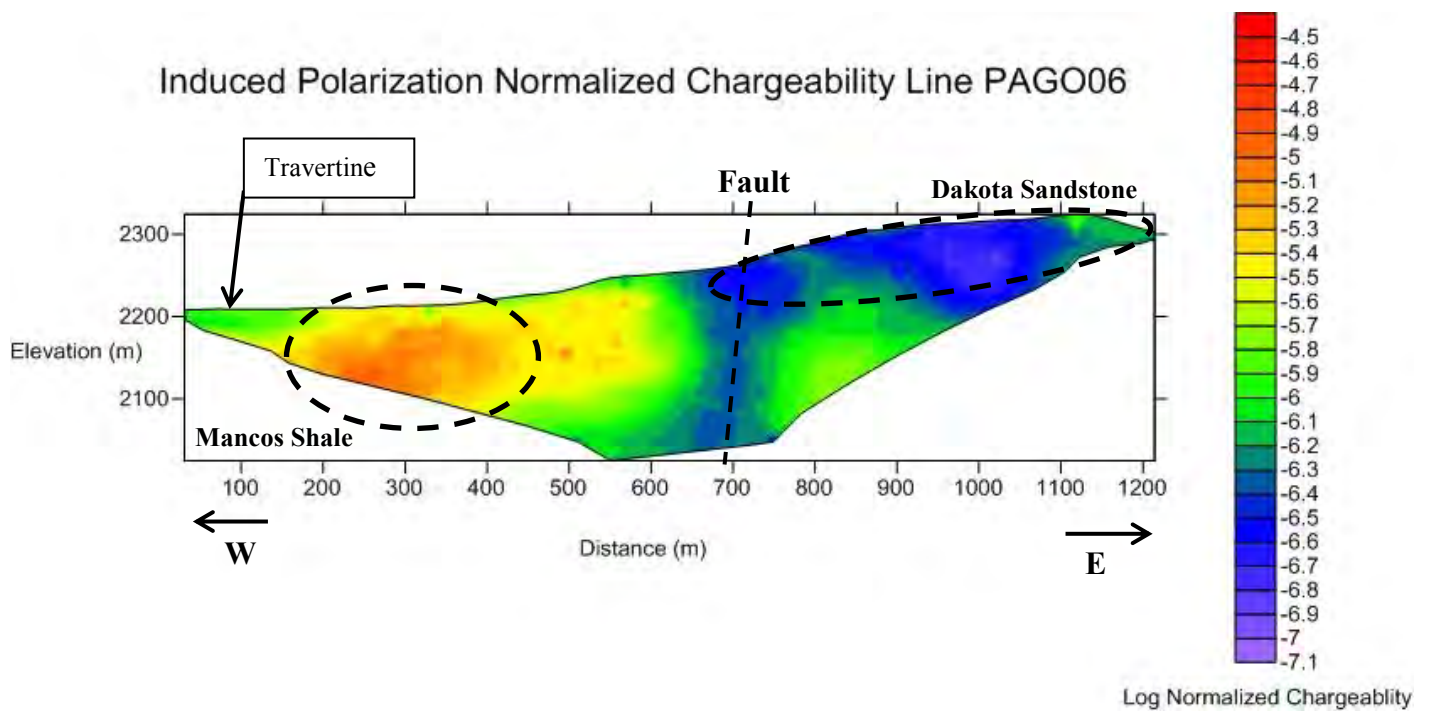


Figure 12.12 Normalized Chargeability Profile for PAGO06



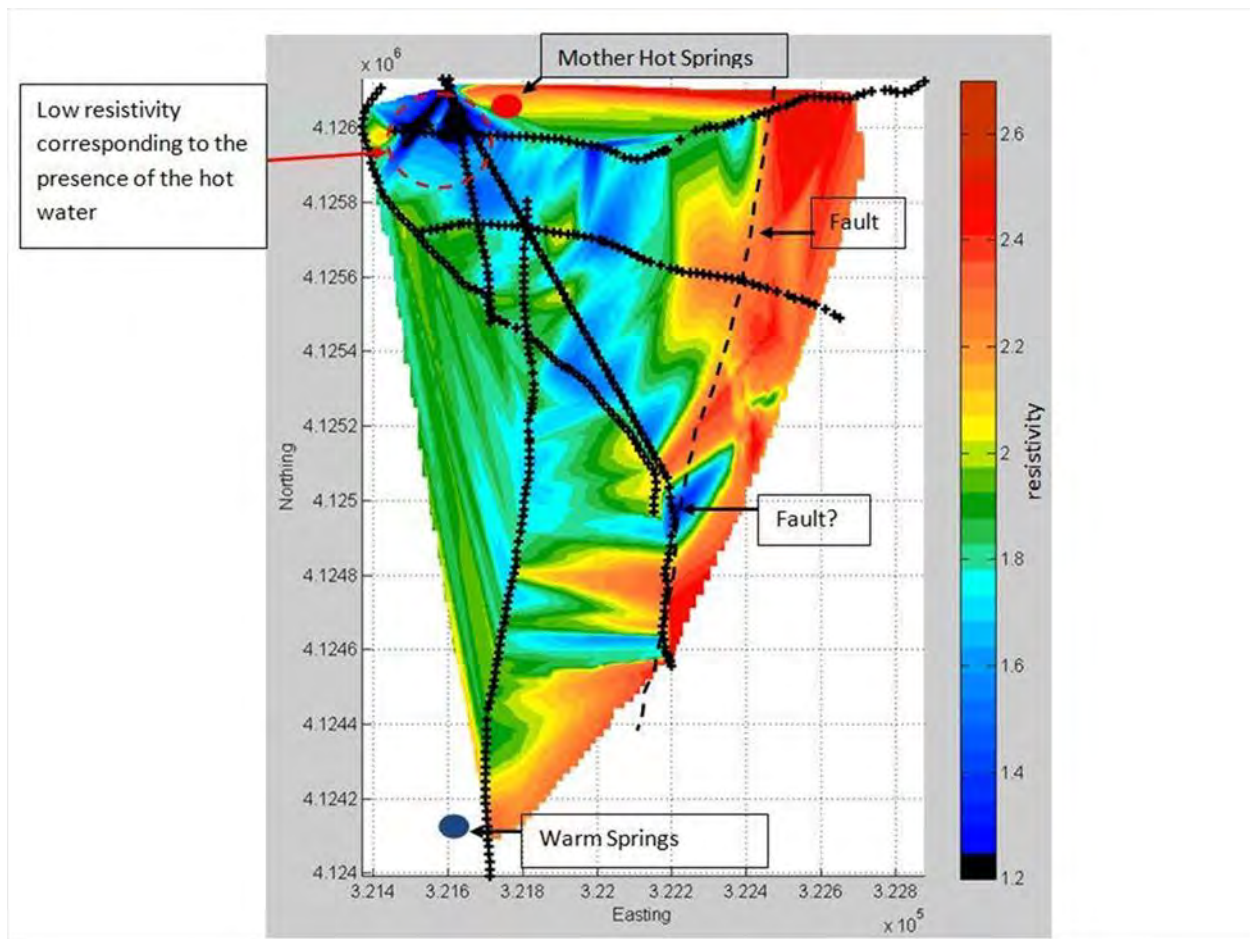


Figure 12.13 Kriging of PAGO 01, 02, 04, 05, 06, and 07

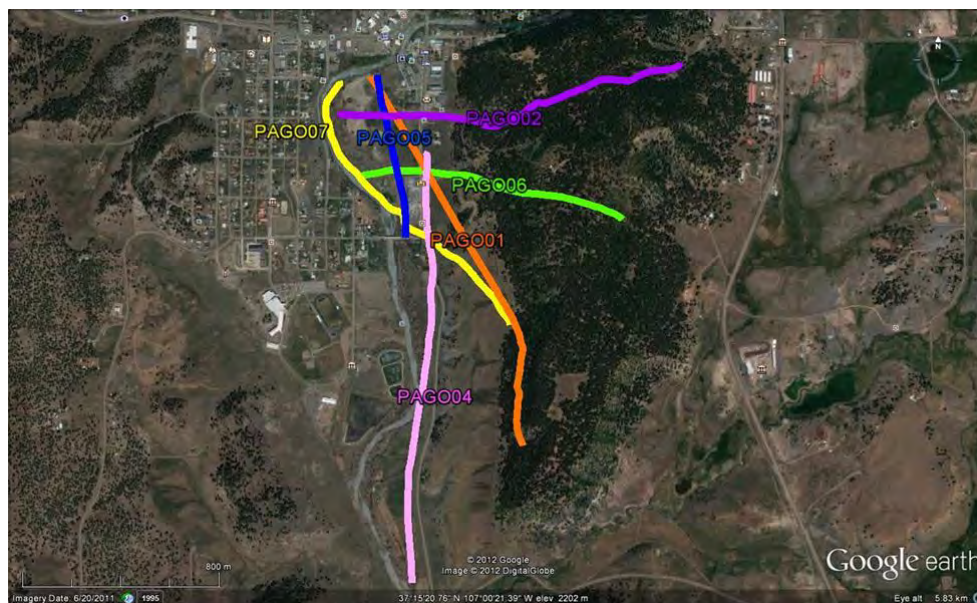


Figure 12.14 Hot Springs Site Overview



## 12.3 Warm Springs

### 12.3.1 Introduction

The Warm Springs site was analysed as it exhibited some geothermal activity; an initial geological survey showed warm water was flowing into the San Juan River from the river bank, interpreted as shallow ground water. On the other side of the river the contact between the Dakota Sandstone and the overlying Mancos Shale was exposed, leading to the hypothesis that the shale was acting as a seal above the porous sandstone, with the contact between the two lithology's forming a pathway that enabled the fluid flow observed at the river bank.

Shallow seismic, gravity, resistivity and SP surveys were carried out in an attempt to determine the subsurface geology and map any fluids that might be flowing under the site. Shallow seismic data was acquired on a single profile, whilst the gravity, resistivity and SP surveys were conducted on the Warm Springs grid. The grid consisted of 7 lines, each 300 meters long, with 10 m spacing between each line as shown in Figure 12.15.

GPS data shows the site to be relatively flat lying, with an increase in elevation of approximately 5 m to the east over the survey area.

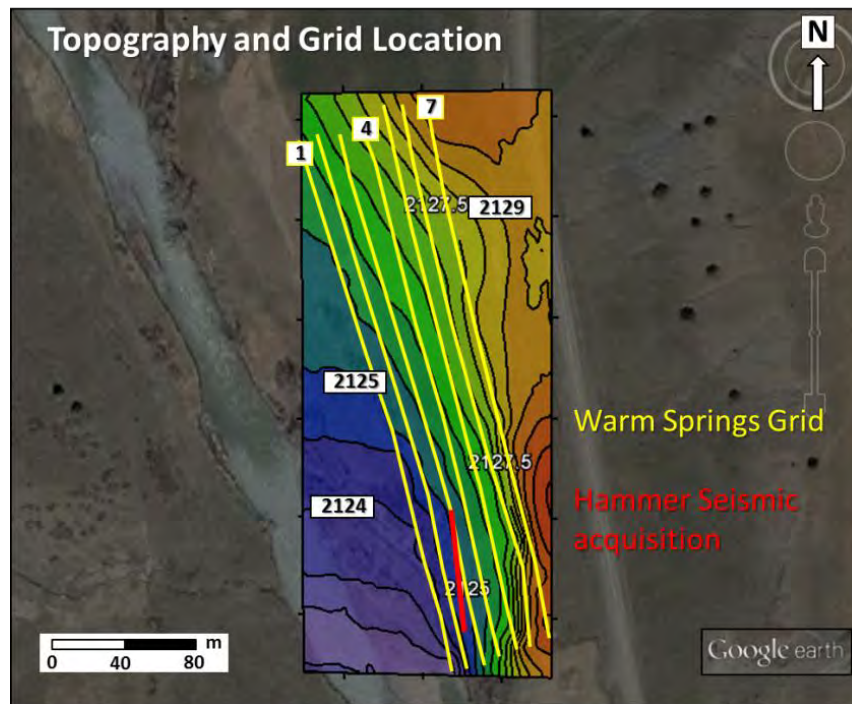


Figure 12. 15 Map of the Warm Springs site, showing the Grid and Hammer Seismic profile

### 12.3.2 Shallow Seismic

The North-South trending profile at this location displayed sub horizontal layers, with low velocity unconsolidated sediments extending down to 1.5-3 meters depth. The sediments were too loosely packed to enable a confident lithological description based on seismic data.

Beneath these was a higher velocity layer interpreted as the Dakota Sandstone. A relatively low p-wave velocity of 2833 m/s indicated that it had undergone some weathering, which is to be expected considering its shallow position.

The depths to the Dakota Sandstone given at either end of the shallow seismic profile, shown in Figure 12.16, indicated some component of dip in the South direction. However, a change in depth of less than 1 meter along a 48 meter profile is more likely to be caused by topography along the contact.

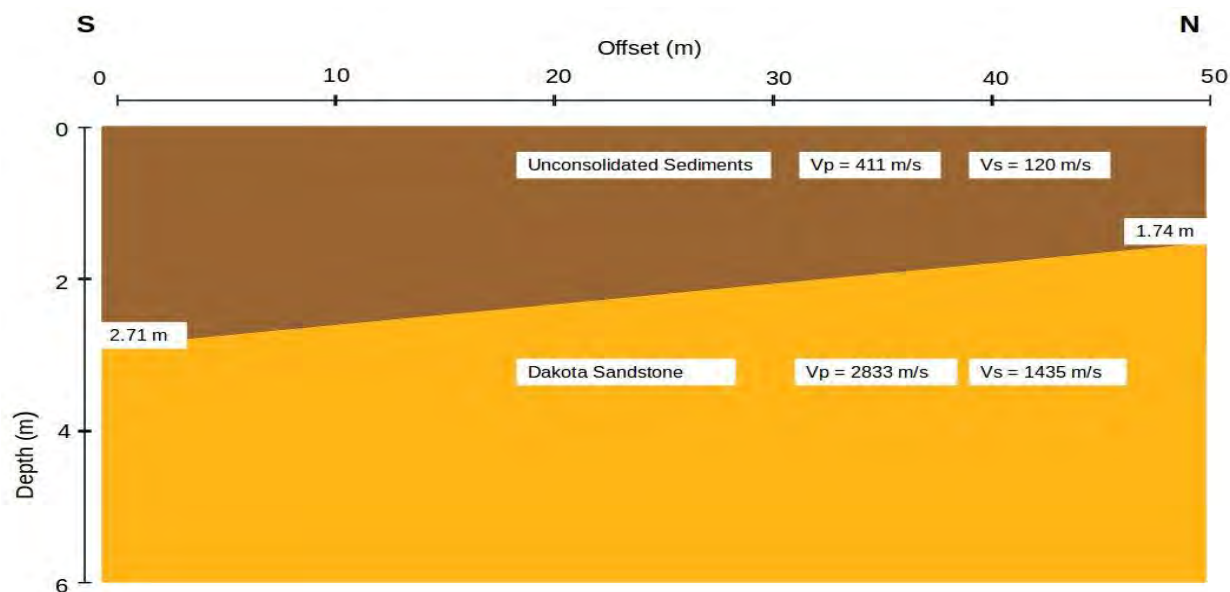


Figure 12. 16 Subsurface model along the Warm Springs shallow seismic profile, showing the loose sediments and the underlying Dakota Sandstone

### 12.3.3 Gravity

The CG5 gravity measurements were taken on the Warm Springs Grid, at every 10 meters along Line 4 until station 32 (Figure 12.17). The observed measurements gave a small negative anomaly to the south and a small positive anomaly to the North, interpreted as a small component of dip to the North at this site causing pinching out of the Mancos Shale against the surface at the southern end of the survey line.

The lack of any major gravity anomalies is consistent with the conclusion from the shallow seismic data that the layers are sub horizontal, with little or no geological features to disrupt the layer cake model.

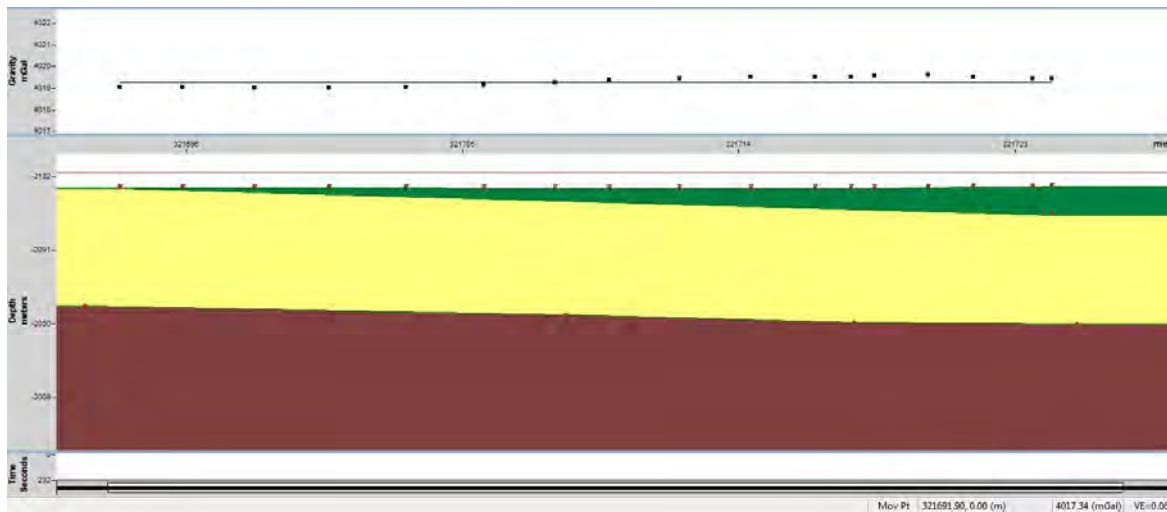


Figure 12. 17 Interpreted gravity data, with the Mancos Shale (Green), Dakota Sandstone (Yellow) and Morrison Formation (Red), with the gravity anomaly plotted above the figure.

#### 12.3.4 Resistivity profiles

Seven resistivity lines were measured at the Warm Springs area at every 5m along a 300m profile. Even if the depth of penetration is limited (50 meters), the 2D resistivity inversion supports the idea of the 2-layer model previously introduced by the other surveys. Indeed, as shown below, the 2D slices contain a distinct shallow conductive layer with an increasing thickness in the NE. The warm colors stand for a resistive body while cold ones refer to a more conductive body. In this way, this blue shallow layer is consistent with the other surveys by indicating a highly conductive body such as the Mancos Shale. According to the well data, the sandstone thickness is expected to be around 60m. The resistivity anomaly pointed out 30 meters deep in Figure 12.18 is more likely to be related to water presence.

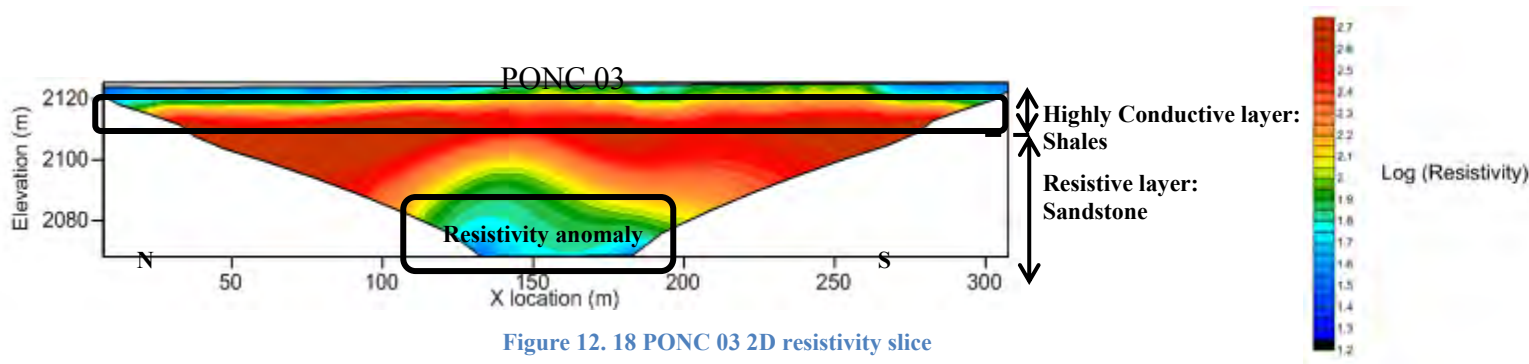


Figure 12.18 PONC 03 2D resistivity slice

A 3D interpolation of the slices in Figure 12.19 confirms the water presence within the Dakota Sandstone. It tends to be concentrated along the river and dips away from it.

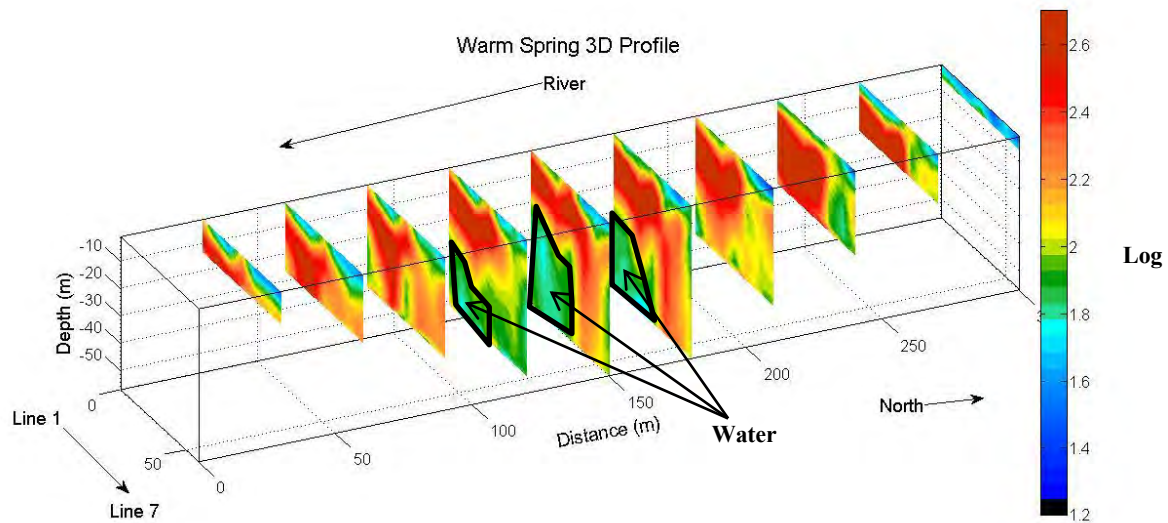


Figure 12.19 Warm Spring 3D resistivity profile

### 12.3.5 SP profile

From the resistivity surveys, water has been located in the Warm Springs area. Thus a deep understanding of the water system is required and to do so, a SP survey was carried out as it can help in determining fluid flow which could in turn explain the presence of the spring.

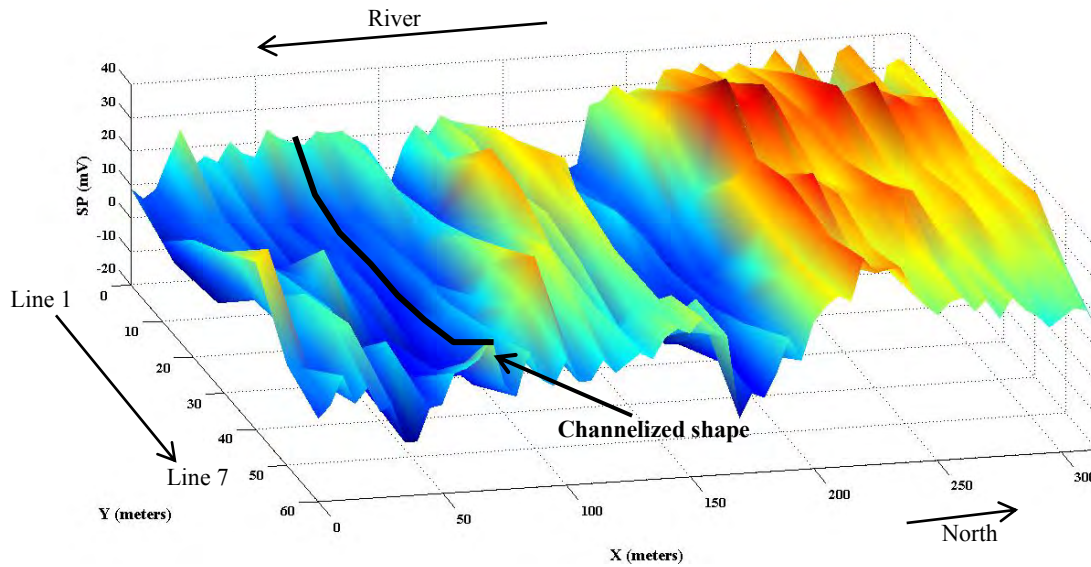


Figure 12.20 Warm Spring 3D SP profile

Even if data has been biased by a flooded field on the northern part, a channelized pattern can be observed in the southern part. This suggests a lateral flow of the water perpendicular to the river i.e. from west to east. Moreover, based on Figure 12.20, the additional fault discovered is actually on the western side of the survey grid. It can then be assumed that the fault enables the water to percolate from the basement to the porous Dakota Sandstone which in turn flows to the surface with the help of the fractured Dakota Sandstone unit.

### 12.3.6 Conclusion

Several types of surveys have been acquired near the Warm Spring and they consistently show a dipping layered system (towards NE) with a thin Mancos Shale above the Dakota Sandstone and the Morrison Formation. However, the resistivity and the SP lines tend to show a water presence within the Dakota Sandstone flowing from the eastern fault to the river shore. Nevertheless, it must be borne in mind that this interpretation relies on a few lines located in a small area (300\*60 m). Further surveys (resistivity, DC and electromagnetic) might be required to confirm the fault play in this geothermal system and to locate precisely the fluid path.



## 12.4 Zen Garden

Initially the primary target at the Zen Garden site was the surface expression of the crack within the travertine. Integration of multiple geophysical methods at the site revealed a much more complex geologic story than first anticipated. It has been surmised that there is a layer of shale that bends upwards towards the surface on the western edge of the Zen Garden. An alluvial deposit lies on top of the shale and is capped by a layer of travertine towards the eastern edge of the grid. This section will present an integrated view of the data collected by each method in order to show that this model of shale, alluvial deposits, and travertine exists at the Zen Garden Site. It will also be shown that the alluvial deposit is north trending, perhaps providing a path for fluid flow in the subsurface.

Models based on the EM31 and EM34 data both show a high-low-high conductivity trend running from east to west (Figure 12.21). In the middle of the grid it is possible to see a more conductive body that diminishes with depth – this is associated with an alluvial deposit that lies on top of less conductive shale (Figure 12.22). Travertine is present on the eastern edge and GPR shows that the travertine extends approximately five meters into the alluvial deposit, Figure 12.23. Although shale appears to extend down to (and possibly beyond) the depth of investigation, it is more plausible that there is an alluvial deposit ten to fifteen meters deep that lies on top of the shale. Multiple methods display anomalies that indicate a conduit running north/south through the upper alluvium.

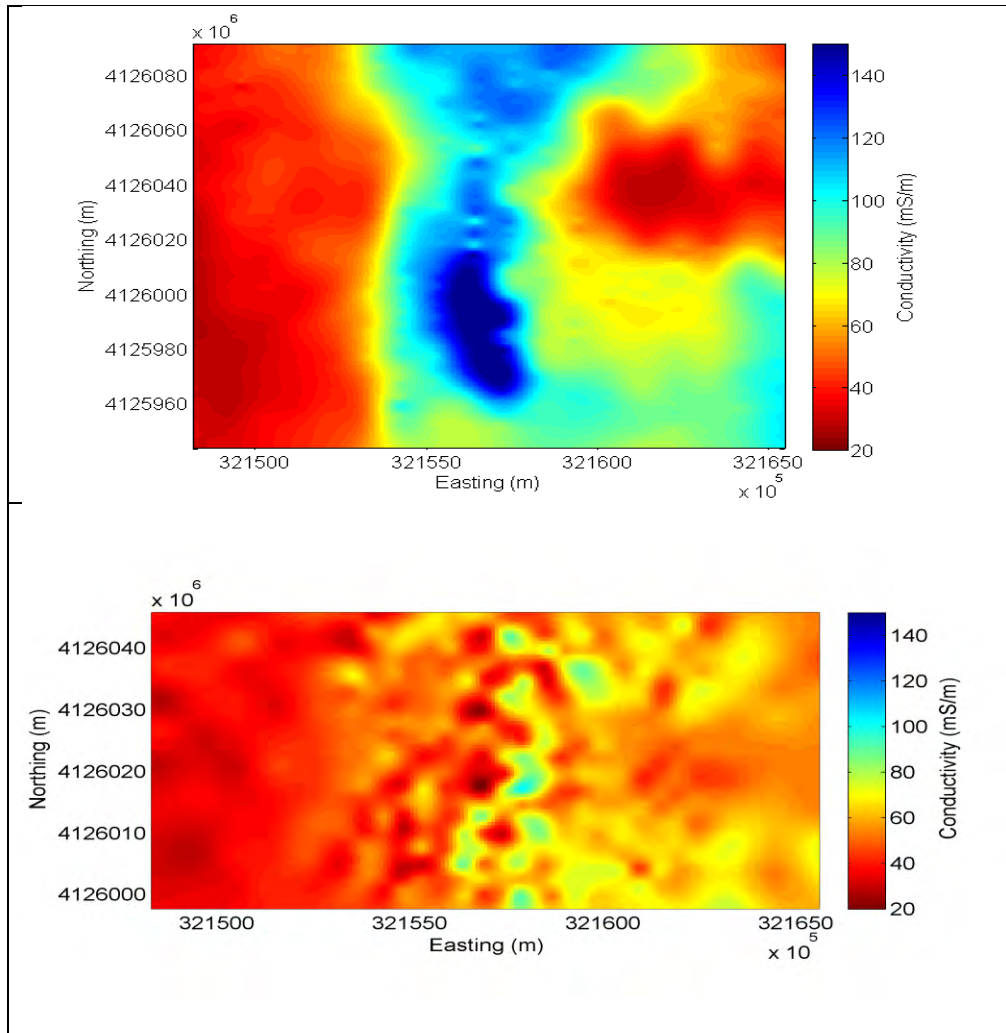


Figure 12.21 Conductivity maps from quadrature EM31 (top) and EM34 (bottom) data display similar trends that diminish with depth. EM31 has an approximate depth of investigation of six meters and the EM34 has a depth of investigation close to fifteen meters.

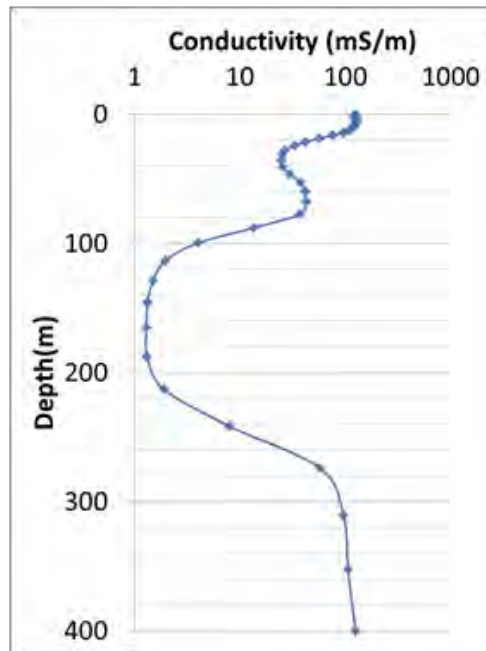


Figure 12.22 EM47 data displaying the change in conductivity with depth at one point in the Zen Garden site. The Mancos Shale ranges from 15 meters to 60 meters in depth.

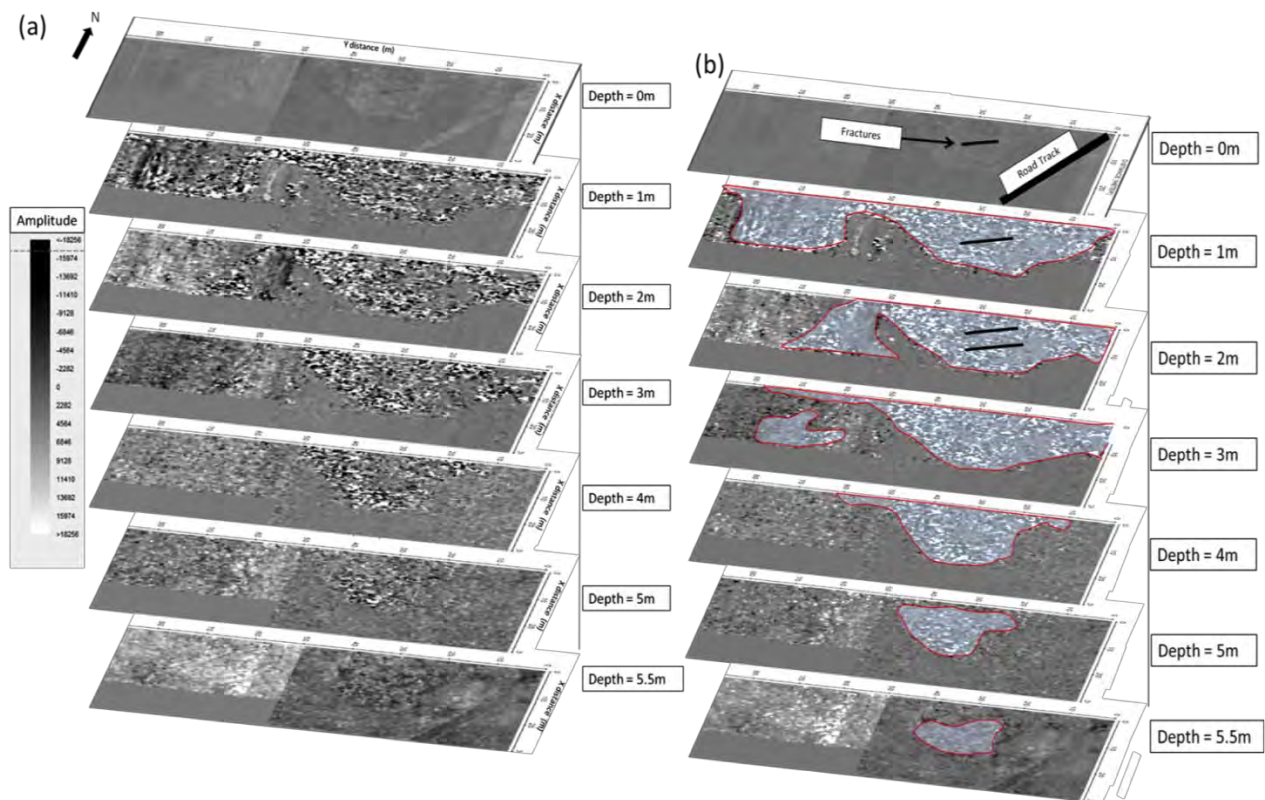
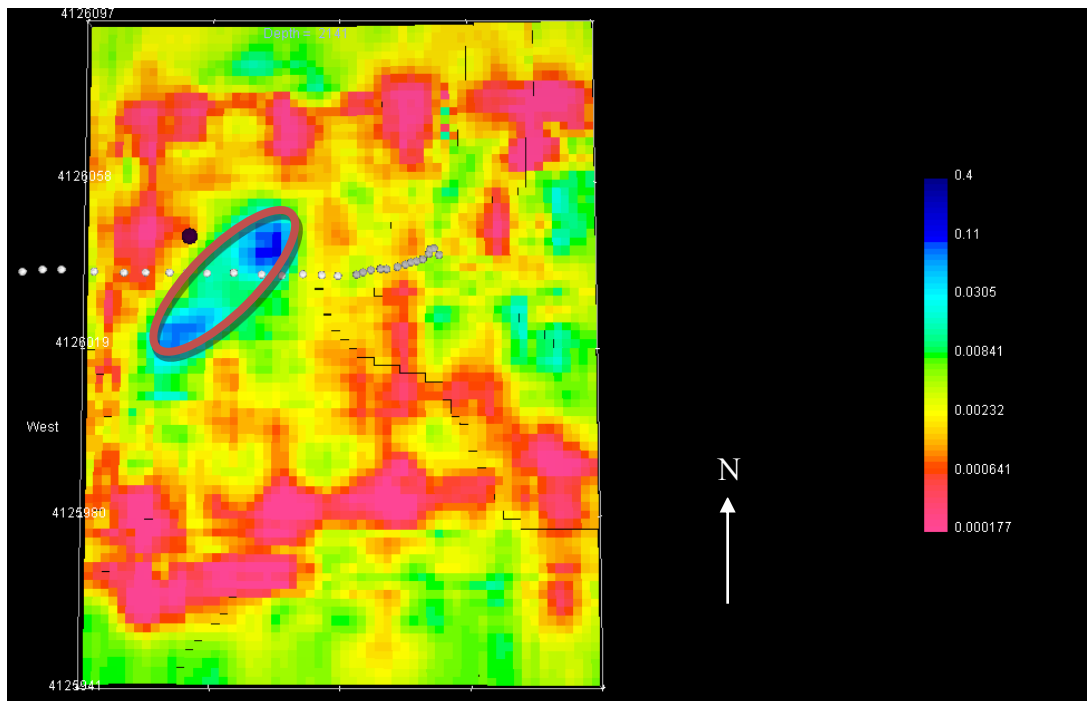


Figure 12.23 GPR layer images of the fracture in the travertine. Results show the travertine extends approximately five and a half meters into the subsurface.

Figure 12.24 displays the surface conductivity of the Zen Garden site. The DC resistivity model indicates that a conductive body follows the path of the fracture with an east/west orientation at a depth of approximately 20 meters (Figure 12.25). From the surface to a depth of approximately 20 meters there appears to be a NE/SW conductive trend to the southwest of the pipe that is congruent with other methods. The 2D resistivity models display trends similar to the EM data and Figure 12.26 reinforces this notion.



**Figure 12. 24 Surface conductivity of the DC resistivity model. Notice the conductive trend running from the southwest to the northeast.**

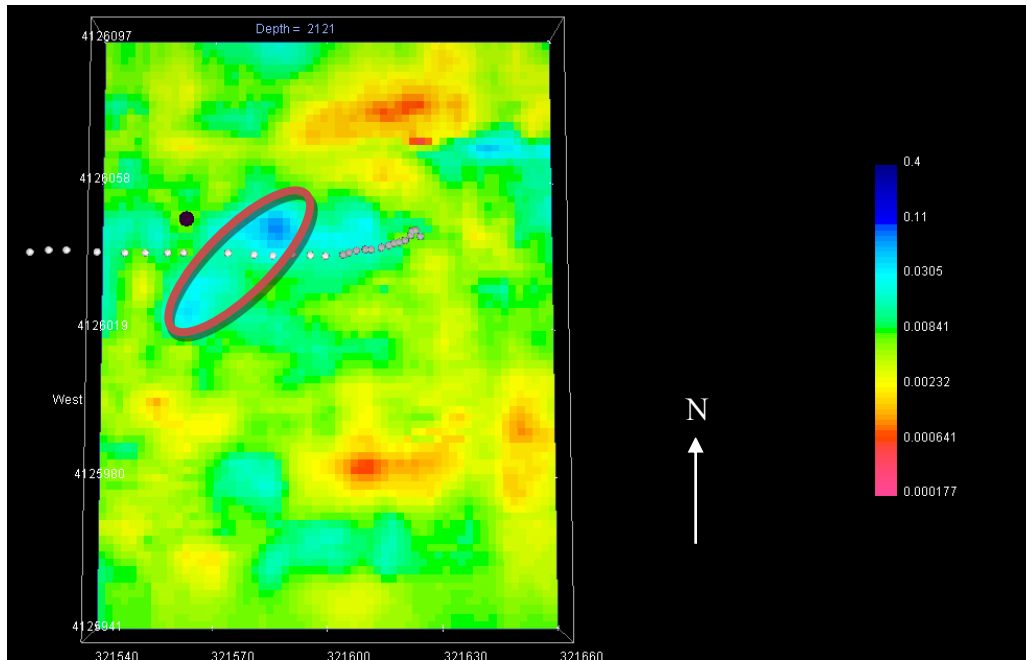


Figure 12.25 20 meters depth of the DC resistivity model. Notice the conductive trend running from the southwest to the northeast.

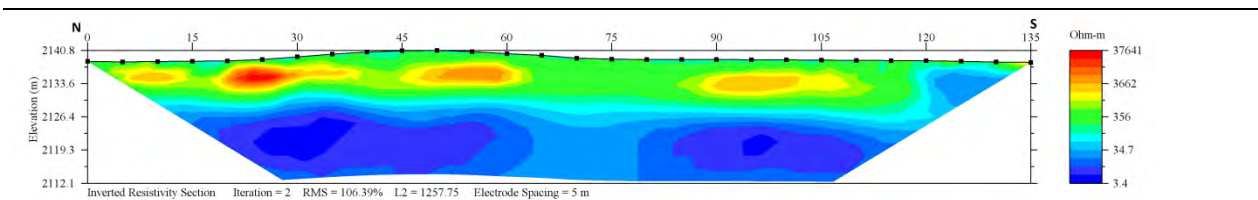
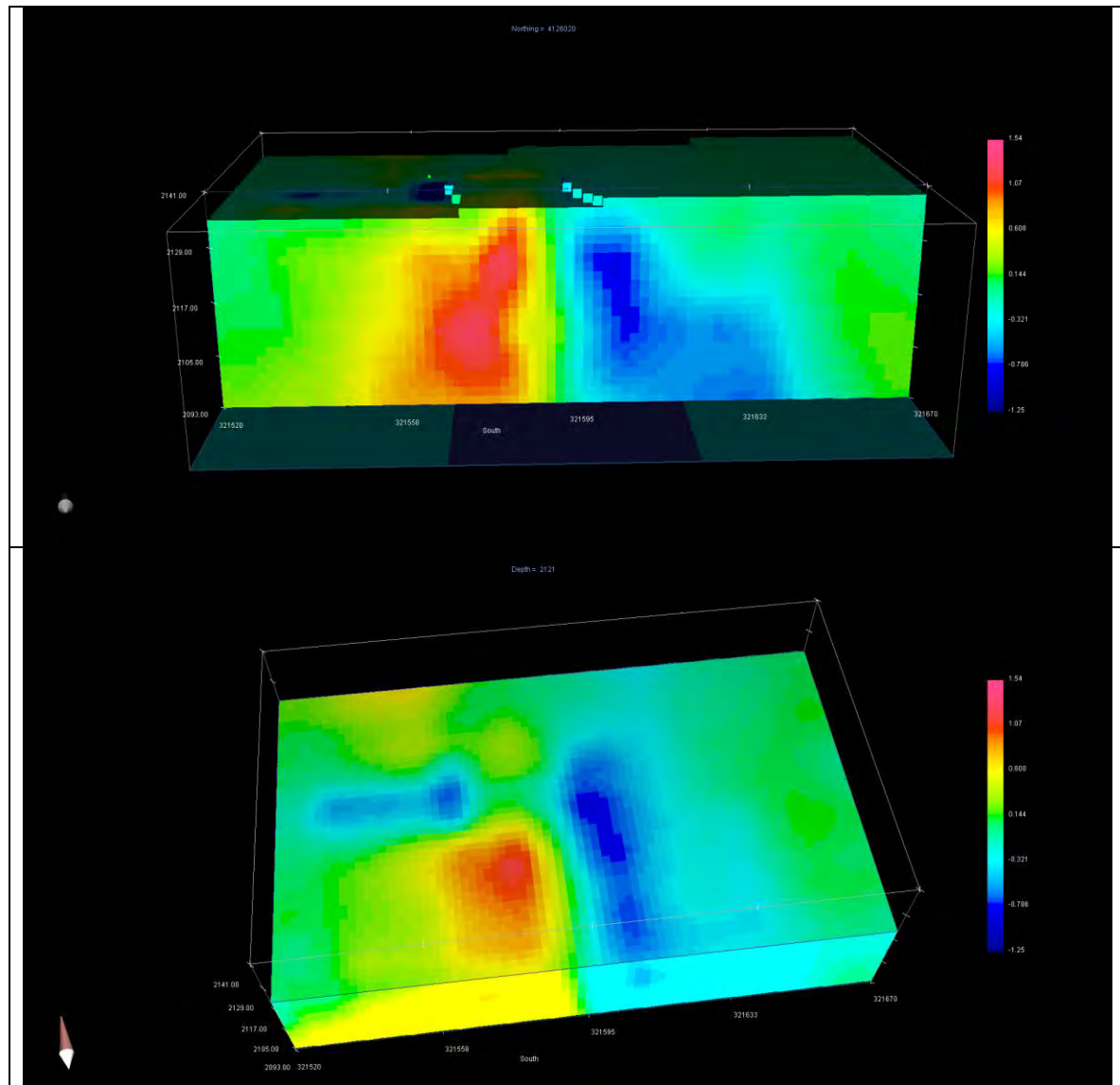


Figure 12.26 Line E of the DC resistivity survey. Notice the low conductivity on the edges, with a higher value in the middle.

As we cross the Zen Garden from east to west we notice a change from high density values to low density values. The low density anomaly is possibly a porous alluvium that reaches a depth of approximately ten to fifteen meters. Magnetic data shows a low susceptibility at nearly the same location as the low density anomaly (Figure 12.27). The magnetic susceptibility of the Zen Garden correlates very well with the density contrast, which emphasizes our hypothesis of shale on the western edge with alluvium and travertine towards the east (Figure 12.28). Figure 12.28 also shows the correlation between the in-phase EM31 data and how it correlates with the magnetic susceptibility. The negative phase of the western edge of the Zen Garden is indicative of a high magnetic susceptibility, which agrees with the magnetic data. There is a low susceptibility and an in-phase EM31 trend on the eastern edge of the Zen Garden, which is close



to the suspected travertine area. Another low susceptibility trend runs north/south to the west of the PVC pipe and could be associated with a conduit at approximately ten to fifteen meters depth. There is a region of high susceptibility in the immediate vicinity of the PVC pipe.



**Figure 12.27 Gravity model cross section (top) and top view at twenty meters depth (bottom) of the Zen Garden. Notice the high to low density trend from east to west. The low density anomaly could be due to the low porosity of the alluvial deposit that has the north/south conduit running through it.**

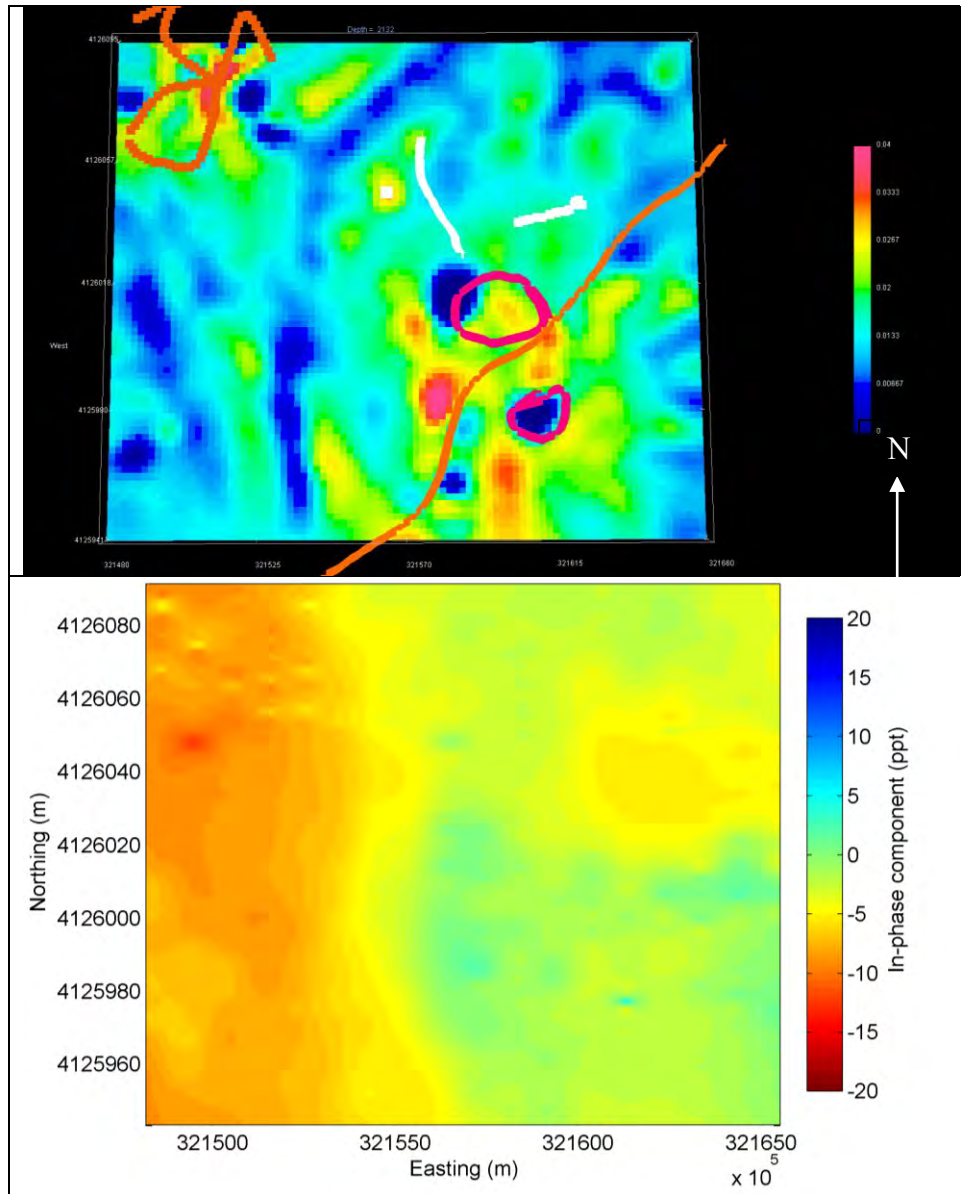


**Figure 12. 28** Surface magnetic susceptibility map (top) and in-phase EM31 map (bottom) of the Zen Garden. Notice the low susceptibility trend that runs from southeast to northwest.

Within the Zen Garden, PAGO 02 displays a low-high-low conductivity trend from east to west that is consistent with both the EM31 and EM34 conductivity maps. There is a north to south trend of highly conductive material, which could indicate the conductive alluvial deposit of the Zen Garden that contains the conduit (Figure 12.29). In this figure we see a high SP anomaly, indicating either upwelling of fluid or lateral flow. The location of this anomaly is consistent with the suspected northern trending conduit.

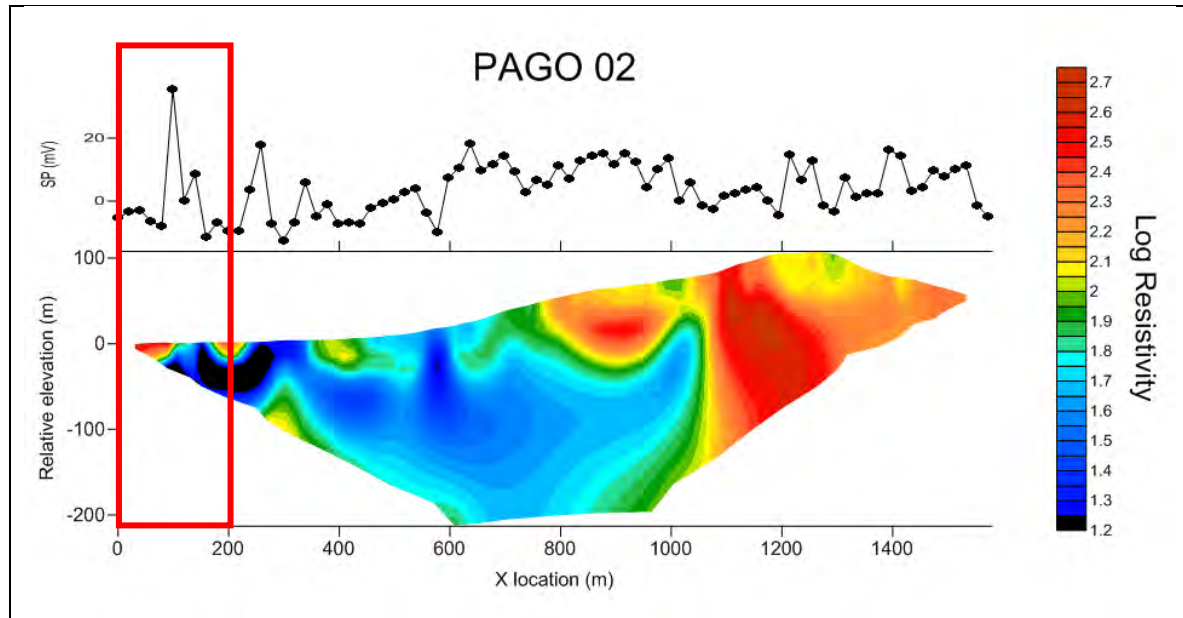


Figure 12.29 SP data (top) and DC resistivity (bottom) for PAGO 02. The Zen Garden is located within the red box. Notice the high SP anomaly, which is commonly associated with moving fluids. The DC model also indicates a conductive body moving into the page.

Figure 12.30 displays the geologic cross section derived from the many geophysical methods used to survey the Zen Garden site. The EM methods all concur that there is a body of high conductivity that is oriented in the north/south direction. A high SP anomaly over the PVC pipe in the Zen Garden indicates flowing water, which coincides with a north/south conduit within the alluvial deposits. The Mancos shale appears to have a high magnetic susceptibility compared to the alluvium and the travertine. Density models show clear contrasts between the three main bodies. EM, SP, DC, and magnetics all indicate a conduit in the alluvium that travels from north to south. Phase EM31, EM34, magnetics, gravity and GPR all agree upon the boundaries of the shale, alluvial deposit, and travertine.

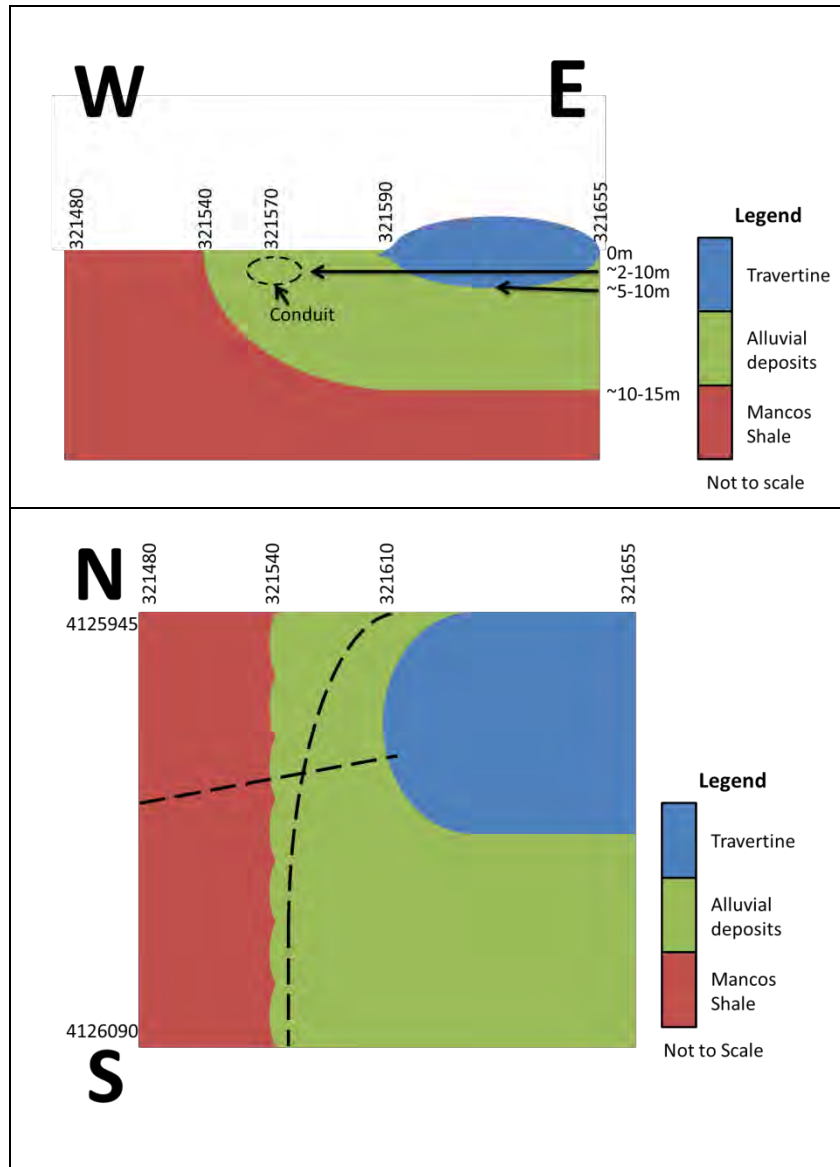


Figure 12. 30 Geologic cross section (top) and map (bottom) based on the integration of the geophysical surveys preformed at the Zen Garden.

It is suggested by the DC data (both pago\_02 and the Zen Garden models) that there is an east/west conduit, but this cannot be stated definitively without further study using east/west running lines. It has also been suggested by hammer seismic that there is a saturation zone below 1.6 meters, further investigation would be necessary to confirm this.

## 12.5 Barn 3

The Barn 3 site is located in Alpine Ranch, shown in Figure 4.5. This site was chosen during the field camp by the survey design team. The objective of this site was to better image the Eight Mile Mesa Fault and structural geology in the Pagosa Springs area. The survey design of this site was mainly directed towards deep seismic acquisition, with other geophysical techniques acquired along the line. The Eight Mile Mesa Fault is found within the north east of the ranch suggesting that it can be imaged by 2D deep seismic acquisition running perpendicular to the fault plane. The survey line runs northeast to southwest and is bisected by the Archuleta County Road 500.

### 12.5.1 Data acquired

Geophysical method	Objective
Ground penetrating radar	Determine the depth and thickness of shallow layers and identify obstacles to deep seismic acquisition
Electromagnetics	Observe contrasts in conductivity of the earth for a given depth, thus interpreting faults, lithology and other structural geology
Gravity	Observe contrasts in gravity of the earth, thus interpreting the Eight Mile Mesa Fault and other structural geological changes
Deep seismic	Measure reflected seismic sound waves to provide an image of the subsurface. The goal is to image the Eight Mile Fault, observe the expected geology and identify additional faults and structure in the subsurface

### 12.5.2 Interpretation

Ground penetrating radar (GPR) was acquired northeast of the Eight Mile Mesa Fault on the survey line for 50m. No shallow obstacles were observed and therefore no shallow anomalies or obstacles were expected in the deep seismic acquisition line. The top of the Dakota Sandstone is interpreted in Figure 12.31 as having a weathered and un-weathered layer overlain by a soft rich soil produced from the weathering of the Dakota Sandstone. The thickness of this upper



weathered layer is estimated at 1 - 1.2 m. The thickness of this layer can be used as input into more accurate deep seismic processing of the same line at a later date; this improves the near surface model.

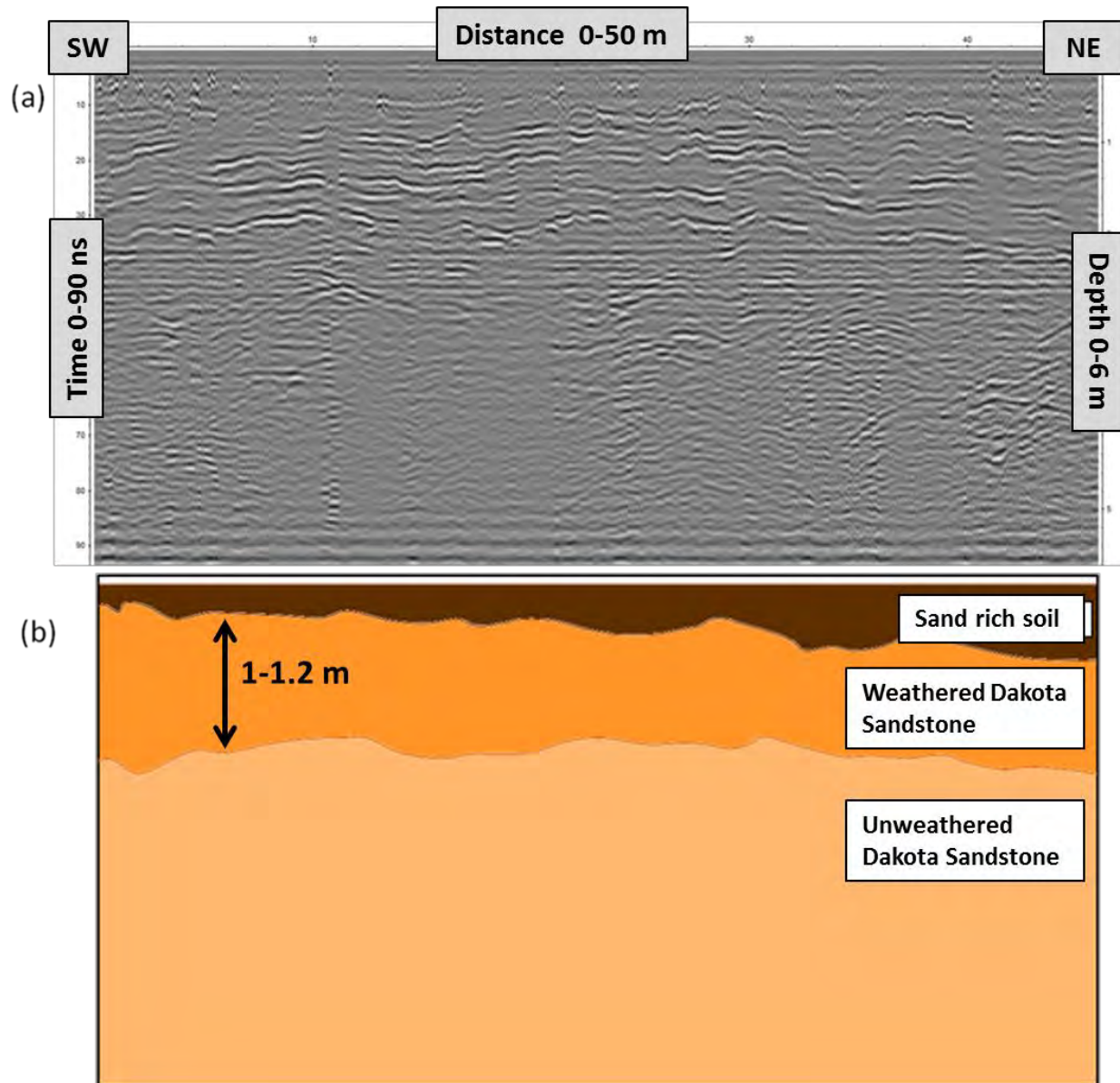


Figure 12.31 Seismic Section at Barn 3 and its interpretation in relation to the Dakota Sandstone

To measure the electrical conductivity using the electromagnetic method, an EM-34 was used to provide maximum depth of investigation. As the line extends over the entire survey and has an estimated depth of investigation of 60m; the upper geologic layers can be observed. From the

petrophysics analysis it was observed that the conductivity of both the Mancos Shale and Dakota Sandstone are 80 mS/m and 40 mS/m respectively. Any faults will be observed as a sharp contrast in conductivity. Figure 12.32 shows electrical conductivity measurements and is overlain by an indication of what shallow layers are dominant in the subsurface. Starting in the northeast, conductivity is very low ( $\sim 5$  mS/s) and sharply but gradually increases to  $\sim 40$  mS/m. This occurs where we expect the Eight Mile Mesa Fault to be and fits how we expect the Dakota Sandstone's response to be significantly lower than the Mancos Shale. Through the length of the Mancos Shale a linear trend of reducing conductivity is observed (from  $\sim 40$  mS/m to  $\sim 10$  mS/m); this trend can be explained due to the thinning of the Mancos Shale towards the peak of the Stinking Springs Anticline in the southeast of the line. As the Dakota Sandstone becomes exposed at the surface and is the dominant shallow rock layer low conductivities are observed of  $\sim 10$  mS/m. This conductivity then increases gradually to  $\sim 25$  mS/m as the Dakota Sandstone thins towards the peak of the anticline and the more conductive Morrison Formation comes into dominance. At northing 4122400 a spike in the data is observed and is considered an anomaly caused by a man made power line interfering with the measurements.

The electromagnetic interpretation fits the geology we expect to see in the shallow subsurface along this survey line. However, where the fault is interpreted, we would expect a less gradual change in conductivity and this could suggest more fine faulting as opposed to just one main fault.

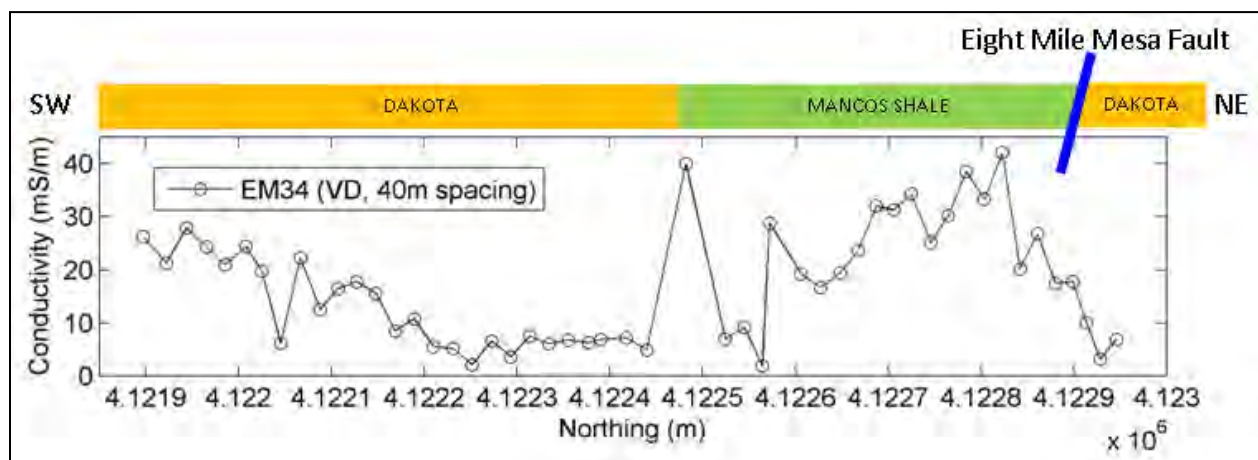


Figure 12. 32 Electrical conductivity measurements of the EM34 at Barn 3 and the interpretation of the geology

The gravity investigation was used to observe contrasts in gravity of the earth across the survey line. The gravity data is expected to follow the shape of the geological layers underlying the line and to show a large contrast over the fault. The dense crystalline basement is expected to influence the gravity data heavily and trends in the data should represent the shape of the basement layer.

The gravity data was forward modelled based on the expected underlying geology as shown in Figure 12.33. As shown there is a sharp change in gravity over where we expect to see the fault. The data also follows the shape of the basement layer; however there are two anomalies in the middle of the line of relatively very low and high gravity respectively. This may be due to either an additional fault system (normal or strike-slip/flower) or from a sharp change in dip of the basement as it approaches the Eight Mile Mesa Fault. More iterations of the forward model with better constraints are required to better fit the model to the geology.

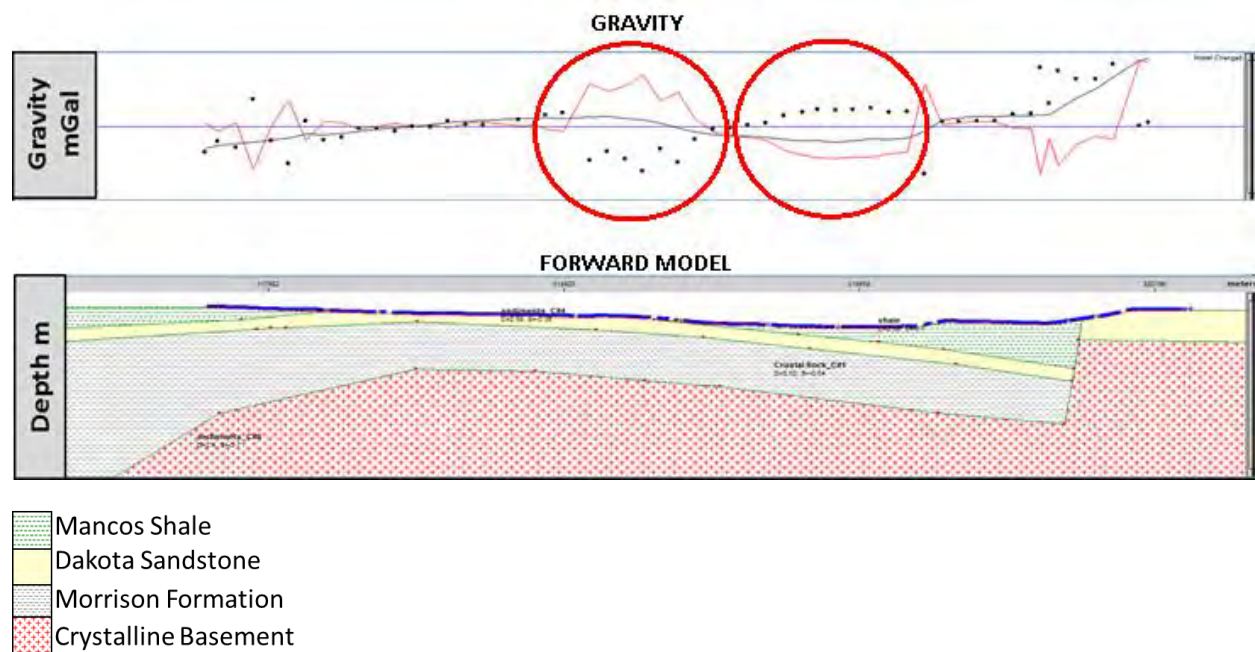


Figure 12.33 Interpreted Gravity data at Barn 3

The deep seismic investigation was used to measure reflected seismic sound waves to provide an image of the subsurface and produce a depth image. Figure 12.34 shows the final depth

converted migrated section of the survey line. At the southwest part of the line we observe a strong reflection at ~380m (1250ft) interpreted in brown to be the top of the crystalline basement. Due to the processing still required to allow full interpretation, the north east section of the line is a preliminary interpretation based on what is expected. Two faults have been interpreted with the northern most fault being the Eight Mile Mesa Fault and just south of that a large additional fault. The throw of the fault is expected to be between 50 and 100 m based on the known geology. Note that the seismic data will undergo further processing to better image the Eight Mile Mesa Fault, additional faults and structural geology.

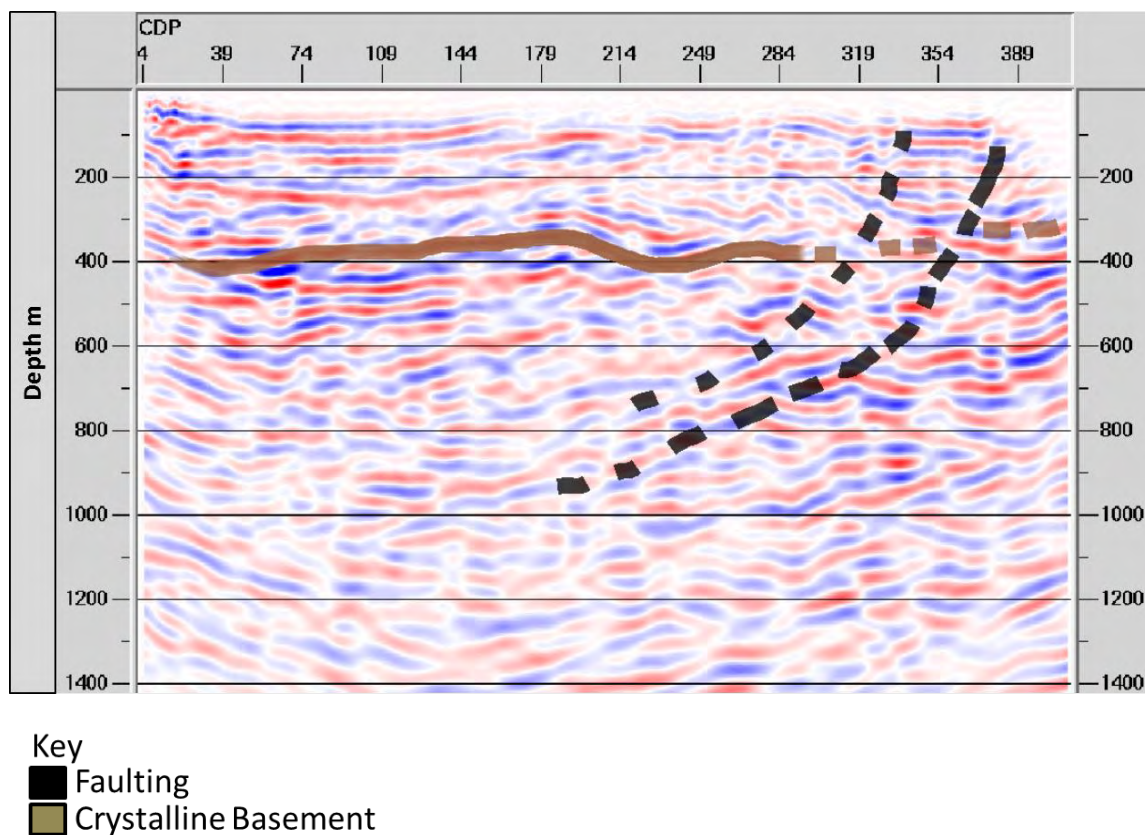


Figure 12. 34 Final depth converted migrated section of Barn 3 with interpretation

### 12.5.3 Conclusions

The known geology of the area is observed by most of the methods used. The gravity data observed the anticlinal nature of the layers. Both gravity and EM observed sharp contrasts over the Eight Mile Mesa Fault as expected, thus the general geology of the area that was expected

was observed. The seismic data successfully recovered the basement reflection. Together these data share anomalies over the central and northeast part of the survey line. These may be explained by additional faulting or sharply dipping layers into the Eight Mile Mesa Fault plane.

## 12.6 North Line Hot Springs

This line was around 1 km long running approximately East-West just north of the Goodman property, Figure 12.36a. The line was chosen to better characterizing the fault systems north of the town. From this we can conclude interesting results as to previously uncharacterized faults and their orientations.

From this section we found two faults located around 250m and 650m down the line respectively, shown in Figure 12.36b. The faults are characterized by sharp changes in conductivity similar to the results from fault found in the East-West PAGO lines located at the warm springs site. Figure 12.36a shows the 2D deep resistivity data collected at this line. Here we can see large conductivity contrasts at around 250m and 650m down the line. These are interpreted to be faults similar to what was found in the other East-West Hot Springs lines.

Samples of calciferous crystals were collected near each of these fault zones which suggest past and/or present hydrothermal water moving along the fracture zones, shown in Figure 12.36b. The most important result however is that we can assume due to local topography that these faults are oriented along the West edge of each ridge and move South towards Pagosa Springs where they likely meet and eventually converge with the large fault found in the other East-West PAGO hot spring lines. This could explain how the current hydrothermal system developed in Pagosa Springs characterized by splaying fracture zones which show evidence of past hydrothermal waters. These faults will be further characterized in the Fall of this year when some students return to produce more DC resistivity coverage North and South of Pagosa Springs.



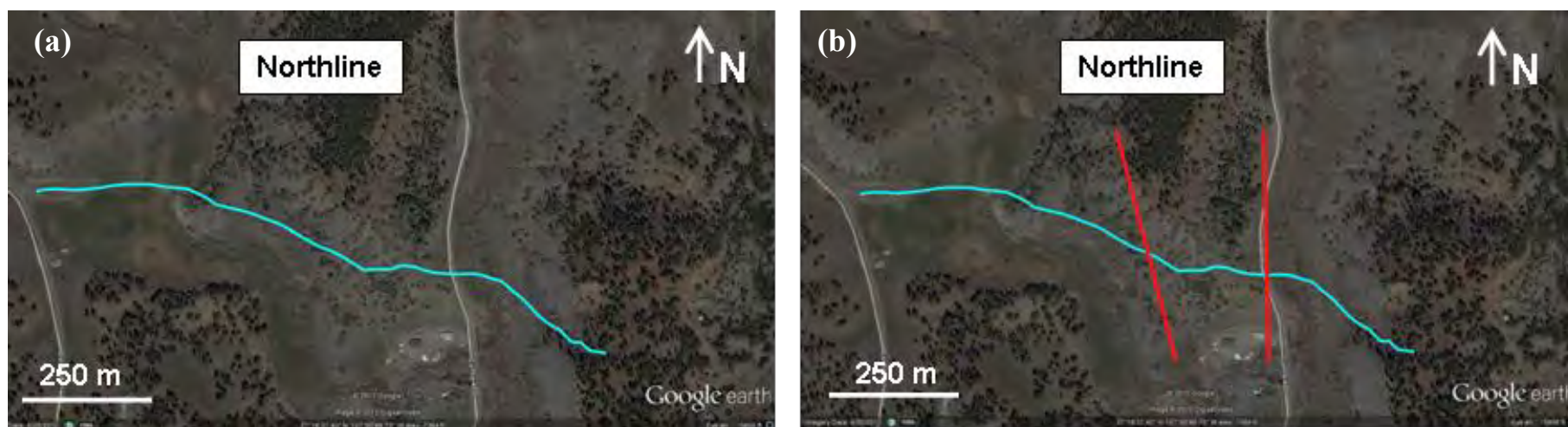


Figure 12.35 (a) Location of Northline – PAGO 08 (blue line) on a Google earth image. (b) Northline with fault plane locations (red lines) superimposed on top.

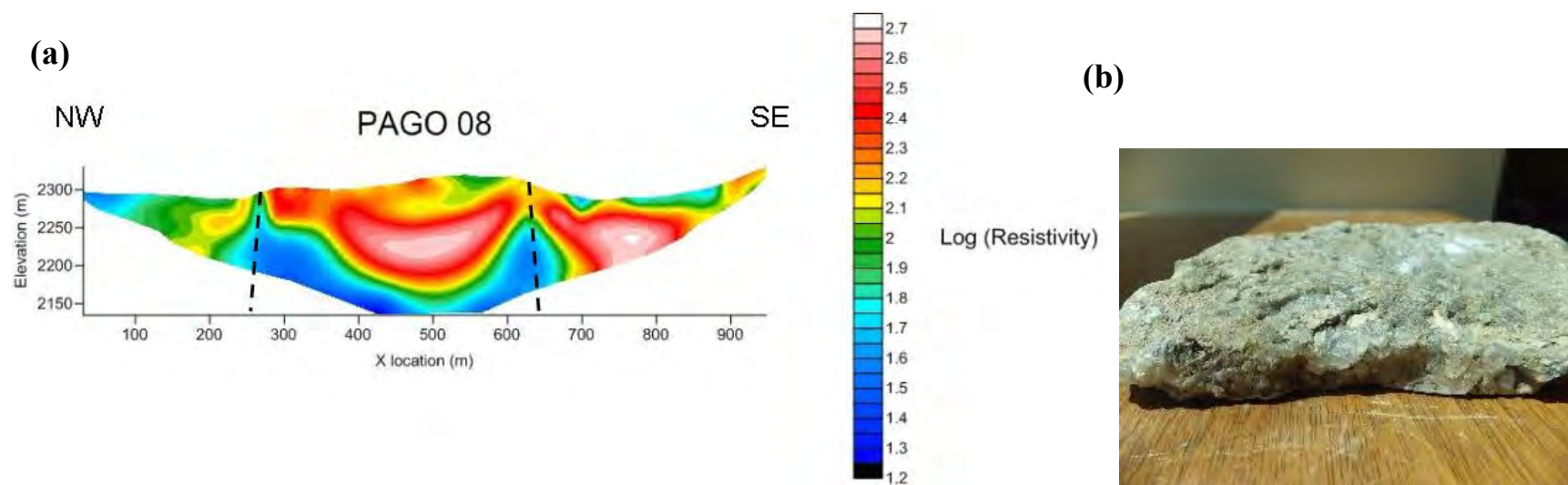


Figure 12.36 (a) 2D deep resistivity data collected at line PAGO 08, Northline site location. (b) Calciferous crystals samples found near both fault zones suggesting past hydrothermal system along fault planes

# 13. Conclusions

---

Through the geophysical investigation done in Pagosa Springs, the known geologic structures were examined and new structures were explored. These structures have importance to the hydrothermal system in the area. Using complementary geophysical methods, new faults and fracture zones were discovered which allowed for a hydrothermal circulation model to be created for the area.

Through the geophysical surveys, several valuable pieces of information were revealed about the geologic structure of the Pagosa hot spring system. First, the seismic results from both the Stevens Airport and the Barn 3 line show that the Eightmile Mesa Fault, and possibly other faults nearby, penetrates the basement material. This discovery shows that faults in the area can penetrate the basement and provide a conduit for deep and hot water transport. These surveys also showed a complex system of faults within the basement material, which could provide an area for cold water to circulate and gain heat deep in the basement.

Geochemical studies have confirmed that the water the hot springs produce is meteoric water, which requires the water to be transported along layers and conduits in the subsurface. By examining data from the P-1 well drilled within city limits, it was confirmed that a significant amount of fluid travels updip along the highly fractured Dakota sandstone and along the contact between the Entrada formation and the basement material. Through studies of EM, magnetic, gravity, electrical and GPR methods at the Zen Garden site just south of the Mother Spring, it was confirmed that the fluids flow near the surface in that area. This discovery shows that the fracture zones occur in and around the area of the Mother Spring, providing a conduit for the flow of hot fluids through the otherwise impermeable Mancos Shale that dominates the surface exposures at the Mother Springs site.

Finally, several previously undiscovered faults were found in the area around the Pagosa Hot Springs (Figure 13.1). A web of DC resistivity lines southwest of the Mother Springs identified a large north-south trending fault along the western ridge (Figure 13.2). For the purposes of this investigation, this fault will be referred to as the Victoire Fault. Other methods such as EM, magnetics, and gravity confirmed this fault's presence. Field samples of igneous rocks gathered along one of these lines indicated that small amounts of magma may have traveled up the fault to produce a small dike structure. Although it is hard to determine fault geometry, using known features in the area, the fault was interpreted to be a steeply dipping normal fault dipping towards the west.

With continued exploration, another DC resistivity line was constructed north of town which allowed

the discovery of two more faults only a few hundred meters apart, trending north to south (Figure 13.3). We interpreted this to be a fault system following the ridges in the area corresponding to the stresses of an extensional basin, similar to the Victoire fault. However, DC resistivity was the only method used at this site, and further studies will be needed to determine the exact characteristics of these faults and their relevancy to the larger geothermal system.

Given these pieces of evidence, a geothermal system can be constructed and provide an explanation of how and why hot water reaches the surface at Pagosa Springs (Figure 13.4). Based on drill reports, water enters the system through the highly fractured Dakota Sandstone and along the Entrada-Pre Cambrian contact, the water travels on an updip. Because both of these formations are deep below the surface downdip of Pagosa Springs, this flow continues uninterrupted until it encounters the Victoire fault. We suspect this fault penetrates the basement due to the results of the DC resistivity lines, which show an area of high resistivity on the east side of the fault characteristic of the Dakota sandstone. In order for this to occur, this fault needs a throw in excess of 150ft, which allows it to be large enough to penetrate the basement. The presence of dike material along this fault supports this theory, as magma would likely originate within the basement material. When this fault crosses the Dakota Sandstone and the Entrada-basement contact, cold water can flow down it to penetrate the basement material. Fractures within the basement material allow the water to remain in the basement for long periods of time, allowing for a heat source in the basement, likely the natural geothermal gradient, to heat the water to high temperatures. This water becomes less dense as the water increases in temperature, allowing it to flow back up Victoire's fault and back into the western member of the Dakota sandstone where it reenters the fractures. The water does not continue back up the fault because meteoric water entering the fault will eventually seal the fault with precipitates such as calcite derived from calcium carbonates within the Mancos Shale. The samples collected on the north line (PAGO08) consisting of crystalline calcite filling in small fractures supports this proposed concept. This concept is also confirmed by the P-1 well, which reported hot water emerging from fractures within the Dakota Sandstone as well as from faults penetrated deeper in the subsurface. Finally, this water can enter minute fractures in the Mancos Shale that intercept the Dakota Sandstone, allowing it to travel through the impermeable layer in high concentrations and emerge at the surface at the Pagosa Hot Springs.

Because of other springs in the area that report occurrences of hot water, it is likely that this system holds in the area between the Victoire fault and the first Dakota Sandstone exposure east of the Eightmile Mesa Fault. This is confirmed by the warm springs system which occurs directly south of the Mother Spring as well as the locations of other springs reported in the area, which occur along a linear system between these two features. Contrary to initial suspicions, the Eightmile Mesa Fault is not crucial to the geothermal system even though seismic surveys confirm that it penetrates the



basement. This is because the Victoire fault cuts off the Dakota Sandstone which carries the system's main source of cold water, removing the majority of water from the member that encounters the Eightmile Mesa Fault. Finally, the faults interpreted along the north line may be similar to, or even an extension of, the Victoire fault and may allow this system to extend northward. However, more data will be necessary to positively confirm this theory as part of the system.

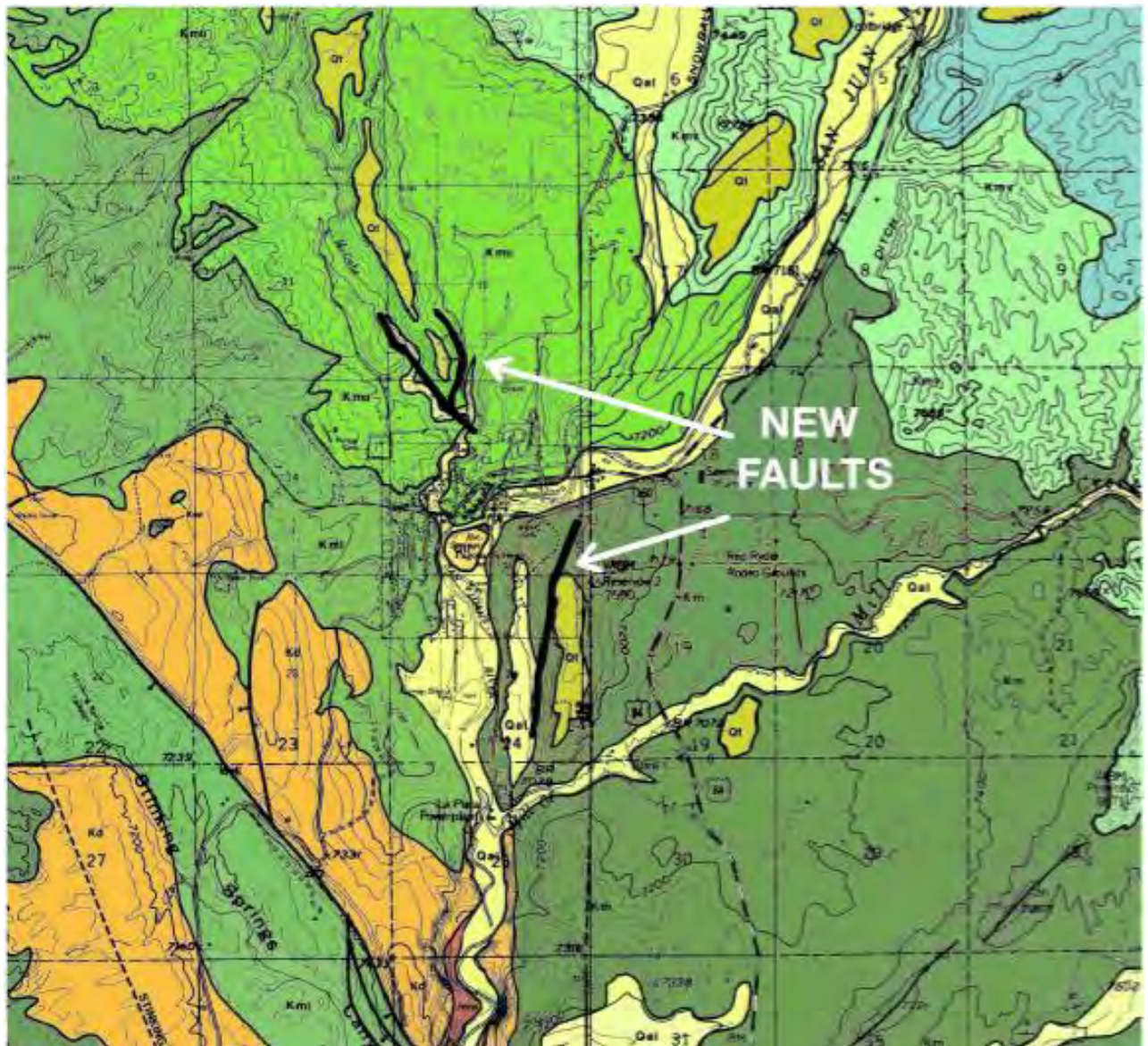


Figure 13. 1: Subset of geologic map showing locations of interpreted faults (in black).



Figure 13. 2 Interpretation of the location of the Victoire fault with the Hot Spring lines.





Figure 13. 3 Interpretation of the location of the Northline faults with the Northline survey.

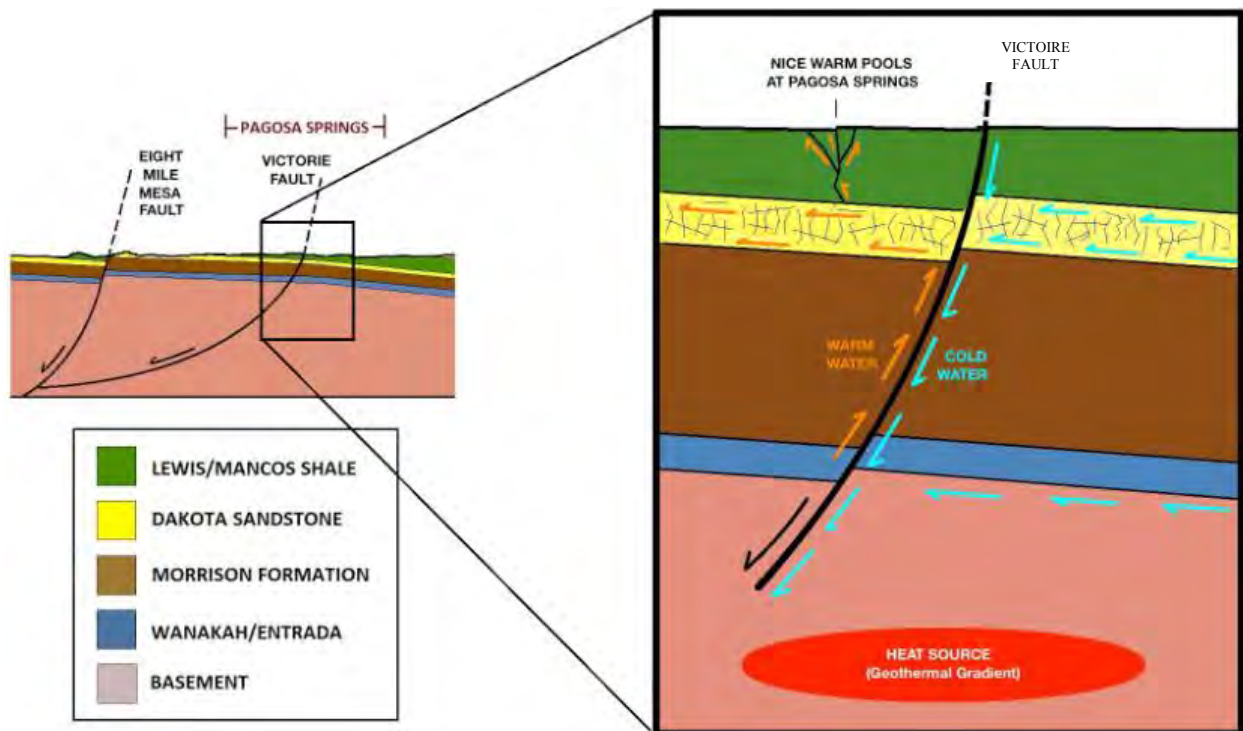


Figure 13. 4 Geothermal system of the Pagosa Hot Springs with associated cross-section.

# 14. Recommendations

---

This investigation of Pagosa Springs provided a greater insight to the geothermal system beneath Pagosa Springs. However, further characterization is needed, and there are many aspects of this investigation that require improvement and future work.

Much of what could be improved in this investigation lies in the extent and completeness of the surveys conducted. Along the Steven's Airport deep seismic line, the largest shortcoming was the inability to provide a strong image of the Eight Mile Mesa Fault. To improve this, it would be necessary to extend the south end of the line further south past the golf course, and increase the number of shots taken. The combination of these two changes would allow the fault to be seen more clearly and to image a larger portion of the fault. At the Zen Garden site, the survey should be redone for each method with the lines perpendicular to their current location. After further examination, it was determined that the fluid flow in that site was perpendicular to the lines, and changing the survey in this way would allow us to better image and characterize this flow pattern. After talking to Matt Meese, the owner of the land where the Zen Garden survey was conducted, it was explained that several springs known as the "Hippie Dip" had been filled in several decades prior to this investigation were located south of the survey site. Re-performing the Zen Garden survey at this site may provide greater insight into the geothermal system, particularly the fracturing and fluid flow in the Mancos shale at this location. Extending the Northline survey into a grid would create a better image of the suspected faults found during the initial survey. The scope of this survey could be extended with the other DC resistivity lines in the area to create a 3D resistivity model of the area, which would help better characterize both the geology and the fluid flow of the area and improve the final model. To better help the town itself, it would be useful to investigate better ways to evaluate their current geothermal piping system. The initial attempt failed to image the pipes correctly, so future investigation will be necessary. Finally, more field samples would be taken, and a better analysis of the surrounding geology would be used to improve the quality of the geologic observations in order to correlate with the geophysical data when the data is processed back in the lab.

Colorado School of Mines is planning a future investigation of the Pagosa Springs hot springs system to improve upon this investigation. These surveys will primarily utilize the DC Resistivity and related methods, focusing on conductivity contrasts to characterize the presence and flow of water as well as changes in the shallow geology. This investigation will re-perform and extend some of the surveys in this investigation as well as construct new lines in the area. One of these new areas will be an extension of the Northline survey. The initial investigation showed two faults with a small separation

north of the city of Pagosa Springs. With more lines the extent of these faults as well as their depths, the geology that these structures create, and finally if and how fluid flows within these faults would be better characterized. Investigations south and east of the Zen Garden and Hot Springs site would be used as well. This would help us better characterize the length and offset of the Victoire fault, as well as help determine if other faults are in the area that could help improve the system, particularly east of the current sites. Further locations are also being planned for this investigation, which should take place sometime in the September of 2012.

# Appendix A

---

Please note: The processing flows for the Steven's Airfield and the Barn 3 lines are very similar. For brevity, the figures and descriptions in this section deal only with the Steven's Airfield line, unless otherwise stated.

## A.1 Initial Processing

Seismic processing aims to convert hundreds of individual shot records into a faithful image of the subsurface. Accurate geometry data is essential for this task, and the positions of each receiver and source point were obtained to a high level of accuracy (on the order of centimeters) by the use of Differential GPS for both lines. The geometry data is then input into ProMAX with the shot records.

Before seismic processing begins, the data must be displayed. Data can be displayed in different viewing types. These include wiggle view, variable area view, variable density, etc. After displaying the data, the editing begins. This step entails removing bad data such as bad channels, bad shots, excessive noise, etc. This is a tedious but vital step that requires human judgment and intervention. After having edited the data, an amplitude correction is applied to the data. There are two types of amplitude corrections which are deterministic and data-dependent amplitude correction. The goal of this step is to get "true" amplitude recovery and amplitude balancing. This step is often applied as a preconditioner for other processes. Deterministic amplitude correction is used for true amplitude correction. This step corrects for propagation effects. We used spherical divergence for our deterministic amplitude corrections. Spherical divergence is a principle that states that there is apparent loss of energy from a wave as it spreads during travel. Thus, the spherical divergence processing method compensates for an expanding wavefront. For spherical divergence we multiplied the amplitudes by two way time squared. We also dealt with the Airblast Attenuation which we used a 350 ms envelope for with a velocity of 331m/s. One then begins to filter the data. This step in processing has a lot of different types of methods and applications in its arsenal to be used. Bandpass filter is one of these filters. It controls the spectrum of output and can exploit spectral differences between signal and noise. Because noise is often localized at particular frequencies, a bandpass filters is able to remove the noise by filtering those frequency that represent the noise. The bandpass filter that we applied was 5-10-60-120 Hz. Thus, it filtered



the high frequencies of 60 Hz and above that were recorded. After amplitude correction and filtering is applied, the amplitudes must be balanced. One can use Automatic Gain Control (AGC). Automatic Gain Control (AGC) is a system which controls the gain, or the increase in the amplitude of a signal from the original input to an amplified output, automatically. AGC is often used in seismic processing to improve visibility of late-arriving events in which wavefronts divergence or attenuation has caused amplitude decay. For our initial AGC, we used a 1000 ms window. After having completed all these steps, the initial processing is done.

## **A.2 Shot Records**

Seismic surveys record individual shot records, which record two-way travel time on the vertical axis and channel number on the horizontal. As discussed in the report, the wave nature of the energy passing through the subsurface means that several physical effects may be recorded at the same time. In a typical shot gather, we expect to see a direct wave, ground roll, refractions and reflections. Figure A. 1 shows two example shot records from the initial data.

A direct wave, or airwave, travels from source to receiver through the air. It travels at the sonic velocity of air,  $330 \text{ ms}^{-1}$ , which is far slower than all subsurface velocities. Importantly, the velocity of a wave on the shot record is inversely proportional to its slope; so a slow velocity airwave manifests itself as a very strongly dipping linear event.

Ground roll is the name given to energy travelling from shot to receiver across the surface layer as a Rayleigh wave. Again, its velocity tends to be slower than p-wave velocities in rock, but greater than the airwave. As a result, we see ground roll as the second most strongly dipping linear event.

Refractions travel along an interface between two rocks layers at the speed of a p-wave in the second medium, they then break off and travel back up towards the receivers. As velocities tend to increase with depth, refractions are seen as weakly dipping linear events on the record.

Reflections are the main target of seismic processing, with each step undertaken with the aim of reducing the noise in the data and preserving reflections. In a simple horizontal reflector

model of the subsurface, reflections have hyperbolic behavior with offset. This is known as Normal Moveout (NMO), and must be corrected for in order to make a horizontal reflector appear as a flat event in the data. This will be dealt with later. Presently, it is enough to know that reflections appear as hyperbolae on a shot gather.

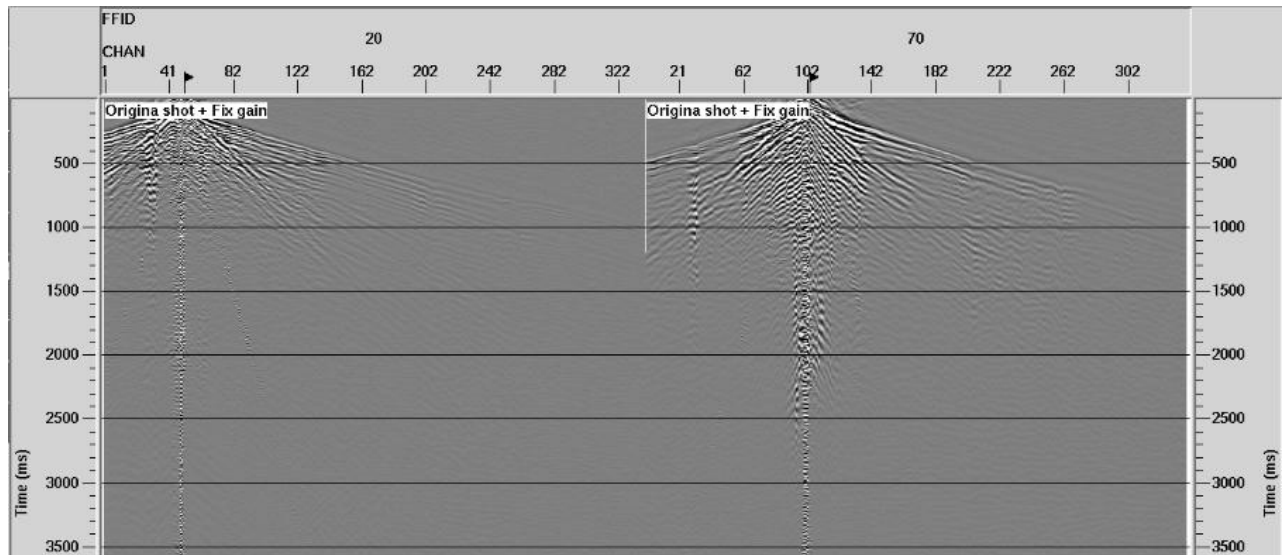


Figure A. 1 - Example initial shot records

### A.3 Filtering and Deconvolution

An FK filter was applied to the dataset to discriminate events by their velocity and remove noise. By transforming into the FK domain, noise trends can be identified and removed from the data. The process is particularly good at removing the ground roll. It contains no geological information but is of fairly high amplitude; making its removal highly desirable. As the airwave travels with the sonic velocity of air ( $330\text{ms}^{-1}$ ), which is far below rock travel times. The airwave is removed by application of the “Airblast Attenuation” module in ProMAX. Figure A. 3 illustrates the reduction in the airwave and ground roll, particularly at shallow depths, leading to an improvement in the signal to noise ratio.

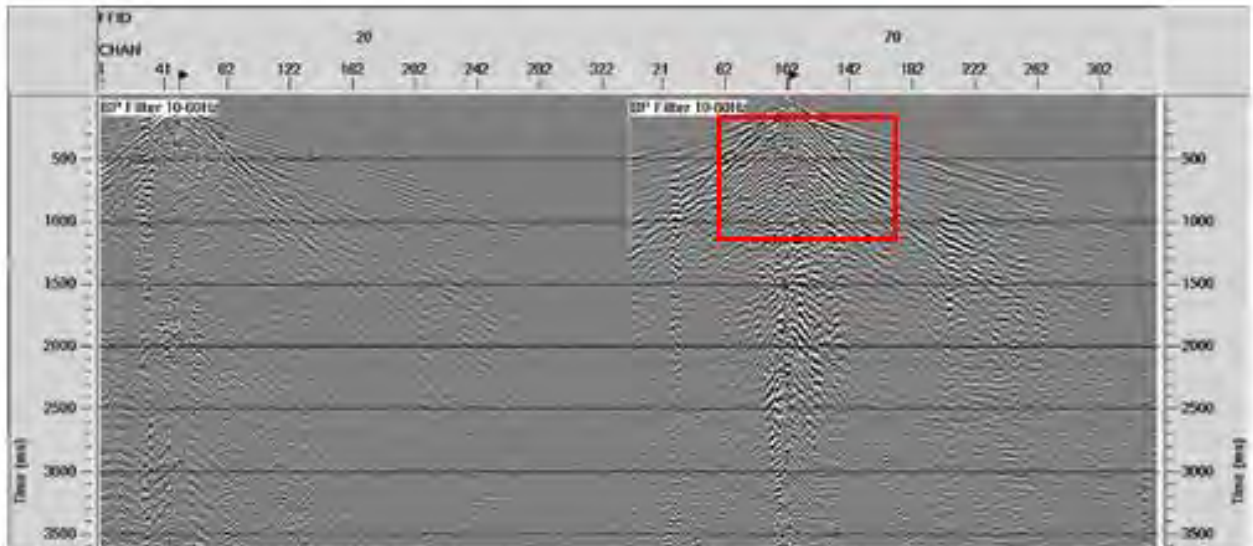


Figure A. 2 - Post bandpass filter (10 - 60 Hz), AGC Applied.

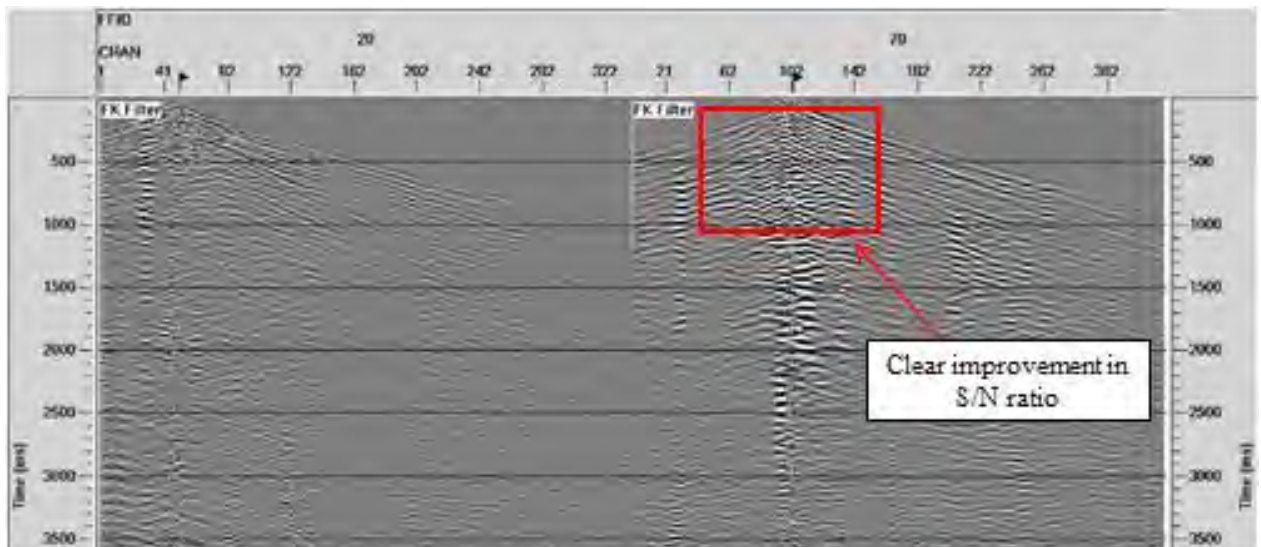


Figure A. 3 - Post FK filter. AGC applied. FK filter has attacked the ground roll whilst the Airblast Attenuation module has targeted the airwave, leading to an improvement in the signal to noise ratio compared to Figure A. 2 .

Predictive deconvolution was carried out with the aim of suppressing any short period multiples or reverberations in the data. The process aims to remove events which are periodic in time by zeroing a range of the autocorrelation function, known as the operator length, whilst leaving the first predictive lag of the autocorrelation untouched to preserve the wavelet. Several tests were carried out to determine the optimum predictive lag and operator length. These were chosen as 32ms and 240ms, respectively, with the result shown in Figure A. 4

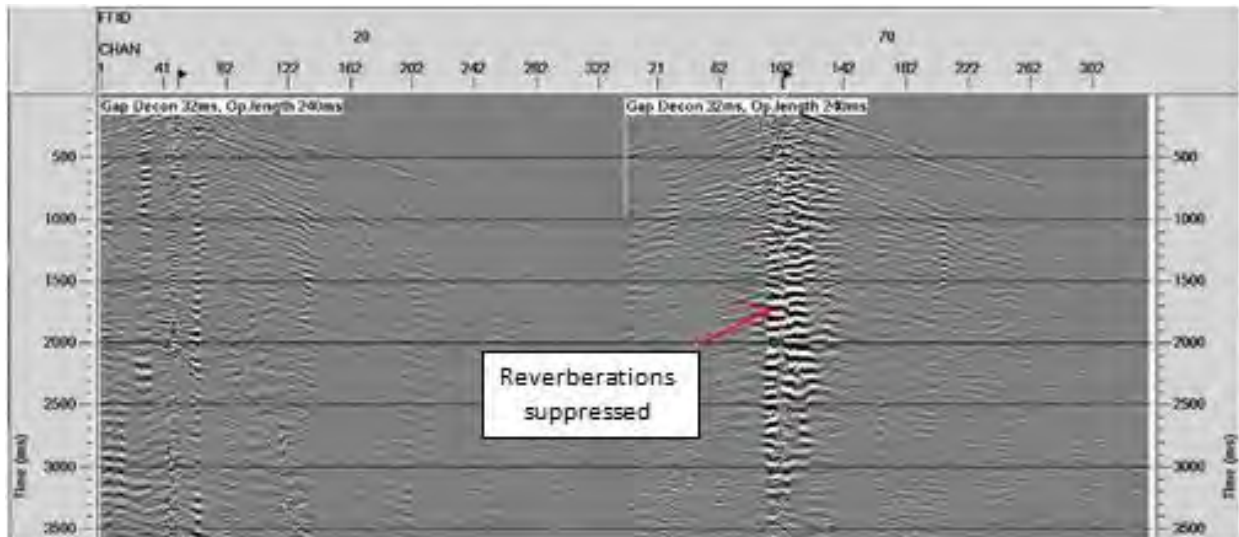


Figure A. 4 - Post predictive deconvolution. AGC applied. Short period multiples and reverberations suppressed

#### A.4 Static Corrections

Static corrections were made to the data. This is achieved by picking first breaks on all shots and making the assumption that rays travel vertically within the weathering layer. This allows the static corrections to be made purely as time shifts. The datum was set as 2300 m with a replacement velocity of  $1700\text{ms}^{-1}$ . A top mute was then applied to the data to clean up and remove as much of the refraction data as possible whilst taking care to conserve reflections.

#### A.5 Velocity Analysis

The data are now ready for Common Depth Point (CDP) sorting and stacking, which converts shot records into a subsurface image. To achieve this, an initial velocity field was created by picking velocities on a semblance plot. Semblance plots show bright spots where a velocity leads to the best NMO correction; i.e. a maximally flattened hyperbola. An example of a picked semblance plot is seen in Figure A. 5 below. These semblance plots were picked every 25 CDPs before being smoothed to create the final velocity field.



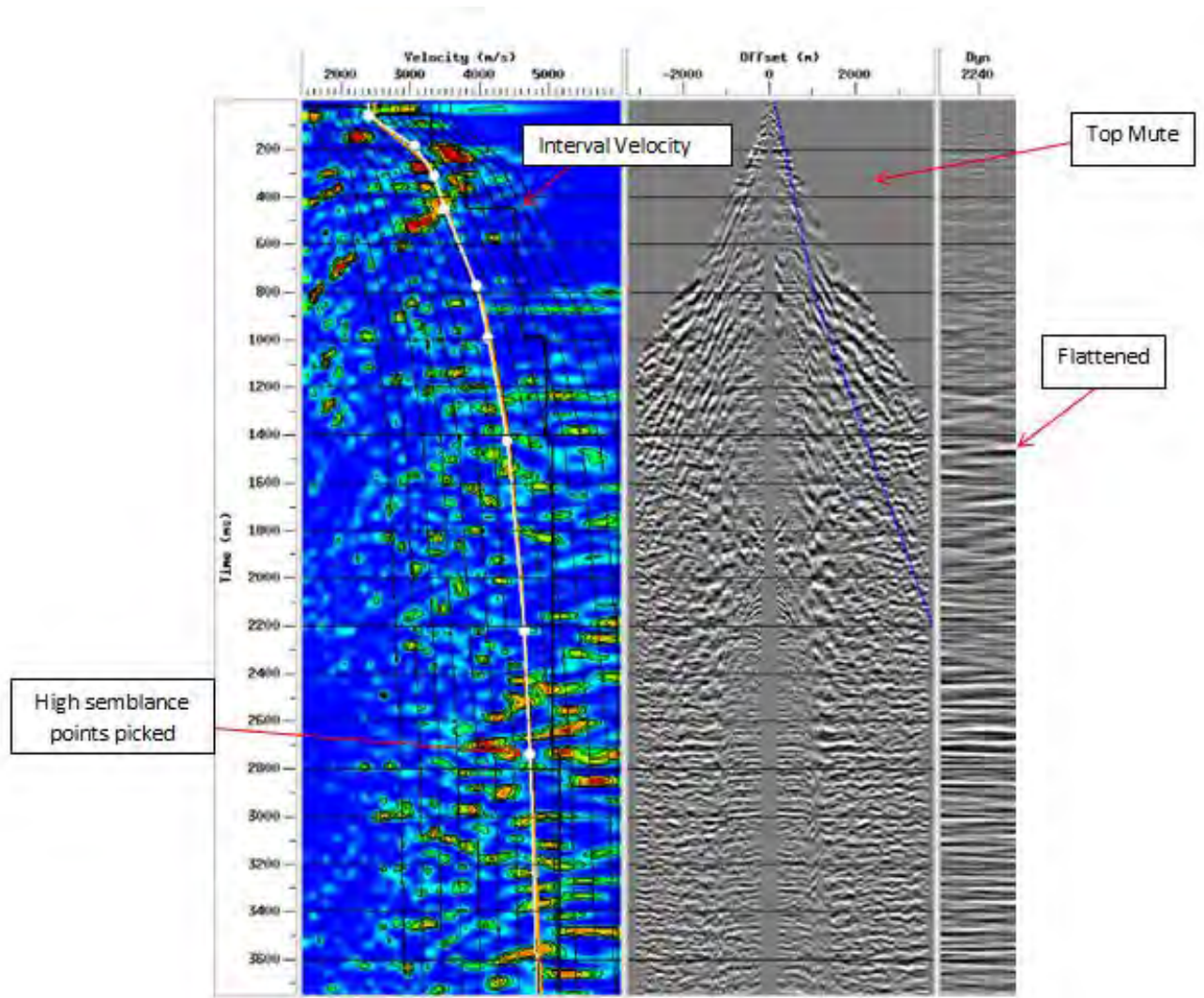


Figure A. 5 - Velocity Analysis. Example semblance plot (left) picked to maximally flatten gathers

Applying NMO corrections leads to stretching in the far offset; this must be removed by use of an NMO stretch mute. The resulting stacked section is shown in Figure A. 6.



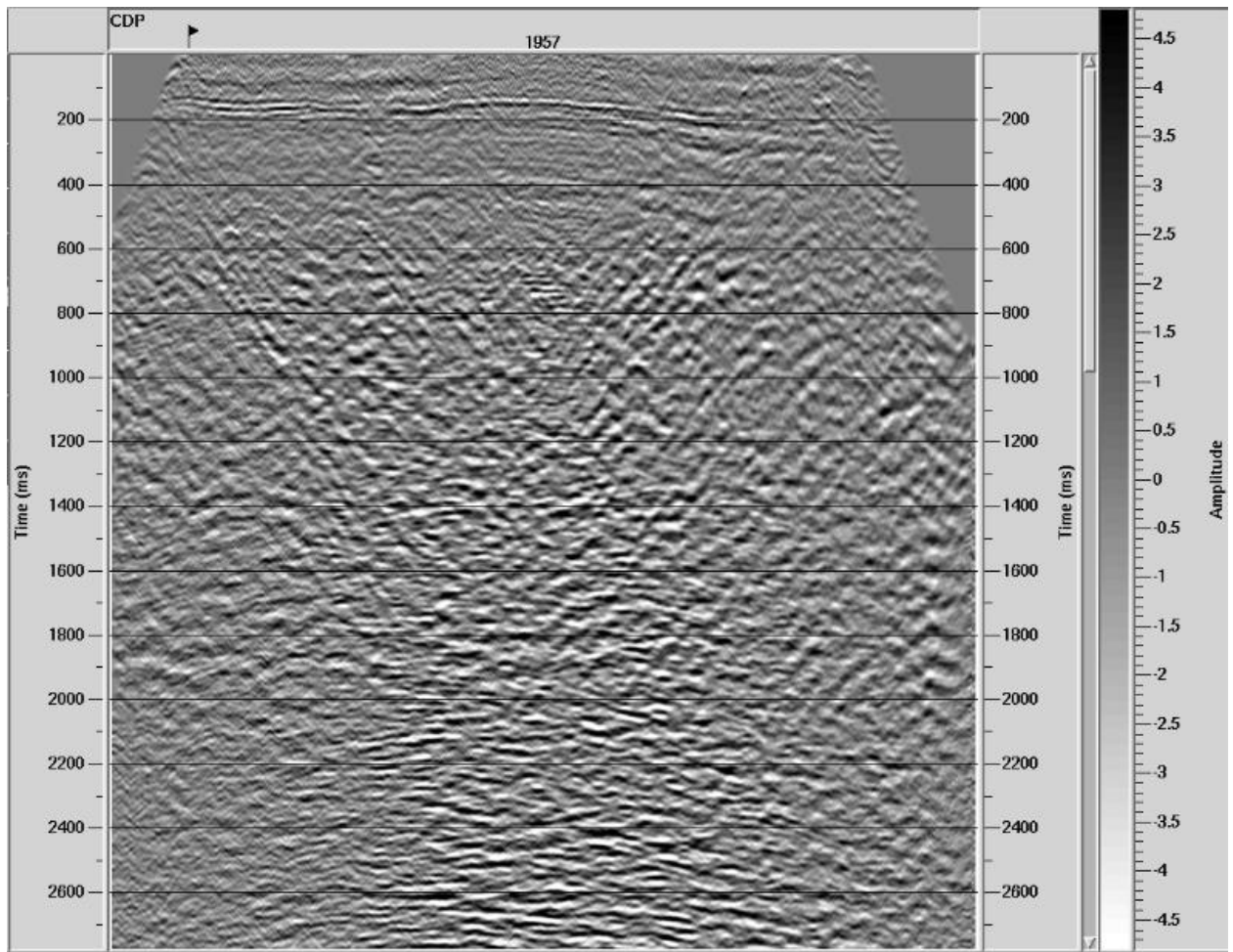


Figure A. 6 - First pass velocity stack (Stevens Airfield Line)

The accuracy of any velocity analysis is limited by several factors. Therefore, three velocity models are created iteratively. Each model makes revisions on the previous model in order to work towards the most suitable velocity field for stacking and migration. The final velocity fields for the Stevens Airfield line Figure A. 7 and the Barn 3 Figure A. 8 line are shown below. One can see that velocities vary from around  $3000 \text{ ms}^{-1}$  in the near surface to around  $6000 \text{ ms}^{-1}$  deeper.

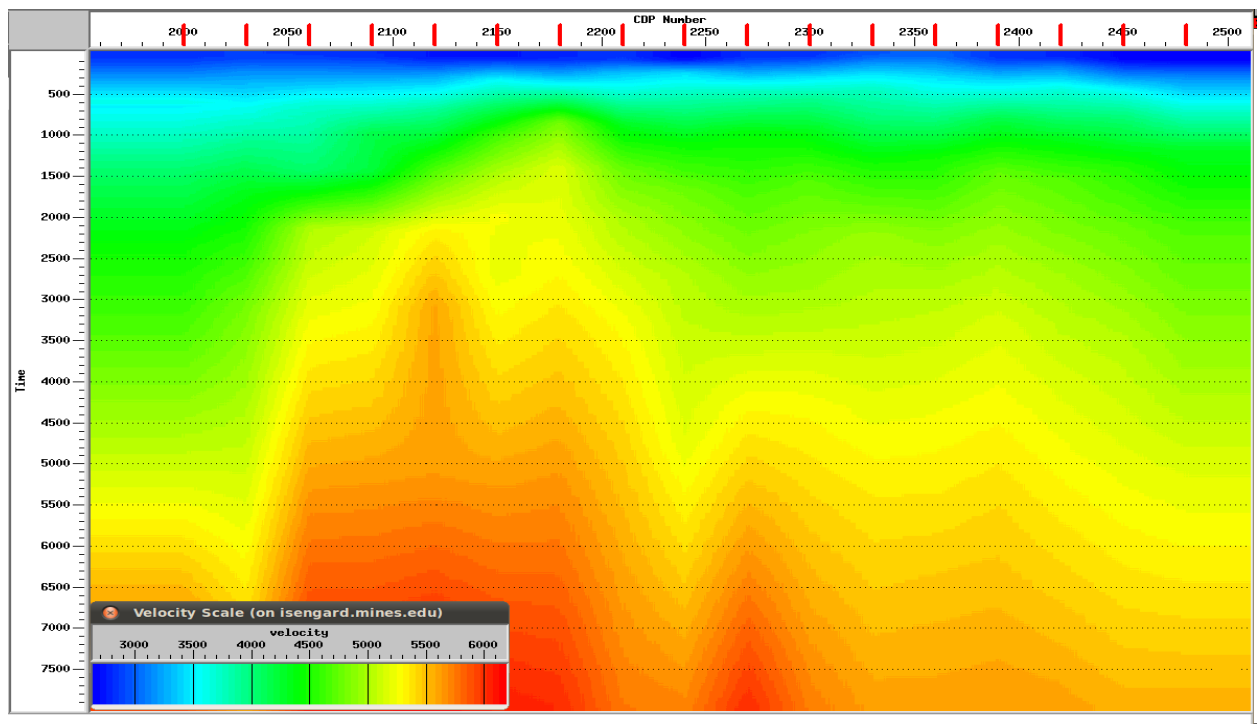


Figure A. 7 - Final velocity field, Stevens Airfield line

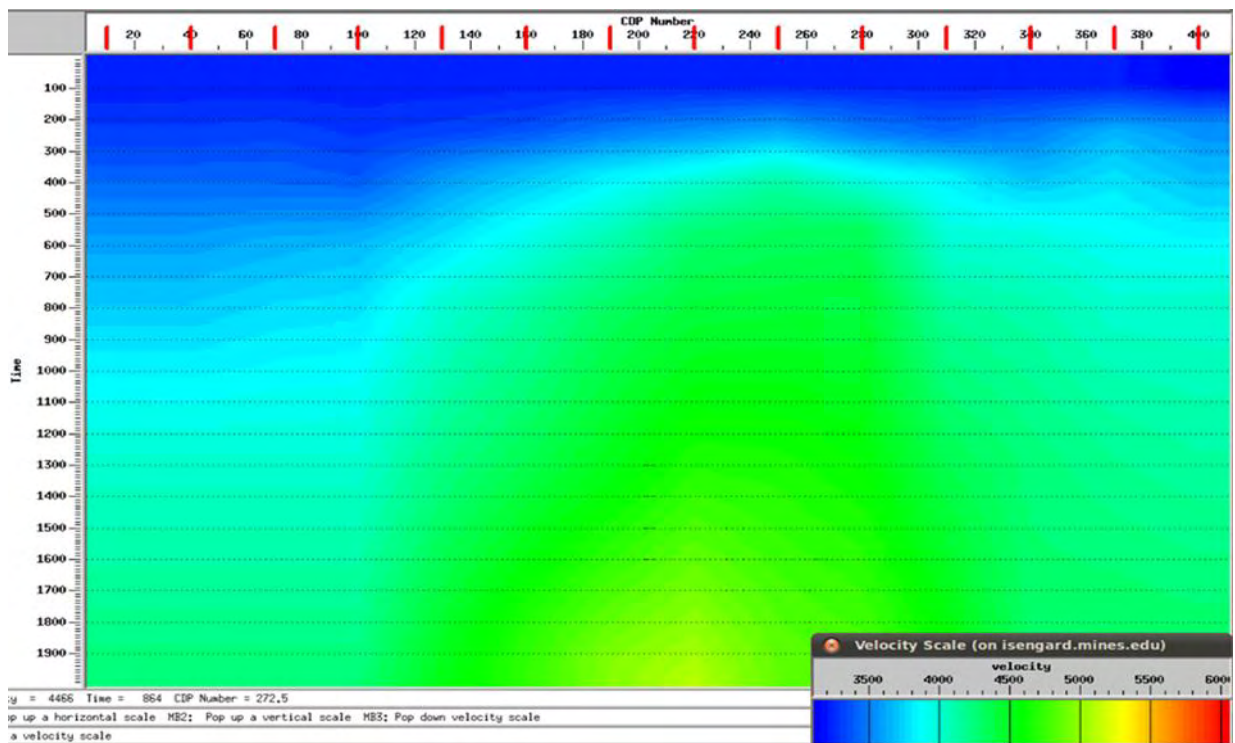


Figure A. 8 - Final velocity field, Barn 3 line

## A.6 Migration

One of the most important steps of processing is migration. A 2D stacked section, as we currently have, is not a true representation of the subsurface; reflections are not reflectors. Migration is the process of shifting reflection events to their true geological position and dimensions.

Migration may be carried out with a number of methods and either pre or post stack. Whilst various factors result in pre-stack migration being accepted as the more accurate method, it is far more expensive in terms of computing power and time. Pre-stack migration is particularly superior when dealing with very complex structural geology. However, with the general geology of the subsurface layers expected to be relatively simple, gently dipping at 8 degrees, post stack Kirchhoff migration was considered more than sufficient for the task. Due to computational power and time constraints, more advanced pre-stack migration methods were not tested. For example, dip-moveout (DMO) was not carried out due to the lack of complex, dipping layers.

Kirchhoff migration is based on the idea that all data can be built up from point reflections, with the final reflector image resulting from the sum of all point reflections. This method can handle any structure, including steep dips up to 90 degrees and may be easily adapted to any velocity behavior.

Migration was carried out twice, with fixed velocity field of  $3000 \text{ ms}^{-1}$  and with the smoothed RMS final pass velocity analysis field. As expected, the latter gives the best migrated image. The unmigrated images and final pass velocity migrated images are shown for the Steven's Airfield in Figure A. 9 and Figure A. 10. For Barn 3, see Figure A. 11 and Figure A. 12.

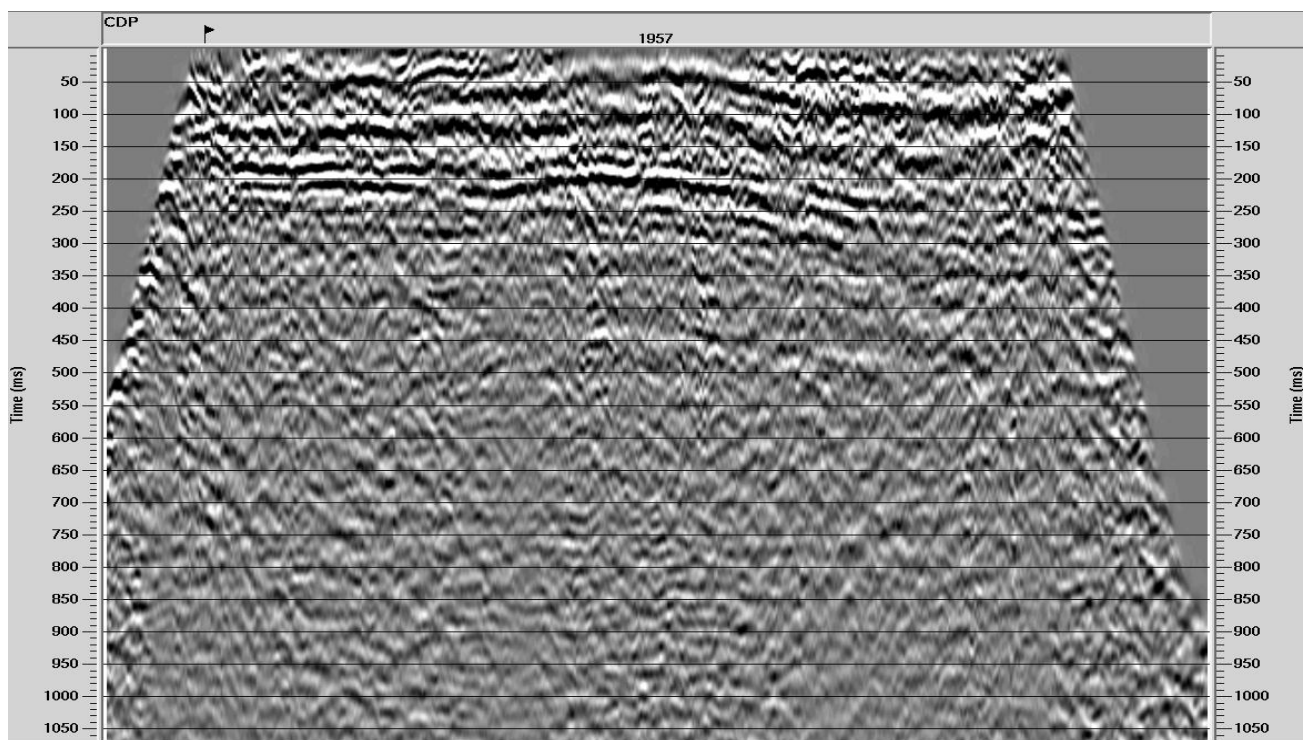


Figure A. 9 - Stevens Airfield, unmigrated

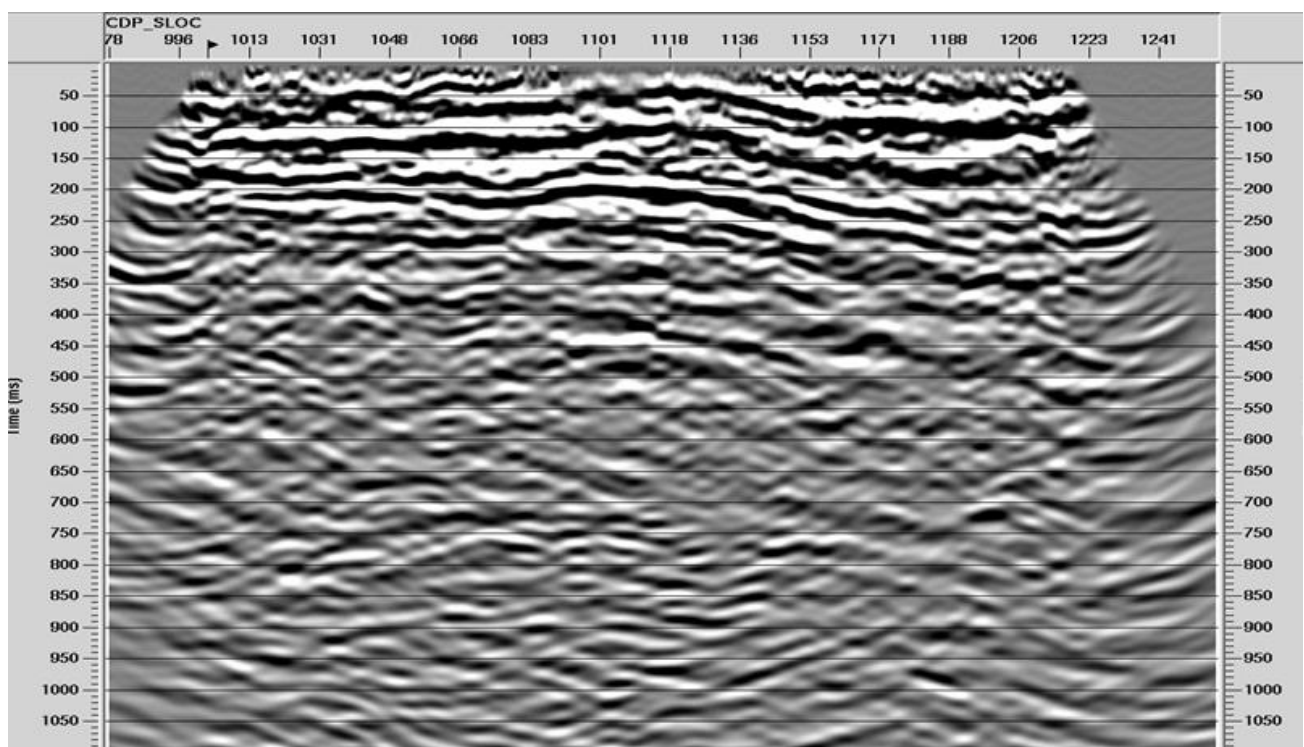


Figure A. 10 - Stevens Airfield, after post-stack Kirchhoff migration



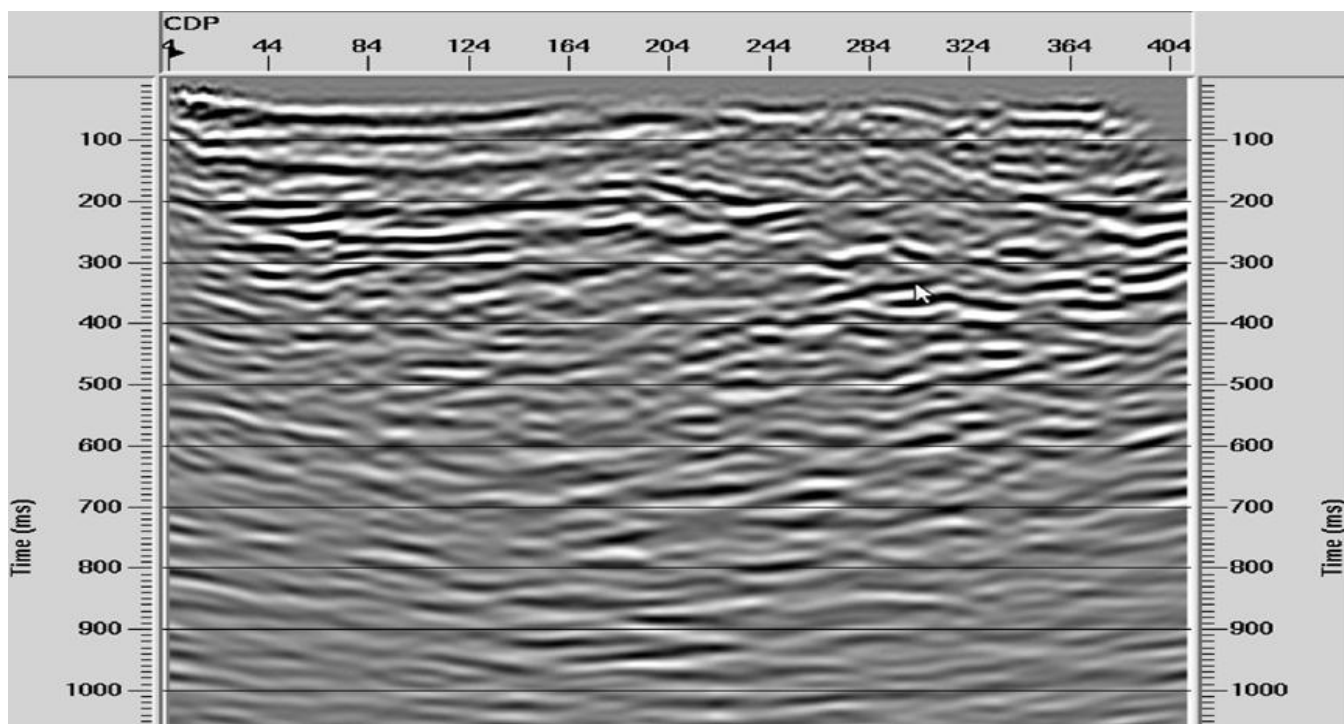


Figure A. 11 - Barn 3, unmigrated

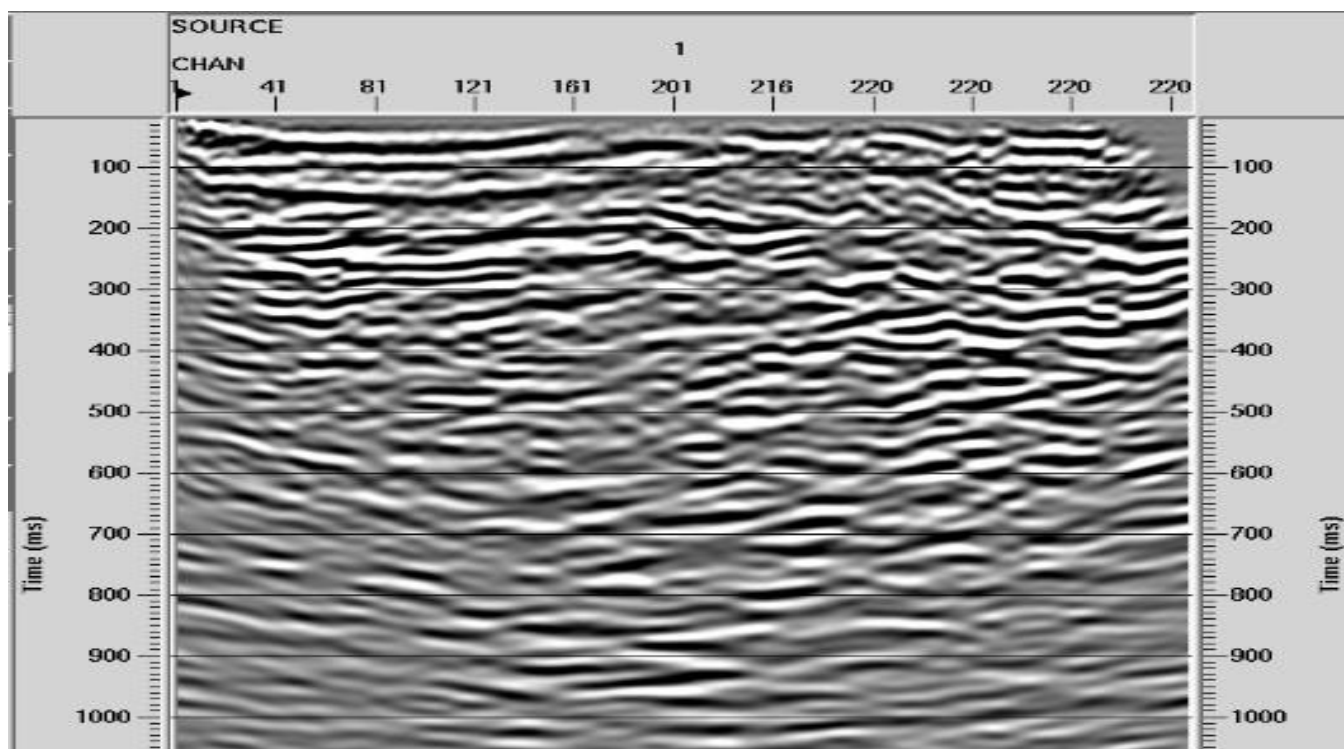


Figure A. 12 - Barn 3, after post-stack Kirchhoff migration



### A.7 Depth Conversion

The seismic sections created so far have remained in the time domain. Depth migration is the process of converting a seismic section from the time domain into the depth domain by use of a velocity model.

A simple depth conversion was carried out on both lines by picking a central velocity model and extending it across the survey. For the airport line, the depth conversion velocity function was picked at CDP 2240. For the Barn 3 line, the function was picked at CDP 190.

The depth converted sections are displayed as Figure A. 13 and Figure A. 14 for the Stevens Airport line and Barn 3 line respectively.

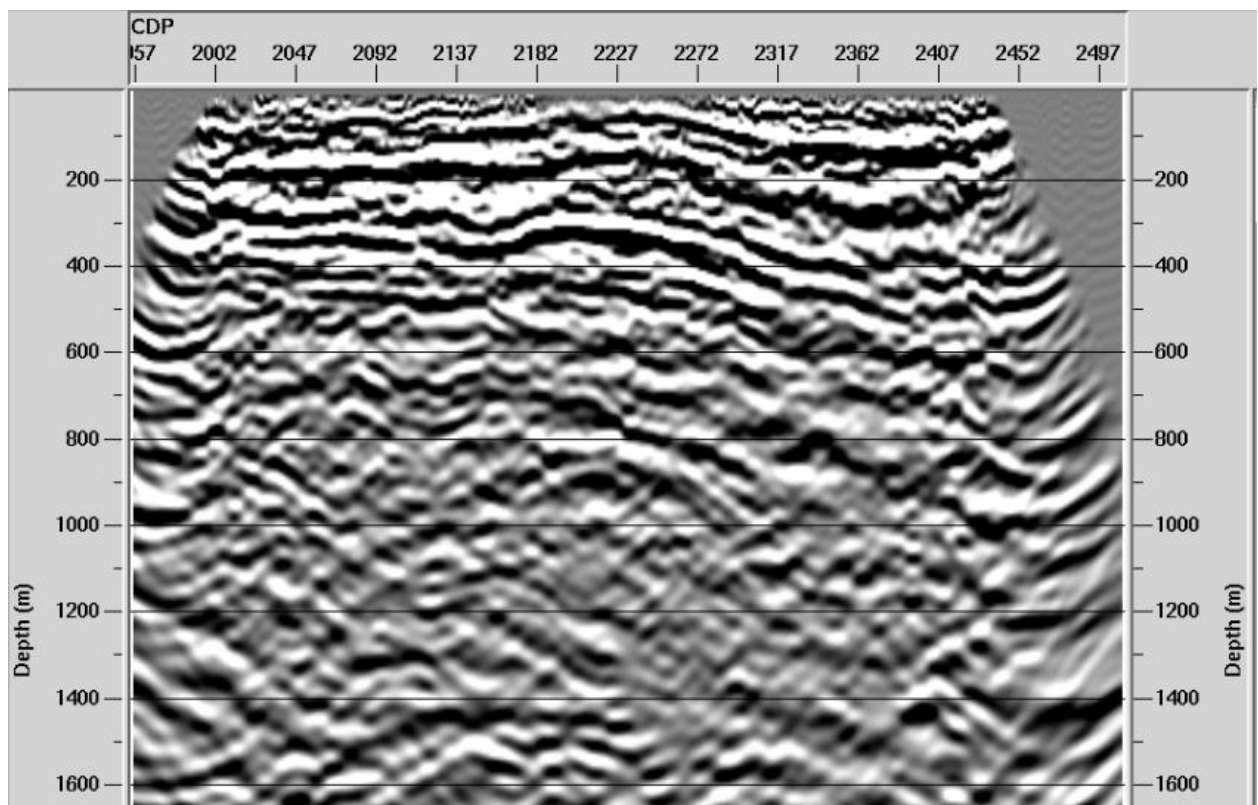


Figure A. 13 - Depth converted Stevens Airport Line

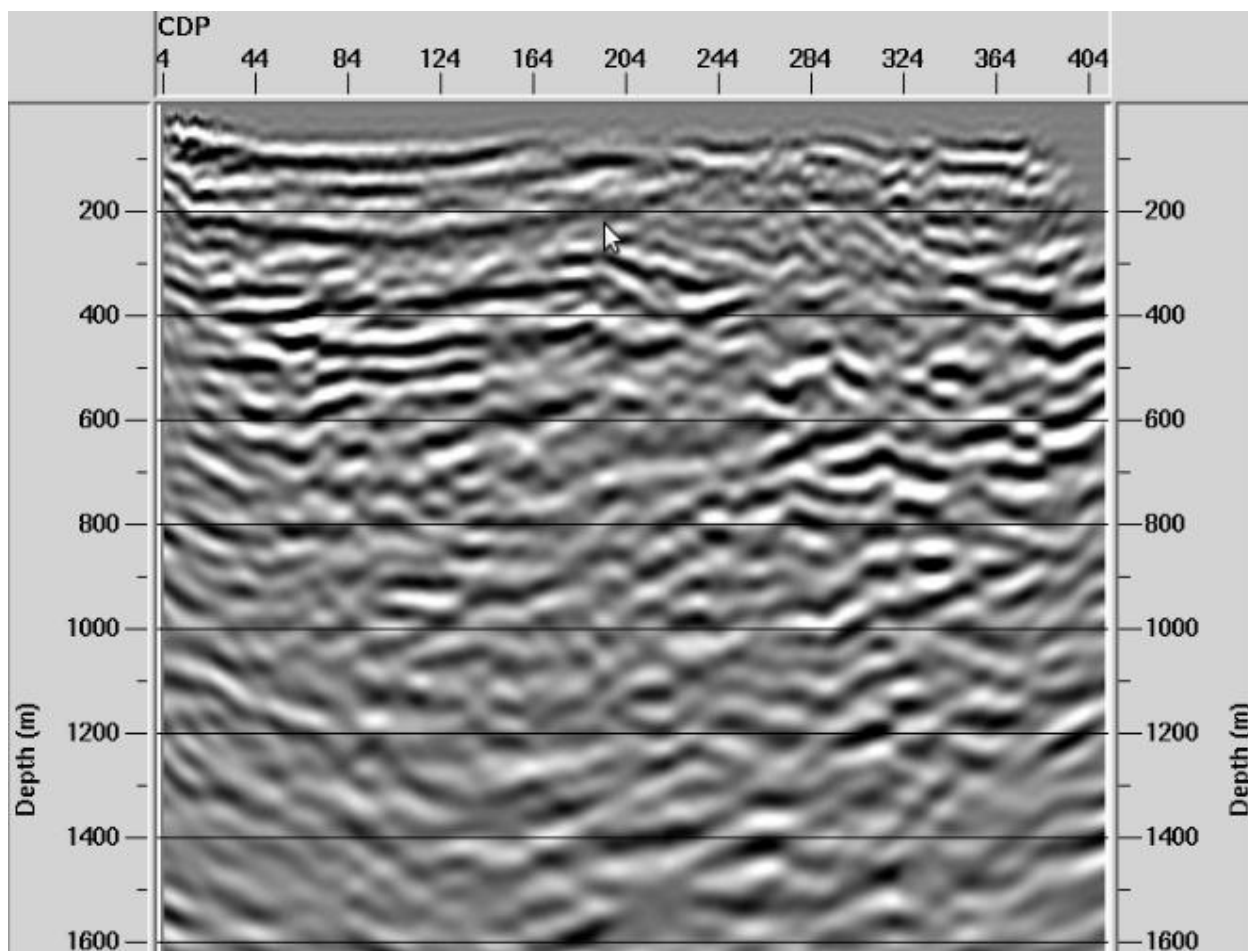


Figure A. 14 - Depth converted Barn 3 Line

# Appendix B

---

## B.1 Site Maps



## B.2 Acquisition Parameters

<b>Line</b>	<b>Student Site 1</b>
<b>Trend</b>	North-South
<b>Length</b>	72 meters
<b>Number of Channels</b>	24
<b>Geophone Spacing</b>	3 meters
<b>Shot Spacing</b>	3 meters, halfway between geophones
<b>Line</b>	<b>Student Site 2</b>
<b>Trend</b>	North-South
<b>Length</b>	96 meters
<b>Number of Channels</b>	24
<b>Geophone Spacing</b>	4 meters
<b>Shot Spacing</b>	4 meters, halfway between geophones
<b>Line</b>	<b>Anisotropy 1</b>
<b>Trend</b>	North-South
<b>Length</b>	48 meters
<b>Number of Channels</b>	24
<b>Geophone Spacing</b>	2 meters
<b>Shot Spacing</b>	2 meters, halfway between geophones
<b>Line</b>	<b>Anisotropy 2</b>
<b>Trend</b>	East-West
<b>Length</b>	48 meters
<b>Number of Channels</b>	24
<b>Geophone Spacing</b>	2 meters
<b>Shot Spacing</b>	2 meters, halfway between geophones
<b>Line</b>	<b>Warm Springs</b>
<b>Trend</b>	North-South
<b>Length</b>	48 meters

<b>Number of Channels</b>	24
<b>Geophone Spacing</b>	2 meters
<b>Shot Spacing</b>	2 meters, halfway between geophones

### B.3 Processing Sequences

<b>Dataset</b>	<b>Zen Garden 1 P-Waves</b>
<b>Processing Step</b>	<b>Notes</b>
<b>Bandpass Filter</b>	Ormsby bandpass filter. Minimum phase. Attenuated low and high frequency noise. Dimensions of filter 20-30-150-200
<b>Automatic Gain Control</b>	Mean scalar. Operator length 500 ms

<b>Dataset</b>	<b>Zen Garden 1 S-Waves</b>
<b>Processing Step</b>	<b>Notes</b>
<b>Bandpass Filter</b>	Ormsby bandpass filter. Minimum phase. Attenuated low and high frequency noise. Dimensions of filter 20-30-150-200
<b>Automatic Gain Control</b>	Mean scalar. Operator length 500 ms

<b>Dataset</b>	<b>Zen Garden 2 P-Waves</b>
<b>Processing Step</b>	<b>Notes</b>
<b>Trace Mute</b>	Muted 3 bad traces, channel number 13, 27, 28
<b>Bandpass Filter</b>	Ormsby bandpass filter. Minimum phase. Attenuated low and high frequency noise. Dimensions of filter 30-40-150-200
<b>Automatic Gain Control</b>	Mean scalar. Operator length 500 ms

<b>Dataset</b>	<b>Zen Garden 2 S-Waves</b>
<b>Processing Step</b>	<b>Notes</b>
<b>Trace Mute</b>	Muted 3 bad traces, channel number 13, 27, 28
<b>Bandpass Filter</b>	Ormsby bandpass filter. Minimum phase. Attenuated low and high frequency noise. Dimensions of filter 20-30-150-200
<b>Automatic Gain Control</b>	Mean scalar. Operator length 500 ms

<b>Dataset</b>	<b>Barn 3 Anisotropy Survey (N-S and E-W) P-Waves</b>
<b>Processing Step</b>	<b>Notes</b>
<b>Bandpass Filter</b>	Ormsby bandpass filter. Minimum phase. Attenuated low and high frequency noise.



	Dimensions of filter 30-40-150-200
<b>Automatic Gain Control</b>	Mean scalar. Operator length 450 ms
<b>Dataset</b>	<b>Barn 3 Anisotropy Survey (N-S and E-W) S-Waves</b>
<b>Processing Step</b>	Notes
<b>Bandpass Filter</b>	Ormsby bandpass filter. Minimum phase. Attenuated low and high frequency noise. Dimensions of filter 30-40-100-150
<b>Automatic Gain Control</b>	Mean scalar. Operator length 450 ms
<b>Dataset</b>	<b>Warm Spring P-Waves</b>
<b>Processing Step</b>	Notes
<b>Bandpass Filter</b>	Ormsby bandpass filter. Minimum phase. Attenuated low and high frequency noise. Dimensions of filter 30-40-100-150
<b>Automatic Gain Control</b>	Mean scalar. Operator length 500 ms
<b>Dataset</b>	<b>Warm Spring S-Waves</b>
<b>Processing Step</b>	Notes
<b>Bandpass Filter</b>	Ormsby bandpass filter. Minimum phase. Attenuated low and high frequency noise. Dimensions of filter 30-40-100-150
<b>Automatic Gain Control</b>	Mean scalar. Operator length 500 ms

## B.4 Equations to calculate layer thickness

### Two Layer Model

To calculate the thickness of the first layer, i.e. the depth to the top of layer 2, the following formula was used:

$$h_1 = \frac{t_i}{2} \frac{V_2 V_1}{(V_2^2 V_1^2)^{\frac{1}{2}}}$$

Where:  $h_1$  = thickness of layer 1,  $t_i$  = zero offset intercept time of layer 2,

$V_1$  = velocity of layer 1,  $V_2$  = velocity of layer 2

### Three Layer Model

The calculation of the layer 1 thickness is the same as the method used in the two layer model. The thickness of the second layer is calculated using the formula below. The depth to the third layer is given by summing the thicknesses of the first and second layer.

$$h_2 = (t_{i_2} - \frac{2h_1(V_3^2 - V_1^2)^{\frac{1}{2}}}{V_3V_1}) \frac{V_3V_2}{2(V_3^2V_2^2)^{\frac{1}{2}}}$$

Where:  $h_2$  = thickness of layer 2,  $h_1$  = thickness of layer 1,  $V_1$  = velocity of first layer,  
 $V_2$  = velocity of layer 2,  $V_3$  = velocity of layer 3

# Appendix C

---

## C.1 Theory

The gravity method is based on the equation of gravitational force. This equation is as follows:

$$F = \frac{G \times M \times m}{R^2}$$

Equation C. 1 Equation of gravitational force

In theory, acceleration due to gravity is approximately 9.8 m/s<sup>2</sup>. However, this is not constant everywhere because our earth is not a continuous, homogenous mass. There are many different densities in the earth and we can measure the acceleration due to gravity over these density contrast locations. An anomaly occurs where there is a large concentration of mass present. If this mass is high density the anomaly will be positive. Low density masses or open spaces will produce a negative anomaly [22].

This is a very useful method when trying to detect bodies in the sub-surface, but there are some inconveniences. The shape of the earth is due to the balance between gravitational and centrifugal accelerations. The earth's shape is referred to as an ellipse of rotation. At the sea surface, if there are no winds, this is known as the geoid. Since the distribution of mass is uneven in the near surface this means the geoid is not the same as the ellipse of rotation [23]. Gravitational forces are affected by other outside sources such a terrain, drift, elevation and tidal effects. To account for this there are several corrections that must be considered when undergoing processing. These corrections are discussed in section 6.4 of this report.

## C.2 Equipment

### CG-5:

1. Initial set-up
  - a. Turn gravimeter on
  - b. Go to set-up menu and press 'OK' to go to a screen that allows you to edit your survey ID name
  - c. When you have entered a name exit this screen and return back to set-up menu

- d. Choose the Autograv icon and make sure automatic corrections are on and then return to set-up menu
- e. Choose the Clock icon and make sure the date is correct and then return to set-up menu
- f. Choose the Measure Clear button on the gravimeter to go to the options screen
- i. For this camp we set read time to be 30 seconds and number of cycles to be 2
- g. Exit this screen and enter the station designation screen. You may edit the station number so it will correspond with your survey
- h. Press F5 to start the levelling process
- 2. Level the CG-5
  - a. Push metal plate into ground until levelling bubble is in center
  - b. Set CG-5 evenly on plate
  - c. The gravimeter should already be on the levelling screen
  - d. Follow on screen instructions to turn levelling knobs as indicated
  - e. When a smiley face comes on the screen the gravimeter is level
- 3. Take a reading
  - a. Press the Read Gravity icon
  - b. Walk approximately 20-30 feet away from the gravimeter as to not affect the measurement
  - c. When a measurement is being taken a blue light on the front of the gravimeter will turn on. This will be on for 30 seconds. Make sure no moving objects come within 20-30 feet of the gravimeter during this time.
  - d. When the blue light turns off, walk to the gravimeter and check the data screen. The gravimeter automatically stores this data if you select F5, but we always hand-recorded as a back-up. Record the gravity reading, standard deviation and time.
  - e. Once you press F5 repeat these steps beginning at 1(g) for the rest of your survey.

#### **L&R:**

- 1. Level the L&R
  - a. Set meter evenly on ground
  - b. Turn the three levelling knobs until the two levelling bubbles are in the center
- 2. Take a reading
  - a. Unlock the gravimeter and turn on the light
  - b. Look through the eye piece and adjust the dial until you see the cross hair at 2.4.

- c. Record this value by hand. Note: there is a decimal after the fourth digit. For processing, the L&R readings must be converted to mGals. Conversion table is in Figure C-1.
- d. Lock the gravimeter, turn off the light and repeat all of these steps for the rest of your survey.

TABLE 1

MILLIGAL VALUES FOR LACOSTE & ROMBERG, INC. MODEL G GRAVITY METER CG- 509

COUNTER READING*	VALUE IN MILLIGALS	FACTOR FOR INTERVAL	COUNTER READING*	VALUE IN MILLIGALS	FACTOR FOR INTERVAL
000	000.00	1.02310	1600	1691.92	1.02257
100	102.41	1.02305	1700	1794.17	1.02255
200	204.80	1.02305	1800	1896.41	1.02252
300	307.16	1.02309	1900	1998.68	1.02249
400	409.51	1.02335	2000	2099.93	1.02246
500	511.84	1.02323	2100	2193.18	1.02242
600	614.17	1.02311	2200	2295.42	1.02238
700	716.48	1.02302	2300	2397.66	1.02233
800	818.78	1.02293	2400	2499.89	1.02228
900	921.07	1.02286	2500	2602.12	1.02223
1000	1023.36	1.02280	2600	2704.34	1.02217
1100	1125.64	1.02273	2700	2806.56	1.02210
1200	1227.91	1.02268	2800	2908.77	1.02203
1300	1330.18	1.02261	2900	3010.97	1.02195
1400	1432.44	1.02260	3000	3113.16	1.02187
1500	1534.70	1.02255	3100	3215.35	1.02179
1600	1636.96	1.02250	3200	3317.53	1.02172
1700	1739.21	1.02247	3300	3419.70	1.02163
1800	1841.46	1.02243	3400	3521.87	1.02154
1900	1943.70	1.02240	3500	3624.02	1.02143
2000	2045.94	1.02238	3600	3726.16	1.02132
2100	2148.18	1.02237	3700	3828.29	1.02119
2200	2250.41	1.02235	3800	3930.41	1.02105
2300	2352.65	1.02236	3900	4032.52	1.02096
2400	2454.88	1.02238	4000	4134.60	1.02066
2500	2557.12	1.02242	4100	4236.67	1.02045
2600	2659.36	1.02245	4200	4338.72	1.02022
2700	2761.61	1.02248	4300	4440.76	1.01999
2800	2863.86	1.02251	4400	4542.74	1.01974
2900	2966.11	1.02255	4500	4644.71	1.01946
3000	3068.36	1.02256	4600	4746.66	1.01914
3100	3170.62	1.02258	4700	4848.57	1.01881
3200	3272.88	1.02260	4800	4950.45	1.01847
3300	3375.14	1.02260	4900	5052.30	1.01813
3400	3477.40	1.02260	5000	5154.11	
3500	3579.66	1.02259			

\* Note: Right-hand wheel on counter indicates approximately 0.1 milligal.

7-12-78  
CR

Figure C. 1 L&R Gravimeter Conversion Table [24][25]



### C.3 Inversion

Inversion and forward modelling:

The goal of the inversion is to produce a reasonable model that generates data, given field survey observations. A summarized procedure for implementing inversion follows:

- **Given:** In order to obtain models of the subsurface by inversion, it is necessary to start with field data, estimates of errors and noise on those data, a forward modelling calculation procedure, and well described prior information or assumptions about the situation.
- **Discretize:** Describe the earth by dividing it into cells, each with fixed size and unknown but constant value of the relevant physical property.
- **Choose decision criteria:** The choices made for how data predictions and survey measurements are compared, and how an optimal model is chosen (based upon prior information) are crucial for obtaining useful results.
- **Inversion:** Find values for cells which are consistent with both the measured data and the prior information. The inversion process is implemented using mathematical optimization theory.
- **Evaluate the inversion result:** Use a comparison between predicted data and field measurements, and take into account what is known or expected about the earth's properties and structures.
- **Interpret the result:** models of physical properties must be interpreted in terms of useful geologic or geotechnical parameters. The models must be easy to understand and convenient to manipulate

# Appendix D

---

The magnetic field of the earth is created by a rotating magnetic core. This magnetic field is not constant and varies throughout each day. The magnetic field has a different intensity and declination for each location on the earth. Some of these variations in the earth's magnetic field are due to diurnal variations. These are caused by the varying currents in the ionosphere. Diurnal corrections can be made to magnetic data through the use of a base station.

When a mass is placed in a magnetic field it acquires a magnetization. This magnetization is caused by the alignment of many magnetic dipoles within the mass. This mass then acts like one large dipole in the place of lots of small dipoles. This dipole gets aligned in the direction of the inducing field. A drawing of this scenario is shown in Figure D.1.

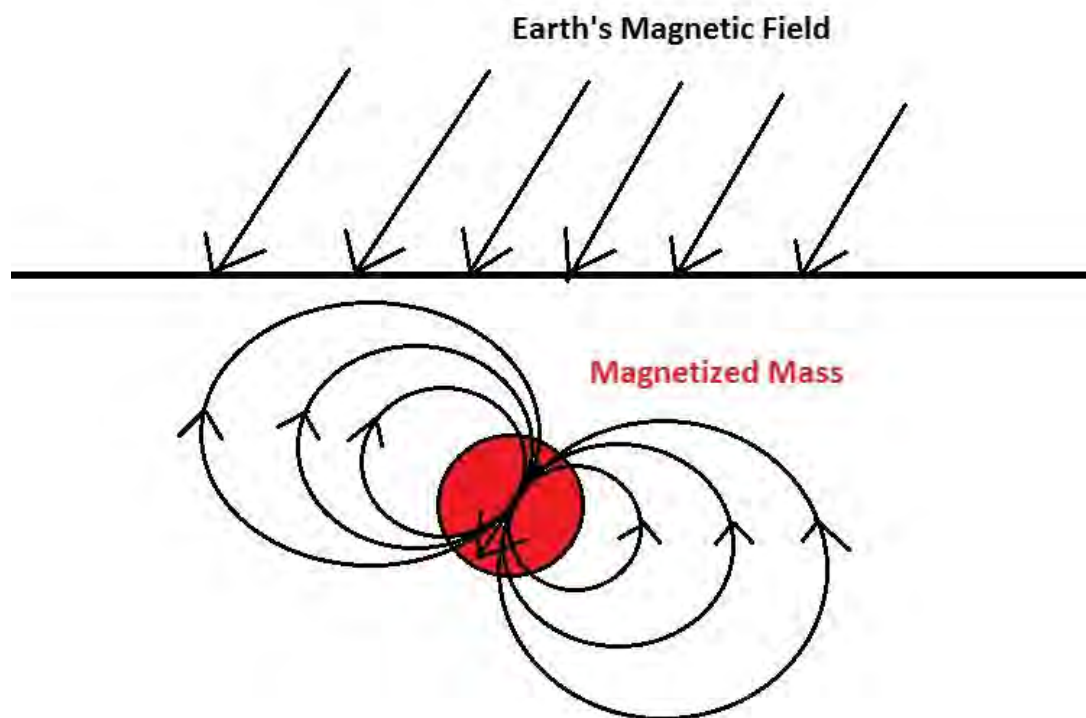


Figure D.1 Cartoon showing how the Earth's magnetic field magnetizes a body.

## D.1 Proton precession magnetometers

Proton magnetometers work by injecting a current into a copper wire that is wound around a bottle of hydrocarbon fluid. This aligns the protons in the fluid in one direction and creates a strong magnetic field. This current is then switched off and the protons realign to direction of the earth's magnetic

field and rotate around this axis at a rate that is proportional to the magnitude of the field [31]. This rate is measured and recorded as the magnetic field measurement.

## D.2 Cesium magnetometers

Cesium magnetometers use the same initial set-up as the proton magnetometers, but with cesium vapors in place of the hydrocarbon fluid. This is done in order to observe the electron moments in place of the proton moments. Very high frequency waves act on the bottle which increases the signal by several orders of magnitude. The increased sensitivity of cesium magnetometers make them ideal for continuous collection.

The Matlab code shown below is for the program that was written to linearly interpolate between the GPS marker points on the magnetic surveys:

```
function [position] = magInterpolateLine( MagDat, GPS )
npoints=length(GPS);
ndat=length(MagDat);
initc=1;

for jj=1:npoints-1
    mark2N = GPS(jj+1,2);
    mark1N = GPS(jj,2);
    mark2E = GPS(jj+1,3);
    mark1E = GPS(jj,3);
    mark2El = GPS(jj+1,4);
    mark1El = GPS(jj,4);
    time1 = MagDat(initc,6);
    c = initc;
    while(c+1<ndat&&MagDat(c,8) == MagDat(c+1,8))
        c = c+1;
    end
    nextc=c+1;
    time2=MagDat(nextc,6);

    for ii=initc:c
        position(ii,1) = ((mark2N-mark1N)/(time2-time1))*(MagDat(ii,6)-
time1)+mark1N;
        position(ii,2) = ((mark2E-mark1E)/(time2-time1))*(MagDat(ii,6)-
time1)+mark1E;
        position(ii,3) = ((mark2El-mark1El)/(time2-time1))*(MagDat(ii,6)-
time1)+mark1El;
    end
    initc=nextc;
end
position(ndat,1) = ((mark2N-mark1N)/(time2-time1))*(MagDat(ndat,6)-
time1)+mark1N;
position(ndat,2) = ((mark2E-mark1E)/(time2-time1))*(MagDat(ndat,6)-
time1)+mark1E;
position(ndat,3) = ((mark2El-mark1El)/(time2-time1))*(MagDat(ndat,6)-
time1)+mark1El;

end
```

This function reads in two files. The first is a file containing the magnetics data along with the flag and line information for each data point. The second is a file containing the GPS points for all of the marker locations. An extra GPS point was needed if the survey did not end on a marker. The function created a file that contained the northing, easting, and elevation of each data point that was continuously collected.

# Appendix E

---

## E.1 Theory

### E.1.1 Basics

Electromagnetics theory revolves around Maxwell's equations which describe the interactions between electrical charges and currents and the electrical and magnetic fields they create. One of the basic principles that makes EM methods work is that a time-varying magnetic field will produce an electric field, as shown in Equation 8.E.1 where  $\vec{E}$  is the electrical field and  $\vec{B}$  is the magnetic field.

$$\nabla \times \vec{E} = -\frac{d\vec{B}}{dt}$$

Equation 8.E.1 Maxwell's equation relating time-varying magnetic fields to electric fields.

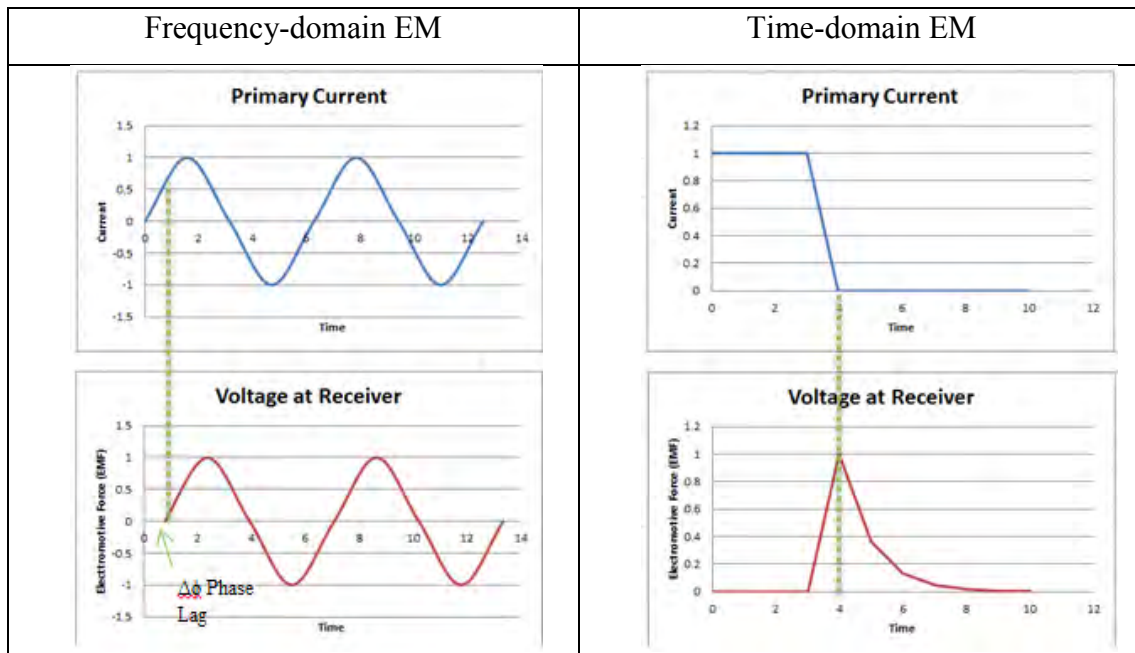
### E.1.2 TEM vs. FEM

Both time-domain and frequency-domain electromagnetic methods use an electrical current as a source. The type of current is different for the two methods as shown in



Table 8.E. 1. Frequency-domain EM uses an alternating current to produce a magnetic field in the ground. FEM is generally faster to implement, uses a single frequency (narrow band) receiver, and measures both the primary and secondary magnetic field. Time-domain EM uses a constant electrical current which is shut-off to create a magnetic field. The advantages of TDEM are that it covers several frequencies (broad band) and only the secondary magnetic field is measured with no interference from the primary magnetic field. It is slower to implement in the field but it does not necessarily need contact to the ground.

Table 8.E. 1 A comparison of FEM and TEM [32]



### E.1.3 Apparent conductivity

The primary and secondary magnetic fields are used to calculate apparent conductivity as shown in Equation 8.E. 2 where  $i$  is  $\sqrt{-1}$ ,  $\omega$  is the frequency in Hertz,  $\mu_0$  is the permeability of free space,  $\sigma$  is the conductivity of the medium in milliSeimen per meter, and  $s$  is the inter-coil spacing in meters.

$$\frac{H_s}{H_p} \cong \frac{i\omega\mu_0\sigma s^2}{4}$$

Equation 8.E. 2 Ratio of the secondary and primary magnetic fields used to calculate apparent conductivity.

There are two types of responses measured when an electromagnetic field is induced in the subsurface: in-phase and quadrature, measured in parts per thousand (ppt) and milliSemens per meter (mS/m), respectively. The response parameters, which are both dependent on properties of frequency ( $\omega$ , or  $2\pi f$ ), self-inductance ( $L$ ), and resistance ( $R$ ). Their relationship is shown in Equation 8.E. 3.

$$\alpha = \omega\tau = \omega L/R = 2\pi fL/R$$

Equation 8.E. 3 Response parameters.

At higher frequencies, the in-phase dominates the quadrature component as shown in Figure 8.E. 1. The in-phase component is sensitive to conductive objects like metal drums and is often used to map buried hazardous waste in metal containers [32]. The quadrature

component is more sensitive to changes in geologic formations and is used to map groundwater flow in faults and fractures [35].

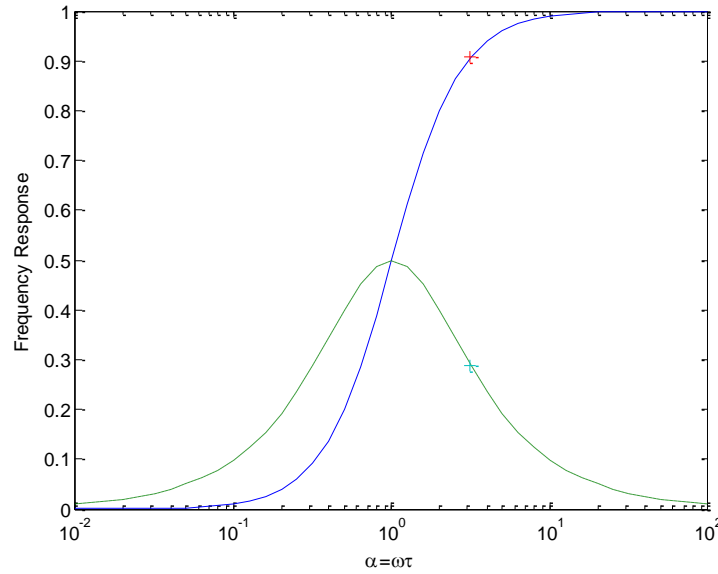


Figure 8.E. 1 Example frequency response of a target at 5000 Hz. The in-phase component is shown in blue, while the quadrature component is shown in green. ‘ $\alpha$ ’ denotes the response parameter.

#### E.1.4 Signal dissipation

The signal for EM methods is dependent on the electromagnetic wave equation which is found by applying a curl to Maxwell’s equation. Equation 8.E.4 describes how the signal propagates in a medium. The left hand side of the equation is a spatial derivative and the right hand side contains temporal derivatives. The first term of the right hand side is the diffusive part and the second is the wave portion.

$$\nabla^2 \vec{E} = \mu\sigma \frac{\partial \vec{E}}{\partial t} + \mu\epsilon \frac{\partial^2 \vec{E}}{\partial^2 t}$$

Equation 8.E.4 Electromagnetic wave equation.

For low frequency measurements (i.e. TEM and FEM data acquisitions), the wave portion of Equation 8.E.4 becomes much smaller than the diffuse part and simplifies to Equation 8.E. 5.

$$\nabla^2 \vec{E} = \mu\sigma \frac{\partial \vec{E}}{\partial t},$$

Equation 8.E. 5 Electromagnetic wave equation for low frequencies.

This is why for low frequency and low induction number data acquisitions in the subsurface, the electromagnetic wave diffuses out more in the form of heat.

### E.1.5 FEM instrument sensitivity

The apparent conductivity measured by frequency-domain EM methods is an average of the portion of the earth the signal reaches. The depth of investigation for EM31 and EM34 instruments can be found in Table 8. 1. These were determined by the percentage of the response that reaches the depth to investigation. For example, if the coil spacing is 40m in vertical dipole mode then at a depth of 60m the percentage of the cumulative response from all the material at 60m and below is around 33%. The cumulative response for vertical and horizontal dipoles is shown in Figure 8.E.2 where  $z$  is the depth normalized by coil spacing and  $\phi_{v(z)}$  is the relative response for a vertical dipole. The distribution of the response from different portions of the earth aids in the interpretation of the data. The response is affected by the various conductivities of the earth the signal passes through. A graph of the conductivities for various rocks and soils is shown in Figure 8.E.3.

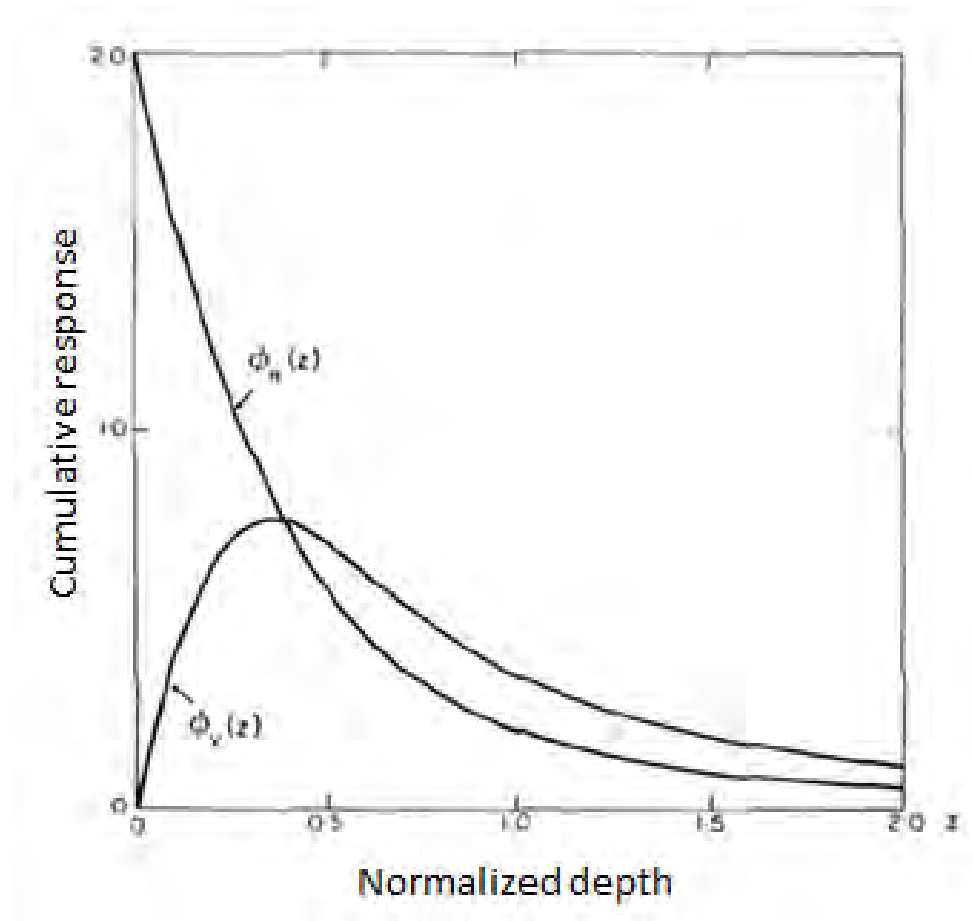


Figure 8.E.2 FEM instrument relative response for horizontal and vertical dipoles where  $z$  is depth normalized by coil spacing and  $\phi_{v(z)}$  is the relative response for a vertical dipole [36].

## E.1.6 Apparent conductivity table

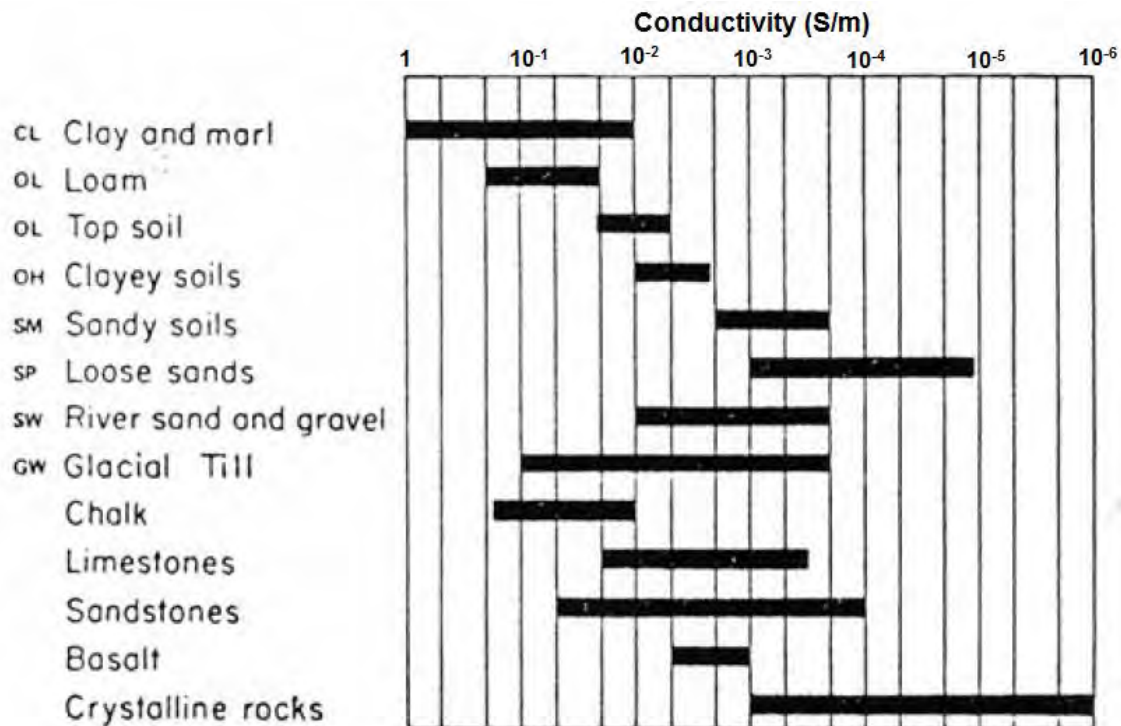


Figure 8.E.3 A graph of different soils/rocks conductivity in S/m [42].

## E.2 Instrument specifications

### E.2.1 EM31-MKS specifications

Table 8.E.2 EM31-MKS instrument details [42].

MEASURED QUANTITIES	1: Apparent conductivity in millisiemens per metre (mS/m) 2: In-phase ratio of the secondary to primary magnetic field in parts per thousand (ppt)
INTERCOIL SPACING	3.66 meters
OPERATING FREQUENCY	9.8 kHz
POWER SUPPLY	8 disposable alkaline "C" cells (approx. 20 h continuous)
MEASURING RANGES	Conduct: 10, 100, 1K mS/m; In-phase: +/- 20 ppt
MEASUREMENT RESOLUTION	+/- 0.1 % of full scale
MEASUREMENT ACCURACY	+/- 5 % at 20 mS/m
NOISE LEVELS	Conductivity: 0.1 mS/m; In-phase: 0.03 ppt
DATA STORAGE	10,000 records (2 components); 16,500 records (1 component); ext. memory available
DIMENSIONS	Boom: 4m xt.; 1.4m stored; Case: 145x38x23cm
WEIGHT	Instrument: 12.4; Shipping: 28 kg



## E.2.2 EM34 specifications

Table 8.E.3 EM34 instrument details [35].

MEASURED QUANTITIES	Apparent conductivity in millisiemens per metre (mS/m)
PRIMARY FIELD SOURCE	Self-contained dipole transmitter
SENSOR	Self-contained dipole receiver
REFERENCE CABLE	Lightweight, 2 wire shielded cable
INTERCOIL SPACING & OPERATING FREQUENCY	10 m at 6.4 kHz 20 m at 1.6 kHz 40 m at 0.4 kHz
POWER SUPPLY	Transmitter: 8 disposable or rechargeable “D” cells Receiver: 8 disposable or rechargeable “C” cells
CONDUCTIVITY RANGES	Conductivity: 10, 100, 1K mS/m;
MEASUREMENT RESOLUTION	+/- 0.1 % of full scale
MEASUREMENT ACCURACY	+/- 5 % at 20 mS/m
NOISE LEVELS	Conductivity: 0.2 mS/m (can be greater in regions of high power line interference)
DIMENSIONS	Rx Console: 19x13.5x26 cm Tx Console: 15.5x8x26 cm Rx & Tx Coil: 63 cm diameter
WEIGHTS	Instrument: 20.5 kg; XL; 26.5 kg Shipping: 43 kg; XL: 51 kg

## E.2.3 EM47 specifications

Table 8.E.4 EM47 instrument details [37].

CURRENT WAVEFORM	Bipolar rectangular current with 50% duty cycle
BASE FREQUENCY	30, 75, or 285 Hz where powerline frequency is 60 Hz 25, 62.5 or 237.5 Hz where powerline frequency is 50 Hz
TURN-OFF TIME	2.5 $\mu$ s at 3 A into 40x40 m loop; faster into smaller loop
TRANSMITTER LOOP	5x5 to 100x100 m single turn loop, or 5x5 m 8- turn loop
OUTPUT VOLTAGE	0 to 9 V, continuously variable
POWER SUPPLY	Internal 12 V rechargeable battery
BATTERY LIFE	5 h continuous operation at 2 A output
DIMENSIONS	10.5x24x32 cm
WEIGHT	5.3 kg

## E.3 EM method limitations

EM methods have limitations because of the nature of the electromagnetic source, coupling between transmitter and receiver coils, and frequency ranges used in the EM surveys.

In general, EM methods do not work well in highly resistive areas because as explained in the section 8.1, to induce the eddy currents, which result in a secondary magnetic field to be detected by the receivers, a conductive (low resistive) medium is necessary. Moreover, if there are highly conductive materials such as metal pipes, cables, fences and power lines near the area in which EM survey is conducted, eddy currents will be induced inside of those materials rather than the target. The signals coming from those conductive materials are treated as noise.

The variation in the coupling between source and receiver coils causes noise specifically in frequency-domain EM methods because those methods have a primary magnetic field. To suppress this noise, the separation and relative orientations of the coils is kept constant as much as possible [19]. However, depending on the conditions in the field, this may not be possible.

Each EM method works well in a certain frequency range. Those ranges limit the depth of the investigation of the methods. Therefore, using the EM methods, only the layers in the depth of investigation can be resolved.

**Table 8.5 TLA's used in this chapter.**

TDEM	Time Domain Electromagnetics
TEM	Transient Electromagnetics
FEM	Frequency Electromagnetics
CWEM	Controlled Wave Electromagnetics
Tx	Transmitter Coil
Rx	Receiver Coil

# Appendix F

---

## F.1 Theory

### F.1.1 DC Resistivity Methods

The geophysical method of DC resistivity uses arrays of voltage potential measurements in order to image a sectioned resistivity profile of the subsurface. Through several array designs, by inducing current and taking measurements at points along an array, a section of apparent resistivities in the subsurface is generated. In the past, these acquisitions were performed manually point for point, however with advances in technology, acquisitions are performed in a fraction of the time. Using laid out spools of cable with many electrical takeouts all connected to a power source and controller box, a program automatically runs through a predefined system of arrays spacings and takes and records all measurements. Also, using these controller boxes, many array types and acquisition methods can be used from the same array (ex. Wenner, Dipole-Dipole, IP, etc.)

### F.1.2 Apparent Resistivity

The property of resistivity defines a material's resistance to the flow of electricity. With rocks in the subsurface, this property can be affected by many variables such as fluid saturation, rock porosity, mineral and fluid types, temperature, and inter-grain properties. This allows for DC resistivity to be a very powerful method to measure and image groundwater problems. In this method, the measured value represents the total resistivity of the subsurface between electrodes plus the electrode contact resistance known as the apparent resistivity. This required processing through inversion techniques to convert to real resistivity in the subsurface. This method used the basic physical concepts as expressed by Ohm's Law (Equation F. 1) and the apparent resistivity equation (Equation F. 2).

$$I = VR$$

Equation F. 1 Ohm's Law

$$R_a = lA$$

Equation F. 2 Apparent Resistivity

Where I is current, V is voltage, R is resistance,  $R_a$  is apparent resistivity,  $\rho$  is resistivity, l is length, and A is cross sectional area. These equations are used to convert the measured resistivity scaled by a geometric factor specific to each array to solve for the resistivity at each survey point.

### F.1.3 Self Potential

Instead of inducing a current in the ground and directly measuring resistance of the subsurface, indirect potential fields can also be measured resulting from both natural and manmade sources. These fields can be generated from many sources including but not limited to, redox reactions, sulphide weathering, moving charged fluids, induction by manmade current flows, and direct induced potential. This method measures these natural and induced potentials to map how electrical potential changes through the subsurface. This method can be particularly useful when imaging the flow of mineral rich waters in a hydrothermal system.

### F.1.4 Induced Polarization

Similar to time domain EM methods, Induced Polarization injects a time varying square wave of current into the subsurface, and then measured the change in potential of the decay of current. In this case however, this measures the property of chargeability.

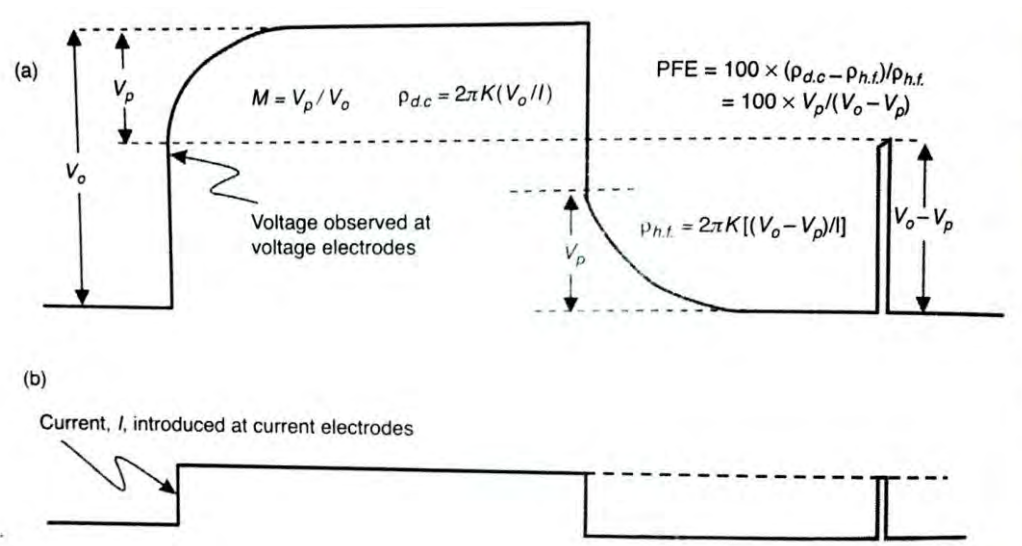


Figure F. 1 (a) Induced polarization decay (b) Injected current signal [43]

This defines a rock's (or more specifically the grains) resistance to charge polarization as the current decays in the subsurface. This can be important to understanding geology as different rock types will give different readings for instance most clays will have a high chargeability while clean sandstone would be very small. From this, the inversion produces an IP model and a resistivity profile. These are then used to calculate and plot the normalized chargeability using the normalized chargeability equation (Equation F. 3).

$$MO = MIP$$

### Equation F. 3 Normalized chargeability equation

Where  $M$  is normalized chargeability,  $\rho_a$  is measured conductivity,  $MIP$  is the IP values from the IP inversion model, and  $\rho_a$  is apparent resistivity. Using this, a normalized chargeability model can be generated and correlated with geology.

## F.2 Equipment

### F.2.1 ABEM

#### Setup and Acquisition

The ABEM Terrameter SAS4000 uses 64 takeouts on spools of cable connected in series to run through predefined routines of electrode arrays to induce and measure resistance in the subsurface. Once an acquisition is complete, these lines of cable can then be rolled over to extend the line indefinitely to extend the section horizontally.



Figure F. 2ABEM [44]

#### Data Formatting

The ABEM produces data in proprietary .s4k files which can then be converted using the accompanied device software “Terrameter SAS4000/SAS1000 Utilities” to more usable file formats such as .amp or .dat files which can then be read by inversion software.



## F.2.2 SuperSting

### Setup and Acquisition

For DC resistivity surveys, the SuperSting uses cables with eight takeouts for electrodes, but multiple cables can be connected for a survey with more than eight electrodes. Before any survey is conducted, it is necessary to run a test on the electrodes to check for good coupling and cable connections.



Figure F. 3 SuperSting [45]

### Data Formatting

The SuperSting generates data in .stg files that contain arbitrary x, y, and z coordinates for each of the A, B, M and N electrodes. In order to be compatible with the inversion software, DCIP3D v2.5, the .stg files are converted to .dat or .txt. DCIP3D requires three types of files: .dat datafiles, a .msh mesh files, and a .dat topography all accessed through a .inp input file. For 2D inversions, the original .stg files are compatible with the AGI Earth Imager 2D software.

## F.2.3 Self Potential

### Setup and Acquisition

For SP surveys, a pair of non-polarizing lead/lead chloride electrodes are used because they do not cause their own self-potential effects along with a high impedance multimeter and a large spool of orange SP cable. One electrode is the reference electrode and is buried at the beginning of a survey while the other is the roaming electrode. The orange SP cable is connected to the reference electrode and at every flag location along the survey is then connected to the multimeter which is always connected to the roaming electrode. The SP value is measured at every flag or station along the DC Resistivity survey profiles.

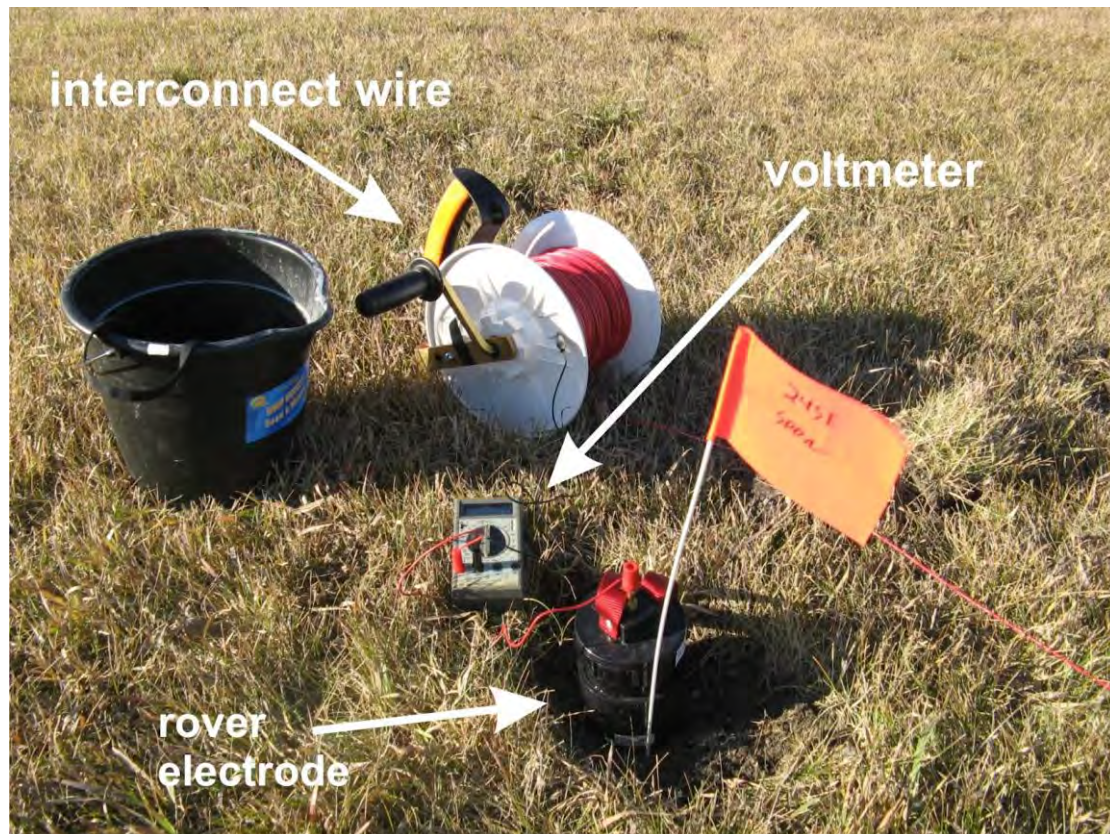


Figure F. 4 SP equipment [46]

### Data Processing

Self-potential data is collected manually in the field with pen and paper. The flag or station number, the SP value in mV, the occasional contact resistance value in  $k\Omega$ , and notes describing the soil or any features that might affect the survey.

## F.3 Array Types

### F.3.1 Wenner

The Wenner array is one of the classical arrays used in DC Resistivity methods. The basic form of this array consists of two outer electrodes called A and B which inject the current, while electrodes in between called M and N measure the resistance. What defines this as a Wenner array is the regular spacing between AM, MN, and NB. In an acquisition, this array is moved laterally to take horizontal constant depth measurements and can be expanded to increase depth of investigation. This array preserves a high signal to noise ratio and serves as a good array for most cases.

## Wenner

$$\rho_a = 2\pi a \frac{V}{I}$$

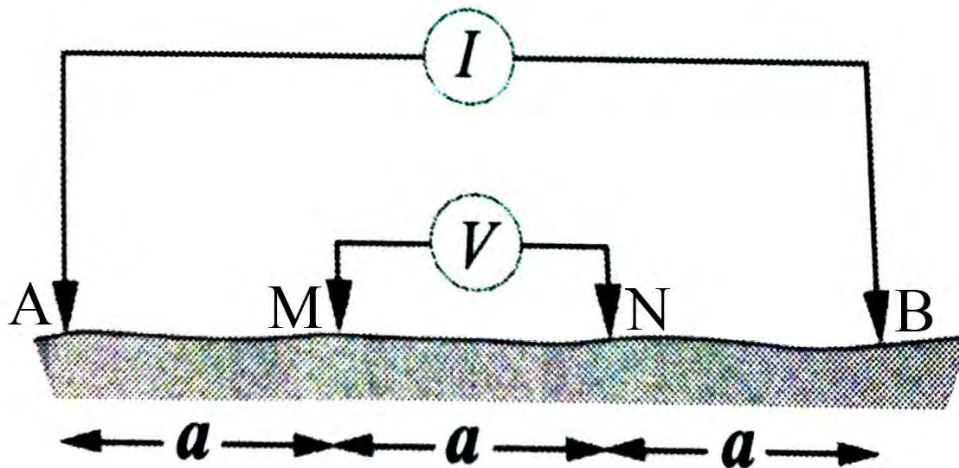


Figure F. 5 Wenner array layout [19]

### F.3.2 Dipole-Dipole

Similar to the Wenner, in the Dipole-Dipole array, current is injected on A and B, and the resistance is measured between M and N. In this case the MN and AB spacing are the same and the AB and MN pairs are separated by a distance multiple of the spacing. This array can also be moved laterally to expand the constant depth section horizontally and also can be expanded to increase depth of investigation. This array is better at imaging vertical features such as dikes and faults at the cost of a low signal to noise ratio.

## Dipole-dipole

$$\rho_a = \pi n(n+1)(n+2) a \frac{V}{I}$$



Figure F. 6 Dipole-Dipole array layout [19]

## **F.4 Processing**

### **F.4.1 Reduction**

For electrical methods, the main data reduction necessary for processing is the integration of topography with electrode position. ABEM acquisitions require an elevation for each electrode - the easting/northing coordinates are not as necessary for accuracy due to the longer lengths of the acquisition lines. The SuperSting electrode positions require UTM coordinates (including elevation) in order to run inversions with the same spatial parameters for all of the student site methods.

### **F.4.2 Assumptions**

In order to process and invert DC resistivity data, it is necessary to make several assumptions regarding the conditions of the survey design and parameters. One important assumption is that the survey areas cover subsurface features of interest that electrical methods can successfully capture. During acquisition, we assume that there are no major electrical disturbances in the area that would skew the data, such as CSAMT and other electrical methods within the area. For the purposes of processing and inversion, we assume that the geology outside the survey area is relatively constant (seen in the padding parameters of the inversion). Also concerning inversion, we assume that we can produce an accurate three dimensional model by connecting several individual two dimensional surveys.

### **F.4.3 ABEM Processing**

The resistivity inverse problem is to invert the model resistivity using the resistivity data we acquired, i.e. the measured apparent resistivity, which only gives us the pseudo section instead of the real resistivity section. There could be more than one model that will fit the data, known as the non-uniqueness. Resistivity sections in real world do not have sharp jumps, so our model should be smooth as well. Thus, smoothness-constrained least square method is used to minimize the difference between the observed data and the calculated data based on the model.

Inversion software Res2Dinv ver. 3.59.108 can do all the above automatically with many parameters adjustable. Firstly we can decide the forward modelling and model discretization parameters. Among other adjustable parameters, damping factor is to control the smoothness add to the model change vector at each iteration, larger indicates smoother model, smaller indicates less smooth and more unstable model; we can add smooth constraint to model resistivity values too; besides, by doing combined Marquardt (ridge regression) and Occam (smoothness constrained) inversion, the distortion in the data due to a very low resistivity shallow layer can be reduced. Convergence limit is the criteria for the iteration to stop, usually it's when the improvement between 2 iterations is small enough, e.g. the data misfit reduction less than 5%. Continuing the inversion beyond this point can result in fitting

the data. The default largest number of iterations is 5. We can do more iterations but usually 4 to 6 is enough.

When displaying the inversion results, it will show the measured apparent resistivity pseudo section, the calculated apparent resistivity pseudo section and the inverse model resistivity section, all plotted in logarithm, from the top to bottom for comparison. Different contour colors and vertical exaggerations can be chosen to help interpretation. The RMS error showed is the error between the measured and calculated resistivity, usually less than 10% is good. Furthermore, RMS error statistics show the histogram of the RMS error of all the data points and we can exterminate the bad datum by discarding the data points of which the RMS error is higher than a certain level, like 20%. We can also remove datum points from the data set by manually selecting those whose amplitude is too large or too small compared to proximity, which indicates noise. When topography information is added to the .DAT file, it can be shown in the inversion result.

IP data is processed in the same method as with DC resistivity with only with the added step of using the outputted IP and resistivity models to calculate normalized chargeability.

3D inversion based on 2D acquisition. 3D acquisition is hard due to having a limited length of cable, limited numbers of electrodes, and require a lot of work, making 2D acquisition more realistic and we can still obtain a 3D model out of the data.

#### **F.4.4 Kriging Processing**

Kriging is a group of interpolation methods widely used in geostatistics, variants of linear regression estimators. It is to estimate the value at unobserved locations from nearby observed scattered data by doing weighted sum of their values, and the weights are derived from covariance or semivariogram, a function of lag describing the spatial dependence. The weights are obtained by minimizing the prediction error. We can use Kriging to interpolate a 2D plot, or to combine several 2D lines into a 2D map or a 3D map. We can do Kriging using software like Surfer, Voxler or Matlab.

#### **F.4.5 SuperSting Processing**

The SuperSting data is processed using DCIP3D v2.5 and AGI EarthImager 2D software for three and two dimensional inversions, respectively. The 2D resistivity inversions for the SuperSting follow a similar ideology. Running 3D inversions with DCIP3D software is a very hands on experience in that one needs to generate many files and choose parameters that the software agrees with.

To adjust the spatial resolution of the inversion, it is necessary generate a mesh file [.msh] that defines the cell sizes of the inversion volume and the padding cells (input table with mesh parameters). The elevation of the top layer of the mesh needs to have the elevation of the highest point in the



topography file and it is necessary to know the point location of the southwest corner of the survey in order to provide adequate room for padding cells.

After the mesh file is generated, the data needs to be formatted correctly into .dat files. The data file consists of a line with the AB electrode location and the number of MN electrodes that correlate to the specified AB electrodes. Following this line is all of the MN combinations that correlation with the aforementioned AB electrode position. The lines with MN electrode locations also contain the apparent resistivity and error values, which can be changed manually if necessary.

A topography file [.dat] is not necessary for 3D inversions, but if the survey area covers a wide range of elevations, then it is prudent to incorporate topography. The topography file contains easting, northing, and elevation data in three columns.

After the mesh and data files (and optional topography) have been constructed, these are placed into an input file that DCIP3D can read and process. The input file is where one changes the weighting factors and types of inversions. If the desire to run multiple inversions in a row arises, it is necessary to create a batch file [.bat]. The batch file holds the purpose of knowing the location of each input file and also knowing where to save the completed inversions.

## **F.5 Error analysis**

### **F.5.1 ABEM**

High contact resistance between the electrode and the ground can cause data inaccuracy. Disturbances from metal pipes, fences or other conductive objects in the ground can result in false anomalies.

### **F.5.2 SP**

Poor coupling between the electrodes and the ground surface can cause error within the measurements. A large difference between the reference and roaming electrodes and drift of that difference that might not be completely linear, which is our assumption, will cause correction values to have some uncertainty or error.

### **F.5.3 SuperSting**

Integrating the UTM coordinates and topography with the SuperSting data files produced a few sources of error in that not every electrode has an accurate GPS location. Attaining good coupling was major issue during SuperSting acquisition and due to poor coupling; some lines may not be able to fully utilize all of the electrodes. Losing the use of electrodes results in less data, which is less information that is available to create a representative model.

# Appendix G

---

Ground Penetrating Radar in short, GPR, is a near surface geophysical tool that uses electromagnetic waves with frequencies from 10 Mhz to 4 Ghz. It detects changes in electrical properties such as the electric permittivity and conductivity. The operation of GPR is simple and similar to that of seismic. A GPR source transmits an electromagnetic wave into the ground. The transmitted wave then hits a boundary which then gets reflected back to the receiver. These waves are then recorded as two-way-time travel, usually measured in nanoseconds (ns). A schematic diagram of a radar acquisition is as shown in the figure below.

The main cause for electromagnetic waves such as radar to get reflected from a boundary within the subsurface is primarily due to the contrasts in electrical conductivity and permittivity. Electrical conductivity measures the relative potential of a material to conduct electricity. It is concurrently used together with the electrical resistivity as they are directly interchangeable by its law of proportionality. The electrical permittivity describes both in the sense that electrical permittivity defines the ability of a material to transmit and/or permit an electromagnetic field. Since radar waves are classified as an electromagnetic wave, it then honours the Maxwell's constitutive equation for electromagnetic case. They are described as follows:

$$\mathbf{d} = \epsilon \cdot \mathbf{E} \quad (\text{Eq. 1})$$

$$\mathbf{b} = \mu \cdot \mathbf{H} \quad (\text{Eq. 2})$$

(Milsom and Eriksen, 2011)

Equation 1 as written above describes the notion of electric charges,  $\mathbf{d}$ , as a function of electric field,  $\mathbf{E}$ . It describes how electric charges move in response to electric field. This phenomenon is known as electric permittivity,  $\epsilon$ . Equation 2 describes the atomic and magnetic moments,  $\mathbf{b}$ , respond to a magnetic field,  $\mathbf{H}$  where  $\mu$  is the magnetic permeability. However, in GPR, the magnetic permeability,  $\mu$ , is kept constant such that  $\mu=1$ . This is to allow the reflection, dispersion and attenuation of the radar wave to be caused by primarily the changes in electrical conductivity,  $\sigma$ , and permittivity,  $\epsilon$  [19].

## G.1 Wave properties

The radar wave in GPR has a physical wave character whereby, as observed in all propagating waves, possesses velocity as a function of wavelength and wave frequency. The radar wave velocity and wavelength is given in the equation below.

$$V = \frac{c}{\sqrt{\epsilon}} \quad (\text{Eq. 3})$$

Where  $v$  is the wave velocity,  $c$  is the velocity of light in empty space and  $\epsilon$  is the electric permittivity.

$$\lambda = \frac{c}{f_c \sqrt{\epsilon}} \quad (\text{Eq. 4})$$

Where  $\lambda$  is the wavelength and  $f_c$  is the centre wave frequency.

The centre frequency,  $f_c$ , is the dominant frequency at which the pulses of electromagnetic energy emanates. This means that the centre frequency,  $f_c$ , spans over a band of frequencies usually an octave higher or lower. The performance of GPR is highly dependent on this factor. High frequencies are needed to resolve small object and lower frequencies are needed to detect deeper objects.

As in many waves, a change in physical property of a material as the wave propagates may mean wave reflection and refraction to occur. In other words, it obeys the simple rule of Snell-Descartes law. This phenomenon is also observed in electromagnetic wave e.g. the radar wave. If a GPR wave encounters a discontinuity in conductivity and permittivity, some of the primary signal from the transmitter will be reflected. The degree at which the reflection occurs is marked primarily by the size of the target, the angle of incidence at which the reflector hits the boundary and the amplitude of the radar energy reflected back to the surface indicated by the reflection coefficient, RC. The reflection coefficient is described in the equation below.

$$RC = \frac{\sqrt{\epsilon_1} - \sqrt{\epsilon_2}}{\sqrt{\epsilon_1} + \sqrt{\epsilon_2}} = \frac{V_1 - V_2}{V_1 + V_2} \quad (\text{Eq. 5})$$

Where  $\epsilon_1$ ,  $\epsilon_2$  are the electric permittivity of two dielectric media and  $V_1$  and  $V_2$  are the wave velocity of two different materials.

The RC provides a numerical indicator of the contrast between two media. In terms of GPR, It gives out the relative change in electric permittivity within the media if any reflections were detected.

Like many waves, the radar waves also suffer from wave attenuation. This is because the movement of current due the presence of an electrical energy induced by the electromagnetic field converts them to heat energy. This phenomenon is known ohmic dissipation. The primary signal of the radar wave will essentially fall below detectable levels. Clays are known to dissipate radar wave due to its high attenuation nature. GPR fails to perform well in imaging clay due to this effect. A field example to this is illustrated in figure 2.

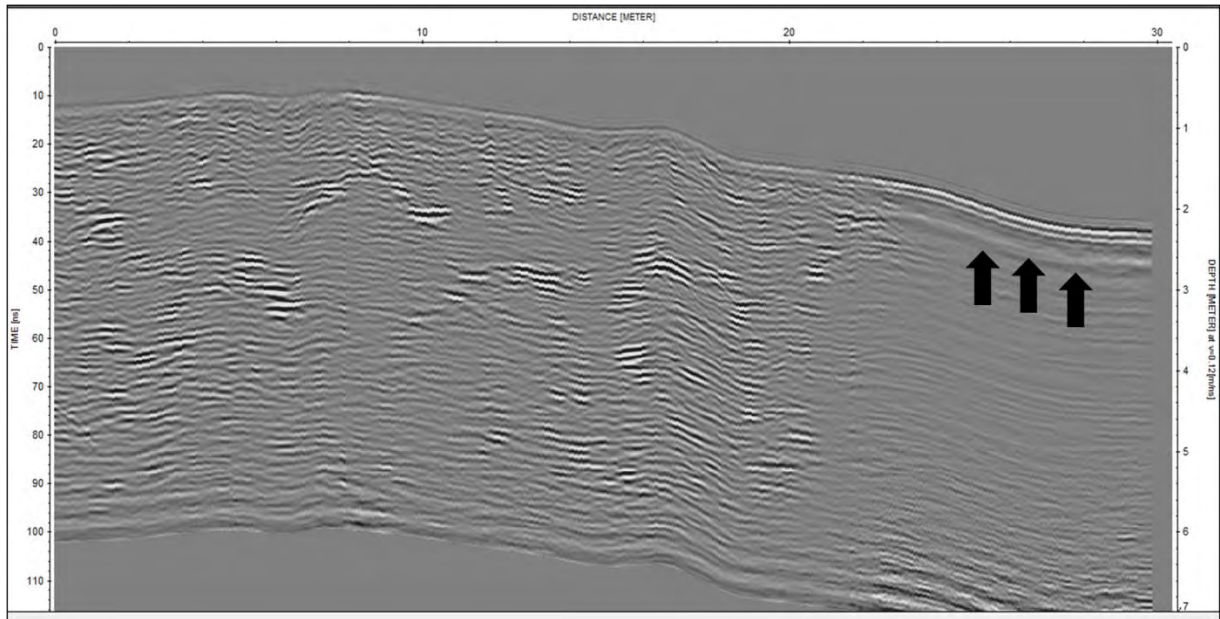


**Figure 2.** A field example of a radar cross section. This section illustrates the transition between a fractured travertine layer to shale. The black arrows mark the region where the wave attenuation effect can be seen clearly.

The equations above are useful in determining the radar range and the lateral resolution. The lateral resolution is simply the minimum distance that must exist between two objects if they are to be seen as separate [19]. The lateral resolution takes into account of the targeted depth because the zone of influence of the radiated pulse from any wave increases as function of depth and velocity. This zone of influence is referred to as the Fresnel zone as illustrated in figure 3. The interference of this zone causes the data to be aliased [47]. The range resolution is then the opposite of lateral resolution whereby instead of looking laterally, it measures the minimum distance of two interfaces at which it can be resolved by a radar signal.

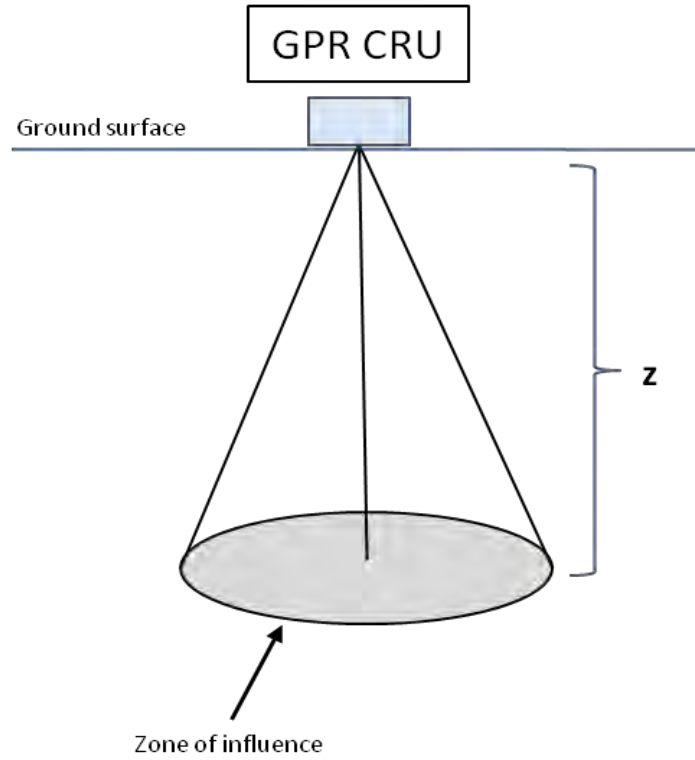


Figure 3. A schematic diagram of the zone of influence of a radar pulse. GPR CRU stands for Ground Penetrating Radar Control and Recorder Unit.

A simple rule of thumb to work out the range resolution,  $\Delta R$ , and the lateral resolution,  $\Delta L$ , is given in the equations below.

$$\Delta R \geq \frac{\lambda V}{4} \quad (\text{Eq. 6})$$

$$\Delta L = \sqrt{\frac{V z \lambda}{2}} \quad (\text{Eq. 7})$$

Where  $z$  is the target depth.

## G.2 Instrumentation

GPR comprises for a control and receiver unit that are linked to the receiver and transmitter units (figure 4). The antennas comprising of receiver and transmitter units are linked to the CRU by using optical cables. This is to ensure low interference whilst acquisition. The CRU serves to determine the radar frequency, sampling interval, the time period at which the data is recorded and the number of individual traces to be stacked.



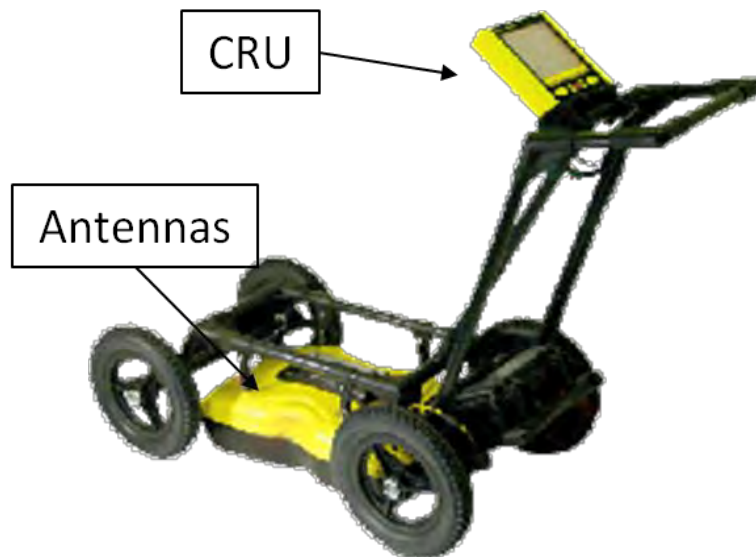


Figure 4. A ground penetrating radar instrument mounted with a control and recorder unit (CRU) (top) and the antennas (bottom).

### G.3 Survey types

Figure 5 illustrates the two types of acquisition profiling used in radar. The most common type is the common offset profiling as shown in figure 5(a). In this case, the transmitter and the receiver antenna separation are kept constant. An alternative radar acquisition type is the common midpoint profiling (or) CMP (figure 5(b)). In CMP, it uses a fixed midpoint between two antennas. This is to obtain optimal fold coverage of the data. With CMP, velocities can be calculated from the variations in the recorded time with offset. However, CMP operating time is slow and therefore rarely used in GPR acquisition.

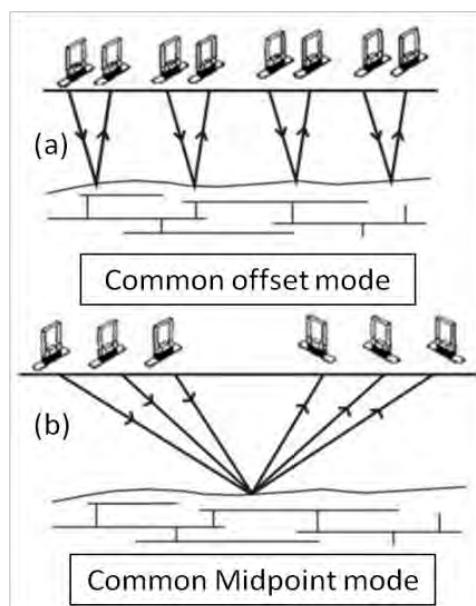


Figure 5. Two types of acquisition profiling used in GPR (a) common offset mode and (b) common midpoint mode.

#### **G.4 Interference in the data**

There are many sources of interference in the data. Radio transmitters are potential sources of interference as they can saturate the receiver antennas. Metal objects buried beneath the ground can also affect the GPR data. If the ground conductivity is high, features at the surface can produce strong interference patterns within the data. This is because of the substantial amount of radiation energy along the ground.

# References

---

- [1] “Colorado seeks a renewable energy peak,”  
<http://news.nationalgeographic.com/news/2010/05/100505-energy-colorado-renewable-power/>  
Accessed June 4, 2012.
- [2] Geothermal Energy Association, <http://geo-energy.org/basics.aspx> Accessed June 4, 2012.
- [3] Geothermal Department, Pagosa Springs Colorado,  
[http://www.townofpagosasprings.com/index.asp?Type=B\\_BASIC&SEC=%7BE4D74380-5C86-4626-972B-C735CE3280D9%7D](http://www.townofpagosasprings.com/index.asp?Type=B_BASIC&SEC=%7BE4D74380-5C86-4626-972B-C735CE3280D9%7D) Accessed June 4, 2012.
- [4] V. C. Kelly, “Regional Structure of the San Juan Basin.” Guidebook of the San Juan Basin- New Mexico and Colorado- First Field Conference, New Mexico Geological Society, New Mexico Bureau of Mines and Mineral Resources, November 1950.
- [5] E. C. Beaumont and C. B. Read, “Geologic History of the San Juan Basin Area.” Guidebook of the San Juan Basin- New Mexico and Colorado- First Field Conference, New Mexico Geological Society, New Mexico Bureau of Mines and Mineral Resources, November 1950.
- [6] M. J. Galloway, “Hydrogeologic and Geothermal Investigation of Pagosa Springs, Colorado.” Colorado Geological Survey Department of Natural Resources, Denver CO, 1980.
- [7] V. C. Kelly, “Pre-Cambrian Rocks of the San Juan Basin.” Guidebook of the San Juan Basin- New Mexico and Colorado- First Field Conference, New Mexico Geological Society, New Mexico Bureau of Mines and Mineral Resources, November 1950.
- [8] S. A. Wengerd, “Triassic Rocks of Northwestern New Mexico and Southwestern Colorado.” Guidebook of the San Juan Basin- New Mexico and Colorado- First Field Conference, New Mexico Geological Society, New Mexico Bureau of Mines and Mineral Resources, November 1950.
- [9] F. C. Barnes and G. A. Hemenway, “Generalized Geologic Column of the San Juan Basin.” Guidebook of the San Juan Basin- New Mexico and Colorado- First Field Conference, New Mexico Geological Society, New Mexico Bureau of Mines and Mineral Resources, November 1950.
- [10] R. H. Pearl “Colorado’s Hydrothermal Resource Base: An Assessment.” Colorado Geological Survey Department of Natural Resources, 1979.
- [11] J. K. Barrett and R. H. Pearl, “Hydrogeochemical Data of Thermal Springs and Wells in Colorado.” Colorado Geological Survey Department of Natural Resources, Denver CO, 1976 (Revised 1993). Provided by Paul Morgan. Colorado Geological Survey.

- [12] "What Is GPS?," <http://www8.garmin.com/aboutGPS/> Accessed June 4, 2012.
- [13] "Why we need Differential GPS?," <http://www.trimble.com/gps/dgps-why.shtml> Accessed June 4, 2012.
- [14] "Earthquake Glossary - seismic reflection or refraction line," <http://earthquake.usgs.gov/learn/glossary/?term=seismic%20reflection%20or%20refraction%20line> Accessed June 4, 2012.
- [15] S. S.Haines, 2007, "A Hammer-impact, aluminum, shear-wave seismic source," U.S. Geological Survey Open-File Report 2007, <http://pubs.usgs.gov/of/2007/1406/> Accessed June 1, 2012.
- [16] H. R. Burger, A. F. Sheehan, and C. H. Jones, *Introduction to Applied Geophysics: Exploring the Shallow Subsurface*, W.W. Norton & Company, 2006.
- [17] "What is a Gravitational Field?," <http://www.wisegeek.com/what-is-a-gravitational-field.htm> Accessed May 29, 2012.
- [18] P. Przyborski, "Gravity Anomaly Maps and The Geoid," <http://earthobservatory.nasa.gov/Features/GRACE/page3.php> Accessed May 30, 2012.
- [19] J. Milsom and A. Eriksen, *Field Geophysics*, 4<sup>th</sup> ed. West Sussex, United Kingdom: John Wiley and Sons Ltd, 2011.
- [20] T. M. Boyd., "Introduction to Geophysical Exploration," [http://galitzin.mines.edu/INTROGP/notes\\_template.jsp?url=GRAV%2FNOTES%2Fspring.html&page=Gravity%3A%20Notes%3A%20Mass%20and%20Spring%20Measurements](http://galitzin.mines.edu/INTROGP/notes_template.jsp?url=GRAV%2FNOTES%2Fspring.html&page=Gravity%3A%20Notes%3A%20Mass%20and%20Spring%20Measurements). Accessed May 31, 2012.
- [21] "International Gravimetric Bureau," <http://bgi.omp.obsmp.fr/index.php/eng/Media/Images/Relative-gravity-meter-Scintrex-CG52> Accessed May 31, 2012.
- [22] "Geophysical Characterization of a Neal Hot Springs, Oregon, USA," <http://geophysics.mines.edu/UserFiles/File/geophysics/fieldcamp/GP%202011%20Field%20Camp%20Final%20Report.pdf> Accessed June 5, 2012.
- [23] J. M. Reynolds, *An Introduction to Applied and Environmental Geophysics*. Chichester: John Wiley and Sons, 1997.
- [24] "LaCoste and Romberg Gravimeter Instructions," <http://crack.seismo.unr.edu/ftp/pub/louie/class/field/lacoste.html> Accessed June 5, 2012.
- [25] "Characterization of the Upper Arkansas River Basin, Chaffee County Colorado," <http://geophysics.mines.edu/UserFiles/File/geophysics/fieldcamp/2009%20Field%20Camp%20Report.pdf> Accessed June 5, 2012.

- [26] P. Kearey, M. Brooks and I. Hill, *An Introduction to Geophysical Exploration*, 3rd ed. Oxford, United Kingdom: Blackwell Publishing, 2002.
- [27] “Geosoft Resources.” <http://www.geosoft.com/resources> Accessed June 5, 2012.
- [28] F. Jones, “The Inversion Process.” <http://www.eos.ubc.ca/ubcgif/iag/tutorials/invn-concepts/how.htm> Accessed June 5, 2012.
- [29] R. Krahenbuhl. Class notes (2011).
- [30] “Drift Corrections for Gravity Data.” Accessed June 5, 2012.  
[http://www.cas.umn.edu/geosciences/faculty/sheriff/438-Gravity\\_Electromagnetics/drift\\_corrections.htm](http://www.cas.umn.edu/geosciences/faculty/sheriff/438-Gravity_Electromagnetics/drift_corrections.htm).
- [31] “G-858 MagMapper,” <http://www.geometrics.com/geometrics-products/geometrics-magnetometers/g-858-magmapper/> Accessed June 6, 2012.
- [32] “Frequency domain electromagnetic methods,”  
[http://www.epa.gov/esd/cmb/GeophysicsWebsite/pages/reference/methods/Surface\\_Geophysical\\_Methods/Electromagnetic\\_Methods/Frequency\\_Domain\\_Electromagnetic\\_Methods.htm](http://www.epa.gov/esd/cmb/GeophysicsWebsite/pages/reference/methods/Surface_Geophysical_Methods/Electromagnetic_Methods/Frequency_Domain_Electromagnetic_Methods.htm) Accessed May 30, 2012.
- [33] “Time Domain Electromagnetic Physics,”  
[http://www.ncwater.org/Education\\_and\\_Technical\\_Assistance/Ground\\_Water/TDEM/](http://www.ncwater.org/Education_and_Technical_Assistance/Ground_Water/TDEM/) Accessed May 30, 2012.
- [34] “EM31 Operating Instructions,” [http://www.geonics.com/pdfs/documentation/eM31\\_manuals/](http://www.geonics.com/pdfs/documentation/eM31_manuals/) Accessed May 30, 2012.
- [35] “EM34-3,” <http://www.geonics.com/html/em34-3.html> Accessed May 30, 2012.
- [36] J. McNeill, “Technical Note 6: Electromagnetic terrain conductivity measurements at low induction numbers,” <http://www.geonics.com/pdfs/technicalnotes/tn6.pdf> Accessed May 30, 2012.
- [37] “TEM47,” <http://www.geonics.com/html/tem47.html> Accessed May 30, 2012.
- [38] K. Richards, A. Revil, A. Jardani, et al., “Pattern of shallow ground water flow at Mount Princeton Hot Springs, Colorado, using geoelectrical methods,” *Journal of Volcanology and Geothermal Research*, vol. 198, pp.217–232, 2010.
- [39] A. Revil, M. Karaoulis, T. Johnson, and A. Kemna, "Review: Some low-frequency electrical methods for subsurface characterization and monitoring in hydrogeology," *Hydrogeology Journal*, pp. 617-658, 2012.
- [40] S. Barde-Cabusson, and A. Finizola, “Tutorial for Self Potential data processing,” April 10, 2012.
- [41] J. McNeill, “Technical Note 5: Electrical conductivity of rocks and soil,”  
<http://www.geonics.com/pdfs/technicalnotes/tn5.pdf>. Accessed May 30, 2012.



- [42] “EM31-MKS,” <http://www.geonics.com/html/em31-mk2.html> Accessed May 30, 2012.
- [43] J. Milsom and A. Eriksen, “7.2.4 Frequency effects,” in *Field Geophysics*, 4th ed., Wiley, 2011, pp. 141-142.
- [44] “Terrameter LUND Imaging System,” <http://abem.se/products/sas4000/sas4000.php> Accessed June 5, 2012.
- [45] “AGI USA,” <http://www.agiusa.com/agicatalog.shtml> Accessed June 5, 2012.
- [46] “Surface Surveys: Self Potential,” <http://www.agiusa.com/agicatalog.shtml> Accessed June 5, 2012.
- [47] J. P. Lindsey, “The Fresnel zone and its interpretive significance,” *The Leading Edge*, vol. 10, pp. 33-39, 1989.